

# ***PROCEEDINGS***

*of the*



## ***1992 Battlefield Atmospherics Conference***

**Fort Bliss, Texas  
1-3 December 1992**

---

---

**BATTLEFIELD ENVIRONMENT DIRECTORATE  
U.S. Army Research Laboratory  
White Sands Missile Range  
New Mexico**

APPROVED FOR PUBLIC RELEASE; DISTRIBUTION IS UNLIMITED.

19971215 129

## **NOTICES**

### **Disclaimers**

The findings in this report are not to be construed as an official Department of the Army position, unless so designated by other authorized documents.

The citation of trade names and names of manufacturers in this report is not to be construed as official Government endorsement or approval of commercial products or services referenced herein.

### **DESTRUCTION NOTICE**

When this document is no longer needed, destroy it by any method that will prevent disclosure of its contents or reconstruction of the document.



**PROCEEDINGS**  
**of the**  
**1992 BATTLEFIELD ATMOSPHERICS CONFERENCE**

**1-3 December 1992**

**Sponsor**

Battlefield Environment Directorate  
U.S. Army Research Laboratory  
White Sands Missile Range, New Mexico

**Conference Manager**

Mr. Robert Lee  
U.S. Army Research Laboratory

**Conference Chairman**

Mr. Edward Creegan  
U.S. Army Research Laboratory

**Host**

Fort Bliss, El Paso Texas

**DTIC QUALITY INSPECTED 3**

---

---

## **PROGRAM COMMITTEE**

**Battlefield Environment Directorate  
U.S. Army Research Laboratory**

**Conference Manager**

Mr. Robert Lee (505) 678-4006 or DSN 258-4006

**Conference Chairman**

Mr. Edward Creegan (505) 678-4684 or DSN 258-4684

**Conference Advisers**

Dr. Franklin E. Niles (505) 678-3721 or DSN 258-3721

Dr. Bernard F. Engebos (505) 678-1489 or DSN 258-1489

Dr. Mary Ann Seagraves (505) 678-4200 or DSN 258-4200

Mr. Don R. Veazey (505) 678-3331 or DSN 258-3331

**Administrative Assistant**

Mrs. Nancy Fudge (505) 678-4450 or DSN 258-4450

**Science and Technology Corporation  
Meetings Division, Hampton, Virginia**

**Conference Administrator**

Ms. Jeanne P. Hawtin

**Conference Coordinators**

Mr. Keith A. Hicks

Ms. Lisa H. McCormick

---

---

## CONTENTS

---

---

Preface .....	ix
Keynote Address .....	xi
<i>Major General Robert D. Orton, Commanding General, Fort McClellan, Alabama</i>	

### SESSION I: ATMOSPHERIC MODELING

A Multi-Stream Radiative Transfer Model for Inhomogenous, Three-Dimensional Aerosol Clouds .....	3
<i>Donald W. Hoock, Battlefield Environment Directorate, U.S. Army Research Laboratory; John C. Giever, Sean G. O'Brien and Edward J. Burlbaw, Physical Science Laboratory, New Mexico State University</i>	
Visualization of Multiple Battlefield Obscurants .....	13
<i>Geoffrey Y. Gardner, Grumman Data Systems; G. Michael Hardaway, U.S. Army Topographic Engineering Center</i>	
Mesoscale Data Analysis Using a Mesoscale Model .....	23
<i>Kenneth E. Eis and Jan L. Behunek, METSAT Inc.; Donald L. Reinke and Thomas H. Vonder Haar, Colorado State University; Craig J. Tremback, ASTeR Inc.</i>	
An Optical Profile Function for Modeling Extinction and Backscatter Coefficients in Very Low Stratus Clouds and Subcloud Regions .....	33
<i>Neal H. Kilmer, Physical Science Laboratory, New Mexico State University; Henry Rachele, Battlefield Environment Directorate, U.S. Army Research Laboratory</i>	
Acoustical Scattering From Atmospheric Turbulence .....	43
<i>Harry J. Auvermann, Battlefield Environment Directorate, U.S. Army Research Laboratory; George H. Goedecke, New Mexico State University</i>	
Modification of Atmospheric Aerosol .....	53
<i>Austin W. Hogan, U.S. Army Cold Regions Research and Engineering Laboratory</i>	
Intermittency, Events, and Coherent Structures in Vegetative Canopies .....	59
<i>Ronald M. Cionco, Battlefield Environment Directorate, U.S. Army Research Laboratory; William D. Ohmstede, Wm Ohmstede, CCM</i>	
The Zephyrus, Vaporous, Thermotics Connection .....	69
<i>H. Rachele, A. Tunick and F. Hansen, Battlefield Environment Directorate, U.S. Army Research Laboratory</i>	

### SESSION II: SENSORS AND SYSTEMS

The Met Improvement Program: Key to Unlocking Target Area Meteorology .....	81
<i>M. A. Seagraves, R. E. McPeck and MAJ A. A. Grunwald, U.S. Army Research Laboratory</i>	
The Double Beam Interferometer Sounder (DBIS): A Device for the Passive Remote Sensing of Atmospheric Profiles .....	91
<i>J.-M. Thériault, DREV-Defence Research Establishment Valcartier, Canada; J. Giroux, J. Coté and M. Fournier, BOMEM, Inc., Canada; G. P. Anderson and J. H. Chetwynd, Phillips Laboratory</i>	

Battlefield Atmospheric Soundings in Near Real Time Using Satellite and Ground-Based Remotely Sensed Data .....	101
<i>James Cogan</i> , Battlefield Environment Directorate, U.S. Army Research Laboratory	
Use of SSM/I Data During Operation Desert Storm .....	111
<i>C. R. Holliday, K. A. Nash and K. H. North</i> , Air Force Global Weather Central, Offutt Air Force Base	
Comparison of Defense Meteorological Satellite Program (DMSP) Capabilities and Army Tactical Weather/Environmental Data Specifications for Observations (Abstract) .....	115
<i>Richard J. Szymer</i> , Battlefield Environment Directorate, U.S. Army Research Laboratory	
Wind Radar Interference with the ARL Microwave Temperature Radiometer .....	117
<i>Teddy L. Barber and Edward M. Measure</i> , Battlefield Environment Directorate, U.S. Army Research Laboratory; <i>Randall J. Hulsey</i> , Physical Science Laboratory, New Mexico State University	
Remote Sensors Comparison Analysis .....	123
<i>R. J. Okrasinski and G. J. Cook</i> , Physical Science Laboratory, New Mexico State University; <i>R. O. Olsen and T. L. Barber</i> , Battlefield Environment Directorate, U.S. Army Research Laboratory	
Characterization of Imager Spectral Response for Optimized Atmospheric Propagation ....	133
<i>Daniel R. Billingsley, Fernando R. Palacios and Wendell R. Watkins</i> , Battlefield Environment Directorate, U.S. Army Research Laboratory	

### SESSION III: DATA BASES AND ANALYSES

Climatology of Cloud Statistics (C Cloud S) .....	145
<i>Paul H. Lewis and Richard W. Hartman</i> , USAF Environmental Technical Application Center, Scott Air Force Base; <i>Albert R. Boehm</i> , Hughes STX Corporation	
High-Resolution Cloud Climatologies .....	151
<i>Kenneth E. Eis</i> , METSAT Inc.	
Cloud Information Reference Library and Archive .....	161
<i>Ronald J. Nelson</i> , Science and Technology Corporation	
REBAL '92 — A Cooperative Radiation and Energy Balance Field Study for Imagery and E.M. Propagation .....	165
<i>Arnold Tunick</i> , Battlefield Environment Directorate, U.S. Army Research Laboratory; <i>Terry A. Howell and Jean L. Steiner</i> , U.S.D.A.—Agricultural Research Service Conservation and Production Research Laboratory	
VORTEX: A New Tool for Observing Vertical Structure of Smoke/Obscurant Clouds .....	175
<i>Max P. Bleiweiss</i> , U.S. Army Research Laboratory; <i>Roger E. Davis</i> , Science and Technology Corporation; <i>Thomas A. King and Kenneth C. Payne</i> , Physical Science Laboratory, New Mexico State University	

---



---

**SESSION IV: ATMOSPHERIC EFFECTS**

The Use of Analytic Approximations in Providing Meteorological Data for Artillery .....	189
<i>Fernando Caracena</i> , NOAA, National Severe Storms Laboratory	
Analysis of Simultaneous Scintillometer Measurements Over Four Unique Desert Terrain Paths .....	199
<i>Gail Tirrell Vaucher</i> , Science and Technology Corporation; <i>Robert W. Endlich and John W. Raby</i> , U.S. Army Research Laboratory	
The Three Faces of Clutter .....	209
<i>Patti S. Gillespie</i> , Battlefield Environment Directorate, U.S. Army Research Laboratory	
Mark III Electro-Optical Tactical Decision Aid Sensor Performance Model Evaluation .....	219
<i>Kimberley Scasny and J. Michael Sierchio</i> , Naval Research Laboratory Monterey	
The Green's Function Parabolic Equation for Acoustic Propagation in the Atmosphere .....	227
<i>David H. Marlin</i> , Battlefield Environment Directorate, U.S. Army Research Laboratory	
Modeling the Optical and Mechanical Properties of Exotic Battlefield Obscurants .....	237
<i>Robert A. Sutherland</i> , U.S. Army Research Laboratory; <i>James D. Klett</i> , PAR Associates	
Progress in Atmospheric Propagation Modeling at Frequencies Below 1000 GHz .....	247
<i>H. J. Liebe, G. A. Hufford and M. G. Cotton</i> , Institute for Telecommunication Sciences	
Radar Backscatter from Snow Surface (Verification of Model and Prediction) .....	257
<i>Oskar Essenwanger</i> , University of Alabama in Huntsville	
The Importance of Ducting in Atmospheric Acoustics .....	267
<i>John M. Noble</i> , Battlefield Environment Directorate, U.S. Army Research Laboratory	

**SESSION V: WEATHER DECISION AIDS**

IR Visibility .....	277
<i>C. N. Touart</i> , Hughes STX Corporation	
The Next Generation of Forecaster Decision Aids .....	287
<i>Jeffrey E. Passner</i> , Battlefield Environment Directorate, U.S. Army Research Laboratory	
Forecasting Using a Hybrid Statistical-Neural Net Method .....	291
<i>Jerrold S. Foster</i> , Command Control, Inc.; <i>Kenneth C. Young</i> , University of Arizona	

**SESSION I POSTERS: ATMOSPHERIC MODELING**

SOUP—A Battlefield Atmosphere .....	301
<i>Robert E. De Kinder, Jr.</i> , U.S. Army Research Laboratory, Battlefield Atmospheric Simulation Division	
Some Flow Characteristics of Surface Layer Micrometeorology Over Complex Terrain Using Field Measurements .....	305
<i>Brian L. Orndorff</i> , Battlefield Environment Directorate, U.S. Army Research Laboratory	

A Mesoscale Numerical Simulation of the Persian Gulf Wind Fields: Case Study of 28-29 March 1991 .....	315
<i>Robert E. Dumais, Jr. and Teizi Henmi</i> , Battlefield Environment Directorate, U.S. Army Research Laboratory; <i>John Barnes</i> , Computer Sciences Corporation	
Surface Wind Speed Distributions .....	325
<i>Elton P. Avara and Bruce T. Miers</i> , Battlefield Environment Directorate, U.S. Army Research Laboratory	
An Examination of the Evolution of Radiation and Advection Fogs .....	335
<i>Montie M. Orgill</i> , Science and Technology Corporation; <i>Robert A. Sutherland</i> , U.S. Army Research Laboratory	
Quantitative Determination of How Smoke Obscuration Varies with Observer Height .....	345
<i>Scarlett D. Ayres</i> , Battlefield Environment Directorate, U.S. Army Research Laboratory	

## SESSION II POSTERS: SENSORS AND SYSTEMS

The U.S. Army Atmospheric Profiler Research Facility: Overview and Preliminary Intercomparison .....	357
<i>John R. Hines, Frank D. Eaton, Scott A. McLaughlin, and William H. Hatch</i> , Battlefield Environment Directorate, U.S. Army Research Laboratory	
An Acoustic Meteorological Test Bed Uses and Applications .....	367
<i>J. Fox and R. Olsen</i> , Battlefield Environment Directorate, U.S. Army Research Laboratory; <i>R. Okrasinski and P. Chintawongvanich</i> , Physical Science Laboratory, New Mexico State University	
A Review of Selected Remote Sensor Measurements of Temperature, Wind and Moisture, and Comparison to Rawinsonde Measurements .....	377
<i>Bruce T. Miers, James L. Cogan and Richard J. Szymer</i> , Battlefield Environment Directorate, U.S. Army Research Laboratory	
A Fresh Look at the Planetary Boundary Layer: High Resolution Profiling with the U.S. Army Research Laboratory FM-CW Radar .....	387
<i>Scott A. McLaughlin</i> , Battlefield Environment Directorate, U.S. Army Research Laboratory	
Tactical Weather Support Concept for Austere Field Operations .....	393
<i>John R. Elrick</i> , Battlefield Environment Directorate, U.S. Army Research Laboratory; <i>Phillip R. Raihl</i> , New Mexico State University; <i>MSGT Timothy J. Smith</i> , Headquarters Air Weather Service	
Acoustic Source Generation System .....	397
<i>Jeff Balding and John M. Noble</i> , Battlefield Environment Directorate, U.S. Army Research Laboratory	
The Mobile Atmospheric Spectrometer: Enhancements in Data Acquisition and Analysis for Smoke Week XIV .....	403
<i>Frank T. Kantrowitz</i> , Battlefield Environment Directorate, U.S. Army Research Laboratory; <i>William M. Gutman and Troy D. Gammill</i> , Physical Science Laboratory, New Mexico State University; <i>Jerry V.B. Rice</i> , Science and Technology Corporation	
Own the Weather: A Vision for Army Meteorology .....	413
<i>James Cogan, Richard Szymer and Robert McPeck</i> , Battlefield Environment Directorate, U.S. Army Research Laboratory	

---



---

**SESSION III POSTERS: DATA BASES AND ANALYSES**

Digital Signal Processing Techniques Used to Reduce Acoustics Data from the JAPE Test . .	425
<i>Thelma Chenault, René Klein and Ascencion Acosta, Jr., Battlefield Environment Directorate</i>	
Pyrolysis-Mass Spectra of Biological Aerosols Interpreted by Factor Analysis-Rank Annihilation . . . . .	435
<i>David Rosen, Battlefield Environment Directorate, U.S. Army Research Laboratory; Alice Harper, U.S. Army Edgewood Research, Development, and Engineering Center</i>	
A Comparison of Low Level Wind and Temperature Profiles from a Radiosonde, Sodar and Mesoscale Model . . . . .	443
<i>Ian D. Todd and Jonathan D. Turton, Meteorological Office, U.K.</i>	
Errors in Sky-Cover Observation by Ground-Based Observers . . . . .	453
<i>Donald L. Reinke, Thomas H. Vonder Haar, Kenneth E. Eis, and D. Neil Allen, Colorado State University and METSAT Inc.</i>	
The MIDAS/ATLAS Video Imagery Database: An Advanced System for Storing and Accessing Digitally Compressed Video Imagery . . . . .	459
<i>Michael Rollins, Science and Technology Corporation; Max P. Bleiweiss, U.S. Army Research Laboratory; Rebecca Tipton, New Mexico State University</i>	
Modernized Graphics Codes for Use with Project Wind Data . . . . .	465
<i>John D. Kincheloe, New Mexico State University</i>	
The CASTFOREM Graphics Postprocessor's Smoke Display Demonstration . . . . .	475
<i>Robert E. De Kinder, Jr., Battlefield Atmospheric Simulation Division, U.S. Army Research Laboratory; Steven J. Lamotte, Physical Science Laboratory, New Mexico State University; Thomas C. Loncarich and Joseph F. Bebbs, Jr., U.S. Army TRADOC Analysis Command</i>	

**SESSION IV POSTERS: ATMOSPHERIC EFFECTS**

Simulating Atmospheric Effects on Infrared Images Used at the Night Vision Electro-Optics Directorate . . . . .	479
<i>James Williams, David Tofsted and Alan Wetmore, Battlefield Environment Directorate, Richard Dutro, New Mexico State University</i>	
Correlation of $C_n^2$ with Image Distortion at the REBAL Test . . . . .	489
<i>Fernando R. Palacios, Wendell R. Watkins, Samuel B. Crow and Daniel R. Billingsley, U.S. Army Battlefield Environment Directorate</i>	

**SESSION V POSTERS: WEATHER DECISION AIDS**

The Integrated Weather Effects Decision Aid: A New Planning Tool . . . . .	501
<i>Robert R. Lee and Sue E. Bussells, Battlefield Environment Directorate, U.S. Army Research Laboratory</i>	

## Contents

---

Weather and Terrain Analysis for Aerial Intelligence Preparation of the Battlefield .....	511
<i>Gary McWilliams and Steve Kirby</i> , Battlefield Environment Directorate, U.S. Army Research Laboratory	
The Airland Battlefield Environment (ALBE) Program at BED .....	517
<i>David Sauter</i> , Battlefield Environment Directorate, U.S. Army Research Laboratory; <i>John B. Spalding and Danforth C. Weems</i> , Physical Science Laboratory, New Mexico State University	
Local Spatial Influences on Temperature and Relative Humidity: Phoenix, Arizona .....	523
<i>Bruce L. Gwilliam</i> , United States Military Academy	

## APPENDICES

Appendix A: Agenda .....	531
Appendix B: List of Attendees .....	539
Author Index .....	555



---

---

## PREFACE

---

---

The 1992 Battlefield Atmospheric Conference was held 1-3 December 1992 at Fort Bliss, El Paso, Texas, under the sponsorship of the U.S. Army Research Laboratory, Battlefield Environment Directorate, White Sands Missile Range, New Mexico. The Conference included oral presentations, poster, and demonstration sessions on five topics: Atmospheric Modeling, Sensors and Systems, Data Bases and Analyses, Atmospheric Effects, and Weather Decision Aids. The Conference had over 200 attendees, including representatives from Canada, France, Germany, Israel, and the United Kingdom.

The Conference is the primary forum for usage of and additions to the Electro-Optical Systems Atmospheric Effects Library (EOSAEL) and Tactical Weather Intelligence (TWI) and for comparison of results with measurements and EOSAEL models.

The reader will find the items related to the Conference itself (the agenda and the list of attendees) in the appendices following the papers collected for these proceedings. An author index is also included.

**Opening Session**

**KEYNOTE ADDRESS**

**Keynote Speaker**

**MAJ GEN Robert D. Orton  
Commanding General  
Fort McClellan, Alabama**



U.S. ARMY



CHEMICAL CORPS

# PURPOSE



TO DISCUSS THE MOST RECENT CONCEPT  
FOR  
FUTURE OPERATIONS

TO IDENTIFY IMPACT OF BATTLEFIELD CONDITIONS  
ON  
FUTURE OPERATIONS



# KEY POINTS



- ARMY IN TRANSITION FROM FORWARD DEPLOYED/FORWARD DEFENSE TO POWER PROJECTION/CONTINGENCY OPERATIONS/FORWARD PRESENCE
- FORWARD PRESENCE FORCES TAILORED TO MISSIONS AND CAPABLE OF CONTINGENCY OPERATIONS
- POWER PROJECTION REQUIRES
  - DEPLOYABLE, VERSATILE (TAILORABLE), LETHAL, AND EXPANSIBLE FORCES
  - GRABBING AND MAINTAINING THE OPERATIONAL INITIATIVE UPON ARRIVAL
  - EFFECTIVE COMMAND AND CONTROL (C2)
- JOINT, COMBINED, AND INTERAGENCY OPERATIONS ASSUME EVEN GREATER IMPORTANCE
- AIRLAND OPERATIONS
  - AN EVOLUTIONARY CONCEPT WHICH EXPANDS ALB DOCTRINE
- A MORE GLOBAL PERSPECTIVE; VARIETY OF CONDITIONS (NBC/CLIMATE)
  - ACROSS THE OPERATIONAL CONTINUUM
- FUTURE BATTLEFIELDS INCREASINGLY NONLINEAR
- TECHNOLOGY (SENSORS, WEAPONS, AND C2) PERMITS FIGHTING WITH PRECISION AND WINNING
- LOGISTICS MUST BE ANTICIPATORY, TIMELY, AND TAILORED



# THE RECENT PAST TRENDS



## INTERNATIONAL INFLUENCES

- NEW ORDER IN EUROPE  
-- CHANGING, BUT STILL DANGEROUS EASTERN EUROPE
- UNSTABLE THIRD WORLD: INCREASED DEMANDS,  
LETHAL WEAPONS
- GROWING GLOBAL ECONOMIC INTERDEPENDENCE

## DOMESTIC INFLUENCES

- REDUCED BUDGETS
- SOCIAL DEMANDS/DRUG DILEMMA

**SIGNIFICANT REDUCTIONS  
IN MILITARY PROGRAMS AND FORCE LEVELS**

## THE DYNAMIC PRESENT TRENDS

- CFE REDUCTIONS / NEGOTIATIONS AND HIGH COST OF MODERN ARMIES

SMALLER ARMIES

- TECHNOLOGY

ENHANCED SENSORS

SMART / BRILLIANT WEAPONS

MOBILE COMMAND & CONTROL

- ARMY'S MISSION

POWER PROJECTION / CONTINGENCY  
OPERATIONS / FORWARD PRESENCE

- REGIONAL INSTABILITIES / CONFLICTS

GREATER EMPHASIS ON GLOBAL  
REQUIREMENTS AND SHORT OF WAR  
(LOW INTENSITY CONFLICT-LIC)

TRAINING AND DOCTRINE COMMAND

**FUTURE BATTLEFIELD  
WILL BE MORE NONLINEAR**

- FEWER FORCES FIELDDED...LARGE "GAPS  
IN THE LINES"
- CHARACTERIZED BY...RAPIDITY AND  
FLUIDITY OF ACTION
- GRAB AND MAINTAIN THE INITIATIVE

**A CONDITION OF FUTURE WARFARE...NO CHOICE!**

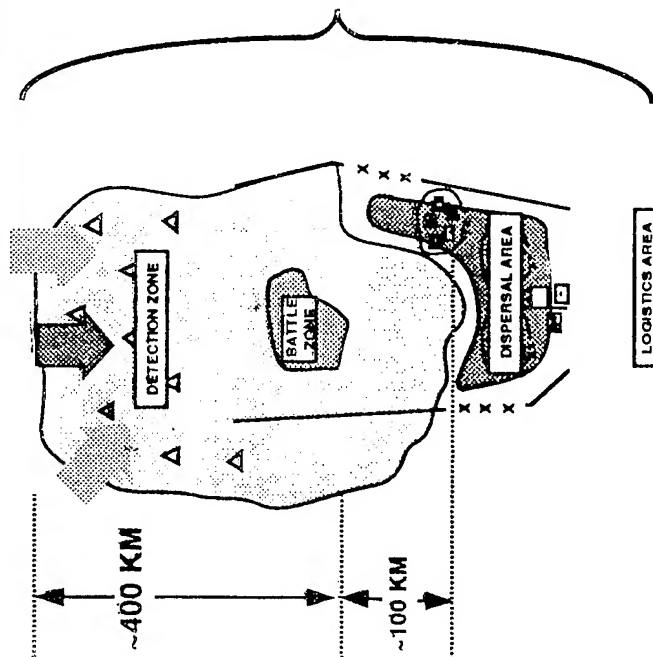


## **FUTURE BATTLEFIELD CYCLE**

- **DISPERSE**
- **MASS**
- **FIGHT (HIGHLY SYNCHRONIZED)**
- **REDISPERSE**
- **RECONSTITUTE**

**AVOID THE GRINDING ATTRITION BATTLE**

# FUTURE BATTLEFIELD

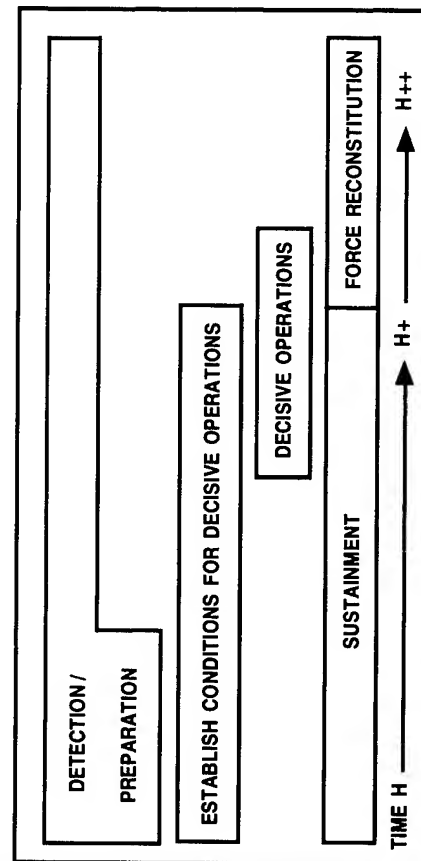


## --- BATTLEFIELD GEOMETRY

- DETECTION ZONE SIZED TO FIND ENEMY, DEVELOP SITUATION AND PROVIDE SECURITY
- BATTLE ZONE IS WHERE THE COMMANDER CHOOSES TO CONDUCT DECISIVE MANEUVER - ORIENTED ON DEFEAT OF ENEMY
- DISPERSAL AREA PROVIDES RELATIVE SAFETY TO SELECTED FORCES
- LOGISTICS IS ANTICIPATED AND PROJECTED WHEN AND WHERE NEEDED

## --- STAGES

- INITIALLY SEQUENTIAL: THEN CONTINUOUS AND OVERLAPPING
- CYCLES VARY BY STAGE AND ECHELON
- PROVIDES FOCUS AT OPERATIONAL AND TACTICAL LEVELS

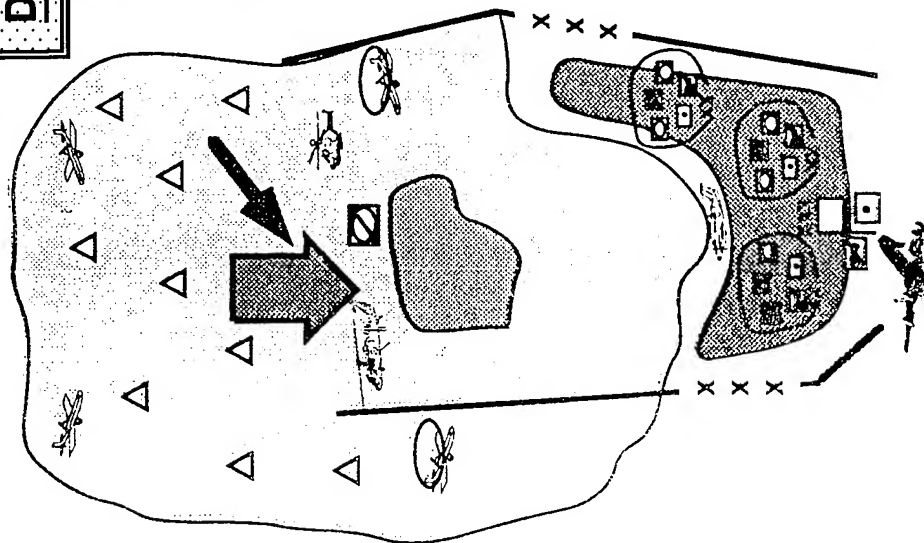


# TRAINING AND DOCTRINE COMMAND

## DEFENSE

## FUTURE BATTLE

## OFFENSE

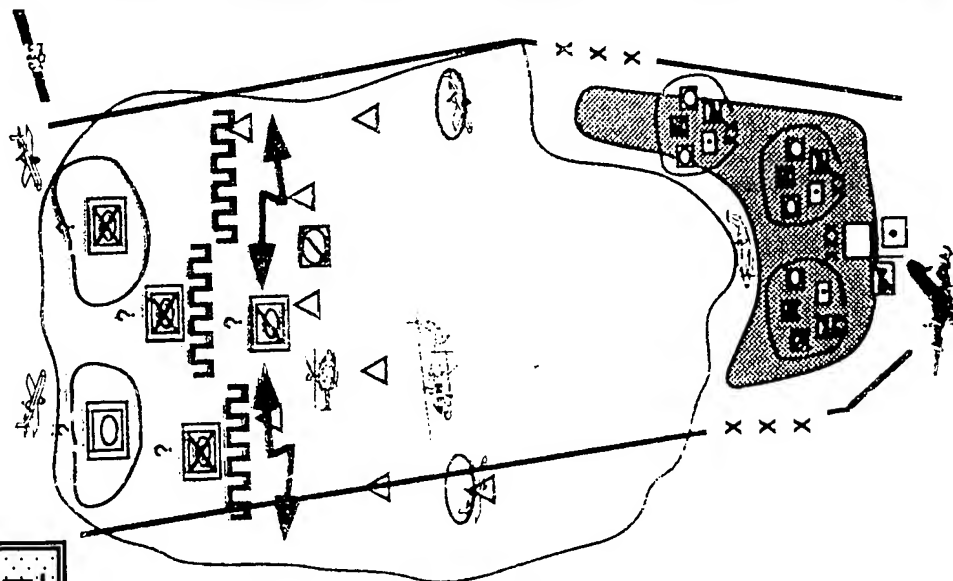


### DETECTION / PREPARATION

- WITH SENSORS / INTEL SYSTEMS
  - GROUND
  - AIR
  - SPACE
  - FUSION
- WITH RECCE
  - CAPABILITIES
  - UNITS

### COMMANDER'S INTENT

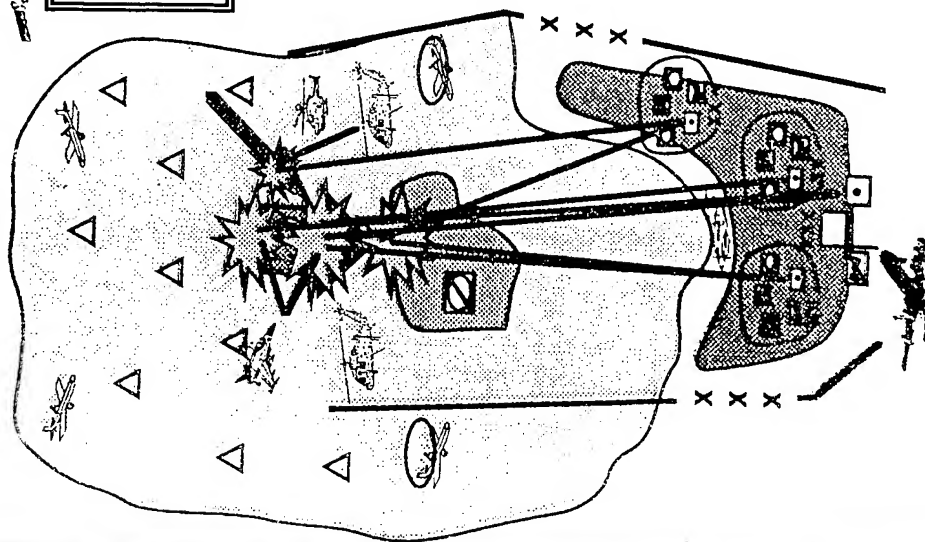
- DEPLOY THE FORCE
- PROTECT THE FORCE
- PREPARE THE BATTLEFIELD
- DECIDE: WHERE  
HOW  
WHEN  
TO FIGHT



## DEFENSE

## FUTURE BATTLE

## OFFENSE

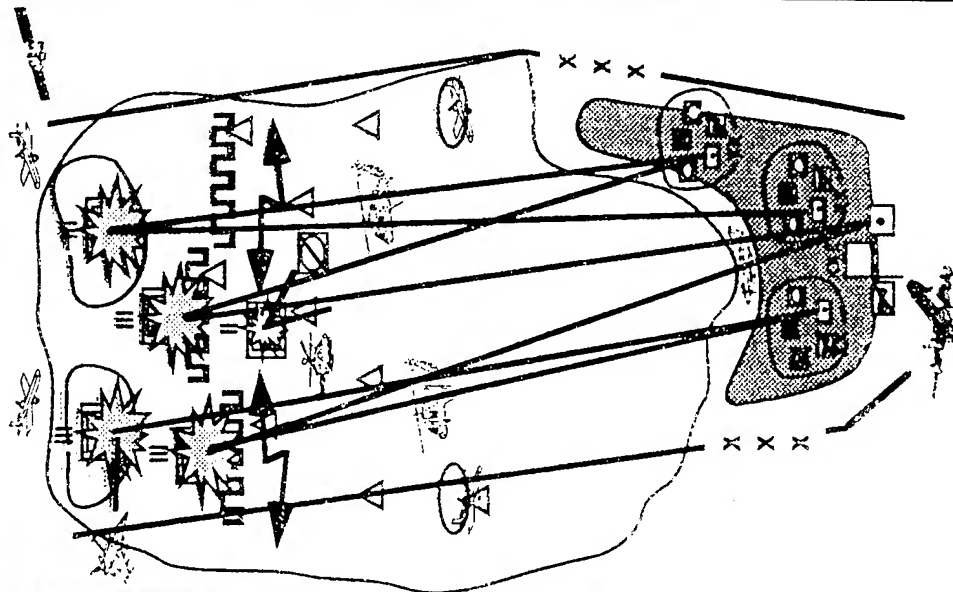


**ESTABLISH THE  
CONDITIONS FOR  
DECISIVE OPERATIONS**

WITH CORPS CONTROLLED  
LONG RANGE  
FIRE SPT 

### COMMANDER'S INTENT

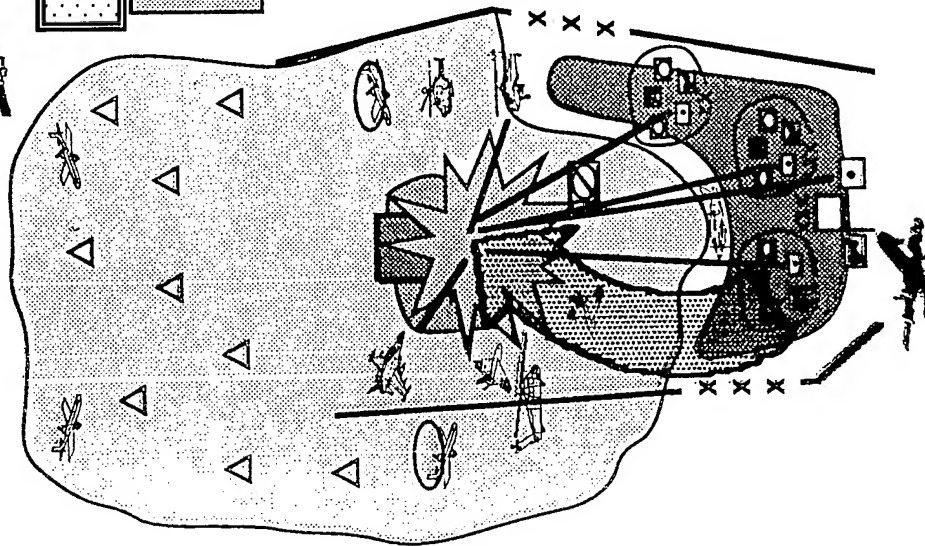
- SET THE CONDITIONS FOR DECISIVE OPERATIONS
- GRAB THE INITIATIVE EARLY
- SEPARATE THE ENEMY IN SPACE AND TIME
- CONTROL THE BATTLE FROM THIS STAGE FORWARD



## DEFENSE

## FUTURE BATTLE

## OFFENSE



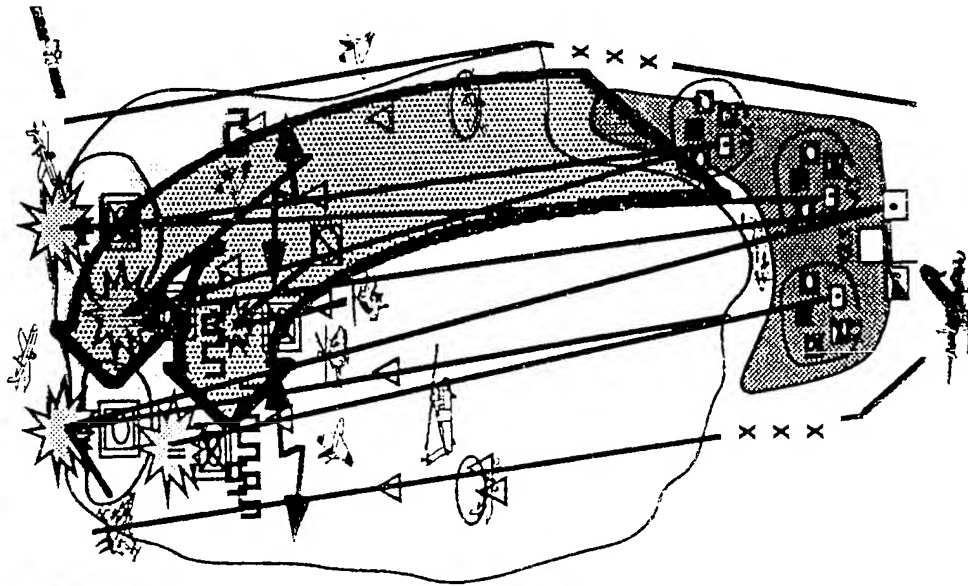
### DECISIVE OPERATIONS

WITH DIV CONTROLLED

- MANEUVER FORCES
- SUPPORTING FIRES

### COMMANDER'S INTENT

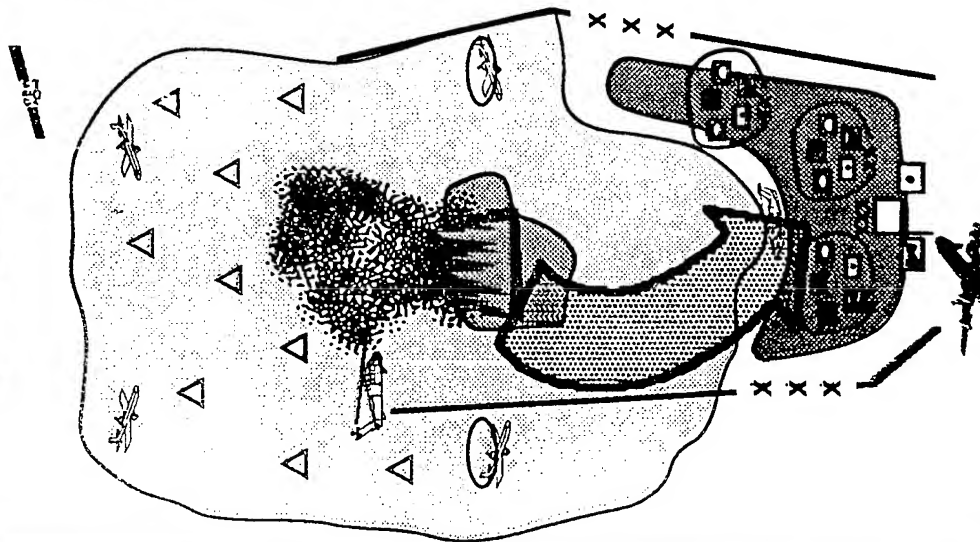
- INITIATE DECISIVE MANEUVER
- MANEUVER SUPPORTED BY FIRES
- DESTROY THE ENEMY



## DEFENSE

## FUTURE BATTLE

## OFFENSE



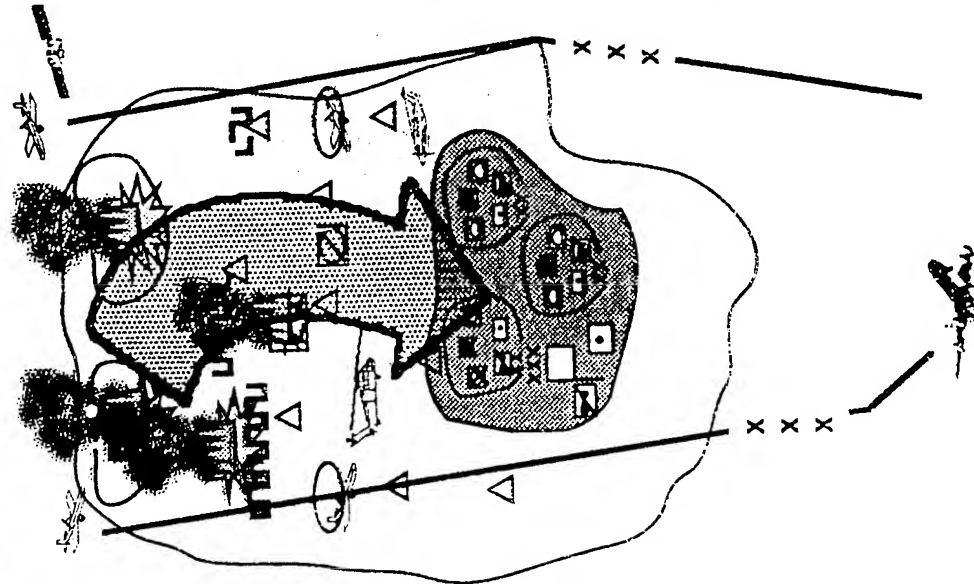
**FORCE RECONSTITUTION**

FIRST-DISPERSE / SECURE FORCES... THEN RECONSTITUTE

- RECOVER
- REORGANIZE
- REARM
- REFUEL
- REPAIR
- REPLACE

**COMMANDER'S INTENT**

- SECURE then
- RESTORE FORCE CAPABILITY FOR FUTURE OPERATIONS



## DESERT STORM



## FIRST IMPRESSIONS

TRAINING AND DOCTRINE COMMAND

## THE SENSOR BATTLE

- THE IRAQI SENSOR THREAT IN THE CLOSE BATTLE
  - PREDOMINANTLY VISUAL
  - LIMITED NIGHT VISION CAPABILITY
    - ACTIVE NEAR INFRARED THE STANDARD
    - SOME IMAGE INTENSIFIERS
    - SOME THERMAL SIGHTS
- THE U.S. SENSORS ADVANTAGE
  - THERMAL SIGHTS THE STANDARD
- THE RESULT: IN LIMITED VISIBILITY CONDITIONS
  - U.S. ENGAGES AND DESTROYS AT RANGE AT WILL
  - IRAQI FIRST WARNING = EXPLODING T72
- THE PAYOFF: VERY LIMITED ALLIED CASUALTIES



## THE OBSCURANT ROLE

- SCREEN PORTS AND AIRFIELDS
- SCREEN VULNERABLE TROOP CONCENTRATIONS
- SUPPORT DECEPTION OPERATIONS
- SCREEN BREACHING FORCES
- SCREEN FLANKS OF MANEUVER FORCES
- SYNERGY WITH OTHER COUNTERMEASURES

MANY TIMES PLANNED BUT NOT USED  
USE TIED TO THREAT

U.S. ARMY



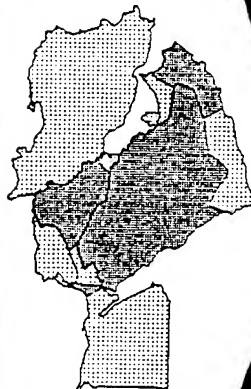
# DESERT STORM EXPERIENCE



CHEMICAL CORPS

## *What They Did:*

- Weaponized CW Agents
- Developed Biological Capability
- Threatened CW through:
  - Tactical Ballistic Missiles
  - Battlefield Artillery / Air Assets



## *What We Did:*

- Executed a multifaceted defense stressing:
  - Contamination Avoidance
  - NBC Protection
  - Decontamination
- Field and demonstrate the effectiveness of Fox Recon System

Chemical C2 structure required to synchronize efforts.

CDTF gives confidence to soldiers.

FOX provides Contamination Avoidance platform

ANBACIS has potential for NBC Warning and Reporting

NBC Battlesoft has high buy-off in units

Stop-gap Bio Detection fielded

Lightweight Decon System responsive to units

Antidotes/Pretreatments fielded

## *Lessons Learned / Observations*

- Emphasize Contamination Avoidance over Decontamination
- Need to develop standoff detection capability for CB weapons
- Coordinate all NBC Assets to fully exploit the advantages of Contamination Avoidance, Protection and Decontamination
- Must be capable of adapting to humidity and extreme climatic conditions

U.S. ARMY

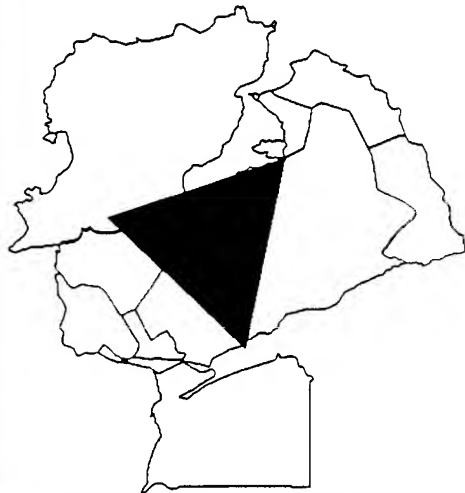


CHEMICAL CORPS

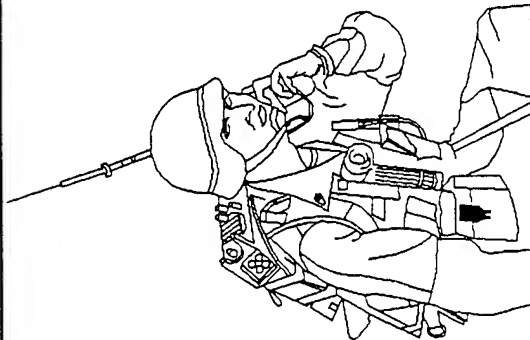
# DETECTION



HAZARD LEVELS  
VAPOR CLOUDS  
SENSITIVITY



## WEATHER

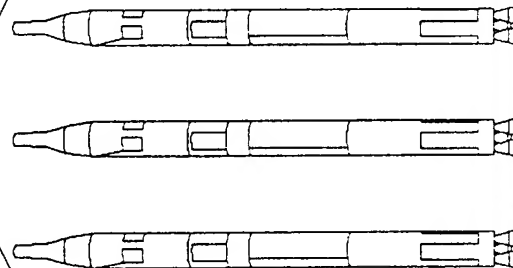


### EFFECTS

PROTECTION  
CASUALTIES  
CONTAMINATION  
TREATMENT

### EMPLOYMENT

BIOLOGICAL  
CHEMICAL  
NUCLEAR  
(FALLOUT)





# IMPLICATIONS



A STRATEGIC ARMY OF THE NINETIES AND BEYOND REQUIRES:

- ABILITY TO RAPIDLY EVOLVE AND ADJUST TO NEW CONDITIONS AND REVISED REQUIREMENTS
- MORE VERSATILE, DEPLOYABLE, AND EXPANSIBLE NBC DEFENSE AND OBSCURANT DELIVERY SYSTEMS
- COMPLEMENT TO EMERGING SENSORS, C2 (TO INCLUDE AUTOMATION TECHNOLOGIES), TARGETING, AND SMART WEAPONS

LEADS TO IMPLICATIONS IN :

DOCIRINE

COMBAT DEVELOPMENTS

- ORGANIZATIONS
- EQUIPMENT

LEADER

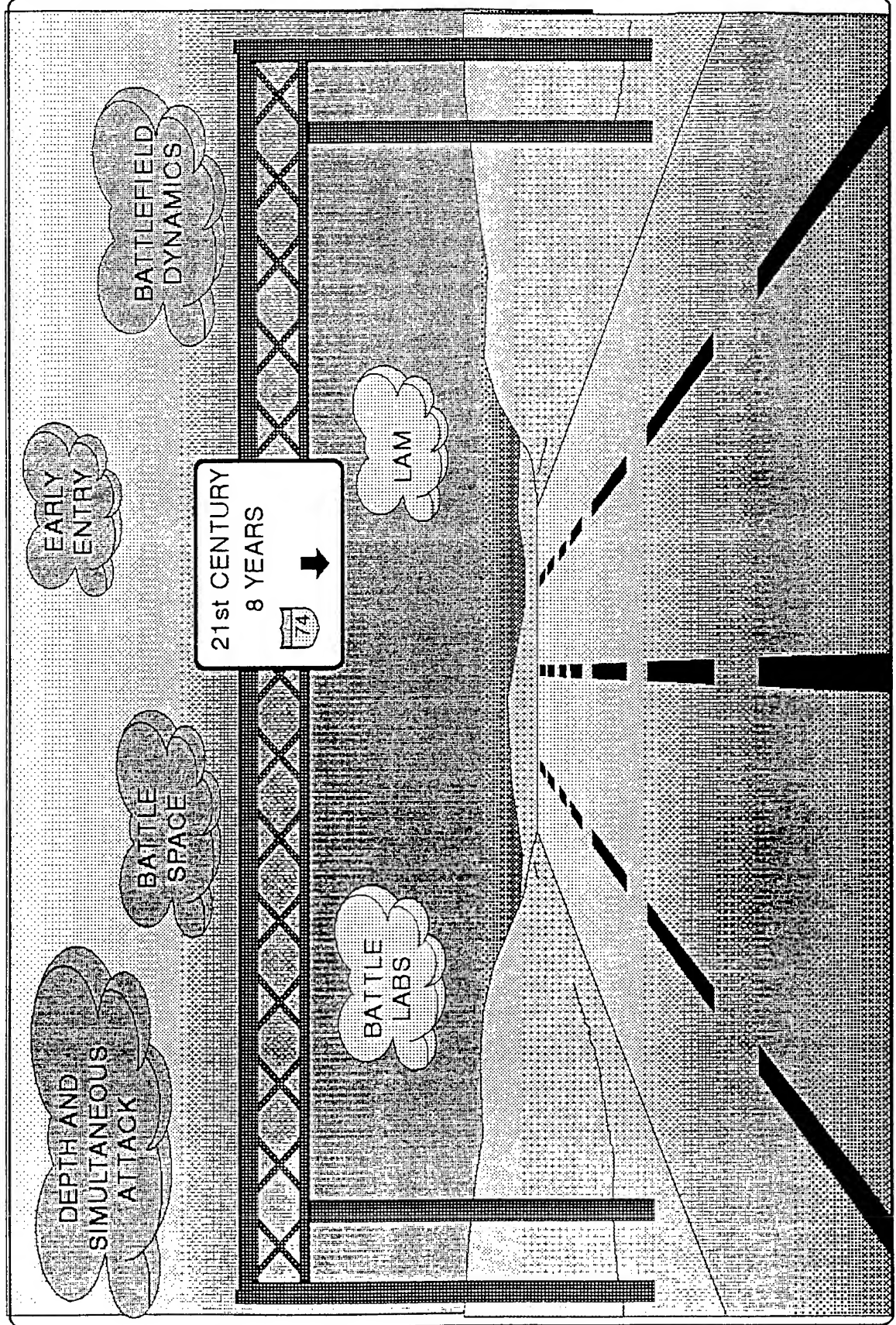
DEVELOPMENT

TRAINING

U.S. ARMY

# WINDS OF CHANGE NEW LANGUAGE

CHEMICAL CORPS



**Session I**

**ATMOSPHERIC MODELING**

**Session Chair**

**COL Grant Aufderhaar  
OUSD(A)ODDDR&E(R&AT)E&LS**

**A MULTI-STREAM RADIATIVE TRANSFER MODEL  
FOR INHOMOGENEOUS, THREE-DIMENSIONAL AEROSOL CLOUDS**

Donald W. Hoock  
U. S. Army Research Laboratory  
Battlefield Environment Directorate  
White Sands Missile Range, NM 88002-5501

John C. Giever, Sean G. O'Brien, Edward J. Burlbaw  
Physical Science Laboratory, New Mexico State University  
Las Cruces, NM 88003-0002

**ABSTRACT**

Electromagnetic radiance depends on three spatial variables, two angular variables and wavelength. Directional radiance and spectral intensity (color) are quantities required in the calculation of scene contrast and target signatures. The improved Battlefield Emission And Multiple Scattering (BEAMS) model has been developed to compute the transmission and radiance fields produced by finite, inhomogeneous aerosol clouds. Analytic methods for computing radiative transfer exist only for simple cloud geometries, for uniform concentration, or for uniform illumination along one or more dimensions. However, natural and battlefield aerosol clouds rarely have such simple properties. Thus, numerical solutions to cloud electromagnetic multiple scattering and emission must be used. The BEAMS model computes radiant interactions along 26 directions on a regular 3-dimensional cubic lattice. Scattering and emission calculations assume that aerosol concentrations are uniform in each volume element but are different between elements. Multiple scattering within and between elements is computed by repeatedly applying the interaction over the lattice until the results converge, and the incident radiation boundary conditions are matched. The method and its ability to treat spatial fluctuations in output radiance, transmission, and propagated contrast are shown in support of scene visualization, intermittent target acquisition and contrast propagation.

**1. INTRODUCTION**

The battlefield environment impacts the employment of high tech weapons, and it influences hardware and software requirements. In particular, battlefield dust, smoke, chaff, fog, and other airborne particles affect electromagnetic (EM) propagation. The battlefield environment is a major contributor to altering signatures of targets and backgrounds at visual,

infrared and millimeter wavelengths, resulting in reduced or intermittent target acquisition and tracking. However, clouds of aerosols and particles do more than obscure. They also have their own distinctive appearance and electromagnetic signatures. These signatures provide cues, alter EM backgrounds, and produce scene clutter both in the real world and in computer-generated battlefield environments.

Except for simple cloud and illumination geometries, it is not easy to analytically compute the detailed electromagnetic transmission, multiple scattering, and emission environment for the battlefield. Radiance  $L(\mathbf{r}, \Omega)$  varies with direction and at each point in space. Its units are power per unit solid angle per unit area perpendicular to the propagation direction, and thus radiance is a five-dimensional quantity. One effect of increasing the concentration of interacting particles along a propagation path is to remove more of the original power propagating along that direction. This loss of radiant power is caused by the combination of increased absorption along the path and by increased scattering of energy away from the path. However, even while radiance is reduced by this interaction, increased concentrations can also increase radiant energy scattered into the path from all other incoming directions and from the emission of radiant energy by the particles themselves.

Modeling this complex interaction process for arbitrary spatial distributions of particle concentrations and incident electromagnetic radiance conditions is a formidable task. The Battlefield Emission and Multiple Scattering (BEAMS) model is a numerical approach to computing these effects. The theoretical basis for BEAMS and examples of modeling finite and inhomogeneous clouds are given in the next sections.

## 2. THEORY

### 2.1 THE RADIATIVE TRANSFER EQUATION

The equation for radiative transfer is (cf. Van de Hulst, 1980):

$$\hat{\Omega} \cdot \nabla L(\mathbf{r}, \Omega) = -\alpha C(\mathbf{r}) [L(\mathbf{r}, \Omega) - \omega \int L(\mathbf{r}, \Omega') P(\Omega', \Omega) d\Omega' - (1 - \omega) L_b(\mathbf{r}, \Omega)] \quad (1)$$

where  $\mathbf{r}$  is a position in space and  $\Omega$  is a direction. In terms of a distance  $s$  from a point  $\mathbf{r}_0 = (x_0, y_0, z_0)$ , one can also write  $\mathbf{r}$  as

$$\mathbf{r} = (x, y, z) = (\alpha s + x_0, \beta s + y_0, \gamma s + z_0); \quad \hat{\Omega} = (\alpha, \beta, \gamma) \quad (2)$$

with  $\Omega$  defined by the direction-cosines between  $(\mathbf{r} - \mathbf{r}_0)$  and the  $x$ ,  $y$  and  $z$  axes. This results in an equivalent radiative transfer equation:

$$\frac{dL(s, \Omega)}{ds} = -\alpha C(s) [L(s, \Omega) - \omega \int L(s, \Omega') P(\Omega', \Omega) d\Omega' - (1 - \omega) L_b(s, \Omega)] \quad (3)$$



where

- $L(s, \Omega)$  - radiance at point  $s$  in direction  $\Omega$  ( $\text{w m}^{-2} \text{sr}^{-1}$ ). If explicit wavelength variation in  $L$  is also included, then this spectral radiance has units of power per unit area per unit solid angle per unit wavelength.
- $P(\Omega', \Omega)$  - scattering phase function ( $\text{sr}^{-2}$ ). The function  $P$  is the fractional power per unit solid angle from incoming direction  $\Omega'$  that scatters per unit solid angle into direction  $\Omega$  by the aerosol.
- $\alpha$  - mass extinction coefficient ( $\text{m}^2 \text{g}^{-1}$ ). This is the cross section per unit mass of aerosol for the removal of direct radiance by both absorption and scattering.
- $\omega$  - single scattering albedo (dimensionless) is the fraction of  $\alpha$  attributable to scattering.
- $C(s)$  - mass concentration of aerosol ( $\text{g m}^{-3}$ ). Concentration is the mass of aerosol suspended per volume of air.
- $L_b(s, \Omega)$  - source radiance (for example, blackbody emission radiance) at point  $s$  in direction  $\Omega$  ( $\text{w m}^{-2} \text{sr}^{-1}$ ).  $L_b$  can also be used for other effective sources of radiance within the cloud.

In general,  $P(\Omega', \Omega)$ ,  $\alpha$ ,  $\omega$  and  $C(s)$  can all vary with position within the cloud. This can occur, for example, for inhomogeneous mixtures of obscuring particles or can result from different settling rates of particle sizes and turbulence-generated variations in particle orientation.

## 2.2 BASIC SOLUTIONS

Define the term "limiting path radiance"  $L_s(s, \Omega)$  as

$$L_s(s, \Omega) = \omega \int L(s, \Omega') P(\Omega', \Omega) d\Omega' + (1 - \omega) L_b(s, \Omega) \quad (4)$$

which is independent of concentration. It represents the angle-averaged contribution of illumination  $L$  to the diffuse (scattered) radiance plus diffuse emission. If  $L_s$  is independent of position  $s$  over some interval, for example, then over that interval the solution of eq. 3 is simply

$$L(s, \Omega) = T L(s_0, \Omega) + (1 - T) L_s(\Omega) = T L(s_0, \Omega) + L_p(s, \Omega) \quad (5)$$

where the direct transmittance  $T$  is defined over the interval  $s_0$  and  $s$ :

$$T = e^{-\alpha \int_{s_0}^s C(s') ds'} = e^{-\tau} \quad (6)$$

The path-integral of the product of extinction and concentration from  $s_0$  to  $s$  is called the optical depth  $\tau$ , and the combined effect of  $L_s$  and  $T$  is called the path radiance  $L_p$ .

Equation 5 has practical importance for its simplicity, and thus its use in computer visualization. Note that transmittance  $T$  becomes a simple

interpolating factor that varies between one (clear conditions) and zero (total obscuration). At low transmittance  $T$  only the radiance  $L_s$  remains along the path, and thus its name as the "limiting path radiance". Some graphics systems actually implement eqs. 5 and 6 in hardware as a "haze" function with  $s$  at the observer's position and  $s_o$  at the object being observed. However, most graphics systems do not allow the user to vary  $L_s$  with position or, perhaps more importantly, with direction.

The purpose of BEAMS is therefore to compute  $L_s$  over a relatively coarse 3-D grid enveloping the cloud and to combine the resulting diffuse radiance with detailed effects of direct transmittance  $T$  on a finer 3-D grid through the cloud. This is shown in figs. 1 and 2. The path radiance  $L_p$  combines the more slowly-varying diffuse radiation effects of  $L_s$  with the more rapid spatial variations in  $T$ .

Direct Beam, Scene Transmission and Forward-Scatter through the Cloud:  $L(s) = T(s) L_b(0)$  with Aspect, FOV

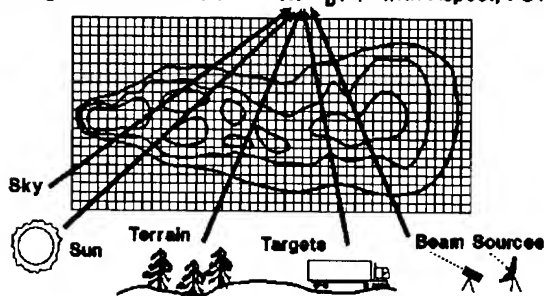


Figure 1. BEAMS computed direct transmittance grid.

Angular and Space-Dependent Diffuse Multiple-Scattering and Cloud Emission  $L(s) = T(s) L_b(0) + L_p(s)$

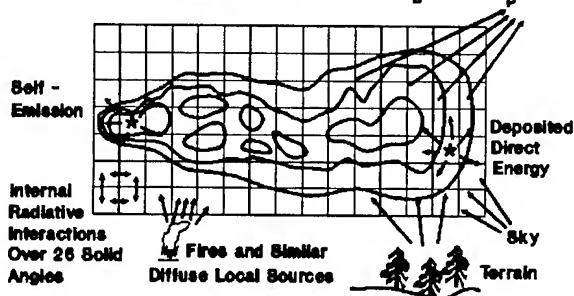


Figure 2. BEAMS computed path radiance grid.

More generally, one would like to model a continuous variation in  $L_s$  within the cloud. If  $L_s$  is computed and fit as a piece-wise linear function in  $\tau$ :

$$L_s(s, \Omega) = L_{s0}(s_o, \Omega) + L_{sd}(\Omega) \tau \quad (7)$$

where  $L_{s0}$  is the value at  $s_o$  and  $L_{sd}$  is the gradient in  $L_s$ , then the solution of the radiative transfer function over the interval becomes:

$$L(s, \Omega) = T L(s_o, \Omega) + (1-T) L_s(s, \Omega) - [1 - (1-\tau) T] L_{sd}(\Omega) \quad (8)$$

### 2.3 BEAMS SOLUTIONS

BEAMS solves the radiative transfer equation numerically on a three-dimensional cubic lattice enclosing the cloud. The x-axis points downwind, the y-axis points cross-wind, and the z-axis points upward from the ground. Within each element the concentration, phase function, extinction and scattering properties are constant inputs. Incident direct and diffuse radiance illuminates the outer boundary of the cloud, and each element can introduce a diffuse volume source such as thermal radiation or scattered beam radiation. While the numbers of cubic elements  $N_x$ ,  $N_y$ ,  $N_z$  along each direction are arbitrary, they are typically constrained by computer memory and execution time to the range of 5 to 50 for the diffuse  $L_s$  calculations.

A general form for the radiative transfer solution for  $L$  (and thus for  $L_s$ ) is obtained within each element using radiant interactions between neighboring cubes and matching radiances on the boundaries. Computations are repeatedly applied between all elements until the interacting radiance fields settle down to some final set of values over the entire lattice. As discussed below, multiple scattering and matrix solutions to two-stream calculations across parts of the lattice are also implemented.

In addition to using discrete spatial elements, BEAMS averages diffuse radiance scattering over a finite number of solid angle directions. The earliest version of BEAMS (Version 0) used only 6 solid angles, each of  $4\pi/6$  sr, with principal directions along the positive and negative x, y and z axes. Newer versions (BEAMS 1.0 and 2.0) use 26 solid angles with principal directions defined as those from the center of each cubic element to the centers of each of its 26 nearest-neighbor cubes. Thus, there are 6 solid angles (of 0.806 sr) connecting through the centers of the 6 faces of the cubes and parallel to the x, y and z axes; 12 solid angles (of 0.482 sr) passing through the midpoints of each of the 12 edges of the cube; and 8 solid angles (of 0.244 sr) passing through the 8 corners of the cube. These solutions convert the continuous phase function to a matrix of single-scattering fractions integrated over the incoming solid angles  $\Delta\Omega_j$  and averaged over the outgoing solid angles  $\Delta\Omega_i$ :

$$P_{ij} = \frac{1}{\Delta\Omega_j} \int_{\Delta\Omega_j, \Delta\Omega_i} P(\Omega_i, \Omega_j) d\Omega_i d\Omega_j \quad (9)$$

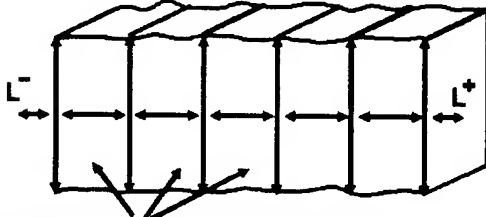
For output direction  $j$ , the matrix  $P$  sums to one over all incoming directions  $i$ . For incoming direction  $i$ ,  $(\Delta\Omega_j/\Delta\Omega_i) P_{ij}$  sums to one over  $j$ .

Examination of eq. 5 shows the limitation in using it as a method to find  $L_s$ , even when the incoming radiance  $L$  is precisely known on the boundary. In particular, consider a single cube uniformly filled with a dense concentration of aerosol such that the transmittance  $T$  from the boundary to the center is nearly zero. Then eq. 5 gives no usable information about  $L_s$  since it implies that  $L_s$  simply equals  $L$  at the center and vice versa. Thus, while eq. 5 is very useful for visualization, it is only useful for computing  $L_s$  if the cloud is first partitioned into smaller elements having reasonably small optical depths (on the order of one or less) corresponding to a relatively large transmittance (on the order of 0.3 or larger). Then the spatial variation in  $L_s$  can be computed through the multiple scattering interactions of radiance between different elements. This was the method used in the original 6-angle version of BEAMS (Hoock, 1987).

Two other methods are used in newer versions of BEAMS. First, uniform radiance is applied at one angle across the face of a  $5 \times 5 \times 5$  (or similar) cube having a small uniform optical depth  $\tau_1$  in each element. The face-averaged output radiance is reused as an effective multiple-scattering phase function  $P$  for elements of optical depth  $5\tau_1$  in larger problems with inhomogeneous concentrations. A second method employs the well-known two-stream solution techniques (Coakley, 1975). The two-stream method is often used for radiative transfer through infinite layered slabs as shown in fig. 3. In BEAMS (Version 2.0) this two-stream multiple scattering is computed along each of the 13 pairs of opposing directions as shown in fig. 4.

$$\frac{dL^+}{d\tau} = -[L^+ - \omega P_{ff} L^+ - \omega P_{bf} L^-]$$

$$-\frac{dL^-}{d\tau} = -[L^- - \omega P_{bb} L^- - \omega P_{fb} L^+]$$

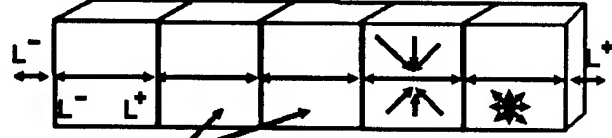


Slabs of Different Optical Depths

Figure 3. Two-stream problem for infinite slabs.

$$\frac{dL^+}{d\tau} = -[L^+ - \omega P_{ff} L^+ - \omega P_{bf} L^- - L_{s1}^+ - L_e^+]$$

$$-\frac{dL^-}{d\tau} = -[L^- - \omega P_{bb} L^- - \omega P_{fb} L^+ - L_{s1}^- - L_e^-]$$



Different Concentrations  
Phase Functions, Albedos  
Finite Cubic Elements

Figure 4. Two-stream problem for finite columns.

For  $L^+$  in one direction (for example,  $+x$ ) and  $L^-$  in the opposite direction:

$$\frac{d}{d\tau} \begin{bmatrix} L^+ \\ L^- \end{bmatrix} = \begin{bmatrix} -(1 - \omega P_{ff}) & \omega P_{bf} \\ -\omega P_{fb} & (1 - \omega P_{bb}) \end{bmatrix} \begin{bmatrix} L^+ \\ L^- \end{bmatrix} + \begin{bmatrix} L_{s1}^+ \\ -L_{s1}^- \end{bmatrix} + \begin{bmatrix} L_e^+ \\ -L_e^- \end{bmatrix} \quad (10)$$

where the limiting path radiance is separated into scattering along the forward  $f$  ( $+x$ ) and backward  $b$  ( $-x$ ) directions as:

$$L_{s1}^+ = \omega (P_{ff} L^+ + P_{bf} L^- + \sum_{j \neq b, f} L(\Omega_j) P_{jf}) = \omega (P_{ff} L^+ + P_{bf} L^- + L_{s1}^+) \quad (11)$$

$$L_{s1}^- = \omega (P_{bb} L^- + P_{fb} L^+ + \sum_{j \neq b, f} L(\Omega_j) P_{jb}) = \omega (P_{bb} L^- + P_{fb} L^+ + L_{s1}^-) \quad (12)$$

This also defines the incoming diffuse side radiance  $L_{s1}$  that scatters into the positive direction  $L_{s1}^+$  and into the negative direction  $L_{s1}^-$ , assumed to change linearly along the path according to eq. 7. Element emission source radiance terms are similarly identified as

$$L_e^+ = (1 - \omega) L_b^+ \text{ (forward)}; \quad L_e^- = (1 - \omega) L_b^- \text{ (backward)} \quad (13)$$

Then eq. 10 can be diagonalized using the eigenvalues:

$$\lambda_{1,2} = \omega \left( \frac{P_{ff} - P_{bb}}{2} \right) \pm \left\{ \left[ 1 - \omega \left( \frac{P_{ff} + P_{bb}}{2} \right) \right]^2 - \omega^2 P_{fb} P_{bf} \right\}^{1/2} \quad (14)$$

with the solutions

$$L^+(\tau) = (1 - \lambda_1 - \omega P_{bb}) A^+ e^{\lambda_1 \tau} + \omega P_{bf} A^- e^{\lambda_2 \tau} + g(\tau)$$

$$L^-(\tau) = \omega P_{fb} A^+ e^{\lambda_1 \tau} + (1 + \lambda_2 - \omega P_{ff}) A^- e^{\lambda_2 \tau} + h(\tau) \quad (15)$$

where

$$\begin{aligned}
g(\tau) = & -\left(\frac{1}{\lambda_1 \lambda_2}\right) \left\{ (1 - \omega P_{bb}) (L_{s1}^+ + L_e^+) + \omega P_{bf} (L_{s1}^- + L_e^-) \right\} \\
& + \left(\frac{1}{\lambda_1 \lambda_2}\right) \left[ 1 - (1 - \omega P_{bb}) \left(\frac{\lambda_1 + \lambda_2}{\lambda_1 \lambda_2}\right) \right] L_{s1d}^+ \\
& - \left(\frac{\omega P_{bf}}{\lambda_1 \lambda_2}\right) \left(\frac{\lambda_1 + \lambda_2}{\lambda_1 \lambda_2}\right) L_{s1d}^-
\end{aligned} \tag{16}$$

$$\begin{aligned}
h(\tau) = & -\left(\frac{1}{\lambda_1 \lambda_2}\right) \left\{ (1 - \omega P_{ff}) (L_{s1}^- + L_e^-) + \omega P_{fb} (L_{s1}^+ + L_e^+) \right\} \\
& - \left(\frac{1}{\lambda_1 \lambda_2}\right) \left[ 1 + (1 - \omega P_{ff}) \left(\frac{\lambda_1 + \lambda_2}{\lambda_1 \lambda_2}\right) \right] L_{s1d}^- \\
& - \left(\frac{\omega P_{fb}}{\lambda_1 \lambda_2}\right) \left(\frac{\lambda_1 + \lambda_2}{\lambda_1 \lambda_2}\right) L_{s1d}^+
\end{aligned} \tag{17}$$

$A^+$  and  $A^-$  are free coefficients that are determined by matching  $L^+$  and  $L^-$  to the incoming radiance on the element boundaries. In fact, these equations hold for every element in a column stretching across the cloud. All the coefficients  $A^+$  and  $A^-$  for each element in the column can thus be solved for simultaneously by inverting a (mostly) diagonal matrix. Once all columns across the cloud in one direction are processed, then interactions along other directions are computed using these updated radiance values. This process continues until computed values of  $L$  and  $L_s$  converge.

### 3. EXAMPLES

Outputs from the BEAMS model have been compared to those produced from other models and approaches. Fig. 5 shows a cube-shaped cloud having single scattering albedo  $\omega$  of 0.9, with incident radiation from the lower right along the direction through the midpoint of one edge toward the center of the cube. Figs. 6 through 9 compare the BEAMS output radiance to that produced by a Monte Carlo multiple scattering model. The cases shown here are for two practical extremes in optical depth of  $\tau = 1$  and  $\tau = 16$  across the cloud. Two aerosol phase functions were considered: an isotropic phase function characteristic of scattering by particles much smaller than the EM wavelength; and a moderately forward-peaked phase function for visible scattering from the Deirmendjian Haze-L particle distribution

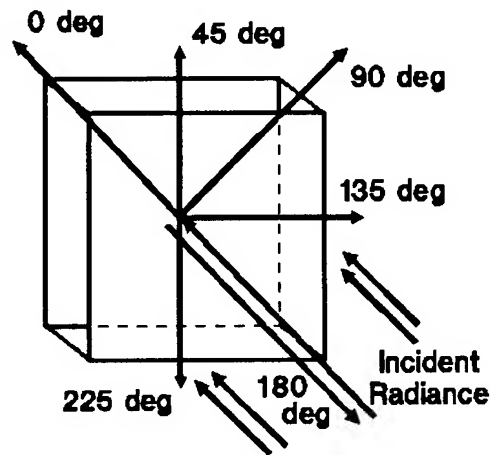


Figure 5. Incident and output radiance directions.

model (McCartney, 1976). The Monte Carlo code used was a modified version of the U. S. Army Electro-Optical Systems Atmospheric Effects Library (EOSAEL) Multiple Scattering (MSCAT) code (O'Brien, 1984). It is "exact" in that the Monte Carlo probability approach is very robust to complex geometries and to different particle properties. However, Monte Carlo methods suffer from a requirement that many photons must be launched into a cloud to produce sufficient scattering histories for accurate statistics.

The Monte Carlo results are given for 5,000 and 10,000 photon histories, and thus the spread in multiple data points at some scattering angles are indicative of the Monte Carlo computational "noise". The BEAMS-computed radiance is given as curves with dots at the principal ray directions. Scattering angles exceeding 180 deg represent the directional output radiance continuing in a circle around the output plane. BEAMS outputs are symmetric about the back-scattering (180 deg) direction for these symmetric phase functions. But the Monte Carlo outputs continue to exhibit different fluctuations at each angle so they need not be completely symmetric about 180 deg. This can be seen in fig. 7. Note that for isotropic scattering and the low optical depth of fig. 6, the output radiance is angle-independent as expected. (The forward peak at 0 deg is part of the forward scatter of the original incident beam). In fig. 7, however, at a large optical depth of 16, one sees that the forward

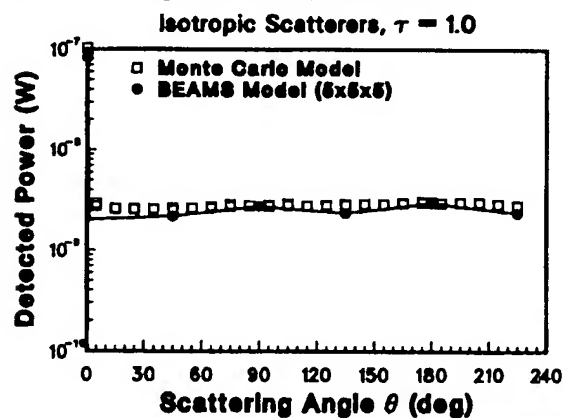


Figure 6. Isotropic,  $\tau = 1$ .

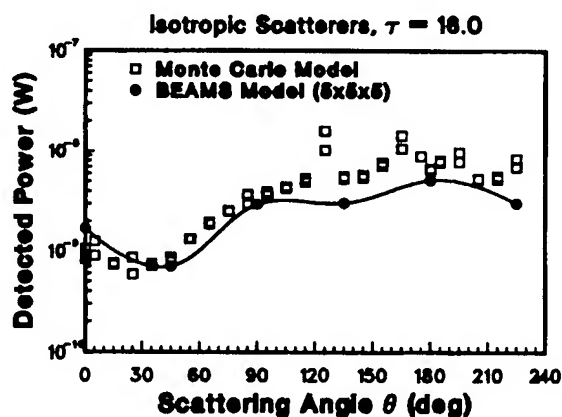


Figure 7. Isotropic,  $\tau = 16$ .

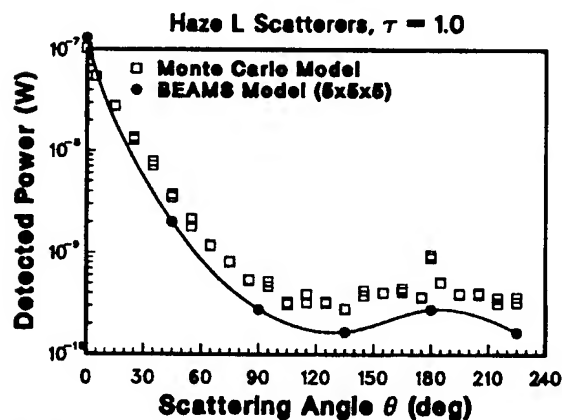


Figure 8. Haze-L,  $\tau = 1$ .

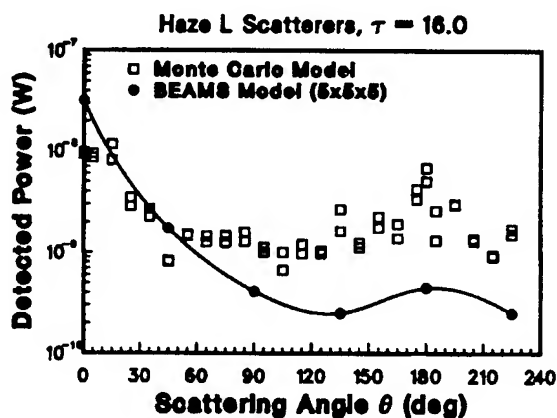


Figure 9. Haze-L,  $\tau = 16$ .

scattered radiance is small but non-zero due to multiple scattering. This radiance decreases for scattering angles out to 45 deg since at this angle the outgoing distance to the side of the cube is smallest, and less path length is available for scattering in that direction. At 90 deg this path again reaches a maximum length and the radiance increases. The continued increase in the backward directions is due to the high reflectance properties of the cloud at this large optical depth. Figs. 8 and 9 show effects of a forward-peaked phase function. Relatively poor agreement in the backward direction in Fig. 9 can be attributed to the fact that the BEAMS calculation was performed on only a 5x5x5 element grid. Thus, each element has an optical depth greater than 3, leading to multiple scattering within the elements themselves and exceeding the requirement that the optical depth per element not be much greater than one.

Figs. 10 through 13 illustrate cloud radiance and obscuration computed from BEAMS. Fig. 10 is an unobscured visible image of a pickup truck (lower left center) at 1 km in a desert background of moderate clutter. Fig. 11 shows the same background image, but with a synthetic, inhomogeneous 30 gal/h fog oil cloud inserted in front of and to the left of the truck. The cloud concentration variations are simulated inputs to BEAMS from a statistical model (Hooch, 1991). BEAMS does not itself compute the dynamic flow or turbulent structure of the aerosol cloud. The transmission and radiance computed from BEAMS were used to generate cloud transparency and brightness for the scene modification. Figs. 12 and 13 are similar to fig. 11. However, the amount of smoke has been somewhat reduced from fig. 11, and the sun position is different. In fig. 12 the sun is at the observer's back, 30 deg above the horizon. In fig. 13, the same cloud with the same concentration is used, but the sun is placed on the far side of the cloud, 30 deg above the horizon. The large apparent change in scene contrast produced by the sun-cloud interaction is the same as that one often experiences while driving a car in late afternoon or early morning. At those times of day, any haze, dust or smoke between the sun and the driver

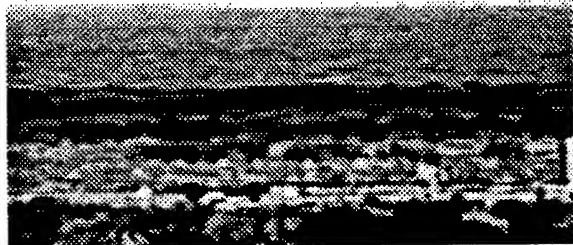


Figure 10. Clear image.



Figure 11. Simulated fog oil.



Figure 12. Sun at back.



Figure 13. Sun in eyes.

can appear quite bright, greatly reducing the available contrast of objects beyond the cloud. Yet the same haze or dust cloud, when viewed with the sun at one's back, might only be slightly visible and have little effect on scene contrast.

#### 4. CONCLUSIONS

The Battlefield Emission and Multiple Scattering (BEAMS) model is a research-level code for computing the transmission and path radiance through finite and inhomogeneous three-dimensional aerosol clouds. External illumination fields can be applied for diffuse radiance sources such as sky and terrain light, for finite illuminated areas such as finite beams and shadows, and for direct beam sunlight. Internal radiance sources and reflective boundaries are also supported. Multiple scattering interactions are computed between cubic elements having uniform concentrations and optical properties. The output diffuse radiance is produced in three space dimensions and in 26 directions. Once the diffuse path radiance has been computed for the cloud on the coarse computation lattice, then more detailed transmittance calculations are generated over a finer lattice to model higher order spatial fluctuations. Background scenes can thus be propagated through the cloud from any direction for obscuration analysis, cloud signature calculations and scene simulations.

Polarization, wavelength dependent effects, and phase functions for non-symmetric particles are now being examined in the model. Future research will also investigate methods to derive statistics of radiance fields from realistic concentrations and particle orientations. These statistics will be applied to the deriving fast, realistic methods to visualize battlefield atmospheres and their effects.

#### REFERENCES

- Coakley, James A. and Peter Chylek, 1975: The Two-Stream Approximation in Radiative Transfer, Including the Angle of the Incident Radiation, Journal of Atmospheric Sciences, Feb 1975, pp. 409-418.
- Hoock, Donald W., 1987; A Modeling Approach to Radiative Transfer through Inhomogeneous Dust and Smoke Clouds, in Proceedings of the 7th Annual EOSAEL/TWI Conference, Las Cruces, NM, pp. 575-596.
- Hoock, Donald W., 1991: Theoretical and Measured Fractal Dimensions for Battlefield Aerosol Cloud Visualization and Transmission, in Proceedings of the 1991 Battlefield Atmospheric Conference, Ft. Bliss, TX, pp 46-55.
- McCartney, Earl J., 1976: Optics of the Atmosphere, John Wiley and Sons, New York
- O'Brien, Sean G., 1984: Volume 18. Aerosol Multiple Scattering Module MSCAT, Technical Report TR-0160-18, U.S. Army Atmospheric Sciences Laboratory, White Sands Missile Range, NM.
- Van de Hulst, H. C., 1980: Multiple Light Scattering, Academic Press, NY.



# **VISUALIZATION OF MULTIPLE BATTLEFIELD OBSCURANTS**

by

Geoffrey Y. Gardner  
Grumman Data Systems  
Woodbury, NY 11797

G. Michael Hardaway  
U.S. Army Topographic Engineering Center  
Fort Belvoir, VA 22060-5546

## **ABSTRACT**

The "Battlefield Obscurants" contract (DACA76-90-C-0026) sponsored by the U.S. Army Topographic Engineering Center (TEC) was extended to include visualization of multiple COMBIC obscurants and to integrate the battlefield obscurant software with TEC's Battlefield Visualization Testbed (BVTB) system. Any number of COMBIC obscurant types can now be included in the scene and any number of sources of each type can be specified with arbitrary starting times and positions. The transmittance of the multiple obscurant model can be computed for any of the COMBIC wavelengths, ranging from visual to radar. The visualization software, which models each obscurant by filling the COMBIC envelope time history with fractal ellipsoids, has been extended to integrate the ellipsoids with a polygon depth-buffer scene image generated on the TEC BVTB. The increased capability will allow the Army to study the effects of different obscurants viewed by different sensors under different environmental conditions. The resulting technology will be demonstrated with video animations.

## 1. INTRODUCTION

The U.S. Army Topographic Engineering Center (TEC) initiated contract DACA76-90-C-0026 to study the feasibility of visualizing battlefield obscurants by integrating Grumman Data Systems computer graphics techniques with physical models defined by the U.S. Army Atmospheric Sciences Laboratory's Electro-Optical Systems Atmospheric Effects Library (EOSAEL) (Shirkey et al., 1987). The initial contract developed techniques to visualize any of the thirty obscurant types contained in the Combined Obscuration Model for Battlefield Contaminants (COMBIC) EOSAEL module (Hooch et al., 1987). The initial effort was successful in demonstrating the capability to visualize a single obscurant source set in a synthetic terrain background. The study produced two software modules: COMB\_I and COMBICV. COMB\_I was a reduced version of COMBIC, containing the essential subroutines of Phase I needed to generate envelope and mass production time history data for a single obscurant source. COMBICV generated images of the obscurant by filling the time histories with fractal ellipsoids and by processing the volumes using COMBIC Phase II equations combined with Grumman graphics algorithms (Gardner, 1991; Gardner and Hardaway, 1991).

To apply this new technology to their battlefield visualization effort, TEC extended the contract to allow visualization of multiple obscurant sources and to allow integration with the TEC Battlefield Visualization Testbed (BVTB) software. The contract extension produced two extended software modules: COMB\_I\_M and COMBICV\_M.

## 2. BATTLEFIELD OBSCURANT EXTENSIONS

The contract extension included two tasks. The first task called for providing the capability to generate multiple obscurants, including multiple source types and multiple sources of each type. The second task called for integrating the obscurant software with the BVTB scene generation software to allow inserting battlefield obscurants into BVTB scenes, which include real terrain and accurate models of surface features such as targets and trees.

### 2.1 EXTENSION TO MULTIPLE OBSCURANTS

COMBIC allows the inclusion of multiple obscurants in the scene. COMB\_I had been simplified for the original contract by removing a single loop in COMBIC Phase I which processed multiple obscurant sources and generated time history tables for each. By replacing this loop, a new version of COMB\_I, called COMB\_I\_M, was produced with the capability to generate tables including time histories for any number of obscurants.

COMBICV was extended by adding a loop to read in these tables for multiple obscurant types. In addition, the ellipsoid generation modules in COMBICV were extended to allow generation of multiple sources of each type. The new software allows positioning each source at an arbitrary location and assigning an arbitrary start time and mass scale. The extended version of COMBICV was called COMBICV\_M.

### 2.1.1 Multiple Level-of-Detail Modeling

It was anticipated that the computation load for image generation would increase with the number of obscurants generated. Initial software tests confirmed this and indicated that the large number of obscurants needed to simulate complex battle scenes realistically would require an undesirable amount of time. To solve this problem we applied a multiple level-of-detail modeling scheme we had used successfully on tree cluster models. This scheme reduces the number of ellipsoids used in each source model depending on the range of the source from the eye. To implement this process smoothly, the size and spacing of the ellipsoids is increased continuously with range. As ellipsoids move toward the plume or puff envelope boundary, they are assigned greater translucence by the Gaussian mass distribution model and tend to "fade away" by the time they move beyond the boundary. This technique proved to work quite well in animations where the eyepoint moved toward or away from the sources, and computation time was cut in half.

The extended COMB\_I\_M and COMBICV\_M software provides TEC with the capability to experiment freely with the insertion of multiple obscurants in a scene. Different types of obscurants, with different numbers of each type can be positioned anywhere in the scene and turned on at arbitrary start times. Different environmental conditions, such as wind speed and direction, can be defined to study the effects of changing conditions. The capability to generate multiple obscurants will produce much more valid simulations of cluttered battlefields.

Figure 1 shows 3 COMBIC obscurants, with multiple sources for each, modeled in a synthetic terrain background. COMBIC obscurant type 25 (fog oil) has 2 sources, and types 10 (White Phosphorus or WP) and 28 (dust) each have 6 sources. Two meter reference ellipsoids are included at each source.



Figure 1. Multiple obscurants (time = 30 seconds)

## 2.2 INTEGRATION WITH TEC BVTB SOFTWARE

TEC's BVTB software generates depth buffer images of scenes including terrain and surface features such as targets and trees, all modeled with polygons. These images are designed to be machine independent to facilitate display on different computer systems. The depth buffer data includes RGB color values and depth values for each image pixel.

COMBICV\_M generates images on a scan-line basis using a multi-level scan-line depth buffer with 32 depth levels. COMBICV\_M processes the background terrain polygons first and inserts their color and depth at each pixel into the first level of the depth buffer. The obscurant ellipsoids are processed and added to the depth buffer. If the obscurant is closer than the terrain at a given pixel, the terrain values are pushed down one level behind the current ellipsoid. If the obscurant is farther than the terrain polygon, it is not added to the depth buffer pixel.

A straightforward approach to integrating COMBICV\_M with the BVTB depth buffer would be to replace the terrain polygon processing by initializing the multi-level scan-line buffer with the data already generated by the BVTB. This would require processing the obscurant ellipsoids at the same resolution as the BVTB image. Since BVTB images are high resolution, and obscurant ellipsoids do not require high resolution rendering, this would result in an unnecessary delay in image generation.

Instead, we chose to generate the ellipsoid image data independently at lower resolution and then integrate the resulting depth buffer data with that of the BVTB image. Although this scheme took more effort to implement, it provides the option of multi-resolution rendering which is much more flexible and efficient. It also offers the potential for parallel processing of obscurants and background.

Because we did not have immediate access to BVTB data, and to make the process more generic, we developed the basic algorithms using depth image data generated by GDS scene generation software. This approach gave us more control of the test image data to assure our technique would handle a wide range of cases.

### 2.2.1 Integration with GDS Depth Buffer Images

Using GDS scene simulation software, we generated depth buffer images similar to BVTB depth buffer images. By using large numbers of fractal ellipsoids, we were able to produce very complex depth images of treed terrain to test the integration of the obscurant ellipsoids. To simulate the BVTB polygon features, we removed all translucence from the trees to produce totally opaque backgrounds and generated images at high (1024-line) resolution. We stored the RGB and depth data for each image in a disk file called *deprgb.dat* in a scan-line format similar to that of the BVTB image (left to right, top to bottom). We also stored the focal length and eyepoint parameters used to generate the image.

We added an option to COMBICV\_M to read in file *deprgb.dat* and set the focal length and eyepoint values to generate the obscurant ellipsoids from the same perspective. We also used the

same terrain elevation data to assure that the ellipsoids would have the proper vertical positions. With this data we generated the multi-level scan-line depth buffer data for the obscurant ellipsoids without any terrain background. This process was independent of the GDS depth image data, allowing rendering of the ellipsoids at any resolution, using a technique we developed called "multi-resolution rendering."

#### 2.2.1.1 Multi-Resolution Rendering

Multi-resolution rendering allows rendering the obscurant ellipsoids at a much lower resolution than the background depth image. This reduces rendering time dramatically and yet loses very little in image quality because the fractal ellipsoids are so soft and blurry. A cost-effective resolution for rendering the obscurant ellipsoids is 1/4 full resolution or 256 lines. To describe the integration procedure, we will use this typical 256-line resolution, which means that one scan-line of the ellipsoid image will be replicated and integrated with 4 scan-lines of the GDS depth image.

The ellipsoid processing is performed one scan-line at a time for each of the 256 scan-lines, filling the scan-line depth buffer to as many levels as necessary for each pixel. The resulting 256 scan-line depth buffer is then integrated with each of 4 scan-lines of the GDS depth image. Integration is performed at each pixel by comparing the ellipsoid depths with the GDS image depth and keeping only those ellipsoids closer than the GDS image feature. Similarly, on each of the 4 GDS image scan-lines, each ellipsoid pixel is integrated with 4 GDS pixels. Although the integration process adds overhead computation, the variable resolution technique still reduces rendering time by a factor of 10 for 1/4-resolution obscurants.

Figure 2 shows images of multiple obscurants integrated with a GDS scene generated using the multi-resolution rendering technique, with the obscurant ellipsoids rendered at 1/4 the 1024-line GDS image resolution. COMBIC obscurant types 23 (generator ABC M3A3) and 8 (WP) each have 3 sources, and type 30 (diesel oil fire) has 1 source simulating a tank fire.



Figure 2(a). GDS test scene depth buffer image



Figure 2(b). Multiple obscurants integrated with GDS image  
(time = 30 seconds)

### 2.2.2 Integration with BVTB Depth Buffer Images

Integration with GDS depth images involved the most difficult part of the technical development needed for integration with the BVTB depth image. The remaining development effort was dedicated to providing flexible capability to extract data from BVTB scene files and to allow different BVTB image formats.

Utility programs were developed to provide COMBICV\_M with BVTB elevation, depth image and graphics data to provide accurate integration of the obscurants with the TEC background scene.

To integrate obscurants with a BVTB scene, the user links the pertinent BVTB scene files to the input files of these utility programs and then runs the programs. At this point, the user is free to select any obscurant parameters for COMB\_I\_M and COMBICV\_M and then run these programs as before.

The user can render the obscurants at any resolution, as with the GDS integration, and can use any size BVTB image. Animations can be generated as well as single images.

Figures 3 and 4 show images generated using this technique. Figure 3 shows 5 sources of COMBIC obscurant type 13 (WP) integrated with a 1024-line BVTB visual image. The obscurants were rendered at 1/8th (128-line) resolution using COMBIC wavelength 1 (visible). Figure 4 shows the same obscurants integrated with a 480-line BVTB IR (8-12 micrometers) image. The obscurants were rendered at 128-line resolution using COMBIC wavelength 5 (IR 8-12). Note the difference in obscurant transmittance depending on wavelength and the difference in shading due to differences in sun and ambient contributions defined in the BVTB graphics input files.

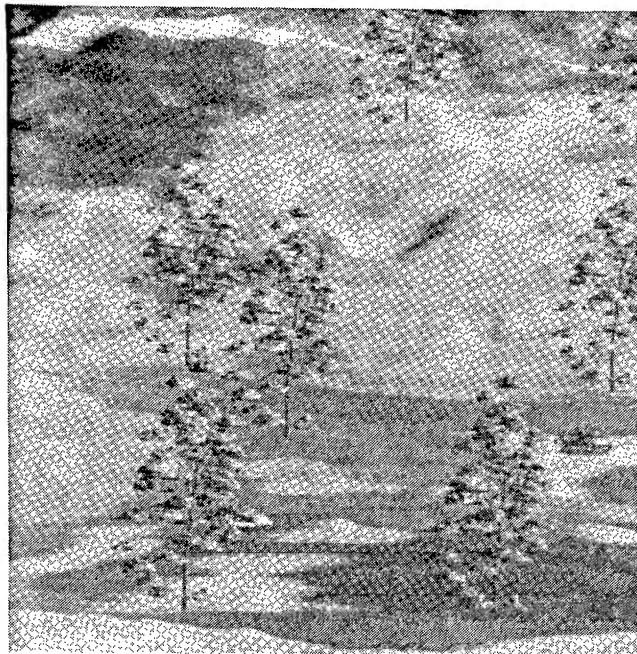


Figure 3(a). 1024-line BVTB visual scene image  
(time = 0 seconds)



Figure 3(b). Multiple obscurants integrated with BVTB image  
(time = 30 seconds)



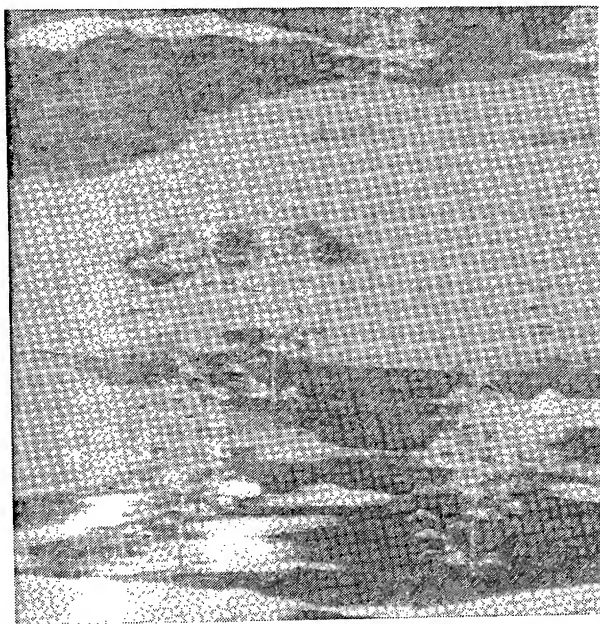


Figure 4(a). 480-line BVTB IR scene image  
(time = 0 seconds)



Figure 4(b). Multiple obscurants integrated with BVTB IR image  
(time = 30 seconds)

### 3. ANTICIPATED BENEFITS OF THE EXTENSIONS

These extended capabilities will allow TEC to simulate battlefield scenes more realistically by including multiple obscurant types and multiple sources of each type. TEC will now be able to integrate these obscurants with their BVTB imagery to enhance ongoing studies in mission planning and smart weapons evaluation. Different obscurant types can be selected and positioned at any location with arbitrary start times. Any of the seven COMBIC wavelengths can be selected to compare the effectiveness of the different obscurant types relative to the corresponding sensors. Environmental factors such as wind speed and direction can be changed to simulate a variety of possible situations.

The multiple level-of-detail modeling and multi-resolution rendering techniques provide an efficient computational environment allowing the generation of complex images on common workstations. In addition, the BVTB integration scheme allows for parallel processing of the obscurant ellipsoids and the BVTB polygons because the obscurants are processed independently. With the steadily increasing capability of graphics workstations, these factors point to the potential for real-time generation of complex battlefield scenes including realistic obscurants.

### REFERENCES

Gardner, G. Y., 1991: Battlefield Obscurants, Final Technical Report. Contract DACA76-90-C-0026, U.S. Army Topographic Engineering Center, Ft. Belvoir, VA 22060-5546.

Gardner, G. Y., and Hardaway, G. M., 1991: Visualization of Battlefield Obscurants. Proceedings of the 1991 Battlefield Atmospherics Conference, pp 56-65.

Hoock, D. W., Sutherland, R.A., and Clayton, D., 1987: Combined Obscuration Model for Battlefield Contaminants (COMBIC). ASL-TR-0221-11, U.S. Army Atmospheric Sciences Laboratory, White Sands Missile Range, NM 88002-5501.

Shirkey, R. C., Duncan, L. D., and Niles, F. E., 1987: Electro-Optical Systems Atmospheric Effects Library (EOSAEL-87). ASL-TR-0221, U.S. Army Atmospheric Sciences Laboratory, White Sands Missile Range, NM 88002-5501.

## MESOSCALE DATA ANALYSIS USING A MESOSCALE MODEL

Kenneth E. Eis and Jan L. Behunek  
METSAT Inc.  
Fort Collins, Colorado 80521, USA

Donald L. Reinke and Thomas H. Vonder Haar  
Cooperative Institute for Research in the Atmosphere (CIRA)  
Colorado State University, Foothills Campus  
Fort Collins, CO 80523

Craig J. Tremback  
ASTeR Inc.  
Fort Collins, CO 80522

### ABSTRACT

The Air Force and Army are currently developing new tactical weather observing and forecast system requirements which are complicated by sensor dependence on data fusion, analysis, and forecasting methods. The forecasting and analysis portion of these systems are dependent on sensor: type, exposure, distribution, and reporting frequency. Operations research (OR) studies are attempting to resolve the interrelationships between the data and analysis segments. A study, using existing mesoscale data coupled to a mesoscale analysis and forecast model would reduce the uncertainties in the system selection process. METSAT is developing specific applications of this "coupled" analysis approach. We will present a methodology and some preliminary results using automated surface station and remote sensing data coupled to the Colorado State University RAMS model. RAMS is representative of high performance local area models available for application in the 1990s. A forecast accuracy, and sensor distribution test, based on this coupled approach would give DoD managers a clear indication of how mesoscale analysis and forecast model accuracies depend on sensor spacing and temporal update frequencies.

### 1. INTRODUCTION

The DoD is about to build a new Combat Weather System (CWS). This combination of sensors, computers, communications, and software technology will support Army and USAF field and base operations well into the 21st century. Acquisition managers, about to spend millions on the CWS and IMETS need to know what kind of sensors, computers, and software to purchase. These decisions are based on two sets of factors. The first set focuses on the external inputs to the CWS. This includes satellite data, CONUS-based

weather central data, and long-line communications capability. The second set of factors are internal. What, and how many sensors to place in a theater of operations depends on in-theater communications and the initialization needs of the mesoscale forecast and analysis software that is fielded. Similarly, the forecast and analysis model is dependent on the spatial and temporal frequency of the in-theater data as well as the specific parameters collected.

Since there is a strong coupling between forecast initialization and the fielded data grid, you cannot treat one as an independent variable to solve the requirements questions of the other.

This paper outlines a pilot study using the CSU RAMS mesoscale model and mesoscale grid of surface automated weather observing systems in eastern Colorado. Although its scope was small, several issues critical to the CSW and IMETS acquisition were addressed.

## 2. NUMERICAL MODEL OVERVIEW

The Regional Atmospheric Modeling System (RAMS) was developed at Colorado State University in order to merge three mesoscale and cloud scale numerical weather simulation codes being used side by side at the same site (Tripoli and Cotton, 1982; Tremback et al., 1985). By merging the capabilities of the different models, a range of specific enhancements were introduced to RAMS, of which the telescoping, interactive nested-grid capability is one of the most significant. Based on the two-way grid interactive procedures of Clark and Farley (1984), RAMS has the ability to represent a large-scale area (e.g., the synoptic scale) and then to nest progressively to smaller scales (e.g., the mesoscale or even the microscale). More than one set of telescoping nests can be specified within a larger-scale grid and user-specified, and movable, grids can be activated. RAMS has hydrostatic and non-hydrostatic options so that all meteorologically relevant spatial scales can be represented. The concept of "plug-compatible" modules is used in RAMS in order to assist developers of parameterizations to interface into RAMS. RAMS incorporates several other options, including various levels of initialization complexity, a range of turbulence, radiation and cumulus convection parameterizations, and several methods of representing microphysical processes.

The RAMS simulations for this study utilized nested grids with 80, 20 and 5 km horizontal resolution. The domain of the finest grid is depicted by the contoured area in fig. 1b. Observational data were assimilated by a Barnes objective analysis scheme.

## 3. DATA DESCRIPTION

Several data sets were collected for use in the evaluation of numerical model responses to varying input data resolution. These data sets were used to intercompare the Barnes objective analyses with and in the absence of the highest spatial resolution surface observations, to initialize the numerical simulation, and to evaluate the accuracy of that simulation. Macroscale data sets encompassing most of North America were supplied by the

U.S. National Meteorological Center. Other data sources are noted below. The case that was analyzed began at 00 UTC on 28 July 1992, which also was the initialization time for the model simulation. The data archive included the 48 hours from 00 UTC 28 July through 00 UTC 30 July. The northeastern Colorado region chosen for study experienced relatively quiescent weather during this period, with high pressure at the surface and light northwesterly winds aloft. The lack of large-scale forcing allowed the undisturbed development of mesoscale circulations driven by terrain, land use, and other similar factors.

Data set characteristics and their value to the current investigation are described as follows:

### 3.1 CONVENTIONAL SYNOPTIC SURFACE OBSERVATIONS

These hourly surface observations were collected in the U.S., Canada, and northern Mexico by human observers and (in the U.S.) some automated stations. They supplied the numerical model with information regarding the macroscale and large mesoscale condition of the atmosphere over and surrounding the region of interest over northeastern Colorado. Parameters measured included surface air temperature, humidity, wind speed and direction, and altimeter setting. These data were important for establishing the initial and boundary conditions for the numerical simulation.

### 3.2 MESOSCALE SURFACE NETWORK DATA

These data were acquired from automated stations deployed by the NOAA/Forecast Systems Laboratory (FSL) and the National Center for Atmospheric Research (NCAR). The NCAR stations are known collectively as the Portable Automated Mesonet (PAM-II). These stations measured surface air temperature, humidity, wind speed and direction, and station pressure. The NOAA/FSL mesonet stations reported every five minutes, whereas PAM-II transmitted one-minute data via satellite. These mesonet data were used in all aspects of the analysis and modeling effort, including comparison with the analysis from synoptic surface observations, and model initialization and validation.

### 3.3 NMC GRIDDED ANALYSES

These analyses are created by NMC for initializing operational forecast models. They are generated from a number of data sources, including synoptic surface observations, upper air measurements from rawinsonde, ocean-going ship reports, coastal buoys, aircraft reports, and satellite estimates of required parameters. These analyses are valid twice per day at 00 and 12 UTC. The gridded data utilized in this study had 2.5 degree horizontal resolution. The grids covered the U.S. and surrounding coastal regions, plus parts of Canada and Mexico. Standard reporting levels in the vertical were used, including 1000, 850, 700, 500, 400, 250, and 200 mb pressure levels. The NMC gridded data were useful for initializing and establishing boundary conditions for the mesoscale simulation.

### 3.4 RAWINSONDE DATA

These data provided vertical profiles of atmospheric temperature, humidity, and wind velocity. The data were collected for the U.S., Canada, and Mexico twice daily at 00 and 12 UTC. These data supplemented the gridded analyses, providing greater resolution of vertical atmospheric structure within the region of interest.

### 3.5 LAND USE CATEGORIES, LAND AND WATER PERCENTAGES, WATER BODY TEMPERATURES

These data were required to initialize RAMS modules that parameterize surface-atmosphere interactions. Land use and land/water percentages were provided on 25 km grids for northeastern Colorado. The land use data were derived from a U.S. Geological Survey (USGS) compilation of data from the Advanced Very High Resolution Radiometer (AVHRR) carried aboard the polar-orbiting NOAA satellites. Those data were translated to a Biosphere-Atmosphere Transfer Scheme (Dickinson et al., 1986). Water body temperatures were estimated from representative measurements taken by the authors for use in the RAMS soil/vegetation scheme.

## 4. DATA ANALYSIS AND MODEL SIMULATION RESULTS

Two types of analyses were accomplished using the data sets and numerical simulations generated during this investigation. The first analysis intercompared the representation of surface atmospheric fields from the relatively coarse synoptic surface observations with the analysis of data from the surface mesonets. The second analysis intercompared the mesonet surface analysis with the model simulation valid at that time. The surface analysis based on mesonet data was considered to represent the true state of the atmosphere in both cases because of the high spatial resolution of those data.

### 4.1 SURFACE TEMPERATURE

Figure 1 shows analyses and simulations of surface temperature valid at 1200 UTC on 28 July 1992. Figure 2b depicts the temperature analysis based on mesonet data. A pocket of relatively warm air existed just east of the Front Range of the Colorado Rocky Mountains, west of the 105 West meridian (vertical dashed line). Cool air was trapped in the South Platte River Valley in the upper right quadrant of that figure. The analysis based on sparser synoptic surface observations, shown in fig. 1a, displays reasonable agreement with the mesonet analysis. The warm pocket in the northwest corner of the domain (fig. 1b) is a notable exception. It is obvious that the mesonet data allow small scale features to be resolved in greater detail than is possible from the synoptic data.

Comparison of the 12 hour RAMS forecast valid at 1200 UTC with the mesonet analysis for that time reveals several interesting features. Figure 1c indicates considerably greater structure and detail in the simulation than was present in the synoptic surface observations used to initialize that simulation. The model also correctly simulates cooler temperatures in the

Figure 1a.

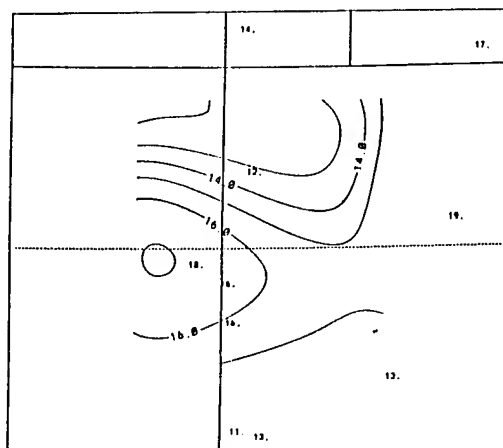


Figure 1b.

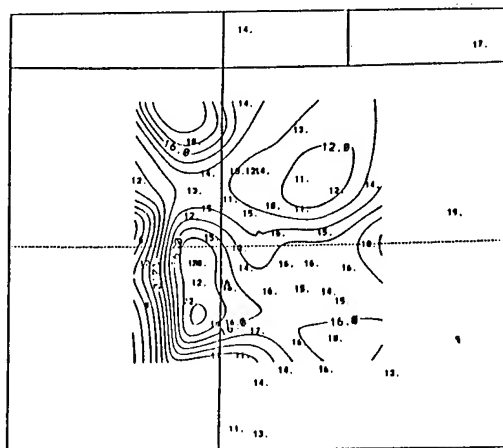


Figure 1c.

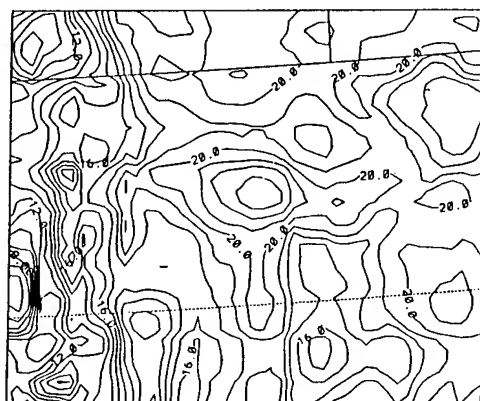


Figure 1. Surface Temperature Analyses and Simulation. Surface temperatures and isotherms (degrees Celsius, one degree intervals) over northeastern Colorado valid at 1200 UTC 28 July 1992; (a) from synoptic network observations; (b) from mesonet observations; (c) 12 hour RAMS forecast based on 0000 UTC data. State borders of Wyoming and Nebraska are seen at the top. Dashed lines indicate 105 degrees West longitude and 40 degrees North latitude.

South Platte Valley, although not as cool as observed. However, the warm air observed along the Front Range is placed too far east by the model. Table 1 summarizes the error characteristics of the temperature and relative humidity analyses and forecasts. It indicates that the simulation differs from the mesonet analysis more than the synoptic analysis does. The differences between those comparisons are not great, however.

#### 4.2 SURFACE RELATIVE HUMIDITY

The analyses and simulation of surface relative humidity at 1200 UTC 28 July 1992 are shown in fig. 2. As with the surface temperature plots, fig. 2a. shows that the synoptic analysis contains less detail than the mesonet analysis. The model forecast restores much of the missing detail, but it also introduces significant errors in the location and magnitude of humidity features. The reason for this error is the inadequate initialization of soil characteristics such as moisture and temperature. Table 1 reinforces the conclusion that significant errors exist in the humidity forecast compared to the mesonet analysis.

### 5. CONCLUSION AND SOME MILITARY CONSIDERATIONS

Despite the limited data and model analysis of this study, it illustrated several points that need to be considered in the DoD's push into the world of mesoscale weather support. Meso-model forecasts are dependent upon:

- synoptic forcing (the external grid),
- the physics of the model (hydrodynamic and radiative processes),
- the radiation and moisture fluxes in the boundary layer, and
- terrain and the frictional features of the terrain such as vegetation and the landscape roughness.

In our case study we had selected a situation where there was weak synoptic forcing. As a result, the RAMS forecast ran with the lower boundary physics and terrain being the dominating features.

#### 5.1 FUTURE CONSIDERATIONS

Sensor packages will have to include more measured parameters than the PAM sensors i.e., wind speed and direction, pressure, temperature, and dew point. These parameters are sufficient during a frontal passage or when major synoptic features are advecting into the area of concern, but during the periods when major synoptic scale features are not dictating local conditions, surface layer heat and moisture fluxes (or alternately, soil/vegetation temperature and moisture content) would also be helpful.

Databases that include detailed surface radiative, roughness, liquid water surface area and temperature, and evapo-transpiration characteristics should be maintained for mesoscale forecast model use. These quasi-constant values will dominate the forecast results at the mesoscale in the absence of well-defined synoptic-scale features.

Data grids at the mesoscale, many times larger than the forecasted area of interest, are needed to run a mesoscale forecast. As an example, a Desert



Relative Humidity			Error Analysis		
	Pam Analysis	SAO Analysis	12 RAMS Fcst	SAO Analysis	12 RAMS Fcst
Plains Stations					
1	97	76	22	-21.00	-75.00
2	48	57	26	9.00	-22.00
3	71	61	35	-10.00	-36.00
Lee side Stations			Average	-7.33	-44.33
1	73	63	20	-10.00	-53.00
2	90	57.5	21	-32.50	-69.00
3	56	47	24	-9.00	-32.00
Mountain Stations			Average	-17.17	-51.33
1	39	66	20	27.00	-19.00
2	38	45	23	7.00	-15.00
			Average	5.61	-28.44
Temperature					
Plains Station	Pam	SAO	12 RAMS		
1	11	13.2	21	2.20	10.00
2	16	15.3	16	-0.70	0.00
3	16	15.2	17.5	-0.80	1.50
Lee side Stations			Average	0.23	3.83
1	14	14	16.5	0.00	2.50
2	11	15	18	4.00	7.00
3	14	16.3	13	2.30	-1.00
Mountain Stations			Average	2.10	2.83
1	18	12.8	18	-5.20	0.00
2	12	15.3	9.5	3.30	-2.50
			Average	0.07	0.11

Table 1. Numerical Error Analysis Results. Error analysis (absolute deviation) for surface relative humidity and temperature for synoptic observations and RAMS simulation compared to mesonet observations.

Figure 2a.

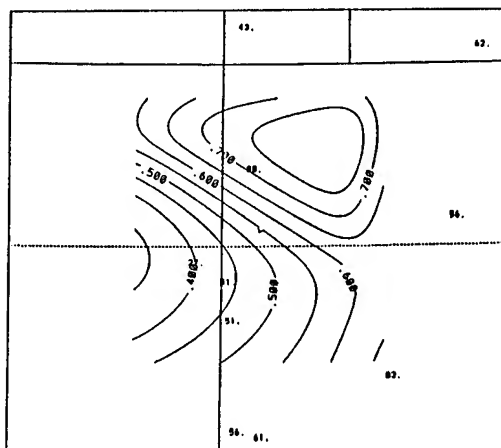


Figure 2b.

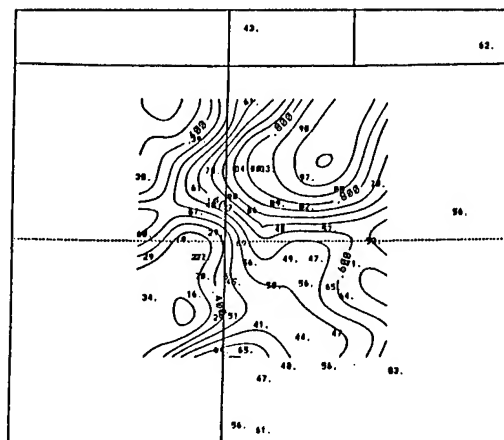


Figure 2c.

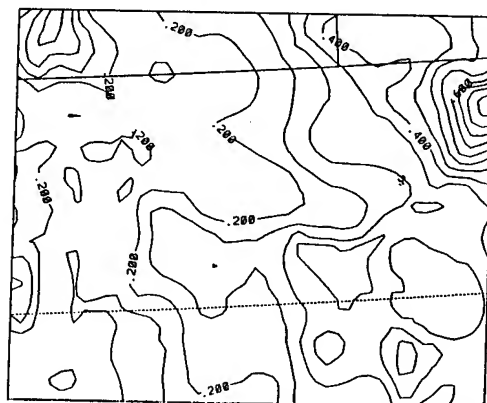


Figure 2. Surface relative humidity analyses and simulation. Relative humidity (percent) and contours (0.05 intervals) over northeastern Colorado valid at 1200 UTC 28 July 1992; (a) from synoptic network observations; (b) from mesonet observations; (c) 12 hour RAMS forecast based on 0000 UTC data. State borders of Wyoming and Nebraska are seen at the top. Dashed lines indicate 105 degrees West longitude and 40 degrees North latitude.

Storm forecast for Kuwait and Iraq would have needed a mesoscale data grid extending to Turkey and the Middle East, through India and southern Saudi Arabia. Since this is not a practical solution for a military contingency, remote satellite-based sounding, global analyses, and other data will have to be incorporated into the forecast model's initial data assimilation routines.

Data assimilation methods are currently a major weakness in the initialization of mesoscale forecast models. Barnes objective analysis schemes are typical of the methods used to analyze data. The terrain and physical processes, currently used in the forecast runs, are usually not used in the data analysis schemes. A true 4-dimensional data assimilation scheme such as adjoint or variational technique, will be needed along with the computer power to run these computationally demanding techniques.

#### 6.0 SUGGESTED FUTURE ACTIVITY

Develop a turn-key Observation System Simulation Experiment (OSSE) system. OSSEs are run to determine propagation errors and sensor requirements with the same objectives as this paper. Unfortunately, OSSE runs are done under contract constraints that make them expensive and less responsive to DoD managers than would be liked. A turn-key system could be developed and installed at USAFETAC or at a system program office to provide hard cost benefit information.

Combine the current generation of prognostic models, such as RAMS, with a high-quality diagnostic model. In the short-term the diagnostic models could improve the initialization quality and could be run iteratively with the prognostic model to improve our understanding of current conditions in regions of sparse observation.

Mesoscale planning scenarios could be run using prevailing climatological patterns fed through a mesoscale computer code. These scenarios could provide insight into local wind flows and temperature patterns associated with terrain, land/sea boundaries and so on. These scenarios could be run at very high resolution and archived for all likely contingency regions.

#### ACKNOWLEDGEMENTS

This paper was supported by METSAT Inc.'s internal R&D program.

#### REFERENCES

- Barnes, S.L., 1973: Mesoscale Objective Map Analysis Using Weighted Time-Series Observations. NOAA Tech. Memo. ERL NSSL-62, March, NSSL, NOAA, Norman, Oklahoma, 38 pp.
- Clark, T.L. and R.D. Farley, 1984: Severe Downslope Windstorm Calculations Two and Three Spatial Dimensions Using An Elastic Interactive Grid Nesting: A Possible Mechanism for Gustiness. J. Atmos. Sci., 41, 329-350.
- Dickinson, R.E., A. Henderson-Sellers, P.J. Kennedy, and M.F. Wilson, 1986. Biosphere-Atmosphere Transfer Scheme (BATS) for the NCAR Community Climate Model: NCAR Technical Note 275+STR, National Center for Atmospheric Research, Boulder, Colorado.
- Tremback, C.J., G.J. Tripoli, and W.R. Cotton, 1985: A Regional Scale Atmospheric Numerical Model Including Explicit Moist Physics and a Hydrostatic Time-Split Scheme. Preprints, 7th Conference on Numerical Weather Prediction, June 17-20, 1985, Montreal, Quebec, AMS.
- Tripoli, G.J., and W.R. Cotton, 1982: The Colorado State University Three-Dimensional Cloud/Mesoscale Model - 1982. Part I: General Theoretical Framework and Sensitivity Experiments. J. de Rech. Atmos., 16, 185-220.

AN OPTICAL PROFILE FUNCTION FOR MODELING  
EXTINCTION AND BACKSCATTER COEFFICIENTS  
IN VERY LOW STRATUS CLOUDS AND SUBCLOUD REGIONS

Neal H. Kilmer  
Physical Science Laboratory  
New Mexico State University  
Las Cruces, New Mexico 88003-0002, USA

Henry Rachele  
Battlefield Environment Directorate \*  
U.S. Army Research Laboratory  
White Sands Missile Range, New Mexico 88002-5501, USA

ABSTRACT

A theoretically based microphysics model developed by the authors was used to simulate a large number of vertical profiles of drop size distributions in very low stratus clouds and subcloud regions. These profiles were computed as a function of air mass type (maritime, rural, and urban), maximum liquid water content, and surface values of temperature, relative humidity, and visibility representative of worldwide conditions. These drop size distribution profiles were used with Mie efficiency factors to simulate vertical profiles of extinction and backscatter coefficients for eight wavelengths (0.55, 1.06, 3.0, 4.0, 5.0, 8.0, 10.6, and 12.0  $\mu\text{m}$ ). The extinction and backscatter profiles were then fit with the Rachele-Kilmer (RK) optical profile function to significantly simplify the computation procedure for Electro-Optical Systems Atmospheric Effects Library (EOSAEL) users. All constants required to evaluate the RK optical profile function have been placed on a disk pack, and a computer program for performing the calculations has been prepared. A step-by-step procedure for computing the extinction and backscatter coefficient profiles is presented in this paper, as well as results for a few selected input sets.

1. BACKGROUND AND INTRODUCTION

To optimize the design and operational capability of electro-optical systems for use in the lower atmosphere, one must have quantitative knowledge of the vertical structure of extinction, backscatter, and absorption. This understanding is needed for sensors operating at different transmission

---

\* formerly U.S. Army Atmospheric Sciences Laboratory

wavelengths. Limited knowledge of vertical structure of drop size distributions, extinction, backscatter, and absorption was documented before 1980. This knowledge was based largely on 18 vertical profiles of drop size and number data collected by the U.S. Army Atmospheric Sciences Laboratory (ASL) at Grafenwöhr and Meppen, Germany (Duncan et al., 1980). Additional data and research were needed to adequately address electro-optical problems in Europe, especially Germany. Consequently, ASL conducted additional field experiments at Meppen, Germany, in 1980. These field experiments, which were included in Project Meppen 80, were designed to measure drop sizes and number with height in conditions of moist haze, fog, and very low stratus clouds. These measurements were made with Knollenberg FSSP-100C aerosol spectrometers suspended from a tethered balloon that was allowed to descend, often through a cloud. These vertical profiles of drop size distributions were then used as input (assuming the drops were pure water) for Mie calculations (Miller, 1983), resulting in vertical profiles of extinction, backscatter, and absorption coefficients for wavelengths of 0.55, 1.06, 4.0, and 10.6  $\mu\text{m}$ . From these data, an early empirical vertical profile model was evaluated and modified.

Vertical profiles of extinction coefficients ( $\sigma_e$ ) have been approximated (in many ASL studies) by a double exponential function (Heaps, 1982; Rachele and Kilmer, 1991; Kilmer and Rachele, 1992) of height ( $z$ ) above ground level; that is,

$$\sigma_e = A \exp [B \exp (Cz)] , \quad (1)$$

where  $A$ ,  $B$ , and  $C$  are constants with appropriate values for the case being approximated. In the past, the values of  $A$ ,  $B$ , and  $C$  have been determined empirically by fitting data collected from a limited number of specific locations. The Heaps version of an empirical model (the double exponential form) was coupled with a U.S. Air Force model that includes drop size distribution expressions by Shettle and Fenn (1979), resulting in the vertical extinction profile model currently in the XSCALE module of EOSAEL.

In addition to the empirically developed electro-optical models, ASL opted to develop a theoretically based microphysical model that together with Mie theory would produce extinction, backscatter, and absorption coefficients. The evolution of the Rachele-Kilmer microphysics model (hereafter designated the RK model) has been documented in several papers, with Kilmer and Rachele (1992) being the most recent proceedings paper. The current RK model (Rachele and Kilmer, 1992) is based on the concept that a cluster of drops embedded in a mass of moist air rises from a reference height to the top of a cloud. The initial drops of the cluster are characterized by the reference level drop size distribution, but as the cluster rises the drop sizes change. The physical and thermodynamical changes of the drops and their environment are computed as though a hypothetical completely permeable sphere envelops the drops and their environment.

The purpose of this paper is to present a relatively simple continuous function, the RK optical profile function, discussed in section 3, that can be executed easily by EOSAEL users to simulate vertical profiles of extinction and backscatter coefficients in very low stratus clouds and subcloud regions representative of worldwide conditions for various combinations of air mass type, maximum liquid water content, and surface level temperature, relative humidity, and visibility. The extinction and

backscatter coefficient profiles were simulated for eight wavelengths (0.55, 1.06, 3.0, 4.0, 5.0, 8.0, 10.6, and 12.0  $\mu\text{m}$ ). All constants required to evaluate the RK optical profile function for the given combinations have been placed on a disk pack, and a computer program for performing the calculations has been prepared. A step-by-step procedure for computing the extinction and backscatter coefficient profiles is presented in this paper, as well as results for a few selected sets of input values.

## 2. MODEL CONCEPT

The RK microphysics model is described in a detailed technical report (Rachele and Kilmer, 1992). Execution of this model requires an estimate of the cloud top height; dry particle chemistry; air mass type (maritime, rural, or urban); and reference level (2 m above ground level) values of temperature, pressure, relative humidity, and visibility. The relative humidity, visibility, and air mass type are required to define the Shettle-Fenn (1979) bimodal lognormal distributions, which are used to define the reference level drop size distributions. In this work, each of these distributions is truncated to omit drops that would form from condensation nuclei having radii less than 0.004  $\mu\text{m}$ .

Our approach is to compute Shettle-Fenn drop size distributions at the reference level for different combinations of relative humidity, visibility, and air mass type. Each of these drop size distributions then varies with height in accordance with the thermodynamics of an ascending cluster. For 15 systematically selected combinations of reference level Shettle-Fenn parameters, we vary the reference level ambient air temperature (0, 15, and 30  $^{\circ}\text{C}$ ). The estimated cloud top height, which also can be varied using the full RK model, was chosen to be 500 m above ground level for all of the cases simulated in this study. The pressure at the reference level is always set at 1000 mbar (1 mbar = 1 hPa) since the drop size distribution is not sensitive to pressure changes. However, we have found that the distribution in the cloud varies with the liquid water content of the cloud. Hence, we also vary input parameters to make the maximum liquid water content approximately 50, 75, and 100 percent of the quasi-adiabatic values. (In this work, a "quasi-adiabatic" simulation is near adiabatic, differing from truly adiabatic by allowing small amounts of entrainment and diffusion from outside the ascending sphere.) The 15 reference level combinations of Shettle-Fenn parameters, 3 choices of maximum liquid water content, and 3 choices of temperature lead to  $15 \times 3 \times 3 = 135$  drop size profiles. Applying Mie theory, we then obtain 135 extinction coefficient profiles and an equal number of backscatter coefficient profiles for each of 8 wavelengths. The fitting method indicated in the next section is used in determining the RK optical profile function constants for approximating each of the  $135 \times 8 \times 2 = 2160$  resulting profiles. Fitting constants have been determined for all of the 2160 cases.

## 3. THE RK OPTICAL PROFILE FUNCTION

Several functions were considered for approximation of vertical profiles of extinction coefficients. The most promising is the following function, eq. (2), which is designated as the "RK optical profile function," where  $\sigma_e$  is the extinction coefficient. For backscatter,  $\sigma_e$  is replaced with  $\beta$ .

$$\sigma_e = \sigma_{e1} \left( \frac{\sigma_{e2}}{\sigma_{e1}} \right) \left( \frac{z - z_1}{z_2 - z_1} \right)^{N(z)} \quad (2)$$

In this equation,  $z_1$  is the reference height or the height of the hinge point, and the corresponding  $z_2$  is the height of the hinge point or the "highest forced match" near the top of the cloud, respectively. The hinge point defines the boundary between the function's two pieces. The hinge point typically is chosen to be the inflection point at the base of the cloud on a  $\ln \sigma_e$  or  $\ln \beta$  versus  $z$  curve defined by RK model data. Both pieces are described according to eq. (2) but have different values for the constants and (in at least some of the cases involving backscatter) may have different functional forms to describe  $N(z)$ .  $N(z)$  is a function of  $z$  and is represented as

$$N(z) = \exp (c_* + d_* z + e_* z^2 + f_* z^3) , \quad (3)$$

or

$$N(z) = A_0 + 2 \sum_{n=1}^{N_A} A_n \cos \left[ \frac{2\pi n(z - z_{F1})}{z_{F2} - z_{F1} + 1} \right] - 2 \sum_{n=1}^{N_B} B_n \sin \left[ \frac{2\pi n(z - z_{F1})}{z_{F2} - z_{F1} + 1} \right] \quad (4)$$

in the range  $z_{F1} \leq z \leq z_{F2}$ . In this pair of equations,  $A_0$ , the  $A_n$  values, the  $B_n$  values,  $z_{F1}$ ,  $z_{F2}$ ,  $c_*$ ,  $d_*$ ,  $e_*$ , and  $f_*$  are constants. When polynomial fitting is used for  $\ln N(z)$  versus  $z$  data in the second piece, the height at which the maximum extinction or backscatter coefficient between 440 and 492 m, inclusive, above ground level occurs is often used as the height of "highest forced match." When short-range structure causes this maximum to be significantly greater than the general trend, such as happens in some simulated backscatter coefficient profiles for wavelengths of 0.55 and 1.06  $\mu\text{m}$ , then the height of "highest forced match" may be refined on a case-by-case basis to improve the goodness of fit. When Fourier analysis is used to fit  $N(z)$  versus  $z$  data in the second piece, the height of "highest forced match" is selected on a case-by-case basis, and each resulting series of Fourier coefficients is truncated to retain only the lowest-frequency components. The number of coefficients retained is selected on a case-by-case basis. The number of Fourier constants retained,  $N_A + N_B + 1$ , is always much less than the number of RK modeled height levels (data points),  $z_{F2} - z_{F1} + 1$ , used in the Fourier analysis.

Equation (2) was solved for  $N(z)$  as a function of  $z$  and  $\sigma_e$  simulated by the RK model. The resulting expression for  $N(z)$  is

$$N(z) = \frac{\ln \left( \frac{\ln \sigma_e - \ln \sigma_{e1}}{\ln \sigma_{e2} - \ln \sigma_{e1}} \right)}{\ln \left( \frac{z - z_1}{z_2 - z_1} \right)} \quad (5)$$

Using a vertical profile of  $N(z)$  thus obtained,  $\ln N(z)$  versus  $z$  data were fitted with two cubic polynomials (one for data below the hinge height



representative of the subcloud region and the other for data above the hinge height for the cloud region) to determine values of the constants in eq. (3) for all of the extinction coefficient profiles and some of the backscatter coefficient profiles. For some of the backscatter coefficient profiles, the second (higher) piece was fitted using Fourier analysis of  $N(z)$  versus  $z$  data, resulting in the fitting expression given by eq. (4). Even for those profiles, the first (lower) piece was fitted by using a cubic polynomial to fit  $\ln N(z)$  versus  $z$  data, as in the other cases. We anticipate that fits to many more of the backscatter coefficient profiles can be improved by using Fourier analysis for the second piece. Work is continuing in this area.

The range typically chosen for fitting  $\ln N(z)$  versus  $z$  data by polynomial in the upper piece is from the second height level at or above the hinge height (since a perfect match is forced at the first height level at or above the hinge height) to a level somewhat below the height of "highest forced match." The range used for fitting  $N(z)$  versus  $z$  data by Fourier analysis in the upper piece is chosen on a case-by-case basis from the data between the hinge height and the height of "highest forced match."

#### 4. COMPUTER PROGRAM FOR EVALUATING THE RK OPTICAL PROFILE FUNCTION

The computer program RKOPF (RK optical profile function) is designed for interactive use and prompts the user at each step. Stored fitting information is located, applied in calculations, and used to determine whether eq. (3) or eq. (4) is to be used to calculate  $N(z)$  for the second piece. The fitting information is stored on a disk pack available immediately to Battlefield Environment Directorate (formerly ASL) computer users. If approval is obtained, this information can be made available to other users also. The RK optical profile function is programmed into the user computer program.

The first set of user choices is employed to determine which set (or sets) of fitting constants is to be applied. The user is to indicate each of these choices by entering an integer corresponding to the number of the desired choice. First, the user is presented with a choice of three air mass types (maritime, rural, and urban) and is asked to select one. Next, the user is asked to choose one of three values (90, 95, or 99 percent) for the relative humidity at the reference height. If 95 percent is chosen, the user is informed that the visibility at the reference height is set automatically at 5 km. If one of the other relative humidity values is chosen, the user is asked to select the visibility (either 2 or 10 km) at the reference height. The user is then presented with a choice of three reference height ambient air temperatures (0, 15, and 30 °C) and asked to choose one. The user is then prompted to select the desired value for the maximum liquid water content in terms of a percent (50, 75, or 100 percent) of the quasi-adiabatic (100 percent) value that would be obtained if all of the other input parameters were the same. The user is then asked to choose one of the eight available wavelengths. This set of selections is completed when the user indicates the type(s) of profile(s) desired (extinction coefficient, backscatter coefficient, or both).

The next set of user responses enables the user to define some details about the profiles he/she is to receive. If "both" is selected in the last choice above, this set of choices is repeated for the second profile. The user is

prompted for the name of the file that is to contain the profile data and is to respond by entering a character string. After that, the program reveals the height limits of validity of the calculated profile. The user may accept these as the bounds of the profile to be calculated, or he/she may specify some range within the range of validity by entering two real numbers (not necessarily integers). Since the RK optical profile function is continuous, function values can be calculated for any desired height spacing, as long as all of the heights are within the range of validity. Therefore, the user may specify the height spacing desired for output data. When prompted to do so, the user is to enter a real number (not necessarily an integer).

The one or two profiles requested are written as one or two ASCII files readable by a Fortran program. The first line, in 3i5 format, gives the number of data points and two small integers, which can be ignored or interpreted by some software as the line type and symbol type requested for a plot. The rest of each output file contains the data and uses one line for each data point. Each of those lines may be read as free format and contains the RK optical profile function value, which approximates the extinction coefficient in  $\text{km}^{-1}$  or backscatter coefficient in  $\text{km}^{-1} \text{sr}^{-1}$ , followed by the height in meters above ground level for which this coefficient is approximated.

## 5. RESULTS

RK optical profile function constants were determined by using simulated extinction or backscatter coefficient profiles one at a time. When the RK optical profile function was used for extinction coefficient profiles with  $N(z)$  calculated according to eq. (3), agreement of calculated curves with RK model curves generally appeared very good. For RK model extinction coefficient profiles that appeared wavy, calculated fitting curves appeared to be reasonable, strongly smoothed curves. The form of the RK optical profile function that uses eqs. (2) and (3) matched simulated extinction coefficient profiles to within 9 percent (root mean square of the residuals divided by mean extinction coefficient, where both quantities are taken from 2 m above ground level to the height at which the maximum extinction coefficient between 440 and 492 m, inclusive, above ground level occurs) for every one of our tries and to within 2 percent for 88.4 percent of our tries. Figure 1 shows a typical example, which was selected because it is very close to the fiftieth percentile in goodness of fit ranking among extinction coefficient profiles. This figure includes the full RK microphysics model curve for a wavelength of  $10.6 \mu\text{m}$  as a solid line and an RK optical profile function fitting curve as a dashed line.

Polynomials were not nearly as successful in fitting  $\ln N(z)$  when  $N(z)$  was to be approximated according to eq. (3) for upper pieces of backscatter coefficient profiles. Many RK model backscatter coefficient profiles showed such extensive structure that we decided not to eliminate it by smoothing. Instead, we successfully fitted  $N(z)$  for upper pieces of selected backscatter coefficient profiles with Fourier series to obtain constants for use with a combination of eqs. (2) and (4). In the case of backscatter coefficient fits involving Fourier series, we found that the goodness of fit depends mainly on the number of terms used. Enough terms were used to retain the major

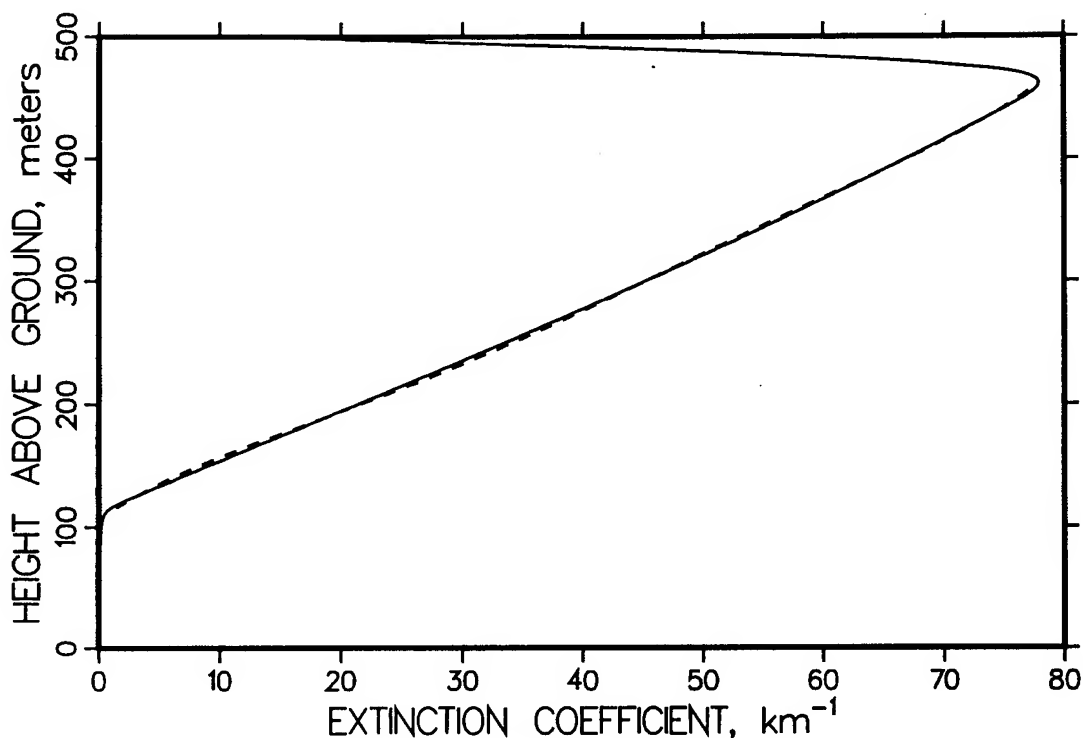


Figure 1. An extinction coefficient profile simulated using full RK model (solid line) and then approximated using RK optical profile function (dashed line).

oscillations as well as the trends in the profiles. For highly oscillatory curves, as many as 24 Fourier constants were used. Results for fitting one simulated backscatter coefficient profile for a wavelength of  $4.0 \mu\text{m}$  with Fourier fits using different numbers of constants are shown in fig. 2.

Out of the 2160 sets of RK optical profile function constants generated in this study, a few sets were chosen for simulating profiles to use in this paper to illustrate results. Effects on calculated RK optical profile function extinction coefficient profiles from varying the maximum liquid water content and reference level relative humidity are shown in figs. 3 and 4 for a wavelength of  $0.55 \mu\text{m}$ .

## 6. SUMMARY AND CONCLUSIONS

The authors have developed a theoretically based very low stratus cloud/subcloud model, which is documented in other papers. Drop size distribution data simulated using this model are used with Mie efficiency factors to simulate vertical profiles of extinction and backscatter coefficients for a variety of atmospheric conditions that can occur worldwide. This model was used in this study to generate extinction and backscatter coefficient profiles that vary with air mass type, maximum liquid

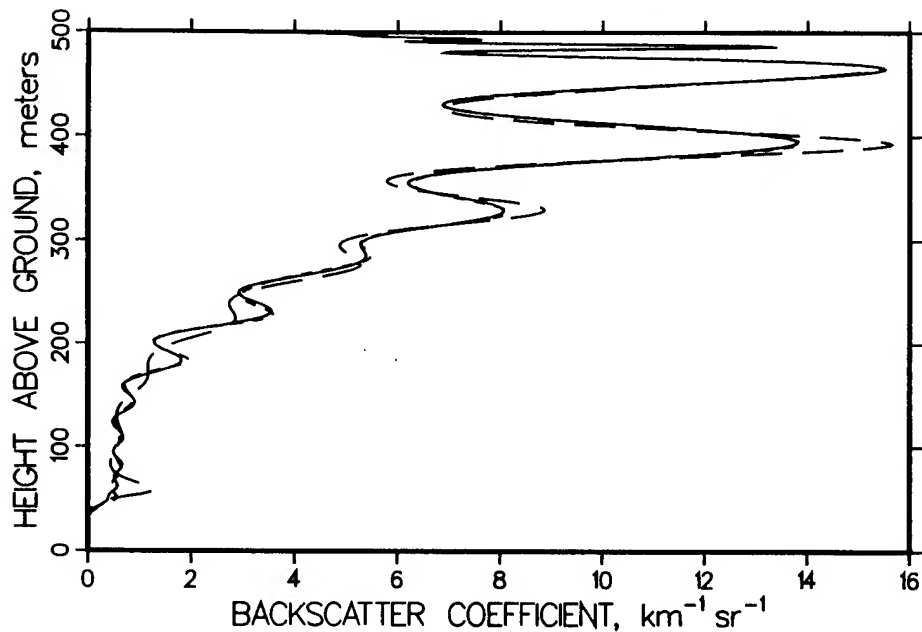


Figure 2. A backscatter coefficient profile simulated using full RK model (solid line) and then approximated using RK optical profile function with Fourier series containing 14 (long dashes) and 24 (short dashes) constants.

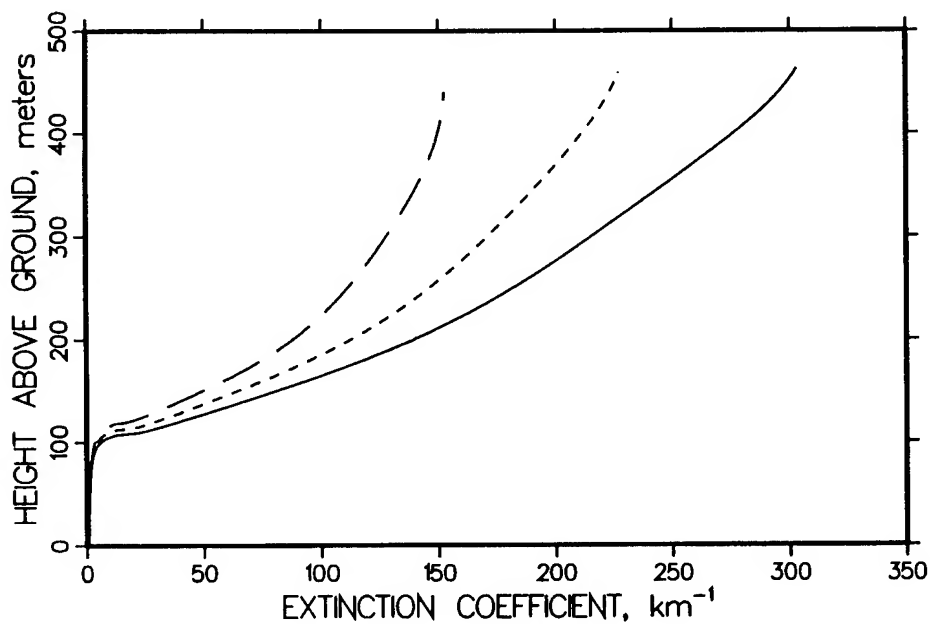


Figure 3. Effect of maximum liquid water content (solid line: 100 percent of quasi-adiabatic; short dashes: 75 percent; long dashes: 50 percent) on extinction coefficient profiles calculated using RK optical profile function.

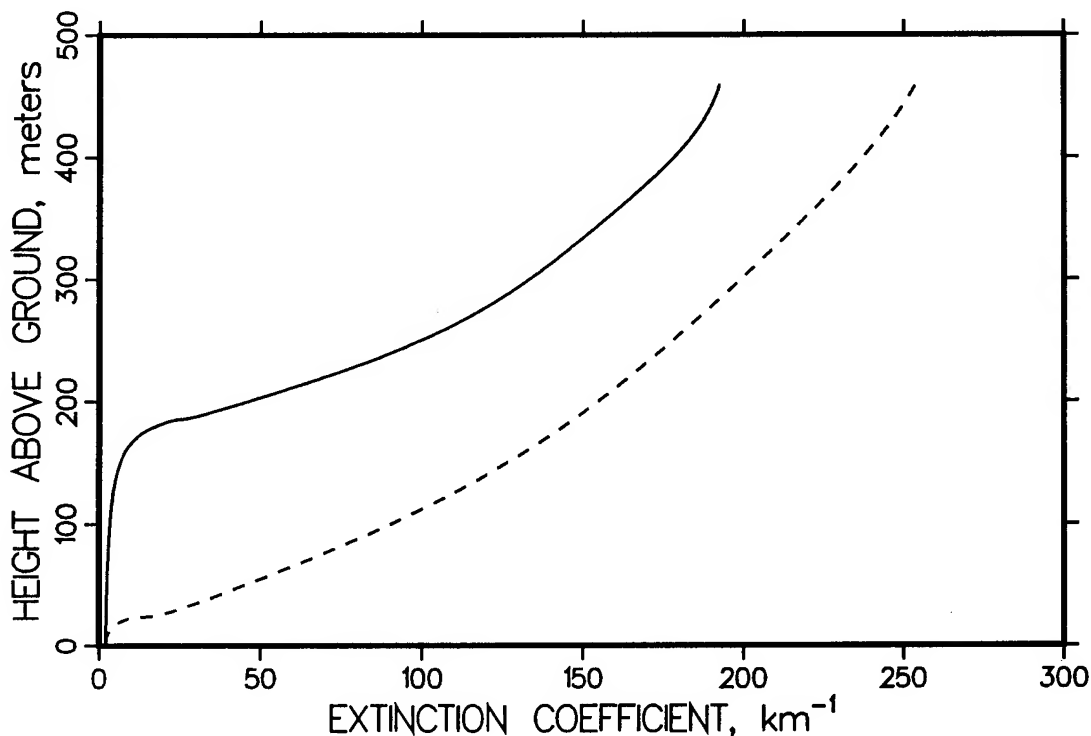


Figure 4. Effect of reference level relative humidity (0.90 for solid line; 0.99 for dashed line) on extinction coefficient according to RK optical profile function.

water content, and reference level values of temperature, relative humidity, and visibility. These profiles were then fitted individually with the RK optical profile function. To determine values of the constants in eq. (3) or (4) for each combination of RK microphysics model input and wavelength, a fitting procedure was used with vertical profiles of the natural logarithm of extinction or backscatter coefficient from the full RK microphysics model and Mie calculations.

Constants for the RK optical profile function were determined for 1080 simulated extinction coefficient profiles and 1080 simulated backscatter coefficient profiles. Curves calculated with the appropriate form of this function generally appeared to be very good approximations of profiles simulated using the full RK model. When used to approximate RK model profiles that exhibited high-frequency waviness in addition to general trends, calculated curves appeared to be reasonable, strongly smoothed curves that represented the general trends well. For some backscatter coefficient profiles, fitting  $N(z)$  with Fourier series was used to preserve low-frequency waviness that seemed too significant to discard. Since fitting with Fourier series is performed on a case-by-case basis with considerable human intervention, this type of fitting is quite time-consuming. Apparently there are still a number of cases among the 2160 simulated profiles for which the fits can be improved significantly by changing from polynomial fitting to Fourier fitting. Work is continuing in this area.

The RK optical profile function constants for the 1080 extinction coefficient profiles and 1080 backscatter coefficient profiles have been placed on a disk pack for access by Battlefield Environment Directorate computer users. We propose that these constants be made available to any EOSAEL users. Use of a computer program to calculate the extinction and backscatter coefficient profiles for a given set of inputs is outlined in section 4 of this paper. Proper execution of this program produces profiles that are in excellent agreement with the essence of profiles (this sometimes implies smoothing) produced by using the complete RK microphysics model. Calculation of extinction and backscatter RK optical profile function constants for some other cloud top heights (other than 500 m) is planned.

#### ACKNOWLEDGMENT

The authors appreciate the work done by Gregory N. Whitfield and Michael S. Paz of the Physical Science Laboratory. They used the full RK model many times to determine self-consistent sets of values to use as input and obtained most of the full RK model extinction and backscatter coefficient profiles used in this study. They have helped considerably in the creation of a very large number of plots. Further, Mr. Whitfield has helped in some of the Fourier fitting.

#### REFERENCES

- Duncan, L. D., J. D. Lindberg, and R. B. Loveland, 1980: An Empirical Model of the Vertical Structure of German Fogs. ASL-TR-0071, U.S. Army Atmospheric Sciences Laboratory, White Sands Missile Range, NM 88002.
- Heaps, M. G., 1982: A Vertical Structure Algorithm for Low Visibility/Low Stratus Conditions. ASL-TR-0111, U.S. Army Atmospheric Sciences Laboratory, White Sands Missile Range, NM 88002.
- Kilmer, N. H., and H. Rachele, 1992: Analytic Functions for Modeling Vertical Profiles of Extinction in and Beneath Very Low Stratus Clouds. In Atmospheric Propagation and Remote Sensing, Anton Kohnle and Walter B. Miller, eds., Proceedings SPIE, 1688, 132-143.
- Miller, A., 1983: Mie Code Agaus 82. ASL-CR-83-0100-3, U.S. Army Atmospheric Sciences Laboratory, White Sands Missile Range, NM 88002.
- Rachele, H., and N. H. Kilmer, 1991: A Derivation for Determining Double Exponential Liquid Water Content and Extinction Profiles from Discrete Data. ASL-TR-0290, U.S. Army Atmospheric Sciences Laboratory, White Sands Missile Range, NM 88002.
- Rachele, H., and N. H. Kilmer, 1992: Unified Very Low Stratus Cloud/Subcloud Microphysics Model. ASL-TR-0309, U.S. Army Atmospheric Sciences Laboratory, White Sands Missile Range, NM 88002.
- Shettle, E. P., and R. W. Fenn, 1979: Models for the Aerosols of the Lower Atmosphere and the Effects of Humidity Variations on Their Optical Properties. AFGL Technical Report AFGL-TR-79-0214, Air Force Geophysics Laboratory, Hanscom AFB, MA 01731.

## ACOUSTICAL SCATTERING FROM ATMOSPHERIC TURBULENCE

Harry J. Auvermann  
Battlefield Environment Directorate\*  
White Sands Missile Range, New Mexico 88002-5501, USA

George H. Goedecke  
New Mexico State University  
Las Cruces, New Mexico 88003, USA

### ABSTRACT

The objective of the ASL research effort in acoustic propagation is to provide the Army with a multi-stream model for investigating acoustic detection systems. The first step in developing this model is to account for turbulent scattering. Five elements are necessary to accomplish this step--(1) model the turbulent region as a collection of vortices with a distribution of characteristic sizes/velocities; (2) characterize each vortex (turbule) as a known (or assumed) velocity distribution in three space; (3) solve the fluid equations to determine the scattering from each turbule; (4) sum the contributions to the scattered sound pressure level at the detector location of all turbules accounting for the propagation characteristics of the atmospheric medium; and (5) incorporate the algorithms devised above into existing (or appropriately modified) propagation models. Progress in these five areas will be reported.

### 1. INTRODUCTION

Acoustic propagation in the atmosphere is influenced by a number of factors that have to be considered in any model designed to predict detector response at battlefield distances. Figure 1 illustrates a possible scenario that, along with fig. 2, incorporates most of the factors of interest. Figure 1 shows an object of interest marked S that is a source of the acoustic field marked F. An acoustic detector marked D is some distance from the source. An obstruction marked O illustrated as a ridge intervenes between S and D. Atmospheric turbulence is marked T and the reflecting ground surface is marked P. E, M, and R are the diffracted, turbulence scattered, and reflected fields, respectively. The electronic signal from D marked V is produced by a superposition of the direct field F (if any) with E, M, and R plus the intrinsic detector noise denoted by N. The problem of interest is to determine theoretically the total field given the scenario. The importance of acoustics as a non-line-of-sight detection tool for the Army is also illustrated in fig. 1. The detector is shown in what is known as a shadow zone by analogy with ray propagation from optics.

A shadow zone can also be produced by an upwardly refracting atmosphere. This effect is illustrated in fig. 2. In the figure, a source is located at an elevation of 10 m in an atmosphere with a constant sound speed gradient. The ray

---

\*formerly U.S. Army Atmospheric Sciences Laboratory (ASL)

path shown just grazes the ground and is known as the limit ray. The shadowzone is to the right of the curve minimum and between the curve and the range axis. The indicated height at a range of 7000 m is 174.89 m. The shadow zone begins at a range of 1351.32 m. Current acoustic propagation models do not account for terrain induced shadow zones as depicted in fig. 1 but are able to model propagation in a stratified atmosphere whose characteristics vary only with height as that depicted in fig. 2.

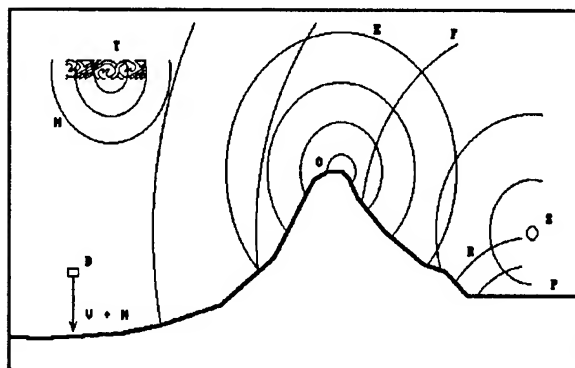


Figure 1. Acoustic detection scenario.

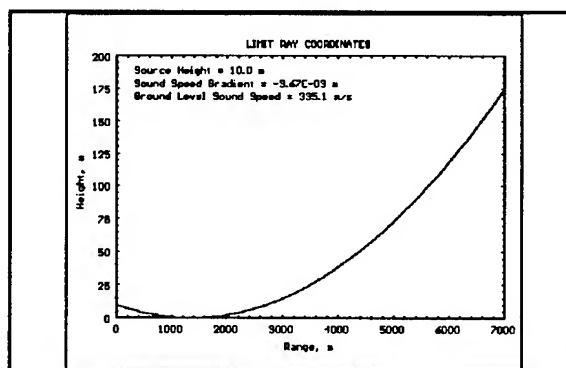


Figure 2. Limit ray coordinates locating the shadow zone.

## 2. WAVE SOLUTIONS FOR ACOUSTIC FIELDS

While the ray solution shown in fig. 2 accounts for the constant atmospheric sound speed gradient, it does not account for the reflections that occur at the ground nor does it account for the wave nature of sound. Figures 3 and 4 illustrate the effect of the ground but not the full-wave nature of sound. As a check on the more sophisticated models, a propagation model called here SPHERICAL was written that models a uniform atmosphere situated above a flat earth, the latter modeled by an impedance change. These plots using data produced by SPHERICAL are essentially ray solutions with the ground effect modeled as an image source below ground level, with the image field phase and amplitude modified according to the impedance discontinuity. Figure 3 shows a contour plot from SPHERICAL that represents the sound field for a uniform atmosphere, frequency of 170 hertz, source height of 10.0 m, sound speed 335.1 m/s, and a ground impedance ratio of  $8.44 + j10.0$ . The heavy line is the limit ray position from fig. 2. Figure 4 shows the region near the origin in greater detail with the horizontal and vertical scales the same. Interference between the direct and the ground reflected waves is clearly demonstrated.

To demonstrate the full-wave nature of sound propagation, a more sophisticated model is necessary. The fast field program (FFP) (Raspet, 1985) is a full-wave solution to the propagation equation that accounts for a nonuniform atmosphere using horizontal planar layers, the propagation constants of each layer being uniform. Ground effects are introduced by an impedance boundary just as in the SPHERICAL program. Since the ultimate goal was to model turbulence effects as scattering, FFP was included as a subroutine in a driver that produced data from multiple sources, multiple scatterers, and multiple detectors. This program is named the acoustical multistream propagation program (AMPP) (Auvermann, 1992). AMPP loops through a set of sources, a set of scatterers, and a set of detector positions, saving the sound field results of each calculation. The



results for the detector position set provides the data for contour plots shown below. AMPP preserves the sound pressure amplitude and phase, as well as the exitance (watts/square meter) so that a coherent summation is possible for a reasonable number of sources or scatterers. This coherent summation capability of AMPP has not been exercised because of the diversion caused by the interesting feature of the field in shadow zones that is discussed below.

To exercise the AMPP program, the scenario of fig. 1 was calculated for an upward refracting atmosphere. The results are shown in figs. 5 and 6. The uniform sound speed gradient was  $-3.67 \cdot 10^{-3} \text{ s}^{-1}$ , with speed at zero height of 335.1 m/s and a ground impedance ratio as in the SPHERICAL program results of figs. 3 and 4. The heavy line in each figure is the limit ray path from figure 2. As seen by comparison of fig. 5 with fig. 3, SPHERICAL and AMPP show virtually identical contours out to a range of 1000 m. Beyond 1000 m, the AMPP upper contour parallels the limit ray path to a high degree of accuracy. The plot in fig. 6 shows in greater detail the sound exitance level in the shadow zone below the limit ray path for the range interval 5000 m to 7000 m.

Finding unexpectedly high sound levels in the shadow zone has diverted the investigation of turbulence scattering into this region because the expected scattered level was approximately the same. The nature of the nonturbulence related sound level was investigated. To eliminate the possibility that computational precision was inadequate, AMPP was changed to 64-bit precision. The code was run at higher frequencies, which should produce faster roll-off at the shadow zone boundary. Changes of ground impedance by an order of magnitude in either direction and a three-to-one increase of sound speed gradient were tried. All these changes produced no material change in the results. The conclusion was that the sound levels reported by AMPP are real and to be expected. The mechanism is most likely the reflection of a spherical wave by a plane boundary, which will produce a field somewhat more complicated than that of the reflection of a plane wave at a plane boundary. To expedite the turbulence investigation, an artificially attenuated shadow zone contour picture was constructed as reported in section 5.

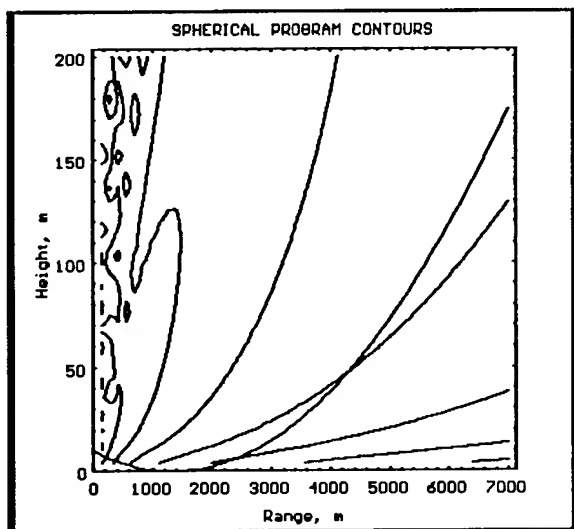


Figure 3. Uniform atmosphere contours.

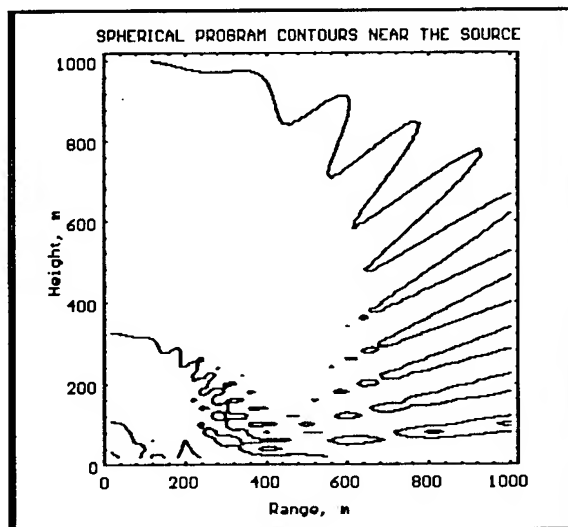


Figure 4. SPHERICAL program contours near the source.

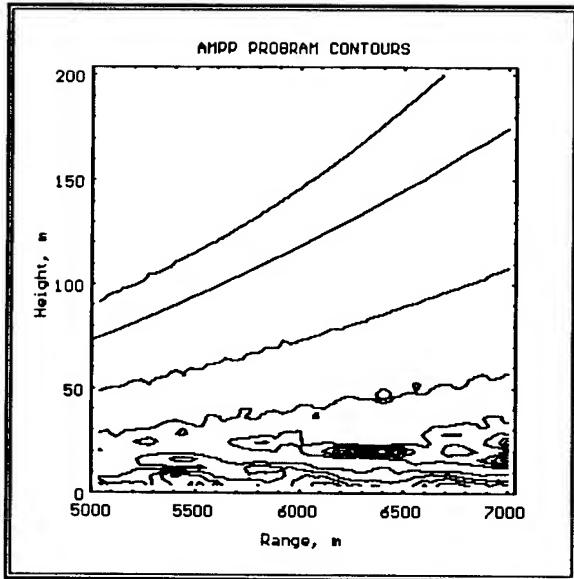


Figure 5. Upward refracting atmosphere results.

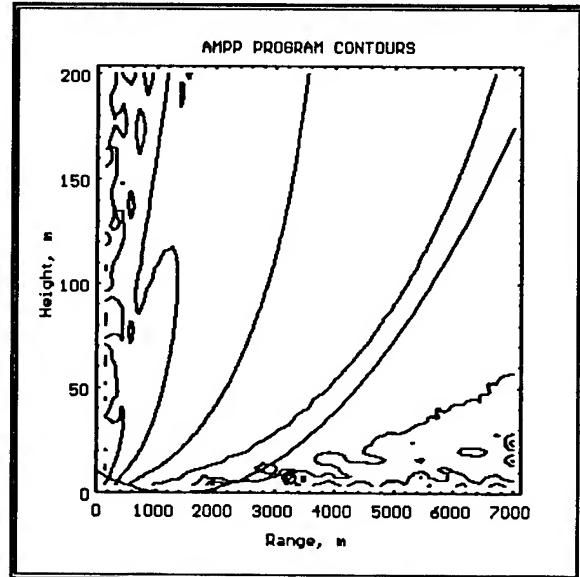


Figure 6. Expanded AMPP program results for longer ranges.

### 3. SCATTERING BY TURBULENCE

Following the "structural approach" to turbulence, acoustical scattering from turbulence is by analogy with optical scattering from aerosols considered as scattering from a collection of eddies (or turbules as hereinafter referred to) of different sizes with a number concentration assigned to each size. If the scattering cross section and number concentration for each size class is available, then a scattering calculation can be made using the geometry of fig. 7. Figure 7 shows a source, a detector, and a turbule positioned over flat ground. The coordinate system to be used is also shown. The horizontal coordinate variable is  $r$  and the vertical coordinate variable is  $z$ . The scattering angle variable  $\theta$  is also shown. The quantities  $R_{st}$ ,  $R_{td}$ , and  $R_{sd}$  are slant ranges. In this paper, all distances are expressed in meters. The coordinates of the principal objects chosen for this scenario and the associated slant ranges are as follows:

$r_s = 0.0$ ,	$z_s = 10.0$	$R_{st} = 5,053.588$
$r_t = 5000.0$ ,	$z_t = 744.0$	$R_{td} = 1,246.409$
$r_d = 6000.0$ ,	$z_d = 0.0$	$R_{sd} = 6,000.008$

Subscripts  $s$ ,  $t$ , and  $d$  stand for source, turbule, and detector, respectively. With this geometric arrangement the scattering angle is  $\theta = \pi/4$  radians. Symbols to be used and not already defined are listed in table 1 along with units and values.

The value of  $\Omega_d$  in table 1 was chosen as representative, leading to the determination of the scattering volume from eq. (1).

$$\Omega_d = 2\pi[1 - \cos(\phi)] \quad r_v = R_{td} \sin(\phi) \quad V_{sca} = \pi r_v^2 l \quad (1)$$

Assuming an isotropic source in an infinite, lossless uniform medium, the exitances at the turbule and at the detector are

$$E_{It} = E_s (R_s/R_{st})^2 = 3.9156 \cdot 10^{-8}$$

$$E_{Id} = E_s (R_s/R_{sd})^2 = 2.7777 \cdot 10^{-8}$$

$$L_{It} = 10 \log_{10}(E_{It}/E_s) = -74.07 \text{ dB}$$

$$L_{Id} = 10 \log_{10}(E_{Id}/E_s) = -75.56 \text{ dB}$$

The logarithmic equivalent of these quantities, called level and expressed in decibels (dB), is given above also. The letter I in the subscripts indicates these quantities are infinite space values. In table 1,  $E_t$  was set equal to  $E_{It}$ . Equation (2) is used to calculate the scattered exitance.

$$\sigma_{sca}(a, v, \theta) = \pi a^2 \langle Q^{(1)}(k, \hat{r}) \rangle \quad \sigma_{sca}(v, \theta) = \int_0^\infty da \sigma_{sca}(a, v, \theta) n_a(a)$$

$$E_d = \frac{E_t \sigma_{sca}(v, \theta) V_{sca}}{R_{td}^2} \quad (2)$$

The nature of the turbule concentration function  $n_a(a)$  in eq. (2) is not known at this time so an approximate evaluation of the integral over turbule size will be made. This approximation will involve selection of a typical size  $a_t$  and a corresponding typical number concentration  $n_t$  with the integral being given by the product of  $n_t$  and  $\sigma_{sca}(a_t, v_t, \theta)$ , where  $v_t$  is the velocity of the typical turbule. The scattering volume  $V_{sca}$  is that of a length  $l$  cylinder with a radius at midpoint set by the detector field of view  $\Omega_d$ .

The scattering efficiency of turbules was determined previously (Goedecke, 1992). Theory was developed for acoustical scattering by localized quasi-static atmospheric turbules that contain both flow and sound speed variations. Differential and total cross-section expressions have been found for a Gaussian spinning turbule model of effective radius  $a$  by using the first Born approximation, which is estimated to be valid for  $ka < 5$  for  $v_{max}/c_\infty < 0.1$ . The contributions of the sound speed variation are about three orders of magnitude smaller than those of the flow. The latter are proportional to  $(ka)^6$  and  $[\sin(\theta) \cos(\theta) \cos(\theta_\alpha) \sin(\phi - \phi_\alpha)]^2$ , where  $(\theta, \phi)$  are the (polar, azimuthal) scattering angles,  $(\theta_\alpha, \phi_\alpha)$  are the spin axis angles. The contributions of the sound speed inhomogeneities vary as  $(ka)^4$  and have a somewhat Rayleigh-like dependence on  $\theta$ .

Analytical results from this theory for turbule scattering efficiency averaged over turbule spin axis orientation are used above. These results are summarized here. A model spinning turbule was chosen to have the following (quasi) static flow velocity  $\vec{v}(\vec{r})$ :

$$\vec{v}(\vec{r}) = (\vec{\Omega} \times \vec{r}) \exp(-r^2/a^2) \quad \Omega = (2e)^{1/2} v_t/a \quad (3)$$

This equation represents a nonuniformly spinning turbule, with angular velocity parameter  $\Omega$  about an axis  $\vec{\Omega}$  through the origin of coordinates. The quantity  $c_\infty$  is the background wave speed far from the turbule; the parameter  $a$  is an "effective radius" of the turbule; and  $\vec{r}$  is the position vector. The expression for  $\Omega$  relates the angular velocity to the maximum turbule velocity which occurs at  $r = a/2^{1/2}$ .

If an acoustic plane wave with propagation vector  $\vec{k}$ , where  $k = 2\pi/\lambda$ , is incident upon this model turbule, then the first order in  $\Omega$  differential scattering

efficiency, which is defined to be the scattering cross section divided by the physical cross-section  $\pi a^2$ , averaged over all spin axis orientations is

$$\langle Q^{(1)}(k, \hat{r}) \rangle = \left( \frac{1}{3} \right) \left( \frac{\Omega a}{4c_*} \right)^2 (ka)^6 (\sin\theta \cos\theta)^2 \exp[-(ka)^2 (1 - \cos\theta)] . \quad (4)$$

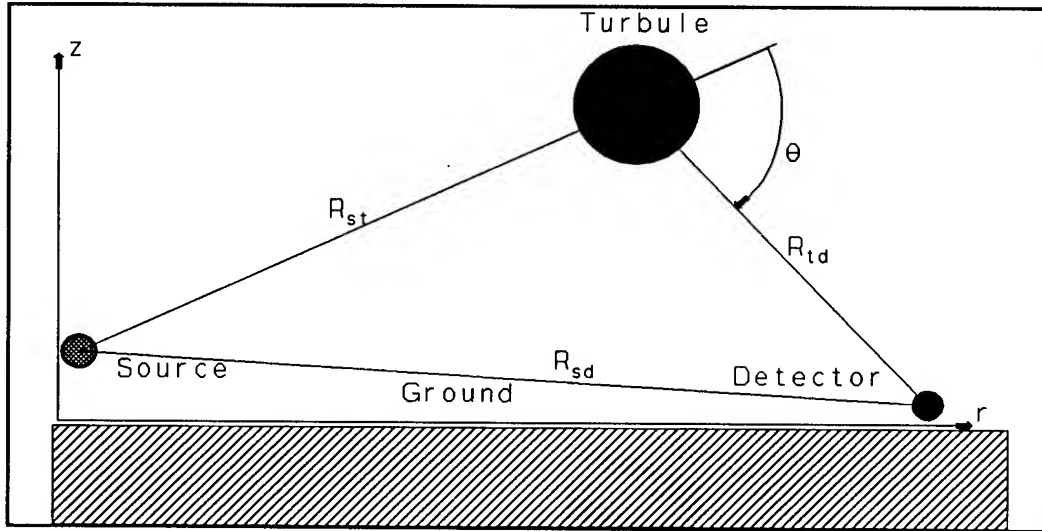


Figure 7. Turbulence scattering geometry.

TABLE 1. SYMBOL DEFINITIONS

Symbol	Definition	Value	Units
$a$	turbule characteristic size		m
$a_t$	typical turbule size	$17.5/\pi$	m
$v$	turbule characteristic velocity		$m \cdot s^{-1}$
$v_t$	typical turbule maximum velocity	1.340	$m \cdot s^{-1}$
$\Omega$	turbule angular velocity	0.561	$rad \cdot s^{-1}$
$\lambda$	acoustic wavelength	10.0	m
$\theta$	propagation to detector angle	$\pi/4$	radian
$\langle Q^{(1)}(k, \hat{r}) \rangle$	differential scattering efficiency	$5.52 \cdot 10^{-5}$	
$\sigma_{sca}(a, v, \theta)$	differential scattering cross section	$1.49 \cdot 10^{-3}$	$m^2$
$R_s$	reference distance from source	1.0	m
$E_s$	exitance of source at $R_s$	1.0	$w \cdot m^{-2}$
$E_t$	exitance at scattering volume	$3.92 \cdot 10^{-8}$	$w \cdot m^{-2}$
$E_d$	scattered exitance at detector	$9.99 \cdot 10^{-12}$	$w \cdot m^{-2}$
$\Omega_d$	detector solid angle field	1.0	str.
$n_a(a)$	turbule concentration distribution		$m^{-3}$
$n_t$	typical turbule concentration	$(1/17.5)^3$	$m^{-3}$
$l$	length of scattering volume	1000.0	m
$r_v$	radius of scattering volume	674.6	m
$\phi$	detector field half-angle	0.572	radian
$V_{sca}$	scattering volume	$1.43 \cdot 10^9$	$m^3$

Figures 8 and 9 show the turbule scattering properties to first order in  $\Omega a/c_\infty$ .

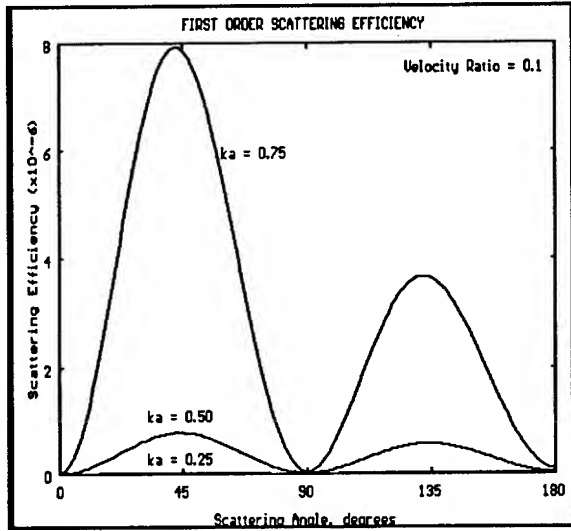


Figure 8. Average differential scattering efficiency.

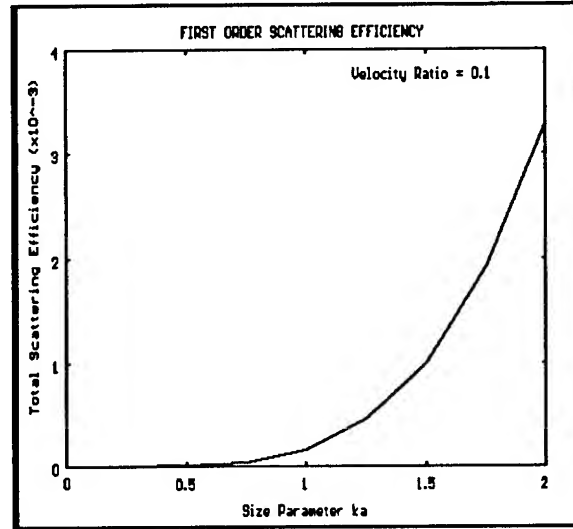


Figure 9. Total average scattering for a spinning turbule.

The typical value for turbule size was chosen from the size parameter for which the cross section is near maximum. Solving for  $a_t$  gives the value in table 1.

$$2\pi a_t/\lambda = 3.5 \quad (5)$$

Since the diameter of the turbule is approximately  $35/\pi$ , a cell size is chosen to be 17.5 or slightly larger than the turbule. The cell is thought of as a cube that completely contains one turbule. The number concentration will be the reciprocal of the cell volume, which is the value for  $n_t$  given in table 1. The final parameter to be determined is the typical turbule velocity. To make a reasonable choice of  $v_t$ , it is appropriate to choose an outer scale size related to the dimensions of the scattering volume and to choose the velocity of the maximum sized turbule as a reasonable wind speed. Thus, if the maximum turbule size is considered to be 500.0 m and the wind speed is  $6.0 \text{ m} \cdot \text{s}^{-1}$ , the one-third power law of velocities determines the typical maximum velocity from the relation

$$v_t = 6.0 (a_t/500.0)^{1/3}, \quad (6)$$

again giving the value in table 1. The differential scattering efficiency is determined by using eq. (4); the turbule scattering cross section, the scattering cross section per unit volume, and the scattered exitance at the detector are determined by using eq. (2).

#### 4. COMPARISON OF RESULTS

The purpose of this section is to compare the scattered exitance derived in section 3 with that calculated from the "statistical approach" relations as well as with experimental results (Gilbert, 1990). The standard statistical approach scattering cross section is (Tatarskii, 1971)

$$\sigma_{Tat}(\theta) = 0.38 k^{1/3} \left[ \frac{(\cos(\theta))^2}{(2 \sin(\theta/2))^{11/3}} \right] \left[ \frac{C_v^2}{C_\infty^2} (\cos(\theta/2))^2 + 0.13 \frac{C_T^2}{T_\infty^2} \right]. \quad (7)$$

The symbols that have not been defined before are  $C_v^2$ , the velocity structure constant,  $C_T^2$ , the temperature structure constant, and  $T_\infty$ , the ambient temperature. Equation (7) has been rederived with fewer approximations but the result has not been reported. The derivation is too lengthy to include here, but the final result is

$$\sigma_{sta}(\theta) = 2 \pi k^4 \left[ \frac{B^v(k)}{C_\infty^2} (\cos(\theta) \cos(\theta/2))^2 + \frac{B^T(k)}{4 T_\infty^2} \right] \quad (8)$$

$$B^v(k) = 4.16 C_v^2 \quad B^T(k) = 4.16 C_T^2$$

$$C_v^2 = 0.04 (m \cdot s^{-1})^2 m^{-2/3} \quad C_T^2 = 0.00043 k^2 m^{-2/3}.$$

The numerical constant 4.16 (dimensions of  $m^{11/3}$ ) in the expressions for  $B^v(k)$  and  $B^T(k)$  in eq. (8) follows approximately the angle dependence of the first bracket in eq. (7) and has been determined for an angle of  $\pi/4$  radians. The structure constants were taken from the literature of Brown (1976). When an asymptotic wave speed of 335.1, a temperature of 300 k, and eqs. (7) and (8) are used, the statistical and Tatarskii cross sections are

$$\sigma_{sta}(\theta) = 6.2417 \cdot 10^{-7} m^{-1} \quad \sigma_{Tat}(\theta) = 1.3217 \cdot 10^{-7} m^{-1}. \quad (9)$$

Detected exitance using eq. (2) and excess loss levels for the four cases of interest are brought together in table 2.

TABLE 2. DETECTED FIELDS COMPARISON

Symbol	Definition	Value	Units
$E_d$	exitance, structural approach	$9.99 \cdot 10^{-12}$	$w \cdot m^{-2}$
$E_{sta}$	exitance, statistical approach	$2.25 \cdot 10^{-11}$	$w \cdot m^{-2}$
$E_{Tat}$	exitance, Tatarskii formula	$4.76 \cdot 10^{-12}$	$w \cdot m^{-2}$
$L_d$	excess loss, structural approach	34.44	dB
$L_{sta}$	excess loss, statistical approach	30.91	dB
$L_{Tat}$	excess loss, Tatarskii formula	37.66	dB
$L_{lit}$	excess loss, literature value	20 - 30	dB

A number of issues impact the validity of the excess loss values in table 2.  $L_d$  was calculated using an assumed turbule number concentration and velocity and a typical turbule size rather than an integration over a size distribution.  $L_{sta}$  was calculated using eq. (8), which was derived using a realistic structure function that became constant at large separations. Perhaps this is the reason for the difference between  $L_{sta}$  and  $L_{Tat}$ .  $L_d$  and  $L_{sta}$  are near the spread in  $L_{lit}$ . The latter, however, was measured for a different geometry and different frequency. The fact that the new results, as crude as represented here, give answers in general agreement with the statistical approach and with the experiment is encouraging.

## 5. TURBULENT SCATTERING IN A PROPAGATION MODEL

Figures 10 through 12 show inclusion of turbulent scattering in a propagation model by running AMPP twice and summing the results. The first run preserves the field produced by the source (fig. 10). Figure 10 is a reproduction of figure 6 except the shadow zone has been artificially cleared of residual sound levels. The second run preserves the field produced by an isotropic scatterer, the results being shown in fig. 11. The two results are combined after the second run results have been modified by the source to turbule loss. This final result is shown in fig. 12 where the summation has been done incoherently. Figure 12 only gives a representative picture of the superimposed fields because the solution algorithm of AMPP (from FFP) can only model isotropic scatterers; whereas, it is known that scatterers have patterns resembling fig. 8. The scattered exitance in fig. 12 has been adjusted to give an excess loss at the detector location of fig. 7 of approximately 25 dB.

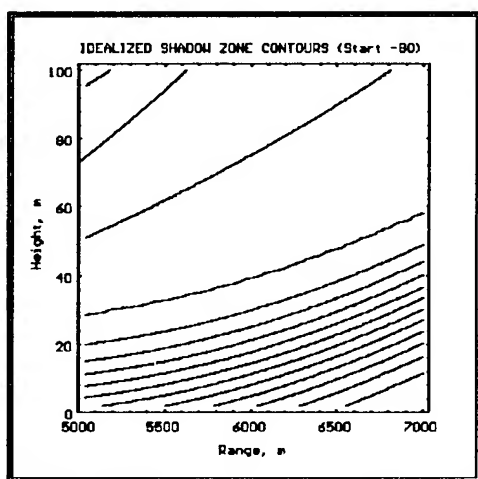


Figure 10. Idealized shadow zone zone contours (contours at -80 to -145).

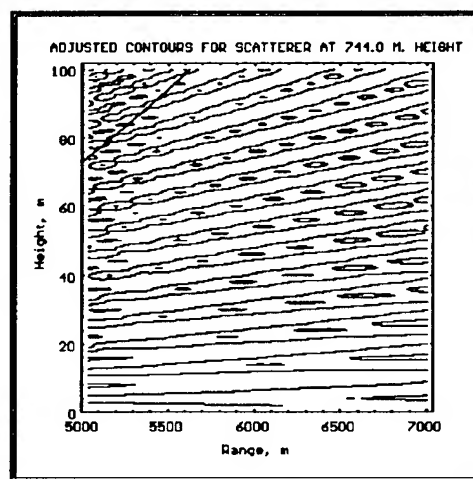


Figure 11. Adjusted scattered field (contours at -100, -105, and -110).

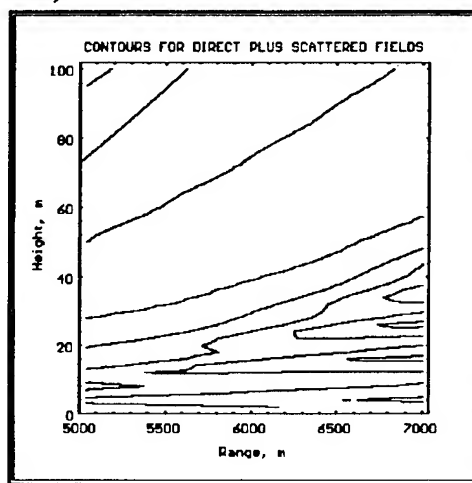


Figure 12. Combined primary and scattered fields (contours at -80 to -110 in 5 dB intervals).

## 6. CONCLUSIONS

The "structural approach" to modeling turbulence produces scattered sound levels that are in general accordance with those calculated using the "statistical approach." They are also in accordance with the experiment. The claim is not that a turbulent region is made up only of a collection of turbules of various sizes. Rather, the claim is that such a concept is a first approximation to the true distribution of motion, energy, and density in the turbulent region. Furthermore, as far as scattering is concerned, this concept yields reasonable answers. The significance of the work reported here is that a pathway has been charted that breaks the shackles imposed by the isotropic and homogeneous requirements of the statistical approach. Boundary layer theory and the vertical structure capability of current acoustic propagation models both attest to the recognized fact that the atmosphere is not isotropic and homogeneous. The structural approach supported by analytical or numerical knowledge of the scattering properties of turbules does work. What has not been done yet is to determine the number concentration distribution appropriate for use. Additionally, knowledge of the scattering properties of large turbules is yet to be determined. The true internal structure of a turbule has not been determined, but the scattering results do not seem to be very sensitive to this structure. Use of the structural approach requires that the analyst know something more of the details of the turbulent region than the statistical approach. A simulation of flow in the actual environment being analyzed is indicated. Calculation of scattering from such unusual features as intermittent turbulent regions is possible. It will be necessary to devise a method by which anisotropic sources and scatters can be included in propagation models.

## REFERENCES

- Auermann, H. J., R. L. Reynolds, and D. M. Brown, 1992: Development of a Multistream Acoustic Propagation Model Including Turbulent Scattering. Technical Report (Draft), U. S. Army Atmospheric Sciences Laboratory, White Sands Missile Range, NM 88002.
- Brown E. H., and S. F. Clifford, 1976: On the attenuation of sound by turbulence. J. Acoust. Soc. Am. 60(4).
- Gilbert, K. E., R. Raspet, and Xiao Di, 1990: Calculation of turbulence effects in an upward-refracting atmosphere. J. Acoust. Soc. Am. 87(6).
- Goedecke, G. H., 1992: Scattering of Acoustical Waves by a Spinning Atmospheric Turbule. Contractor Report (Draft), U. S. Army Atmospheric Sciences Laboratory, White Sands Missile Range, NM 88002.
- Raspet, R., S. W. Lee, E. Kuester, D. C. Chang, W. F. Richards, R. Gilbert, and N. Bong, 1985: A fast-field program for sound propagation in a layered atmosphere above an impedance ground. J. Acoust. Soc. Am., 77(2).
- Tatarskii, V. I., 1971, The Effects of the Turbulent Atmosphere on Wave Propagation. TT-68-50464, National Technical Information Service, Springfield, VA 22161.



## MODIFICATION OF ATMOSPHERIC AEROSOL

Austin W. Hogan  
USA Cold Regions Research and Engineering Laboratory  
Hanover, New Hampshire 03755-1290, U.S.A.

### ABSTRACT

The physical properties of the particulate fraction of aerosol are continuously modified by coagulation processes within the aerosol throughout its life in the atmosphere. A model, based on the Fuchs multi-component coagulation theory, was originally derived to predict diurnal changes in aerosol concentration and size distribution due to photochemistry. This model has been refined to incorporate first principles consideration of mean free path, diffusion coefficient and equilibrium electrical charge, and it can be applied to any tropospheric layer. An area/mass conservation algorithm has been incorporated in the model to allow estimation of modifications of particle surface properties due to coagulation with material of differing properties.

Examples are given showing the rate at which soot aerosol interacts with other aerosols. The generality of the model allows comparison of the modification of surface properties in cold, stably stratified layers to modifications of those properties in regions of more vigorous exchange.

### 1. INTRODUCTION

The particulate fraction of the atmospheric aerosol is very dynamic with respect to chemical and physical properties of the particles. The chemical and physical changes that can occur over brief time periods greatly influence the optical properties of the atmosphere and its ability to transport chemical compounds. The fundamental cause of the major influence of relatively small masses of aerosol on several physical and chemical properties is the relatively great surface to mass ratio presented by the particulate matter. This paper presents a descriptive model predicting some aspects of modification of the surface properties of aerosol by describing the interaction among the size classes of the aerosol and the interaction with new small particles generated through chemical reactions in the atmosphere.

The aggregation of fine smoke particles of similar size through Brownian diffusion was first described by Smolochowski (1917). Fuchs (1963) provided a more general Brownian coagulation theory, which described the mutual coagulation among particles of differing sizes. Junge (1963) and Hogan (1977, 1979) have presented mutual coagulation calculations to explain variations in aerosol size distribution with time. These models attempted to conserve total aerosol mass as sizes changed through coagulation by considering the aggregate to be a sphere of volume equal to the sum of the volumes of the initial particles. This allowed prediction of evolution of particle size with time, but it did not preserve the modification of the nature of surface or chemical composition of the particles. The model calculations presented here preserve the relative area of the agglomerate contributed by the components of the aerosol, and it can be used to examine the nature of the aerosol surface for application to chemical, radiative and cloud physics problems.

## 2. THEORETICAL DEVELOPMENT OF CALCULATION SCHEME

The family of coagulation equations used in the calculation scheme are based on the Fuchs general two-component coagulation equation:

$$\frac{dN_{1,2}}{dT} = 4\pi \frac{(D_1 + D_2)}{2} \frac{(R_1 + R_2)}{2} N_1 N_2 \quad (1)$$

which provides the time rate of coagulation of  $N_2$  smaller particles of  $R_2$  with  $N_1$  larger particles of  $R_1$ . The larger particle is considered the survivor in each collision, and the loss of particles of radius  $R_2$  from the concentration  $N_2$  in an interval  $t$  is given by

$$N_{2t} = N_{20} - \left( \frac{dN_{1,2}}{dt} \right) t. \quad (2)$$

Previous work has generally been restricted to the use of diffusion coefficients ( $D$ ) given by Fuchs (1963) or Hinds (1982) based on laboratory work at sea level and 20°C. This work allows the specification of altitude and temperature of the layer in which coagulation occurs, and it provides the mean free path and viscosity of air in the layer to calculate Stokes parameters and diffusion coefficient for each particle radius class.

Each radius class is allowed to coagulate with itself and with every smaller radius class through a matrix of (1). The loss of particles in each class is tabulated through summation of (2) as in previous work. An accounting is made of the volume (mass) of smaller particles amassed by the larger, and the surface area of the larger covered by cross section area of the smaller. The radii classes are defined by a "root two" progression, and the particles are moved upward in size through coagulation by

$$\Delta N = \frac{R_2^3/R_1^3}{(2 \times 2.83) \left( \frac{dN_{1,2}}{dt} \right) t} \quad (3)$$

which moves the number of particles that statistically exceed the mass midpoint of the adjacent classes into the larger class. An equal number is subtracted from the collecting class. This surface area accounting convention is illustrated in Fig. 1.

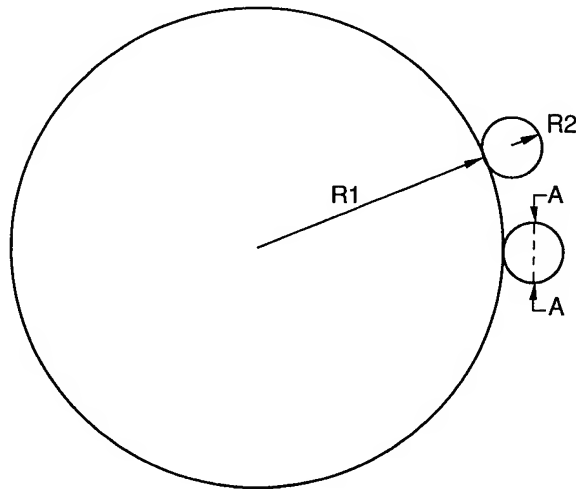


Figure 1. Geometric consideration of the modification of particle surfaces through coagulation. Smaller particles aggregating upon larger particles influence the surface of the large particle in proportion to the cross section area, rather than the surface area, of the small particle.

A "root two" progression in particle radius classes provides resolution of a factor of two in area of the particle classes and realistically approximates our ability to resolve particle size in this range. The use of a finite step boundary in the calculation causes an apparent increase in total aerosol mass with time in the calculation while conserving aerosol number concentration. This mass increase can be canceled with an algorithm, but is less than 0.2 in the calculations to follow and does not influence the parameters to be discussed.

### 3. APPLICATION OF MODEL CALCULATION

The oil field fires following the Kuwait war caused the largest tropospheric aerosol cloud of recent history, and certainly the most quantitatively studied smoke plume (Ferek et al., 1992). This smoke aerosol had two somewhat unanticipated properties: Hudson and Clarke (1992) found the particles to be active cloud condensation nuclei, and elemental analysis of impacted smoke particles by Parungo et al. (1992) showed them to be coated with sulfate.

The size distribution of particles in this smoke, measured with an electrostatic aerosol analyzer in the  $2 \times 10^{-6} < R < 3 \times 10^{-5}$  cm range by Hudson and Clarke (1992), has been translated to the root two progression above, and entered into the model. An hypothetical sulfate aerosol of  $R < 1 \times 10^{-6}$  cm has been "mixed" with the smoke aerosol at production rates proportional to the rate of sulfur dioxide conversion given by Ferek et al. (1992). Examples, calculated for a sulfate aerosol production rate of  $2.8 \times 10^{-10}$  gm/m<sup>3</sup>-s are given in Fig. 2 and 3.

Figure 2 shows the composite size distribution of smoke aerosol obtained in the merged plume downwind of the Kuwait fires by Hudson and Clarke (1992). The size distribution of an aerosol produced by adding particles of  $1 \times 10^{-6}$  cm to this aerosol, at the rate above, for four hours, is shown by the shaded lines. The concentration of  $1 \times 10^{-6}$  cm particles equilibrates at  $5 \times 10^4/\text{cm}^3$  (indicated by the arrow on the figure) after a few hundred seconds, as these fine particles aggregate through the remainder of the size distribution. Particles in size classes greater than

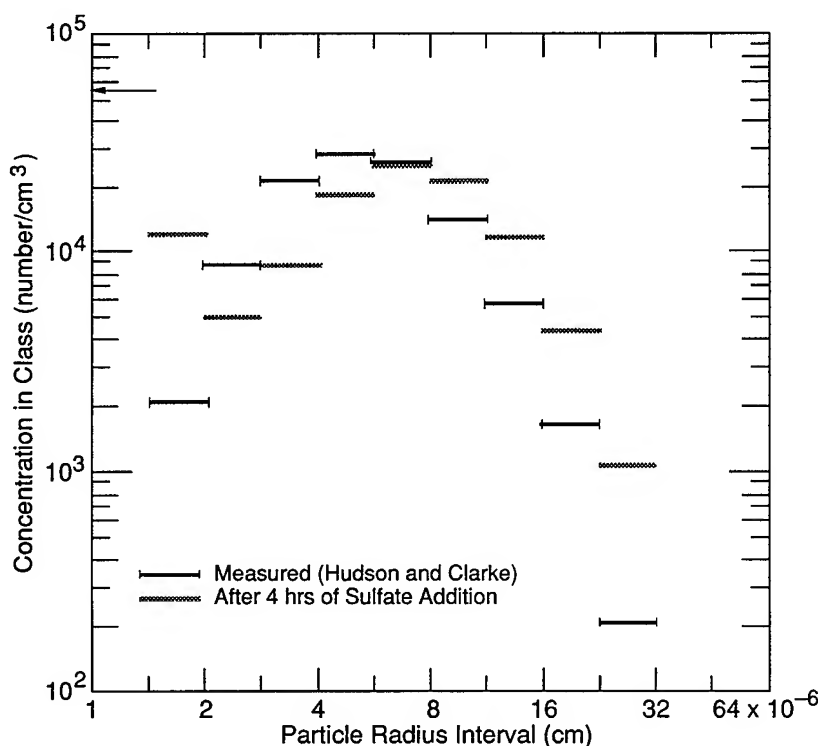


Figure 2. Size distribution of Kuwait smoke, measured by Hudson and Clarke, compared with a model aerosol resulting from coagulation of that smoke after adding smaller particles.

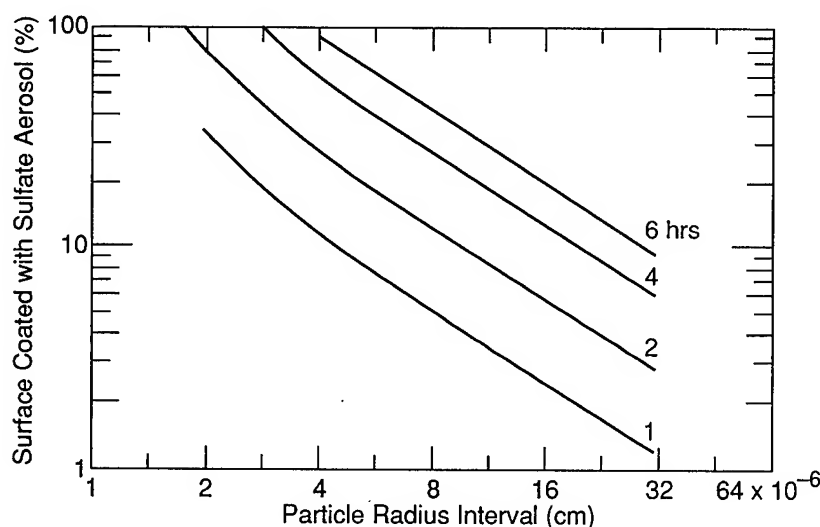


Figure 3. Amount of particle surface, with respect to size, of the model aerosol in Fig. 2 covered by collected smaller particles.

$8 \times 10^{-6}$  cm increase in concentration, while those in classes less than  $5.6 \times 10^{-6}$  cm decrease in concentration, with the exception of the smallest class.

The rate at which the small sulfate particles might cover the surface of the smoke aerosol is given in Fig. 3, for periods of 1, 2, 4 and 6 hours, at the sulfate production rate given. Six hours would seem a reasonable limit to calculations based on the observed size and concentration, as exchange would certainly be active in diluting the original smoke on this time scale. The smaller particles become totally covered (statistically) in 4 hours, and all particles have at least 10% surface coverage in 6 hours. This may provide an insight into the activity of these particles as cloud condensation nuclei, as a thin covering of soluble material may constitute a surface suitable to begin water accretion at small saturation.

#### 4. DISCUSSION AND CONCLUSION

A number and area conservative coagulation model has been applied to a unique smoke aerosol. Preliminary calculations using the model show that vapor-to-particle conversion in the atmosphere at rates comparable or less than those of  $\text{SO}_2$  loss measured in the smoke plume by Ferek et al. (1992) provide changes in particle size distribution over time periods comparable with plume stability. The consideration that the vapor homogeneously produces small particles allows consideration of modifying the surface of chemically inactive particles, as these fines aggregate on the larger particle surface through Brownian coagulation. Coagulation provides a mechanism that can alter the surface chemistry, index of refraction and nucleating properties of aerosol through the addition of a very small mass amount to the surfaces of particles.

#### REFERENCES

- Ferek, R.J., P.V. Hobbs, J.A. Herring, K.K. Laursen, R.E. Weiss and R.A. Rasmussen, 1992: Chemical Composition of Emissions from the Kuwait Oil Fires, *Journal of Geophysical Research*, **97**, 14483–14490.
- Fuchs, N.A., 1963: *The Mechanics of Aerosols*, Pergamon Press, N.Y.

- Hinds, W.C., 1982: *Aerosol Technology*, Wiley Interscience.
- Hogan, A., 1977: A Simplified Aerosol Coagulation Model, *Journal of the Air Pollution Control Association*, **27**, 759-762.
- Hogan, A., 1979: *Aerosol Detection by Condensation Nuclei Counting Techniques in Aerosol Measurement* (D.A. Lundgren, Ed.), University of Florida Press, Gainesville, Fl., p. 497-514.
- Hudson, J.G. and A.D. Clarke, 1992: Aerosol and Cloud Condensation Nuclei Measurements in the Kuwait Plume, *Journal of Geophysical Research*, **97**, 14533-14536.
- Junge, C.E., 1963: *Air Chemistry and Radioactivity*, Academic Press, N.Y.
- Parungo, F., B. Kopcewicz, C. Nagamoto, R. Schnell, P. Sheridan, C. Zhu and J. Harris, 1992: Aerosol Particles from the Kuwait Oil Fire Plumes: Their Morphology, Size Distribution, Chemical Composition, Transport, and Potential Effect on Climate, *Journal of Geophysical Research*, **97**, 15867-15882.
- Smolochowski, M., 1917: *Z.Phys Chem*, **92**, 129.



# INTERMITTENCY, EVENTS, AND COHERENT STRUCTURES IN VEGETATIVE CANOPIES

Ronald M. Cionco  
Battlefield Environment Directorate\*  
US Army Research Laboratory  
White Sands Missile Range, New Mexico 88002-5501, USA

William D. Ohmstede  
Wm Ohmstede, CCM  
Las Cruces, New Mexico 88005, USA

## ABSTRACT

The occurrence of intermittency, events, and coherent structures associated with boundary layer shear flow has been recognized for sometime now. They are often made manifest by the observed phenomena of intermittency and temperature ramps. These coherent structures appear to be particularly in association with substantial vegetative canopies. The coherent structures are often said to be associated with a "microfront"; which is preceded by slow wind speed and upward motion (ejection) and followed by descending motion and increased wind speed (sweep). The coherent structures appears like a longitudinal wave. The often observed temperature ramps are indeed an effect rather than a cause of the wave. Basic features of the coherent structure can be modeled quite simply using perturbation theory. We assume a steady longitudinal wave moving downwind at the speed of the wind in the upper part of the surface layer. Given the mean wind speed profile and the wave speed, separate solutions are obtained for ejection and sweep regions within and above a vegetative canopy by matching boundary conditions at the jump and assuming that the vertical motion vanishes at the ground. Examples of coherent structures are illustrated using data from Project WIND. The solutions show substantial agreement with observations taken in a canopy domain.

## 1. INTRODUCTION

It has long been recognized that atmospheric turbulence is not just random disorder but rather partly composed of organized motions. The occurrence of vertically coherent structures was first noted in conditions of free convection. Gravity waves are the opposite example of buoyancy dominated coherent structures.

---

\* Formerly U.S. Army Atmospheric Sciences laboratory

There is much less recognition of the occurrence of coherent structures associated with boundary layer shear flow. These events' are often made manifest by 'intermittency', 'wind gusts', or 'temperature ramps.' There have been several useful reviews of this subject area. Mollo-Christensen (1973) summarized the subject of intermittency in large-scale turbulent flows. 1981 was a very good year for relevant reviews. Cantwell (1981) described organized motion in turbulent flow, largely pertaining to laboratory and engineering flow regimes; Antonia (1981) reported on conditional sampling techniques used to study such structures; and Raupach and Thom (1981) pointed out the significance of coherent structures in regard to turbulence in and above plant canopies. More recently, Raupach et al (1991) have reviewed the role of organized motion in the general context of rough-wall turbulent boundary layers.

Particularly interesting recent accounts of observed coherent structures are reported by Marht (1991), Shaw et al (1990), Gao, et al (1989), Gardiner (1991), and Bergström and Högström (1989). These phenomena appear to be especially in association with substantial vegetative canopies. The objective of this paper is to explore further the manifestations of coherent atmospheric structures in vegetative canopies.

## 2. PHYSICAL REPRESENTATION

Data collected for previous studies (Cionco, 1971) were analyzed during 1969 to also depict the occurrence of events and intermittency within and above a simple canopy. Wind speed data collected in a geometrically uniform field of corn plants exhibited how the establishment of organized daytime flow within the canopy evolved from a drift and disorganized 'flow' of the night regime. Figure 1 presents the isotach analysis of five minute averaged data beginning at 0700 hours. Prior to 0700, flow was composed predominately of speeds of 15 cm/sec or less and behaved in a disorganized manner. After 1300 hours, the well-established, organized flow with speeds exceeding 100 cm/sec continued past sunset. Between 0700 and 1300 during the summer of 1968, the flow of the ambient surface layer began its first gusty penetration into the canopy followed by more frequent and longer lasting events before the flow was fully established. Between the disorganized and organized regimes, notable gusty events attempted to penetrate the upper levels of the canopy with events every 40 to 45 minutes without success at 0840, 0920, 1000, 1040, and 1130. The intermittency of this flow for the morning occupied as much as 40 minutes before the "five minute energy event" occurred. At the 1200-1215 Hr event, the flow was virtually ready to set in. When the events occur continuously or on top of each other, you no longer have intermittency such as after 1300 hours when the surface layer was established for the daytime hours (not shown in figure 1). What is surprising is that we could discern these fine events with somewhat coarse five minute averages. Recent investigators are sampling at 20 and 10 Hz to resolve similar but high resolution events. The balance of this paper will focus on the behavior of



the high resolution events.

The coherent structures are often said to be associated with a 'micro-front' or 'gust front', which is preceded by slow wind speed and upward motion (ejection) and followed by downward motion and increased wind speed (sweep). In part, we find this terminology misleading. A front denotes a quasi-horizontal interface separating two air masses of different density and which moves primarily by advection. In our view the coherent structure is a longitudinal wave with a quasi-vertical jump surface that propagates at its own wave speed which is independent of any local advection. Since the Mach number is quite small, it follows from the Rankine-Hugoniot jump conditions that the density, pressure, and normal (longitudinal) velocity must be essentially continuous through the jump. However, their derivatives as well as the tangential (vertical) velocity can be discontinuous (neglecting viscous effects). Any difference in temperature across the jump is incidental and due to differential transport. It is an effect rather than a cause. Nevertheless, it turns out that the temperature (as well as other passive scalars) is an easily observable indicator of the jump associated with the coherent structure as long as it has a mean vertical gradient.

Surprisingly, the basic features of coherent structures can be modeled quite simply using perturbation theory. We assume a steady, isolated longitudinal wave moving downwind at a wave speed corresponding with the wind speed at the upper part of the surface layer. Coherent structures are three-dimensional, but here we neglect any lateral variation and assume the longitudinal wave is marked by a vertical jump surface, or wave front, of extensive lateral breadth. The mean wind is assumed to correspond with the log-law above the vegetation and with the exponential wind profile within the vegetation. A Galilean transformation is performed corresponding with the wave speed and the resultant dynamic equations are linearized using perturbation theory. This includes linearization of the canopy drag. The resultant perturbation equations are steady and homogeneous with coefficients which are only functions of height. Separation of variables is applicable.

The objective in solving the perturbation equations is to demonstrate qualitatively that many of the basic features of coherent structures are explained by our assumption of a longitudinal wave. For illustrative purposes we chose, somewhat arbitrarily, a single complex, exponential eigen-function for each side of the jump to represent the longitudinal variation. The corresponding vertical eigen-functions were evaluated by numerical integration requiring that the vertical motion vanish at the ground. The real and imaginary parts of the two solutions are combined to minimize, in a least-squared sense, any incongruities at the jump interface.

Figure 1a is taken from Shaw, et al (1990) and pertains to observations within and above an 18 m high forest at Camp Borden, Ontario, Canada. It shows the "association between ejection/sweep

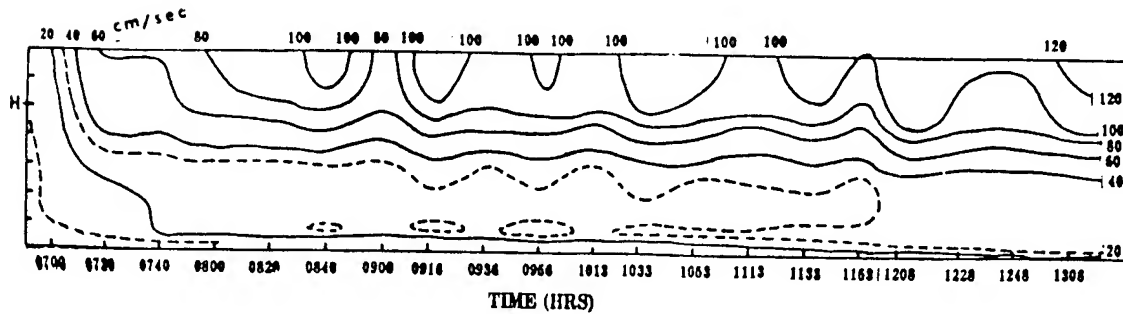


Figure 1. Isotach analysis (of wind speed in cm/sec) depicting intermittency and events of canopy flow during the Canopy Density Experiment - 1968, Ellis Hollow, NY (After Cionco, 1971)

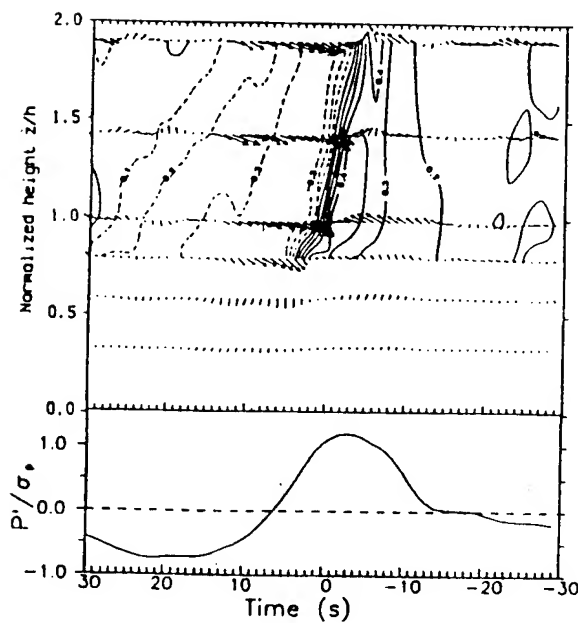


Figure 1a. Observations of velocity vectors, humidity contours, and static surface pressure normalized by Shaw et al, 1990.

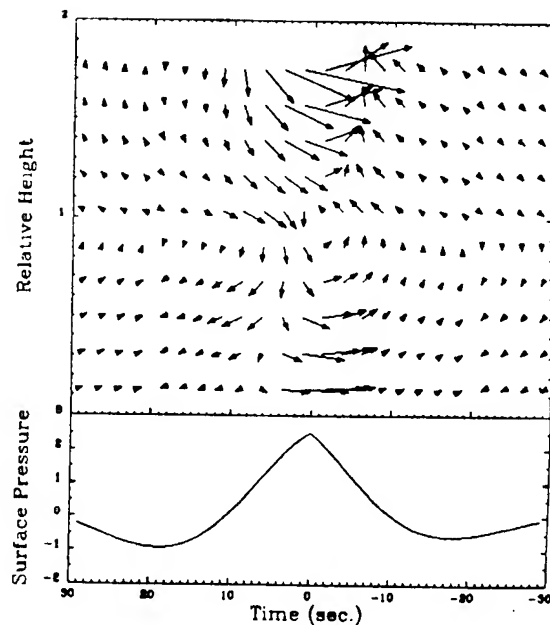


Figure 1b. Perturbation Theory solution of velocity vectors and the surface pressure.

coherent structure identified by fluctuations in humidity (contour interval  $0.1 \text{ g/m}^3$ ) and by fluctuation velocity vectors (maximum arrow length represents  $2.0 \text{ m/sec}$ ) and surface static pressure normalized by its unfiltered standard deviation. Each part of the diagram is an ensemble average of events during one 30 min period." Gao, et al (1989) report that the shift in the sign of the vertical velocity occurs almost simultaneously at all levels.

Figure 1b is a corresponding perturbation solution. The magnitudes of the vectors and pressure are arbitrary since the equations are homogeneous. There are many things wrong with Figure 1b; space limitations preclude their enumeration. The solution is especially suspect near the top and the bottom. Nevertheless, the solution shows good qualitative agreement with Figure 1a in the region surrounding the mean velocity inflection point at the top of the canopy. The ejection and sweep cycles are clearly evident.

We believe that Figures 1a/b provide sufficient evidence to conclude that the coherent structure is a longitudinal wave moving at a wave speed which is independent of local advection -- particularly within the vegetation. In the solution of Figure 1b, the wave speed was taken to be equal to the wind speed at twice the height of the canopy.

### 3. OBSERVATIONAL EVIDENCE

We previously noted some of the studies which provide observational accounts of coherent structures. New data have become available to allow us to further study this phenomenon. The Project WIND database (Cionco, 1989a) is the source of these data.

Four phases of Project WIND were successfully conducted by the USA Atmospheric Sciences Laboratory in and about the Sacramento River Valley of northern California during the period beginning June 1985 and ending October 1987. The design of Project WIND (Cionco, 1989a) was based on the multiple-scale data requirements of ASL's hierarchical system of nested meso- and microscale models (Cionco, 1987 and 1985). Project WIND was therefore designed with nested measurement domains to address scales ranging from mesoscale to microscale. More than 54 measurements sites were established within the WIND domain. Only two were major sites collecting data on all scales: one in and about a geometrically-neat orchard on flat terrain and the other in and about a complex forest on mountainous terrain. Data were collected over a two week time span for selected periods resulting in two full sets of daytime, nighttime, and transition (sunrise and sunset) periods and two full 24-hour diurnal periods. A significant portion of Project WIND's database is composed of horizontal micrometeorological surface layer measurements as well as vertical measurements within and above vegetative canopy domains (Cionco 1989b). For example, three micrometeorological towers of eight levels of identical sensors were placed deep in the 8 m high orchard canopy, near the edge of the canopy, and upwind in the ambient surface layer of a large

clearing. Measurements of wind components ( $u, v, w$ ), temperature, and humidity were collected in  $x, y$ , and  $z$  with a sampling rate of one per second. Data from the zone of established canopy flow and the ambient surface layer directly above the trees are used in the analysis that follows.

At this time, we have only scratched the surface of this vast resource. Merely a fraction of the data from the orchard site have been reviewed and analyzed. Even a casual examination of the data reveals the presence of coherent structures. This is to say, when viewing contemporaneous time series plots of the observed variables at all measurement levels, we infer the occurrence of a coherent structure when there is present significant vertical coherence of the observed perturbations. For example, Figure 2 is a 300-second time series of temperature observations within and above the orchard. Two rather classical appearing temperature ramps are apparent. Figure 3 is a vector plot showing the velocity perturbations associated with the left temperature ramp. (Note that the abscissa of Figure 3, like Figures 1a/b, is reversed to emphasize the ejection/sweep progression.) The warm ramp is associated with the ejection and the cooler bulge corresponds with the sweep.

Figures 2 and 3 pertain to a cool winter's morning (1024 PST, JD38) with a modest north wind (1.8 m/sec at 2h). Figure 2 is exceptional; most of the hour was marked by lesser temperature perturbations. Nevertheless, numerous coherent structures were evident in the time series plots of the vertical motion. Although a sunny day, the thermal effects during this period were minimal due to the low sun angle.

Figure 4 is a vector plot of the wind perturbations for another cool winter's day (JD29) which was cloudy with occasional rain. Temperature perturbations were minimal. The wind was from the southeast (2.6 m/sec at 2h). The time series for the period studied (1100-1200 PST) are in general more confused than in the other interval because the period of the organized motions is shorter (due to stronger wind speed).

The examples of Figures 2, 3, and 4 describe events for these given times. When we analyze the ensemble average of these types of events for the full hour of data, the behavior of the ejections and sweeps for both JD38 and JD29 are remarkable in their coherent structure. Figures 5 and 6 each confirm that these perturbations have vertical coherence in the time domain with little or time lag and that the wave motion suggested earlier in this paper is valid. Our ensemble averaged event statistics agree quite well with results reported by others (Shaw, et al, 1990; Gardiner, 1991).

We deliberately chose to review only data for which we anticipated minimal thermal effects. In this we succeeded. The object was to demonstrate that the coherent structures which were of interest are derived from the boundary layer shear rather than buoyancy forces. Because of space limitations, we have illustrated only a small

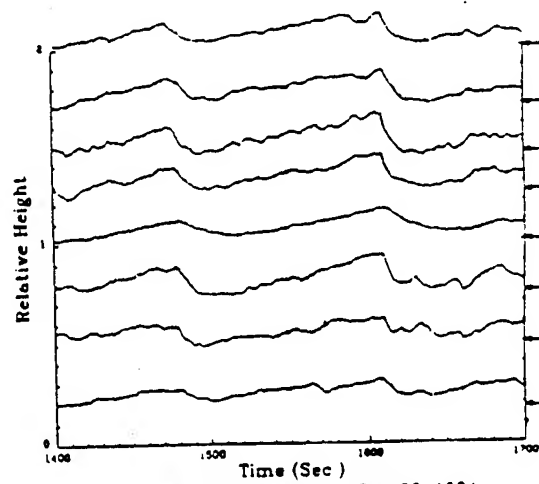


Fig 2 Temperature - Day 38, 1024

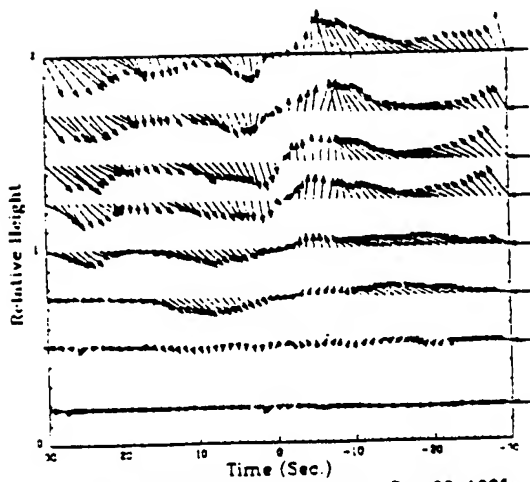


Fig 3 Velocity Perturbations - Day 38, 1025

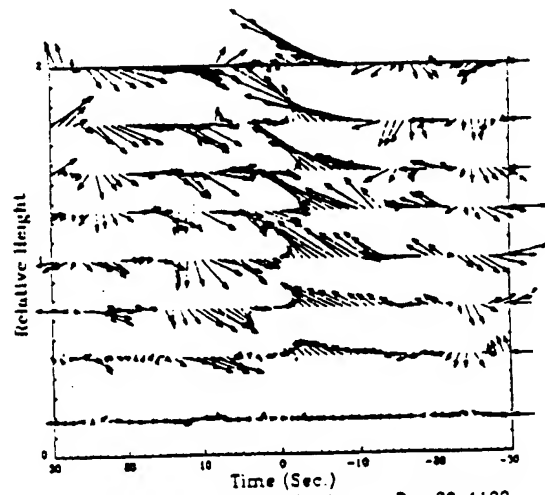


Fig 4 Velocity Perturbations - Day 29, 1102

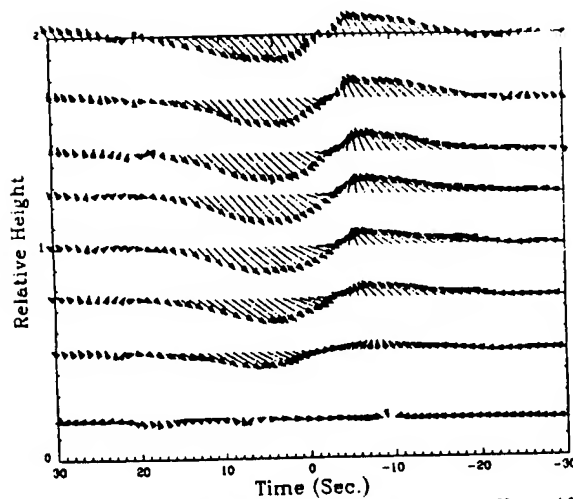


Figure 5. Jump-Averaged Vectors - Day 38, Hour 10

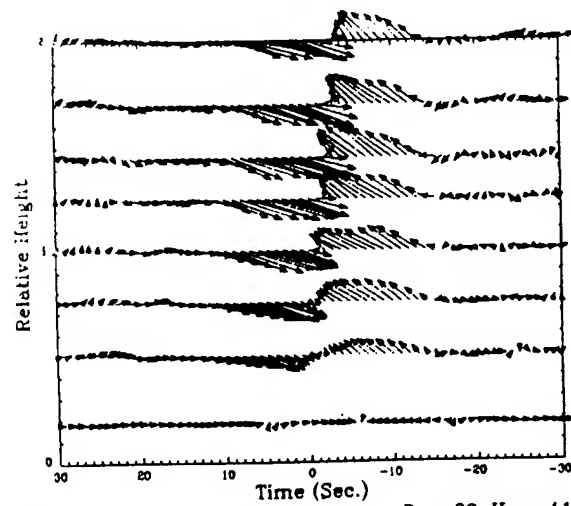


Figure 6. Jump-Averaged Vectors - Day 29, Hour 11

fraction of the data. The data for the figures were chosen with care. Nevertheless, the reader can be assured that for the two one-hour periods reviewed and analyzed, there were present numerous coherent structures. Indeed, for the period associated with Figure 4 (JD29), they were so abundant as to appear to interfere with one another. They may not all have the ideal appearance, but they are there ejecting and sweeping. Certainly for the ensemble averaged event statistics of Figures 5 and 6, the coherence exhibits ideal behavior.

The overriding point is that the data show perturbations with vertical coherence in the time domain with little or no lag. If this vertical coherence is to be maintained in the space domain, then the coherent structure must be moving at a uniform speed -- which is many times larger than the mean speed within the canopy. We interpret this organized motion to constitute a wave. Unfortunately, the Project WIND database contains no observations of the concomitant pressure perturbations. If it did, this would further verify our findings.

#### 4. DISCUSSION

It has been estimated that anywhere from 50% to 90% of the vertical flux of momentum is associated with coherent structures. If this be the case, then they cannot be mere intellectual curiosities. The tendency has been to address the coherent structure from the standpoint of an isolated event. However, there must be many events if these organized motions are to dominate the momentum flux. Most students of coherent structure use various conditional sampling techniques to study the events singly or collectively; the key here is the detection of the event, more precisely, the jump. Figure 1a is an elementary example of event statistical analysis based on condition sampling. The eigen-structure analysis used by Marht (1991), and others, is a far more sophisticated technique.

The occurrence of coherent structures calls into question the use of brute-force statistical procedures and modeling approaches which ignore the existence of these phenomena. How does one reconcile the mixing-length hypothesis, or any other local closure scheme (1-st or 2-nd order), with such organized motion throughout a depth comparable with that of the surface layer? The parallel with the problem of convective boundary layer diffusion is obvious. This is especially true in the vegetation where one can witness virtual calm conditions interspersed with bursts of activity which systematically transport material in or out of the canopy.

Perhaps a parameterized numerical model of coherent structures could be of value. However, many questions should be answered before seeking such solutions. We need to better understand what determines the depth and wave speed. The coherent structures are three-dimensional; much more information is needed to appreciate this aspect of the problem.

## 5. CLOSURE

The history of micrometeorology has been marked by the search for the perfect experimental site -- billiard table flat with mowed grass. Perhaps this was because such sites more nearly paralleled laboratory flow regimes. However, most land surfaces are not composed of golf course fairways and estate lawns. Consequently, the last decade was marked by a number of significant field programs at sites with substantial vegetation such as Project WIND. The manifestations of coherent structures are such a dominant factor in deep canopies, they are difficult to ignore. They are, indeed, an important factor within the surface layer as a whole. Perhaps the course of micrometeorological history has changed to emphasize rough rather than smooth boundaries.

Project WIND was not designed primarily to investigate the coherent structures of interest; if it were, it would have included fast-response pressure measurements. (It is strongly recommended that future experiments include these important measurements.) Nevertheless, the Project WIND database is seen as a valuable resource for providing new data which can contribute to a better understanding of surface layer diffusion as well as air/earth interaction with particular emphasis on vegetated sites. Analysis of these data may lend support to development of models (statistical or numerical) which establish the basic properties of coherent structures and their manifestations.

## 6. REFERENCES

- Antonia, R. A., 1981: Conditional Sampling in Turbulence Measurements. Annual Review of Fluid Mechanics, 13, 131-156.
- Bergström, H. and U. Högström, 1989; Turbulent Exchange Above a Pine Forest II. Organized Structure. Boundary-Layer Meteorology, 49, 231-263.
- Cantwell, B. J., 1981: Organized Motion in Turbulent Flows. Annual Review of Fluid Mechanics, 13, 457-515.
- Cionco, R.M. 1989a: Design and Execution of Project WIND. Proceedings of the 19th Conference on Agricultural and Forest Meteorology, 156-159, AMS, Boston.
- Cionco, R.M., 1989b: Micrometeorological Measurements of Canopy Domains during Project WIND. Proceedings of the 19th Conference on Agricultural and Forest Meteorology, 165-168, AMS, Boston, MA.
- Cionco, R. M., 1987: Windfield Simulations from a Hierarchy of Nested Meso- and Micrometeorological Models. Proceedings of the Symposium on Mesoscale Analysis and Forecasting, IUGG, ESA SP-282, Vancouver, CA.
- Cionco, R. M., 1985: Modeling Windfields and Surface Layer Profiles over Complex Terrain and Within Vegetative Canopies.

Forest-Atmosphere Interactions, Eds: B. A. Hutchison and B. B. Hicks. D. Reidel Publishing Co, Holland.

Cionco, R. M., 1971: Application of the Ideal Canopy Flow Concept to Natural and Artificial Roughness Elements, Master of Science thesis, Cornell University, Ithaca, NY.

Gao, W., R.H. Shaw, and K.T. Paw U, 1989: Observations of Organized Structure in Turbulent Flow Within and Above a Forest Canopy. Boundary-Layer Meteorology, 47, 349-377.

Gardiner, B.A., 1991: Observations of Airflow Above and Within Conifer Plantations. Proceedings of the 20th Conference on Agricultural and Forest Meteorology, 68-71, AMS, Boston.

Mahrt, L., 1991: Eddy Asymmetry in the Sheared Heated Boundary Layer. J. Atmos. Sci., 48, 472-492.

Raupach, M. R., and A. S. Thom, 1981: Turbulence in and above Plant Canopies. Annual Review of Fluid Mechanics, 13, 97-129.

Raupach, M. R., R. A. Antonia, and S. Rajagopalan, 1991: Rough-wall Turbulent Boundary Layers. Applied Mechanics Review, 44, 1-25

Shaw, R.H., K.T. Paw U, X. J. Zhang, W. Gao, G. Den Hartog, and H.H. Neumann, 1990: Retrieval of Turbulent Pressure Fluctuations at the Ground Surface Beneath a Forest. Boundary-Layer Meteorology, 50, 319-338.



## THE ZEPHYRUS, VAPOROUS, THERMOTICS CONNECTION

H. Rachele, A. Tunick, and F. Hansen  
Battlefield Environment Directorate\*

U.S. Army Research Laboratory  
White Sands Missile Range, New Mexico 88002-5501, USA

### ABSTRACT

Dynamic similarity of flows theory as applied to the surface boundary layer of the atmosphere must be treated as an interwoven quadripartite function of trivariant orthogonal turbulent motion, the thermal structure and associated vertical gradients, evaporation at the interface, and vertical transport of water vapor with respect to the specific humidity as a function of height. Physical studies of the surface layer are typically conducted with respect to the buoyant heat flux and the momentum flux. Buoyancy is associated with the sensible and latent heat fluxes. The key parameters for establishing the vertical fluxes are the scaling velocity, scaling temperature, and scaling humidity. An interpretation of the similarity theory developed from the basics of the mean value theorem of calculus allows evaluation of the scaling parameters without using the mathematically complex diabatic influence functions, but directly from the vertical gradients of wind, temperature, and specific humidity.

### 1. INTRODUCTION

The Obukhov (1946) dynamic similarity of flows theory is universally accepted for mathematically describing the shape of the vertical wind, temperature, and specific humidity profiles for the surface boundary layer of the atmosphere. Applications of dynamic similarity to micrometeorological or mesometeorological analyses exercises require a facile and rapid assessment of the scaling parameters, that is, the surface friction velocity  $u_*$ , the scaling temperature  $\theta_*$ , and the scaling humidity  $q_*$ . These entities, in conjunction with the surface roughness length  $z_0$ , and either the scaling length  $L$  or the scaling ratio  $z/L$ , are used to provide reliable estimates of the surface energy balance, the turbulent kinetic energy budget, and the vertical shapes of the profiles in the surface boundary layer.

A recent exercise by Rachele, Tunick, and Hansen (1991) concerned with the validity of the law of natural growth and the mean value theorem for the analysis of vertical profiles in the surface layer has led to a unique and uncomplicated technique for establishing the similarity scaling parameters and will be put to the proof. Baseline analysis via the Obukhov theory is dubbed the O'KEYPS\*\* scheme; our new technique shall be known as MARIAH.\*\*

---

\*formerly U.S. Army Atmospheric Sciences Laboratory

\*\*See appendix

## 2. DYNAMIC SIMILARITY OF THE SURFACE LAYER

Obukhov (1946) ascertained that the diabatic surface boundary layer could be effectually described by a singular scaling length representative of the ratio of mechanical production of energy to that of the production of convective energy. Obukhov initially derived the scaling length for a dry atmosphere. Busch (1973) properly interpreted the definition of  $L$ , so that the presence of water vapor in the atmosphere and its effect upon the dynamics of the surface layer could be accounted for. Thus, the scaling length is now correctly written as

$$L = - \frac{u_*^3 c_p \rho \bar{\theta}}{kg (H + 0.07 L'E)} = \frac{u_*^2 \bar{\theta}_v}{k g \theta^*} \quad (1)$$

where  $u_*$  is the friction velocity,  $c_p$  the specific heat of air at constant pressure,  $\rho$  density,  $\bar{\theta}$  potential temperature,  $\bar{\theta}_v$  virtual potential temperature,  $k$  karman's constant,  $g$  the gravitational acceleration,  $\theta^*$  the virtual scaling temperature,  $H$  the sensible heat flux, and  $L'E$  the latent heat flux where  $L'$  is the latent heat of vaporization and  $E$  the evaporation of water vapor from the soil to the atmosphere.

By definition the scaling length  $L$  is related to the gradient Richardson (1920) number  $Ri$  by

$$\frac{z}{L} = Ri \phi_M \frac{K_H}{K_M} = Ri \frac{\phi_M^2}{\phi_H} \quad (2)$$

where  $z/L$  is the Monin and Obukhov (1954) scaling ratio,  $K_H$  and  $K_M$  the exchange coefficients for heat and momentum respectively, with  $\phi_H$  a dimensionless lapse rate and  $\phi_M$  a dimensionless wind shear.

In unstable conditions, according to Dyer (1974) and Hicks (1976),  $\phi_H = \phi_M^2$  so that  $z/L = Ri$ . In a stable regime,  $\phi_H = \phi_M$  so that  $z/L = Ri\phi_M$ . Based upon these relationships, the O'KEYPS diabatic equations for unstable flow assume the form listed a priori in table 1.

The MARIAH scheme is not dependent upon first calculating the gradient Richardson number by using eq. (16) in table 1 to obtain values of  $L$ , but will yield  $L$ 's directly. If eqs. (4), (6), and (9) are substituted into eq. (1), the result is

$$L = \frac{\bar{\theta}_v \phi_H (\Delta \bar{V})^2}{\phi_M^2 [\Delta \bar{\theta} + 0.61 \bar{\theta} \Delta \bar{q}] g \Delta \ln z} \quad (3)$$

an exact solution for the Obukhov length in terms of the measured profile gradients in the surface boundary layer. The scaling length  $L$  is no longer dependent upon the friction velocity  $u_*$ , the buoyant heat flux  $(H + 0.07 L'E)$ , or a concurrent evaluation of the evaporation rate  $E$  as suggested in eq. (1).

Equation (3) is also universal, as it applies to the stable as well as the unstable regime. The friction velocity, scaling temperature, and scaling humidity are calculated by using eqs. (4), (6), (8), and (9) after establishing  $\phi_M$  and  $\phi_H$  from eqs. (5) and (7).

TABLE 1. THE O'KEYPS SIMILARITY FORMULA FOR AN UNSTABLE REGIME

$$u_* = \frac{k \Delta V}{\phi_M \Delta \ln z} \quad (4) \quad \bar{V} = \frac{u_*}{k} \left[ \ln \frac{z}{z_o} - \psi_M \left( \frac{z}{L} \right) \right] \quad (11)$$

$$\phi_m = (1 - 15 z/L)^{-1/4} \quad (5) \quad \psi_M \left( \frac{z}{L} \right) = \int_{z_o}^z \frac{1 - \phi_M}{z/L} d \frac{z}{L} \quad (12)$$

$$T^* = \frac{k \Delta \bar{\theta}}{\phi_H \Delta \ln z} \quad (6) \quad \bar{\theta} - \theta_o = \frac{\theta^*}{k} \left[ \ln \frac{z}{z_o} - \psi_H \left( \frac{z}{L} \right) \right] \quad (13)$$

$$\phi_H = \left( 1 - 15 \frac{z}{L} \right)^{-1/2} \quad (7) \quad \psi_H \left( \frac{z}{L} \right) = \int_{z_o}^z \frac{1 - \phi_H}{z/L} d \frac{z}{L} \quad (14)$$

$$\theta^* = T^* + 0.61 \bar{\theta} q_* \quad (8) \quad \bar{q} - q_o = \frac{q_*}{k} \left[ \ln \frac{z}{z_o} - \psi_H \left( \frac{z}{L} \right) \right] \quad (15)$$

$$q_* = \frac{k \Delta q}{\phi_w \Delta \ln z} \quad (9) \quad \frac{z}{L} = Ri = \frac{g (\partial \theta / \partial z)}{\theta_v (\partial \bar{V} / \partial z)^2} \quad (16)$$

$$\phi_w = \phi_H \quad (10)$$

Notes:  $T^*$  is scaling temperature;  $\theta^*$  is a virtual scaling temperature;  $q^*$  is scaling humidity;  $\phi_w$  is dimensionless water vapor gradient;  $\bar{q}$  is specific humidity;  $\psi_M (z/L)$  and  $\psi_H (z/L)$  are the diabatic influence functions for wind and temperature; and  $z_o$  is the surface roughness length.  $\theta_o$  is the potential temperature at  $z_o$ .

In a stable regime, the law of natural growth is only approximately valid, as demonstrated by Rachele, Tunick, and Hansen (1991); and the vertical gradients are no longer tangent to the profiles at the geometric mean of the layers since, from the mean value theorem,

$$z = \frac{\Delta z}{\Delta \ln z} \quad (17)$$

This relationship requires that the gradient Richardson number be rewritten as

$$Ri = \frac{g}{\theta_v} \frac{(\Delta \theta + 0.61 \bar{\theta} \Delta \bar{q})}{(\Delta \bar{V})^2} \Delta z \quad (18)$$

for computational purposes. Hansen (1977), based upon the concept that  $z/L = Ri \phi_M$  in stable conditions, determined from an extensive analysis of experimental profile data extracted from the Great Plains turbulence study reported on by Lettau and Davidson (1957) and Project Prairie Grass, Barad (1958), that the constant  $\beta$  in the log-linear profile model is a variable. Because of the log-linear nature of the mean flow in the surface boundary layer, the MARIAH approach cannot be separated from the O'KEYPS function. This becomes apparent from the MARIAH expression for the stable Obukhov length

$$L = \frac{\bar{\theta}_v (\Delta \bar{v})^2}{g(\Delta \bar{\theta} + 0.61 \bar{\theta} \Delta \bar{q}) \left( \Delta \ln z + \frac{15 \Delta z}{\phi_M L} \right)} \quad (19)$$

which will simplify to

$$L = \frac{\bar{\theta}_v (\Delta \bar{v})^2}{g \Delta \ln z (\Delta \bar{\theta} + 0.61 \bar{\theta} \Delta \bar{q})} - \frac{15 \Delta z}{\phi_M \Delta \ln z} \quad (20)$$

The barrier to an independent MARIAH approach for stable conditions lies in the second term on the right side of eq. (20) that necessitates the calculation of the dimensionless shear  $\phi_M$  before evaluating  $L$ , which is not required in an unstable regime.

The similarity approach for stable flow for O'KEYPS and MARIAH is listed in table 2. However, the basic approach for both dynamic similarity concepts, as shown in table 2, can be improved by considering the ramifications of eq. (17) as derived from the mean value theorem. Applying this concept to the scaling parameters leads to

$$u_* = \frac{k \Delta \bar{v}}{\Delta \ln z + \frac{15 \Delta z}{\phi_M L}} \quad (21)$$

$$T^* = \frac{k \Delta \bar{\theta}}{\Delta \ln z + \frac{15 \Delta z}{\phi_M L}} \quad (22)$$

$$q_* = \frac{k \Delta \bar{q}}{\Delta \ln z + \frac{15 \Delta z}{\phi_M L}} \quad (23)$$

Equations (21), (22), and (23) are much better approximations for establishing the scaling parameters; and although each is dependent upon the O'KEYPS solution, the derivation comes directly from the MARIAH approach.

TABLE 2. THE O'KEYPS AND MARIAH SIMILARITY FORMULA  
FOR THERMALLY STRATIFIED STABLE REGIME

$$z = \frac{\Delta z}{\Delta \ln z} \quad (17) \quad \bar{V} = \frac{u_*}{k} \left[ \ln \frac{z}{z_o} + \psi_M \left( \frac{z}{L} \right) \right] \quad (27)$$

$$Ri = \frac{g}{\theta_v} \frac{(\Delta \bar{\theta} + 0.61 \theta \Delta \bar{q})}{(\Delta \bar{V})^2} \Delta z \quad (18) \quad \psi_M \left( \frac{z}{L} \right) = \beta \frac{z}{L} = \frac{15}{\phi_M} \left( \frac{z}{L} \right) \quad (28)$$

$$\frac{z}{L} = Ri \phi_M \quad (24) \quad \theta - \theta_o = \frac{\theta^*}{k} \left[ \ln \frac{z}{z_o} + \psi_H \left( \frac{z}{L} \right) \right] \quad (29)$$

$$\Phi_w = \Phi_H = \Phi_M = 1 + 15 Ri \quad (25) \quad q - q_o = \frac{q_*}{k} \left[ \ln \frac{z}{z_o} + \psi_w \left( \frac{z}{L} \right) \right] \quad (30)$$

$$\beta = 15 \phi_M^{-1} \quad (26) \quad \psi_w \left( \frac{z}{L} \right) = \psi_H \left( \frac{z}{L} \right) = \psi_M \left( \frac{z}{L} \right) = \beta \frac{z}{L} \quad (31)$$

Notes: Calculate  $u_*$ ,  $T^*$ , and  $q_*$  using eqs. (4), (6), and (9).

### 3. DISCUSSION

Evaluating the MARIAH concepts and comparing the MARIAH hypothesis with the more traditional O'KEYPS profile solutions require a few additional concepts, such as establishing the virtual potential temperature from

$$\bar{\theta}_v = \bar{\theta} (1 + 0.61 \bar{q}) \quad (32)$$

and the relevant specific humidities from vapor pressures in the form

$$q = 0.621 \frac{e}{p - 0.379e} \quad (33)$$

where  $e$  is vapor pressure and  $p$  is the ambient atmospheric pressure. Saturation vapor pressure is given by

$$e_s = 6.11 \exp \left[ \frac{17.4 (\bar{\theta} - 273.15)}{\bar{\theta} - 34.16} \right] \quad (34)$$

and relative humidity is simply the ratio  $e/e_s$ .

To complete the comparison, the diabatic influence functions for O'KEYPS are evaluated by using Benoit's (1977) methodology, whereby

$$\Psi_M\left(\frac{z}{L}\right) = \ln \left[ \frac{(\mathcal{L}_o^2 + 1)(\mathcal{L}_o + 1)^2}{(\mathcal{L}^2 + 1)(\mathcal{L} + 1)^2} \right] + 2 [\tan^{-1}(\mathcal{L}) - \tan^{-1}(\mathcal{L}_o)] \quad (35)$$

$$\text{where } \mathcal{L} = \left(1 - 15 \frac{z}{L}\right)^{1/4}, \quad \mathcal{L}_o = \left(1 - 15 \frac{z_o}{L}\right)^{1/4},$$

and

$$\Psi_H\left(\frac{z}{L}\right) = 2 \ln \left( \frac{\lambda_o + 1}{\lambda + 1} \right) \quad (36)$$

$$\text{with } \lambda = \left(1 - 15 \frac{z}{L}\right)^{1/2}, \quad \lambda_o = \left(1 - 15 \frac{z_o}{L}\right)^{1/2}.$$

Figure 1 shows a comparison of the Obukhov (1946) lengths for MARIAH and O'KEYPS calculated using eqs. (16) and (3). The agreement is considered to be excellent. The divergence is near neutral conditions; that is, large negative  $L$  in figure 1 can be attributed to terrain effects at the Project Prairie Grass field site. An inspection of the upwind terrain relief revealed that the fetch from approximately  $130^\circ$  to  $150^\circ$  was nonhomogeneous, creating a reverse pseudoadvective process upon the normalized wind profile as illustrated in figure 2. Also contributing to the divergence is a humidity effect upon the dynamic stability. Large relative or specific humidities will modify the vertical temperature gradients, creating a destabilizing effect upon the lower portion of the atmosphere.

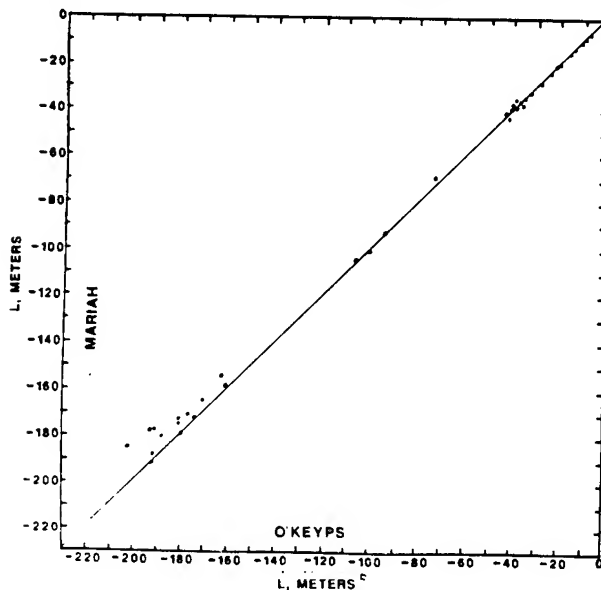


Figure 1. Obukhov lengths for O'KEYPS and MARIAH.

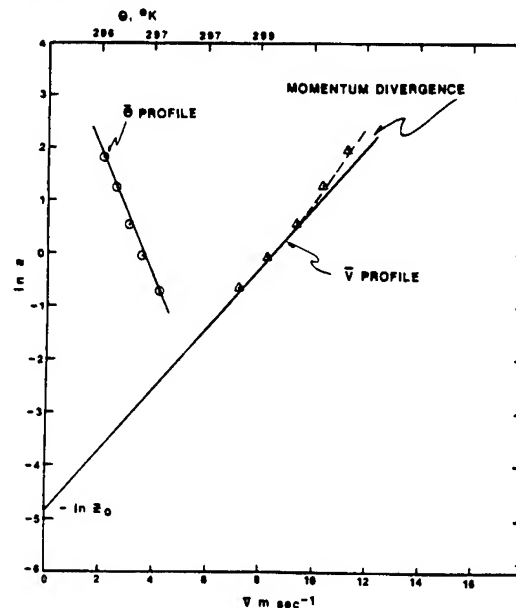


Figure 2. Momentum divergence in the windspeed profile.

Figures 3, 4, and 5 compare the scaling parameters  $u_*$ ,  $\theta^*$ , and  $q_*$ . Again the agreement is considered to be excellent. The experimental data symbolized by (o) represents the thermally stratified stable regime and were evaluated by using eqs. (4), (5), and (8) for O'KEYPS and eqs. (21), (22), and (23) for MARIAH.

The negative values of  $q_*$  for stable flow verify that evapotranspiration continues well into the nocturnal hours and on many occasions continues all night. If the surface temperature cools to near the dew point temperature, then the moisture profiles become isohumic. As the dew point is reached, the specific humidity profile will invert and mass is transported downward with dew formation on the surface.

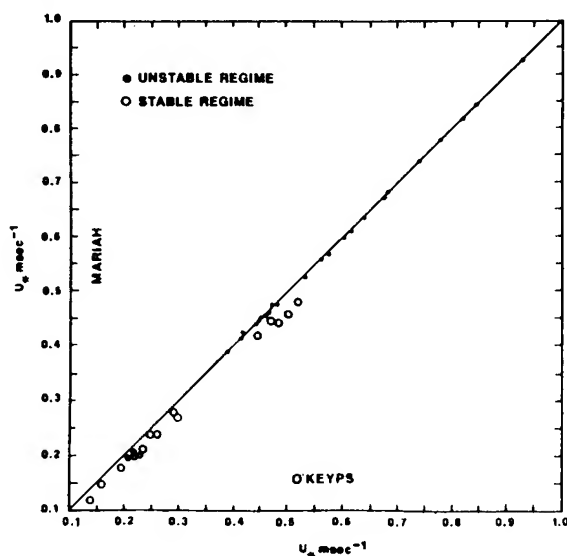


Figure 3. Comparison of friction velocities for O'KEYPS and MARIAH.

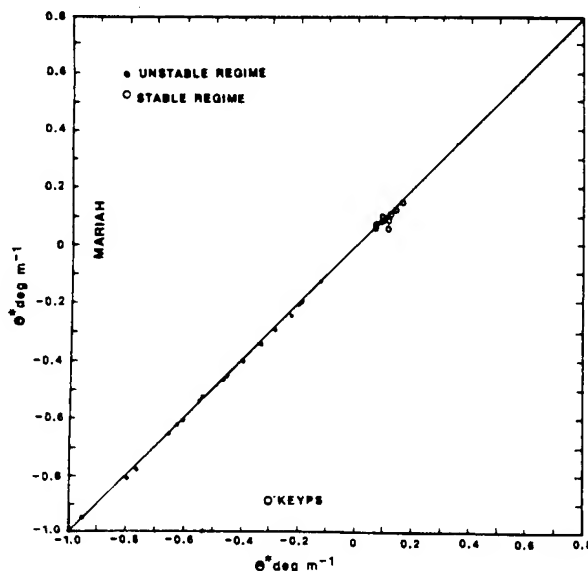


Figure 4. Virtual scaling temperatures for O'KEYPS and MARIAH.

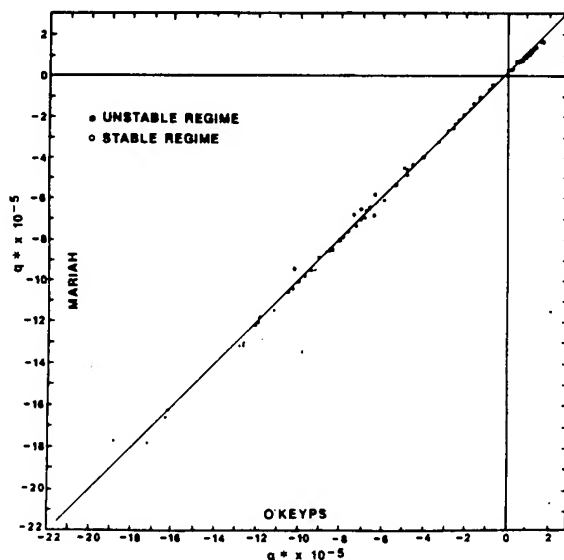


Figure 5. Scaling specific humidities for O'KEYPS and MARIAH.

A total of 21 Project Prairie Grass profiles were analyzed for this study, 12 unstable and only 9 for thermally stratified stable flow. In all, 247 profiles were initially inspected; 226 were being rejected for various reasons, such as obvious nonstationary or heterogeneous defects including horizontal advection of heat and momentum and obvious instrument failures. Of the 21 analyzed profiles only 4 could be assumed to be "ideal." This is about 1.6 percent of the total. This would suggest that advection and convection in the surface layer are the rule, rather than the exception.

Surface boundary layer data must be filtered and smoothed to glean any intelligence concerning atmospheric processes. After the data are temporally averaged, additional massaging includes least squares polynomial fits to the vertical profiles before the dynamic stability and scaling parameters are evaluated. Statistical smoothing is a final step and involves invoking Lettau's (1957) approximation of the height derivative of the Obukhov length in the form

$$L^{-1} = \frac{\sum (Ri)_z}{\sum (z)_i} , \quad i = 1, 2, 3, \dots \quad (37)$$

for unstable flow, and

$$L^{-1} = \frac{\sum (Ri \phi_M)_z}{\sum (z)_i} \quad (38)$$

for the stable regime.

The forced stationarity invoked by application of eqs. (37) and (38) yields the best available estimates of the dynamical physical processes in the surface layer.

#### 4. CONCLUSIONS

The MARIAH approach to similarity theory profile analysis is simpler than the O'KEYPS methodology, especially if the more formal analysis involving the evaluation of the diabatic influence functions  $\psi_M(z/L)$  and  $\psi_H(z/L)$  is used to solve eqs. (11), (13), and (15) and subsequently to evaluate the scaling parameters  $u_*$ ,  $\theta^*$ ,  $q^*$  in unstable flow. The experimental results shown in figures 3, 4, and 5 indicate that the use of eqs. (4), (8), and (9) for calculating the scaling parameters yields accurate results.

The requirement for proper filtering and smoothing of experimental profile data needs to be reemphasized. Forced stationarity is apparently a necessity.

Both O'KEYPS and MARIAH appear to function well in the stable regime, especially after water vapor is included in the models. The approach to an isohumic state and the inversion of the specific humidity profiles do not seem to affect the profile analysis scheme whatsoever. This would indicate that expansion of the MARIAH scheme by estimating specific humidity profiles for



shelter height relative humidities will be highly feasible for both the stable and unstable regimes.

#### REFERENCES

- Barad, M. L., 1958: Project Prairie Grass, A Field Program in Diffusion. Geophysical Research Paper No. 59, Air Force Cambridge Research Center, Bedford, MA, II, 209 pp.
- Benoit, R., 1977: On the Integral of the Surface Layer Profile-Gradient Functions. J. Appl. Meteorol., 16:859-860.
- Busch, N. E., 1973: On the Mechanics of Atmospheric Turbulence. In Workshop on Micrometeorology, D. A. Haugen, ed., American Meteorological Society, Boston, MA, 392 pp.
- Dyer, A. J., 1974: A Review of Flux-Profile Relations. Boundary Layer Meteorol., 7:363-372.
- Hansen, F. V., 1977: The Critical Richardson Number. ECOM-5829, U.S. Army Atmospheric Sciences Laboratory, White Sands Missile Range, NM 88002-5501
- Hicks, B. B., 1976: Wind Profile Relationships from the Wangara Experiment. Quart J. Roy. Meteorol. Soc., 102:535-551.
- Lettau, H. H., 1957: Computation of Richardson Numbers, Classification of Wind Profiles, and Determination of Roughness Parameters. Exploring the Atmosphere's First Mile, Vol. 1. H. H. Lettau and B. Davidson, eds, Pergamon Press, New York.
- Lettau, H. H., and Davidson, B., 1957: Exploring the Atmosphere's First Mile, I and II, Pergamon Press, New York.
- Monin, A. S., and A. M. Obukhov, 1954: Basic Regularity in Turbulent Mixing in the Surface Layer of the Atmosphere. Trans. Geophys. Inst. (Trudy) Acad. Sci., USSR, 24:163-187.
- Obukhov, A. M., 1946: Turbulence in an Atmosphere of Non-Homogeneous Temperature. Trans. Inst. Theor. Geophy., USSR, 1:95-115.
- Rachele, H., A. Tunick, and F. V. Hansen, 1991: A Method for Estimating Similarity Scaling and Obukhov Lengths from Discrete Vertical Profile Data. ASL-TR-0303, U.S. Army Atmospheric Sciences Laboratory, White Sands Missile Range, NM 88002, 27 pp.
- Richardson, L. F., 1920: The Supply of Energy from and to Atmospheric Eddies. Proc. Roy. Soc., (A):97:354-373.

## APPENDIX A. ORIGINATION OF O'KEYPS AND MARIAH

The O'KEYPS function used generically as a "nom'de plume" for all diabatic conditions was coined by Panofsky<sup>1</sup> and Yaglom.<sup>2</sup> The acronym represents the initials of the major authors who pioneered the linear-quartic form of the profiles of wind temperature and specific humidity and to a lesser extent the log-linear forms for stable flow. These were: Obukhov, Kasanski and Monin, Ellison, Yamamoto, Panofsky, and Sellers.

MARIAH has no relationship to any meteorological phenomena or to any individual, except that fictitious fellow "Rotten Luck Willie" of the Broadway musical Paint Your Wagon\* who sang,

"---Way out there they have a name for rain and wind and fire,  
the rain is Tess, the fire's Joe, and they call the wind MARIAH!"

---

\*copyright, MCA Records, Inc. Universal City, CA.

<sup>1</sup>H. A. Panofsky, 1963: Determination of Stress from Wind and Temperature Measurements. Quart. J. Roy. Meteorol. Soc., 89:85.

<sup>2</sup>A. M. Yaglom, 1977, Comments on Wind and Temperature Flux-Profile Relationships. Boundary Layer Meteorol., 11:89-102.

**Session II**

**SENSORS AND SYSTEMS**

**Session Chair**

**Mr. Chad George  
AMC Smart Weapons Management Office  
Redstone Arsenal**

## **THE MET IMPROVEMENT PROGRAM:**

### **KEY TO UNLOCKING TARGET AREA METEOROLOGY**

**M. A. Seagraves, R. E. McPeck and MAJ A. A. Grunwald  
U.S. Army Research Laboratory  
White Sands Missile Range, New Mexico 88002-5501, USA**

#### **ABSTRACT**

The U.S. Army Research Laboratory Battlefield Environment Directorate is conducting research and developing equipment in a Met Improvement Program that will lead to an understanding of target area meteorology for artillery fires. Systems to observe and model weather in data-denied areas will provide Army commanders with data needed for fire planning and direct target servicing using conventional and high-technology weapons. The Mobile Profiler System (MPS) will fuse data from satellite and ground-based profilers to build 3-D databases out to 200 km. Research into time and space variability of data and satellite sensor data calibration and validation will be conducted to ensure that only highest quality 3-D data are produced by the MPS. Satellite data exploitation techniques for inferring visibility in varying spectral regions are also being pursued. All data produced by the MPS will be provided to both the Integrated Meteorological System and the Computer Assisted Artillery Meteorology (CAAM). The CAAM software is being developed to reside on artillery Army Tactical Command and Control System (ATCCS) computers. It will optimize available met data for effective employment of artillery fires. The CAAM development team will also investigate and develop new techniques for displaying and transmitting information for artillery weapons selection and aiming decisions.

#### **1. INTRODUCTION**

The Field Artillery has long been aware of the effects of the atmosphere on their weapon systems. An accurate knowledge of the atmosphere and its effects along the expected path of an artillery shell is essential in pointing the gun to hit the target.

As the range of artillery weapons increases, so do the atmospheric effects. An analysis of all the factors known to affect artillery accuracy has shown that the effect of meteorological (or met) conditions is the largest contributor to artillery miss distances and that frequently updating the met data used in aiming, especially wind,

significantly improves accuracy and effectiveness (Blanco, 1992a). It is estimated that as much as 50% of the artillery miss distance is due to inaccuracies in the met data. With longer-range weapons coming into the inventory, the need for accurate, timely data is becoming even more critical.

The U. S. Army Field Artillery School has recognized the requirement for improved met data and has initiated a Mission Need Statement (MNS) for a Target Area Meteorological Sensors System (TAMSS) to address the requirement. This MNS recognizes the need for timely and accurate met data for ballistic corrections for cannon and rocket systems. Low-level wind data and visibility restraints, such as precipitation type and rate, sky cover, cloud base altitude, and fog, out to 200 km in the target area, are needed for selecting the optimal munition and determining its aiming point. The mission of TAMSS is to provide an enhanced target area met capability to assist in projecting lethality forward. TAMSS addresses a suite of sensors and software to acquire data in the target area. The initial operation capability is required in fiscal year 2000 with full operational capability in fiscal year 2005. The MNS was approved by TRADOC on 14 Sep 92.

The Met Improvement Program at the U.S. Army Research Laboratory Battlefield Environment (BE) Directorate is designed to lead to an understanding of target area met for artillery fires and to fulfill requirements stated in the TAMSS MNS. This is a two-thrust program consisting of the Mobile Profiler System (MPS) and the Computer Assisted Artillery Meteorology (CAAM).

## 2. MOBILE PROFILER SYSTEM (MPS)

The purpose of the MPS is to determine accurate values for vertical profiles of wind, temperature, density, and humidity from the surface to 30 km altitude and out to 200 km horizontally. The MPS will fuse satellite-derived wind, temperature, density, and humidity data with similar data obtained from direct measurements using state-of-the-art remote radar and microwave sensors. Figure 1 illustrates the sources of the MPS data for various altitudes above the surface, where RASS refers to the Radio Acoustic Sounder System. Further information about the components and capabilities of the MPS may be found in McPeck and Seagraves (1992).

When operating in a "stand-alone" mode, the MPS sensors exhibit over-all accuracies that are not sufficient to result in any improvement in met data that might increase the accuracy of artillery fires (Miers et al., 1992). However, each sensor can provide certain types of useful data, and when complementary sensors are used in combination, they have the potential to equal or exceed the accuracy of conventional rawinsonde observations. Accuracy studies of the MPS are on-going, but it is expected that the largest errors in the MPS wind data will occur near the tropopause (approximately 10-12 km AGL) during conditions of strong wind shear such as caused by the jet stream. Temperature and humidity errors are also expected to be larger near the tropopause and during precipitation conditions.

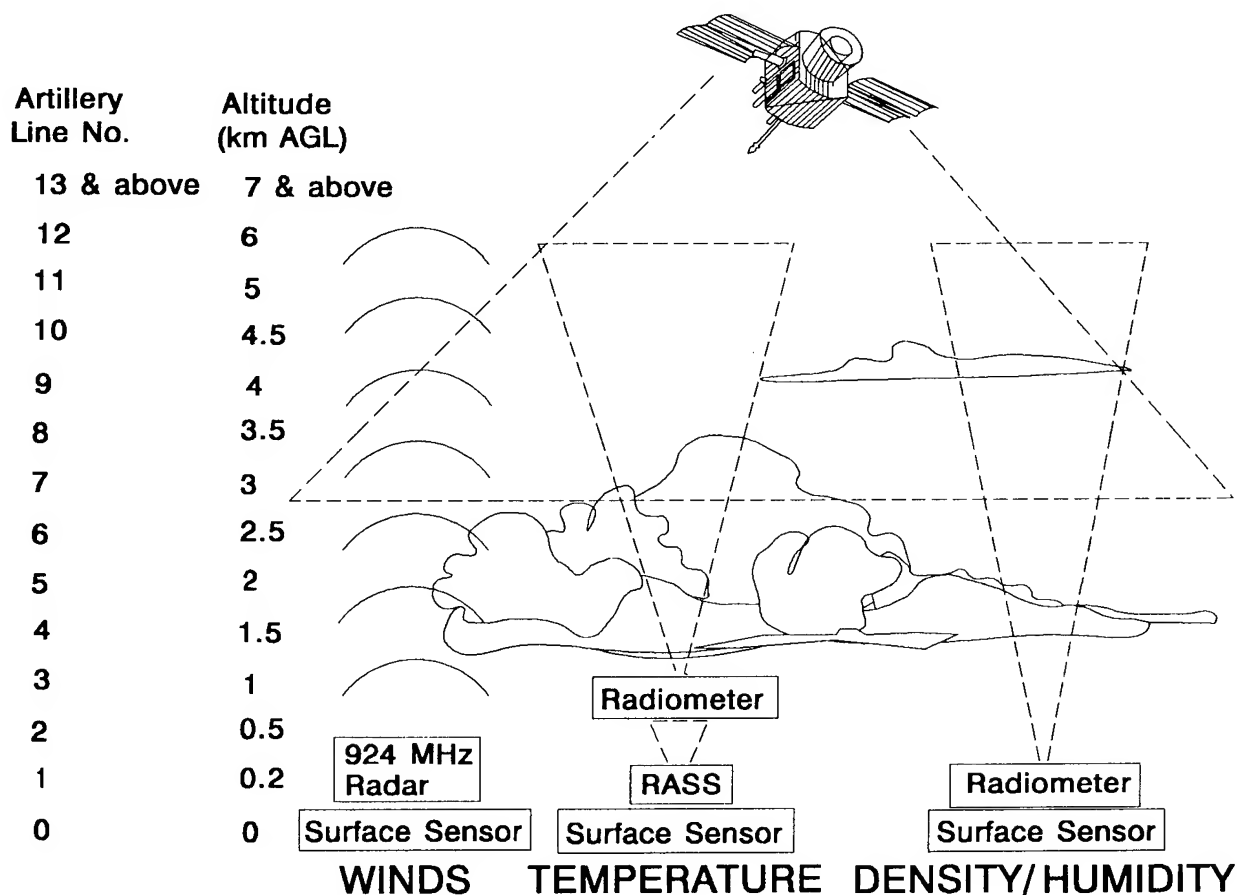


**Figure 1.** MPS data sources, where RASS refers to the Radio Acoustic Sounder System.

A major advantage to be offered by the MPS in improving met data used by the Field Artillery is the great increase in the temporal and spatial resolution of the data. Currently, upper air profiles are measured using radiosondes at best every two hours. Measurement frequency is more likely to be every four hours. The MPS is expected to be able to provide data to update the lower portion of the profile as often as every 15 minutes using data from the ground-based sensors. New data will be available from the satellites for the upper portion of the profile at least every 2-4 hours and methods of "advecting" the data using isentropic models will provide information comparable in frequency to that from the ground-based sensors.

A second major advantage of the MPS is its ability to provide met data for the target area. The fusion of met profiles from ground-based sensors with those generated from satellite sounders offers much improved temporal and spatial resolution. The ground-based profiling segment can produce winds, temperature, pressure and humidity every 15 minutes. The satellite-based segment produces profiles over a swath 1700 km wide for the Defense Meteorological Satellite Program (DMSP) platforms and 2200 km wide for the National Oceanographic and Atmospheric

Administration (NOAA) TIROS satellites. The temporal refresh capability of the MPS ground-based segment combined with the battle-area spatial capability of the space-based segment provides a synergism of time and space scales heretofore not available to Army commanders.

All data collected by the MPS will be fused to form a 3-dimensional (3-D) database suitable for use in employing cannons, rockets, and smart weapons delivered by tactical missile carrier vehicles. This database will be updated when new data are received from the MPS ground segment, space segments, other available sources, or output from the isentropic model that will move the satellite data forward in time between satellite passes. Data will be automatically made available to the CAAM software for artillery application and dissemination. Further, the 3-D data will be made available to the Integrated Meteorological System (IMETS) for input to 4-dimensional forecast models and tactical decision aids.

### 3. COMPUTER ASSISTED ARTILLERY METEOROLOGY (CAAM)

The second thrust of the Met Improvement Program is the development of CAAM. As indicated in the Field Artillery's MNS for TAMSS, there is no single system envisioned that will be capable of providing the artillery with all of its target area met needs. It will take a suite of sensors and associated software techniques to accomplish this mission--sensors that provide a variety of data, in different resolutions, at various locations and times. This requirement drives the need for CAAM, a software package that can integrate a wide variety of met data, build an understanding of the atmospheric conditions in the target area, generate products that describe these conditions in artillery formats, and disseminate this information to all fire support users. Thus, the purpose of CAAM is to optimize available met data for the more effective employment of artillery fires. The CAAM concept is illustrated in figure 2.

Utilizing advanced met modeling techniques, CAAM will integrate available met sensor data and generate area-of-interest met messages that closely represent the actual conditions in the target area at the time of firing. This available met information will include:

- upper-air profiles, initially, from the Artillery Met Sections and, eventually, from the MPS,
- met satellite-derived profiles obtained from the MPS or IMETS,
- dropsonde profiles for the target area, once the Field Artillery develops and fields such as system,
- automated surface sensor data obtained via IMETS from a network of sensors that will exist when the Automated Meteorological Sensor System (AMSS) is fielded,
- and, eventually, met sensor data from unmanned aerial vehicles.

The integrated area-of-interest met messages will be used to improve ballistic corrections for both cannon and rocket systems, to adjust the aiming points for carrier

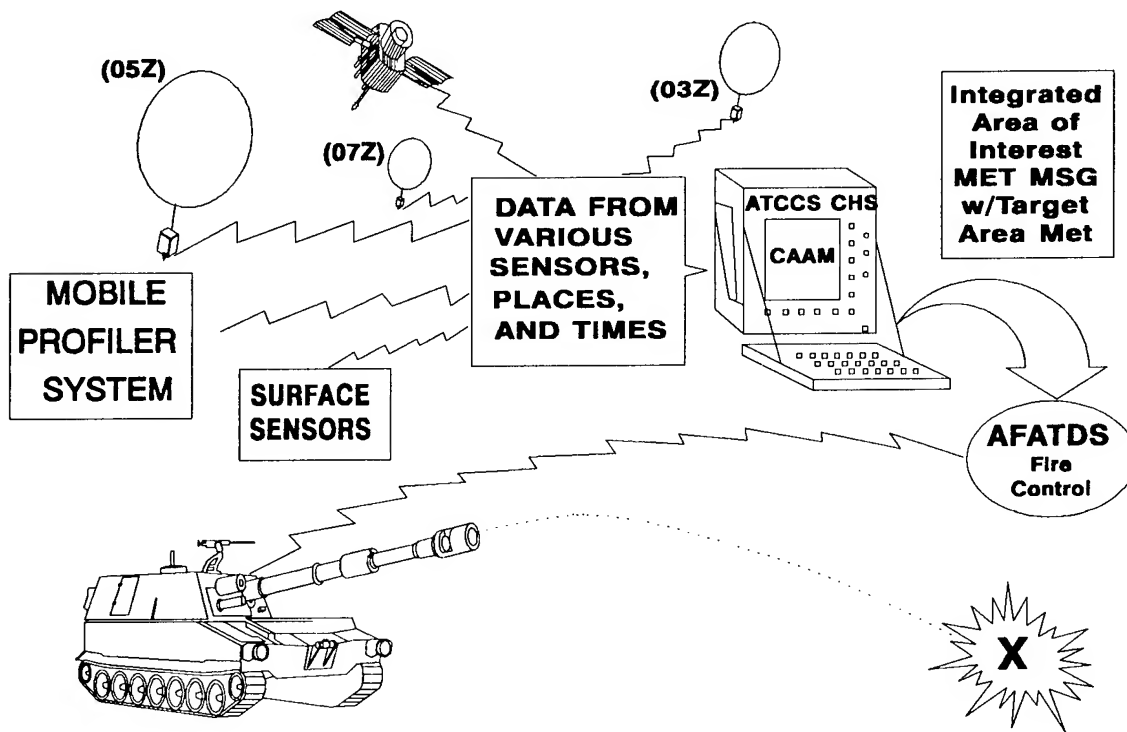


**Figure 2.** Computer Assisted Artillery Meteorology (CAAM) concept.

munitions, and to select the best munition or means of fire support to engage targets based on an understanding of the expected atmospheric conditions in the target area.

The objective of the CAAM effort is to develop, evaluate, and demonstrate a software package that will integrate available battlefield met data on ATCCS common hardware and derive improved ballistic and target area met for Field Artillery applications. In addition, CAAM is being developed as a system improvement, or technology insertion, to the Field Artillery Meteorological Data System (MDS) (AN/TMQ-31) and Meteorological Measuring Set (AN/TMQ-38).

The CAAM program has several technical objectives, the first of which focuses on the selection of a met model that best meets the needs of the Field Artillery. To accomplish this task, an approach has been taken that essentially competes four existing models against specific Field Artillery-related criteria. The four candidate models chosen for evaluation are the Time Space Weighted Analysis Model (Blanco, 1992b); the Analytic Approximation Scheme Model (Caracena, 1992), the Optimum Interpolation Objective Analysis Model (Stenmark, Olmstead, and Veazey, 1977), and the Higher Order Turbulence Model for Atmospheric Circulation (HOTMAC) (Yamada



and Bunker, 1989). Each model has been adapted to ingest data from the array of met sensors that are expected to be available on the battlefield in the near-term and to derive met information in artillery formats over a 100 km wide and 200 km deep area-of-interest (the dimensions of this area correspond to the Artillery's definition of the target area). These models will be evaluated under a wide variety of scenarios where the quantity, type, and characteristics of the input is varied. To examine the accuracy of each model with respect to ballistics, the met messages derived by each model under a given scenario will be input to both cannon and rocket trajectory models. Comparisons will then be made against the expected impacts calculated by each model for each scenario. Other criteria that will be examined during model evaluation include ease of model implementation, hardware requirements, level of training required for the operator, and accuracy in providing wind profiles at the target area for aiming point adjustments of carrier munitions.

To provide the necessary arrays of sensor data needed to support model evaluation, an extensive met data collection exercise was conducted at White Sands Missile Range. The test exercise was designed to provide data from those sensors that could reasonably be expected to exist on the near-term battlefield, covering a 100 km by 200 km targets area. Eight upper-air rawinsonde sites were located so that their data could represent the Artillery Met Sections located behind the forward edge of the battle area, surrogate dropsonde flights in the target area, and measurements of truth in the target area needed to validate model outputs. Radiosondes were released at each of these sites 5 times each day. To represent automated surface sensor data, 15-minute and hourly-averaged data from an extensive network of automated surface sensors were recorded for each 24 hour period. Met satellite profiles were also recorded for each pass of NOAA and DMSP satellites that occurred on test days. Radar profiler and RASS data were recorded to represent the MPS. Present Weather Sensor data, which includes temperature and precipitation data, were recorded at selected locations, as were local observations from observers at the upper-air sites, including ceilometer measurements. Weather radar and lightning detection data were recorded for each test day. Attempts were also made to simulate unmanned aerial vehicle met data over the target area by using a met sensor flown on a manned aircraft. However, due to technical difficulties, the data that resulted from this operation were not usable. All data will be entered into a relational database to support model evaluation.

The second technical objective of the CAAM program focuses on the dissemination of target area met for fire support applications. While the need for target area met is well understood both in terms of what and why, methods for disseminating this information to all of the fire support users is largely unresolved. Current practices assume that the atmospheric conditions measured by the Artillery Met Section are homogeneous in both time and space. Thus, met information can be disseminated across the battlefield with a single message that covers the entire area of operations and is assumed to be valid until replaced with newer message. As the Field Artillery develops new techniques to enhance and modernize its capabilities so that target area

met can be obtained, it must also develop the necessary techniques to display and transmit the information to the various users.

Dissemination of accurate and timely target area met information could cause a significant increase in the amount of met data that will flow over the Field Artillery command, control, and communications (C3) network--a network that is already overtaxed with existing requirements. Even though problems associated with this increase in traffic may eventually be solved with future communications and data distribution systems, disseminating target area met in such formats as 4-dimensional grids that cover a 100 km by 200 km area is not realistic for the near future. In response to the need for target area met, the Field Artillery has developed a new low-level target area met message that includes a profile of wind and temperature at the target location, height of cloud bases, precipitation type and rate, and refractive index. However, there are many unresolved issues associated with the generation and dissemination of this message. Therefore, innovative new approaches for displaying and transmitting target area met information over the Artillery's existing and near-term C3 networks are being investigated.

The final major technical objective is the development of the CAAM demonstration package. Once the model has been selected and the outputs determined, an entire CAAM software package will be developed to support a technology demonstration (TD). This package will be designed to run on an ATCCS computer and will include met databases, met message generation functions, executive and user interfaces, displays, and communications interfaces. In addition, research will be conducted to incorporate met data management functions into the CAAM software. These functions will employ a set of rule-based techniques to assist the operator in directing artillery met measuring activities by recommending balloon release rates. These release rates will be based on a trend analysis of the sensor data in the database such that a slower rate can be recommended when the atmosphere is relatively stable, and a more frequent rate can be recommended when the weather is changing rapidly. In addition, research will be conducted to develop functions that assist in the dissemination of met messages. Again, rule-based techniques will be employed to compare newly generated met messages with the last message transmitted and recommend dissemination of a new message only when a specified level of artillery accuracy is threatened. This management technique will assist in the conservation of communications resources. To demonstrate CAAM as a technology insertion, the entire CAAM software package will be integrated into an MDS.

#### 4. MET IMPROVEMENT PROGRAM TECHNOLOGY DEMONSTRATION

A Technology Demonstration of the MPS and CAAM will be conducted in April 1994. The TD will demonstrate that the CAAM modification will give MDS the capability to:

- (1) receive and database met data from other sources to include other Artillery Met Sections, the MPS, and a prototype IMETS,

(2) integrate met data from the database through the use of an objective analysis or a mesoscale model to derive upper-air profiles and target area met parameters at a user specified location and time,

(3) convert the derived and or databased data into the Field Artillery's Computer Met (MET-CM) and Target Area Low Level Meteorological Messages (MET-TALL),

(4) transfer the MET-CM and MET-TALL messages to a designated firing element where these messages will be employed to improve artillery accuracy, and

(5) better manage artillery met operations through the use of specialized management software.

For the demonstration, upper-air systems will be used as surrogate Artillery Met Sections and BE's Technology Exploitation Weather Testbed will be used as a prototype IMETS. The MPS will provide two products for CAAM integration--computer met messages every 15-30 minutes, measured at the profiler location, and satellite profiles over the general area of interest with each pass of a NOAA or DMSP satellite. The firing element in this demonstration will be represented by a computer that will run Battery Computer System (BCS) software that has been modified to use both the MET-CM and MET-TALL messages. Figure 3 illustrates the concept for the TD. Improvements in accuracy will be demonstrated through the use of firing simulation software that will combine a general trajectory model with user displays and graphics. Firing simulations will be conducted to show the differences in "should hit" data when four-hour-old met messages from a single dedicated station are used versus integrated "best met" messages from CAAM.

The TD will also demonstrate that a CAAM-modified MDS can exchange met data with the prototype IMETS over a surrogate Multiple Subscriber Equipment (MSE) communications link. These techniques will be used to show how upper-air data from the Artillery can be transferred to IMETS, while parameters such as satellite profiles, precipitation forecasts in the target area, and other required data can be transferred to a CAAM modified MDS from IMETS. Figure 4 provides a data flow diagram for the TD. The demonstration will be conducted in two parts. First, CAAM will ingest previously archived met data to demonstrate improvements in artillery accuracy under various scenarios of sensor availability and weather. Secondly, CAAM will run in real-time with actual met data to demonstrate data transfer, modeling, and message generation techniques in an operational context.

## 5. CONCLUSIONS

The Met Improvement Program as outlined in this paper is designed to greatly decrease the miss distance of artillery fire due to stale, inaccurate met data. As the range of the artillery cannon is increased, this improved accuracy is essential in achieving the mission. It will become even more crucial as rockets and cannons are used to deliver smart munitions at very long ranges when target area met is critical.

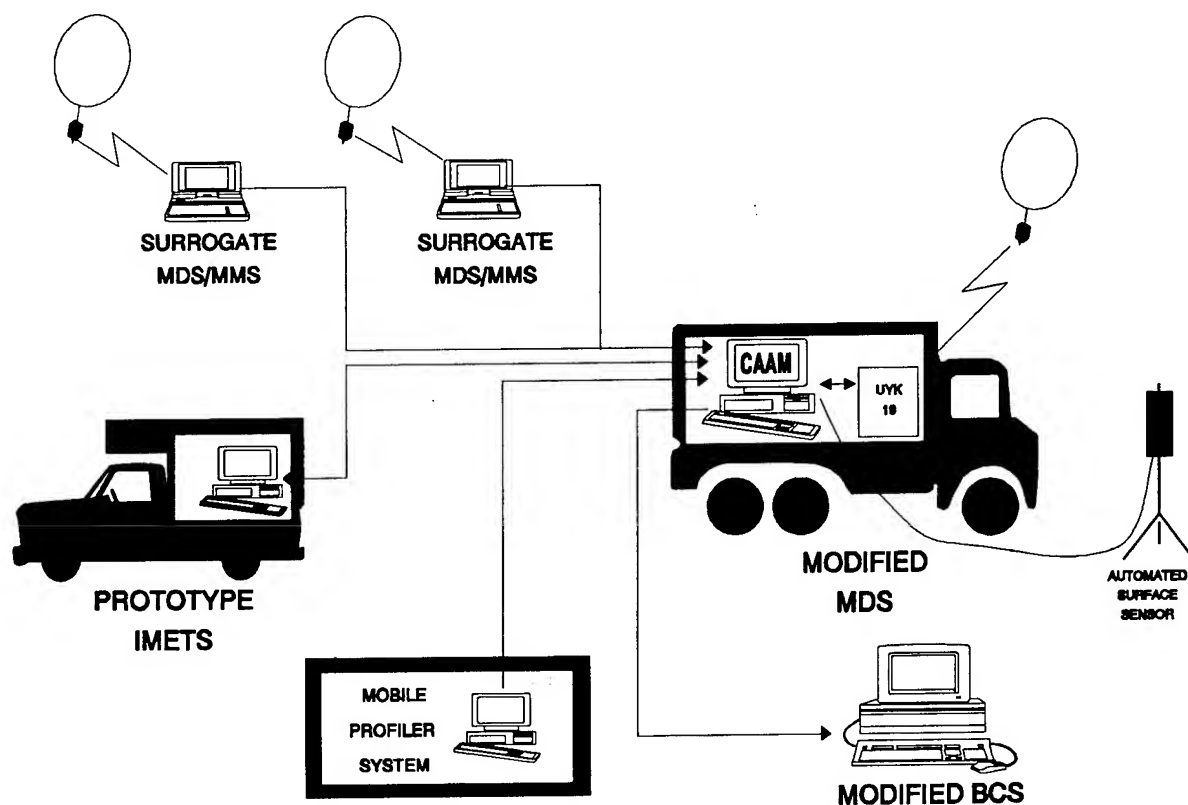


**Figure 3.** Met Improvement Program Technology Demonstration Concept.

## REFERENCES

- Blanco, A., 1992a: personal communication.
- Blanco, A., 1992b: personal communication.
- Caracena, F., 1992: The Use of Analytic Approximation in Providing Met Data for Artillery, Proceedings of the 1992 Battlefield Atmospherics Conference, U.S. Army Research Laboratory, White Sands Missile Range, NM 88002-5501.
- Marty, F. F., 1992: Draft Mission Need Statement (MNS) for the Target Area Meteorological Sensors System (TAMSS), memorandum dated 4 Jun 92, U.S. Army Field Artillery School, Fort Sill, OK 73503-5600.
- McPeck, R. E., and M. A. Seagraves, 1992: Mobile Profiler System (MPS): The Army's Future Target Area Meteorology Data Collection System, Proceedings of the 1992 Battlefield Atmospherics Conference, U.S. Army Research Laboratory, White Sands Missile Range, NM 88002-5501.

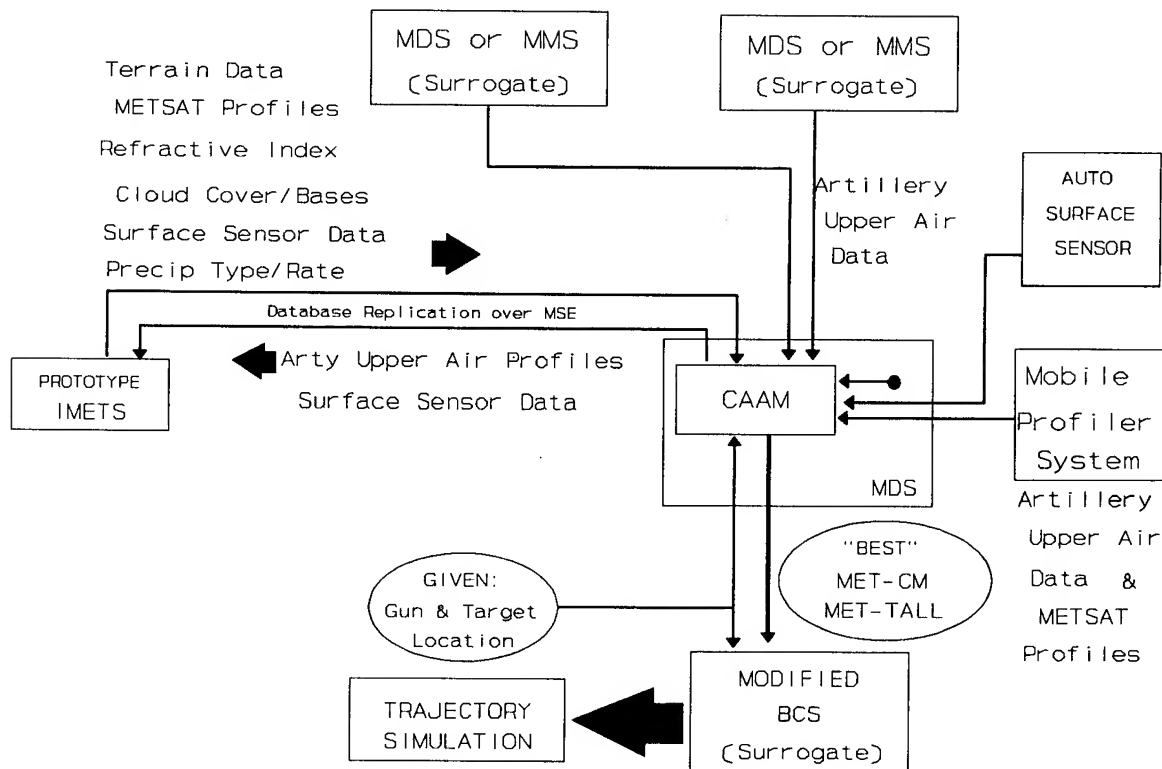


**Figure 4. Technology Demonstration Data Flow.**

Miers, B. T., J. L. Cogan, and R. J. Szymber, 1992: Review of Selected Remote Sensor Measurements of Temperature, Wind, and Moisture, and Comparison to Rawinsonde Measurements, ASL-TR-0315, U.S. Army Atmospheric Sciences Laboratory, White Sands Missile Range, NM 88002-5501.

Stenmark, E., W. Olmstead, and D. Veazey, 1977: Proposed AMS-A (Automatic Meteorological System--Artillery) for Corps TACFIRE (PACT) System Description, Internal ECOM Report, U.S. Army Atmospheric Sciences Laboratory, White Sands Missile Range, NM 88002-5501.

Yamada, T., and S. Bunker, 1989: A Numerical Model Study of Nocturnal Drainage Flows with Strong wind and Temperature Gradients, J. Appl. Met., 28:545-554.

**THE DOUBLE BEAM INTERFEROMETER SOUNDER (DBIS):  
A DEVICE FOR THE PASSIVE REMOTE SENSING  
OF ATMOSPHERIC PROFILES**

J.-M. Thériault

DREV-Defence Research Establishment Valcartier  
P.O. Box 8800, Courcelette, Québec, Canada, G0A 1R0

J. Giroux, J. Côté and M. Fournier

BOMEM INC. 450 St-Jean-Baptiste, Québec, Canada, G2E 5S5

G. P. Anderson and J. H. Chetwynd

Geophysics Directorate, Phillips Laboratory /GPOS  
Hanscom Air Force Base, MA 01731, USA

**ABSTRACT**

In order to develop a method for the retrieval of temperature and water vapor profiles from IR emission spectra, the Defence Research Establishment Valcartier (DREV) has recently acquired an instrument referred to as the Double input Beam Interferometer Sounder (DBIS). The sounder is a portable device composed of a Fourier spectrometer and one or two telescopes that measures the atmospheric emission in the IR region from 3 to 20  $\mu\text{m}$  at a spectral resolution of  $1\text{ cm}^{-1}$  and at any prescribed viewing angles. Preliminary tests performed in the laboratory with the DBIS indicate a radiometric accuracy better than 0.4 K in terms of brightness temperature. Several field measurements achieved with the sounder in clear sky conditions have been compared to calculations with FASCODE and MODTRAN models. In both cases the agreement is remarkably good. The quality of the measurement-model comparisons suggests implementing an algorithm based on the minimum information approach.

**1. INTRODUCTION**

The Defence Research Establishment Valcartier (DREV) is currently developing a Tactical Decision Aid (TDA) to provide field commanders with continuously updated predictions of their EO systems based on remotely determined information of the slant path transmission (Bissonnette, 1989). An important component of the TDA development program is concerned with the remote determination of atmospheric temperature and water vapor profiles along the optical path. In this case, the DREV approach is founded on ground-based measurements of the infrared radiation emitted by the atmosphere. In order to investigate the many possible avenues of such a method, a spectrometer system especially designed for remote sensing applications has been recently acquired. The instrument is referred to as the Double input Beam Interferometer Sounder (DBIS). The prime capability of the DBIS is to produce calibrated IR emission spectra in the 3-20  $\mu\text{m}$  region at a resolution of  $1\text{ cm}^{-1}$  for any angle of observation. One measurement provides approximately 2000 spectral elements of useful information. The magnitude and the shape of emission spectra are direct functions of temperature and

constituent profiles. Conversely, the temperature and the constituent profiles can be retrieved by applying to these spectra a proper inversion algorithm.

The purpose of this paper is to report the current research related to this new remote sensing project. First, the design and the mode of operation of the sounder are described. Second, recent field measurements of atmospheric emission spectra are presented, analyzed and compared to models predictions. Finally, the general retrieval approach selected for the inversion of DBIS spectra is described and discussed in terms of the speed and accuracy requirements.

## 2. DESCRIPTION OF THE SOUNDER

As represented in Fig. 1, the DBIS consists of one or optionally two telescope modules, a Fourier transform spectrometer-interferometer and two output optics modules. The sounder has the following specifications:

- Cassegrain 10-in diameter F/5.1 telescopes,
- Bomem MB100 spectrometer including an intel 386 computer with the radiometric software,
- spectral coverage: output optics-1 with an MCT detector, 5-20  $\mu\text{m}$ ; output optics-2 with an InSb detector, 2-5  $\mu\text{m}$
- variable resolution from 1 to 128  $\text{cm}^{-1}$
- throughput (clear optical cross section),  $\sim 9 \text{ cm}^2$
- system field of view, 5 mrad.

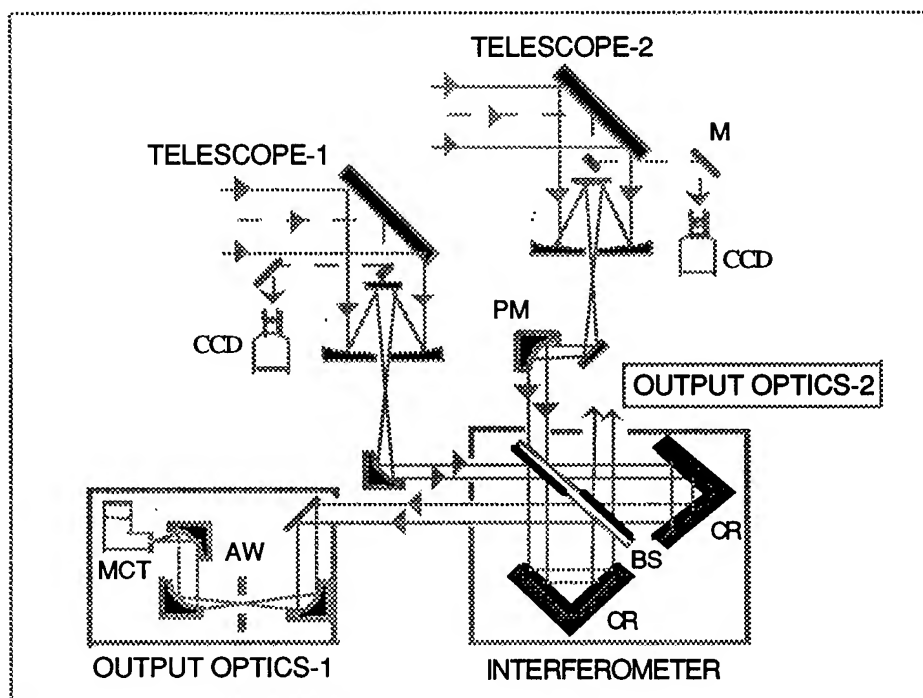


Figure 1. Schematic representation of the Double input Beam Interferometer Sounder (DBIS).

As a part of the input modules, a large flat plate mirror (scene mirror) placed in front of each telescope can be either rotated to the selected scene or oriented in a position for the acquisition of calibrated reference spectra. The pointing capability of the scene mirror allows slant path measurements at any zenith angles from 0 to 360 degrees with a tilt adjustment of  $\pm 10$  degrees in azimuth and an accuracy of 0.1 degree. The coarse adjustment in azimuth is simply achieved by rotating the whole sounder assembly which is mounted on a tripod. After reflection on the scene mirror, the optical beam is then successively focussed by the Cassegrain telescope and reflected by an off-axis parabolic mirror (PM) to produce a collimated beam of proper diameter at the entrance pupil of the interferometer. As illustrated in Fig. 1, the interferometer is a modification of the Michelson configuration where the conventional flat plate mirrors have been replaced by corner reflectors (CR). This design has numerous advantages. First, the use of corner reflectors is a simple and efficient way to insure the parallelism between the two interfering beams. Second, it is a natural solution for the design of a real double input, double output ports interferometer. With such an interferometer (ideal case), two beams coming from different scenes can be optically combined and spectrally subtracted in real time. Basically, this arises from the fact that the modulated components of the two interferograms associated to each input port are out of phase. The development of a differential observation technique based on spectral subtraction with the DBIS is a major goal of our project. However, preliminary tests of this technique have not been totally successful. For this reason, the field measurements performed so far have been done with the single beam configuration. In this case, the second telescope module has been replaced by a stable cold blackbody (liquid nitrogen). The two outputs modules are identical, except that channel-1 includes a MCT detector while channel-2 includes a InSb detector (note that module-2 optics are not explicitly shown in Fig. 1). Essentially, these modules contain parabolic and condensing mirrors that focus the beam coming from the interferometer onto a detector (MCT or InSb) of 1 mm diameter. An aperture wheel (AW) mounted with stops of different diameters permits the adjustment of the field of view of the instrument (5 mrad or smaller).

The methodology for the radiometric calibration of DBIS spectra is based on the two temperature calibration method. Two temperatures are required because there are two unknowns: the gain and the offset (self emission) of the instrument. The implementation of this method is fully consistent with the solution given by Revercomb et al. (1988). To this end, two large flat plate blackbodies (12"x12") kept at constant temperatures have been used: one, referred to as the hot blackbody, is stabilized at a temperature of 50° C while the other, referred to as the ambient blackbody, is stabilized at a temperature near the ambient conditions of operation ( $\sim 25^\circ$  C). The accuracy of both blackbodies is of the order of 0.1° C. To obtain a calibrated emission spectrum, three measurements are required: the raw spectrum corresponding to the emission of the atmosphere and two raw spectra from the reference blackbodies. Each raw spectrum is obtained by coadding 40 individual scans ( $\sim 4$  minutes) taken at a resolution of  $1\text{ cm}^{-1}$  (apodized). In these conditions of operation, the accuracy of the DBIS has been evaluated to be better than 0.4 K in terms of brightness temperature with an RMS noise component below 0.1 K almost everywhere in the usable portion of the 3-20  $\mu\text{m}$  region.

### 3. ATMOSPHERIC MEASUREMENTS AND CALCULATIONS

From May to July 1992, in a series of field experiments organized by the Phillips Laboratory (Hanscom, AFB) at Ft. Devens annex in Sudbury MA, the DBIS has been run successfully in a wide variety of clear and cloudy sky conditions. One major objective of the experiment was the acquisition of coincident radiosonde and spectral data to be used as a support for the development and the validation of inversion algorithms. Typical measurements of atmospheric emission spectra ( $1\text{ cm}^{-1}$  res.) performed with the sounder in hot-dry conditions for two zenith angles are shown in Fig. 2. For the purpose of a qualitative comparison, Fig. 3 summarizes the issue (note the resolution of  $2\text{ cm}^{-1}$ ). The general shape of emission spectra is entirely dominated by the temperature and the absorption properties of the constituents along the optical path. In spectral region where the



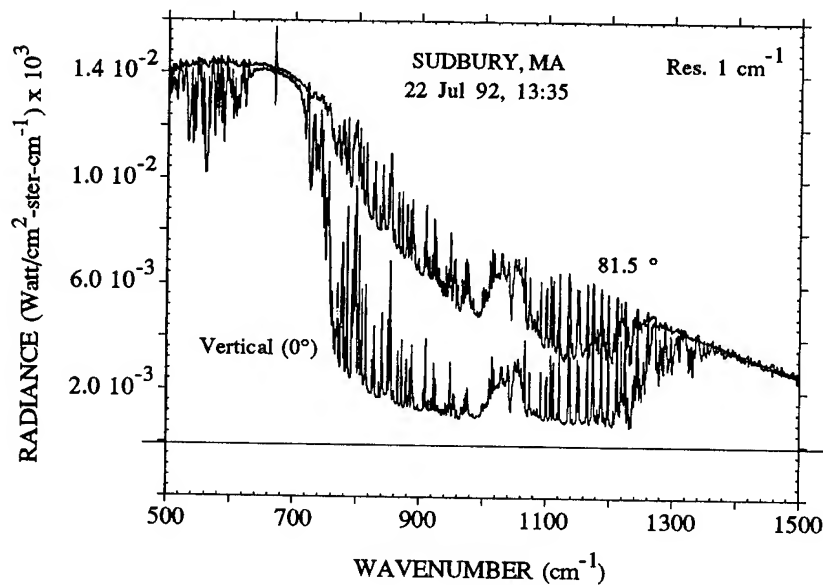


Figure 2. Atmospheric slant path IR emission measurements performed with the Double input Beam Interferometer Sounder (DBIS) in hot-dry conditions for two zenith angles.

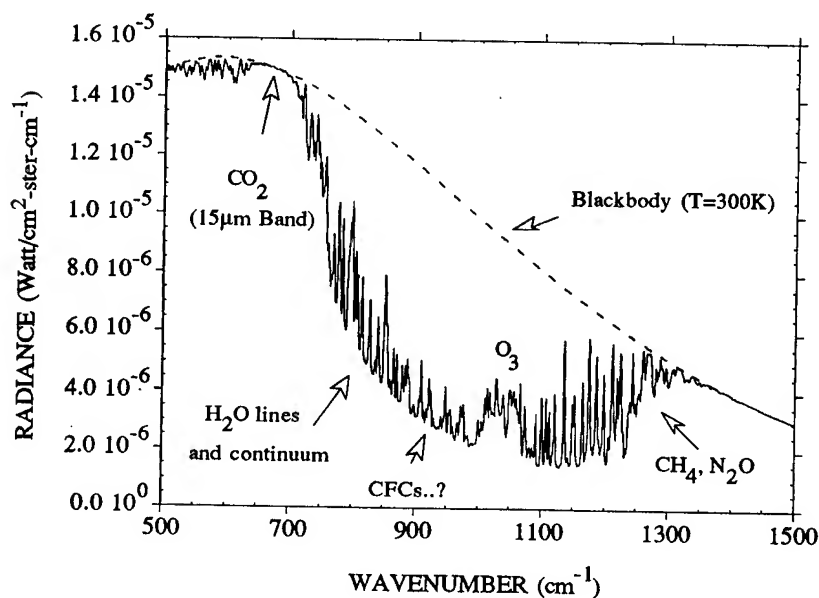


Figure 3. Atmospheric IR emission spectrum ( $2\text{ cm}^{-1}$ , uplooking) computed with the MODTRAN2 model for a typical summer condition and the theoretical curve of a blackbody at 300 K, together with a representation of some of the most active species in the  $500\text{-}1500\text{ cm}^{-1}$  region.

absorption is strong, the atmosphere radiates its energy like a blackbody at a temperature roughly equal to the one near the sounder. This is observed in the strong absorption band of CO<sub>2</sub> near 15  $\mu\text{m}$  (660  $\text{cm}^{-1}$ ) and also in the 1350-1500  $\text{cm}^{-1}$  region where the absorption is mainly due to water vapor. If we exclude the important emission band of the O<sub>3</sub> near 9.6  $\mu\text{m}$  (1040  $\text{cm}^{-1}$ ), the atmospheric window region from 800 to 1300  $\text{cm}^{-1}$  is dominated by the water vapor absorption lines (fine spectral structure) and continuum (smooth spectral shape). Finally, for slant path measurements, the number of intervening molecules is increased and the overall effect is to increase the IR emission accordingly.

The accuracy of measurements is a major factor for achieving adequate retrievals of atmospheric profiles. Also important is the precision of radiative transfer models used in the inversion algorithm to simulate emission spectra. A detailed evaluation of the two models, FASCOD (Clough et al., 1981) and MODTRAN (Berk et al., 1989), based on DBIS spectra is now being pursued. Figure 4 is a typical comparison between measurements and calculations performed with the FASCOD3 model (Anderson et al., 1989) while Fig. 5 is a comparison with the MODTRAN2 model (note that the spectral resolution is 2  $\text{cm}^{-1}$ ). In these cases, radiosonde profiles (temperature and humidity) has been used as inputs for calculations together with a midlatitude summer atmosphere for other constituents. In both cases, the agreement is remarkably good. Of the two models, FASCOD is the most accurate but also the less efficient in terms of computing time; MODTRAN is approximately 100 times faster. To a certain extent, these comparisons validate our experimental methodology and provide a solid foundation for the development of a retrieval method based on these two models.

#### 4. GENERAL RETRIEVAL APPROACH

The optimized algorithm for the retrieval of temperature and water vapor profiles from DBIS spectra is not finalized yet. However, a definitive retrieval approach has been adopted and is now being developed. Essentially, the approach is based on a formulation often referred to as the minimum information method (see for example Fleming and Smith, 1972). The two main advantages of this formulation are: first, no a priori information on the statistics of atmospheric profiles is required and second, it allows the simultaneous retrieval of temperature and constituents profiles (Smith et al., 1991; and Isaccs 1988). The theory of this method can be formulated as follows. First, the problem is linearized by considering that the measured radiance  $R(\nu)$  is a first order perturbation of the radiance  $R^0(\nu)$  computed with first guess profiles of temperature  $T^0(z)$  and absolute humidity  $\rho^0(z)$  i.e.

$$R(\nu) = R^0(\nu) + \delta R(\nu). \quad (1)$$

A multi-variable Taylor expansion of eq. 1 in terms of the first guess profiles, evaluated at  $L$  predefined discrete levels leads to

$$\begin{aligned} \delta R(\nu) = & \left( \frac{\partial R^0}{\partial T_1} \right) \delta T_1 + \left( \frac{\partial R^0}{\partial T_2} \right) \delta T_2 + \dots \left( \frac{\partial R^0}{\partial T_L} \right) \delta T_L \\ & + \left( \frac{\partial R^0}{\partial \rho_1} \right) \delta \rho_1 + \left( \frac{\partial R^0}{\partial \rho_2} \right) \delta \rho_2 + \dots \left( \frac{\partial R^0}{\partial \rho_L} \right) \delta \rho_L \end{aligned} \quad (2)$$

where  $\delta T_1, \delta T_2 \dots \delta T_L$  and  $\delta \rho_1, \delta \rho_2 \dots \delta \rho_L$  represent the unknown profiles ( $T_1 = T_1^0 + \delta T_1 \dots$ ) to be evaluated,

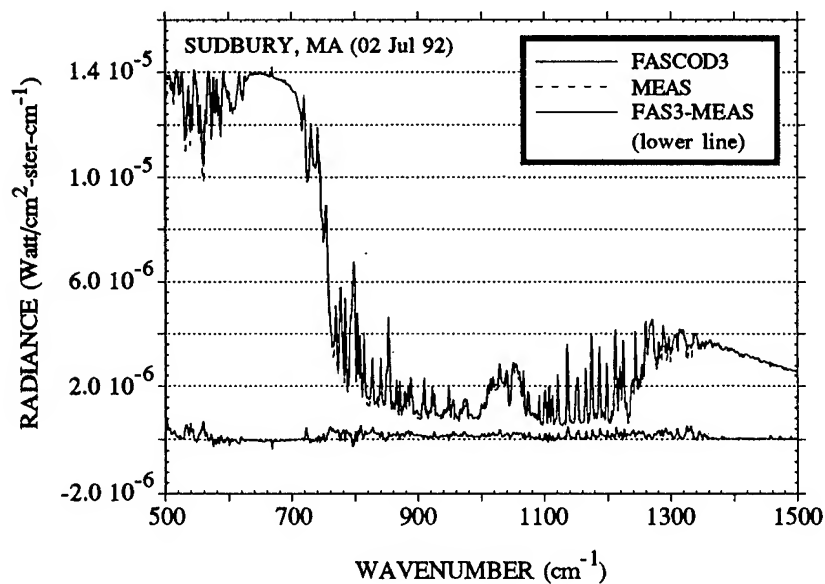


Figure 4. Atmospheric IR emission spectra ( $2 \text{ cm}^{-1}$  res.) in hot-dry conditions for the uplooking case: a typical comparison between FASCOD3 calculations and DBIS measurements.

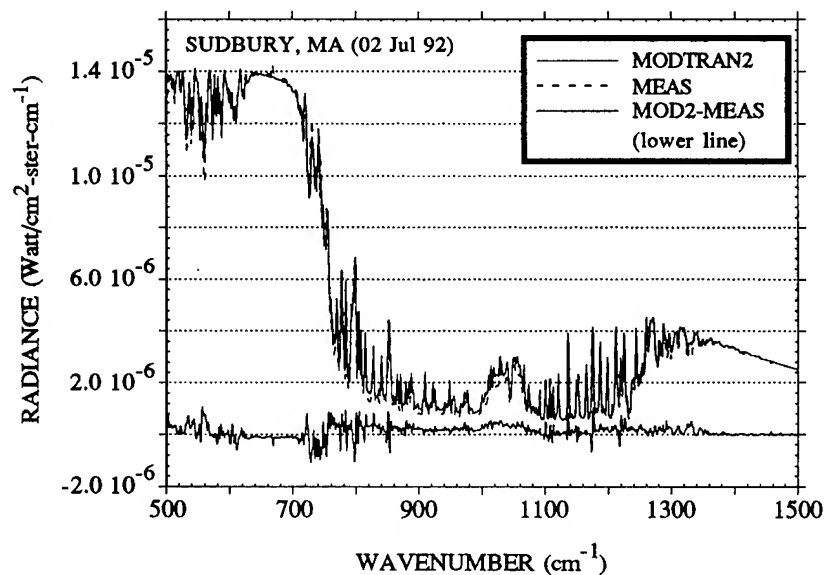


Figure 5. Atmospheric IR emission spectra ( $2 \text{ cm}^{-1}$  res.) in hot-dry conditions for the uplooking case: a typical comparison between MODTRAN2 calculations and DBIS measurements.

$R^0$  and the related partial derivatives are computed using a radiative transfer model. Equation 2 may be written in a matrix form

$$r = K x \quad (3)$$

where  $r$  is the vector of spectral measurements,  $x$  is the vector of the unknown profiles (temperature and humidity merged) and  $K$  is the matrix of partial derivatives often referred to as the Jacobian. The solution of this overdetermined system of equations ( $\sim 2000$  spectral elements for  $\sim 80$  unknowns) is given by the minimum information method

$$x = [K^t S_e^{-1} K + S_b^{-1}]^{-1} K^t S_e^{-1} r \quad (4)$$

where  $S_e$  is a diagonal matrix having for elements the noise standard deviation associated with spectral measurements and  $S_b$  is a diagonal matrix composed of damping parameters adjusted for each level and each constituent. These damping parameters are introduced to stabilize the solution which oscillates when improperly adjusted. Because of the linearization constraint in the problem, eq. 4 provides only an approximate solution of the actual profiles. The final solution may be obtained by iterations on eq. 4 for which the  $K$  matrix is updated with the previous profiles estimate.

The two main difficulties encountered in the practical implementation of this method are first, there is no systematic procedure to optimize the matrix of damping parameters ( $S_b$ ). It has to be adjusted empirically based on retrieval simulations performed with typical atmospheres. Second, the method requires the evaluation of the Jacobian (partial derivatives) for each level and each parameter (temperature and humidity) at each step of the iterative procedure. In our approach, the Jacobian is evaluated numerically by computing the spectral radiance of an atmosphere that contain a small perturbation (2 K for temperature or 0.1 g/m<sup>3</sup> for humidity) at a given level, subtracting it from the radiance computed without perturbation and dividing the result by the corresponding normalization factor. This operation involves a large number of radiance computations and consequently represents the main limiting factor of the method in terms of speed or efficiency.

Figure 6 shows an example of a Jacobian element computed with the MODTRAN model for water vapor perturbations at three different levels. This representation is useful because it shows the spectral region of sensitivity for the retrieval of water vapor profiles from the ground. For instance, at an altitude of 0.2 km the maximum sensitivity is recorded in the 500-600 cm<sup>-1</sup> region while near 15  $\mu$ m (660 cm<sup>-1</sup>) the sensitivity is minimum because of the strong absorption due to CO<sub>2</sub>. Overall, for sounding from the ground sensitivity peaks at the earth surface and decreases exponentially (approximately) with the altitude.

Preliminary tests of the minimum information method using a prototype algorithm based on the FASCODE model have shown promising results. The benefit of using FASCODE as a forward model to compute the radiance and the  $K$  matrix is its accuracy. However, this approach is very inefficient in terms of computing time: a single retrieval can require days, even with a fast minicomputer. To avoid this limitation, we are now developing a fast retrieval algorithm that uses FASCODE for the radiance calculations and MODTRAN for updating the  $K$  matrix. This would reduce the computing time by several orders of magnitude. Figure 7 represents a typical comparison of the Jacobians computed with FASCOD3 and MODTRAN2 for the water vapor case at an altitude of 1.8 km. The very good agreement between the two models support the choice of MODTRAN for  $K$  matrix computations. The final step in the optimization of the method is the adjustment of the damping parameters required in the solution (eq. 4), which will be easily accomplished by a series of

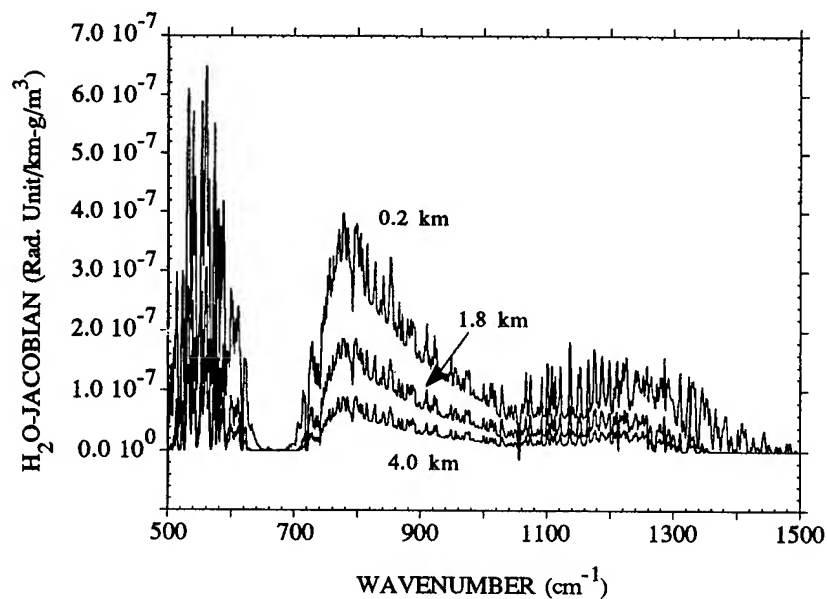


Figure 6. Water vapor Jacobian (normalized) computed with the MODTRAN2 model for three different levels in a typical summer condition.

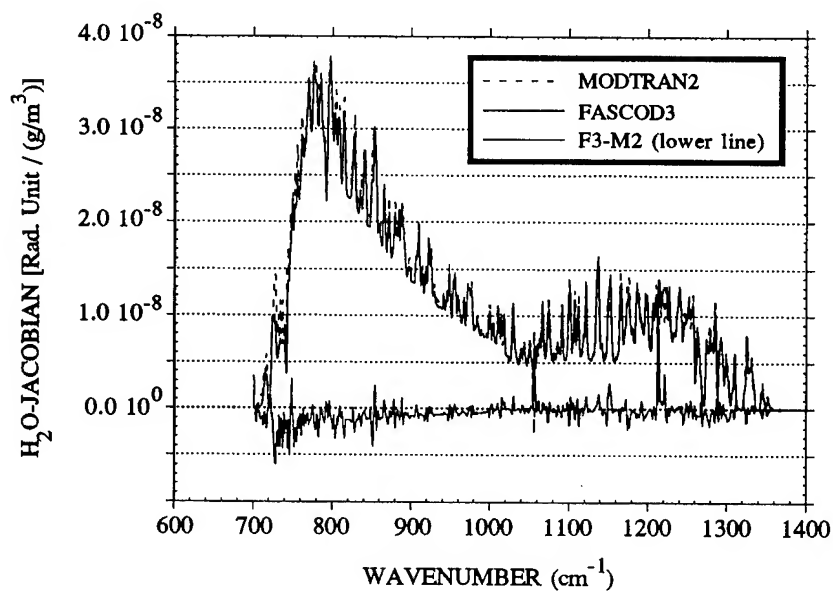


Figure 7. Typical comparison of the Jacobians (no normalization,  $2 \text{ cm}^{-1}$  res.) computed with FASCOD3 and MODTRAN2 models for the water vapor case: altitude 1.8 km.

simulations performed with the fast retrieval algorithm.

## 5. CONCLUDING REMARKS

The retrieval of atmospheric temperature and water vapor profiles from ground-based IR emission measurements is technically achievable. However, several issues remain to be addressed prior to the definitive implementation of such a technique. The Double input Beam Interferometer Sounder (DBIS), described in this paper, is a device designed to address these issues. The sounder has been conceived to match the needs encountered in many remote sensing scenarios: Slant path capability, small field of view (5 mrad), very wide spectral coverage (3-20  $\mu\text{m}$ ) and high spectral resolution (1  $\text{cm}^{-1}$ ). Preliminary tests of the DBIS indicates a radiometric accuracy better than 0.4 K in terms of brightness temperature. In a series of field measurements, the instrument has been run successfully in a wide variety of clear and cloudy sky conditions. Several atmospheric emission spectra recorded with the sounder have been compared to calculations with FASCODE and MODTRAN models. In both cases, the agreement is remarkably good. To a certain extent, these comparisons validate the experimental methodology developed for the sounder. Finally, the proposed approach for the retrieval of temperature and water vapor profiles from DBIS spectra is founded on the minimum information method. For its implementation, a new algorithm has been design to take advantage of first, the accuracy of the FASCODE model for radiance calculations and second, the efficiency (speed) of the MODTRAN model for the computation of the matrix elements required in the inversion.

## REFERENCES

- Anderson, G. P. et al., 1989: FASCOD3 Update. Proceeding, 12th Annual Review Conference on Atmospheric Transmission Models, Geophysics Laboratory, Hanscom AFB, MA: 163-187.
- Bissonnette, L., 1989: Remote Sensing of Aerosol Scattering Coefficient with a Multi-Field-of-View Lidar. AGARD Conference Proceedings (Operational Decision Aids for Exploiting or Mitigating Electromagnetic Propagation Effects), 453 : 39.1-39.13.
- Berk, A., Bernstein, L. S., and Robertson, D. C., 1989: MODTRAN: A Moderate Resolution Model for LOWTRAN7. GL-TR-89-0122, Geophysics Laboratory, Hanscom AFB, MA 01732.
- Clough, S. A., Kneizys, F. X., Rothman, L. S. and Gallery, W. O., 1981: Atmospheric Transmittance and Radiance: FASCOD1B. Proc. Soc. Photo-Opt. Instrum. Eng., 277 : 152-166.
- Fleming, H. E. and Smith W. L., 1972: Inversion Techniques for Remote Sensing of Atmospheric Temperature Profiles. Harmon H. Plumb Ed. (Temperature: Its Measurements and Control in science and Industry), Pittsburgh, 4 : 2239-2250.
- Isacacs, R. G., 1988: Retrieval Technics for Atmospheric Path Characterization. Proc. Soc. Photo-Opt. Instrum. Eng., 928 : 136-164.
- Revercomb, H. E., et al. 1988: Radiometric Calibration of IR Fourier Transform Spectrometers: Solution to a Problem with the High-Resolution Interferometer Sounder. Appl. Opt., 27 :3210-3218.
- Smith, W. L., Woolf, H. M. and Revercomb, H. E., 1991: Linear Simultaneous Solution for the Retrieval of Temperature and Absorbing Constituents from Radiance Spectra. Appl. Opt., 30 : 1117-1123.



BATTLEFIELD ATMOSPHERIC SOUNDINGS IN NEAR REAL TIME USING  
SATELLITE AND GROUND-BASED REMOTELY SENSED DATA

James Cogan  
Battlefield Environment Directorate\*  
U.S. Army Research Laboratory  
White Sands Missile Range, New Mexico 88002-5501, USA

ABSTRACT

A near real-time sounding of the atmosphere from the surface to  $\geq 30$  km may be obtained by combining atmospheric profiles from a meteorological (met) satellite and a ground-based system for remotely sensing wind and temperature. This type of capability is essential for optimum use of Army assets such as artillery and defense against biological and chemical attack. This paper describes the method for merging data from satellite and ground-based remote sensing systems and briefly discusses the algorithms used to evaluate the combined soundings. The current software allows the user to generate output in a standard form or in the format of an artillery met message. Initial results of this merging method are compared with data from nearly coincident rawinsondes. Preliminary comparisons of individual combined and rawinsonde sounding pairs, and individual met message zones for a number of sounding pairs, give an initial insight into the technique and the satellite/ground-based system concept.

1. INTRODUCTION

Systems currently used by the Army for measurement of atmospheric profiles rely on balloon sondes that are not state of the art. The time between balloon launches normally runs from about 2 to 4 h, possibly longer. The combination of satellite sounders and newer ground-based systems provides a means of updating the current system. Meteorological (met) satellite sounders operating in the infrared or microwave currently provide a means of obtaining atmospheric soundings on a routine basis for remote areas where surface and upper-air stations are normally absent. However, for mesoscale areas over land, satellite sounder data may have horizontal and vertical resolutions that are too large for certain applications, especially for the lower troposphere. Orlanski (1975) defines various mesoscale size ranges; herein mesoscale is considered to cover a range from about 2 to 500 km. Also, within the lowest 2 or 3 km satellite sounders are increasingly less accurate as the surface is approached.

---

\*formerly U.S. Army Atmospheric Sciences Laboratory



In the lowest 1 or 2 km over land, satellite temperature soundings without ancillary data generally have errors of as much as 5 to 8 K (Le Marshall, 1988; Reale, 1990). Le Marshall (1988) showed that root mean square (rms) values of precipitable water derived from TIROS operational vertical sounder (TOVS) data differed from those derived from radiosonde data by 40 to 60 percent for the 1000 to 400 hPa layer and around 20 to 30 percent for the 850 to 400 hPa layer, suggesting that lower level error contributed significantly to the overall differences. For derived variables such as wind velocity, the situation may be even less desirable (Franklin and Lord, 1988). Vertical and horizontal resolutions typically are about 3 to 5 km and around 30 to 200 km, respectively, depending on spectral region and amount of spatial averaging for noise reduction (Shenk et al., 1987; Kidwell, 1988).

Some of the newer ground-based systems can provide soundings in the lowest few kilometers at a rate of one every 30 min, or less if a lower accuracy is sufficient. The smaller microwave radar profilers (for example, 924 MHz) can provide consistent wind profiles up to 2 to 4 km, depending on vertical resolution (100 or 200 m) under average conditions. With a radio acoustic sounding system (RASS) added, they can produce virtual temperature soundings up to 700 or 800 m in an average atmosphere at a vertical resolution of about 100 m. Kaimal (1990) and Miers et al. (1992) and their references provide information on radar profilers and other ground-based sounding systems. Miers et al. (1992) also present numerous charts and tables that list the accuracies and other characteristics of those systems. Comparisons with balloon sonde data give an idea of how these systems compare with more traditional systems.

The merging method described in this report is a considerably revised version of the technique described in Cogan (1990a, b). Certain topics from these earlier reports are included in an abbreviated form to have a coherent presentation of the material. Cogan (1990c) describes the technique for converting an atmospheric sounding from the "standard" form to that of an artillery meteorological (met) message. This report contains a brief summary of the technique for the sake of continuity and describes the slight modifications. For the comparisons, a new method generates difference profiles for each of the several variables. A difference profile is the vertical profile of the differences between values of a variable for a merged sounding and those for a "coincident" rawinsonde sounding. A difference is computed for each met message zone. In addition, means and standard deviations are calculated for each pair of soundings. Finally, means and standard deviations can be computed for each met message zone for a number of difference profiles, along with a confidence test (t-test) of the statistics for each zone.

## 2. ALGORITHMS

### 2.1 MERGED SOUNDING

The merging algorithms are described in some detail in Cogan (1990a, b, c). Here we discuss the highlights of this technique and the modifications for combining satellite and ground-based radar profiler data. Figure 1 shows the basic concept of the method. Radar profiler and RASS provide data below the lowest satellite level. Where ground-based and satellite profiles overlap,

the satellite data are weighted in accordance with the spatial and temporal separation of the sounding from the location of the radar profiler and RASS (here we will refer to the radar profiler and RASS combination as the profiler). Cogan (1990a, b) describes the spatial and temporal weighting schemes. The spatial weighting function has an elliptical form. The equation is

$$W = 1 - X^2/A^2 - Y^2/B^2 \quad (1)$$

where  $W$  = weight,  $A$  and  $B$  are the semimajor and semiminor axes of the assumed elliptical area represented by the satellite sounding, and  $X$  and  $Y$  are the distances along those axes from the profiler to the center of the satellite sounding area. For polar orbiting satellites a circular area may be sufficient away from the edges of the swath, within about 500 to 1000 km of the subsatellite track. The temporal weighting function has a short period when the two sources of data have equal weight (for example, 30 min), followed by a period of linear decrease to some time (usually 3 to 6 h) when the satellite data are ignored (temporal weight = 0). The final weight given to the satellite sounding is the product of the spatial and temporal weights times an accuracy ratio. The ratio relates typical accuracies (Miers et al., 1992) of the radar profiler (wind velocity) and RASS (virtual temperature) to those of the satellite sounder.

In the overlap region satellite data are interpolated to profiler heights. The equation for combining the two sets of data for those heights has the following form:

$$Q = W(Q_p + Q_s)/2 + (1 - W)Q_p \quad (2)$$

where  $Q$  is a variable at some height,  $W$  is the combined temporal and spatial weight, and subscripts  $p$  and  $s$  refer to profiler and satellite, respectively. The algorithm ignores the satellite data where  $W = 0$ , and simply averages the two types of data where  $W = 1$ .

If a gap exists between the highest altitude of the profiler data and the lowest height of the satellite data, the satellite data are extrapolated down to the maximum altitude of the profiler data. Wind and temperature profiles are treated separately since profiler wind values normally extend to considerably greater heights than RASS virtual temperature values. If humidity data are available, satellite values of temperature are converted to virtual temperature. Otherwise a default routine computes virtual temperature based on the surface humidity. Virtual temperature is set equal to temperature if the temperature or dewpoint is less than 233 K (maximum difference between temperature and virtual temperature at 233 K is  $< 0.1$  K). Above the highest altitude of the profiler data for either virtual temperature or wind velocity, the satellite value is adjusted according to a scheme described in Cogan (1990a, b). This scheme is based on the difference between satellite (actual or extrapolated) and profiler values at the maximum profiler height for the particular variable. If the gap exceeds a preset value (for example,

2 or 3 km), the algorithm skips the extrapolation routine and does not adjust the satellite data.

## 2.2 ARTILLERY MET MESSAGE

A method to convert a meteorological sounding into an artillery met message format is described in Cogan (1990c). The basic met message format has 27 zones from the surface to 20 km. The first zone is the surface; subsequent ones represent layers. The second and third zones extend from the surface to 200 m and from 200 to 500 m, respectively. From 500 to 5000 m the zones (layers) are 500 m thick, becoming 1000 m thick from 5000 to 20,000 m. An extended form of the met message has another five zones of 2000 m thickness from 20 to 30 km. Zones are numbered from 00 to 26 (to 31 for the extended message). For each zone the message lists values of wind direction in tens of mils (6400 mils =  $360^\circ$ ), wind speed in knots, virtual temperature ( $T_v$ ) in tenths of kelvins, and pressure in millibars. Additional surface data in the header provide, for example, location and date/time.

The computer program developed for this paper produces a sounding for the artillery met message zones in met message units. The program computes values of each variable for the boundary levels (200, 500, 1000 m, and so forth) by interpolation of values from heights immediately above and below. Linear interpolation is used except for pressure where standard algorithms compute pressure at the particular level given  $T_v$  at that level and pressure and  $T_v$  at the one immediately below. For each variable a simple integration scheme generates a mean value for each layer using values at the boundary and at heights within the layer. Cogan (1990c) discusses details of the algorithm and shows sample input and output.

## 3. SENSOR CHARACTERISTICS

Before applying the merging algorithm, one should have an idea of the accuracies and other relevant measurement parameters of the data sources. In particular we concentrate on satellite sounders and ground-based radar profilers and accompanying RASS. Miers et al. (1992) and their references provide considerable information on both satellite and ground-based sensing systems. Table 1 summarizes certain information extracted from Miers et al. and their references. These values may be compared with similar data for common rawinsonde systems (Fisher et al., 1987), also presented in table 1.

Table 1 shows that ground-based radar profilers and RASS have accuracies that approach those of some rawinsonde systems. However, in the case of RASS the measured variable is virtual temperature versus temperature from rawinsonde. The difference may be significant for a warm ( $> 300$  K) moist atmosphere (difference  $> 1$  K). Also, a radar profiler obtains a mean wind over a volume and a number of measurements are averaged to reduce noise. The horizontal scales of these volumes are on the order of tens to hundreds of meters, depending on distance from the radar and frequency. For a system such as the 404 or 50 MHz radars, the area represented by the three (or five) beams used to measure the horizontal and vertical wind may have a diameter exceeding 10 km near 15 or 20 km altitude. The time needed to reach a consensus (reduce noise to an acceptable minimum) may be considerable. The values in table 1 represent 30- to 60-min consensus averages. A rawinsonde acquires a mean

layer wind velocity along its path, over a period of perhaps a minute or less (most rawinsondes rise at about 300 m/min). Temperature measurements may be considered as point values. Satellite sounders measure radiances that are converted to temperatures that represent means for large volumes of atmosphere according to the weighting functions and horizontal field of view. A temperature may represent the mean over a vertical extent of 3 to 5 km and over a horizontal area of tens to over 100 km diameter (assuming a circular area). Wind velocity is derived from the satellite temperature profile (usually geostrophic or thermal wind equations). In spite of the differences, table 1 can provide approximate indicators of the relative "quality" of data from the several systems. The better present day rawinsondes generally give the best accuracies, followed by radar profilers with RASS. However, satellite sounders are the only means of obtaining large area or global coverage, while radar profilers/RASS have the best time resolution.

The situation with regard to satellite sensors should improve significantly as we enter the next century. The most dramatic potential improvement may appear in measurement of wind velocity. The laser atmospheric wind sounder (LAWS) is the first system for direct measurement of wind profiles from satellite. The accuracy and spatial resolution should improve relative to present methods that derive wind velocity indirectly. For example, the LAWS will measure wind velocity to  $\pm 1$  to  $5 \text{ ms}^{-1}$  (vector error estimate) at a vertical resolution of 0.3 to 1 km, depending on turbidity of the atmosphere. Fortunately, the better vertical resolution normally would occur in the lower atmosphere (more aerosols) where greater variability in wind usually is expected. Merging data from the LAWS and other planned sensors should greatly improve the upper part of merged profiles, thereby coming closer to high quality rawinsonde profiles. Information on some of the satellite sounders planned for launch as part of the Earth Observing System (EOS) may be found in NASA (1991).

A rough idea of the expected measurement error may be obtained by computing the root mean square error (rmse) for a combined or merged sounding derived from "typical" present day satellite and radar/RASS systems (for example, table 1). These rmse values strictly apply to the overlap region where both satellite and radar/RASS values are available for merging. Table 2 contains rmse values for selected combinations of systems where the satellite and ground-based data have equal weight, including the potential future case of LAWS and radar profiler. Outside the overlap region the expected accuracy should roughly equal the accuracy of the individual system (for example, the RASS accuracy below the lowest satellite data level). An exception is the altitude region immediately above the highest data level of the ground-based system where the satellite data are modified as noted above. In that region the error may be expected to lie between the rmse of table 2 and the error for satellite data alone. The values shown in table 2 suggest that for present day systems the satellite should be given less than equal weight in the overlap region, as in the merging method of this paper.

TABLE 1. CAPABILITIES OF SEVERAL REMOTE SENSING AND RAWINSONDE SYSTEMS.\*

System	Variable	Capabilities			
		Accuracy	Temporal Resolution	Vertical Resolution	Vertical Range
Radar Profiler (924 MHz)	Wind Spd	$\pm 1.5$ - $2.5 \text{ ms}^{-1}$	0.5 to 1 h	100 m	100 to
	Wind Dir	$\pm 5$ - $10^\circ$		200 m	2500 m
RASS (with 924 MHz profiler)	Virt Temp	$\pm 1 \text{ K}$			100 to 850 m
Satellite sounder (TOVS and SSM/T-1)	Temp	$\pm 2$ - $2.5 \text{ K}$	6 h (2 sat)	3 to	2 to
	Wind Spd	$\pm 4$ - $14 \text{ ms}^{-1}$	4 h (3 sat)	5 km	40 km
	Wind Dir	$\pm 10^\circ$	(1-2 h near poles)		
Rawinsonde	Temp	$\pm 0.5$ - $1 \text{ K}$	1 to 3 h	pt value	Surface
	Wind Spd	$\pm 0.5$ - $2 \text{ ms}^{-1}$	depending on max height	60- to 600-m layers	to 30 km
	Wind Dir	$\pm 5$ - $10^\circ$			

\*The listed systems are a sample of the large number discussed in Miers et al. (1992), their references, and Fisher et al. (1987). The values shown represent averages for most current systems in each group. Note that the satellite values are valid for altitudes  $> 2$  or  $3 \text{ km}$  above a land surface and not near the tropopause (for example, temperature to  $\pm 5$  to  $8 \text{ K}$  and  $\pm 3$  to  $5 \text{ K}$  near the surface and tropopause, respectively). Temporal resolution for the profiler/RASS as short as  $15 \text{ min}$  may be possible. Temporal resolution of  $< 1 \text{ h}$  may be achieved for the rawinsonde if there is a capability for multiple launch and multiple transmitter frequencies.

TABLE 2. RMSE VALUES COMPUTED FOR SELECTED COMBINATIONS OF SENSORS IN TABLE 1\*

Systems combined	Variable	rmse
Radar profiler and satellite	Wind speed: best	$3.0 \text{ ms}^{-1}$
	Wind speed: worst	$10.1 \text{ ms}^{-1}$
Radar profiler and satellite-LAWS	Wind speed: best	$1.3 \text{ ms}^{-1}$
	Wind speed: worst	$4.0 \text{ ms}^{-1}$
RASS and satellite	Virtual temperature: best	$1.6 \text{ K}$
	Virtual temperature: worst	$1.9 \text{ K}$

\*Best and worst values were computed for the best and worst accuracies listed in table 1, plus wind speed values expected from the LAWS ( $\pm 1$  to  $5 \text{ ms}^{-1}$ ). The listed rmse values are valid when and if the listed systems overlap. Overlap is likely for wind measurements, less probable for temperature. Virtual temperatures computed from satellite temperature and humidity data (if available) are assumed to have the same accuracy as satellite temperatures. For each combination both systems have equal weight.

#### 4. MERGED SOUNDING AND COMPARISON TO RAWINSONDE

In this section we present a sample case of a merged sounding before conversion to an artillery met message format and compare the results with a rawinsonde. As a consequence of the manner of collecting the data from the radar profiler/RASS and rawinsonde, the comparison is not entirely straightforward. Specifically, no surface data were taken with the profiler/RASS system, and the navigation aid rawinsonde system does not produce directly measured wind data below about 600 m above the surface. The rawinsonde processor interpolates between the surface value (directly measured) and the value at about 600 m, using an Ekman Spiral algorithm. Between 600 and 1200 m the system generates a combination of computed and measured wind velocity, with the weight given to the measured values increasing with height. To have surface values to "tie down" the remotely sensed profiles and to compute pressure with height, we took measured values from the rawinsonde surface data. Therefore, differences between combined and rawinsonde soundings should be ignored for values at the surface and the lowest layer computed for artillery met messages. For wind comparisons the method for computing rawinsonde wind velocity may lead to differences that have no meaning at met message zones below 1000 m, and may be questionable for the 1000 to 1500 m zone.

Figure 2 shows input soundings taken on 28 May 1992, at White Sands Missile Range, for virtual temperature as a function of height, and figure 3 presents the combined sounding along with the nearest rawinsonde in space and time. The rawinsonde ascent began within a few minutes of the beginning (about 2000 UT) of the half-hour period of the wind and virtual temperature profiles, and was several kilometers distant. The satellite sounding has a listed time of about 20 min later and the center of the horizontal resolution area was about 60 km slightly south of west.

For this preliminary investigation only eight sounding pairs had been processed as of the writing of this paper, too small for a valid statistical sample. However, the output can serve as an initial indicator of potential accuracy (not a final result). Figure 4 shows difference profiles for virtual temperature and wind speed (profiler - rawinsonde), and table 3 has certain statistics for the entire profile. Because the satellite covers the larger vertical extent, the statistics are dominated by the satellite accuracies and do not accurately portray profiler results. The "bump" in the temperature difference profile between 1 and 3 km resulted from a combination of the increasing error from the satellite data as the surface was approached and the accuracy of the RASS "forcing" the profile to better values in the lowest kilometer. Table 4 shows preliminary results for virtual temperature and wind speed and wind direction for the zone comparisons. Despite the small sample size, some trends seem to appear. Mean differences and standard deviations generally follow published results (Miers et al., 1992) for both profiler and satellite, although the wind direction error appears excessive. The worst case for comparison of wind direction would happen during light winds, as occurred for much of this data set (29 April to 4 June 1992). Confidence tests were not performed since the small sample size could lead to misleading results. Nevertheless, the preliminary output indicates that the combined sounding method will produce results in line with accuracies of the individual systems, perhaps better at satellite levels immediately above the highest profiler or RASS altitude.

TABLE 3. PROFILE STATISTICS FOR THE MERGED SOUNDING/RAWINSONDE  
PAIR OF 28 MAY 1992, ABOUT 2000 UT

Variable	Pressure	Virtual Temperature	Wind Speed	Wind Direction
Mean	0.7 hPa	-0.1 K	8.9 ms <sup>-1</sup>	-19.0°
Standard deviation	0.8 hPa	3.0 K	6.2 ms <sup>-1</sup>	57.2°

TABLE 4. DIFFERENCE PROFILE STATISTICS BY MET MESSAGE ZONE: MEANS  
AND STANDARD DEVIATIONS (sd); ZONES 2-16, 18, 20\*

Zone	Height	Mean dT	SD dT	Mean dS	SD dS	Mean dD	SD dD
2	500	0.29	0.70				
3	1000	1.39	1.46	2.9	1.3	- 19.7	37.6
4	1500	2.06	2.80	3.7	3.2	- 36.1	62.3
5	2000	2.16	2.28	5.1	3.3	- 25.1	39.1
6	2500	2.12	2.11	5.2	2.0	20.3	64.3
7	3000	1.92	1.87	5.8	2.0	- 24.5	64.1
8	3500	1.39	1.65	6.7	2.9	- 7.7	34.3
9	4000	0.87	1.81	8.5	3.4	- 25.6	71.5
10	4500	0.22	1.53	10.4	4.5	17.6	67.9
11	5000	- 0.78	1.34	11.0	5.7	- 13.4	21.6
12	6000	- 1.67	1.20	11.2	6.0	- 18.5	23.9
13	7000	- 1.82	0.69	12.7	6.9	- 32.6	30.0
14	8000	- 1.21	0.88	14.2	7.4	- 57.3	61.4
15	9000	- 0.74	1.24	15.1	7.4	- 11.0	80.4
16	10000	0.35	1.46	16.1	7.7	- 8.4	68.2
18	12000	- 0.34	1.59	16.7	7.7	- 27.4	48.6
20	14000	- 4.40	2.76	15.3	6.3	- 8.3	27.3

\*No zone 2 wind values shown because of the poor quality of rawinsonde values below at least 600 m (see text). The prefix d refers to the difference value. T, S, D = virtual temperature (K), wind speed (ms<sup>-1</sup>), and wind direction (deg), respectively.

## 5. CONCLUSION

The merging method discussed here as applied to profiler/RASS and satellite data appears to have promise as a means of computing met soundings for the battlefield. Clearly more comparisons with better data are required for valid statistical results. Comparisons using a statistically significant sample are planned when further data are processed into the proper input format. The effect of varying certain processing parameters for the satellite data is planned (for example, the lowest height for use of satellite data). In addition, better rawinsonde data are required, especially for the lowest 1200 m above the surface, as well as useful surface data as part of the ground system data set. All test data of the type

described here require good quality control. A test of an early prototype of the MPS planned at the Wave Propagation Laboratory (WPL) for January 1993 should provide comparison data of high quality, especially at the lower heights. Further comparisons using a 404- or 50-MHz profiler and associated RASS in place of the rawinsonde are planned that will eliminate the problem of drift of the rawinsonde and allow a comparison of measurements of similar type (for example, mean virtual temperatures of volumes). Software for the merging method has transitioned to WPL for inclusion in the prototype system.

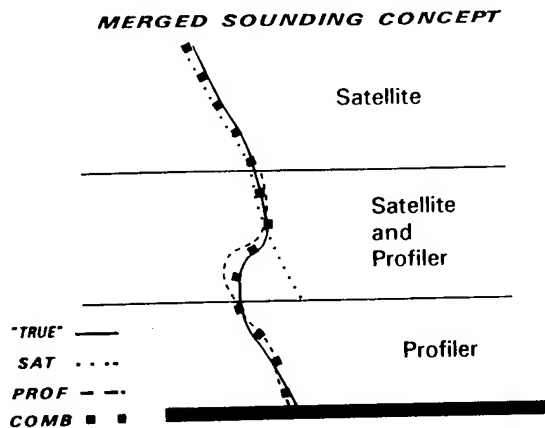


Figure 1. Basic concept of the merging technique as applied to satellite sounder and radar profiler (with RASS) data. Virtual temperature profiles shown.

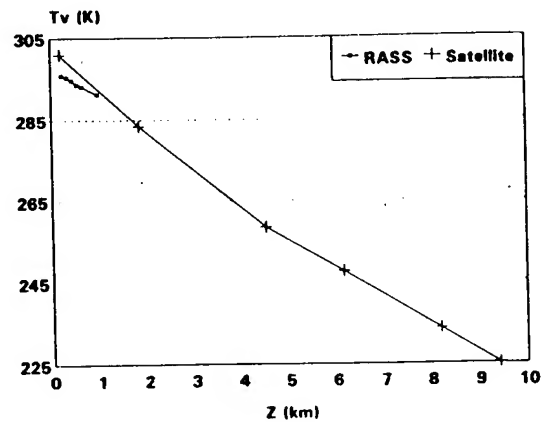


Figure 2. Input soundings for virtual temperature profile.

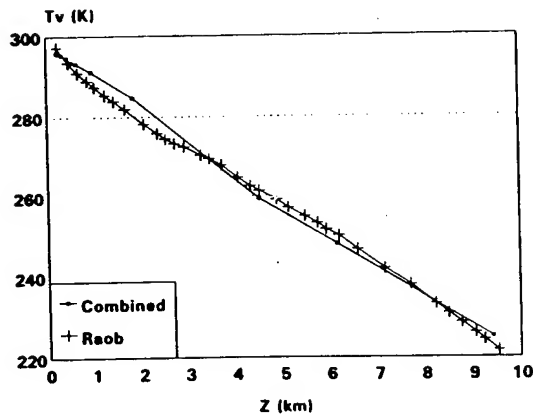


Figure 3. Output combined sounding for virtual temperature along with nearest rawinsonde in space and time for comparison.

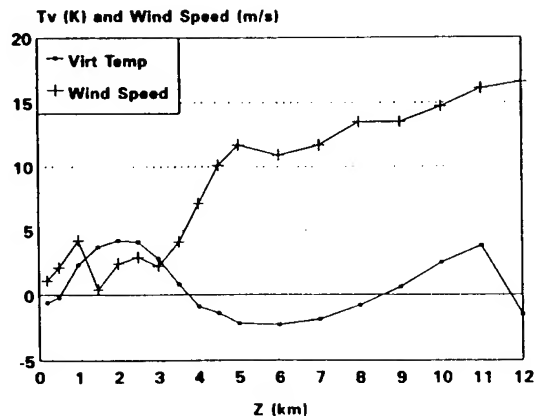


Figure 4. Difference profiles for virtual temperature and wind speed for one sounding pair.



## 6. ACKNOWLEDGMENT

The author acknowledges Mr. Aldo Izaguirre of the University of Texas at El Paso, TX (Student Short Form Contract) for his effort in reformatting the input data.

## REFERENCES

- Cogan, J., 1990a: A Method for Obtaining Remote Area Meteorological Soundings in Near Real Time. Preprints of the Fifth Conference on Satellite Meteorological and Oceanic, London, UK, pp. 98-103.
- Cogan, J., 1990b: A Method for Obtaining Remote Area Meteorological Soundings in Near Real Time. ASL-TR-0287, US Army Atmospheric Sciences Laboratory, White Sands Missile Range, NM 88002.
- Cogan, J., 1990c: A Technique for Computation of Meteorological Variable Profiles for User Defined Heights and Layers. ASL-TMR-0005, US Army Atmospheric Sciences Laboratory, White Sands Missile Range, NM 88002.
- Fisher, E. E., F. Brousaides, E. Keppel, F. J. Schmidlin, H. C. Herring, and D. Tolzene, 1987: Meteorological Data Error Estimates. Document 353-87, Meteorology Group, Range Commanders Council, White Sands Missile Range, NM 88002.
- Franklin, J. L., and S. J. Lord, 1988: Comparisons of VAS and Omega Dropwindsonde Thermodynamic Data in the Environment of Hurricane Debby (1982). Mon Wea Rev, 116:1690-1701.
- Kaimal, J. C., (Editor), 1990: Remote Atmospheric Profiling Systems for Tropospheric Monitoring. NOAA Technical Memorandum ERL WPL-175, National Oceanic and Atmospheric Administration, Washington, DC.
- Kidwell, K. B., 1986 (revised 1988): NOAA Polar Orbiter Data (TIROS-N, NOAA-6, NOAA-7, NOAA-8, NOAA-9, NOAA-10) Users Guide. Satellite Data Services Division, National Climate Data Center, NESDIS, National Oceanic and Atmospheric Administration, Washington, DC.
- Marshall, J. F., 1988: An intercomparison of temperature and moisture fields derived from TIROS operational vertical sounder data by different retrieval techniques. Part I: basic statistics. J Appl Meteorol, 27:1282-1293.
- Miers, B., J. Cogan, and R. Szyrmer, 1992: A Review of Selected Remote Sensor Measurements of Temperature, Wind and Moisture, and Comparison to Rawinsonde Measurements. ASL-TR-0315, US Army Atmospheric Sciences Laboratory, White Sands Missile Range, NM 88002.
- NASA (National Aeronautics and Space Administration), 1991: EOS Reference Handbook. Goddard Space Flight Center, Greenbelt, MD.
- Orlanski, I., 1975: A Rational Subdivision of Scales for Atmospheric Processes. Bull Am Meteorol Soc, 56:527-530.
- Reale, A. L., 1990: Baseline Upper Air Network (BAUN) Final Report. NOAA Technical Report NESDIS 52, US Department of Commerce, NOAA/NESDIS, Washington, DC.
- Shenk, W. E., T. H. Vonder Haar, and W. L. Smith, 1987: An Evaluation of Observations from Satellites for the Study and Prediction of Mesoscale Events and Cyclone Events. Bull Am Meteorol Soc, 68:21-35.

## USE OF SSM/I DATA DURING OPERATION DESERT STORM

C. R. Holliday, K. A. Nash, and K. H. North  
Air Force Global Weather Central  
Offutt Air Force Base, NE 68113-4039

### ABSTRACT

During Operation DESERT STORM Air Force Global Weather Central (AFGWC) utilized stored readout data from the Defense Meteorological Satellite Program (DMSP) Special Sensor Microwave Imager (SSM/I) to augment Operational Linescan System (OLS) visual and infrared imagery surveillance of the Mid-East region. During the period of concern two polar orbiting DMSP vehicles with SSM/I sensors viewed the region. This two spacecraft configuration virtually ensured SSM/I coverage over the Mid-East at least once every 12hr. The SSM/I data provided new capabilities for reconnaissance of embedded thunderstorms cells masked by high cloudiness particularly when viewed in nighttime infrared data. In addition, the SSM/I proved an unique data source for mapping ocean surface wind speeds over the Persian Gulf, and other adjacent water bodies to the Arabian Peninsula.

### 1. INTRODUCTION

During Operation Desert Storm Air Force Global Weather Central (AFGWC) utilized data from the Defense Meteorological Satellite Program (DMSP) Special Sensor Microwave Imager (SSM/I) to augment DMSP visual and infrared surveillance of the Mid-East region. The SSM/I data provided additional capabilities for reconnaissance including ocean wind speed estimates and thunderstorm discrimination, particularly at nighttime as cirrus clouds often obscured delineation of deep convective activity in infrared imagery.

### 2. BACKGROUND

The SSM/I sensor is a seven-channel, four frequency, passive microwave system on the DMSP Block 5D-2 spacecraft. The frequencies of the SSM/I are 19, 22, 37, and 85 GHz. Upwelling radiation is vertically and horizontally polarized and expressed in brightness temperatures (BT). Footprint diameters are approximately 15 km, 30 km, and 50 km for the 85 GHz, 37 GHz, and 22/19 GHz frequencies.

### 3. SSM/I COVERAGE

During the period of concern three polar-orbiting DMSP vehicles provided reconnaissance of the Mid-East region. Two satellites, F8 and F10, carried an SSM/I sensor. This two spacecraft configuration virtually ensured SSM/I coverage over the Persian Gulf region at least every 12 hr. AFGWC received stored readout data from all SSM/I sensor channels throughout the period; with the exception of F8's 85 H channel which failed midway through the operation.

### 4. DISPLAY SYSTEM

The AFGWC analysis effort utilized a Mission Sensor Tactical Imaging Computer (MISTIC) (Hughes, 1991a) hosted on a standard SUN workstation and running under the Sunview Windowing system. This unit linked to AFGWC's worldwide SSM/I data base provided display and analytic capabilities through a MSTVUE imaging module (Hughes, 1991b). Critical enhancements to MSTVUE by Aerospace Corp. (Boucher et al, 1992) provided additional display and algorithm manipulation capability.

### 5. OCEAN SURFACE WINDS

AFGWC analysts were able to monitor ocean surface wind speeds over the Persian Gulf, and other adjacent water bodies utilizing SSM/I data. The ocean surface wind speed algorithm developed by Goodberlet et al (1990) provided estimates that matched well with ship reports in these areas and fit within accuracy specification in rain-free conditions of 2 m/s. The range of wind speeds observed varied from 0 to 15 m/s. Shamal high wind events were readily detected. Tactical users of the data remarked favorably on the advantage of an entire wind speed field depiction covering the area of responsibility as compared to sometimes sparse ship observations.

### 6. THUNDERSTORM DISCRIMINATION

The SSM/I 85 GHz channel data with relatively high spatial resolution (15km) proved of particular value in discriminating thunderstorm targets. The dominant signature produced by thunderstorms in these channels arise mainly from the scattering by the precipitation-sized ice particles and graupel associated with the vigorous updrafts. This scattering significantly depresses the BT as compared to the surrounding area, and is readily identifiable in the SSM/I image.

During the initial phase of Desert Storm persistent high cloudiness associated with the subtropical jet covered Northwest Saudi Arabia, Kuwait, and southern Iraq. This cloudiness often acted as a mask for embedded thunderstorms, particularly when viewed in nighttime infrared

imagery. Cirrus spissatus often mistaken for thunderstorm activity in the infrared posed an additional problem. The 85 GHz channel data assisted greatly in delineating between these features.

Diagnostics for 85 GHz thunderstorm identification followed closely with work by Adler et al.(1990) and Spencer et al. (1989), using BT threshold minimums. In addition, BT gradient patterns resembled those of radar echoes, with the addition of some of the anvil debris, aiding identification. However, background signatures such as lakes in Iraq and snow over the Zagros mountains yielded low BT and subsequent spurious targets. Additional screening using 85 GHz polarization differences suggested by Spencer et al. (1989) assisted in removing the false targets.

With the F8 85 GHz channel failure, analysts employed 37 V GHz data with some success. A sharp scattering signal (lower BT) appeared evident for deep convection over land even at this is lower frequency and yielded a distinct signature for analysis. This is consistent with findings of Adler et al (1990) utilizing research aircraft microwave radiometer observations. Although we could detect large thunderstorms, the 37 GHz diminished spatial resolution (30km) didn't resolve smaller cell features. This was readily apparent in independent cross checks between F10 85H and 37V channel imagery.

## 7. SUMMARY

The use of SSM/I data during Operation Desert Storm was of considerable value in discriminating embedded thunderstorms within the extensive high cloudiness associated with the subtropical jet. This was particularly true during nighttime situations when infrared imagery often revealed little detail within a cirrus cold cover mask. Although the 85 GHz data provided the best imagery for surveillance, an alternate method utilizing 37 V channel imagery detected thunderstorm activity but at a loss of spatial resolution.

SSM/I mapping of ocean surface wind speed estimates in the Persian Gulf and adjacent water bodies assisted the synoptic analysis of the region during periods of sparse ship reports. The data compared quite favorably with individual point ship observations.

## 8. REFERENCES

- Adler R. F., R. A. Mack, N. Prasad, H.-Y.M. Yeh, I.D. Hakkarinen, 1990: Aircraft Microwave Observations and Simulations of Deep Convection from 18 to 183 Ghz. Part 1: Observations, J. Atmos Oceanic Techno., 7, 377-391.
- Boucher D., M. Plonski, and K. Ricci, 1991: Interactive Manipulation of SSM/I Data: A New Paradigm for Rapid Algorithm Development, Sixth AMS Conf. on Satellite Meteorology and Oceanography, Atlanta, GA, 5-10 Jan, 1992
- Goodbert, M.A., C.T. Swift, and J.C. Wilderson, 1990: Ocean Surface Wind Speed Measurements of the Special Sensor Microwave/Imager (SSM/I), IEEE Trans. Geosci. Remote Sensing, 28, 823-827.
- Hughes Aircraft Company, Space and Communications Group, 1991a: "MISTIC Users Manual, Ver. A05"
- Hughes Aircraft Company, Space and Communications Group, 1991b: "MSTVUE Users Manual"
- Spencer. R.W., H.M. Goodman and R.E. Hood, 1989: Precipitation retrieval over land and ocean with the SSM/I. Part 1: Identification and characteristics of the scattering signal. J. Atmos. Oceanic Technol., 6, 254-273.

**COMPARISON OF DEFENSE METEOROLOGICAL SATELLITE PROGRAM (DMSP) CAPABILITIES  
AND ARMY TACTICAL WEATHER/ENVIRONMENTAL DATA SPECIFICATIONS FOR OBSERVATIONS**

Richard J. Szymer  
US Army Research Laboratory  
Battlefield Environment Directorate  
White Sands Missile Range, NM 88002, USA

**ABSTRACT**

The objective of this investigation was to establish a baseline for Army tactical weather and environmental data specifications for observations, and compare those specifications to the DMSP's capability for collecting meteorological observations. Army tactical weather and environmental data requirements, as well as the DMSP Block 6 system, are both still evolving. The most current information on future DMSP satellites and Army meteorological support requirements was gathered and analyzed. The DMSP Block 6 and 5D-3 satellites are the only observing system that comes the closest to meeting Army requirements for tactical observations, and form the cornerstone system for providing a capability to satisfy stated Army tactical requirements for weather and environmental data.

Paper distribution authorized to Department of Defense and DoD contractors only. Other requests for this document must be referred to U.S. Army Research Laboratory, ATTN: AMSRL-OP-CI-C, Technical Publications, White Sands Missile Range, NM 88002-5501.



## WIND RADAR INTERFERENCE WITH THE ARL MICROWAVE TEMPERATURE RADIOMETER

Teddy L. Barber and Edward M. Measure  
Battlefield Environment Directorate\*  
U.S. Army Research Laboratory  
White Sands Missile Range, New Mexico 88002-5501, USA

Randall J. Hulsey  
Physical Science Laboratory  
New Mexico State University  
Las Cruces, New Mexico 88003, USA

### ABSTRACT

The Battlefield Environment Directorate\* of the Army Research Laboratory operates two microwave radiometers for remote sensing of atmospheric temperature and moisture. The microwave radiometer, designed to measure the faint thermal radio emission of the atmosphere, incorporates an extremely sensitive, broad-band radio receiver. The detected radiation enters the system through a highly directional horn antenna, and the system is very highly isolated against external signals. Nevertheless, because of the sensitivity of the detectors, the potential for interference exists. During the spring and summer of 1992, while operating in an extremely radar rich environment, several peculiar signals were noticed. This paper discusses our investigation of these signals.

### 1. INTRODUCTION

The Battlefield Environment Directorate\* (BED) of the U.S. Army Research Laboratory is developing remote sensing techniques for measuring meteorological parameters on the battlefield. One component of the suite of sensors being developed is the microwave radiometer, used in measuring atmospheric temperature and moisture profiles. This instrument exploits the information contained in the natural thermal emissions of the atmosphere to infer atmospheric water vapor, liquid water, and vertical profiles of atmospheric temperature. Figure 1 is a picture of one of the instruments, the passive microwave temperature profiler (PMTF), that BED has operated for the past several years.

The top left portion of the radiometer in the figure is a Teflon window through which the microwave radiation enters and is reflected off a plane metal mirror into a horn antenna. The Teflon window can be covered with a

---

\*formerly U.S. Army Atmospheric Sciences Laboratory



metal cover, which is normally used only for protection during shipment. We mention it here because we did have occasion to run the radiometer in cover on mode during the experiments described below.

Since the thermal emission of the atmosphere is exceedingly faint, a very sensitive radio receiver is needed to detect this signal. Although these systems are carefully isolated against stray RF noise, because of their extreme sensitivity such noise remains a potential problem. During spring and summer of 1992, BED operated two microwave radiometers at the profiler test site, a location extremely rich in RF sources, containing a 50-MHz wind radar with 250 kW peak power, a 404-MHz wind radar with a peak power of 7 kW, a 924-MHz wind radar with a peak power of 1 kW and an FM-CW radar. In addition, the entire surrounding area of White Sands Missile Range is replete with radars of many descriptions.

During the period of operation a number of peculiar results were observed, suggesting that nonthermal radio signals were being observed, the most common being a small amplitude jitter in the received signal. At this time the PMTP was mounted on the roof of a van situated about 15 ft from the fence surrounding the 404-MHz radar. The proximity and the elevated position of the radiometer made us suspect that the radiometer was receiving stray radiation from the wind radar side lobes.

Figures 2 and 3 show contrasting cases where the peculiar jitter is seen (fig. 2) and is not seen (fig. 3).

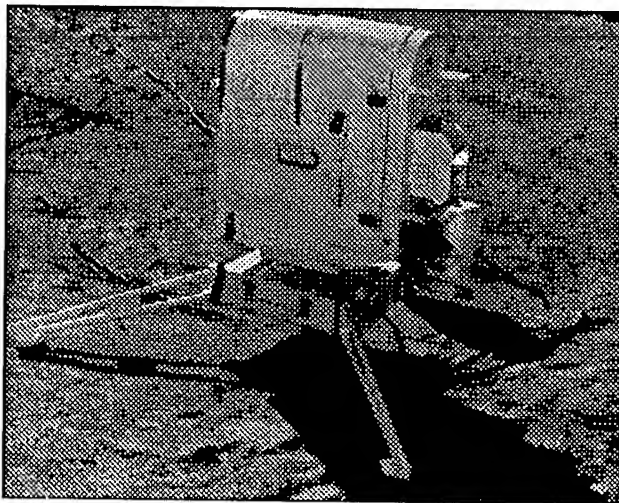


Figure 1. Four-channel microwave radiometer.

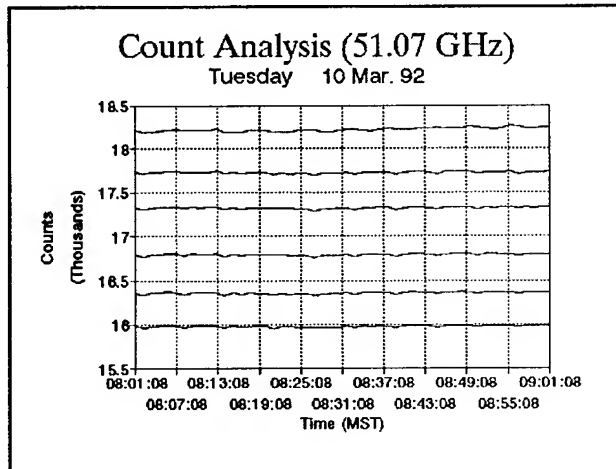


Figure 2. Microwave radiometer data, 57.45 GHz elevation angle (top curve) 9°, 15°, 25°, 40°, 90°. First notice of radio noise. Running within 25 ft of 404-MHz radar.

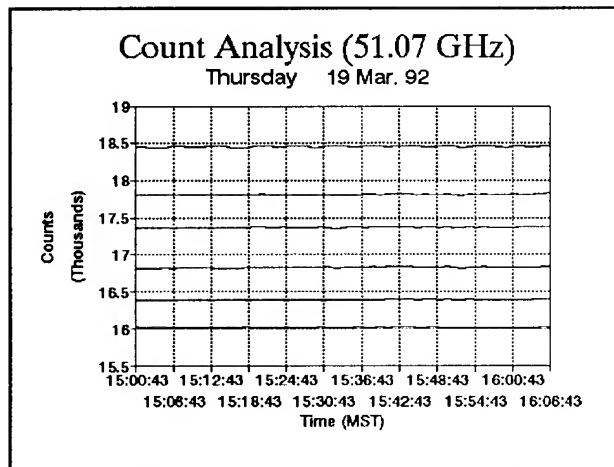


Figure 3. Same frequency and conditions as in fig. 2 except a faster sampling rate.

## 2. METHODOLOGY

Our subsequent efforts were devoted to clearly identifying and isolating the source of interference, the means by which it was entering the radiometer, and the means for avoiding the undesirable interference.

The radiometer signal undergoes several stages of signal processing before being used to compute temperature. Initially the signal is reflected off a flat mirror and into a horn antenna. Next it proceeds through the waveguide to a mixer where it is mixed with the output of a local oscillator to produce an intermediate frequency (IF) signal of about 200 MHz. Subsequently, the IF signal drives a voltage controlled oscillator that produces pulses that are reduced to the digital counts shown in fig. 2.

The PMTP operating frequencies are 51.07 GHz, 53.88 GHz, 55.29 GHz, and 57.45 GHz. It does not appear possible that an interfering signal of 404 MHz entering the horn antenna could propagate far enough through the waveguide to cause interference by that route. It seemed more likely that the interfering signal was entering at the IF stage, or perhaps over power lines or cables.

In its normal operating mode the radiometer takes data at several different look angles and goes through a data taking cycle lasting about 2 min. We felt that this was too slow to reveal the character of the jitter observed, so we modified the control programs to take data at a much faster rate (about one data point every 2 s) along a single line of sight.

Data was then taken in each of several different modes. We experimented with different antenna look angles, running with the radiometer cover on or off, and with various radiometer locations. Figure 4 shows data taken in the original van top location with the metal radiometer cover left off. In this test the radiometer was looking at an internal target. This data clearly shows the periodic character of the interference, which was only vaguely discernible in fig. 2. The interference is periodic with a period of 6 min, matching the 6-min cycle time of the 404-MHz radar (the 404-MHz radar goes through a 6-min cycle of pointing in various directions).

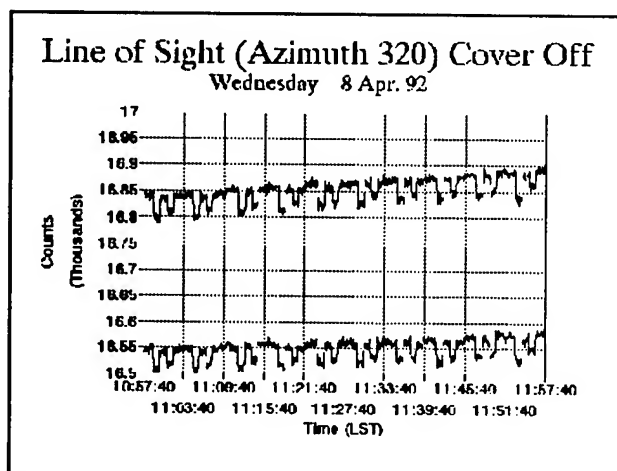


Figure 4. Radiometer within about 25 ft of 404-MHz radar metal cover off. Top curve 57.45 GHz, lower 53.88 GHz elevation held constant.

Next, the metal cover over the radiometer window was replaced and more data was taken. Figure 5 shows this data, and the prominent interference pulses are completely absent. Clearly the interference is entering the radiometer through the radiometer window and not through power lines or cables. This conclusion was confirmed by further tests in which the radiometer azimuth angle was changed, thus changing the orientation of the open radiometer window, but not of the radiometer look angle, which remained pointing straight down at the internal target. The data from these measurements showed a clear dependence of the magnitude of the interference on this aperture orientation, exactly as would be expected if the interfering signal entered through the

radiometer window and then affected the internal radiometer electronics. Figure 6 shows an example with an azimuth of 230; the magnitude of the interference pulses is only about half that at azimuth 320 (fig. 4). At an azimuth of 40° (not shown) interference was essentially abolished.

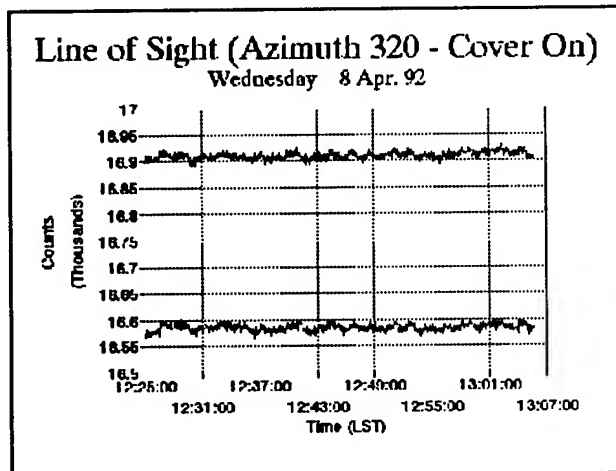


Figure 5. Same conditions as in fig. 4 except metal antenna cover on microwave radiometer.

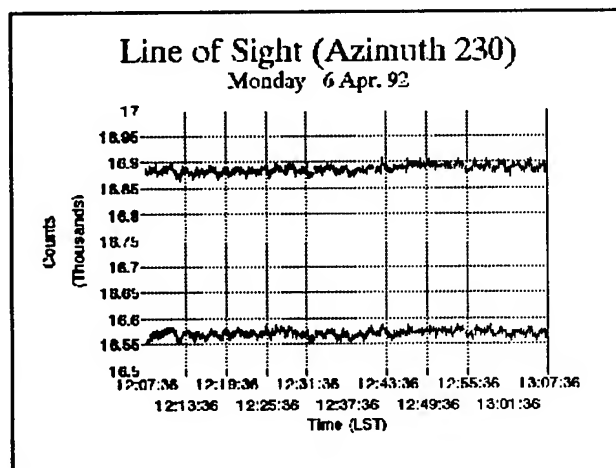


Figure 6. Same conditions as in fig. 4 except several hundred feet from 404 MHz radar essentially noise free microwave data, data reasonably smooth.

Subsequent removal of the radiometer from the immediate vicinity of the 404-MHz radar abolished all signs of interference (it currently operates about 150 m from the radar).

Because the radiometer is expected to be paired with a 924-MHz radar in the Mobile Atmospheric Profiler system, we conducted numerous tests of the radiometer operating in close proximity to the 924-MHz wind radar. None of these revealed any detectable interference.

### 3. CONCLUSIONS

Our results show clearly that there is a potential for interference from powerful radio-frequency sources. They also show that in many cases very simple measures suffice for protection of the radiometer from such interference. In particular, the radar with which it is paired in the (tactical) mobile atmospheric profiler does not appear to present a problem, at least if the profiler is located near ground level.

It is clear that careful attention should be given to isolation of the radiometer from such interference in future (tactical) radiometer designs. It might be difficult or impossible to protect it from directed high-power jamming, but it seems unlikely that such jamming of a relatively low value, passive system would be cost effective for any plausible enemy, especially since the jammer would be an expensive, highly visible target.

## REMOTE SENSORS COMPARISON ANALYSIS

R. J. Okrasinski and G. J. Cook  
Physical Science Laboratory  
New Mexico State University  
Las Cruces, New Mexico, 88003-0002, USA

R. O. Olsen and T. L. Barber  
Battlefield Environment Directorate\*  
White Sands Missile Range, New Mexico, 88002-5501, USA

### ABSTRACT

In recent years, there has been an increased availability of different types of remote sensors for measuring atmospheric boundary layer parameters. With their introduction into field operation, a question arises as to their accuracy and precision. An attempt to address this issue was made by analyzing and intercomparing sets of wind and temperature data obtained during the Joint Acoustic Propagation Experiment conducted at DIRT Site, White Sands Missile Range, New Mexico, in July and August, 1991. The remote sensing systems that were deployed were a 924 MHz wind profiler, two Doppler acoustic sodar, a Radio Acoustic Sounding System (RASS), and a microwave radiometer. In situ measurements of wind, temperature, and humidity were also obtained from radiosondes. Individual system characteristics and the results of intercomparing the derived winds and temperatures from each of the systems are presented.

### 1. INTRODUCTION

The Joint Acoustic Propagation Experiment (JAPE) was conducted at DIRT Site in the extreme southeast corner of White Sands Missile Range in July and August of 1991. Two Doppler sodars, a 924 MHz wind profiler, a Radio Acoustic Sounding System (RASS), and a passive microwave temperature profiler were deployed by the U.S. Army Atmospheric Sciences Laboratory to collect boundary layer wind and temperature data in support of the test. Upper-air wind, temperature, and humidity data were also collected by periodically released rawinsondes.

In this study, data obtained during the experiment was analyzed to evaluate the capabilities of the five remote sensors. Wind data

---

\*formerly U.S. Army Atmospheric Sciences Laboratory (ASL)

from the UHF profiler and temperature data collected by the RASS and the microwave profiler were statistically compared with concurrent rawinsonde measurements. Simultaneous wind data from the two sodars were similarly compared with each other. The percent of the time that wind profiler, RASS, and sodar data were successfully measured at each sampling height was also calculated to determine their functional vertical ranges.

## 2. INSTRUMENT DESCRIPTION

Both sodars, manufactured by REMTECH, Inc., utilize one vertical and two tilted beams to provide data. Changes in the acoustic refractive index caused by temperature fluctuations scatter some of the transmitted energy back to the antennas. Doppler shifts in these backscattered signals are used to derive the wind velocities along the three beam paths. Horizontal wind speeds and directions are then calculated from the radial velocities. The sodars are used to measure winds between 50 and 750 m above the surface.

The older A0 model uses a trailer-mounted array of three acoustic antennas, two of which are tilted  $18^\circ$  from the vertical, and the newer PA2 uses a single phased array antenna with three electronically steered beams, two of which are directed  $30^\circ$  from the vertical and  $90^\circ$  from each other. Frequency coded transmissions are propagated at frequencies centered at 1600 Hz with an acoustic power of 60 W by the A0 and at 2100 Hz with an acoustic power of 140 W by the PA2.

The wind profiler transmits three 924 MHz beams, one vertical and two tilted  $15^\circ$  vertical, from 3 antennas. Doppler shifts in the backscattered signals are used to derive the wind velocities along the beam paths. One-hour averaged horizontal wind data are computed from the radial velocities using a random sample consensus technique. The maximum measurement height is a function of the intensity of the backscattering and the vertical resolution of the wind data, but is usually between 2 and 4 km. Peak pulse power is 500 W.

The vertical radar antenna is also used to track a 2000 Hz acoustic beam transmitted by the conjunctive RASS. Doppler shifts in the backscattered energy are used to measure the speed of the acoustic signal, which is proportional to the virtual temperature of the medium. Maximum measurement height is about 1 km. Both the wind profiler and the RASS were developed by the NOAA Wave Propagation Laboratory.

The microwave temperature profiler was constructed by the Jet Propulsion Laboratory and measures the brightness temperatures at four channels between 51 and 58 GHz in the oxygen-absorbing band. Absorptivity varies significantly with frequency within the band, so that each channel detects radiation from different atmospheric depths. Additional radiometric measurements are obtained by tilting the profiler at five different angles during operation. This information combined with surface temperature, pressure,

humidity measurements, and archival radiosonde data are used to determine the temperature at 14 levels between 30 and 10688 m using a mathematical inversion technique developed by Westwater (1972).

Different radiosonde systems were deployed at DIRT Site for the July and August phases of JAPE. In July, a system manufactured by Atmospheric Instrument Research, Inc. (AIR), was used, consisting of a 1680 MHz sonde tracked by an automatic radio theodolite using a phase array antenna. Height, temperature, humidity, and balloon-to-ground azimuth and elevation angles were recorded for every 4-5 s of flight. In August, Vaisala RS-80 radiosondes were tracked by a Vaisala Digicora ground station to collect data at greater heights. Measurements were outputted for every 10 s of flight. Vaisala sondes were also launched at other White Sands locations during both phases of the experiment. Depending on the sounding, data from these were written on a file for either 152-m or 305-m flight intervals.

### 3. DATA COLLECTION

JAPE was conducted at DIRT Site in the southeast corner of White Sands Missile Range. This is an arid region situated in a broad basin between two mountain ranges. The nearest significant feature is the 300-m high Jarilla Mountains, which are approximately 4 km to the east. The test area slopes from an elevation of 1275 to 1254 m above sea level from south to north.

The A0 sodar, the wind profiler and RASS, and the radiosonde station were located at the same site. The PA2 sodar was situated approximately 4.5 km south, next to a 40-m hill. The temperature profiler was located between the two about 1.5 km south of the radiosonde. Other than the hill, there were no significant terrain features in the vicinity of the three sites.

Fifteen-minute averaged wind data were collected by the PA2 sodar during July 21-29 every 50 m between 50 and 750 m. Concurrent A0 winds were measured every 50 m between 50 and 750 m from 2045 MDT on July 20 to 1515 MDT on July 27 and between 50 and 600 m the rest of the time. Both sodars were operated more than 90% of the time between midnight MDT July 21 and 0930 MDT on July 29.

The UHF wind profiler was operated for several days during July 16-28. Two sets of 1-hour averaged data were collected. Winds with a vertical resolution of 101 m were measured at 25 levels between 167 and 2601 m, and 203-m resolution winds were measured at 24 levels between 246 and 4911 m. The profiler was turned off during several testing periods to avoid interfering with other instrumentation. A total of 84 hours of data were collected.

Five-minute averaged virtual temperatures were collected hourly by the RASS during July 20-28 and August 19-29. Data were obtained every 105 m between 127 and 1283 m above the ground. Forty-five hours of data were collected in July and 144 hours were collected in August.



Temperature measurements were provided by the microwave profiler every 106 s at 30, 61, 91, 152, 213, 305, 457, 762, 1219, 1829, 3048, 4572, 6706, and 10668 m above the surface. Approximately 26 hours of data were collected during July 16-25.

Twenty-two AIR radiosondes were flown at Dirt Site during July 16-28 and tracked to 5 km above the ground. Seven Vaisala sondes, tracked to 15-20 km, were released during August 19-29. Additional July Vaisala flights were launched from two other White Sands locations, 20-30 km from the test site.

#### 4. DATA COMPARISONS

##### 4.1 SODARS

The sodars do not usually collect wind data at all of their programmed altitudes. In many cases, the backscattered signal is too weak to be interpreted, and the wind data fields will be designated as missing. The strength of the returned signal is a function of both the attenuation along the path to the antenna and the intensity and scale of the temperature fluctuations in the region being probed. The highest altitudes that wind data can be obtained, therefore, varies with state of the atmosphere. To investigate how often sodar wind data can be successfully collected, the percentage of wind data obtained at each altitude between July 21 and July 29 were calculated and plotted versus height. The results are shown in fig. 1. The PA2, as expected, had more success at the higher levels. At 600 m, for example, 15-min wind data were collected approximately 40% of the time by the A0 and 85% of the time by the PA2.

The comparability of the two sodars was determined by calculating statistics of the differences in simultaneous wind data. Between 300 and 616 concurrent measurements were available for analysis, depending on the height. Standard deviations of the differences ranged from 1.7-1.8 m s<sup>-1</sup> for the wind speed and 41-54° for the wind direction. The largest biases, by contrast, were 0.37 m s<sup>-1</sup> and 7.2° for the wind speed and direction, respectively. In an earlier comparison, the standard deviations of the differences in wind speed and direction measured by two collocated A0 sodars were found to be 1.1-1.4 m s<sup>-1</sup> and 22-32°, respectively (Chintawongvanich et al., 1989). The poorer JAPE statistics may be partially due to the 4.5 km separation of the two sodars.

The rms wind speed and vector wind differences were also computed and are plotted in fig. 2. The latter were calculated by taking the square root of the sum of the mean square differences in the east-west and north-south component winds and are, therefore, a function of the differences in both wind speed and direction. The two statistics were close to 2 and 3 m s<sup>-1</sup> at all heights.

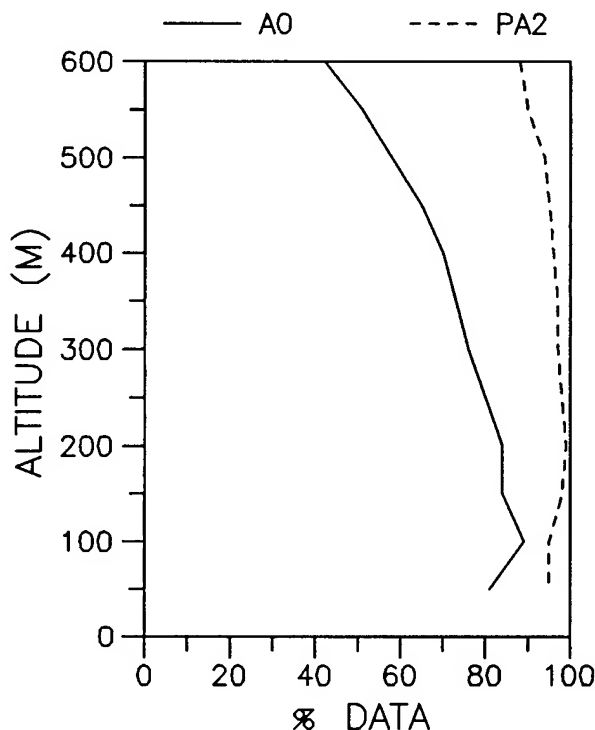


Figure 1. Percent of the time that horizontal wind data were successfully collected by the A0 (solid line) and PA2 (dashed line) sodar.

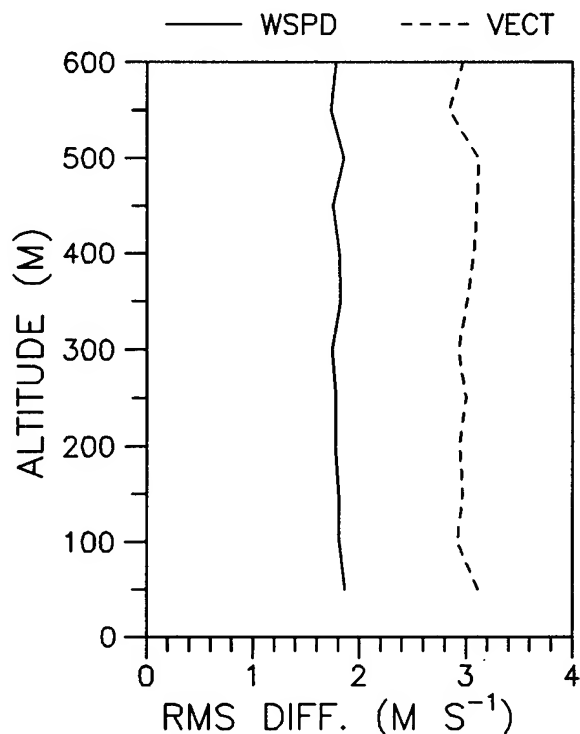


Figure 2. Rms wind speed differences (solid line) and vector wind differences (dashed line) of concurrent A0 and PA2 sodar wind data.

#### 4.2 UHF WIND PROFILER

The height range of the wind profiler varies with the intensity of the turbulent backscattering. Lower resolution winds can be measured at greater heights because longer pulse lengths, and therefore, more energy is transmitted. This is shown in fig. 3, in which the percent of 101-m and 203-m profiler data collected in July is plotted versus height. At 2 km, for example, 101-m and 203-m resolution winds were collected about 55% and 90% of the time, respectively.

To investigate the accuracy of the wind measurements, low-resolution (203-m) wind profiler data collected in July was statistically compared with data from 20 rawinsonde soundings that were launched within 30 minutes of one of the profiler interrogation times. The rawinsonde winds were calculated for 200-m layers and interpolated to the profiler heights so that both data sets had approximately the same vertical scale. There is still a rather large temporal difference, however, since the profiler winds are averaged over 1 hour and the rawinsonde winds were computed

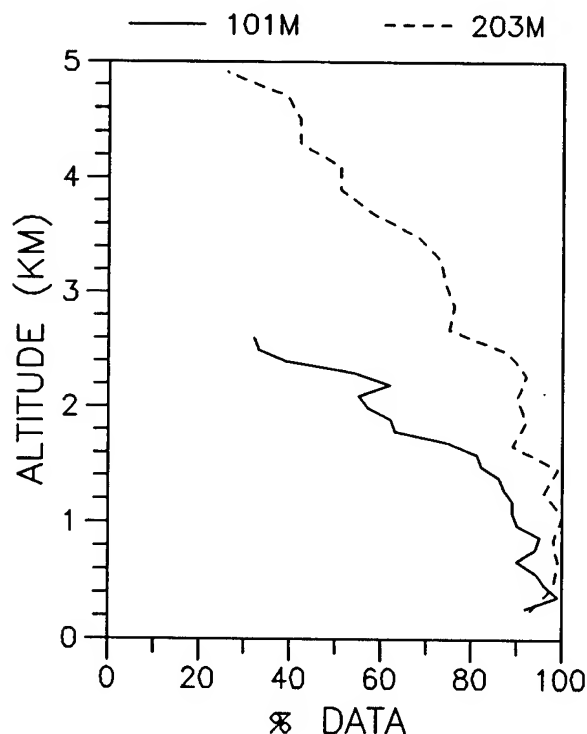


Figure 3. Percent of the time that horizontal wind data were successfully collected by the UHF wind profiler at 101-m (solid line) and 203-m (dashed line) resolutions.

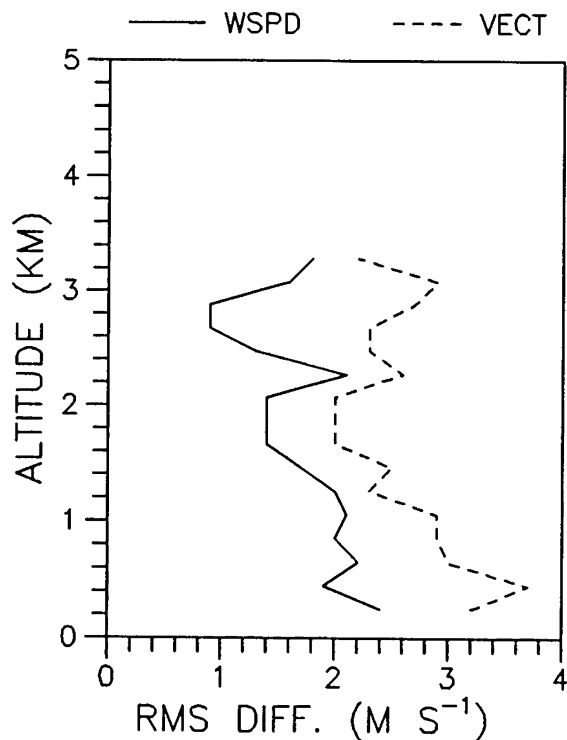


Figure 4. Rms wind speed differences (solid line) and vector wind differences (dashed line) of concurrent UHF wind profiler and rawinsonde data.

for approximately 40 s of flight. In addition, the balloon drifts away from the site as it rises. Nevertheless, the agreement between the rawinsondes and profiler was fairly good, as shown in fig. 4, in which the rms wind speed and vector wind differences are plotted versus height. Most of the rms vector differences were close to  $2.5 \text{ m s}^{-1}$ . This is not much larger than the  $1.5\text{--}2.0 \text{ m s}^{-1}$  vector differences that were found between the same radiosonde system and a reference high-precision radar during a radiosonde intercomparison experiment (Olsen et al., 1991). These statistics also compare favorably with the results of a study by Weber and Wuertz (1990) in which the standard deviation of the differences in the east-west and north-south wind velocities measured by a wind profiler and rawinsondes were found to be about  $2.5 \text{ m s}^{-1}$ .

#### 4.3 RASS

Virtual temperature data collected by the RASS in July and August were similarly analyzed. The percent data measured at each height,

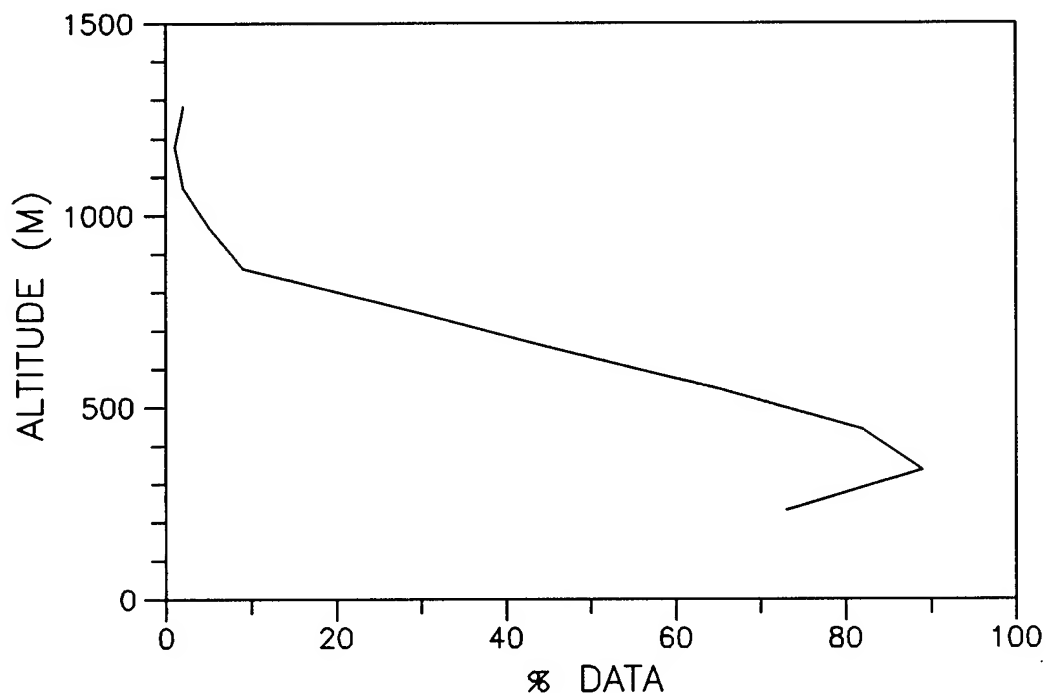


Figure 5. Percent of the time that temperature data were successfully collected by the RASS.

TABLE 1. RASS-RADIOSONDE VIRTUAL TEMPERATURE DIFFERENCES

ALT (m)	MEAN	SDEV (°C)	RMS	NPTS
233	.0	.7	.7	20
338	.3	.7	.8	22
442	.6	.7	.9	21
548	.5	.6	.8	17
652	.4	.7	.8	12

plotted in fig. 5, shows that almost no data were obtained above 652 m. Measurements up to this level were statistically compared with virtual temperatures computed from 22 radiosonde soundings, which were released within 30 minutes of one of the RASS interrogation times. Means, standard deviations, and root-mean-squares of the differences are printed in table 1. The rms differences of 0.8 °C are comparable with those found by May et al. (1989).

TABLE 2. PROFILER-RADIOSONDE TEMPERATURE DIFFERENCES

ALT (m)	MEAN	SDEV (°C)	RMS	NPTS
61	.3	.6	.6	7
91	.2	.6	.6	7
152	-.1	.6	.6	7
213	.1	.5	.5	7
305	.8	.7	1.0	7
457	1.3	.8	1.5	7
762	1.9	.8	2.0	7
1219	2.2	1.0	2.4	7
1829	3.5	1.2	3.7	7
3048	3.2	1.4	3.5	7
4572	2.7	1.5	3.1	7

#### 4.4 MICROWAVE TEMPERATURE PROFILER

Temperature data from the microwave profiler were averaged over seven points and statistically compared with data from seven concurrent radiosondes released in July and tracked to 5 km at DIRT Site. The results are shown in Table 2. The most significant feature is the bias between the two measurements above 213 m, which reaches a maximum of 3.7 °C at 1829 m. Nevertheless, the rms differences, which range from 1 °C at 305 m to 3 °C at 4572 m, are roughly comparable to the specified profiling accuracy of this sensor.

During the periods the profiler was operated, three radiosondes were also released at Oasis, approximately 21 km to the west. One of these flights is plotted in fig. 6 to show how the top two measurements of the profiler compare with radiosonde data. In this case, the temperature bias reaches a maximum at 1829 m and becomes negative at the top two heights. A plot of other White Sands data presented in an earlier paper by Measure et al. (1991) has similar features.

#### 5. SUMMARY

Statistical agreement between the radiosonde data and the wind profiler and RASS measurements collected at JAPE was comparable with the results of other similar studies. The rms temperature and vector wind differences between concurrent measurements were approximately 0.8 °C and 2.5 m s<sup>-1</sup>, respectively. Standard deviations of the differences in the sodar wind speeds and directions were somewhat greater than those that were found between two

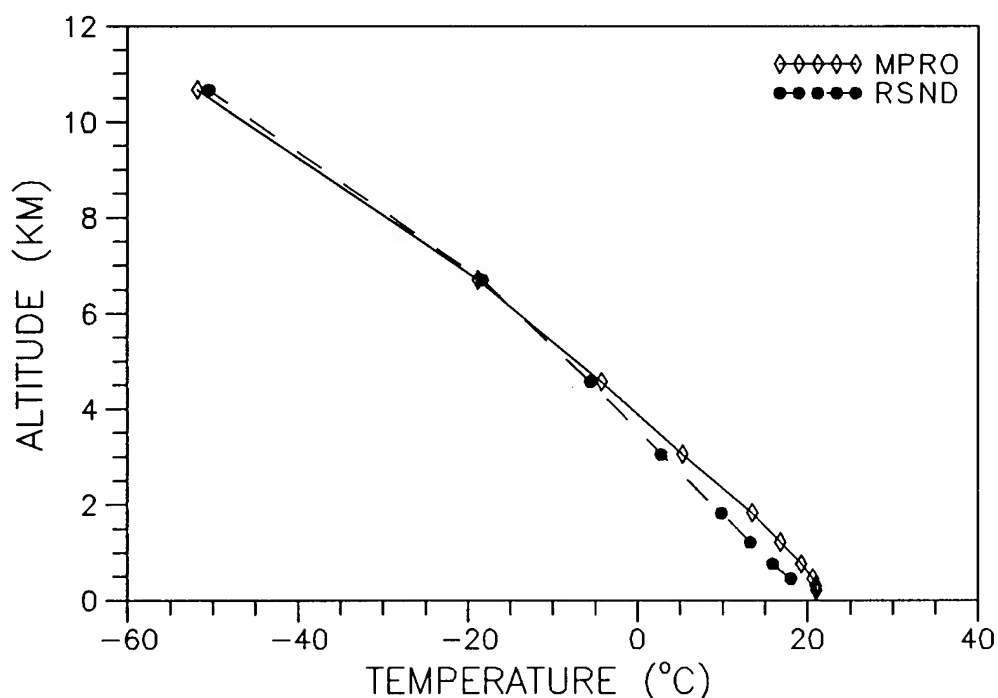


Figure 6. Temperature measured by a radiosonde launched at Oasis on July 23, 1991, at 0855 MDT (solid circles) compared with concurrent JAPE microwave profiler data (diamonds).

collocated sodars in a previous study, however. This may be partially due to the 4.5 km separation of the two sensors. The sodar rms vector wind differences were about  $3 \text{ m s}^{-1}$ . The rms differences between data collected by the microwave temperature profiler and concurrent radiosondes ranged from  $0.6^\circ\text{C}$  for heights below 305 m to  $3\text{--}4^\circ\text{C}$  for heights of 1829 m and above. This is roughly comparable with the specified profiler accuracy.

Data were successfully collected at least 50% of the time at all heights below 600 m by the A0 sodar, below 652 m by the RASS, and below 2.3 and 4.3 km by the UHF wind profiler at 101-m and 203-m vertical resolutions, respectively. More than 85% of the PA2 data were collected at all altitudes up to 600 m.

#### REFERENCES

- Chintawongvanich, P., R. O. Olsen, and C. A. Biltoft, 1989: Intercomparison of Wind Measurements from Two Acoustic Doppler Sodars, a Laser Doppler Lidar, and In Situ Sensors. J. Atmos. Oceanic Technol., 6, 785-797.
- May, P. T., K. P. Moran, and R. G. Strauch, 1989: The Accuracy of RASS Temperature Measurements. J Appl. Meteor., 28, 1329-1335.

- Measure, E. M., T. L. Barber, R. J. Hulsey, and D. R. Larson, 1991: Testing a Microwave Radiometer in Arctic, Temperate, and Tropical Climates. In Proceedings of the 1991 Battlefield Atmospherics Conference, Battlefield Environment Directorate, WSMR, NM, 223-227.
- Olsen, R. O., R. J. Okrasinski, and F. J. Schmidlin, 1991: Intercomparison of Upper Air Data Derived from Various Radiosonde Systems. In Preprints: 7th Symp. on Meteor. Observations and Instrumentation, Amer. Meteor. Soc., Boston, MA, 232-236.
- Weber, B. L., and D. B. Wuertz, 1990: Comparison of Rawinsonde and Wind Profiler Radar Measurements. J. Atmos. Oceanic Technol., 7, 157-174.
- Westwater, E. R., 1972: Ground-Based Determination of Low Altitude Temperature Profiles by Microwaves. Mon. Wea. Rev., 100, 15-28.

#### DISCLAIMERS

The citation of trade names and names of manufacturers in this paper is not to be construed as official Government endorsement or approval of commercial products or services referenced herein.

## CHARACTERIZATION OF IMAGER SPECTRAL RESPONSE FOR OPTIMIZED ATMOSPHERIC PROPAGATION

Daniel R. Billingsley, Fernando R. Palacios  
and Wendell R. Watkins  
U.S. Army Battlefield Environment Directorate  
White Sands Missile Range, NM. 88002-5501

### ABSTRACT

For long-range target detection the degrading effects of atmospheric path radiance must be considered, and have resulted in the use of cold-finger spectral filtering of the Inframetrics, Inc., imagers in the Mobile Imaging Spectroscopy Laboratory (MISL). To demonstrate the effectiveness of the application of the bandpass filters to the MISL infrared (IR) imagers, the authors conducted sets of long-path absorption cell measurements. The first set of these measurements was performed for dry through humid atmospheres for a 1.0-km cell pathlength using filtered and unfiltered mid-IR and far-IR imagers. The mid-IR measurements using a 1,000 °C blackbody source demonstrated that the filter did indeed improve the target contrast sensitivity significantly for the humid conditions. The initial far-IR measurements were inconclusive because the calcium fluoride cell windows did not transmit much beyond 8  $\mu\text{m}$ . Subsequent use of barium fluoride windows proved that the filtered far-IR imagers perform better for humid long-range detection although intermediate ranges and humidities gave the most pronounced improvement.

### 1. INTRODUCTION

In November 1988 at Redstone Arsenal, Alabama, it was observed that in using the commercially available Inframetrics 610 IR imager that uses a mercury cadmium telluride detector there was a detector optimization problem due to the noise contributions from path radiance (Watkins, Kantrowitz, Crow, 1989). Path radiance is due to emissions from atmospheric constituents such as  $\text{H}_2\text{O}$  and  $\text{CO}_2$  and can be a significant contributor to a poor signal-to-noise ratio.

The 610 IR imager has a dual mid-IR and far-IR wavelength response with a corresponding detector for each of these bandwidths. At the above test in Alabama, two of these imagers were used in order to characterize propagated target contrast. One of the imagers was positioned 83 m (near field (NF)) from a fiberglass tank simulator and the other was positioned 1,550 m (far field (FF)) from the target. There were also two visible cameras positioned at these respective distances. The IR imagers were optically matched so their spatial resolutions at the target plane were essentially identical.



The very apparent problem of path radiance observed at this test is illustrated in fig. 1. Figures 1a and 1b are respectively the visible NF and FF scenes. Figures 1c and 1d are respectively the NF and FF 3 to 5  $\mu\text{m}$  mid-IR scenes. Figures 1e and 1f are respectively the NF and FF 8 to 14  $\mu\text{m}$  far-IR scenes. In viewing fig. 1c the target is very distinguishable from the background, but in fig. 1d the target's contrast with the background has been washed out due to the effects of path radiance. The effect of path radiance also shows up in the FF 8 to 14  $\mu\text{m}$  scene (fig. 1f) but is less severe than that of the 3 to 5  $\mu\text{m}$  bandwidth.

In order to mitigate the effects of path radiance, the IR 610 imager needed to be modified. This modification was done in two respects. First, the detector response peak for the mid-IR bandwidth was shifted to a more optimized wavelength by changing the doping concentrations in the detector chip. Second, a cold finger filter was mounted within the dewar of each detector in order to filter out undesirable path radiance. After the modification, measurements showed that there was an enhancement of target contrast ( $\Delta T$ ) in the far-IR region but that in the mid-IR region the modification had not met the desired results. Further analysis showed that the detector response shift in the mid-IR region did not meet the required specifications (Kantrowitz, et al., 1990).

Although the modified imager had not met specifications in the detector response shift in the mid-IR region, it still responded at a more favorable wavelength than its unmodified counterpart. Thus it is the intent of this paper to demonstrate that the mid-IR and far-IR modified imagers have distinct advantages in sensitivity over their unmodified counterparts for a wide range of humidity levels. The tool needed and used to provide the data for this demonstration is the 21-m White cell located in the Imaging Spectroscopy Laboratory of the Battlefield Environment Directorate at White Sands Missile Range, New Mexico (Watkins and Dixon, 1979). The White cell was the prime tool for this test because of its capability of providing a series of rapid succession parametric comparisons between the pairs of imagers.

## 2. BACKGROUND

In deciding how the IR 610 imager needed to be modified, the detector responses for both the mid-IR and far-IR were looked at along with the spectral atmospheric transmission, atmospheric path radiance, and ambient ( $\sim 17^\circ\text{C}$ ) blackbody curves for the respective bandwidths (Kantrowitz, et al., 1990). Two significant observations were made. First, the detector response function in the mid-IR bandwidth was not optimally peaked for maximum signal-to-noise ratio, and second, by implementing cold finger spectral filters within the dewars of the detectors, the noise from the path radiance could be significantly reduced. For the mid-IR detector, it was found that the signal-to-noise ratio was maximized when the mid-IR unfiltered detector peaked near  $2200\text{ cm}^{-1}$  and that a notched cold finger filter with a bandpass of  $2080\text{--}2185\text{ cm}^{-1}$  and  $2400\text{--}2950\text{ cm}^{-1}$  would be appropriate for this detector. For the far-IR detector no detector peak spectral response change was necessary, but a cold finger filter with a bandpass of  $825\text{--}1205\text{ cm}^{-1}$  was needed to reduce path radiance.

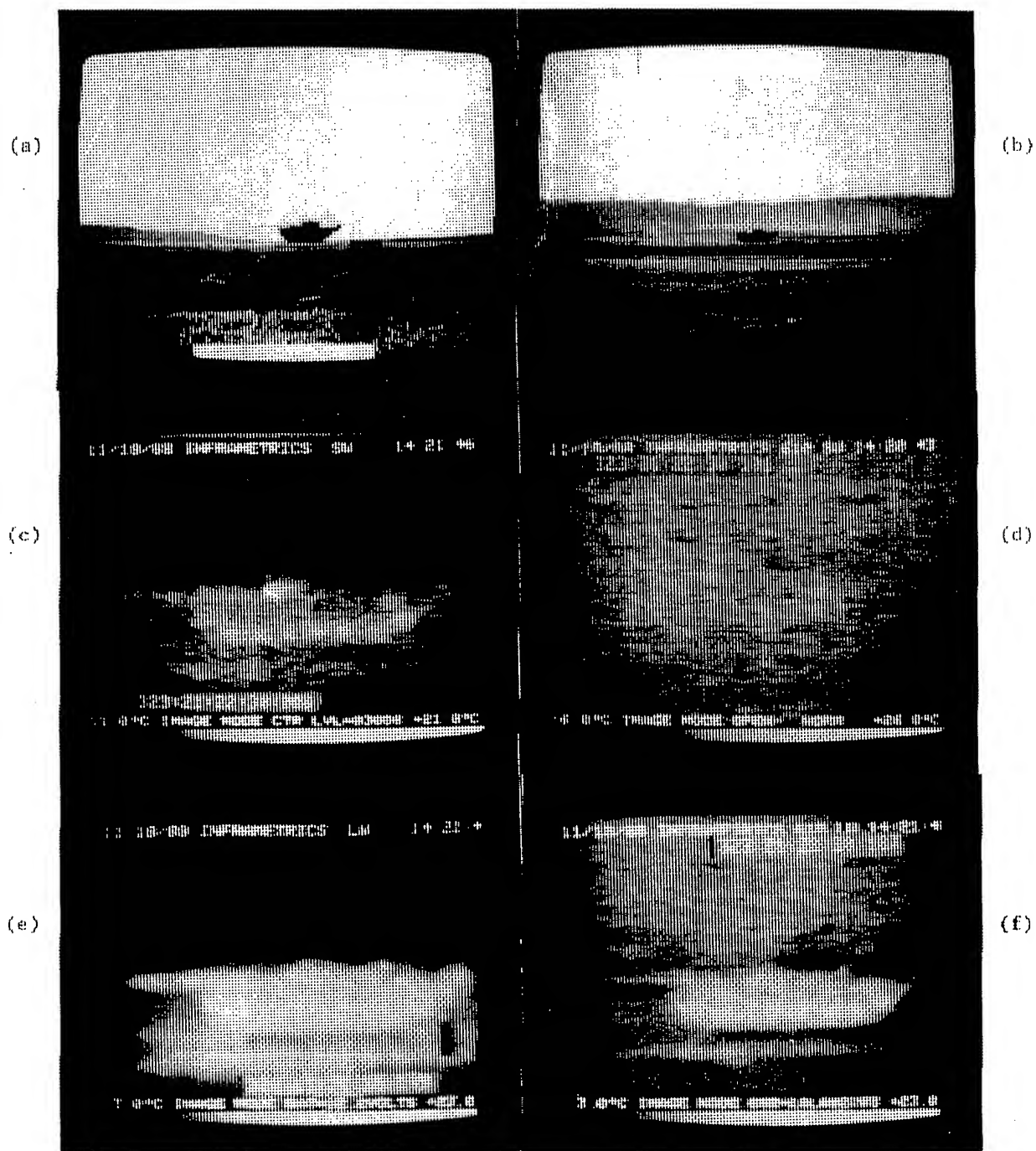


Figure 1. Views of a heated tank simulator for low humidity:  
 (a) NF visible, (b) FF visible, (c) NF 3-5  $\mu\text{m}$ , (d) FF 3-5  $\mu\text{m}$   
 (e) NF 8-14  $\mu\text{m}$ , and (f) FF 8-14  $\mu\text{m}$

After the changes were made, the modified imager was compared to an unmodified one and there was a significant improvement in the far-IR bandwidth over a path length of 557 m (Kantrowitz, et al., 1990). The far-IR detector with the cold finger filter was now able to detect slightly larger  $\Delta T$ s over the unmodified detector. In the mid-IR bandwidth, the modified detector did not achieve the desired results, and it was concluded later that the modified detector had been peaked slightly beyond the desired frequency.

While the above comparison between the two imagers was done in the field, it was known that a more thorough parametric comparison between the two imagers could be done by taking advantage of the Battlefield Environment Directorate White cell. The White cell, which is a 21-m long path absorption cell with three internal mirrors, has distinct advantages in that a controlled environment can be produced for varying gas concentration in the pathlength with rapid turnaround in cycling the cell atmospheres (Watkins and Dixon, 1979). In the field the researcher is greatly restricted to the prevalent amounts of mixed gas levels, including uncharacterized aerosols for a particular day and to change the pathlength would require the picking up and moving of the equipment rather than a minor adjustment of a mirror in the White cell.

### 3. EQUIPMENT SETUP

The 21-meter White cell or long-path absorption cell houses three concave mirrors of equal radius of curvature (James and Sternberg, 1969). Two of these mirrors are of equal dimensions and are positioned at one end of the cell. The third mirror, which is larger, is positioned at the other end of the cell. Between the three mirrors multiple reflections can be established to achieve desired pathlengths. At the same end of the cell as the larger mirror, the input and output windows are located on opposite sides of the mirror with barium fluoride windows giving the best result. On the outside of this end of the White cell are two mirrors that change the direction of the incoming radiation by 180°. Before hitting the first outside mirror, the radiation is emanated from a blackbody set at a temperature of 1000 °C and passes through a collimating lens also composed of barium fluoride (fig. 2).

Barium fluoride windows were used so that the long wavelength end of the spectral transmission bandpass of the optics in the cell would not cut off inside the spectral radiance response of the far-IR detectors. This type of transmission cutoff had occurred in preliminary testing when the cell windows were composed of more durable, less hygroscopic calcium fluoride. Although the cutoff for barium fluoride is around 15  $\mu\text{m}$  with the cumulative thicknesses of the barium fluoride lens and windows, the transmission began to fall off with increasing wavelength starting around 11  $\mu\text{m}$ . Due to this not all the available radiation in the far-IR region was received by the far-IR detector, while in the mid-IR bandwidth there was no preferential spectral attenuation of the radiation.

The reason for the high temperature source, 1000 °C, is because the imagers are unable to resolve the actual apparent temperature of the source after propagating through the White cell. There is roughly a 90 percent loss in received peak radiant energy due to this resolution problem.

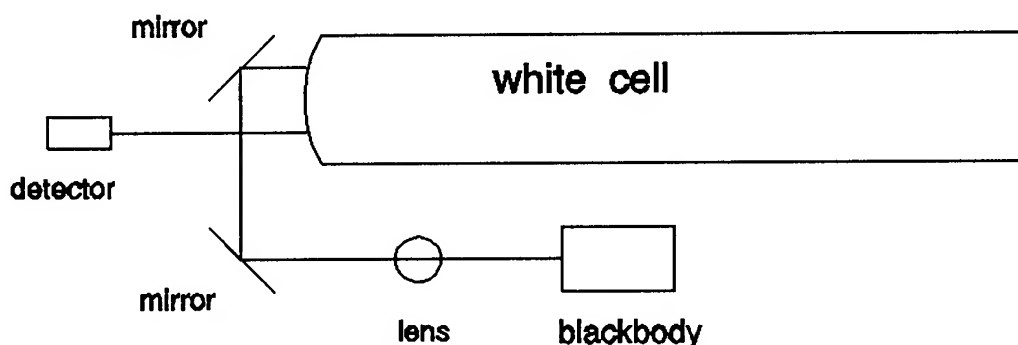


**Figure 2. White cell configuration**

It is also important to explain how the IR imagers detect and recognize a certain temperature level. The imager window has impinged upon it a certain radiant intensity from the scene and a corresponding voltage is produced by the detector. This voltage is then matched against a calibration table corresponding to the optical filter/lens combination in use. Of course if one detector has a spectral filter, its calibration table will differ from that of an unfiltered detector.

#### **4. MEASUREMENT**

The series of tests decided on in comparing the two detectors were at humidity levels of 0 (vacuum), 26, 50, 70 and 90 percent. The last four humidity levels were for ambient pressure (657 torr avg.) atmospheres with local concentrations of the minor constituent gases.

For the first test the White cell was first pumped out until a vacuum level of approximately  $1 \times 10^{-5}$  torr was achieved. Once this was achieved the blackbody, set to approximately 1000 °C, was properly positioned and the radiation then propagated through the cell at an initial pathlength of 1176 m and then stepped down by increments of 168 m until a final pathlength of 168 m was reached. This gave seven different pathlengths for the IR radiation to propagate through, and measurements were taken by both detectors for each pathlength.

After the first test the White cell was filled with regular room atmosphere, which on that particular day had a relative humidity of 26 percent. For the following three tests of increasing humidity levels, the White cell was again pumped out to  $1 \times 10^{-5}$  torr and then a predetermined amount of water (for the respective humidity levels) was allowed to enter the cell under vacuum. After this, outside ambient air was allowed to slowly enter the cell and combine with the water vapor already present until the pressure within the cell balanced with the outside ambient pressure.

## 5. ANALYSIS

In analyzing the data it was necessary to determine the difference between the received radiant temperature and the ambient or room temperature,  $\Delta T$ , for each detector and compare that against its counterpart. Figures 3 through 7 are therefore given with a Y axis that represents  $\Delta T$  (delta T) in  $^{\circ}\text{K}$  and an X axis that represents the incremental pathlengths in meters.

For the first test in which the medium was a vacuum, fig. 3a illustrates that in the far-IR region the unmodified detector clearly outperformed the modified one. This was to be expected as the modified detector received less energy due to the cold finger filter. In the mid-IR region however the situation reversed with the modified detector clearly outperforming the unmodified one (fig. 3b). This is attributed to the detector response function of the modified detector being much more appropriately peaked in that spectral response than its unmodified counterpart.

For the second test with a humidity level of 26 percent, the modified detector slightly outperformed the unmodified in the far-IR bandwidth, demonstrated in fig. 4a. This is because at 26 percent relative humidity the water absorption band is absorbing a significant amount of the source radiation that is replaced by reemitted spectral water emission band radiation at a much lower temperature. The cold finger filtered detector is not calibrated against the radiation absorbed in the water vapor band and thus displays a higher temperature. For the mid-IR region, displayed in fig. 4b, the modified detector significantly outperformed the unmodified detector. This is attributed to the more desirable detector response and the notched cold finger filter of the modified detector.

For the third test atmosphere at a humidity level of 50 percent was used. The results showed that in the far-IR region (fig. 5a), the modified detector had an even bigger advantage over the unmodified one. With the increase in humidity, more of the source radiance was being absorbed and reemitted at a lower temperature. In the mid-IR region (fig. 5b) the modified detector had a big advantage over the unmodified one, but for this bandwidth the increase in performance was only slightly more than the increase demonstrated at 26 percent relative humidity.

For the fourth test an atmosphere at a humidity level of 70 percent was used. The results showed that in the far-IR region (fig. 6a) the modified detector again outperformed the unmodified one, but the difference in performance was only slightly better than that in the prior test at 50 percent relative humidity. For the mid-IR region (fig. 6b) the modified detector maintained performance over the unmodified one, but likewise the difference in performance was only marginal compared to the prior test at 50 percent relative humidity.

For the final test an atmosphere at a relative humidity level of 90 percent was used. The results showed that in the far-IR region (fig. 7a) the modified detector still outperformed the unmodified detector, but now the difference in performance was found to be slightly less than the difference of performance from the 70 percent relative humidity test. The same results were found to be true for the detector operating in the mid-IR region (fig. 7b).

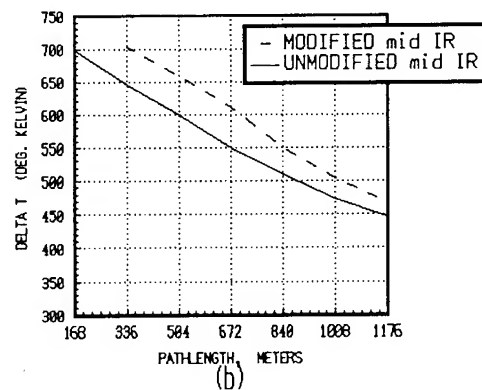
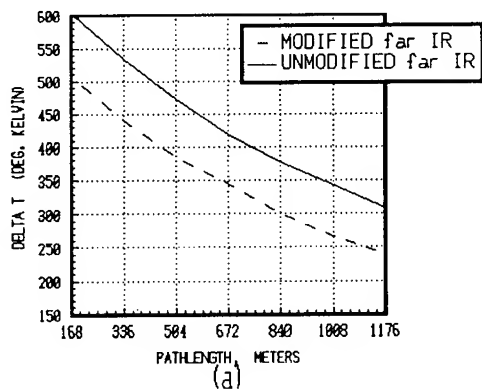


Figure 3. Cell status: vacuum

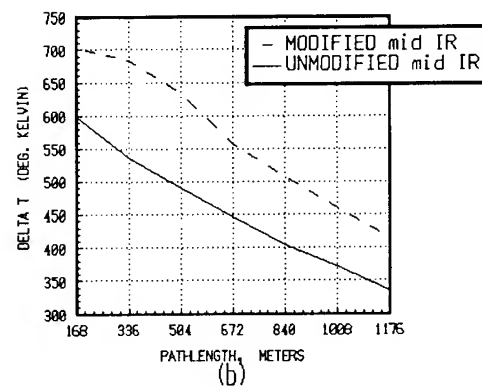
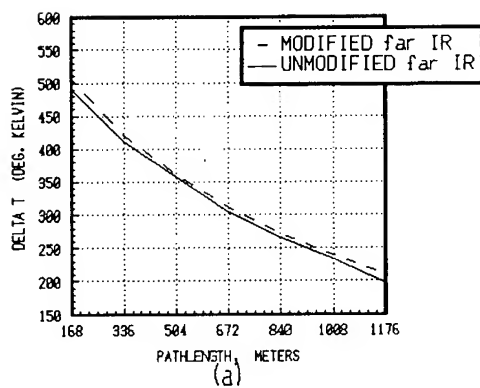


Figure 4. Cell status: 26% Rel. Hum., 655.5 Torr

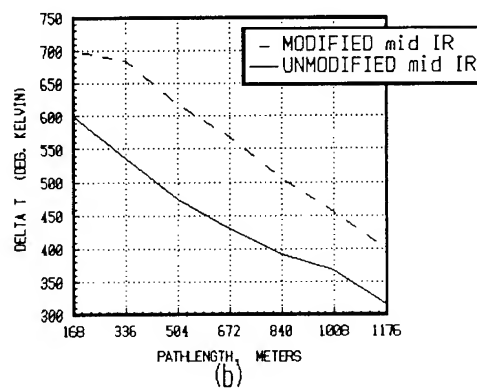
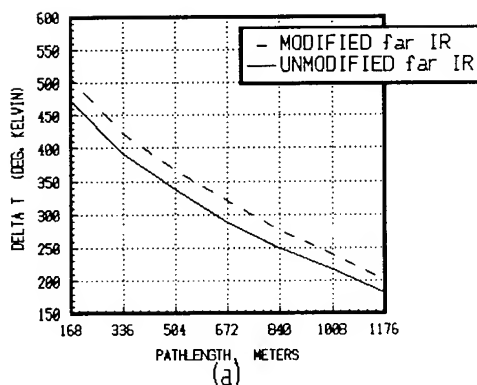


Figure 5. Cell Status: 50% Rel. Hum., 657.7 Torr

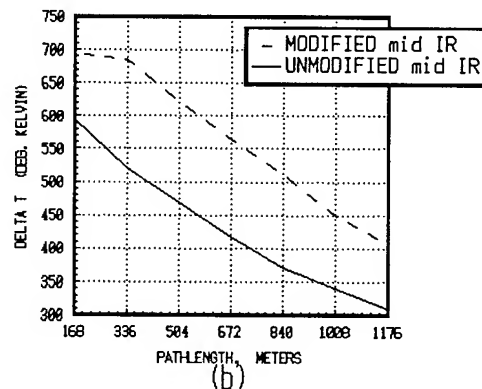
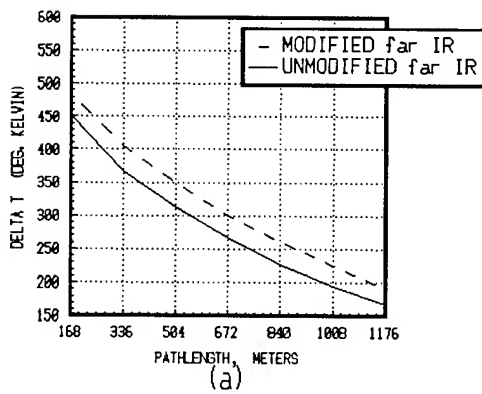


Figure 6. Cell status: 70% Rel. Hum., 658.7 Torr

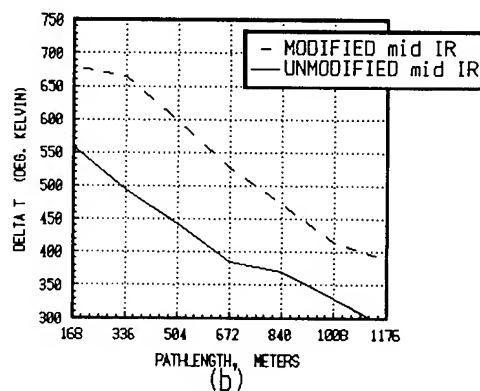
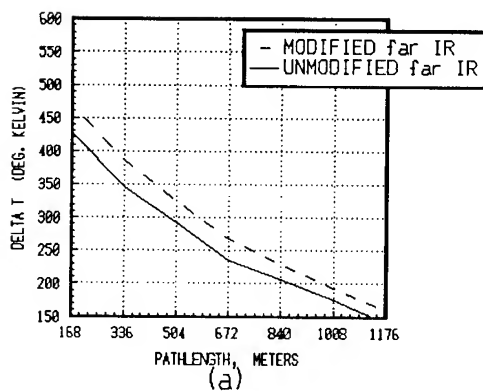


Figure 7. Cell status: 90% Rel. Hum., 655.7 Torr

To quantitatively summarize the results of the tests, table 1 has been provided which displays the average difference of  $\Delta T$  between the better performing detector and its counterpart for each test. Column 1 gives the White cell status for each test, while column 2 gives the bandwidth of interest for the test. In column 3 is denoted the detector with the higher sensitivity for the test, and in column 4 the average difference of  $\Delta T$  is given between the more sensitive detector and its less sensitive counterpart.

The tests convincingly showed that in all of the cases but one (vacuum, far-IR) the modified detector outperformed the unmodified detector. Table 1 shows that both the mid-IR and far-IR detectors had their largest advantage of sensitivity at the 70 percent relative humidity level. Additional tests need to be run with smaller incremental changes in the relative humidity to determine where the respective modified detectors have their greatest advantage, for the appropriately peaked mid-IR detector.

The unmodified far-IR detector had a distinct advantage of sensitivity at 0 percent humidity or a vacuum. This as noted before was to be expected because with no gas absorption the unmodified detector will receive all the radiation within its spectral response while the modified detector is limited by its spectral filter.

TABLE 1.  
DETECTOR SENSITIVITIES COMPARED UNDER DIFFERENT HUMIDITIES

CELL STATUS	BANDWIDTH	DETECTOR OF HIGHER SENSITIVITY	AVERAGE DIFFERENCE OF $\Delta T$ ( $^{\circ}\text{K}$ )
VACUUM	far-IR	UNMODIFIED	82.0
26% REL. HUM., 655.5 TORR	far-IR	MODIFIED	8.7
50% REL. HUM., 657.7 TORR	far-IR	MODIFIED	28.1
70% REL. HUM., 658.7 TORR	far-IR	MODIFIED	32.4
90% REL. HUM., 655.7 TORR	far-IR	MODIFIED	29.6
VACUUM	mid-IR	MODIFIED	53.8
26% REL. HUM., 655.5 TORR	mid-IR	MODIFIED	111.1
50% REL. HUM., 657.7 TORR	mid-IR	MODIFIED	116.0
70% REL. HUM., 658.7 TORR	mid-IR	MODIFIED	130.1
90% REL. HUM., 655.7 TORR	mid-IR	MODIFIED	125.0



## 6. CONCLUSIONS

Use of the White cell, which is a long path absorption cell, shows that a modified Inframetrics 610 IR imager has distinct advantages over its unmodified counterpart for a wide range of humidity levels and varying pathlengths. This is important because over long pathlengths (1 km or more), path radiance, which is primarily from emissions of H<sub>2</sub>O and CO<sub>2</sub>, can have a very degrading effect on the sensitivity of an unmodified imager. Even over moderate pathlengths a wide range of humidity levels can be responsible for a significant loss of detector sensitivity.

The White cell is a preferred instrument or tool in the comparison of these imagers because a controlled environment can be produced for varying gas concentration in the pathlength with rapid turnaround in cycling the cell atmospheres.

## REFERENCES

- James, J. F., and R. S. Sternberg, 1969: The Design of Optical Spectrometers. Chapman and Hall Ltd, 11 New Fetter Lane, London EC4, 239 pp.
- Kantrowitz, F. T., W. R. Watkins, D. R. Billingsley, and F. R. Palacios, 1990: Characterization and Optimization of Infrared Imager Detector Response for Long Path Research. In SPIE Conference Proceedings, 1311, Orlando, FL.
- Watkins, W. R. and R. G. Dixon, 1979: Automation of long-path absorption cell measurements. In Review of Scientific Instruments, 50:86-92.
- Watkins, W. R., F. T. Kantrowitz, and S. B. Crow, 1989: Transmission Measurements with the Target Contrast Characterizer. In SPIE Conference Proceedings, 1115, Orlando, FL.

**Session III**

**DATA BASES AND ANALYSES**

**Session Chair**

**Mr. Anthony Van de Wal  
U.S. Army Research Laboratory**

## **CLIMATOLOGY OF CLOUD STATISTICS**

### **C CLOUD S**

Paul H. Lewis and Richard W. Hartman  
USAF Environmental Technical Application Center  
Scott Air Force Base, IL 62225-5438

Albert R. Boehm  
Hughes STX Corporation  
Lexington, MA 02173-0000

### **ABSTRACT**

C CLOUD S is a PC-based software package that provides rapid access to 14 cloud-cover statistics in four categories: (1) surface-observed sky cover, (2) cloud-free line-of-sight (CFLOS), (3) satellite-based viewing, and (4) database variables. Knowledge of CFLOS is especially important in the design and testing of the optical components of various Department of Defense systems. These statistics represent average conditions. Also generated is the validity of cloud statistics based on natural variability and observed and archived error. One benefit of C CLOUD S is that several of its modeled cloud statistics it provides, such as the probability of CFLOS, are not routinely measured nor available. Another benefit is its ability to store a world-wide cloud climatological database in a very compact form. The database includes surface and ship observations from DOE/NCAR (Department of Energy/National Center for Atmospheric Research), Burger surface observations, and Nimbus 7 Satellite-derived cloud cover.

C CLOUD S is capable of presenting climatological cloud statistics rapidly in several presentation formats. Users may display statistical values as numbers, as contour maps (for area calculations), or as histograms. The information can be sent directly to the screen, to an output file, or to a printer. C CLOUD S runs on IBM-compatible systems with a VGA monitor and at least 640k of memory. A math co-processor is highly recommended.

## 1. INTRODUCTION

For some time the military community has needed an easily transportable global cloud-cover database of optimum size but which can supply a broad spectrum of statistics. C CLOUD S will fill this need.

In this paper, we first present the benefits C CLOUD S provides that previous cloud climatology programs do not. Second, we explain the database compaction used by C CLOUD S. Finally, we give a brief description of the cloud-cover statistics available and of the various methods of output.

## 2. BENEFITS OF C CLOUD S

C CLOUD S provides basic climatology input to stochastic (i.e., random) sky-cover simulators that generate sequences of observations statistically resembling sky-cover observations. The most important benefit of the C CLOUD S model is its ability to store a worldwide cloud climatology database in a very compact format. To provide worldwide cloud cover statistics, C CLOUD S requires only one 3 1/2" floppy diskette for both the model and its associated database. Conventional techniques require look-up tables and large amounts of storage on numerous high density tapes; they take enormous amounts of time to compute the statistics of interest. The C CLOUD S database is not historical; that is, "real data" observed on a given day are not available in the C CLOUD S database. However, "real data" is statistically compressed, using Fourier spectral methods, to create the C CLOUD S databases.

## 3. DATABASE

Although the C CLOUD S data compaction is such a complex process that an explanation is far beyond the scope of this paper, a brief synopsis of the technique follows. The C CLOUD S database is the result of blending and compacting four separate databases: (1) DOE/NCAR surface observations for land and sea, (2) the Burger database for individual stations, (3) the Nimbus 7 satellite database, and (4) a subset of the DATSAV data that provides hourly sequences for temporal and spatial correlation. These databases are very large; for example, DOE/NCAR has 54 years of data over the ocean). They have their own temporal and spatial attributes.

The data is first parameterized by using the mean sky cover and mean correlation. Mean sky cover is average cloudiness over the sky dome. Mean correlation is the average correlation over all pairs of points on the sky dome. These two points can be used to regenerate the complete distribution of sky cover with about a 2% error.

From here the parameters are analyzed using a Fourier spectral method. The 12 monthly values for the monthly database are analyzed using a 12-term Fourier series. Similarly, the eight "time of day" values (every 3 hours) are described by an eight-term Fourier series. In general,

$$A' = \sum_{j=0}^7 A_{ij} F_j(t) \quad (1)$$

where  $F$  is a Fourier function for time  $t$  and  $A_{ij}$  is the Fourier coefficient. This is the basis for the storage of the temporal database, but a more intense process is needed for the spatial database.

Spatially, the elements of the C CLOUD S database can be described by a 225-term spectral analysis. Longitudinally, a Fourier series describes cloud cover rather well since the values along a particular longitude are cyclic. Latitudinally, however, the cloud-cover values are not necessarily cyclic. Therefore, an associated fully normalized Legendre polynomial (Gleason, 1985) is used to describe cloud cover along a particular latitude. Thus,

$$f(x,y,t) = \sum_{i=0}^{224} A'_i F_i(x) L_i(y) \quad (2)$$

in which  $f$  is a general function describing the mean and mean correlation.  $A'$  comes in from Equation 1 and  $F$  is a Fourier function where  $x$  is the longitude and  $L$  is a Legendre function where  $y$  is the sine of the latitude.

#### 4. TYPES OF STATISTICS

The first of the four types of surface-based sky-cover statistics available from C CLOUD S is the probability for a single condition, such as the probability of 0.4 (four-tenths) or less of the sky covered by cloud. The second surface-based statistic is duration probability; that is, the probability time a specified fractional sky-cover condition will last over  $m$  hours; for example, the probability of 0.4 or less sky-cover over a 3-hour time period. Third, the probability of recurrence of a specified fractional sky-cover, without respect to what happened between the times specified; for example, the probability that sky-cover less than 0.4 would occur at noon GMT and at 1500 GMT. The final surface-based sky-cover statistic is conditional climatology, or the probability of a specified fractional sky-cover at a time  $m$  hours later, given an exact sky-cover observation at the initial time. This option is similar to the conditional climatology tables developed and used by Air Weather Service.

The second type is CFLOS. As with the sky-cover statistics, there are four CFLOS statistics available from C CLOUD S. The first of these is the probability a CFLOS can be obtained

for a given elevation angle (the angle above the horizon) or along a line between the point specified on the earth's surface and a satellite location specified by its height above the surface in kilometers and its latitude and longitude. The second and third CFLOS statistics are the probabilities for CFLOS duration and CFLOS recurrence. The final CFLOS probability is the probability that CFLOS for  $N$  sites on the surface can be obtained. The elevation angle can be the same for all sites or can be calculated from each site to a common satellite.

Satellite-based viewing is the next statistical type. First, the probability of a fraction  $N$ , or less, cloud-cover over an area depends on the depression angle, which can be specified or calculated by C CLOUD S given the site and satellite locations. Depression angle is the same as the elevation angle, except that the former is defined for looking up, while the latter is defined for looking down. The size of the area specified ranges from 0 (same as a line of sight) up to an area of 500 km<sup>2</sup>. Second, the probability of a fraction  $N$  or less of cloud-cover over a line also depends on the depression angle. The specified latitude and longitude of the surface locations represent the midpoint of this line. The user also provides the length and orientation of the line.

The last type of C CLOUD S statistic is database variables. This portion of C CLOUD S outputs the rudimentary, raw elements of the database, which are:

- (1) Mean sky-cover as seen by a surface observer.
- (2) Mean sky dome correlation, or the mean of the correlations between all pairs of points in the sky dome; this is closely related to the standard deviation of the sky-cover distribution.
- (3) Mean mesoscale correlation, or the mean of the correlation between all pairs of points in an area 500 by 500 km. This value is closely related to the standard deviation of the distribution of clouds covering the earth for this size area, as seen from a satellite.
- (4) The effective period of record, equivalent to the number of days of observations for a given month.

## 5. METHOD OF PRESENTATION

The C CLOUD S software offers five output data displays: values, graphs, histograms, contour maps, and data files. The value is displayed as the expected value of the cloud statistic as well as of the lowest and highest probable values. The graph option displays an X-Y graph of any cloud statistic. Users may also request a histogram display of coverage, or the fractional area (between 0 and 1) obscured by clouds. The vertical axis is the expected frequency and the horizontal axis is tenths of coverage from clear (0) to overcast (1). Only a limited number of cloud statistics can be displayed with the graph option. The map contouring option presents, on a cylindrical equal area map, the probability of occurrence of a cloud statistic. The area of the map can be changed by selecting different latitude and longitude boundaries. The final presentation option is the data file; C CLOUD S can output results to files which can be used as input to other software programs.

## 6. SUMMARY

The heart of C CLOUD S is its database compression through the use of Fourier series and Legendre polynomials. PC-based C CLOUD S software provides a vast selection of statistics displayed with various means of output. It can give direct results or can output data files for use in other software programs.

## REFERENCE

Gleason, D.M., 1985: Partial sums of Legendre series via Clenshaw summation. Manuscripta Geodaetica,10:115-130





## HIGH-RESOLUTION CLOUD CLIMATOLOGIES

Kenneth E. Eis  
METSAT Inc.  
Fort Collins, Colorado 80521, USA

### ABSTRACT

Mission planning for air interdiction, close air support of ground operations, air-mobile combat elements, and airborne resupply all require a detailed understanding of cloud climatologies for the operations region. Special operations and clandestine forces operating in unfriendly areas require precision paradrop resupply and fire-support planning that can be critically affected by clouds. This detailed planning process could benefit immensely from a cloud climatology that was of much higher resolution than the current 43 x 43 km analysis. Planners could use persistent, climatologically reliable cloud features, anchored to terrain to discriminate between operations in a valley vs. a ridge where persistent cloud cover would decrease the probability of mission success significantly. METSAT Inc. has developed a high-resolution cloud climatology based on GOES visual imagery at a 2.5 x 2.5 km resolution that will meet the DoD's meso-scale cloud climatology needs. This high-resolution composite climatology will allow the Army's Intelligence Preparation of the Battlefield (IPB) activities to have cloud climatologies at their preferred 5 km resolution for the first time. In some regions, climatologies can be produced at a 1 km resolution and 1 HR intervals from GOES visible data. IR composites are produced at an 8 km resolution. The climatologies could also become a powerful forecasting tool when the composites are conditioned on a variety of observed conditions. Possible candidate variables include: current sky conditions, prevailing winds or surface temperature. These conditional climatologies could lead to a new class of forecast aid to be incorporated into the Air Force's AWIDS or the Army's IMETS systems.

### 1. INTRODUCTION

METSAT Inc. has developed a new high-resolution Satellite Cloud Composite Climatology (SCCC) published as the cover article in the March 1992 Bulletin of the American Meteorological Society (Reinke et al., 1992). High-resolution cloud climatologies, beyond their academic interest, have many military applications that could revolutionize military planning and simulations activities. Section 4 of this paper details some of those

applications. Currently, the Army and Air Force rely on the Air Weather Service's Real Time Nephanalysis (RTNEPH) (Kiess and Cox 1988) to support simulations and planning. This cloud analysis, which is produced at the Air Force Global Weather Center (AFGWC), is a 43 x 43 km gridded database. The RTNEPH is based primarily on surface observations of clouds, with Defense Meteorological Satellite Program (DMSP) Infrared imagery used in regions with little or no surface observations.

Reinke et al., (1992) demonstrated that the very fine-scale temporal (1 hour updates) and spatial images (2.5 x 2.5 km), provided by the SCCC, are crucial to a proper understanding of cloud physics, battlefield-scale cloud patterns, and terrain-forced cloud patterns.

The Army's Intelligence Preparation of the Battlefield (IPB) process stipulates a 5 x 5 km data domain to provide the battlefield commander with data such as terrain, weather, and intelligence, specific enough to formulate tactics to engage the enemy. The SCCC is the only cloud climatology with sufficient resolution to meet these needs.

This paper will outline how SCCCs are produced, contrast them to the RTNEPH and describe potential impacts of SCCC products on military operations and meteorology.

## 2. THE SCCC PROCESS

The SCCC process uses geostationary images, such as GOES and METEOSAT, and overlays these images from the same time or month, depending on what statistical accumulation is required. Statistics are accumulated at the pixel level (at the 2.5 x 2.5 km resolution). The accumulated statistic, such as probability of cloud ceilings, are then displayed at the same resolution as the original composited images.

Figure 1 shows the elements of the SCCC production method.

The elements of the process follow:

Navigation: In order for the composite method to work, each image must be correctly navigated. The navigation data provided in the satellite data stream is often not accurate enough to position a given pixel so it registers exactly with the other pixels in the statistic accumulation or stack. To build an accurate statistical accumulation, each image is mapped to within 1 km by finding several known geographic features and assigning them their correct

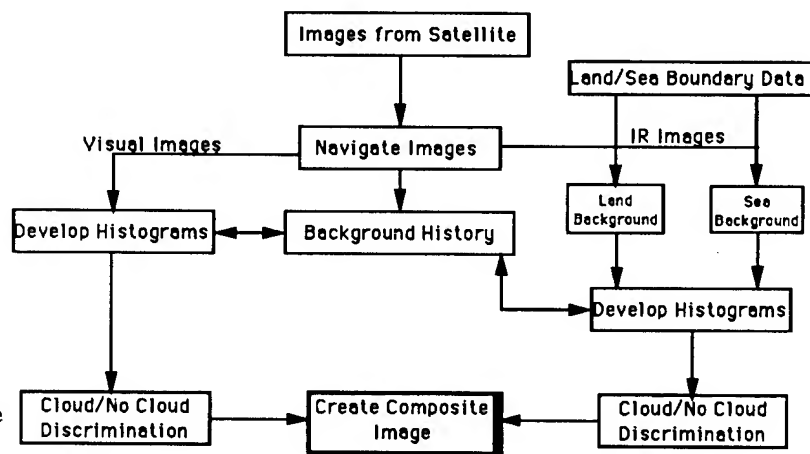


Figure 1. Elements of SCCC Production Method

latitude and longitude. A "rubber sheet" two-dimensional non-linear interpolation scheme is used to map the initial image into a corrected image. Practically, each of the images is remapped to a reference image which acts as the base of the compositing overlays.

Cloud/No Cloud Discrimination: Two methods for cloud/no cloud discrimination were used for the SCCCs.

For the visual images a dynamic background was created by picking the darkest gray-scale value from recent cloud-free imagery for each pixel stack as a clear value. This value is then subtracted from the current image being analyzed. The difference image was then compared to a threshold value. If it exceeds the threshold, the pixel is declared cloudy.

For infrared images, the registered imagery is split into land and sea pixels using a land/sea boundary defined by a Defense Mapping Agency database. Each sub-set of pixels is then run through a structure analysis routine to put it into one of two populations: boundary or centroid pixels. The centroid pixels are ones whose nearest neighbors are of the same radiance value, i.e. they are in the middle of either a clear or cloudy region. This centroid population of pixels is then binned into a histogram and interrogated for two distinct clear and cloudy populations. A clear/cloud radiance value is then picked between the two populations and the entire pixel population is then reinterrogated for a clear/cloudy assignment.

Figure 2 shows an example of a 2 x 2 km resolution composite over Central America. Figure 3 is a 43 x 43 km-resolution smoothed variant of fig. 2. This 43 x 43 km smoothed image approximates the resolution of the RTNEPH. In both images the color scale of fig. 2 depicts the mean probability of having a ceiling within the displayed pixel.

Figure 4, is a July 1990 composite of GOES visual images over the Western U.S. The resolution, because of the distance from the GOES nadir point, is 2.5 km vs 2 km for the Central American images. Figure 5 is again the 43 km-smoothed variant of fig. 4.

### 3. COMPARISON OF SCCC AND RTNEPH

Figures 6 and 7 are graphs that show the error frequency distribution of smoothed images from 10 x 10 km to the illustrated 43 x 43 km or RTNEPH gray scale images. The error was computed by taking the smoothed box mean and subtracting it from each high-resolution pixel value. These departures were then binned by error percentage from -99 to +99 percent error and the frequency distribution of these error values plotted in the figures. The mean error for each smoothing, weighted by the frequency distribution, is as follows:

Central America (Based on 2.0 km initial pixel size)

Pixel x Pixel	Box Size km x km	Mean Weighted Error
4 x 4	10 x 10	3.11
8 x 8	20 x 20	4.31
12 x 12	30 x 30	5.18
17 x 17	43 x 43 (RTNEPH grid size)	7.29

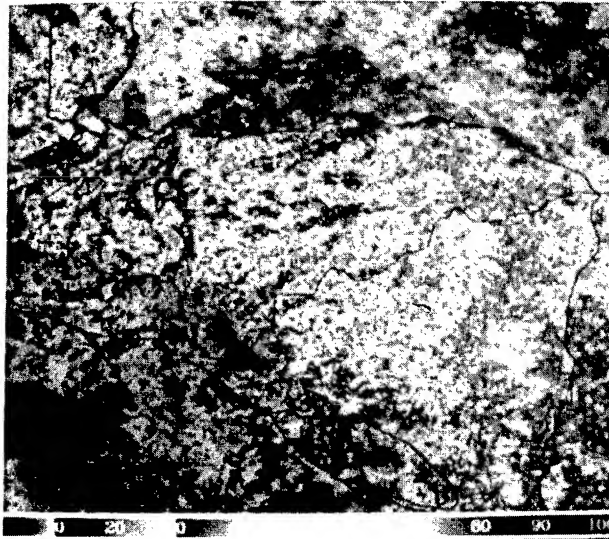


Figure 2. Frequency of Occurrence of Cloud from GOES Visible - 2 km resolution Central American Sector - Sept. 1990, 1800 UTC

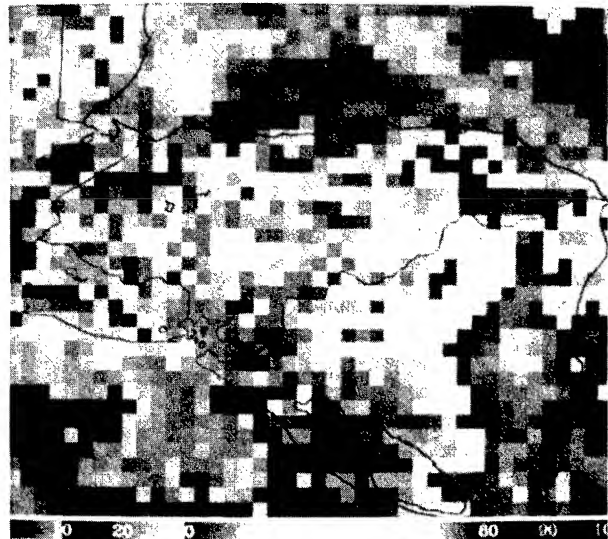


Figure 3. Frequency of Occurrence of Cloud from GOES Visible - 43 km resolution Central American Sector - Sept. 1990, 1800 UTC

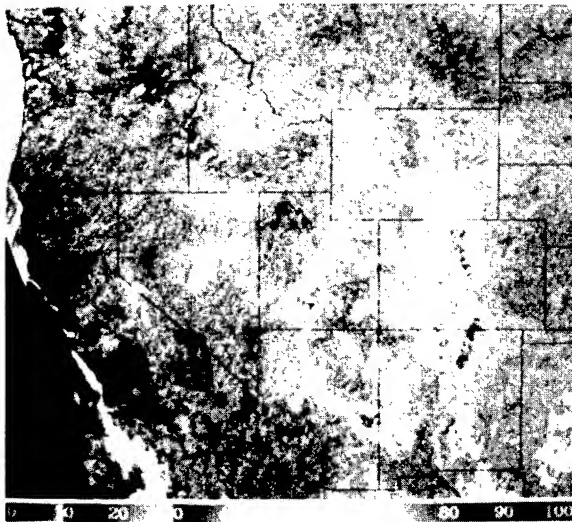


Figure 4. Frequency of Occurrence of Cloud from GOES Visible - 2.5 km resolution Western U.S. Sector - July 1990, 2100 UTC

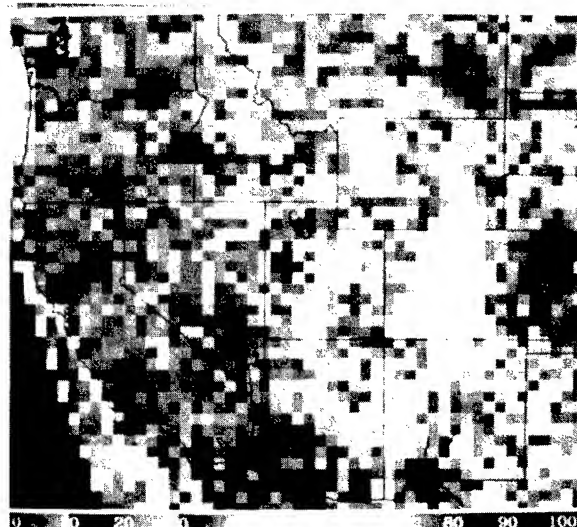


Figure 5. Frequency of Occurrence of Cloud from GOES Visible - 43 km resolution Western U.S. Sector - July 1990, 2100 UTC

Western U. S. (Based on 2.5 km initial pixel size)

Pixel x Pixel	Box Size km x km	Mean Weighted Error
4 x 4	10 x 10	3.00
8 x 8	20 x 20	3.90
12 x 12	30 x 30	4.41
17 x 17	43 x 43 (RTNEPH grid size)	5.05

The mean error more than doubles from a 10 x 10 km smoothing to the 43 x 43 km smoothing in Central America and almost doubles in the U. S. case. This logic has been used to justify using the lower-resolution products. A 7 percent error is often considered an acceptable error given the advantage of a 290 times smaller data set. The true cost of the smoothed product to military applications is masked in the mean statistics. Figures 8 and 9 illustrate the dynamic range of the high-resolution pixels for each of the smoothed boxes for the Central American and Western U. S. cases respectively. In these figures the pixel color represents the difference, or dynamic range of cloud ceiling probabilities that have been smoothed to a single mean number as illustrated in figs. 3 and 5.

In both the U.S. and Central American, areas of complex terrain and land/ocean boundaries show the largest dynamic range. Consequently, these areas are where an analysis at the resolution of the RTNEPH is non-representative. (Note that this conclusion is based on composite images. The composites are averaged in time so an individual real-time image would show even more non-representative behavior than the composite.)

#### 4. APPLICATIONS

SCCC composite products can be applied in the same way the RTNEPH data is currently used as well as some new ways. Fundamentally the SCCC product can be displayed, as the following figures illustrate, as a high-resolution image such as a color photograph. As such, it is shirt-pocket portable. The SCCC is unique in its resolution, both temporal and spatial, as well as its independence from surface-based observations.

##### 4.1 MISSION PLANNING

###### 4.1.1 Fire Support Management

Fire support management would benefit from the detailed knowledge of cloud cover persistence probabilities at different times of day for specific points in the terrain. If a target is identified as in an area of persistent low-level cloud cover artillery support can be planned instead of close air support.

###### 4.1.2 Beach Selection for Amphibious Landings

Beach selection for amphibious landings can be assisted by the use of high-resolution climatologies that are not dependent upon ground-based observations. Using fig. 2 as an illustration, the difference of a few

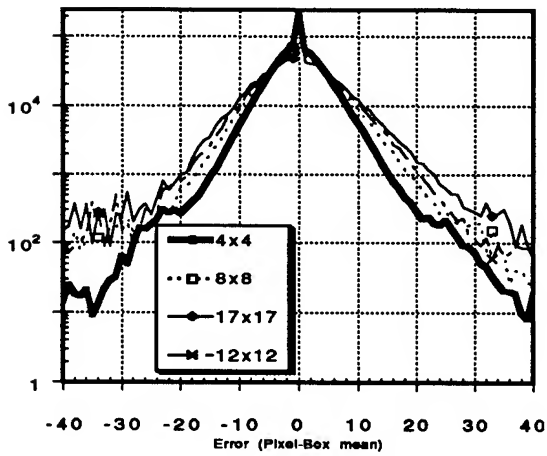


Figure 6. Western U.S. July 1990,  
2100 UTC Error Comparison

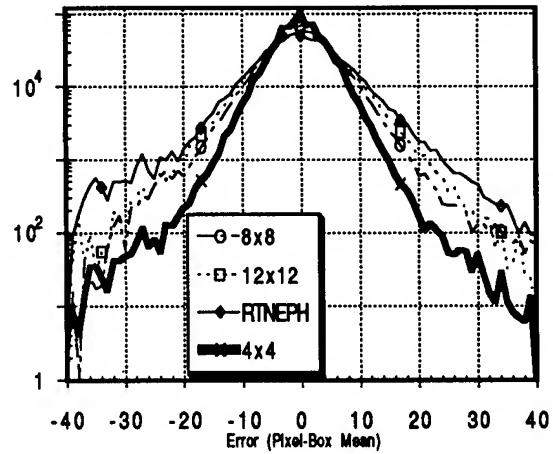


Figure 7. Nicaragua Error  
Frequency Comparison

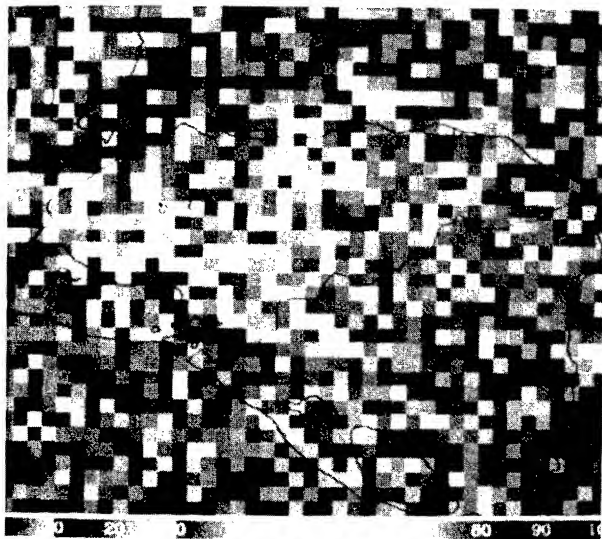


Figure 8. Error Based On Dynamic  
Range of 43 km vs 2 km  
composites, Central American  
Sector - Sept. 1990, 1800 UTC

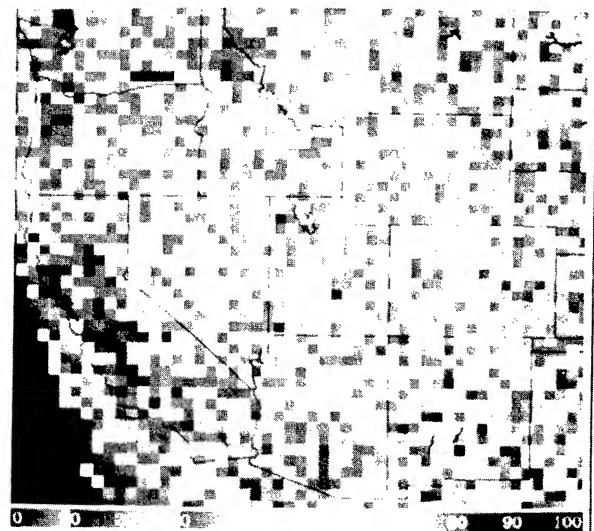


Figure 9. Error Based On Dynamic  
Range of 43 km vs 2.5 km  
composites, Central American  
Sector - July 1990, 2100 UTC

miles of beach can be the difference of 20-40 percent cloud cover probability. Near La Ceiba, Honduras there is a persistent clear area on the north coast that could improve the effectiveness of air cover for an amphibious assault. At locations either east or west down the coast the probability of ceilings increases from 5 percent to over 50 percent. Other persistently clear areas are in the Gulf of Fonseca and along the northern coast of Nicaragua. Since the largest gradients in cloud cover occur near ocean/land boundaries, the higher resolutions of the SCCC will provide the most improvement over planning based on the RTNEPH for amphibious operations. Note the high errors in the RTNEPH-scaled 43 km smoothed image of fig. 7 along the coast and eastern mountains.

#### 4.1.3 Reconnaissance

Reconnaissance, both pre- and post-strike, would be more efficient using the SCCC product. Cloud-free periods over specific target areas could be picked to plan reconnaissance missions. Persistently cloudy times could be avoided in the reconnaissance mission planning process.

#### 4.1.4 Offensive Land Operations

Offensive land operations could be planned using persistent cloud cover to shield these operations from enemy reconnaissance. Similar use of the SCCC products could be made over water to mask fleet operations. Note, in fig. 2, the persistent cloud cover and adjacent clear areas associated with the ridge to the north of the Ulua and Aguan river valleys.

#### 4.1.5 Airlift Operations

Airlift operations could benefit from SCCC-based planning in the positioning of base runways, timing of paradrop operations, and to improve the chance of having VFR conditions at the time of arrival when flying into airdromes without precision-approach equipment. Again fig. 2 shows many locations in central Honduras where moving an air assault operation 20 km would decrease the ceiling probability over 40 percent.

#### 4.1.6 Offensive Air Operations

Offensive air operations can be planned using persistent cloud regions to mask aircraft and helicopter contrails and exhaust plumes. Stealthy airframes would likewise benefit from such tactics by masking their jet/turbine plumes within high probability cloud regions.

### 4.2 ACQUISITION PLANNING

#### 4.2.1 Development of Electro-Optical Sensors

Development of electro-optical sensors for air-to-ground operations could benefit from SCCC-derived statistics like mean cloud-to-cloud distances and probability of cloud-free path lengths equal to the lock-on and detection ranges of specific sensors.

#### 4.2.2 Ground-Based Sensors and Weapons Systems

Ground-based sensors and weapons systems such as ground-based lasers could benefit by precisely locating a site where the terrain-forced clouds are at a minimum. Typically, deep-space trackers and directed energy systems that engage satellites and ballistic missiles are located in mountainous terrain to place them above the bulk of the atmosphere's water vapor and clouds. In doing so, the systems are often located on ridge lines and peaks that, at the meso and micro climatological scale, have a high probability of cloud cover. Surface observations which are used to site such facilities, are typically scarce or non-representative in such regions. The SDI Ground Based Laser program recognized this problem when it fielded a network of whole-sky imagers. Unfortunately, the WSIs were expensive to deploy and they lacked the benefit of an accumulated database. Typically the SCCC analysis can be run against a continuous database that goes back to the mid 1970s.

#### 4.2.3 Optical Tracker Location Planning

Optical trackers, used on military test ranges, like the cinetheatolite systems at White Sands, Holloman, and Edwards are placed to collect and document the test flights of developmental airframes and their subsystems. They are placed on the ranges to cover the entire flight envelope. They, like the systems mentioned above, tend to be placed on hill tops and ridge lines where persistent terrain-forced clouds can lower their collection efficiency.

### 4.3 FORECAST TOOLS

#### 4.3.1 Cloud Persistence Statistics

Cloud persistence statistics can be used to support air bases, test ranges, bombing ranges, and local area flying patterns. Unlike RTNEPH derived statistics, the SCCC can provide statistics for 30 minute, 1, 2, and 3 hour persistence intervals. The RTNEPH interval, 3 hours, is based on the Air Force Global Weather Center's 3-hour production cycle, and not a new data set on which to run a cloud analysis.

#### 4.3.2 Cloud Statistics

Cloud statistics would aid operational planners for denied areas or friendly areas without reliable surface observations. Since the SCCC cloud statistics are derived from satellite imagery only, it can be interrogated for regions without surface-based observations.

#### 4.3.3 Conditional Cloud Statistics

Conditional cloud statistics can be initiated on a clear or cloudy condition. Conditional climatologies can be very powerful tools for a local area forecast. For a given date and time, if a specific location is either cloudy or clear subsequent cloud patterns can be statistically derived from the SCCC overlays.



#### 4.3.4 Conditional Cloud Statistics

Conditional cloud statistics can be initiated on some other prevailing condition such as: wind direction, temperature, humidity, or stability index. This and the conditional statistics based on clouds discussed above, have specific applications for the military. High-resolution SCCCs can be produced for specific locations, times, and dates that are conditioned on a local observation that can be taken by a team behind enemy lines, or a unit out of radio contact with friendly weather information. A hand held anemometer and a series of photographs for each possible conditioning wind speed or direction would provide a highly specific climatological cloud probability. The SCCC images could guide a team to a clear area for extraction or resupply, or to a cloudy area to avoid aerial detection.

#### 4.3.5 Assistance Tools

SCCC's can be used as IMETS, AWDS, TWADS, CWS assistance tools. These new forecast systems, being developed by the Army and Air Force, are intended to improve the forecast products to the operational "shooters". They are a logical place to incorporate the conditional climatologies outlined above. Each station could download the SCCC subsets of local interest from a CD-ROM and use them for local area forecaster familiarization, and forecast preparation.

### 4.4 MILITARY MISSION SUPPORT

#### 4.4.1 Contingency Support

The concept of local area forecaster familiarization, discussed above, could easily be extended to train and support contingency operations. In today's political environment our ability to prepare and train for military contingencies is severely restricted by our inability to predict where the next contingency would occur. Who would have guessed in the 1980s that Kuwait, Yugoslavia, and Panama would be where we would deploy in the early 1990s? Consequently, the military meteorologist needs to be able to perform a quick study of the new area of interest to support operations planning for airlift, intelligence gathering, weapons selection, logistical materials selection and possibly amphibious landing. The SCCCs would provide an instantly available climatological reference that would help the weather support elements move up their step learning curve.

After deployment, weather forecasters could use SCCC products to brief mission planners and flight crews as well as use them as forecaster aids.

#### 4.4.2 Simulation and Operations Research Activities

Simulations and operations research (OR) activities could incorporate the SCCC products directly into their computer programs. The high resolution of the SCCC, both temporal and spacial, lend themselves to the logic tables used in simulations and OR studies.

#### 4.5 COST BENEFIT ANALYSIS

The temporal and the spatial resolution of the SCCC allows analysis of the orbital configuration of the DMSP and the production cycle at the Air Force Global Weather Central. What is the benefit of one hour or even 30 minute updates to the analysis and forecast fields vs the current 3 hour updates? What is gained by going to 1/16, 1/32 or even 1/64-mesh cloud analysis grids?

#### 4.6 PERSISTENCE STUDIES

Persistence studies could be run to help optimize the cloud production cycle. Small, but numerous, highly persistent clear or cloudy regions could be identified and the nephanalysis could be modified to treat them in a more streamlined manner.

### 5. LIMITATIONS AND FUTURE ANALYSIS

Currently, the SCCC analysis is limited by the availability of geostationary data. GOES, METEOSAT, and GMS cover most of the earth's surface but massive extractions of past data, with its attached costs, would be needed to provide SCCC's for all time periods and areas of interest.

Polar orbiting imagery can, and has been, used to produce SCCC's. Currently, the cloud foreshortening at the edges of the line scanner have not been corrected for and will be the subject of future development.

### 6. CONCLUSION

The resolution of the SCCC in time and space allow it to be used in the military decision process in a much more specific way than the lower resolution cloud climatologies currently used by the DoD. The composite images can be stored, retrieved, and analyzed at end-user weather support facilities to improve the quality and reaction time to the customer. The pseudo-image nature of the product is more understandable to the military decision maker and of more use to the practicing forecaster than the data-arrays currently archived for climatological analysis support.

### ACKNOWLEDGEMENTS

This paper has been prepared under METSAT Inc.'s internal R&D program. See Reinke et al. (1992) for citations of sponsors of the original data sets.

### REFERENCES

- Kiess, R.B. and W.M. Cox, 1988: The AFGWC Automated Real-Time Cloud Analysis Model. AFGWC/TN-88/001, AFGWC, Air Weather Service (MAC), Offcutt AFB, Nebraska, 82 pp.
- Reinke, D.L., T.H. Vonder Haar, C.L. Combs, and S.Q. Kidder, 1992: Satellite Cloud Composite Climatologies: A New High-Resolution Tool in Atmospheric Research and Forecasting. Bull. Amer. Meteor. Soc., **73**, 278-285.

## **CLOUD INFORMATION REFERENCE LIBRARY AND ARCHIVE**

Ronald J. Nelson  
Science and Technology Corporation  
Albuquerque, NM 87112

### **ABSTRACT**

Science and Technology Corporation, under contract to the Geophysics Directorate, Phillips Laboratory, is responsible for the design and maintenance of an electronic mail data file called the Cloud Information Reference Library and Archive (CIRLA). CIRLA provides a reference file containing information on cloud and cloud-related data, models, analyses, simulations, and experiments. This information is intended for use by scientists, engineers, and planners of DOD systems development and related analysts working in and for the tactical communities. The information is relevant to sensor and weapon system development, simulation, wargaming, and tactics and training. CIRLA responds to the recent emphasis on increasing the transfer of environmental data and information from DOD to the civilian scientific and engineering communities. It connects those who require cloud and cloud-related data with those who hold the data and, in effect, operates as a facilitator for information transfer. On-line charges are absorbed by the sponsor, so CIRLA is free to all users. This paper describes CIRLA's organization, content, and access procedures, along with hardware/software requirements.

### **SUMMARY**

The Cloud Information Reference Library and Archive (CIRLA) was created in response to a perceived need as voiced by members of the Cloud Impacts on Department of Defense (DOD) Operations and Systems (CIDOS) community. The purpose of CIRLA is to provide the following:

- An information reference listing of cloud and cloud-related data, models, analyses, simulations, and experiments
- Rapid on-line access
- A common communications medium for the cloud data supplier and user community for use in sensor and systems development, simulation and war gaming, tactics and training and, more generally, by anyone interested in the potential effect of clouds on their (usually military) application

CIRLA's sponsor is the Geophysics Directorate, Phillips Laboratory, whose headquarters are at Kirtland AFB, NM. CIRLA is managed by Science and Technology Corporation, whose main office is in Hampton, VA.

CIRLA provides a reference archive containing information on cloud and cloud-related environmental data of the type required by scientists, engineers, and planners of the DOD systems development and tactical communities. Additionally, the initiation of CIRLA responds to the recent emphasis on increasing the transfer of environmental data and information from DOD to the civilian scientific/engineering communities.

Figure 1 shows the organization of CIRLA. The five major categories of Models/Simulations, Databases, Algorithms, Summaries, and Reference Information each devolve to an additional level where detailed information on the selected category of data may be found. Three categories contain adjunct information (recent additions, notices, meetings) on topics of interest to potential users. The actual on-line interaction is menu driven and there is a menu selection that allows a user to communicate with the database manager on any subject.

Note that CIRLA does not hold data explicitly, but contains information that allows users who require cloud and cloud-related data to make contact with those who hold the data, in effect becoming a facilitator for information transfer. CIRLA can benefit both civilian and military communities by reducing duplicate or redundant research through its information archive, which, while targeted for DOD applications, also has wide applicability to many civilian interests, including those focused on global climate change.

Access channels to CIRLA include both OMNET and INTERNET. Figure 2 shows the current access procedures for connecting to CIRLA.

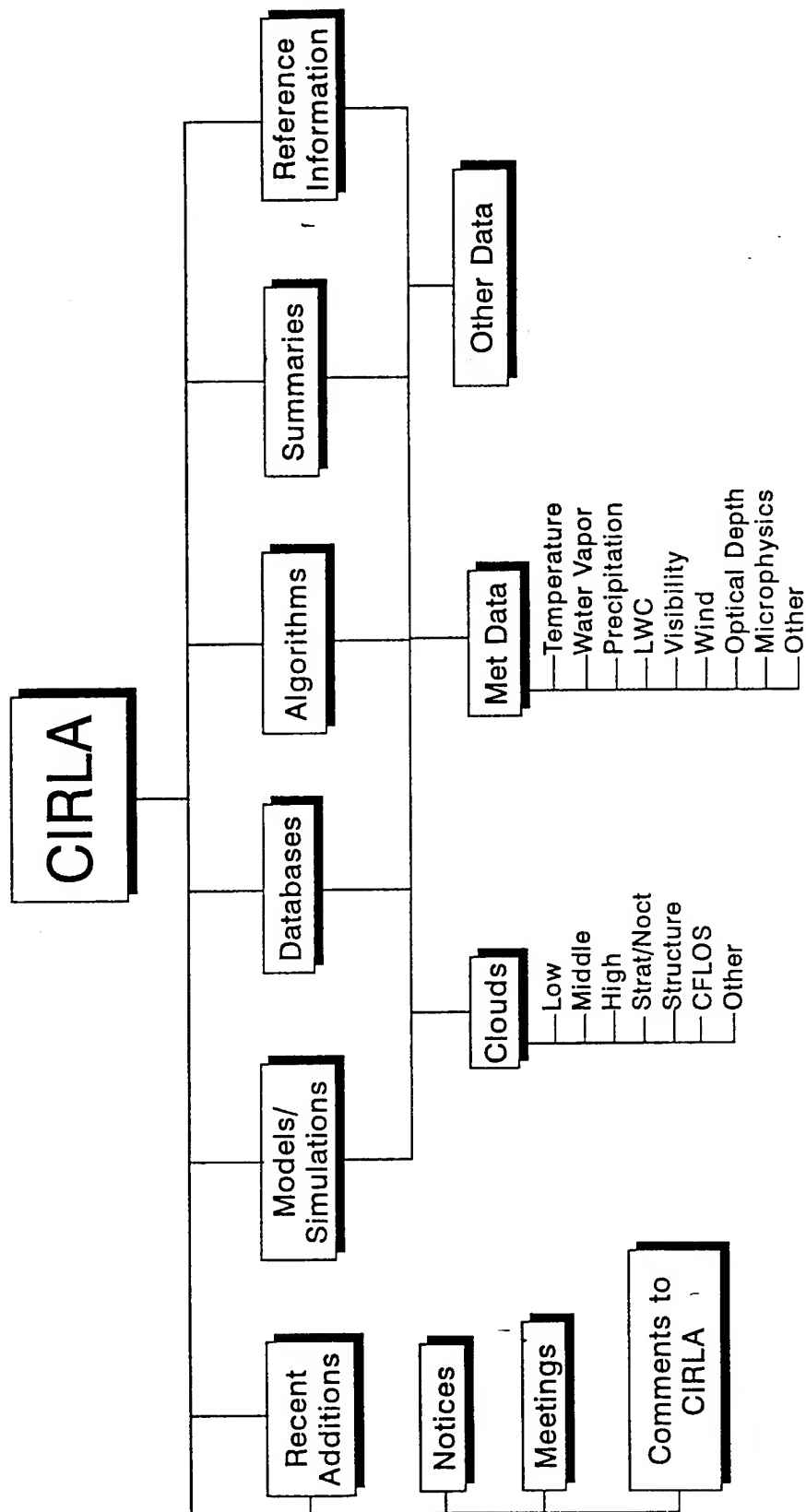


Figure 1. Organization of Cloud Information Reference Library & Archive (CIRLA)

**Managed by: Science and Technology Corporation**

## SAVI &lt;cr&gt;

164

REBAL '92 - A COOPERATIVE RADIATION AND ENERGY BALANCE  
FIELD STUDY FOR IMAGERY AND E.M. PROPAGATION

Arnold Tunick  
Battlefield Environment Directorate\*  
U.S. Army Research Laboratory  
White Sands Missile Range, NM 88002-5501

Terry A. Howell and Jean L. Steiner  
U.S.D.A. - Agricultural Research Service  
Conservation and Production Research Lab  
Bushland, TX 79012

ABSTRACT

The surface energy balance affects the structure of temperature and humidity gradients in the atmospheric surface layer. Temperature and moisture gradients are needed to estimate the intensity of optical turbulence along a given path, but models of these relationships are not adequately validated for imagery and electromagnetic propagation applications. A field study entitled 'Radiation Energy Balance Experiment for Imagery and E.M. Propagation' (REBAL '92) was conducted by the U.S. Army Atmospheric Sciences Laboratory (ASL) and the USDA Agricultural Research Service (ARS), at Bushland, Texas, in May and July 1992. We collected diurnal radiation, evaporation (directly measured by weighing lysimeters), 5-level micro-meteorological profiles of wind speed, air temperature, and relative humidity, soil temperature and water content, soil heat flux, optical turbulence (scintillometer), and near- and far-field infrared imager data over wet and dry bare soil under clear and cloudy sky conditions. Initial model tests indicate excellent agreement between measured and modeled values of the optical turbulence structure parameter,  $C_n^2$ , for one day. Future model evaluation will extend over the wide range of conditions encountered during the field study.

1. INTRODUCTION

Understanding surface radiation/energy balance processes is important for estimating evaporation rates and understanding surface-layer temperature gradient structure. Both Department of Defense (DoD) and United States Department of Agriculture (USDA) are interested in the development of numerically efficient methods or models to describe the partitioning of the net radiative flux into sensible, latent, and soil heat fluxes and the impact of surface fluxes on atmospheric profile structure. To make efficient use of limited fiscal and personnel resources, an integrated, multi-agency effort was initiated to improve current models. This cooperative DoD-USDA research-oriented field program, the Radiation and Energy Balance Experiment (REBAL '92) was organized by the US Army Atmospheric Sciences Laboratory (ASL) and the USDA Agricultural Research Service (ARS), Conservation and Production Research Lab (CPRL). REBAL '92 was conducted at Bushland, Texas at the ARS/CPRL experimental site in May and July 1992. The site was chosen due to the presence of four large weighing lysimeters. Direct measurements of latent (evaporative) heat flux were lacking in several previous micro-meteorological field tests.

\* formerly U.S. Army Atmospheric Sciences Laboratory

REBAL '92 was initiated to improve the knowledge on radiation/energy balance partitioning and to characterize surface layer micro-meteorological processes over wet and dry, soil surfaces. The project's goals were:

1. To collect radiation, evaporation, micro-meteorological profile, and optical turbulence scintillometer data over wet and dry bare soil, under clear and cloud covered skies. In addition, infrared imager data in a near field/far field configuration was collected simultaneously to characterize the effects of optical turbulence on a thermal bar pattern (Watkins et al., 1991a) to determine the temporal turbulent distortions of the imaged target.
2. To evaluate and refine two energy balance models (Evetts et al., 1991; Rachele and Tunick, 1992a).

The effects of the atmosphere are basic to the performance of advanced, high resolution systems and sensors, including lasers and imaging systems. The US Army interests in the REBAL '92 field study focus on atmospheric effects on electromagnetic propagation, imagery (including infrared), and target recognition. These research efforts are influenced by the phenomenon referred to as optical turbulence. Optical turbulence is a function of the character and structure of temperature and moisture gradients in the atmospheric surface layer (Tunick and Rachele, 1991). Reasonable estimations of the energy balance fluxes are required to predict the character and intensity of the optical turbulence. Scintillometer data are critical for verification and evaluation of the energy balance models and electromagnetic propagation models.

The USDA-ARS research interests in the REBAL '92 field study focus on improved knowledge of the energy balance fluxes, especially the evaporative or latent heat flux, for applications such as predicting crop water use and to improve irrigation scheduling and crop growth models.

The purpose of this paper is to present an overview of the REBAL '92 experiment including project objectives and goals, research interests, site description, experimental layout, methodology, instrumentation, and preliminary results from the test.

## 2. THEORY

Carson (1987) defined the energy flux balance at the soil surface as

$$R_n = H + L'E + G \quad (1)$$

where  $R_n$  is the net radiative flux,  $H$  is the sensible heat flux,  $L'E$  is latent heat flux with  $L'$  as the latent heat of vaporization [ $2.45 \times 10^6$  J/kg] and  $E$  as the evaporation rate in  $\text{kg m}^{-2} \text{s}^{-1}$ , and  $G$  is soil heat flux; units are in  $\text{W/m}^2$ . During REBAL '92,  $R_n$ ,  $E$ , and  $G$  were measured directly (net radiometers, lysimeters, and soil heat flux plates/thermocouples, respectively) while  $H$  was computed as the residual. Carson (1987) also defined the net radiative flux at the soil surface as the sum of the net short-wave radiative flux and the net long-wave radiative flux as

$$R_n = R_s - R_{sr} + R_{li} - R_{lg} \quad (2)$$

where  $R_s$  is incident solar radiation,  $R_{sr}$  is reflected solar radiation,  $R_{li}$  is sky emitted long-wave radiation,  $R_{lg}$  is ground emitted long-wave radiation, and the units are in  $\text{W/m}^2$ . The short-wave reflection, albedo, is computed as  $R_{sr}/R_s$ . The effects of surface soil water content, surface roughness, and solar elevation angle on albedo is part of the REBAL '92 study along with the characterization of the net long-wave radiative flux as affected by different cloud type, amount of cloud cover, and surface soil water content.



A key element of the REBAL '92 field study is the application of radiation/energy balance measurement and modeling to imagery and electromagnetic propagation as affected by optical turbulence. The character and intensity of optical turbulence is represented by  $C_n^2$ , the optical turbulence structure parameter. Given reasonable estimations of the energy balance fluxes, one can determine the relative magnitude of  $C_n^2$  (Rachele and Tunick, 1992b). For damp unstable conditions, the optical turbulence structure parameter can be expressed as

$$C_n^2 = A'\theta^{*2} + B'\theta^*q^* + C'q^{*2} \quad (3)$$

where

$$A' = b(2.897 \times 10^{-8}) \frac{p^2}{T^4} k^{-2/3} z^{-2/3} \left(1 - 15 \frac{z}{L}\right)^{-1} \omega \quad (4)$$

$$B' = b(1.444 \times 10^{-8}) \frac{p^2}{T^3} k^{-2/3} z^{-2/3} \left(1 - 15 \frac{z}{L}\right)^{-1} \omega \quad (5)$$

$$C' = b(1.801 \times 10^{-9}) \frac{p^2}{T^2} k^{-2/3} z^{-2/3} \left(1 - 15 \frac{z}{L}\right)^{-1} \omega \quad (6)$$

and where

$$\omega = \left\{ \frac{\left(1 - 15 \frac{z}{L}\right)^{1/2}}{\left[\left(1 - 15 \frac{z}{L}\right)^{-1/4} - \frac{z}{L}\right]^{1/3}} \right\}$$

where  $C_n^2$  is the optical turbulence structure parameter in  $m^{-2/3}$ ,  $b$  is the Obukhov-Corrsin constant [3.2],  $k$  is von Karman's constant [0.4],  $z$  is height in m,  $L$  is the Obukhov scaling length in m,  $T$  is the air temperature at height  $z$  in  $^{\circ}K$ ,  $p$  is barometric pressure in kPa,  $\theta^*$  is the scaling constant for temperature, and  $q^*$  is the scaling constant for specific humidity. The scaling constants for temperature and specific humidity can be expressed in terms of sensible heat and latent heat fluxes as

$$\theta^* = \frac{-H}{C_p \rho u^*} \quad q^* = \frac{-L'E}{L' \rho u^*} \quad (7)$$

where  $C_p$  is the specific heat [ $1003 \text{ J kg}^{-1} \text{ }^{\circ}C^{-1}$ ],  $\rho$  is the density of moist air [ $1.0 \text{ kg m}^{-3}$ ], and  $u^*$  is the surface friction velocity in m/s. Finally, the optical turbulence structure parameter can be expressed in terms of sensible heat and latent heat fluxes as

$$C_n^2 = A' \left( \frac{(-H)^2}{C_p^2 \rho^2 u^{*2}} \right) + B' \left( \frac{(-H)(-L'E)}{C_p L' \rho^2 u^{*2}} \right) + C' \left( \frac{(-L'E)^2}{L'^2 \rho^2 u^{*2}} \right) \quad (8)$$

The surface friction velocity,  $u^*$ , can be determined iteratively given the expression for the Obukhov scaling length  $L = \frac{-u^{*3} C_p \rho \theta}{kgH}$ , and the similarity profile function for the mean horizontal wind speed. This procedure is

discussed in detail in Rachele and Tunick, 1992a.

### 3. SITE DESCRIPTION

The test site at ARS/CPRL in Bushland, Texas (35°N Lat, 102°W Long, 1,170 m elevation MSL) is approximately 16 km due west of Amarillo, Texas. Four weighing lysimeters are located in a 20 ha field with each lysimeter centered in a 4.6 ha sub-field (215 m by 215 m). The topography is relatively level with a slope to the SE of less than 0.15%. There are no vertical obstructions near the field, and over 1,000 m of cropped or fallow agricultural fields provided unobstructed upwind fetch in the predominant summer wind direction (SSW).

The test area (the NW and SW sub-field) was a tilled, bare soil (Pullman clay loam) expanse approximately 215 m by 430 m, containing two of the four weighing lysimeters (fig. 1). Irrigated and dryland wheat fields (NE and SE lysimeter fields, respectively) were directly east of the test area. Prior to the July REBAL '92 study period, these wheat fields, as well as dryland wheat to the south of the test area, were harvested leaving a short stubble residue.

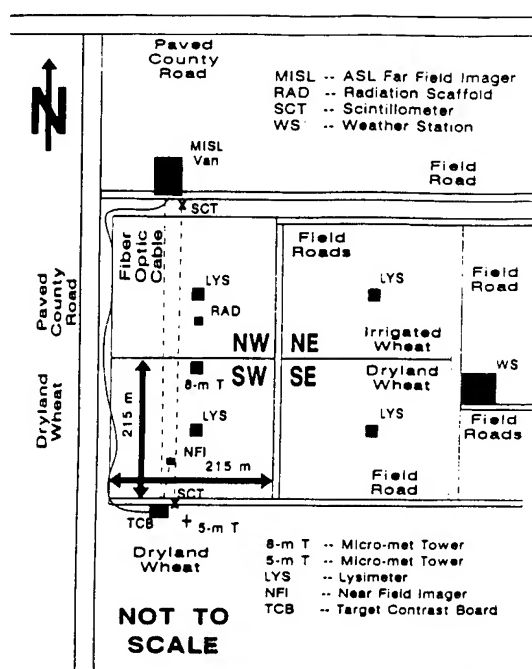


Figure 1. The experimental test area.

### 4. EXPERIMENTAL LAYOUT AND METHODOLOGY

Micro-meteorological profile data (wind speed, air temperature, and relative humidity) were measured with sensors mounted on an 8-m tower centered in the test area (fig. 1) at 0.5-, 1-, 2-, 4-, and 8-m elevations. Six radiometers and one infrared thermometer (IRT) measured the radiation balance components at a site approximately 80 m north of the profile tower (and about 15 m south of the NW lysimeter). Wind speed, wind direction, air temperature, and relative humidity were also measured at the radiation measurement site at the 2-m elevation. Table 1 contains a list of the instruments deployed in the REBAL '92 experiment.

The ASL Mobile Imaging and Spectroscopy Laboratory (MISL) trailer was located at the north end of the test area. The trailer contained the imaging equipment, cameras and recorders. A  $0.94\mu\text{m}$  scintillometer source module was mounted 2 m above ground on a tripod located adjacent to the MISL trailer. The imaging cameras and the scintillometer were aligned and focused down-field (i.e., to the south) over a path of approximately 450 m.

The receiver module of the scintillometer, the target board (a thermal bar pattern), a small source van (a vehicular target), and an auxiliary 5-m micro-meteorological tower were located at the south end of the test area. Instrumentation on the auxiliary micro-meteorological tower measured 2- and 5-m elevation wind speed and direction, air temperature, and relative humidity and solar radiation, barometric pressure, soil temperature (100 mm depth), and visibility near the target board to provide site specific data for the target contrast board environment at a frequency synchronized with the imagery data.

#### 4.1 DATA COLLECTION SUMMARY

Micro-meteorological profile data and radiation/energy balance data were collected in May 1992 (DOY 132 - DOY 141) and in July 1992 (DOY 190 -DOY 196). Scintillometer and infrared image data were collected during selected periods (Table 2) within that time frame. The field was sprinkler irrigated once on DOY 132 while significant rainfall events (i.e., more than trace rainfall) occurred on DOY 136, DOY 141, DOY 191, and DOY 192. Table 2 summarizes weather during the data collection periods. Two daily radiosonde observations and hourly cloud observations were recorded and four daily surface weather charts were provided during both data collection periods by the National Oceanographic and Atmospheric Administration (NOAA), National Weather Service (NWS) Office in Amarillo, Texas (about 35 km east of the field site).

#### 4.2 LYSIMETER MEASUREMENTS

The lysimeter is an intact soil monolith (3 m by 3 m square and 2.4 m deep) that can be weighed to a mass equivalent of 0.02 to 0.05 mm of water which corresponds to an hourly evaporative flux of approximately 14 to 34  $\text{W/m}^2$  (Dusek et al., 1987, Marek et al., 1988, Steiner et al., 1991). The lysimeters directly measured the water mass contained in the soil monolith. The change in this mass in a given time interval is the evaporation rate. The water mass was measured at 0.5-hz frequency, averaged for 5 min periods, the difference between successive 5-min periods was averaged for 15 min periods, and these 15-min evaporation rates were smoothed using a 3-point equally weighted running mean. The latent heat flux (in  $\text{W/m}^2$ ) was computed as the product of the evaporation rate ( $\text{kg m}^{-2} \text{s}^{-1}$ ) and the latent heat of vaporization ( $\text{J/kg}$ ). At each lysimeter, net radiation, reflected solar radiation, surface temperature, soil heat flux (50 mm depth), soil temperature (averaged for the 10-mm and 40-mm depths), and wind speed profile (0.8-, 1.3-, 1.8-, and 2.3-m elevations) and dry- and wet-bulb temperatures (1.3- and 2.3-m elevations) were measured at 0.17 hz and averaged for 15 min. Soil heat flux was corrected calorimetrically to the surface using the change in soil temperature above the plates and the soil heat capacity. Within the NW lysimeter, two arrays of Time Domain Reflectometry probes measured soil water contents at 20 and 40 mm at 30-min intervals. This soil water content was used to estimate the surface soil heat capacity in both lysimeters.

TABLE 1. List of instruments<sup>1/</sup> deployed in REBAL '92.

Parameter/Equipment	Manufacturer/Model	Deployment
<b>8-m Tower</b>		
Air Temperature/Relative Humidity (aspirated)	Rotronics HT225R/ SMP410012	0.5, 1, 2, 4, and 8 m
Air Temperature (non-aspirated)	Climatronics 100093-3	same
Wind Speed	R.M. Young 12102	same
Wind Direction	R.M. Young 12302	8 m
<b>Radiation Scaffold</b>		
Incident Solar Radiation	Eppley PSP	1 m
Reflected Solar Radiation	Eppley 8-48	1 m (inverted)
Sky Long-Wave Radiation	Eppley PIR	1 m
Emitted Ground Radiation	Eppley PIR	1 m (inverted)
Net Radiation	REBS Q*6	1 m
Total Hemispherical Radiation	REBS THRD55	1 m
Surface Temperature	Everest 4000	1 m (nadir; 60° fov)
Air Temperature/Relative Humidity (non-aspirated)	Rotronics HT225R/ SMP 41002	2 m
Wind Speed	R.M. Young 12102	2 m
Wind Direction	R.M. Young 12302	2 m
<b>Lysimeter</b>		
Reflected Solar Radiation	Eppley 8-48	1 m (inverted)
Net Radiation	REBS Q*6	1 m
Surface Temperature	Everest 4000	1 m (nadir; 60° fov)
Soil Heat Flux	REBS TH-1	50 mm
Soil Temperature	Thermocouples (Cu-Co)	10 and 40 mm (averaged)
Soil Water	TDR (3-prong probes)/ARS-CPRL design	20 and 40 mm (averaged)
Wind Speed	Met One 024	0.8, 1.3, 1.8, and 2.3 m
Dry- and Wet-Bulb Temp. (psychrometers)	Thermocouples	1.3 and 2.3 m
Lysimeter Mass	Cardinal FS-7 Scale/Alphatron SL50 load cell	
<b>Optical Turbulence/E.M. Imaging</b>		
Scintillometer	Lockheed Engr. & Mgmt. IV-L	N to S; 450 m path; 2 m
Visible Cameras/Lens	Sony NTSC DX 102s 10 power zoom lens	N to S; 50 and 450 m paths; 2 m
Infrared Imagers	Inframetrics 610s/ 10 power lens	N to S; 50 and 450 m paths; 2 m
Target Contrast Board	US Army ASL	S end of field
Image Recording	Analog tape	N end of field (MISL van)
Image Registration	Recognition Concepts Inc.	N end of field (MISL van)
<b>Target Met Tower</b>		
Solar Radiation	Qualimetrics 3120	2 m
Air Temperature/Relative Humidity (non-aspirated)	Campbell Scientific 207	2 m and 5 m
Soil Temperature	Yellow Springs Instr. 703	100 mm
Barometric Pressure	Intellisensor AIR-DB	2 m
Wind Speed/Direction	R.M. Young 05103	2 and 5 m
Visibility	HSS VF-500-100.	3 m

<sup>1/</sup> The use of corporation or company names with regard to instrumentation and equipment used does not constitute an endorsement by either the US Army or the USDA-ARS.

TABLE 2. Summary of weather conditions during REBAL '92 in May and July, 1992, Bushland, Texas.

Day of Year	T <sub>max</sub> <sup>1/</sup> ° C	T <sub>min</sub> <sup>1/</sup> ° C	T <sub>dew</sub> <sup>1/</sup> ° C	Daily Solar Radiation MJ/m <sup>2</sup>	Daily Mean 2-m Wind Speed m/s	Rain or (Irrigation) mm
132 <sup>2/</sup>	26.4	5.4	2.3	28.3	2.4	(32.00)
133 <sup>2/</sup>	31.5	9.0	2.0	27.1	3.0	0.00
134 <sup>2/</sup>	27.9	12.4	8.5	22.9	4.4	0.00
135	30.1	11.8	7.4	26.6	3.8	0.00
136	29.8	13.4	8.2	25.2	4.1	3.05
137	26.1	11.9	7.5	25.9	4.7	0.00
138	25.0	10.6	8.3	26.0	4.8	0.00
139 <sup>2/</sup>	25.3	9.6	7.9	26.9	2.5	0.00
140 <sup>2/</sup>	26.5	11.7	8.2	25.5	3.1	0.00
141 <sup>2/</sup>	24.3	12.2	10.2	17.4	4.2	15.24
190 <sup>2/</sup>	33.9	17.7	9.2	28.7	5.3	0.00
191 <sup>2/</sup>	33.5	15.9	11.7	28.0	5.3	27.94
192 <sup>2/</sup>	30.1	17.6	15.4	24.3	4.2	6.86
193 <sup>2/</sup>	30.5	17.2	15.2	26.8	6.8	0.00
194	32.1	19.0	13.5	27.9	7.2	0.00
195 <sup>2/</sup>	31.4	17.0	12.8	25.9	3.7	0.00
196 <sup>2/</sup>	30.5	14.5	12.9	26.8	2.7	0.00
197	34.3	18.7	13.1	26.8	4.5	0.25

<sup>1/</sup> T<sub>max</sub>, T<sub>min</sub>, and T<sub>dew</sub> are daily maximum, minimum, and mean dew point temperatures, respectively, measured from a standard weather shelter at 1.5 m height about 220 m east of the REBAL '92 field.

<sup>2/</sup> Days when scintillometer and infrared image data were collected.

#### 4.3 TARGET CONTRAST CHARACTERIZER

The Target Contrast Characterizer (TCC) compares infrared scene features collected simultaneously from an imager located near the target and from an optically-matched imager located far from the target. The imagers share a common line of sight with the target, and the "near-field" images are transmitted over a video fiber-optics data cable to the far-field position for processing and recording. The "far-field" imager is coupled to a telescope of sufficient power to provide "far-field" images of the same dimensional field of view in the target plane as the "near-field" images. Pixel-to-pixel frame

registration, critical to the success of this technique, is obtained through the use of a Recognition Concepts, Inc. real-time image processing system. The TCC quantifies the effect of optical turbulence on imagery by measuring the atmospheric modulation transfer function (AMTF). A large area target board (1.78 m by 1.78 m) with uniform surface temperature was used to measure the AMTF. A bar-pattern mask placed in front of the target board produced sharp hot-to-cold bar radiance transitions needed for measuring the AMTF. Video signals from visible, 3- to 5- $\mu\text{m}$ , and 8- to 12- $\mu\text{m}$  imagers were recorded on VHS video tape. For the REBAL '92 study, the "near-field" imager was placed 48 m from the target board and the "far-field" imager, coupled to a 10-power telescope, was placed approximately 480 m from the target board. The TCC is conceptually depicted in figure 2 and described in detail in Watkins et al. (1991b).

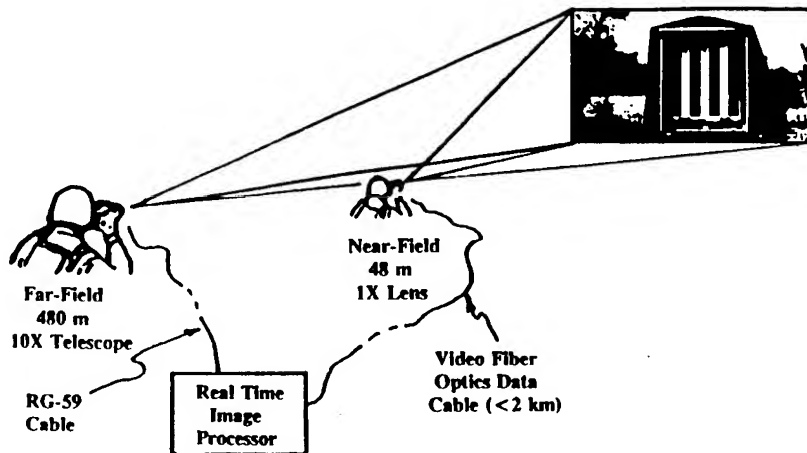


Figure 2. Conceptual use of the Target Contrast Characterizer.

#### 4.4 SCINTILLOMETER MEASUREMENTS

A scintillometer is a ground-based, remote-sensing instrument designed to measure optical turbulence intensity along a line-of-sight path established between a transmitter and a downrange receiver. Scintillometer operation is based on the principle that scintillations or light intensity variations occur as atmospheric density discontinuities create refraction effects in light propagating along a path (Clifford et al., 1974). The optical turbulence structure parameter,  $C_n^2$ , is related to the intensity of these refraction effects.

### 5. PRELIMINARY RESULTS

Energy balance and optical turbulence structure parameter measurements on DOY 134, which was 1-1/2 days after irrigation of the test area in May (Table 2), will be used to illustrate a portion of the data collected during REBAL '92. Figures 3 and 4 show the measured wind speed, temperature and dew point temperature at 2 m for DOY 134. Wind speeds ranged from 2-6 m/s increasing somewhat by 2200 CST. Air temperature at 2 m was between 12.0 and 28.0 °C. Figure 5 illustrates the observed energy balance components on DOY 134. Figure 6 illustrates good agreement between  $C_n^2$  measured by a scintillometer and calculated from the observed sensible and latent heat flux data (Eqn. 8). The comparison shows exceptional agreement considering the complexity of the

problem. Therefore, given reasonable values for the energy flux components, whether measured or modeled, the character of the optical turbulence represented by the optical turbulence structure parameter,  $C_n^2$ , can be accurately determined.

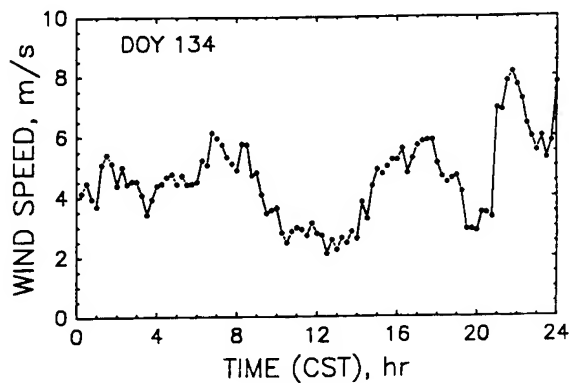


Figure 3. Wind speed a 2-m elevation during DOY-134 above bare soil.

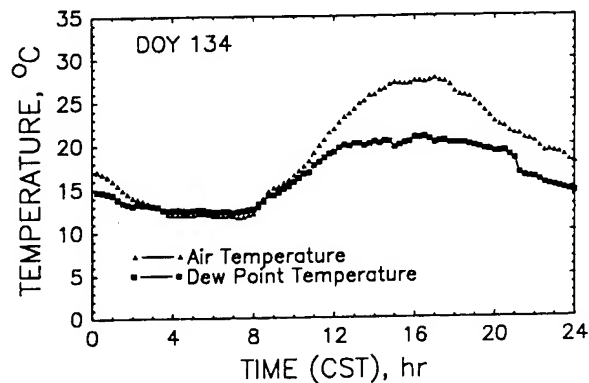


Figure 4. Air temperature and dew point temperature at 2-m elevation during DOY-134 above bare soil.

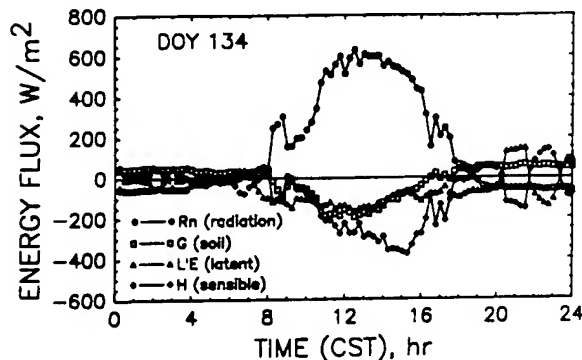


Figure 5. Radiation/Energy Balance Fluxes during DOY-134 at Bushland, TX for bare soil.

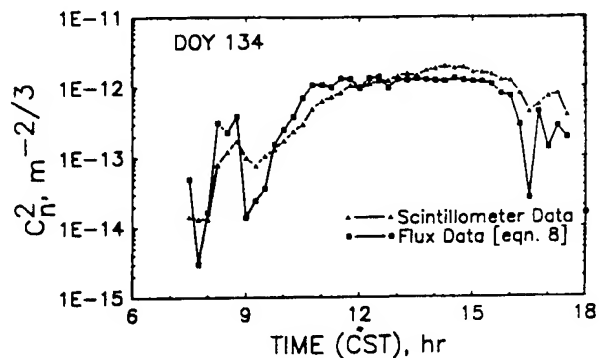


Figure 6. Measured and modeled  $C_n^2$  for DOY-134 at Bushland, TX for bare soil

## 6. SUMMARY

A field study entitled 'Radiation and Energy Balance Experiment for Imagery and E.M. Propagation' (REBAL '92) was conducted cooperatively by the US Army ASL and the USDA-ARS/CPRL at Bushland, Texas in May and July 1992. A unique set of radiation/energy balance, micro-meteorological profile, scintillometer, and infrared image data were collected over wet and dry bare soil, under clear and cloudy sky conditions. Initial evaluations indicate excellent agreement between the measured optical turbulence structure parameter and estimates of the parameter using measured energy fluxes of sensible and latent heat. Models of the radiation/energy balance components will be evaluated in future research. The results from this field test will be used to improve the knowledge base of meteorological processes within the surface boundary layer, radiation/energy balance partitioning, and atmospheric effects on optical turbulence and infrared imagery.

## ACKNOWLEDGMENTS

The authors would like to thank several persons for their exceptional work in the planning, execution, and support of the field project. We gratefully acknowledge Henry Rachele, Frank V. Hansen, Ronald Cionco, Robert Brown, Wendell Watkins, Sam Crow, Daniel Billingsley, Fernando Palacios, Don Lewis, Bob Olsen, and John Fox of the US Army Atmospheric Sciences Laboratory. We also extend our thanks to B.A. Stewart, Don Dusek, Karen Copeland, Arland Schneider, Steve Evett, and Joseph Serda of the USDA-ARS, Conservation and Production Research Lab. Additionally we extend our appreciation to John Eise and Steven Cooper of the NOAA, National Weather Service Office in Amarillo, Texas and to C.L. Tate of the University of Texas, El Paso.

## LITERATURE CITED

Carson, D. J., 1987: 'An Introduction to the Parameterization of Land-Surface Processes: Part 1. Radiation and Turbulence', Meteorological Magazine, No. 1381, 116:229-242.

Clifford, S. F., G. R. Ochs, and R. S. Lawrence, 1974: Saturation Of Optical Scintillation By Strong Turbulence, J. Opt. Soc. Am., 64, 148-154.

Dusek, D. A. , T. A. Howell, A. D. Schneider, and K. S. Copeland, 1987: Bushland Weighing Lysimeter Data Acquisition Systems For Evapotranspiration Research, 1987 International Winter Meeting of the American Society of Agricultural Engineers, Chicago, Illinois, 15-18 December 1987, Paper No. 87-2506.

Evett S. R., T. A. Howell, J. L. Steiner, and J. A. Tolck, 1991: Measured and Modeled Soil and Plant Evaporation, Agron. Abstracts, p. 16.

Marek T. H., A. D. Schneider, T. A. Howell. L. L. Ebeling, 1988: Design and Construction of Large Weighing Monolithic Lysimeters, Transactions of the American Society of Agricultural Engineers, Vol. 31 No. 2, 447-484.

Rachele H. and A. Tunick, 1992a: Energy Balance Model for Imagery and Electromagnetic Propagation, Technical Report ASL-TR-0311, US Army Atmospheric Sciences Laboratory, White Sands Missile Range, NM 88002-5501.

Rachele H. and A. Tunick, 1992b: Sensitivity of  $C_n^2$  to Random Variations of Windspeed, Sensible Heat Flux, and Latent Heat Flux, Technical Report ASL-TR-0308, US Army Atmospheric Sciences Laboratory, White Sands Missile Range, NM 88002-5501.

Steiner J. L., T. A. Howell, and A. D. Schneider, 1991: Lysimetric Evaluation of Daily Potential Evapotranspiration Models for Grain Sorghum, Agronomy Journal, Vol. 83 No. 1, 240-247.

Tunick A. and H. Rachele, 1991: Estimating Effects of Temperature and Moisture on  $C_n^2$  in the Damp Unstable Boundary Layer for Visible, Infrared, Radio, and Millimeter Wavelengths, Proceedings of the 1991 Battlefield Atmospherics Conference, Ft. Bliss, Texas, 3-6 December, 1991.

Watkins W. R., S. B. Crow, D. R. Billingsley, F. R. Palacios, and R. W. Dutro, 1991a: MISL Measurements at the NATO BEST TWO, Proceedings of the 1991 Battlefield Atmospherics Conference, Ft. Bliss, Texas, 3-6 December, 1991.

Watkins W. R., S. B. Crow, and F. T. Kantrowitz, 1991b: Characterizing Atmospheric Effects On Target Contrast, Optical Engineering, Vol. 30 No. 10, 1563-1575.



## **VORTEX: A NEW TOOL FOR OBSERVING VERTICAL STRUCTURE OF SMOKE/OBSCURANT CLOUDS**

**Max P. Bleiweiss**  
U.S. Army Research Laboratory  
White Sands Missile Range, New Mexico 88002

**Roger E. Davis**  
Science and Technology Corporation  
Las Cruces, New Mexico 88001

**Thomas A. King and Kenneth C. Payne**  
Physical Science Laboratory  
Las Cruces, New Mexico 88003

### **ABSTRACT**

Recent analysis of certain Smoke Week XIII single-generator trials has yielded a discrepancy between EOSAEL Gaussian plume model predictions and observed mass concentrations measured with a nephelometer sampling line. In an effort to better understand the source of these differences, the Vertical Orthogonal Transmissometer Experiment (VORTEX) was devised to observe the crosswind integrated concentration (CWIC) vertical structure of the smoke cloud as it passed the nephelometer sampling line. The system was implemented at Smoke Week XIV by erecting a 32-m tower at the far side of the nephelometer line and instrumenting the tower with light sources at 2-m intervals. This vertical light array was imaged with visible and infrared devices from the opposite end of the nephelometer sampling line, which allows 16 transmission lines of sight to be measured. Results of the VORTEX measurements for single-generator trials conducted at Smoke Week XIV were used to study obscurant vertical mass distribution. In this paper, measured obscurant plume centroid heights, standard deviations of obscurant distributions, and obscurant plume vertical meandering are compared with model descriptions of the plumes. Obscurant plume lofting is discussed in the context of obscurant type and meteorology. Possible modifications to the Gaussian plume model are suggested.

### **1. INTRODUCTION**

A recent attempt (Davis et al., 1991) to verify the Gaussian Plume Model (GPM) of EOSAEL raised several questions. In that study, data acquired at Smoke Week XIII were compared with those model parameters suitable for analysis; however, the behavior of the plume in the vertical direction could not be studied because of a lack of measurements. A discrepancy between ground-level measurements of concentration and model predictions could not be resolved. To measure the crosswind two-dimensional structure of a plume in the open atmosphere presents formidable problems. It is not often that even a single crosswind sampling array may be constructed of sufficient size and density because of the extensive logistical, structural, and financial problems associated with such a venture. Nevertheless, these measurements are required not only for the validation of simple models such as used here but

also for the development and understanding of more complicated (time-resolved) models. Study of the vertical profile of mean and variance of concentration with downwind distance can allow discrimination among a variety of physical processes and, perhaps, the choice between, for example, the reflected or dissipated Gaussian models. In addition, the link between K-theory and Gaussian models may be drawn (Netterville, 1979) from these types of data.

The Smoke Week series of field trials, though primarily meant to serve as a test of electro-optical systems in the presence of obscurants and other aspects of the "dirty battlefield," provides some opportunity for analysis of aerosol transport and diffusion. The extensively instrumented test grid and the choice of certain types of trials allows a comparison between model predictions and reality. Specifically, an array of aerosol nephelometers placed crosswind at about 2 m above ground level (AGL), several 10-m and a 32-m meteorological towers, and transmissometer lines of sight coupled with single-generator trials have yielded several trials suitable for analysis. Because of the gap created by nonexistent or limited measurement of plume structure in the vertical direction, the Vertical Orthogonal Transmissometer Experiment (VORTEX) subtest of Smoke Week XIV was devised.

Direct measurement of the vertical structure in a cloud beyond the simple parameters of maximum and minimum height AGL is very difficult. The primary reason for this difficulty is the inability to erect a sampling array of sufficient horizontal and vertical dimensions to capture and probe the cloud. Remote techniques such as lidars do not have sufficient spatial or temporal resolution for proper analysis; in any case, current problems in solving the lidar equation preclude the use of such a system. Most transmissometer systems such as REVIRT or MPTR, which can yield crosswind integrated concentration (CWIC), are not amenable to placement in a vertical array.

Two possible solutions to the problem are the Atmospheric Transmittance Large-area Analysis System (ATLAS) developed by the U.S. Army Atmospheric Sciences Laboratory (ASL) (Bleiweiss et al., 1991) and a variation of the two-dimensional transmissometer proposed by Bleiweiss (1989). ATLAS can, in many instances, provide the information required; however, because of a limited dynamic range and inability to measure all clouds at all times, as well as the requirement to process such large amounts of data, it was decided to use ATLAS in a secondary role for the study described here. Instead, a one-dimensional variation of the two-dimensional transmissometer was developed that would, during most of the trials, capture the whole vertical extent of the cloud.

The next section describes the VORTEX setup in detail as well as the other test instrumentation and its arrangement on the test grid. Following that, the reduction of the VORTEX data is described and examples of several ways in which the data can be presented are given. The analysis of the remaining collateral data is then given and model comparisons are made. A summary and suggestions for further measurements/analysis complete the paper.

## 2. EXPERIMENTAL ARRANGEMENT

The VORTEX setup consists of 16 floodlamps attached at 2-m intervals to a 32-m tower, which is the "transmissometer source," and a variety of imaging devices, which become the "transmissometer receivers." The tower was placed near the far end of the nephelometer array and the suite of imagers located at site M1 so that the lines of sight (LOSs) were parallel to the nephelometer array and, depending on the specific trial, anywhere from 30 m to 300 m downwind from the dissemination point. This arrangement allowed minimal interference with other instrumentation. A "plan" view map of the portion of the Smoke Week XIV test grid pertinent to this study is shown in Fig. 1. Here, the relative placement of the M1 instrumentation site, the nephelometer array, VORTEX, the meteorological towers closest to the nephelometer array, and the REVIRT and MPTR LOSs are shown.

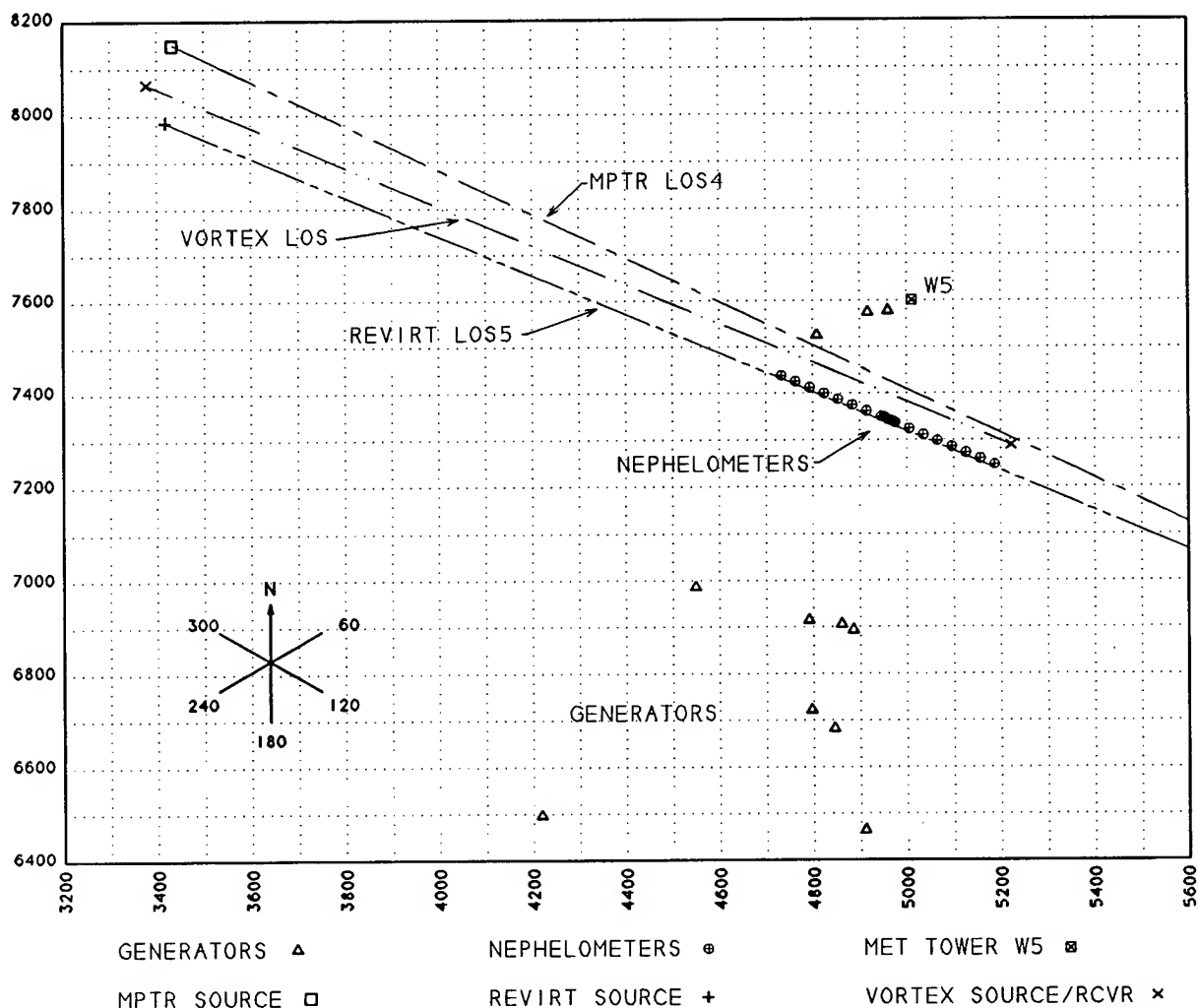


**Figure 1. Plan view of the Smoke Week XIV test grid pertinent to this study.**

A cross-sectional view of the LOSs and the nephelometer placement is shown in Fig. 2. The view in this figure is looking downwind in a northerly direction from the approximate dissemination position.

The imager suite consisted of a CCD video camera sensitive to near infrared radiation in the vicinity of  $1.06\ \mu\text{m}$ , an Agema™ 880 D-Brut thermal imager observing in the mid and far infrared portions of the spectrum, and an Inframetrics™ 210 thermal imager (also dual band). Because of a complicated and varied observing schedule, not all devices were used in all trials. In particular, the imagery reduced so far from which results are presented here is for the CCD video and the 3- to  $5\text{-}\mu\text{m}$  channel of the Inframetrics™ 210 imager. The light sources were Philips™ 150-W Model k150 par/FL floodlamps.

After setup at Smoke Week XIV, the signal from the lamps appeared not to be as strong as had been observed during pretest trials held at White Sands Missile Range to select the best light source. To increase the thermal emission, half of the lamp surface was painted black (Farmer, 1992), which helped considerably. Nevertheless, the dynamic range available for the measurements was small, limiting the usefulness of these data for the intended analysis. Future tests will require a different radiation source such as the MPTR sources, or something similar, in a vertical array.

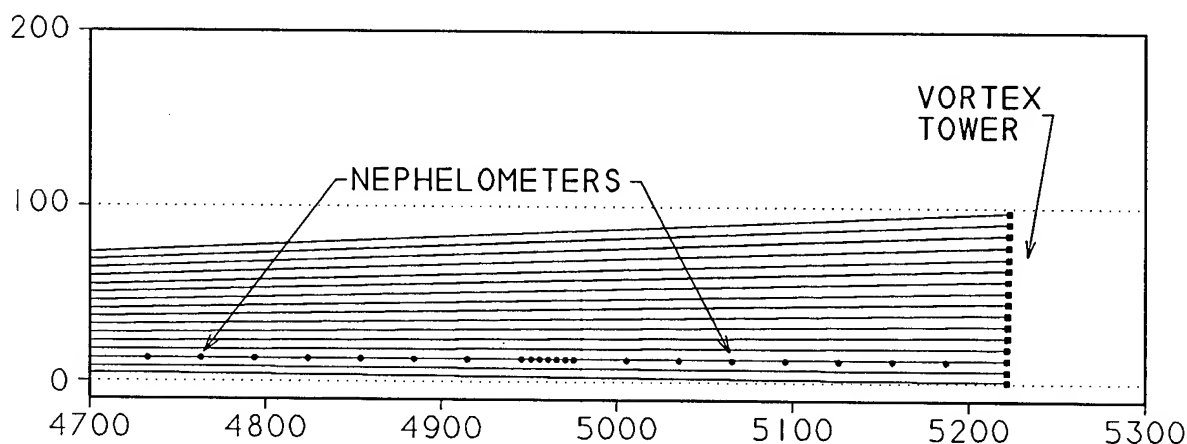


**Figure 2. Cross-sectional view of the test grid in the vicinity of the nephelometer sampling array showing the positions of the 16 VORTEX LOSs with respect to the sampling array.**

### 3. REDUCTION OF THE VORTEX MEASUREMENTS

The conversion of the imaged light array to transmittance values has been described in Bleiweiss (1989) and is similar to the technique used by the MPTR transmissometer system (de Jong et al., 1988). In short, videotapes of the trial, which contain 30 frames per second, are processed by performing an 8-frame running average, which is sampled at 10 frames per second to low-pass filter the raw data. These 10-Hz frames are processed with the following algorithm:

$$T(t) = \frac{L_s(t) - L_b(t)}{L_s(0) - L_b(0)} \quad (1)$$

where the video signal has been digitized and scaled so that "black" is 0 and "white" is 255. The notations (0) and (t) indicate the clear-air period preceding a trial and the time of the measurement during the trial, respectively. To obtain the source and background levels, a box is placed around a given light source so that it just surrounds the light pixels, and the value of  $L_s(t)$  or  $L_s(0)$  is the maximum value within the box depending on the time of the measurement. Two similarly sized boxes are placed in the background, one to the left and one to the right of the light source. The values for  $L_b(t)$  and  $L_b(0)$  are obtained by averaging the average grey level values in each of the two boxes. Equation (1) is processed at 10 Hz for each of the light sources to give 15 transmissometer LOSs (the bottom light was not visible due to screening by the terrain). The choice of the maximum value from the box surrounding the light source instead of an average may have exacerbated the dynamic range problem in that the transmittance value may be held artificially above zero. Using the source box average as was done with the background regions might alleviate this problem. Previous experience indicates that this is not a problem; however, it requires further investigation.

VORTEX data can be presented in a variety of ways to emphasize different aspects of the measurement and the analysis being undertaken. One example of data presentation is shown in Fig. 3, which is a plot of transmittance versus time for trial 05212. For comparison, the trial 05212 MPTR measurements for LOS 4 are overlaid in the plot. More detailed comparisons of this type have been presented

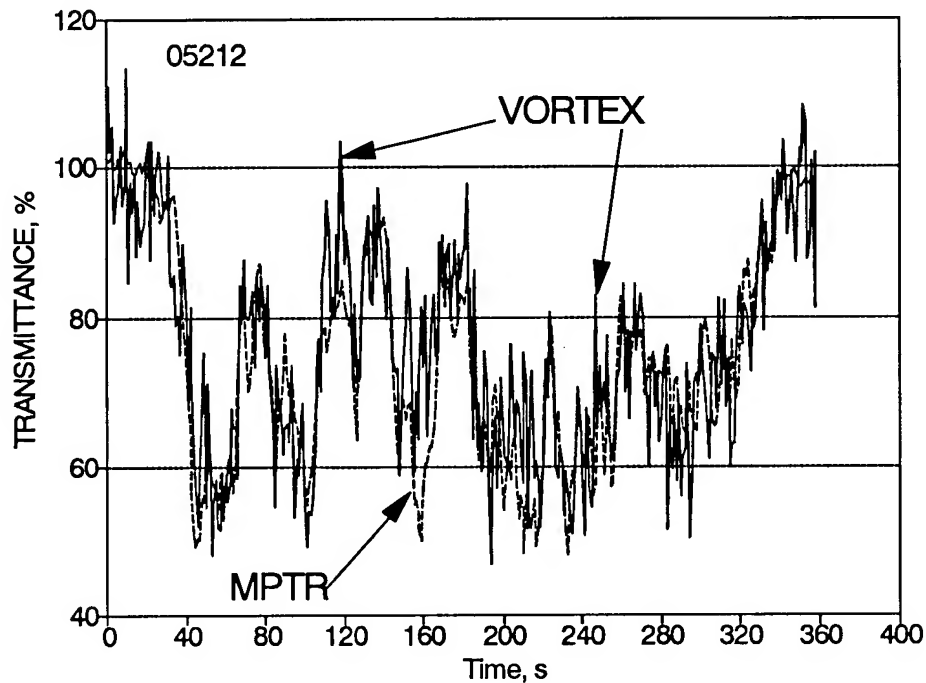


**Figure 3. Transmittance versus time for Smoke Week XIV trial 05212. VORTEX LOS 3 and MPTR LOS 4 data are displayed. These two LOSs are nearly coincident.**

elsewhere (Bleiweiss et al., 1991). Figure 4 is an example of another type of data presentation. It presents the time-dependent vertical structure contours for the obscurant cloud derived from the history of transmittance from each light (that is, each LOS) for trial 05212.

The transmittance data can be converted to a quantity proportional to the CWIC through Eq. (2):

$$CWIC = \frac{-\ln T}{\alpha} \quad (2)$$

where  $\alpha$  is the mass extinction coefficient for the particular aerosol being studied and the wavelength band of the measuring instruments.

The VORTEX data have been processed for height of the mean and standard deviation of the vertical distribution of CWIC. This method is analogous to that used in the previous paper examining the GPM (Davis et al., 1991), except that the earlier paper studied the horizontal structure as seen by the nephelometer array. The trials chosen for our analysis of plume vertical structure had to meet the following criteria:

- (1) single-generator trial
- (2) nephelometer data available
- (3) cloud contained by the nephelometer array during the whole trial
- (4) VORTEX data available

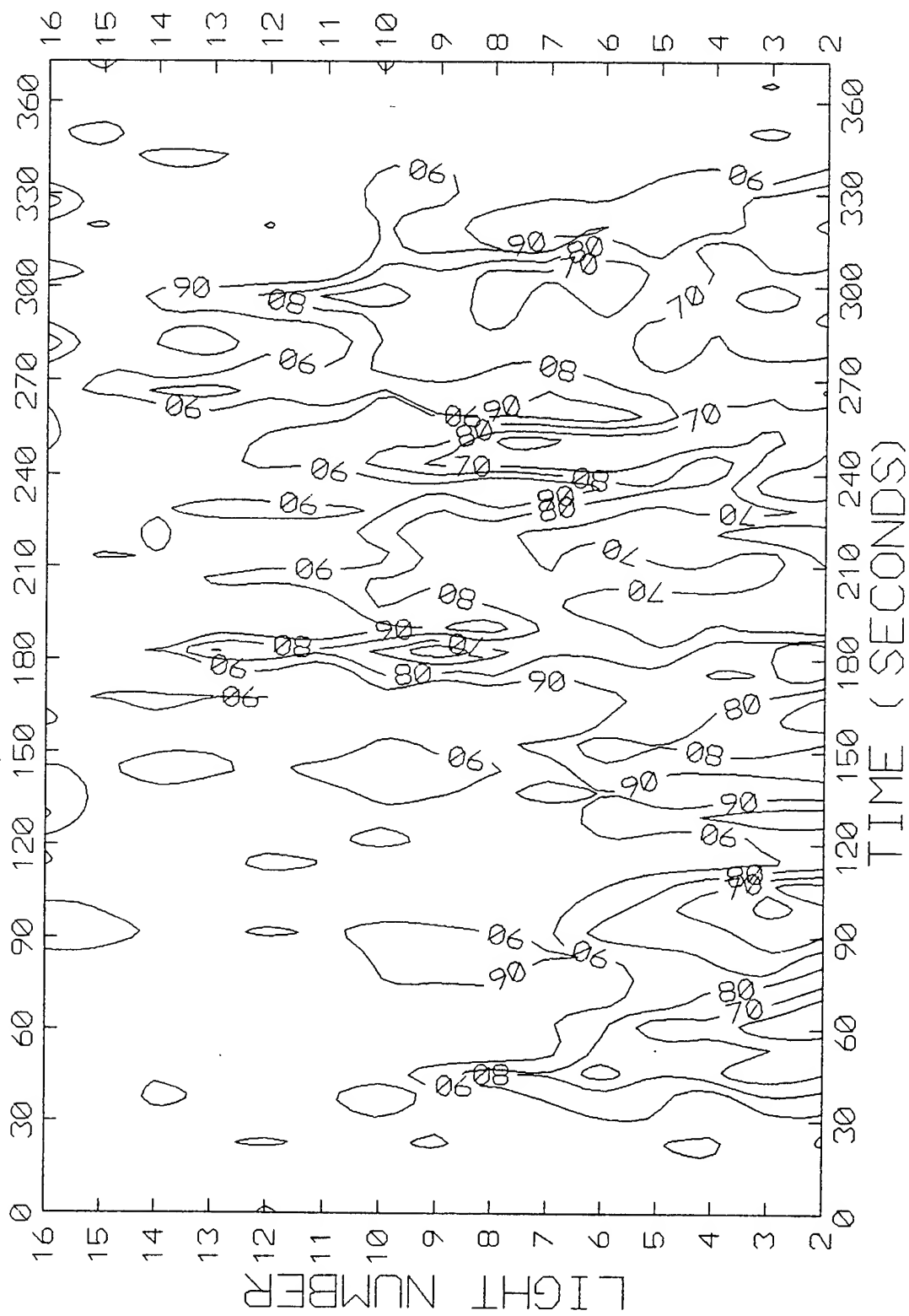


Figure 4. VORTEX vertical transmission history of the plume.

The trials chosen are listed in Table 1 along with other pertinent information. Examination of the data indicates that a minimum transmittance value of about 10% is the least that can be used with any confidence. This transmittance corresponds to a value for  $\alpha \cdot \text{CWIC}$  of  $\approx 2$ . Consequently, for those VORTEX LOSs with large attenuation, it is not possible to do one-to-one comparisons with the nephelometer data, nor is it possible to discuss the overall vertical structure of the plume. Therefore a detailed comparison with the GPM is difficult; however, as the main purpose of this experiment was to investigate the vertical structure of the plume averaged over the trial time and, specifically, any plume "lofting" over the nephelometer array, the VORTEX measurements remain useful diagnostics.

Future work will include far-infrared (FIR) data acquired by the Agema camera. Because many obscurants have different attenuation properties in different wavebands, the FIR measurements will provide supplementary information on cloud vertical structure.

**TABLE 1: SUMMARY OF TRIALS SELECTED FOR STUDY**

Trial	Obscurant	Source Dist <sup>1</sup>	Wind Speed <sup>2</sup>	Wind Direction <sup>3</sup>	PSC	Emission Rate <sup>4</sup>
05212	Kaolin	166	10.9	262	D	226.8
05310	Graphite	132	6.5	199	B	216.0
05414	Silica	132	7.1	196	C	216.0
05513	Brass	131	6.6	207	C	205.2
05613	Brass	137	7.0	208	C	212.6
05715	Aluminum	139	5.9	214	C	216.0
06408	VEES	213	5.9	176	C	53.6
07340	Fog Oil	199	4.2	192	C	33.2
07810	Graphite	53	6.7	337	D	302.4
08014	Silica	49	6.3	342	D	301.6
08309	NEODTC1	74	2.7	352	A	84.6
08409	NEODTC1	82	2.8	344	A	36.7
08507	JP8 VEES	73	3.2	003	B	*****
08608	VEES	71	3.8	013	B	53.6

<sup>1</sup> m  
<sup>2</sup> m s<sup>-1</sup>

<sup>3</sup> referenced to north  
<sup>4</sup> g s<sup>-1</sup>

#### 4. MODEL EVALUATION

The Gaussian model has been extensively utilized for describing aerosol diffusion by many commonly used transport and diffusion programs, including EOSAEL. It has attained workhorse status primarily because it is relatively easy to handle mathematically and it produces results that agree with experimental data as well as any model (Hanna et al., 1982). The general form of the Gaussian plume model is given by:

$$\chi^{\pm}(x,y,z) = \frac{Q e^{-\gamma(x')}}{2\pi\bar{u}\sigma_y(x')\sigma_z(x')} e^{-\left(\frac{y'}{\sigma_y(x')}\right)^2} e^{-\left(\frac{z \pm z_i}{\sigma_z(x')}\right)^2} \quad (3)$$

where $\chi(x,y,z)$	= $\chi^+(x,y,z) + \chi^-(x,y,z)$ , $g\ m^{-3}$
$Q$	= obscurant mass emission rate, $g\ s^{-1}$
$\gamma(x')$	= deposition/scavenging factor
$\bar{u}$	= mean wind speed, $m\ s^{-1}$
$\sigma_y(x')$	= crosswind dispersion coefficient, $m$
$\sigma_z(x')$	= vertical dispersion coefficient, $m$
$x_o, y_o, z_o$	= obscurant release coordinates
$x, y, z$	= coordinates of measurement
$x'$	= $x - x_o$ , $m$
$y'$	= $y - y_o$ , $m$
$z_i$	= $z_o + wt$ , $m$
$w$	= vertical velocity due to buoyancy, $m\ s^{-1}$
$t$	= downwind time, $x'/\bar{u}$ , $s$

The negative  $z_i$  term allows for the reflection of the plume at the surface by assuming a source image at a height  $z_o$  below the surface.

Plume dispersion is controlled by the dispersion parameters  $\sigma_y$  and  $\sigma_z$ , which are functions of downwind distance, Pasquill stability category (PSC), and surface roughness. These parameters account for plume meandering in the horizontal and vertical directions over time scales of tens of minutes.

Davis and Sutherland (1992) and Davis et al. (1991) analyzed single-generator obscurant plume crosswind dispersions using nephelometer data acquired at Smoke Week XIII. These analyses showed good agreement between the measured plume mass concentration dispersion distributions and the Gaussian plume model predictions. It was noted, however, that for most trials studied, the model consistently predicted larger absolute mass concentrations than were measured by the nephelometers. This discrepancy was not resolvable with available data, but could be explained by errors in the nephelometer measurements and/or inaccurate model inputs.

One model input parameter brought into question is the buoyant velocity. Lacking specific information concerning obscurant buoyancy, the buoyant velocity was assumed to be zero in the Smoke Week XIII studies. One of the main purposes of the VORTEX experiment was to verify this assumption through the measurement of the obscurant cloud vertical mass distributions.



To begin analysis of the nonbuoyant Gaussian model, obscurant plume calculations using Eq. (1) were run for trial conditions with  $w = 0$  and  $\gamma = 0$ . These calculations provide a baseline data set of CWICs along each VORTEX LOS for each trial in Table 1. Comparison of VORTEX transmittance measurements and the GPM CWIC calculations is done by converting VORTEX trial-averaged transmittance to CWIC values with Eq. (2). Thus far only the 3- to 5- $\mu\text{m}$  band has been studied.

Figures 5a through 5d present the Gaussian model predictions of CWIC for trials 05212 (kaolin), 05414 (silica), 05513 (brass), and 05715 (aluminum). Each figure also plots VORTEX measurements of optical depth divided by the mass extinction coefficient,  $\alpha$ . Two values for  $\alpha$  have been used for each obscurant: one value from laboratory or field measurements and one arbitrary value. The arbitrary values for trials 05212 and 05414 were set to give a "good" visual fit to the model curve. For trial 05513, the reported VORTEX distribution is such that no single-valued alpha produces a good fit. For trial 05715, the situation is somewhat better but clearly not as satisfying as for the first two trials.

At face value, the VORTEX data for trials 05212 and 05414 appear to support the nonbuoyant assumption. The fact that an adjustment of approximately a factor of two in  $\alpha$  has been made is not particularly alarming. Aside from measurement errors in  $\alpha$  or in the Smoke Week data, it is possible that the obscurants released at Smoke Week XIV were somewhat different from those used several years earlier for determining  $\alpha$ . To the contrary, however, data for trials 05513 and 05715 show a steeper slope in mass distribution than the nonbuoyant GPM distribution, regardless of the choice of a single-valued  $\alpha$ . This result suggests that a possible buoyant term should be included in the GPM calculations.

There were two distinct differences between trials 05212/05414 and trials 05513/05715. First, the obscurants for trials 05212 and 05414 were dusts, while the obscurants for trials 05513 and 05715 were flakes. Secondly, the  $\alpha$  values for the dusts were an order of magnitude smaller than those for the flakes. The differences between the dust and flake shapes may result in significant aerodynamic differences, allowing the flakes to experience a different vertical distribution than that predicted by the GPM. This possibility needs additional study.

The order of magnitude differences in  $\alpha$  values between the dusts and flakes result in much greater attenuation by the flakes than by the dusts for similar CWICs. Because of the dynamic range considerations discussed above, VORTEX may be underestimating the flake CWIC when the attenuation becomes large.

The analysis of plume buoyancy continues as more supplementary data from Smoke Week XIV become available. Of particular interest is the short-path transmissometer data, which will be used to determine Smoke Week obscurant  $\alpha$  values under trial environment conditions.

## 5. CONCLUSION

VORTEX has been described and its implementation at Smoke Week XIV has been discussed. The lack of dynamic range caused by light sources of insufficient strength reduced the number of trials amenable to analysis and comparison with the GPM of EOSAEL. Nevertheless, it has been shown that VORTEX is capable of meeting the goals initially set for it and that further analysis of existing data can still be accomplished. The short time available between Smoke Week XIV and this conference has made it difficult to accomplish a complete analysis because not all supporting data are yet available. VORTEX implementation in future tests for the study of diffusion and transport is warranted in those cases where ATLAS does not function well. The implementation of instrumentation for tomographic analysis of obscurant plumes will eventually allow a complete analysis.

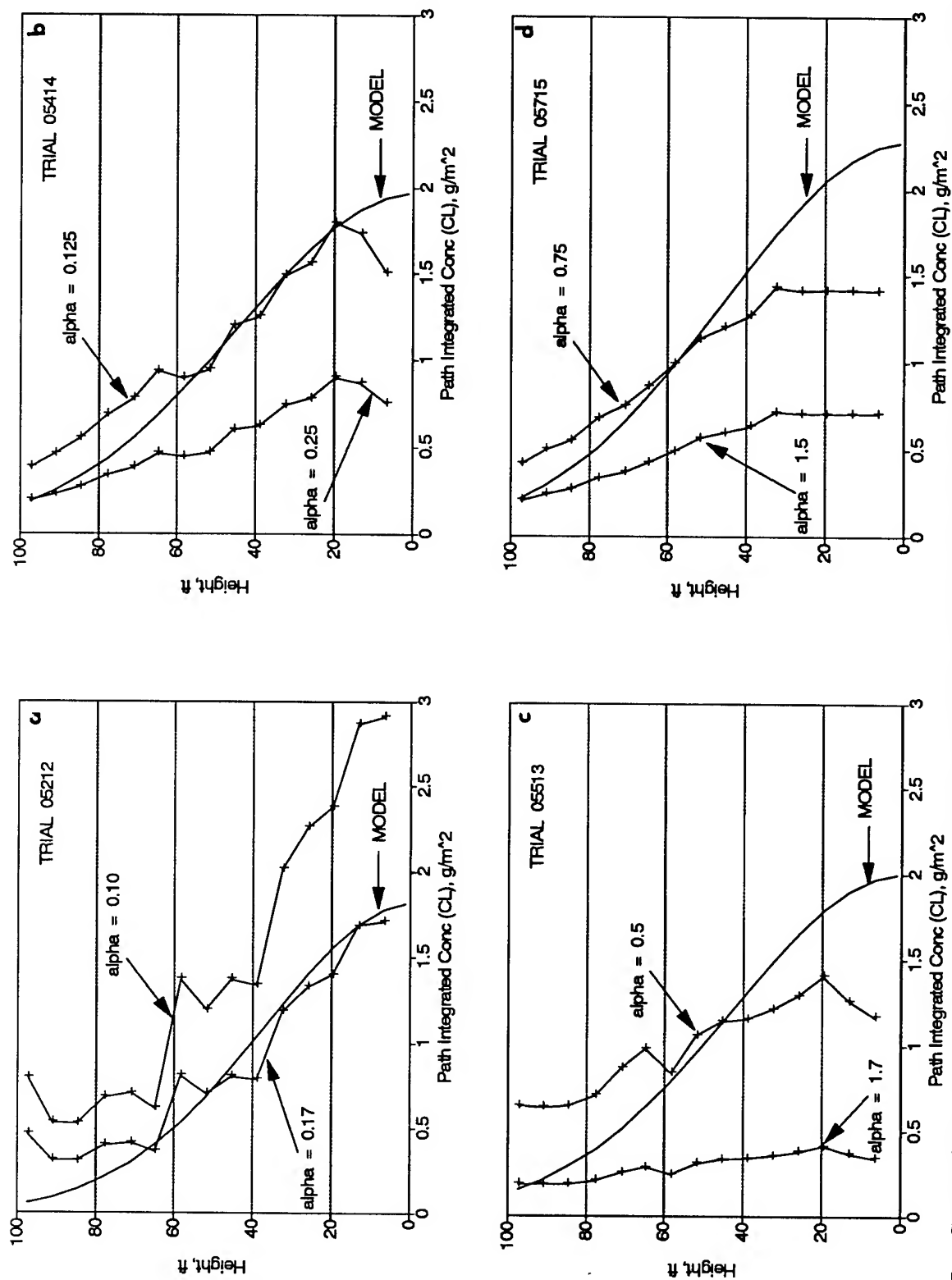


Figure 5. Comparison of GPM vertical mass distributions with mass distributions derived from VORTEX for trials 05212 (a), 05414 (b), 05513 (c) and 05713 (d).

## ACKNOWLEDGMENT

At the time of this analysis, most Smoke Week XIV data were still being processed and were not generally available. The authors acknowledge and thank Mr. Tony Spence and Ms. Karen Hutchison of the Physical Science Laboratory for providing the nephelometer data (Spence) and transmissometer data (Hutchison) in advance. Our appreciation for this effort is also extended to Mr. Bill Bruce (ASL) and Mr. Ed Butterfield (ASL), who run the nephelometer and transmissometer programs, respectively. Without the support of these people this paper would not have been possible.

## REFERENCES

- Bleiweiss, M.P., 1989: A Two-Dimensional Transmissometer. *Proc. of the Smoke/Obscurants Symposium XIII*, Office of the Project Manager, Smoke/Obscurants, Aberdeen Proving Ground, Maryland.
- Bleiweiss, M.P., R. Howerton, R. Valdez, K. Payne, T. King, and K. Hutchison, 1991: A Comparison of the MPTR and ATLAS Transmissometers. *Proc. of the Smoke/ Obscurants Symposium XV*, U.S. Army Chemical Research Development and Engineering Center, Aberdeen Proving Ground, Maryland.
- Davis, R.E., J. Crain, and R.A. Sutherland, 1991: An Application of AAODL Meteorological and Nephelometer Field Test Data: Obscurant Plume Characterization. *Proc. of the 1991 Battlefield Atmospherics Conference*, U.S. Army Atmospheric Sciences Laboratory, White Sands Missile Range, New Mexico.
- Davis, R.E., and R.A. Sutherland, 1992: Obscurant Plume Dispersion Measurements At Smoke Week XIII. *Proc. of the Smoke/Obscurants Symposium XVI*, U.S. Army Armament Munitions Chemical Command, in press.
- de Jong, A.N., M.J. Roos, and P.J. Fritz, 1988: *Smoke Characterization by Means of MPTR*. IR1988-7, FEL-TNO, The Netherlands.
- Farmer, W.M., 1992: private communication.
- Hanna, S.R., G.A. Briggs, and R.P. Hosker Jr., 1982: *Handbook On Atmospheric Diffusion*. DOE/TIC-11223, Technical Information Center, U.S. Department of Commerce, Springfield, Virginia.
- Netterville, D.D.J., 1979: *Concentration Fluctuations in Plumes*. Environmental Research Monograph 1979-4, Syncrude Canada Ltd., 10030-107 Street, Edmonton, Alberta, T5J 3E5.



**Session IV**

**ATMOSPHERIC EFFECTS**

**Session Chair**

**Mr. Don Grantham  
Air Force Geophysics Laboratory**

# THE USE OF ANALYTIC APPROXIMATIONS IN PROVIDING METEOROLOGICAL DATA FOR ARTILLERY

Fernando Caracena

NOAA, Environmental Research Laboratories  
National Severe Storms Laboratory  
Boulder, Colorado 80303

## ABSTRACT

The current approach in artillery of analyzing sounding data in terrain-following layers can yield suitable results over flat terrain, but may have problems over complex terrain. Using a new analysis technique called analytic approximation, sounding data from project PASS for a moderate westerly flow event over the narrow ridge of the Organ Mountains were analyzed to look for such distortions and to check out the analysis scheme over a small mesoscale domain. The analysis gave physically reasonable results, even though no mass continuity constraints were placed on the analysis.

## 1. INTRODUCTION

Wind, temperature, and air density are known to have a significant effect on ballistics, and a knowledge of these is essential for accurately delivering missiles (Blanco and Traylor, 1976). These atmospheric data are conveyed to artillery crews in the field by means of a meteorological message. The analytic approximation scheme (Caracena, 1987) which is a generalization of objective analysis, is being tested at White Sands as one method of generating automated meteorological messages for artillery. This paper serves two purposes: 1) to describe its application, and 2) as a check on the quality of the scheme, to show that an unconstrained analysis produces a realistic appearing flow pattern over a narrow mountain ridge. The analyses presented are based on data collected during project PASS (see Blanco and Traylor, 1976) on 23 November 1974 during westerly flow over the Organ Mountains. One sounding site in Las Cruces sampled the upstream flow, and seven others sampled the lee side flow. No soundings were initiated over the mountains themselves.

The basic meteorological challenge faced in artillery is to maintain an accurate data base of upper-air sounding data. Relative to this task, temporal and spatial variability of these data become moot questions. Field experiments performed at

---

1. Support for this work was furnished by Atmospheric Sciences Laboratory under contract no. HO-2-9J408-HO-00.

White Sands Missile Range have addressed the question of four-dimensional variability in upper-air conditions. Blanco and Traylor (1976) concluded from experiments performed during project PASS that temporal variability was more important than spatial variability, at least over the spatial area sampled (~ 80 km across).

Within small areas (~100 km across) over flat terrain, only shallow variations in the fair weather airflow, temperature, and pressure are expected near the surface, due mostly to changes in surface roughness. The greatest changes should be seen vertically, so that the major effect on the trajectory of a missile would be in changing conditions encountered by the missile as it moved vertically. For fair weather and flat terrain, a single site where soundings were released periodically would suffice to provide data for the purposes of artillery. Because of sharp gradients and rapid changes associated with weather features such as storms and frontal passages, soundings need to be launched at more sites and more frequently during inclement weather, so that both spatial and temporal changes in the atmosphere are observed. Surface wind sensors are important to this task, because they can provide a nearly continuous coverage of the weather near the surface from which one can diagnose changes in upper-level conditions.

Even in fair weather, the flow over complex terrain can sometimes generate three- and four-dimensional variability in atmospheric conditions that not only are difficult to monitor, but also can significantly affect the flight of a projectile. To sample the flow over complex terrain and monitor its changes, one needs to have a number of sounding sites, to release soundings periodically, and to have a steady stream of data from surface sensors. A mesoscale model initialized with synoptic-scale and mesoscale data can be a great aid in providing meteorological data for artillery, but it is not a standalone tool. Numerical models need to be initialized. This requires a good objective analysis package. The state of the atmosphere needs to be updated in models with current data. Numerical models, however, have spinup times of a few hours, during which the models adjust to initial or new data. Therefore, in real-time applications, models need an objective analysis interface that updates model output to reflect current observations.

## 2. REVIEW OF THE ANALYTIC APPROXIMATION SCHEME

Analytic approximation is the reformulation of objective analysis such that each set of observations is approximated as an analytic function that can be evaluated by a computer at any specified point. No longer having a regular computational grid to work with, successive corrections are performed in a novel way. Analytic approximation captures the results of successive corrections (up to an infinite number of successive corrections, or passes) in a matrix, that is a function of  $n$ , the number of passes. This matrix transforms a vector of the original observations into a vector of surrogate observations; a single-pass analysis, based on surrogate observations, yields the equivalent of a conventional objective analysis with  $n$  successive corrections, but without the computational grid. The analytic

approximation method with successive corrections (Caracena, 1987) is reviewed here briefly, beginning with the single-pass analysis scheme, moving onto the successive approximation scheme, and finally to the exact analysis scheme.

## 2.1 THE SINGLE-PASS ANALYTIC APPROXIMATION

Matrix notation allows a compact representation of a single-pass, weighted-sum scheme:

$$\langle F \rangle = w^T(L, r) f, \quad (1)$$

where  $w$  is a column vector (the weighting function vector) containing weighting function elements  $w_i(L, r)$  and the observation vector  $f$ , of one type of observed field, has the discrete observations  $f_i$  as its elements.

In general, the weighting function  $w_i$  in eq.(1) is defined in terms of some unnormalized, isotropic weight basis function (WBF) that is analytic. Here a Gaussian WBF is chosen, so that the analytic approximation developed is a generalization of the Barnes (1964) scheme. The resulting weighting function is then defined as follows:

$$w_k(L, r) = \exp(-|r - r_i|^2 L^{-2}) / \sum_{i=1}^S \exp(-|r - r_i|^2 L^{-2}). \quad (2)$$

Dividing the WBF by the sum of the unnormalized weights over the entire distribution of observations, such as in eq.(2), normalizes the weighting function  $w_k$  such that the sum of all the weights over the index  $k$  is unity at any location  $r$ . The normalizing sum depends on the form of the WBF and the geometry of the observational grid.

The spatial behavior of the normalizing sum for a Gaussian WBF has been discussed (Caracena et al., 1984; Achtemeier, 1987; and Pauli and Wu, 1990). If the observations are not too irregularly distributed, and the scale length is about the same or greater than the average spacing between observations, the normalizing sum for a Gaussian WBF is almost constant for all points inside the boundaries by more than one scale length  $L$ . The weighting functions  $w_k(L, r)$  are then very close to being homogeneous and isotropic. Large irregularities in the distribution of observations cause large, colocated irregularities in the normalized weighting function (Caracena et al., 1984).

All orders of derivatives of the approximating function are defined, also as weighted sums, without truncation errors associated with the finite difference estimates (see Potter, 1973) of finite difference schemes. Taking the appropriate partial derivatives of eq.(1) and using eq.(2), one has an expression for the two-



dimensional gradient that involves only uniformly weighted sums, which are an important feature of *Gaussian* weight-based schemes:

$$\nabla \langle F \rangle(r) = 2 L^{-2} [ \langle F R \rangle(r) - \langle F \rangle(r) \langle R \rangle(r) ] , \quad (3a)$$

where bracketed quantities are defined as weighted sums of products of discrete observations or other corresponding, indexed quantities.

$$\langle A B C \dots \rangle = \sum_{i=1}^S w(L, |r - r_i|) a_i b_i c_i \dots . \quad (3b)$$

Note that eq.(3a) results strictly from using a *Gaussian* WBF. In general, any other choice of WBF would not have resulted in an expression as simple as eq.(3a), but would have involved weights other than  $w$ . The choice of weighting function in an analytic approximation has a strong effect on the complexity of formulas for derivatives.

## 2.2 THE MULTIPLE PASS SCHEME

Analyses resulting from  $n$  successive corrections are expressed very compactly as analytic approximations (see Caracena, 1987). Successive corrections are analyzed using residuals of the previous estimate of the field from the set of observations. Then the analyzed field of residuals gives the next successive correction to the field. The same set of weights is used in every successive pass, because of convenience and the more rapid convergence that is obtained by using weighting functions with unchanging scale factors in each successive pass (Achtemeier, 1987). In traditional objective analysis schemes, the results of each successive correction are accumulated on a regular computational grid, and residuals at the observation sites are computed from values of this regularly gridded field bilinearly interpolated back to the observing sites. Instead of accumulating field approximations on a regular grid, the analytic approximation captures these effects in a square matrix  $B_n$  that is a function of the number of successive corrections  $n$ . This matrix, which produces a simple modification in the single pass scheme eq.(1c),

$$\langle F \rangle = w^T(L, r) B_n f , \quad (4)$$

is given by

$$B_n(L) = W^{-1} [I - (I - W)^n] , \quad (5a)$$

where the matrix  $I$  is the identity matrix.

The analytic approximation that fits the data exactly is the limit of an infinite number of successive corrections. The corresponding correction matrix becomes

$$B_{\infty}(L) = W^{-1} . \quad (5b)$$

Note that choosing a single iteration reduces the value of  $B_n$  in eq.(5a) to the identity matrix,

$$B_1(L) = I , \quad (5c)$$

so eq.(4) reduces eq.(1c).

All analytic approximation schemes can be written as equivalent, one-pass schemes either by writing the expression in terms of an effective weighting function vector

$$\langle F \rangle = w_{eff}^T(L,r) f , \quad (6a)$$

or, in terms of surrogate observations

$$\langle F \rangle = w^T(L,r) f_{sur} . \quad (6b)$$

The effective weighting function vector is given by

$$w_{eff}(L,r) = B_n^T(L) w(L,r) , \quad (7a)$$

and the surrogate observation vector by

$$f_{sur} = B_n(L) f . \quad (7b)$$

### 3. A CASE STUDY FOR 23 NOVEMBER 1974

On 23 November 1974, field tests were conducted at White Sands Missile Range as part of project PASS. During most of the day, the upper-level winds were from the west. Soundings were launched at 2 h intervals from eight sites, one of which, near Las Cruces, sampled the flow on the windward side of the Organ Mountains. One-half the soundings were initiated at 0615 MST, and the other half were released at 0645 MST. Thereafter, soundings were taken on this staggered schedule of two releases, one 15 min after the hour and the other 45 min after, every 2 h.

The series of kinematic and isentropic vertical cross sections depicting the flow over the Organ Mountains presented here, were obtained from unconstrained, four-pass analytic approximations of sounding data using combined releases  $\pm 15$  min on either side of the analysis time. The potential temperature is horizontally stratified, except for a weak effect of flow over and around the mountains. The

winds analyzed in terms of their u and v components, in artillery zones (0 = surface, 1 = average over first 200 m, 2 = average over next 300 m layer, 3 and higher = average over successive 500-m layers), were assigned heights corresponding to the center of each layer. The release level of all radiosondes was taken to be a flat surface, although there are a few tens of meters difference in their elevation, so that heights in the following figures are measured above this fictitious, flat surface.

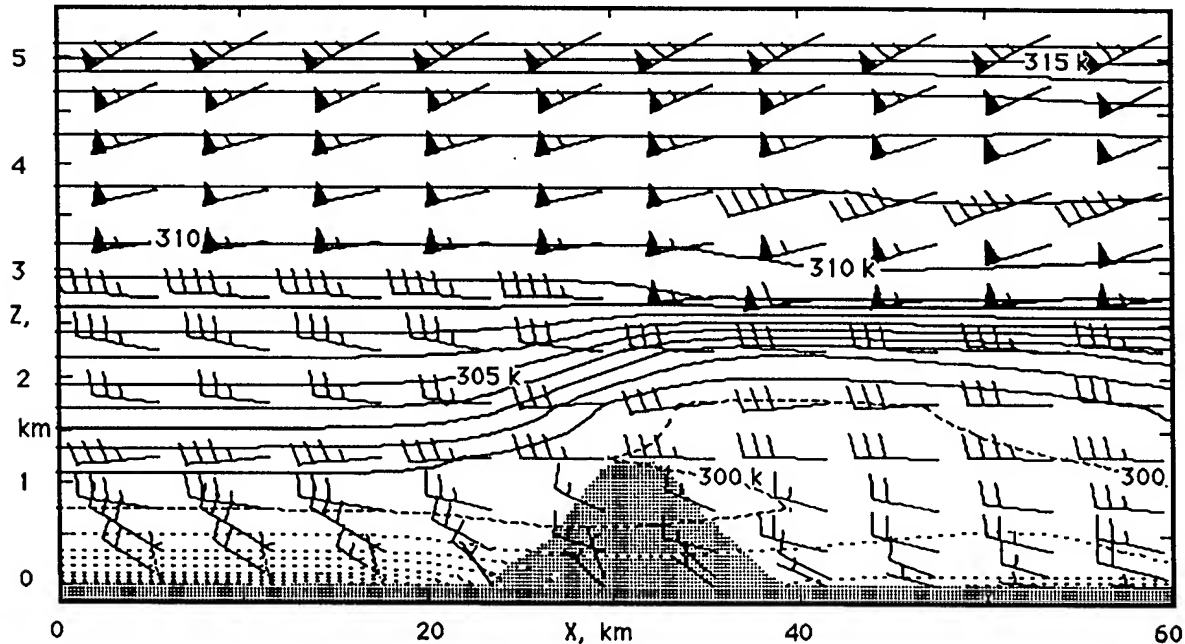


Fig 1a. Vertical E-W cross section over Organ Peak analyzed from 0630 MST, 23 November 1974 soundings. Winds are in knots. Potential temperature contours are in kelvins, solid above 300 K, and dotted below.

Analyzed flow over Organ Peak (fig. 1a) 0630 MST, 23 November 1974 in an east-west, vertical cross section, shows that although the flow is moderate at mountain top level (~35 kt), a stable layer near peak top is visibly displaced upward, and enhanced, suggesting a weak vertical perturbation in the flow near peak top. This conclusion is supported by slight accelerations of winds above the peak and at the top of the stable layer. At the same time, the same kind of perturbation is seen over St. Augustine Pass (fig. 1b), but it has a smaller amplitude. Note that in both figures there is a low-level inversion very near the surface due to nocturnal cooling, which is blocked by the mountains. Although no soundings were released over the mountains, the analytic approximation draws a minimum in the wind, within the space occupied by the mountains, from extrapolated gradients determined from soundings released over flatter terrain.

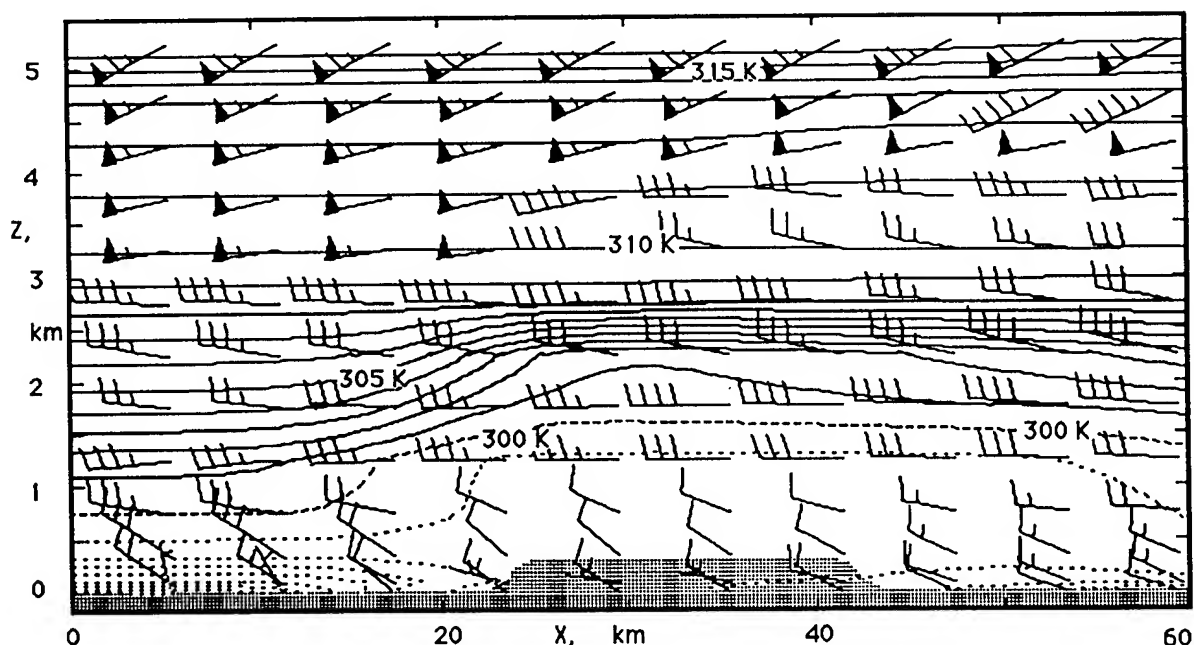


Fig 1b. Vertical E-W cross section over St. Augustine Pass analyzed from 0630 MST, 23 November 1974 soundings. See fig. 1a caption for details.

Soundings taken within  $\pm 15$  min of 0830 MST were combined to produce the analysis depicted in fig. 2. These vertical cross sections show the same kind of structures that are contained in the corresponding figs. 1, but the patterns are weaker in amplitude. The isentropes in fig. 2a suggest that the flow is no longer displaced much above Organ Peak. Apparently the stream of faster flow that was present at 0630 MST at mountain top level has moved eastward by 0830 MST, and the stable layer has lifted higher above the mountain tops. The weaker flow at 0830 is then insufficient to produce a large vertical displacement on encountering the terrain. In contrast, fig. 2b shows evidence that the air is still flowing up and over St. Augustine Pass. As in fig. 1, the analysis places a minimum in the wind within the space occupied by mountains and to their lee.

The tendency of the analysis to put the minimum wind inside spaces occupied by mountains is demonstrated clearly in figs. 3a and 3b. Air approaches the mountain (fig. 3a) with a higher speed below the ridge line upstream than the analysis (fig. 3b) showing the corresponding section occupied by the mountain. Another feature of interest in these analyses is what happens to the contours of constant potential temperature as the flow approaches the mountains. Since potential temperature is a tracer of air parcels in adiabatic motion, the displacement of isentropes is one way to infer vertical air motions. Note that as the flow moves from the upstream side over flat terrain, the isentropes are more or less horizontally stratified. However, in moving over the ridge top, the isentropes are displaced upward over the ridge, indicating that some of the air that encountered the ridge was forced over the top.

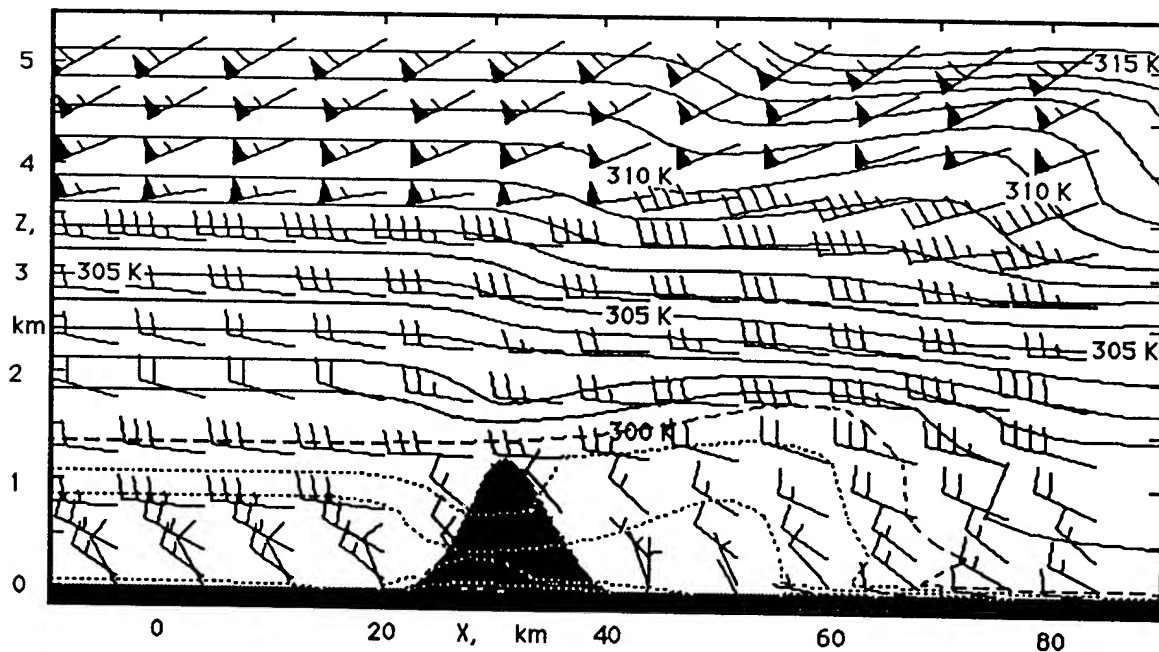


Fig 2a. Vertical E-W cross section over Organ Peak analyzed from 0830 MST, 23 November 1974 soundings. See fig. 1a caption for details. Note change in horizontal scale.

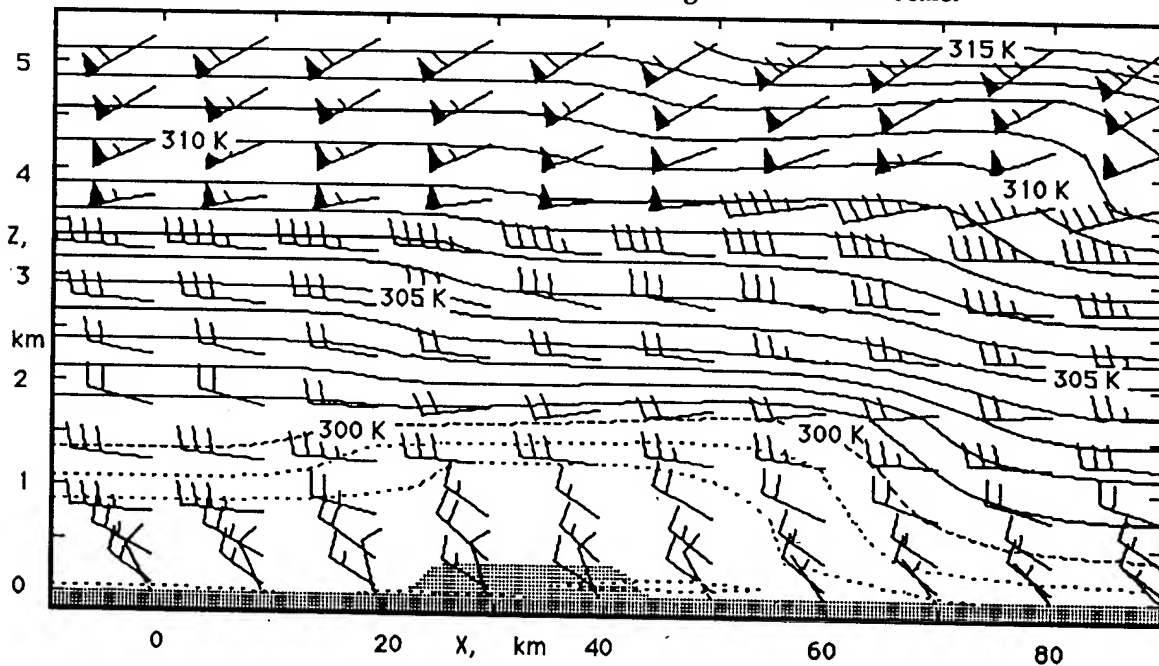
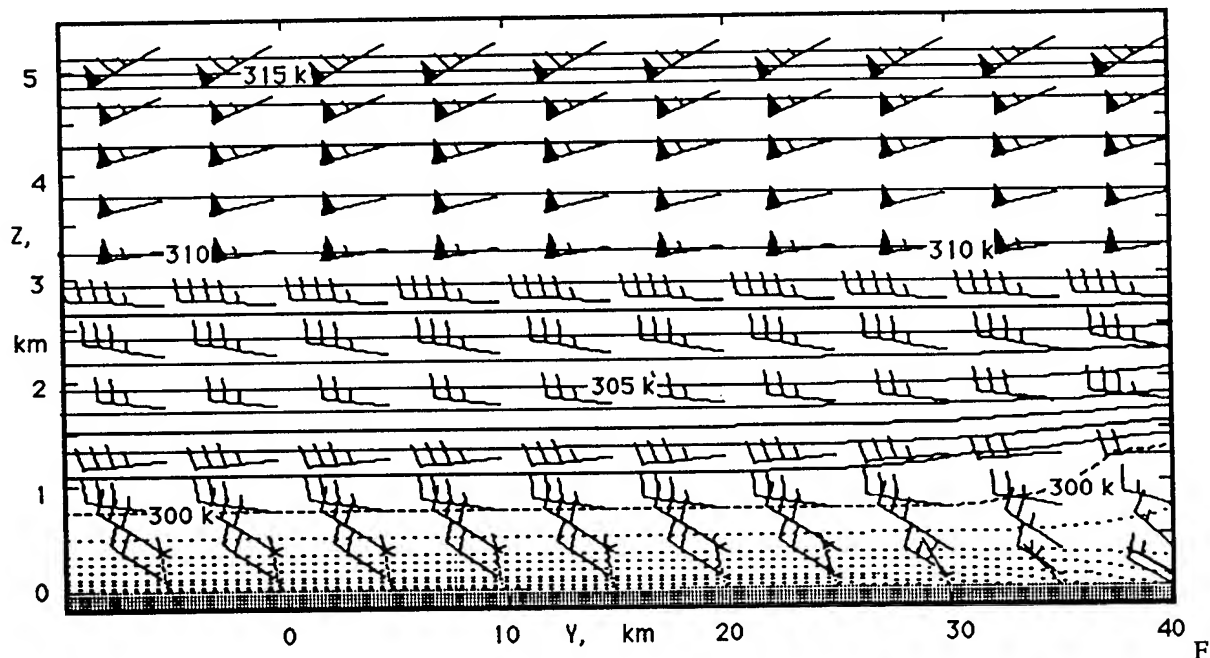


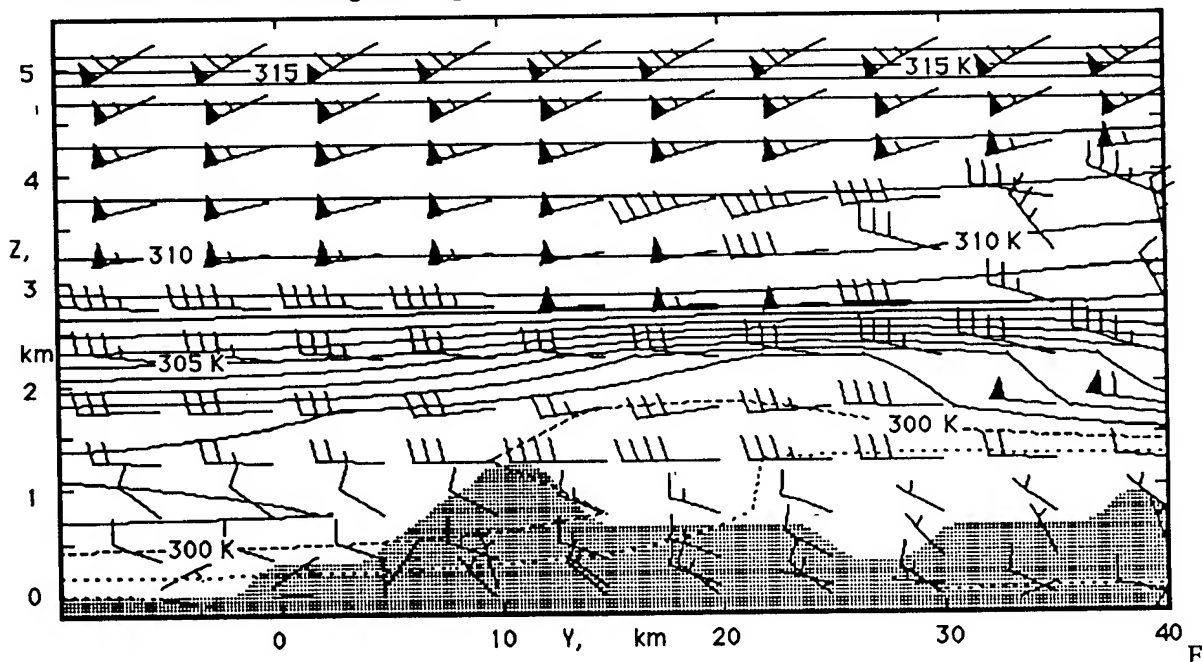
Fig 2b. Vertical E-W cross section over St. Augustine Pass analyzed from 0830 MST, 23 November 1974 soundings. See fig. 1a caption for details. Note change in horizontal scale.

#### 4. CONCLUSION

Space limits the results that can be presented, but from those presented, it is clear that the analytical approximation method does a reasonably good job in analyzing the flow crossing over a narrow ridge, even though it was not directly



ig 3a. Vertical N-S cross section 20 km upwind of the Organ Mountains analyzed from 0630 MST, 23 November 1974 soundings. See fig. 1a caption for details.



ig 3b. Vertical N-S cross section over the Organ Mountain ridge line analyzed from 0630 MST, 23 November 1974 soundings. See fig. 1a caption for details.

sampled by upper-air soundings. Both thermodynamic and kinematic fields look physically reasonable. We conclude from these results is that the analysis can provide good meteorological data for ballistics wherever the upper atmosphere is well sampled and data are current, especially where the results are interpolated

rather than extrapolated. The acid test for the suitability of this scheme, however, will be provided by forthcoming field tests.

#### REFERENCES

Achtemeier, G.L., 1987: On The Concept Of Varying Influence Radii For A Successive Corrections Objective Analysis. Mon. Wea. Rev.: 115, 1760-1771.

Barnes, S.L., 1964: A Technique for Maximizing Details in Numerical Weather Maps Analysis. J. Appl. Meteor., 3: 396-409.

Blanco, A. J. and L. E. Traylor, 1976: Artillery Meteorological Analysis of Project PASS. ECOM-5804, U.S. Army Atmospheric Sciences Laboratory, White Sands Missile Range, NM 88002-5501.

Caracena, F. 1987: Analytic Approximation of Discrete Field Samples with Weighted Sums and the Gridless Computation of Field Derivatives. J. Atmos. Sci.: 44: 3753-3768.

Caracena, F., S.L. Barnes, and C.A. Doswell, III, 1984: Weighting Function Parameters for Objective Interpolation of Meteorological Data. Preprints, 10th Conference on Weather Forecasting and Analysis, American Meteor. Soc., Boston, Mass., 109-116.

Pauley, P. M. 1990: On the Evaluation of Boundary Errors in the Barnes Objective Analysis Scheme. Mon. Wea. Rev., 118:1203-1210.

Pauley, P. M., and X. Wu 1990: The Theoretical, Discrete, and Actual Response of the Barnes Objective Analysis Scheme for One- and Two-Dimensional Fields. Mon. Wea. Rev., 118: 1145-1163.

Potter, D.E., 1973: Computational Physics. J. Wiley, London, New York, 304 pp.

#### ACKNOWLEDGEMENTS

I would like to thank A. Blanco for his helping me in accessing and using PASS data. Also, I would like to thank E. Vidal and Mj. Grunwald and others at ASL and PSL for the help that they have provided me in carrying out this task.

# ANALYSIS OF SIMULTANEOUS SCINTILLOMETER MEASUREMENTS OVER FOUR UNIQUE DESERT TERRAIN PATHS

Gail Tirrell Vaucher  
Science and Technology Corporation  
White Sands Missile Range, New Mexico 88002

Robert W. Endlich  
U.S. Army Research Laboratory  
White Sands Missile Range, New Mexico 88002

John W. Raby  
U.S. Army Research Laboratory  
White Sands Missile Range, New Mexico 88002

## ABSTRACT

A study of optical turbulence, measured at 1 m above ground level in arid desert terrain, was conducted. The parameter used to characterize the optical turbulence was the index of refraction structure function,  $C_n^2$ , measured directly by scintillometers. Following a side-by-side comparison of the scintillometer data along an essentially identical 1-km path, the calibrated sensors were installed along a 3.75-km path for this study. The total path length was subdivided into four nearly equal segments, each equipped with a scintillometer transmitter and receiver pair. The following article describes the terrain variation by segment, discusses the overall scintillometer measurements commenting on pertinent local and synoptic weather conditions, and summarizes the observations/correlations drawn from an analysis of the four simultaneous scintillometer measurements acquired along the full 3.75-km range.

## 1. BACKGROUND

In the spring of 1992, a study characterizing the near-surface optical turbulence along a 3750-m path was conducted at White Sands Missile Range (WSMR), New Mexico. This article describes the meteorological elements and parameters measured, the pre-experiment instrument cross-calibration, the near-surface optical turbulence measurements (NSOTM) experiment and the experiment's initial results.

### 1.1 METEOROLOGICAL MEASUREMENTS

The primary atmospheric optical turbulence parameter sampled was the index of refraction structure function,  $C_n^2$ . By definition,  $C_n^2$  is the ensemble average of the index of refraction ( $n$ ) variance, divided by the  $(2/3)$  root of the distance ( $r$ ) between  $n_2$  and  $n_1$  samples:



$$C_n^2 = \frac{\langle (n_2 - n_1)^2 \rangle}{r^{2/3}}$$

For a more detailed explanation of this parameter, see Tatarski (1961) or Clifford (1978).

Since  $C_n^2$  is related to the vertical heat flux, the vertical temperature difference ( $\Delta T$ ) and incoming solar radiation (insolation) were acquired. These parameters were especially useful, as they provided an unambiguous look at the vertical heat flux sign and estimated magnitude.

In addition to the optical turbulence parameters, basic meteorological elements (temperature, dew-point temperature, wind speed, wind direction, visibility, and cloud cover) were also collected from two SAMS towers. Further details on these measurements are given in Section 2.

## 1.2 PRE-EXPERIMENT SCINTILLOMETER CROSS-CALIBRATION

Prior to the NSOTM experiment, the four  $C_n^2$  sensors, Lockheed Model IV Optical Scintillometers, were mounted at 1 m above ground level (AGL) and subjected to a side-by-side cross-calibration check. The terrain for this test was flat and covered with desert scrub vegetation, similar to the terrain used during the NSOTM. The instrument configuration placed a single scintillometer transmitter at 1 m AGL; 1000 m away, the four scintillometer receivers were mounted side by side, also 1 m AGL. Modified sturdy Celestron tripods supported each sensor. The data, collected every 10 s by a microprocessor and A-D converter, was archived on disk and magnetic tape.

### 1.2.1 Data Analysis Tools

Two types of scintillometer time series plots were employed in the data analysis: an hourly time series displaying 10-s data, and a 24-hr time series comprised of 15-min "bucket" averages. Other time series referenced were temperatures at 2, 4, 8, and 16 m AGL, and insolation sampled at 32 m AGL. The data from 25 March 1992 were selected as a case study based on the relative simplicity of the local weather conditions. On this day, clear skies and light winds dominated, minimizing the heat flux variations.

### 1.2.2 Pre-experiment Results

Review of the time series graphs revealed the following. The diurnal temperature wave amplitude was about 22 C at 2 m AGL. Unstable conditions developed during daytime hours, while inversion conditions occurred during the night. Wave-like temperature traces at night were observed at the 32-m level between 2000 and 2400 MST. The smooth insolation curve displayed almost no solar radiation variations induced by clouds.

The strongest atmospheric optical turbulence was displayed during the midday hours, during the maximum incoming solar flux. Well developed  $C_n^2$  minima occurred around 0700 and 1700 MST. Overlaying the insolation, the four temperature curves, and the  $C_n^2$  time series plots shows that these minima coincided with periods of neutral stability, about 60 min after sunrise and 40 min before sunset. Figure 1 displays the correlation of the vertical temperature gradient passing through the dry adiabat/neutral stability conditions, and the well defined optical turbulence ( $C_n^2$ ) minima, the "neutral event."

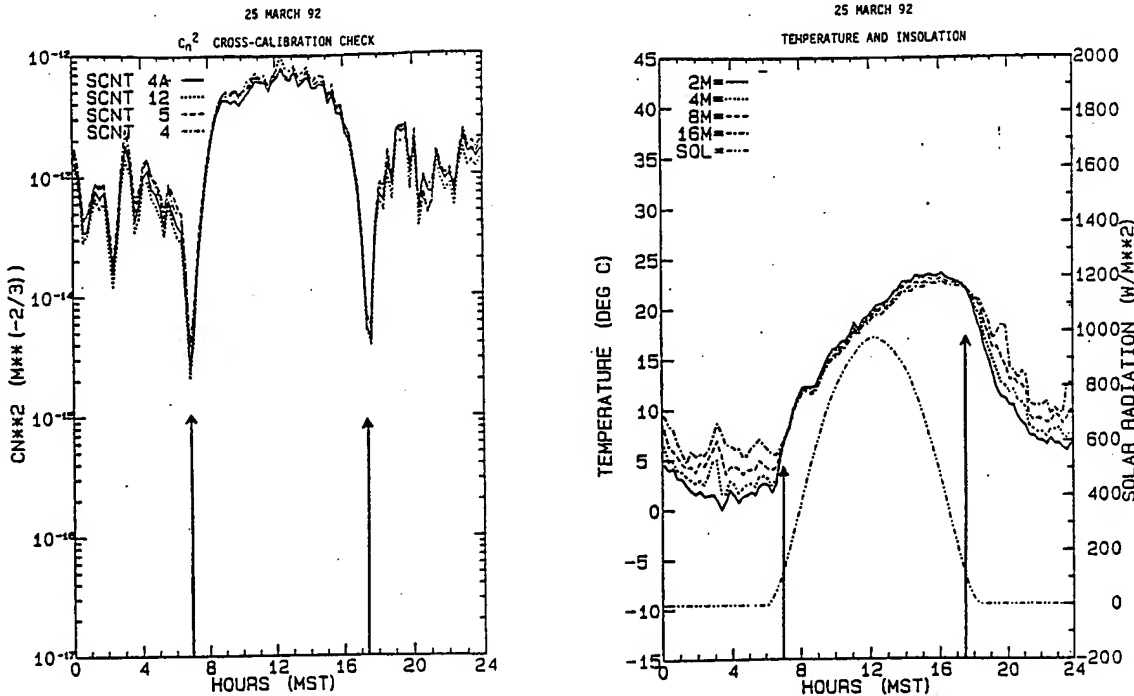


**Figure 1. Day plots of scintillation data, temperatures, and solar radiation for 25 March 1992. a: scintillometer data at 1 m AGL; b: 2-, 4-, 8-, and 16-m temperatures and solar radiation.**

Intercomparing the simultaneous scintillometer measurements, all scintillometers showed essentially the same phenomena. The variation of magnitudes spanned approximately  $0.7 \times 10^{-13}$  during daytime conditions. At night, the strength of the optical turbulence spanned an order of magnitude or more in a short time period. This pattern was interpreted as gravity waves propagating through the stably stratified beam path. While the wave structure affected the turbulence strengths significantly, all scintillometers showed roughly the same variation.

## 2. NEAR-SURFACE OPTICAL TURBULENCE MEASUREMENT EXPERIMENT

The NSOTM experiment conducted in May and June 1992 took place along a 3750-m desert path in the Tularosa Basin, New Mexico. As shown in Fig. 2, the total path was subdivided into three sequential segments of 1000 m (paths 1, 2, 3) and one segment of 750 m (path 4). Table 1 displays the height and approximate location with respect to the four paths of the various meteorological elements sampled.

The following sections present a botanical survey of the four individual paths, as well as a general summary of the weather conditions and optical turbulence measurements acquired during the 1992 June 9-12 data acquisition period.

### 2.1 BOTANICAL SURVEY

The dominant characteristic of the first 1000 m, path 1, was the barren, light-brown soil. Less than 20% of the path was covered with shrubs or grass. The soil surface of the first 275 m was mottled with a low-lying, black fungal growth covering about 40% of the surface.

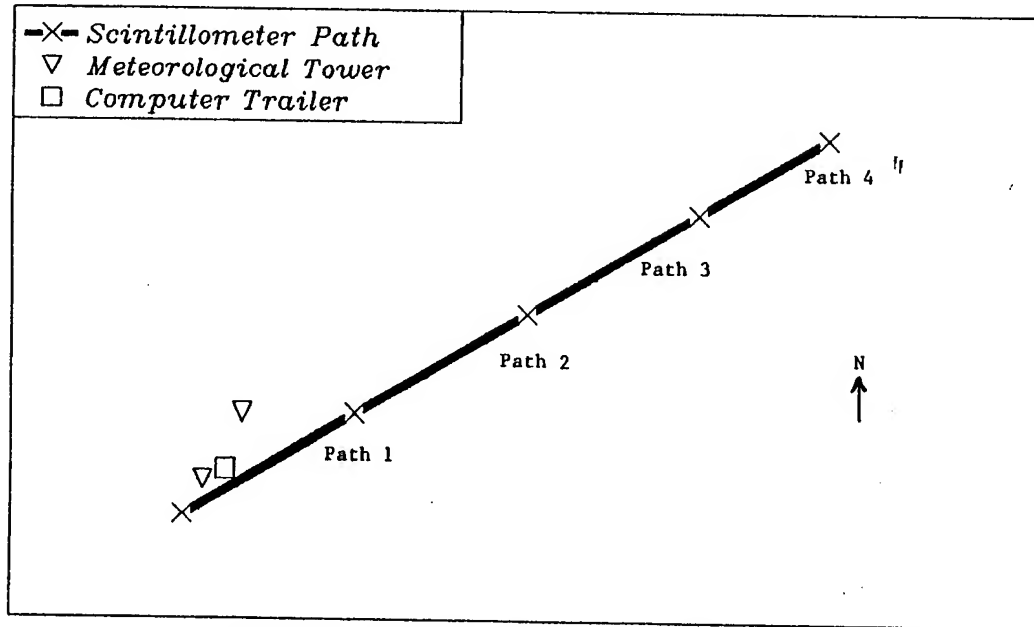


Figure 2. NSOTM Instrument Configuration.

TABLE 1. NSOTM INSTRUMENT PLACEMENT

Element/Parameter	Location (Path)	Height (AGL)
Optical Turbulence	1,2,3,4	1 m
Temperature	1 (Met Tower)	2 m
Dew-point Temp.	1 (Met Tower)	2 m
Wind Direction	1 (Met Tower)	2 m
Wind Speed	1 (Met Tower)	2 m
Visibility	1 (Met Tower)	4 m
Delta Temp.	1 (Met Tower)	16-2 m, 4-0.5 m
Insolation	1 (Met Tower)	1 m

The second 1000 m, path 2, was also dominated (70%) by barren, light-brown soil. The remaining 30% of the ground cover consisted of short (less than 1 ft tall) grasses in the first 500 m and grasses mixed with shrubs in the second 500 m.

Path 3, extending from 2000-3000 m, was about 50% soil and 50% vegetative cover. The increased vegetation consisted of short bunch grass mixed with shrubs. The shrubs included sage, mesquite, and tar-bush. A swath approximately 4 m wide was mowed along the beam path to a height of 5 cm. Vegetation outside this swath stood about 46 cm tall.

The final 750 m, path 4, was fairly densely covered with tall bunch grass (50% ground cover) and shrubs (10% ground cover), with another 40% of the soil surface covered with black fungal growth. A continuation of the 4-m wide mowed path extended the full length of the beam path. Vegetation within the swath was 5 cm tall. Outside the track, vegetation averaged 1 m tall.

## 2.2 WEATHER AND OPTICAL TURBULENCE SUMMARY: 1992 JUNE 9-12

The following sections describe the local and synoptic weather conditions for the 1992 June 9-12 Case. Also presented are the general optical turbulence summaries for each day.

### 2.2.1 Weather and Optical Turbulence: June 9

On June 9, New Mexico was under the destabilizing influence of a passing upper-level trough located over southern Colorado. Residual low-level moisture, in combination with the upper-level trough and intense insolation, resulted in the development of afternoon/evening thunderstorms over the northern and central parts of New Mexico.

During the sampling period (1400-2300 MST), the afternoon skies were mostly clear with scattered cumulus clouds over the Tularosa Basin. Towering cumulus clouds developed in the moist and unstable air over the Sacramento Mountains to the east, as well as to the distant north and west. During the late afternoon and evening, the towering cumulus evolved into thunderstorms. Mid-level debris clouds from distant thunderstorms invaded the Basin's sky, creating broken sky cover by 2100 MST.

Over the experiment site, the atmosphere was clear with over 60 mi visibility. The dew point increased from 40 to 50 °F during the test. The surface winds were light and westerly until approximately 2040 MST, when a thunderstorm outflow boundary shifted the winds to northerly and temporarily increased the wind speed to 10-12 mph. The winds subsided to light and variable by 2145 MST. The air temperature decreased from the day's maximum, 88 °F (1500 MST) to 68 °F by the test's conclusion. The relative humidity ranged from 22% to 52%. Delta-T fluctuated between -1 and -2 °F between 1500 and 1800 MST, then increased in magnitude, crossing through 0 °F at approximately 1815 MST. Delta-T became increasingly positive as the nocturnal inversion developed, reaching a maximum of +10 °F at 2212 MST. Delta-T experienced wide fluctuations, on the order of 4-5 °F, during this inversion.

The afternoon optical turbulence time series displayed large intermittencies that were visually correlated with the occulting of the sun by small cumulus clouds. During this period,  $C_n^2$  decreased from about  $5 \times 10^{-13} \text{ m}^{-2/3}$  (1500 MST) to about  $9 \times 10^{-14} \text{ m}^{-2/3}$  (1700 MST). In the late afternoon, the sun was obscured by cumulus clouds over the San Andreas Mountains, immediately to the west resulting in a 10-min dip in  $C_n^2$ . A combination of low cumulus clouds and higher cirrus clouds moved across the site around 1740 MST, complicating the radiation balance along the beam path. This condition resulted in an abnormal neutral event.

Around 2035 MST, a wind shift line crossed the 3750-m path from north to south, bringing cooler northerly breezes. This feature caused each segment's optical turbulence to decrease from approximately  $7 \times 10^{-14} \text{ m}^{-2/3}$  (2035 MST) to  $2 \times 10^{-14} \text{ m}^{-2/3}$  in the subsequent 15-min period.

### 2.2.2 Weather and Optical Turbulence: June 10

New Mexico's weather for June 10 was dominated by high pressure both aloft and at the surface. As a result of the subsiding air mass, the moisture content decreased from the previous day and the afternoon cumulus cloud development was suppressed. During the test period (1600-2300 MST), the skies were mostly clear, with scattered cumulus and altocumulus clouds. These clouds dissipated after 2000 MST.

The atmosphere over the site was optically clear with over 60 mi visibility. The dew point increased from about 32 °F (1600 MST) to 45 °F (2300 MST). The surface winds were light and westerly, becoming light and variable after 1900 MST. The air temperature decreased from 91 °F (1700 MST) to 69 °F by 2300. The relative humidity ranged from 14% to 16% over the test period. Delta-T increased from -0.5 °F (1700 MST) to 0 °F (about 1830 MST). As the nocturnal inversion developed, delta-T increased to a maximum of +7 °F (2000 MST). Following the establishment of the temperature inversion, delta-T fluctuated widely, on the order of 4 °F over periods of several minutes.

The optical turbulence data for June 10 ranged from a high of  $2 \times 10^{-13}$  (test commencement) to the evening minimum (neutral event) of  $6.5 \times 10^{-15} \text{ m}^{-2/3}$  around 1800 MST. Within 45 min of the neutral event,  $C_n^2$  rose sharply to near  $1 \times 10^{-13} \text{ m}^{-2/3}$ . For the remainder of the evening,  $C_n^2$  behaved erratically, with large intermittencies as large as 2 orders of magnitude. This behavior was typical of nocturnal turbulence, which is largely dependent on wind speed fluctuations in the inversion layer.

### 2.2.3 Weather and Optical Turbulence: June 11

On June 11, a ridge of high pressure aloft remained stationary over New Mexico, while a surface low extended into southern New Mexico from a low center over northern Mexico. During the test period (1000-1600 MST), skies were mostly sunny with scattered cumulus clouds.

Local weather conditions were optically clear with over 60 mi visibility. The dew point remained near 40 °F. The surface winds were light and southeasterly for the first hour, then increased to 10-12 mph until 1315, when the wind shifted slowly to the southwest at 5-10 gusting to 15 mph. The air temperature increased from 89 °F (1000 MST) to the day's maximum of 97 °F (1400 MST). The temperature only dropped 1 °F by the test's completion. The relative humidity decreased from 17% to 12% during the test. Delta-T fluctuated between -1 and -2 °F over the test period.

With the abundance of intense sunshine, the low-level atmospheric optical turbulence was very high.  $C_n^2$  remained at  $3 \times 10^{-13}$  to  $6 \times 10^{-13} \text{ m}^{-2/3}$  throughout the day's sampling period.

### 2.2.4 Weather and Optical Turbulence: June 12

Synoptic weather conditions over New Mexico for June 12 were dominated by a high-pressure ridge aloft, with a low-pressure trough at the surface. During the test period (0800 - 2100 MST), skies were mostly clear with scattered cumulus clouds developing by midday and dissipating after sunset.

The atmosphere over the site was optically clear, with approximately 60 mi visibility. The dew point temperature decreased from the mid-40s in the morning, to the upper 20s by the afternoon. The surface winds were light and northwesterly, becoming southeasterly by midmorning. By afternoon, winds were southwesterly at 5-10 mph, gusting to 15 mph, and subsiding somewhat after sunset. The test's initial air temperature increased from about 75 °F to the day's maximum of 94 °F at approximately 1400 MST. By the test's conclusion, the temperature had decreased to 77 °F. The relative humidity decreased from 30%, (0800 MST), to a minimum value of 10% by 2100 MST. Delta-T fluctuated between -1 and -4 °F shortly before the evening heat flux minimum (1820 MST). Following the neutral event, delta-T increased from 0 to +8 °F, with large intermittencies.

The June 12 atmospheric optical turbulence was between  $3 \times 10^{-13}$  and  $6 \times 10^{-13} \text{ m}^{-2/3}$  until after 1500 MST, when it decreased with the neutral event to approximately  $2 \times 10^{-15} \text{ m}^{-2/3}$ .  $C_n^2$  remained below  $1 \times 10^{-14} \text{ m}^{-2/3}$  for about 25 min during the neutral event.  $C_n^2$  rose sharply to near  $1 \times 10^{-13} \text{ m}^{-2/3}$

during the subsequent hour. The increase continued more gradually, reaching approximately  $2.5 \times 10^{-13} \text{ m}^{-2/3}$  by the tests' completions. The simultaneously sampled optical turbulence data along all four paths displayed a spread of 0.5 to 1 order of magnitude during the final 2 hr of data collection (1900-2100 MST).

### 3. PRELIMINARY INTERCOMPARISON OF SCINTILLOMETER PATH DATA

Isolating the 1992 June 9-12 data set as the representative sample data set, the following three subsets were selected: (1) MAXSUN, representing a period of high heat flux, considered data between 1400 and 1600 MST; (2) NE, for the neutral event, focused on the daily minimum heat flux for June; data ranged from 1700 to 1900 MST; and (3) SUNSET, which centered on the published sunset for the Mountain Time Zone, considered data between 18.2 to 20.2 hrs MST. All data within the three subset intervals were averaged by path and day.

The following sections describe the tools used for the preliminary intercomparison. A discussion of the results, along with two possible causes for the observations, are also presented.

#### 3.1 $C_n^2$ PATH AVERAGES

Table 2 displays the paths from the highest to the lowest average  $C_n^2$  value. In all cases, path 2 measured the lowest  $C_n^2$  average. In 60% of the cases, the highest  $C_n^2$  average was along path 4. For 30% of the cases, path 3 displayed the highest  $C_n^2$  average. Grouping path 4 with path 3 and path 2 with path 1, 60% of the cases show the average  $C_n^2$  value for paths 4:3 to be higher than paths 2:1.

TABLE 2. PATH ORDER OF HIGHEST TO LOWEST AVERAGE  $C_n^2$

Date	MAXSUN	NE	SUNSET
09 June	4,3,1,2	4,3,1,2	4,3,1,2
10 June	3,4,1,2	3,1,4,2	1,4,3,2
11 June	4,3,1,2	No data	No data
12 June	4,3,1,2	3,1,4,2	4,1,3,2

#### 3.2 $C_n^2$ PATH DIFFERENCES

The  $C_n^2$  measurements were further compared by differencing simultaneously sampled  $C_n^2$  magnitudes from the MAXSUN, NE, and SUNSET subsets. An average of these differences was calculated. The results, summarized in Table 3, were translated into positive and negative entries. The cases represented include: M = MAXSUN; N = Neutral Event; and S = SUNSET. The averaged path differential was calculated as implied, that is (2-1) means that the simultaneous samples of path 1 were subtracted from path 2, the differences were then averaged and the sign of the result noted below.

**TABLE 3.  $C_n^2$  PATH DIFFERENCE TREND**

June Date	Path Difference					
	(2-1) <u>M</u> <u>N</u> <u>S</u>	(3-1) <u>M</u> <u>N</u> <u>S</u>	(4-1) <u>M</u> <u>N</u> <u>S</u>	(3-2) <u>M</u> <u>N</u> <u>S</u>	(4-2) <u>M</u> <u>N</u> <u>S</u>	(4-3) <u>M</u> <u>N</u> <u>S</u>
09	- - -	+ + +	+ + +	+ + +	+ + +	+ + +
10	- - -	+ + -	+ - -	+ + +	+ + +	- - +
11	-	+	+	+	+	+
12	- - -	+ + -	+ - +	+ + +	+ + +	+ - +

All cases involving path 2 confirmed that the average  $C_n^2$  sampled between 1000 m and 2000 m was lower than any other path. In contrast, path 4 demonstrated a strong tendency to be greater than the other three paths. That is, 70% of the 4 minus 1 path differential cases were positive. The same was true when path 3 was subtracted from path 4.

Grouping path 4 with path 3, and path 1 with path 2, Table 3 again shows path 4:3 to have the greater  $C_n^2$  averages. Specifically, 88% of the cases show paths 4:3 greater than paths 1:2.

### 3.3 $C_n^2$ PATH DIFFERENCE DISCUSSION

Based on the preliminary survey, the 1992 June 9-12 optical turbulence was the lowest along path 2. In general, optical turbulence was least along paths 1:2 and greatest along paths 4:3. The cause for these observations is still being investigated. Some of the reasons being entertained are ground cover variations and topographical influences on the heat flux along the four paths.

#### 3.3.1 Influence of Ground Cover Variation

A characteristic of the terrain that supports the grouping of paths 3 and 4 and paths 2 and 1 is the fact that paths 3 and 4 had a 4-m-wide swath mowed along the beam path. The height differential of the vegetation within the track to that outside was between 55 and 95 cm. The unmowed area along paths 3 and 4 was densely covered with short bunch grass mixed with shrubs. The first two paths had no mowed area along the beam path. In fact, the dominant characteristic of paths 1 and 2 terrain was the barren, light-brown soil.

One theory is that the height differential of the ground cover created a vertical shear in the airflow, which, when coupled with the normal sharp temperature gradient near the ground, created more optical turbulence than the mostly barren soil of paths 1 and 2. Review of the MAXSUN path differentials shows the consistency with which paths 3 and 4 average greater  $C_n^2$  values than paths 1 and 2. During the NE and SUNSET cases, paths 3 and 4 yielded mixed results. Without a temperature (density) gradient to mix, the vertical wind shear has minimal effect on optical turbulence.

#### 3.3.2 Influence of Topography

While the 0- to 3750-m path was approximately level, the horizons to the east and west were mountainous. Such topography had little effect during the daily maximum heat flux. With the onset of the neutral event, however, the mountains cast a nonhomogeneous array of shadows over the 3750-m path, creating a differential or delayed heating (sunrise) and early cooling (sunset).

Another effect of the surrounding mountains was the daily upslope cumulus. Such cumulus generated random sunblocks and occasional gusty winds (outflow from the cumulonimbus) over the paths. The intermittent occulting of the sun was observed as temporary dips in the individual  $C_n^2$  time series.

#### 4. SUMMARY AND CONCLUSIONS

In the spring of 1992, a near-surface optical turbulence measurement (NSOTM) experiment was conducted at White Sands Missile Range, New Mexico. The purpose of this study was to characterize the low-level (1 m AGL) optical turbulence along a 3750-m arid terrain path. The primary parameter used to characterize the optical turbulence was the index of refraction structure function,  $C_n^2$ . The instrument used to measure  $C_n^2$  was the Lockheed IV Optical Scintillometer. Other meteorological measurements included the basic elements, such as the vertical temperature difference and the insolation.

Prior to the actual study, the four scintillometers were subjected to a side-by-side cross-calibration check along a 1000-m arid terrain path. Data from March 25, 1992 were selected for a pre-experiment case study based on the minimized variation of heat flux observed during that 24-hr period. The results of the preliminary experiment displayed nearly textbook optical turbulence conditions. When the insolation, the four temperature curves, and the  $C_n^2$  plots were overlayed, it was clear that the minima coincided with neutral stability time periods, about 60 min after sunrise and 40 min after sunset (Fig. 1). Intercomparing the simultaneous sampling (March 25 Case), all scintillometers show essentially the same phenomena.

The four scintillometer paths were surveyed and described as:

Paths 1 and 2: dominated by barren, light-brown soil; 30% and less was covered with shrubs or grass.

Paths 3 and 4: a relatively even mix of barren soil and tall grasses and shrubs; a 4-m-wide swath was mowed along the beam path. Ground cover within this path was 5 cm tall. Outside this path the ground cover was between 46 cm and 1 m tall.

Local and synoptic weather conditions for the 1992 June 9-12 case study were mostly sunny, with scattered cumulus clouds. The optical turbulence measurements followed the general diurnal patterns.

Focusing on the 1992 June 9-12 study, three case studies were selected:

<u>Case Reference</u>	<u>Time Interval</u>	<u>Explanation</u>
MAXSUN	14.0-16.0 MST	max heat flux
NE (Neutral Event)	17.0-19.0 MST	$C_n^2$ minimum
SUNSET	18.2-20.2 MST	MST sunset

All data within the time intervals were averaged by path and day. The  $C_n^2$  measurements were further compared by differencing the four paths of simultaneously sampled  $C_n^2$  magnitudes. An average of these differences was calculated and tabulated (Table 3).



Paths 3 and 4 were observed to have higher average  $C_n^2$  values than paths 1 and 2. Path 2 consistently displayed the lowest average  $C_n^2$ . Possible explanations include (1) vegetative ground cover and (2) the topography.

**The ground cover:** Since paths 3 and 4 had a 4-m-wide mowed swath along the beam path, creating a ground cover height differential of 55-95 cm, a vertical wind shear coupled with the normal sharp surface temperature gradient generated higher optical turbulence along these paths. Paths 1 and 2 lack the ground cover variation, and in fact were characterized with mostly barren soil. The MAXSUN, NE, and SUNSET path differentials support this theory by demonstrating that without a temperature (density) gradient to mix (NE/SUNSET), the vertical wind shear has a minimal or mixed effect on optical turbulence.

**Topography:** The NSOTM test was conducted in an arid desert basin along a horizontal path, with a ridgeline several km to the west. Such topography had little effect during the daily maximum heat flux. However, with the onset of the neutral event, the mountains cast shadows over the 3750-m path, creating a differential or delayed heating (sunrise) and early cooling (sunset). Another effect of the mountains was the daily upslope cumulus, which affected the heat flux by generating random sunblocks and occasional gusty winds (outflow from the cumulonimbus) over the paths.

## 5. REFERENCES

- Clifford, S.F., 1978: *The Classical Theory of Wave Propagation in a Turbulent Medium. Topics in Applied Physics. Laser Beam Propagation in the Atmosphere*, v. 25, Springer-Verlag, Germany.
- Tatarski, V.I., 1961: *Wave Propagation in a Turbulent Medium*, Dover Publications, Inc., New York.

## 6. ACKNOWLEDGEMENTS

Special thanks to Elaine Santantonio, for the botanical survey, and to Alan Rishel, for the data management.

## The Three Faces of Clutter

Patti S. Gillespie  
Battlefield Environment Directorate\*  
U.S. Army Research Laboratory  
White Sands Missile Range, NM 88002-5501, U.S.A.

### ABSTRACT

The low, medium, high clutter model has been used in target acquisition models for thermal imagery in the U.S. for some time. This is the model currently being incorporated into the Battlefield Environment Directorate, U.S. Army Research Laboratory target acquisition model TARGAC. This model has been compared to observations of images and calculations of scene statistics. Some correlation of clutter with scene statistics was found. Recently a requirement has surfaced for including the impact of emissive sources on target acquisition. One simple way to do this is to incorporate the effect of emissive sources as clutter and obscuration. Additionally, as the scene shadow model for visible devices has developed, one aspect of scene shadows is the shadowing by small-scale features. This can be modeled as clutter in the sense of low, medium, or high clutter, depending on the amount and type of cloud cover. Features in the terrain may have shadows that contribute significantly to the image. Sharp cloud shadows over a flat landscape can simulate more clutter in the image. This paper discusses the three ways in which the simple low, medium, high clutter model is being and will be used in TARGAC.

### 1. INTRODUCTION

Clutter is a quantity that has been used in target acquisition models for many years. In general, clutter has been used to quantify the confusion of the observer when there are objects in the observed image that may look like or mask the target. This concept has been used principally for thermal models. In fact, the first use of the low, medium, high (LMH) clutter model described here is in the usual sense; a combination of scene contrast and complexity for thermal images. This model has

---

\*formerly U.S. Army Atmospheric Sciences Laboratory

existed for a number of years and is used in many target acquisition tactical decision aids (Petzko, 1989). The second use of this model is for emissive sources modeling, and is an extension of the traditional application of the idea of clutter. The idea here is the incorporation of the effect of emissive sources simply, using both the concept of clutter and extinction. Finally, the idea of clutter is extended to the visible wavebands for scene shadowing. Small-scale features and small clouds under partly cloudy conditions can throw shadows (dark areas) over an otherwise bright landscape. These dark splotches in the visible image can cause confusion for the observer and result in the effect that is called clutter. This is similar to the effect called clutter for infrared wavelengths. The extension of clutter to visual wavelengths was developed by Snapp et al. (1992) for the U.S. Army Research Laboratory's target acquisition tactical decision aid.

## 2. LOW-MEDIUM-HIGH MODEL FOR THE IR

The clutter model now in use in the ASL target acquisition model is the low, medium, or high (LMH) clutter model. This is a traditional application of clutter in which clutter is used to quantify confusing elements in the "scene." The word scene is in quotation marks because the clutter model described here is incorporated into target acquisition models that calculate the probability of detection or the acquisition range, and these models are based on sensor performance characteristics, not imagery. Schmieder (1983) tried to quantify this LMH clutter designation by the signal to clutter ratio. The signal to clutter ratio is based on gray levels of a given scene. The actual use of the LMH model is subjective, but the signal to clutter ratio concept is not. The LMH clutter model is dependent on four quantities: target to background contrast, background to background contrast, target resolution, and scene complexity. It is the scene complexity that is subjectively designated as low, medium, or high. Some preliminary work (Silk, 1990) indicates that there may not always be a good correlation between the signal to clutter ratio and designation of clutter under the LMH model. Another study indicates that there may be correlation of image statistics to the LMH clutter model (Gillespie, 1992). A complete literature search in this area has not been completed, and there may be other references.

The scene contrast and scene complexity are taken together in a matrix form to determine the clutter level. Table 1 shows how clutter is designated in this matrix. The scene contrast is low if the contrast among the four backgrounds chosen is between 1 and 2°K, medium for delta T's of 2° to 4°K, and high for delta T's of greater than 4°K. Scene complexity is judged subjectively by the user of the model to be low, medium, or high based on viewing images that are examples of low, medium, or high

complexity.(MARK III TDA Users Manual, 1989) Low scene complexity images would have few objects in the image that are near the target or could be confused with the target. High scene complexity images have many objects in the scene near the target that can be confused with the target. The scene clutter is determined by finding the appropriate scene contrast on the vertical axis of the matrix in Table 1 and reading across to the appropriate scene complexity on the horizontal axis of the matrix.

Once the decision matrix is used to find the clutter category, the low-medium-high clutter level is used to scale the MRC value as follows. Low clutter scales the MRC value by a value of 0.5, medium clutter scales the MRC value by 1.0, and high clutter scales the MRC value by 2.5. The scaled MRC value is then used by the target acquisition model to calculate probability values.

TABLE 1. Classification Scheme for clutter categories in the Low-Medium-High Clutter Model.

		SCENE COMPLEXITY			
		LOW	MEDIUM	HIGH	
SCENE CONTRAST	LOW $1^{\circ} < K < 2^{\circ}$	LOW	LOW	LOW	
	MEDIUM $2^{\circ} < K < 4^{\circ}$	LOW	MEDIUM	MEDIUM	
	HIGH $K > 4^{\circ}$	LOW	MEDIUM	HIGH	

Since the LMH model depends on the contents of a scene, it would be reasonable to expect that the gray levels of scene may be sorted in some way statistically that would correspond to low, medium, or high clutter. A recent study (Gillespie, 1992) investigated this idea. The scenes chosen for this study were first judged for the scene complexity, and then scene contrast was determined from gray levels. These same scenes were then used to calculate mean and standard deviation values of the gray levels. The main trends drawn from this study were that the average gray level for all clutter cases- low, medium, or high, was about the same. The average standard deviation for both the low and medium clutter cases was about the same, but the high clutter cases had a higher average standard deviation. In a plot of number of pixels versus gray level, the low and high scene complexity cases had a single peak or mode and the medium scene complexity cases had two modes. This causes the medium clutter

cases to have two modes and the low and high clutter cases to have one mode. Some low clutter cases do have two modes, but these are all for cases of medium or high scene complexity, but low contrast.

This study was done with scenes of nearly the same types of images, that is, imagery was taken from three positions over a three week period during which the weather was very constant and mild. The view from each of the three positions from which imagery was taken was very similar in scene content. For these reasons, one would not expect biases from the different scenes, such as varying sky content effecting the average, standard deviation, or modes of gray levels.

This comparison can be likened to a similar comparison of the LMH clutter model to calculations using the Schmieder signal-to-clutter ratio (Schmieder, 1983; Silk, 1990) for which the results are not published. This study did not find a conclusive trend between the LMH clutter model and the Schmieder signal-to-clutter ratio.

### 3. EMISSIVE SOURCE MODEL

The emissive source model that is being incorporated into TARGAC will build on the ideas described in the preceding section on the LMH model. Since an emissive source can provide both obscuration and bright confusing images in the infrared, the emissive source model will use the smoke option in TARGAC for the obscuration component and also specify high clutter.

As discussed previously (Gillespie, 1992), thermal images have been determined to be either low, medium, or high clutter and then image statistics for those images were calculated. Images specified as high clutter generally had larger standard deviations of the gray level than images specified as low or medium clutter. Emissive sources provide the complexity to a scene that is generally associated with high clutter. For that reason, when emissive sources are specified, the LMH clutter model also will be invoked specifying high clutter. Images of emissive sources often appear to have high scene complexity, but the scene contrast also must be high to result in high clutter. For this application, scene contrast will assumed to be high (greater than  $4^{\circ}\text{K}$ ) because emissive sources should provide high contrast in the scene elements.

The point that a scene with emissive sources might have a low or medium contrast between backgrounds provides the main objection to this formulation. The low or medium contrast mitigates the effect of the high complexity and results in either low or medium clutter. An extremely complex image of emissive sources might make it very difficult to discern a "hot" target until the target is very close, resulting in very short acquisition

ranges. Medium or low contrast in the model results in normal or longer acquisition ranges. The designation of emissive sources in a scene as high clutter is something that can be easily changed if data are obtained that shows that it should be changed.

The emissive source model being proposed here also mixes in the effect of attenuation due to the smoke; decreasing acquisition ranges based on attenuation due to the emissive source. The smoke model offers some choice for smoke produced (low, medium, high) scaling the extinction properly. So, in reality, the emissive source model has two factors, one factor that decreases the acquisition range due to extinction, and another factor that decreases the acquisition range through confusion (clutter).

Some immediate verification of this concept is planned. Images generated emissive sources under realistic conditions by Dr. Dorothy Bruce of the U.S. Army Research Laboratory BED will have images statistics calculated for various levels of scene complexity to determine if the images of emissive sources correspond to trends in image statistics discussed in an earlier paper by this author and described here briefly. This work is planned for the near future.

#### 4. SHADOWING BY SMALL-SCALE FEATURES MODEL

The shadowing by small-scale features model is part of the scene shadow program being developed for TARGAC. The shadowing by small-scale features is one of three main ideas in the shadow program. Small-scale features refer to objects whose size and appearance are nearly that of the targets. The importance of small-scale features is that these objects add clutter to the target scene. The other two parts of the scene shadow program are shadowing by clouds and shadowing by large scale features. The effort to implement these changes will occur in the next two years.

Four steps are defined to implement the shadowing by small-scale features. These steps are (1) describe the small-scale scene features and their shadows, (2) discuss the relationship between small-scale features, shadows, and clutter with respect to target acquisition; (3) describe the temporal and spatial characteristics of shadows, including diurnal, latitudinal, seasonal, and terrain effects; and develop an approach to include shadows as a modification to clutter in TARGAC.

Here the clutter would be for visual devices, not thermal. Schmieder et al. (1982) have described clutter effects on target acquisition very extensively. Their conclusions are applied to the thermal imaging sensor, however, they state that the same principles would apply to an observer performing target acquisition tasks with any imaging device. Schmieder et al.

(1982) categorize scenes with targets in terms of a signal to clutter ratio (SCR), ratioing target contrast to clutter contrast. The thermal contrast used for the target contrast is replaced by brightness contrast between target and background for visual imagers. Theoretically, shadows can even be important for image intensifying devices used under moonlit conditions at night (Snapp et al., 1992). This causes scenes with even more spatial content than the original.

One experiment has been conducted on the impact of small-scale scene shadows on target acquisition. This is the SEEKVAL test using a terrain table in a joint agency project (SEEKVAL, vol. 1 & 2, 1975). This terrain table experiment staged observers in aircraft under different solar elevation and azimuth conditions looking at a scene characterized by mixed coniferous and deciduous trees and shrubs as clutter objects. Acquisition performance was determined by the frequency of correct target detections and mean detection range. The study concluded that longer scene shadows so have an adverse effect on target acquisition.

One can note that scene shadows, particularly those of the target can have the opposite effect from above on target acquisition. Target shadows can increase target size and contrast, thereby making the target more visible to the observer. This will be considered as a separate issue in the development of the TARGAC model.

The shadows discussed in this paper are cast by objects illuminated by the sun or the moon, thus limiting this model to visual or near-IR devices. There are a few conditions that limit the sun and moon as direct sources of illumination. To be an effective source of illumination that can produce shadows the source must be above the horizon. Twilight conditions (elevation 0 to minus 18 degrees) produce diffuse lighting that does not produce an effective shadow. When the phase of the moon decreases from full to quarter, the illumination level decreases by over an order of magnitude. Night vision goggles (NVG, second generation) are generally restricted to operating conditions of lunar phase of greater than 23 percent. Newer NVG can operate under starlight conditions, but the effect of shadows under these conditions is small. Snapp (1992) also shows that indirect solar illumination during twilight can exceed most solar illumination at low elevation angles. Snapp then assumes that most lunar shadows will occur when the solar elevation is below 18 degrees. This conservative approximation does not consider the shadowing that occurs for half to full moon conditions when the sun is between minus 12 and minus 18 degrees.

Shadow occurrence as a function of solar or lunar position (azimuth and elevation), latitude, season, day, and time were studied to determine the maximum effect (Snapp et al., 1992). Snapp gives an expression for shadow length based on the height

of the object  $z$ , and the zenith angle  $\theta$  of the sun or moon,

$$L = z \tan \theta \quad (1)$$

for level ground. The situation is more complicated for sloping background, but expressions can be found to express the shadow length in these circumstances also (Snapp, 1992). Figures 1 through 3 depict the variation of shadow length as a function of time of day, season, and latitude for specific places and times of the year. These figures use normalized shadow length where the height of the object is set to one. The normalized shadow length then reduces to

$$L = \tan \theta \quad (2)$$

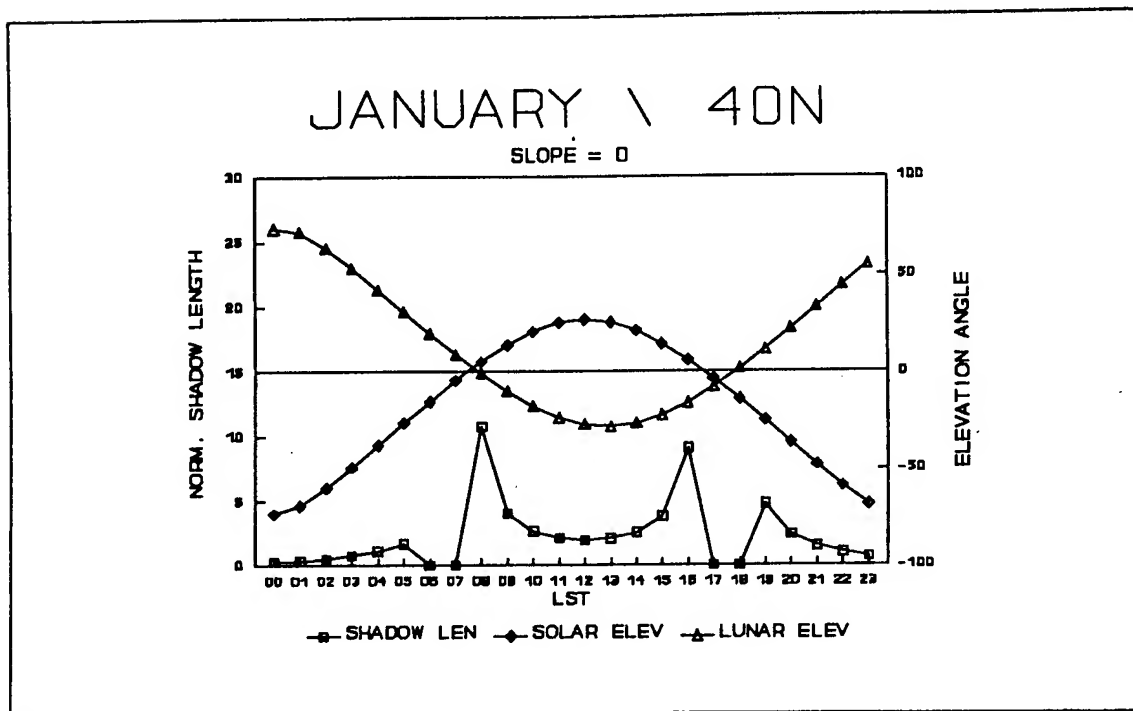


Figure 1. Normalized shadow length for January, 40N latitude.



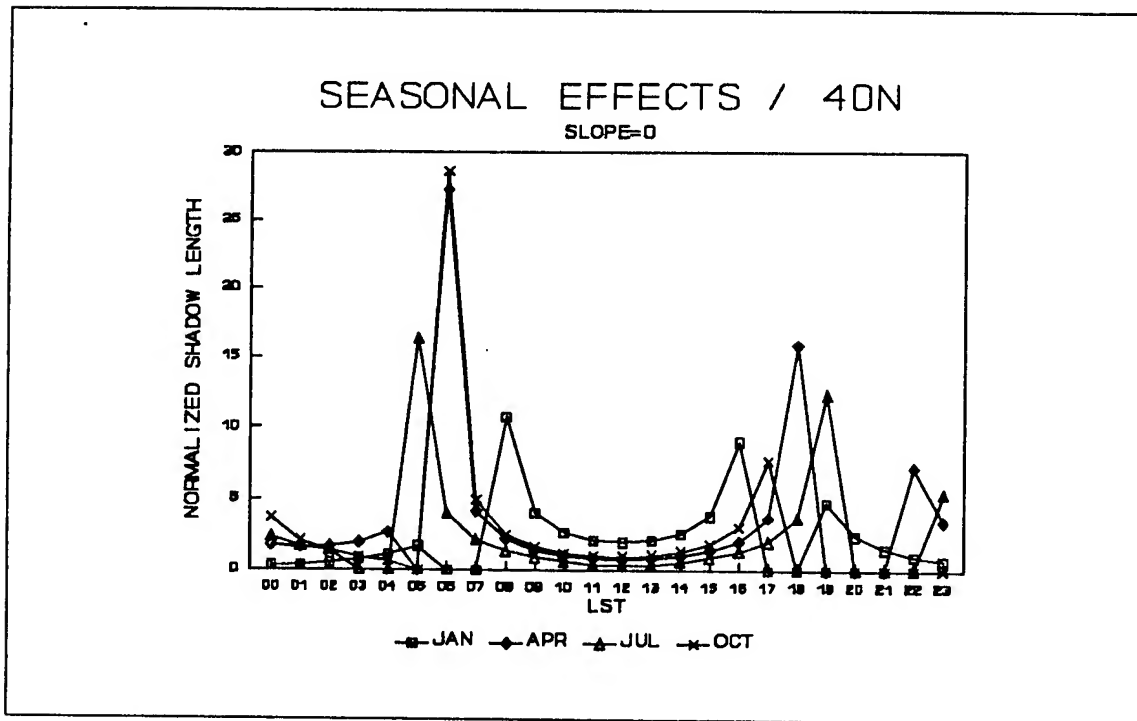


Figure 2. Seasonal effects on shadow length.

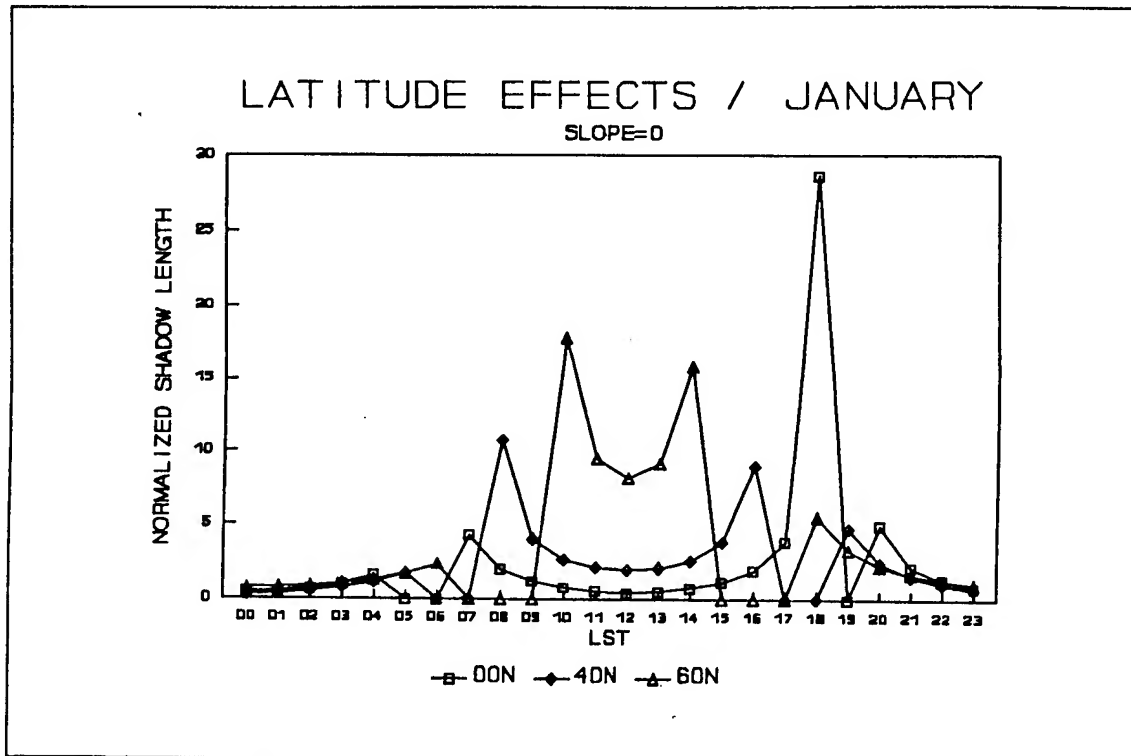


Figure 3. Latitudinal effects on shadow length.

The shadow length for time of day is a maximum for sunrise and sunset, as expected. The example is chosen for maximum effects, but the length of the shadows is about three times the height of the object during the middle part of the day and up to ten times the height of the object at sunrise and sunset. This should produce a significant effect on the visual images.

The seasonal effect on shadow length shows that January stands out as having longer shadows during the midday hours than other months. January also exhibits less tendency for very long shadows around sunset and sunrise. These shadows vary from 5 to 10 times the height of the object. October has the longest shadows in Figure 2, and these are at sunrise and are 25 times the height of the object. April has the second longest shadows in Figure 2, and these are at sunset. July shows significant shadows at sunrise and sunset, almost as long as April's shadows. The shadows for July and April are about 12 to 15 times the height of the object. These shadows also should produce a significant effect on the visual images.

Under latitudinal considerations at the equator, the shadow length remains short and constant, except near sunrise and sunset. To contrast this, calculations for 60 degrees N show the dominance of reduced daylight hours and very low sun angle in producing a very shadowed environment for a few hours. Once again these shadows vary from 5 to 25 times the height of the object.

## 5. COMMENTS

Three diverse phenomena; thermal clutter, emissive source effects, and small-scale feature shadowing; are tied together with a common description as clutter. Two of the models apply to the infrared and the third to the visible. The common thread is that in all three cases there are confusing images to the sensor that interfere with the target acquisition process.

The basic LMH clutter model will be available in the TARGAC in EOSAEL in the very near future. The emissive sources model should be available in TARGAC within the next year. The scene shadow model is part of a two-year program that is slated to start this fall.

Further quantification of the clutter process may enable modelers to make a more precise calculation of the impact of clutter in target acquisition models. The current choice of low, medium, or high scene complexity based on standard images lacks rigor. The use of image statistics is useful to image models, but cannot be applied currently to computational models. We hope to investigate these ideas in the coming months.

## ACKNOWLEDGMENTS

The scene shadow model described in this paper was developed by Michael Snapp at Pacific Sierra Research Corporation and Paul Hilton and Melanie Gouveia at Hughes-STX. This research is ongoing and the author wishes to acknowledge the fine efforts of these collaborators. Figures 1 through 3 are taken from the final report of the Phase 1 SBIR that Pacific Sierra Research Corporation had with the U.S. Army Atmospheric Sciences Laboratory in 1991.

## REFERENCES

Gillespie, Patti, 1992, "A Comparison of Clutter Models for Target Acquisition Modeling," In Proceedings of the Second Symposium on Measuring and Modeling the Battlefield Environment, Paris, France.

1989 MARK III EO Tactical Decision Aids for Microcomputer Systems Users Manual, STX Scientific Report No. 38, Hughes-STX Corporation, 109 Massachusetts Ave., Lexington, MA 02173.

Petzko, D.R., 1989, "Target Acquisition Model Enhancements", Final Report-WAO 8809 Task 1, Volume I, OMI-350, Optimetrics, Inc., 3115 Professional Dr., Ann Arbor, MI48104-5131.

Schmieder, D.E., M.R. Weathersby, W.M. Findlay, and T.J.Doll, 1982, "Clutter and Resolution Effects on Observer Static Detection Performance", AFWAL-TR-82-1059, Georgia Tech Research Institute AD-B071-777, Atlanta, GA 30332.

Schmeider, David E. and Marshall R. Weathersby, 1983, IEEE Transactions on Aerospace and Electronic Systems, AES-19:(4).

SEEKVAL Joint Test Force, 1975, "SEEKVAL Project 1B1 Final Report Aided Visual Terrain Table Experiment, Volume 1", OUSDRE, Washington, D.C., AD-B085-531.

SEEKVAL Joint Test Force, 1975, "SEEKVAL Project 1B1 Final Report Aided Visual Terrain Table Experiment, Volume II", OUSDRE, Washington, D.C., AD-A145-164.

Silk, James, 1990, Institute for Defense Analysis, Presentation at the In Progress Review of the ACQSIM Working Group.

# MARK III ELECTRO-OPTICAL TACTICAL DECISION AID

## SENSOR PERFORMANCE MODEL EVALUATION

Kimberley Scasny and J. Michael Sierchio  
Naval Research Laboratory Monterey  
Monterey CA 93943-5006

### ABSTRACT

The Mark III Electro-Optical Tactical Decision Aids (EOTDAs), developed in a tri-service effort, predict the performance of electro-optical (EO) sensors under various environmental conditions. The EOTDAs consist of three microcomputer based programs supporting infrared, laser and television systems. Each program is comprised of three sub-models: an atmospheric transmission model, a target contrast model, and a sensor performance model. Validation of the EOTDAs has been conducted for Air Force and Army EO systems by the Air Force R&D community. The Naval Research Laboratory Monterey is currently evaluating the sensor performance model portions of the EOTDA for Navy and Marine Corps EO systems. The results of this evaluation will be used to design formal validation tests of the sensor performance model in the future. A database of operational performance and environmental data collected during aircrew training missions is being compiled as part of this study. This paper discusses the data collection and analysis techniques used and reports the preliminary results of the evaluation.

### 1. INTRODUCTION

Air Force weather personnel have been providing weather support for Air Force and Army electro-optical (EO) systems since the early 1980's. This support has evolved from nomogram/look-up tables to calculator Electro-Optical Tactical Decision Aids (EOTDAs) to what is used today, the microcomputer EOTDA (Higgins et al., 1990; and Hilton et al., 1990). Although Navy operational use did not occur until two years ago, the Navy began research into adapting the Air Force's EOTDA for Navy and Marine Corps sensors in 1987.

With the increase of tensions in the Persian Gulf in 1990 the Naval Oceanography Command recognized the immediate need for the EOTDA to support Fleet operations. This decision was made with the knowledge that validation of the EOTDA sensor performance model for Navy/Marine Corps specific sensors had not been accomplished. Now that the EOTDA is being used operationally, it is imperative to ascertain the accuracy and tactical effectiveness of the target acquisition and lock-on ranges provided by the EOTDA.

The Naval Research Laboratory Monterey has been tasked to conduct an evaluation of the Mark III EOTDA Sensor Performance Model for each Navy/Marine Corps sensor. This evaluation uses shore and ship based

oceanography/ meteorology personnel in a cooperative effort with the aviation communities to collect operational and environmental data. Analysis of the databases will provide insight into the accuracy of the predicted performance of the sensor calculated by the EOTDA. This will be accomplished by comparison of the calculated performance values with the observed performance of the sensor gathered during operational training missions.

Sensor detection data on Forward Looking Infrared (FLIR) and Night Vision Goggle (NVG) sensors will be collected from various organizations throughout the Department of the Navy. An information card has been developed to gather the needed sensor and environmental data. This collection effort is currently in the very early stages. A myriad of prospective participants have been contacted and a few have just recently begun initial collection efforts. Even with numerous ongoing projects, very limited data for FLIR systems have been acquired, and NVG data is virtually nonexistent at this time.

Meteorology data for the evaluation is provided gratis and for the most part so is the operational information. However, due to budget cuts for aviation, especially in the Strike Warfare (STW) community, funding must be provided for dedicated data collection flights. NRL has provided funding for one such collection episode thus far. Two dedicated STW flights have already been completed with two to three more scheduled for late October 92. This paper will review the ongoing efforts to collect various Navy/Marine Corps FLIR and NVG sensor data and the preliminary analysis of acquired data.

## 2. METHODOLOGY

As discussed previously, the Navy's EOTDA evaluation requires the comparison between calculated and observed sensor performance. To acquire actual sensor performance, data is being collected in conjunction with normal training missions, Navy and DOD test programs, ship deployments, Reserve cruises, Naval exercises, and Naval Postgraduate School experiments. Potential participants, in both the aviation and weather communities, are contacted to discuss the project and to determine if their operational mission will support FLIR and NVG data collection efforts.

To collect both operational and meteorology data a two-sided "knee-board" information card (Figure 1a-c) is sent to the participants. Side one of the data cards, Figure 1a (1b), is used by the weapon system operators for recording FLIR (NVG) sensor information. Three types of detection ranges are requested: detection range, where the FLIR operator can first distinguish the presence of a target from the background; the recognition range, where the operator can distinguish the target within its classification (e.g. a truck, ship, etc.); and the identification range, where the operator can distinguish that the target is the specific "detection target" (e.g. Ford truck, Frigate, etc.). The NVG data card specifically asks for information on the windscreen condition and amount and type of artificial ambient light. These factors can degrade the performance of the NVGs and help to explain possible discrepancies between the calculated and observed NVG detection ranges.

Figure 1c is the reverse side for each of the FLIR and NVG cards and is used to record meteorological information by the oceanography/meteorology personnel. In addition to the card, the weather personnel are requested to send copies of their observation sheets for the day preceding and the day of the data collection. This provides approximately 12 to 24 hours of

DATE: \_\_\_\_\_ DETECTION TIME (LOCAL): \_\_\_\_\_  
A/C TYPE: \_\_\_\_\_ A/C SIDE #: \_\_\_\_\_  
SENSOR TYPE: \_\_\_\_\_ EVENT #: \_\_\_\_\_  
PILOT: \_\_\_\_\_ BN: \_\_\_\_\_  
TARGET DESCRIPTION: \_\_\_\_\_  
TARGET LAT: \_\_\_\_\_ LON: \_\_\_\_\_  
TARGET HEADING: \_\_\_\_\_  
TARGET ELEVATION: \_\_\_\_\_  
DETECTION RANGE (nm): \_\_\_\_\_ FOV: N W  
RECOGNITION RANGE (nm): \_\_\_\_\_ FOV: N W  
IDENTIFICATION RANGE (nm): \_\_\_\_\_ FOV: N W  
BACKGROUND TYPES: \_\_\_\_\_  
ALTITUDE AT DETECTION (ft msl): \_\_\_\_\_  
AIRCRAFT HEADING: \_\_\_\_\_  
SENSOR HEADING (relative to A/C nose): \_\_\_\_\_  
PRECIP? Y N OAT (°C): \_\_\_\_\_  
OBSERVED WX AT TGT: \_\_\_\_\_  
REMARKS: \_\_\_\_\_  
\_\_\_\_\_  
\_\_\_\_\_

Figure 1a. FLIR Data  
Information Card

DATE: \_\_\_\_\_ DETECTION TIME (LOCAL): \_\_\_\_\_  
A/C TYPE: \_\_\_\_\_ SENSOR TYPE: \_\_\_\_\_  
PILOT: \_\_\_\_\_ COPILOT: \_\_\_\_\_  
FCST ILLUMINATION \_\_\_\_\_ LUX  
TARGET LAT: \_\_\_\_\_ LON: \_\_\_\_\_  
TARGET DESCRIPTION \_\_\_\_\_  
DETECTION RANGE (nm): \_\_\_\_\_  
RECOGNITION RANGE (nm): \_\_\_\_\_  
IDENTIFICATION RANGE (nm): \_\_\_\_\_  
BACKGROUND AT TGT: \_\_\_\_\_  
TARGET HEADING: \_\_\_\_\_  
ALTITUDE AT DETECTION (ft msl): \_\_\_\_\_  
AIRCRAFT/SENSOR HEADING: \_\_\_\_\_  
AMOUNT AMBIENT LIGHTING PROVIDED BY: (circle)  
TOWN CITY FLARE ORNANCE VEHICLE OTHER  
(circle) NONE LOW MED HIGH VERY HIGH  
WINDSCREEN CONDITION: (circle) DIRTY BUGS PITTED  
(circle) POOR FAIR GOOD VERY GOOD  
OBSERVED WX AT TGT: \_\_\_\_\_  
REMARKS: \_\_\_\_\_  
\_\_\_\_\_  
\_\_\_\_\_

Figure 1b. NVG Data  
Information Card

TARGET LATITUDE \_\_\_\_\_ LONGITUDE \_\_\_\_\_  
MAX/MIN TEMP PREVIOUS 24 HRS \_\_\_\_\_ / \_\_\_\_\_  
DATE \_\_\_\_\_ TIME \_\_\_\_\_ TEMP \_\_\_\_\_  
DEWPT \_\_\_\_\_ VIS (mi) \_\_\_\_\_ AEROSOL TYPE(1-14) \_\_\_\_\_  
PRECIP TYPE: NONE RAIN SNOW RATE: LT MOD HVT  
TARGET WINDS: DIRECTION \_\_\_\_\_ SPEED (kts) \_\_\_\_\_  
CLOUDS: 0-NONE 1-St/Sc 2-Cu/Cb 3-Ac/As  
4-Ns 5-Thick Ci/Cs 6-Thin Ci/Cs  
LOW: TYPE 0 1 2 4 HT(hft) \_\_\_\_\_ AMT(1/8s) \_\_\_\_\_  
MID: TYPE 0 2 3 4 HT(hft) \_\_\_\_\_ AMT(1/8s) \_\_\_\_\_  
HIGH: TYPE 5 6 HT(hft) \_\_\_\_\_ AMT(1/8s) \_\_\_\_\_  
INVERSION HEIGHT \_\_\_\_\_ U/L INFO AVAIL Y N  
U/L T \_\_\_\_\_ TO \_\_\_\_\_ VIS \_\_\_\_\_ AEROSOL \_\_\_\_\_  
  
TO BE COMPLETED BY MET PERSONNEL ONLY

Figure 1c. Reverse Side of Data Information Card,  
Meteorology Information

background information for input into the EOTDA. Most of the meteorology information needed is straightforward and requires no explanation. The exception is the aerosol type. The EOTDA atmospheric transmission model requires the input of one of eight aerosol profiles to represent aerosol extinction. These eight aerosol models are: 1) advection fog, 2) radiation fog, 3) rural, 4) urban, 5) maritime, 6) Navy maritime, 7) desert, and 8) tropospheric. The profile that best represents the air mass over the target area is input into the EOTDA.

Complete target and background information is crucial to the accuracy of the EOTDA predictions. Sensor operators are asked to choose detection targets that are closest in description of those targets in the EOTDA Target List or those that can be reproduced using the generic building model or off-menu target option. To obtain the operational sensor detection data FLIR and NVG operators are asked to begin approach of the target from beyond maximum detection range and to maintain a constant altitude and airspeed. As the aircraft nears the target the operator can log the appropriate data. If possible, multiple passes over the target at differing altitudes and approach angles are accomplished. After the flight is completed the data card is handed over to weather personnel for completion of weather data on the reverse side of the card.

Upon return of the completed data cards to the Naval Research Laboratory Monterey, they are categorized by sensor type and data is input into the Mark III EOTDA Version 2.2. (This version is an update to the fielded EOTDA version 2.0 and was specifically used during DESERT SHIELD/STORM operations.) Targets are reconstructed to the best of the EOTDA's ability. The EOTDA is run for each completed data card and the calculated output is then compared to the observed values of detection.

### 3. RESULTS AND DISCUSSION

In spite of vigorous efforts to recruit EOTDA evaluation advocates and the enthusiastic replies from the operational community to participate in collecting sensor detection information, very little data has been received so far. Data collection programs are continuing, however, and with the influx of new monies for fiscal year '93, more dedicated data collection flights are scheduled. Currently sensor data from three FLIR sensors has been obtained and preliminary analysis has begun. The following paragraphs will discuss the comparison of the observed versus predicted detection ranges for each of the sensors.

Observed and EOTDA predicted sensor data collected from the sensors are shown in Table 1. In Figure 2 the observed ranges are plotted against the predicted ranges calculated from the EOTDA Version 2.2 for each sensor. Due to the classification of sensor data information associated with sensor nomenclature, the sensors will be identified in this paper by sensor 1, sensor 2, and sensor 3.

Sensor 1 is a relatively old FLIR with a very narrow field of view (FOV) used extensively to acquire targets within a 5 to 7 nautical mile range. Other airborne equipment is used to acquire the target prior to this FLIR operational envelope. The data listed in Table 1 was acquired using this tactic, consequently biasing the outcome of the data comparison. The EOTDA significantly overpredicts the performance of sensor 1. It may be that the EOTDA is not far off. The sensor may be able to detect the target at longer ranges, should the FLIR be turned on earlier. Most often than not when using

Table 1. SUMMARY OF OBSERVED AND PREDICTED DATA

Sensor #/Event #	FOV	Target	Background	Observed Ranges *	Predicted Ranges *
1/1	N	POL (whole)	Grass	13.00	28.00
1/1	N	POL (DMPI)	Grass	13.00	17.00
1/1	N	POL (whole)	Dirt road	13.00	28.00
1/1	N	POL (DMPI)	POL tank	13.00	12.00
1/2	N	POL (whole)	Grass	13.90	27.00
1/2	N	POL (DMPI)	Grass	13.90	16.00
1/2	N	POL (whole)	Dirt Road	13.90	27.00
1/2	N	POL (DMPI)	POL tank	13.90	16.00
1/3	N	POL (whole)	Grass	14.00	27.00
1/3	N	POL (DMPI)	Grass	14.00	16.00
1/3	N	POL (whole)	Dirt road	14.00	26.00
1/3	N	POL (DMPI)	POL tank	14.00	7.75
1/4	N	Building	Foliage	6.00	14.00
1/4	N	Building	Dirt road	6.00	2.75
1/4	N	Building	Rock	6.00	8.50
1/5	N	Hanger	Concrete	7.00	21.00
1/5	N	Hanger	Asphalt	7.00	22.00
1/6	N	Hanger	Concrete	8.50	28.00
1/6	N	Hanger	Asphalt	8.50	31.00
1/7	N	Building	Foliage	2.00	3.50
1/7	N	Building	Dirt road	2.00	7.50
1/7	W	Building	Rock	2.00	8.00
1/8	W	Bridge (whole)	Trees	5.00	18.00
1/8	W	Bridge (DMPI)	Trees	5.00	13.00
1/8	W	Bridge (whole)	Water	5.00	19.00
1/8	W	Bridge (DMPI)	Water	5.00	16.00
1/8	W	Bridge (whole)	Grass	5.00	18.00
1/8	W	Bridge (DMPI)	Grass	5.00	14.00
1/9	N	Building	Asphalt	2.00	2.50
1/9	N	Building	Foliage	2.00	3.00
1/9	N	Building	Road	2.00	2.50
1/10	N	Hanger	Concrete	3.50	19.00
1/10	N	Hanger	Asphalt	3.50	21.00
1/11	N	Building	Trees	3.00	24.00
1/11	N	Building	Foliage	3.00	25.00
1/11	N	Building	Asphalt	3.00	11.00
1/12	N	Building	Asphalt	4.00	3.25
1/12	N	Building	Water	4.00	22.00
1/12	N	Building	Grass	4.00	15.00
2/1	N	Ship	Water	4.00	13.00
2/2	N	Ship	Water	4.00	13.00
2/3	W	Ship	Water	2.00	14.00
2/4	W	Ship	Water	2.00	14.00
2/5	W	Ship	Water	2.00	14.00
3/1	N	Ship	Water	8.80	8.50
3/2	N	Ship	Water	10.00	9.00
3/3	N	Ship	Water	7.50	9.25

\* Ranges are in relative units of length



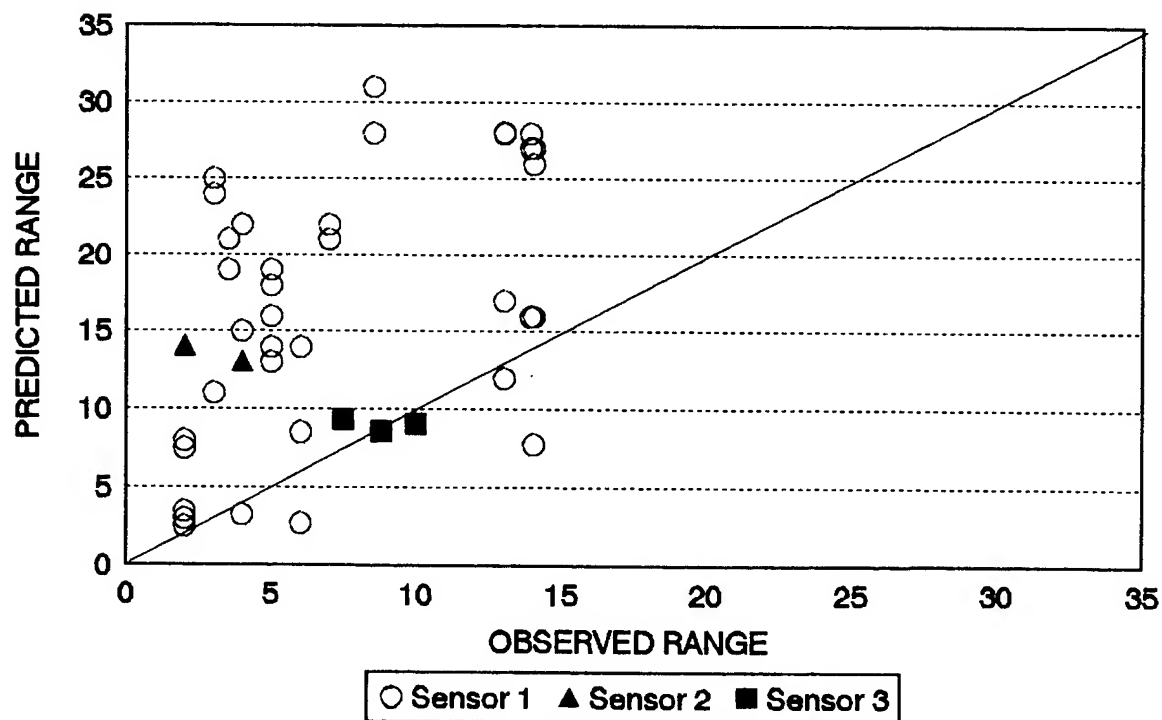


Figure 2. Predicted vs Observed Range  
Ranges are in relative units of length

the tactics described above, the FLIR operator detected the target as soon as the FLIR was switched on. Discussion with the system operators will eliminate this problem on future flights. They will adjust their tactics to use the FLIR at the beginning of the run-in over the target solely for sensor performance data collection.

Only five data points were received for Sensor 2. The data was collected from one mission during overflights of the target ship. The sensor was used just above a dissipating cloud layer and did not have a continuous cloud-free line of sight during the episodes recorded in Table 1. In the EOTDA, predictions of detection range assume a cloud-free line of sight from the sensor to the target. This discrepancy between the reality of the environment and the limitations of simulation with the EOTDA's assumed line of sight may explain some of the differences between the two ranges. Additional data points, collected during various environmental conditions, will need to be analyzed to determine a fair representation of sensor 2 performance and the EOTDA's capability to predict that performance.

Sensor 3 data is also extremely sparse but shows a better correlation between the two ranges. This data was collected during one mission on an overcast day at altitudes well below the cloud deck. The limited data for sensor 3 appears to show that the EOTDA prediction of detection ranges is fairly accurate for this sensor. Unlike sensors 1 and 2, sensor 3 is one of the newer FLIRs in the Naval inventory and the sensor performance parameters probably have not degraded beyond the contractor's specification limitations defined in the EOTDA.

#### 4. CONCLUSION

This paper has described the evaluation of the sensor performance model portions of the EOTDA for Navy and Marine Corps EO sensors. Preliminary analysis of data recently obtained via operational aviation and environmental communities has been discussed. As mentioned above, the data is very limited and many more data points must be collected, under various environmental and operational conditions, to show a statistically sound representation for each sensor's performance. Efforts to collect additional data for these sensors and others are ongoing and will provide the needed information to produce a fair evaluation of the EOTDA's prediction performance for selected Navy and Marine Corps FLIR and NVG sensors.

The efforts to collect the data discussed above proved to be an enlightening experience. Detailed information was attained about the varying methods used in the different types of tactical aviation missions. As scientific researchers, one can get lost in the realm of the "way things should be done" without the legitimate knowledge of the "way things are done" in the operator's or user's world. Discussions with sensor operators provided insight into the "way things are done" and as is always the case in research, the test plan was adjusted. Continuing discussions with the aviation community and sensor operators on their tactics will provide the required information to collect useful sensor detection data.

#### ACKNOWLEDGEMENT

The Navy effort in the tri-service development of the Electro-Optical Tactical Decision Aid (EOTDA) is sponsored by the Oceanographer of the Navy (OP-096) through the Space and Naval Warfare Systems Command program office (PMW-165), CAPT C. Hoffman, Washington D.C., Program Element 0603207N.

#### REFERENCES

- Higgins, G. J., DeBenedictis, D. A., Gouveia, M. J., Hilton, P. F., Hodges, D. B., Hoppes, D. M., and Touart, C. N., 1990: Electro-Optical Tactical Decision Aid (EOTDA) Final Report. STX Scientific Report No. 44. GL-TR-90-0251, Phillips Laboratory, Hanscom AFB, MA 01731-5000.
- Hilton, P. F., DeBenedictis, D. A., Freni, J. M., Gouveia, M. J., Higgins, G. J., Hodges, D. B., Hoppes, D. M., Oberlatz, M. J., Odle, M. S., and Touart, C. N., 1990: Mark III EOTDA Users Manual for Microcomputer System - Version 2. STX Scientific Report No. 41. GL-TR-90-0289, Phillips Laboratory, Laboratory, Hanscom AFB, MA 01731-5000.



# THE GREEN'S FUNCTION PARABOLIC EQUATION FOR ACOUSTIC PROPAGATION IN THE ATMOSPHERE

David H. Marlin  
Battlefield Environment Directorate\*  
Army Research Laboratory  
White Sands Missile Range, NM 88002-5501

## ABSTRACT

A Green's function solution to the parabolic equation has been developed. This approach includes a complex-impedance surface, accounting for both the reflected wave and the surface wave. The direct and reflected wave fields are calculated in the frequency domain, using an FFT. The surface wave contribution is implemented by an integration in the spatial domain. The frequency domain approach allows a range step of several wavelengths, making this model much faster than finite-difference and finite-element parabolic equation methods. Several benchmark cases are compared with the Fast Field Program.

## 1. INTRODUCTION

Parabolic approximations to the reduced wave equation have been used extensively in acoustic propagation since the early 1970's (Tappert, 1974), and in electromagnetics even earlier (Fock, 1965). The advantage of a parabolic equation (PE) is that the solution can be "marched forward" in range; the field at a given range  $r_0$  is not dependant on the field at ranges  $r > r_0$ . In contrast, the reduced wave equation is elliptic, so that the field at range  $r_0$  is dependant on the field at all other ranges. This requires solving a large set of simultaneous equations, a much more demanding problem computationally.

Various PE's have been implemented numerically using finite-differences, finite-elements, and a Fourier transform based method known as the split-step PE. The split-step PE has a significant advantage in that the range step is typically on the order of tens of wavelengths as opposed to tenths of a wavelength for the finite-element and finite-difference models. This makes the split-step much faster, typically by at least one order of magnitude.

---

\*Formerly U.S. Army Atmospheric Sciences Laboratory

It was the underwater acoustic community which first applied the PE, including the split-step, to the acoustic propagation problem. The biggest problem faced in adapting these underwater models to the problem of atmospheric propagation is accommodation of the air-ground boundary. The Green's function parabolic equation (GF-PE) (Di and Gilbert, 1992) is the first split-step PE to include a complex-impedance surface.

Section 2 of this paper develops the GF-PE from the reduced wave equation. A brief discussion of it's implementation using an FFT is also given. In section 3, the GF-PE is compared with the FFP for several specific combinations of sound speed profile and frequency.

## 2. DEVELOPMENT OF THE GF-PE

Our starting point is the reduced wave equation,

$$\nabla^2 p + \frac{\omega^2}{c^2} p = 0, \quad (1)$$

where the pressure disturbance is of the form  $p(r,z)e^{j\omega t}$ . We use cylindrical coordinates (fig. 1) and assume the pressure field is independent of  $\theta$ . This leads to

$$\frac{\partial^2 p}{\partial r^2} + \frac{1}{r} \frac{\partial p}{\partial r} + \frac{\partial^2 p}{\partial z^2} + k^2 p = 0. \quad (2)$$

It is well known that a cylindrical wave will

decrease in amplitude as  $r^{\frac{1}{2}}$ . To separate this cylindrical spreading loss from other effects, we define  $u$  by

$$p(r,z) = r^{-\frac{1}{2}} u(r,z). \quad (3)$$

Then  $u$  satisfies the reduced wave equation

$$\frac{\partial^2 u}{\partial r^2} + \frac{\partial^2 u}{\partial z^2} + k^2 u = 0, \quad (4)$$

and it is to this equation we apply the parabolic approximation.

The current approach to the parabolic equation involves approximations of a certain differential operator, which we consider next. But first, it is interesting to observe that the term "parabolic equation" is really a misnomer, since most of these operator

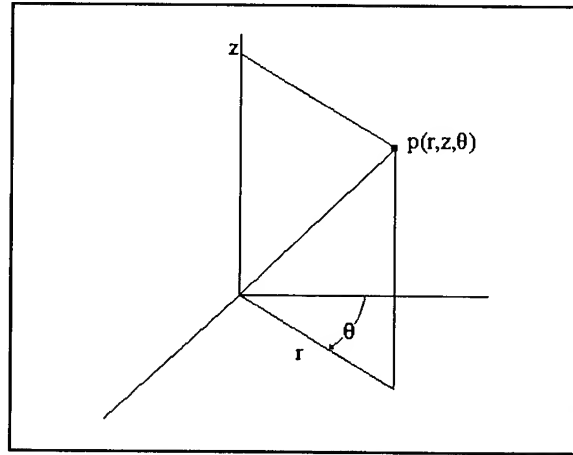


Figure 1. Coordinate system used for PE

approximations result in an equation which is not parabolic. However, we will follow custom and continue to use the name parabolic for equations in this class.

Begin by expressing (4) in operator notation,

$$\begin{aligned} \left[ \frac{\partial^2}{\partial r^2} + Q \right] u &= 0, \\ Q &= \frac{\partial^2}{\partial z^2} + k^2. \end{aligned} \quad (5)$$

$k$  can vary with height but is assumed independent of  $r$ . Then (5) can be factored,

$$\left( \frac{\partial}{\partial r} + i\sqrt{Q} \right) \left( \frac{\partial}{\partial r} - i\sqrt{Q} \right) u = 0. \quad (6)$$

The left and right factors represent inwardly and outwardly propagating waves, respectively. Our interest here is in the wave propagating outwardly from the source, so we use only the right term,

$$\frac{\partial u}{\partial r} = i\sqrt{Q} u. \quad (7)$$

The vertical dependance on height is characterized by

$$k^2(z) = k_0^2 + \delta k^2(z), \quad (8)$$

where the perturbation  $\delta k^2(z)$  is assumed small,

$$\frac{|\delta k^2(z)|}{k_0^2} < 1. \quad (9)$$

The essence of the operator approach involves an approximation of the square root

$$\begin{aligned} \sqrt{Q} &= \left( \frac{\partial^2}{\partial z^2} + k_0^2 + \delta k^2 \right)^{\frac{1}{2}} \\ &= k_0 \left( 1 + k_0^{-2} \frac{\partial^2}{\partial z^2} + \frac{\delta k^2}{k_0^2} \right)^{\frac{1}{2}}. \end{aligned} \quad (10)$$

Several approximations have been discussed in the literature (Tappert, 1977; Feit and Fleck, 1978; Thompson and Chapman, 1983). The approximation used here is

$$\begin{aligned}\sqrt{Q} &\approx \left(\frac{\partial^2}{\partial z^2} + k_0^2\right)^{\frac{1}{2}} + \frac{\delta k^2}{2k_0} \\ &\equiv \sqrt{\tilde{Q}} + \frac{\delta k^2}{2k_0}.\end{aligned}\tag{11}$$

A few comments are in order at this time. This approximation was originally proposed by Tappert (1977). Thompson and Chapman (1983) concluded that it did not result in significant improvement over earlier PE's. However, the implementations in use at that time involved an ad-hoc technique to handle the boundary conditions. This technique is still used by the underwater community, but is unacceptable for the types of surfaces encountered in atmospheric modeling. The advantage of the GF-PE, as will be seen below, is that it incorporates a complex-impedance surface and can be implemented using an FFT for speed. It is the combination of these two features which distinguish the GF-PE from previous implementations.

Returning to the task at hand, we now seek a solution to

$$\frac{\partial u}{\partial r} = i\left(\sqrt{\tilde{Q}} + \frac{\delta k^2}{2k_0}\right) u.\tag{12}$$

Note that were  $\tilde{Q}$  a real-valued constant, this would be a trivial problem in basic calculus. However,  $\tilde{Q}$  is a differential operator, not a number. Nevertheless, a solution does exist, and it is exactly what one would expect,

$$u(r+\Delta r, z) = e^{\frac{i\Delta r \delta k^2}{2k_0}} e^{i\Delta r \sqrt{\tilde{Q}}} u(r, z).\tag{13}$$

This solution is well known in the theory of linear operators, for example (Dunford and Schwartz, 1958). The exponential term on the left is a simple phase term. We now consider the exponential function of the operator  $\tilde{Q}$ .

The form for a general function of  $\tilde{Q}$  is

$$f(\tilde{Q}) = \frac{1}{2\pi i} \oint_C f(x) [xI - \tilde{Q}]^{-1} dx,\tag{14}$$

where  $C$  is the boundary of an open set containing the spectrum of  $\tilde{Q}$ . In the present case, the function is  $f(x) = i\Delta r \sqrt{x}$ , giving rise to

$$e^{i\Delta r\sqrt{\tilde{Q}}} = \frac{1}{2\pi i} \oint_C e^{i\Delta r\sqrt{x}} [xI - \tilde{Q}]^{-1} dx. \quad (15)$$

The change of variables  $x = k_h^2$  leads to

$$e^{i\Delta r\sqrt{\tilde{Q}}} = \frac{1}{\pi i} \oint_{C'} e^{ik_h\Delta r} [k_h^2 I - \tilde{Q}]^{-1} k_h dk_h. \quad (16)$$

This is an operator, and we are interested in its action on  $u$ ,  $e^{i\Delta r\sqrt{\tilde{Q}}}$ . To this end, we note that the integral on the right side of (16) is the limit of a sequence of finite sums over simple operator valued functions. This sequence converges uniformly to the integrand, and uniform convergence implies strong convergence. Thus,  $e^{i\Delta r\sqrt{\tilde{Q}}} u$  may be found by bringing  $u$  inside the integral,

$$e^{i\Delta r\sqrt{\tilde{Q}}} u(r, z) = \frac{1}{\pi i} \oint_{C'} e^{ik_h\Delta r} [k_h^2 I - \tilde{Q}]^{-1} u(r, z) k_h dk_h. \quad (17)$$

Substituting into (13) gives

$$u(r + \Delta r, z) = e^{\frac{i\Delta r\delta k^2}{2k_0}} \frac{1}{\pi i} \oint_{C'} e^{ik_h\Delta r} [k_h^2 I - \tilde{Q}]^{-1} u(r, z) k_h dk_h. \quad (18)$$

Observe that the integrand is no longer an operator valued function. Defining the function

$$\phi(k_h, r, z) \equiv [k_h^2 I - \tilde{Q}]^{-1} u(r, z) \quad (19)$$

leads to

$$u(r + \Delta r, z) = e^{\frac{i\Delta r\delta k^2}{2k_0}} \frac{1}{\pi i} \oint_C e^{ik_h\Delta r} \phi(k_h, r, z) k_h dk_h, \quad (20)$$

with

$$(\tilde{Q} - k_h^2) \phi(k_h, r, z) = -u(r, z). \quad (21)$$

Define the vertical wavenumber



$$k_v^2 = k_0^2 - k_h^2 \quad (22)$$

to arrive at

$$\left(\frac{\partial^2}{\partial z^2} + k_v^2\right)\phi(k_h, r, z) = -u(r, z). \quad (23)$$

Observe that the original solution for  $u$ , equation (13), involving the square root of a differential operator, has been reduced to equation (23), for which a Green's function solution can be found,

$$\phi(k_h, r, z) = \int_0^\infty G(k_h, z, z') u(r, z') dz'. \quad (24)$$

At this point we can apply the surface boundary condition, characterizing the surface by its complex impedance  $Z_g$  (Attenborough, 1985). The resulting Green's function is

$$G(k_h, z, z') = \frac{i}{2k_v} [e^{ik_v|z-z'|} + R(k_v)e^{ik_v(z-z')}] , \quad (25)$$

where

$$R(k_v) = \frac{k_v Z_g - k}{k_v Z_g + k} \quad (26)$$

is the ground reflection coefficient.

Substituting this Green's function into (24) and (20) leads to

$$u(r + \Delta r, z) = e^{\frac{i\Delta r \delta k^2}{2k_0}} \frac{1}{\pi i} \oint_C e^{ik_h \Delta r} \int_0^\infty \frac{i}{2k_v} [e^{ik_v|z-z'|} + R(k_v)e^{ik_v(z-z')}] u(r, z') dz' k_h dk_h. \quad (27)$$

We now make use of a couple of identities,

$$\frac{i}{2k_v} e^{ik_v|z-z'|} = \frac{1}{2\pi} \int_{-\infty}^\infty \frac{e^{i\kappa(z-z')}}{\kappa^2 - k_v^2} d\kappa \quad (28)$$

and

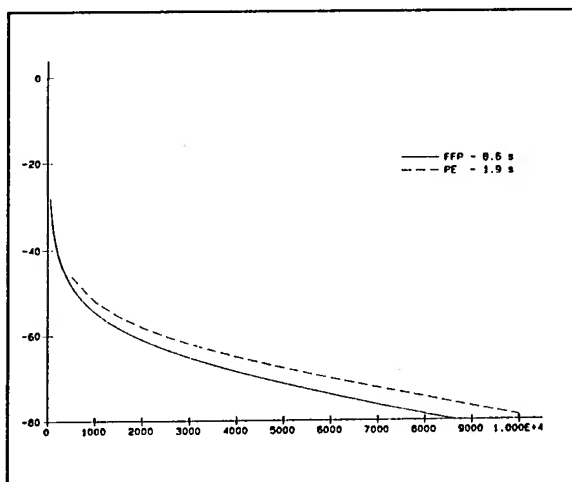


Figure 4 - 10 Hz, upward refracting

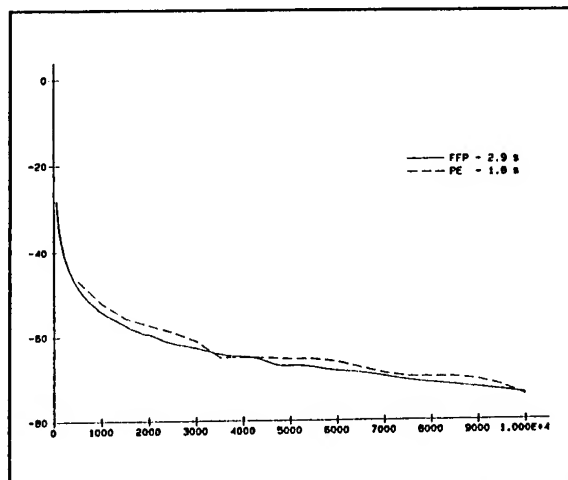


Figure 5 - 10 Hz, surface duct

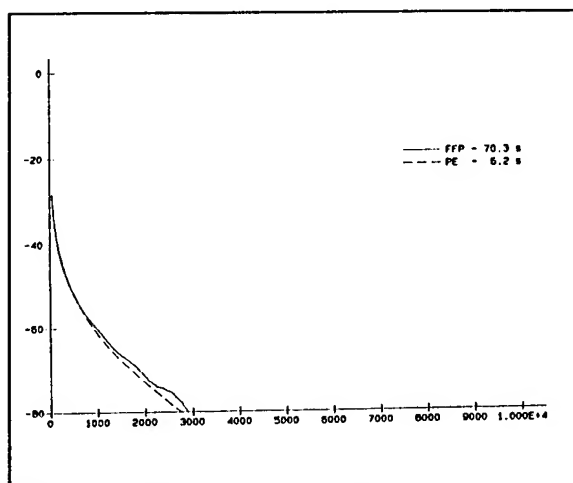


Figure 6 - 100 Hz, upward refracting

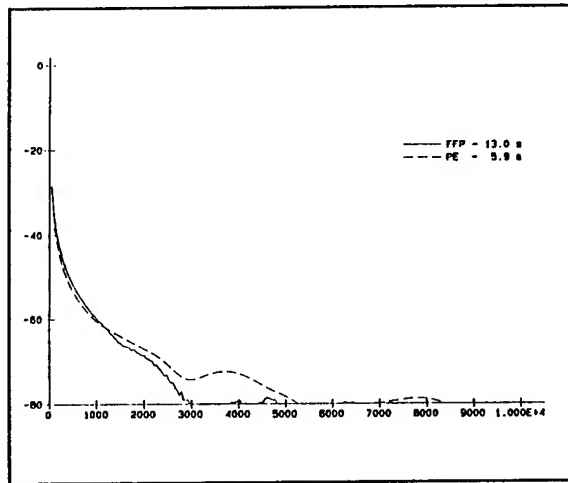


Figure 7 - 100 Hz, surface duct

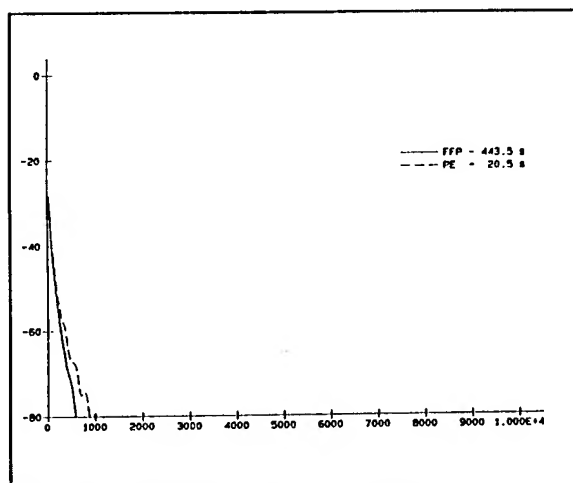


Figure 8 - 1000 Hz, upward refracting

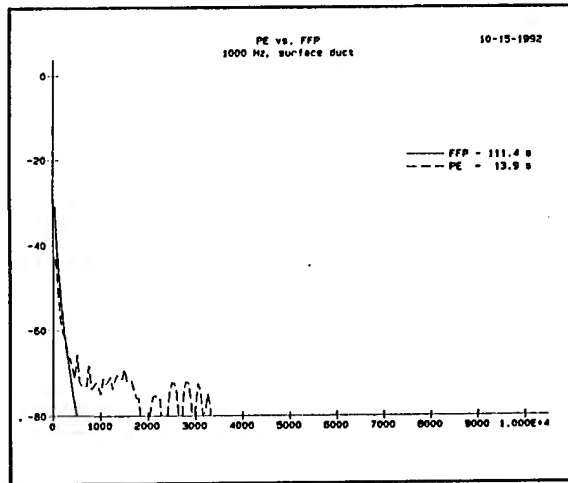


Figure 9 - 1000 Hz, surface duct

$$\frac{i}{2k_v} R(k_v) e^{ik_v(z+z')} = \frac{1}{2\pi} \int_{-\infty}^{\infty} R(\kappa) \frac{e^{i\kappa(z+z')}}{\kappa^2 + k_v^2} d\kappa + 2i\beta \frac{e^{i\beta(z+z')}}{\beta^2 - k_v^2}, \quad (29)$$

where

$$\beta = \frac{k_0}{Z_g}. \quad (30)$$

Substitution of these identities into (27) leads to the formidable looking equation

$$u(r+\Delta r, z) = e^{\frac{i\Delta r \delta k^2}{2k_0}} \frac{1}{\pi i} \oint_C e^{ik_h \Delta r} \int_0^{\infty} \left[ \frac{1}{2\pi} \int_{-\infty}^{\infty} \frac{e^{i\kappa(z-z')}}{\kappa^2 - k_v^2} d\kappa + \frac{1}{2\pi} \int_{-\infty}^{\infty} R(\kappa) \frac{e^{i\kappa(z-z')}}{\kappa^2 - k_v^2} d\kappa + 2i\beta \frac{e^{-i\beta(z-z')}}{\beta^2 - k_v^2} \right] dz' k_h dk_h. \quad (31)$$

However, after performing the contour integration, the remaining integrals take on a very simple form,

$$u(r+\Delta r, z) = e^{\frac{i\Delta r \delta k^2(z)}{2k_0}} \left\{ \frac{1}{2\pi} \int_{-\infty}^{\infty} \int_0^{\infty} u(r, z') e^{-i\kappa z'} dz' e^{i\Delta r \sqrt{k_0^2 - \kappa^2}} e^{i\kappa z} d\kappa \right. \\ \left. + \frac{1}{2\pi} \int_{-\infty}^{\infty} \int_0^{\infty} u(r, z') e^{i\kappa z'} dz' R(\kappa) e^{i\Delta r \sqrt{k_0^2 - \kappa^2}} e^{i\kappa z} d\kappa \right. \\ \left. + 2i\beta e^{-i\beta z} e^{i\Delta r \sqrt{k_0^2 - \beta^2}} \int_0^{\infty} e^{-i\beta z'} u(r, z') dz' \right\}. \quad (32)$$

Note that  $\delta k(z)$  appears only as a multiplicative phase factor. The problem has been decoupled into two steps: propagate from  $r$  to  $r+\Delta r$  in a uniform medium, then apply a phase correction for the variation in  $k$ . The first two terms represent the direct and reflected fields in a uniform medium, respectively. They are found by Fourier transforming the field at  $r$ , applying a vertical-wavenumber dependant phase term in the spatial frequency domain, then Fourier transforming back to the spacial domain. The third term represents a surface, or creeping, wave (Pierce, 1989).

Strictly speaking, the inner integrals in the first two terms are not Fourier integrals, since the lower limit of integration is 0. Also, the signs of the exponents are different, so that using any definition of the Fourier transform, one is an inverse transform. But this can be exploited to our advantage. By forming a single even function which is  $u(-z')$  for  $z' < 0$

and  $u(z')$  for  $z' > 0$ , both integrals can be performed at the same time, via a single FFT. Furthermore, properties of the Fourier transform can be exploited to perform both outer integrals as a single inverse FFT.

## 2. NUMERICAL COMPARISON WITH THE FAST FIELD PROGRAM

The Fast Field Program (Lee, et al., 1986) is another model in wide use in both the atmospheric and underwater acoustic communities. It is a full-wave solution to the reduced wave equation; the only approximations are those inherent to the numerical solution. This is not to imply that the FFP is a more accurate model under all conditions. It is used here only for comparison.

Figures 4-9 show the predictions of both models under varying conditions, as listed in Table 1. The two sound-speed profiles are shown in figs. 2 and 3. The ground impedance model is that of Attenborough (1985). The same surface is used in all cases, and the parameters are flow resistivity  $\sigma = 366$  rayls (cgs), porosity  $\Omega = 0.27$ , pore shape factor ratio  $s_p = 0.5$ , and grain shape factor  $n' = 0.5$ . The run times are listed in seconds on the legend of each fig.

TABLE 1. PARAMETERS USED IN  
NUMERICAL  
MODEL COMPARISONS

Fig.	Freq. (Hz)	Complex Impedance	Sound Speed Profile
4	10	$70.0 + i69.7$	upward refracting
5	10	$22.5 + i21.6$	upward refracting
6	100	$8.53 + i5.70$	upward refracting
7	100	$70.0 + i69.7$	surface duct
8	1000	$22.5 + i21.6$	surface duct
9	1000	$8.53 + i5.70$	surface duct

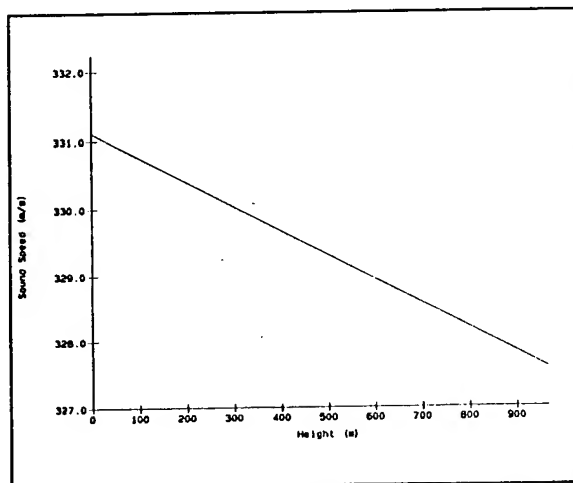


Figure 2. Upward refracting sound-speed profile.

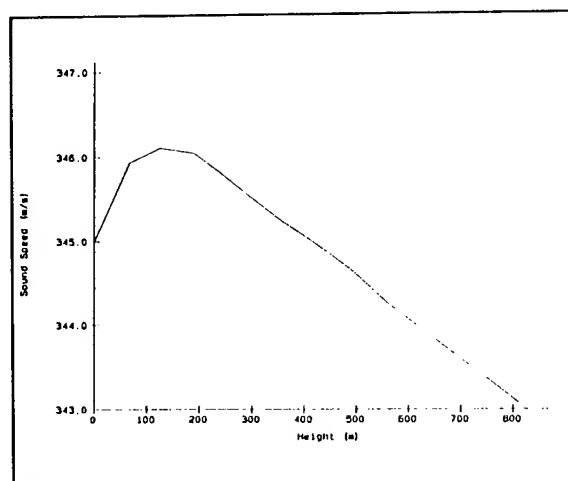


Figure 3. Surface duct sound-speed profile.

In general, the agreement between models is better at lower frequencies and upward refracting profiles. The agreement is quite good in the 10 and 100 Hz cases for the upward refracting profile. In the surface duct cases, both models exhibit some oscillatory behavior. This is due, at least in part, to interference between the direct and reflected waves, since the source is completely coherent. It is well known that the PE has inherent phase errors, which will generally lead to incorrect regions of constructive and destructive interference. This is probably one mechanism leading to the disagreement in oscillatory behavior of the two models. Another contributing factor, particularly at lower frequencies, is the larger range steps used by the PE. This results in lower resolution with respect to range.

Note also the difference in run times at different frequencies. The GF-PE has a significant advantage at higher frequencies, and even at lower frequencies, faster times could be significant for real-time applications or 2-D applications which compute the transmission loss in several directions.

## REFERENCES

- Attenborough, K., 1985: Acoustical Impedance Models for Outdoor Ground Surfaces, *Journal of Sound and Vibration*, 99:521-544
- Dunford, N. and J.T. Schwartz, 1958: Linear Operators, Part I, Interscience Publishers, Inc., New York, NY
- Di, X. and K. E. Gilbert, 1992: A Survey of Acoustic Propagation Predictions for Realistic Atmospheres, final report, contract no. DAAL03-91-C-0034, U.S. Army Research Office, Research Triangle Park, NC
- Feit, M.D. and J.A. Fleck, Jr., 1978: Light Propagation in Graded-Index Optical Fibers, *Applies Optics*, 17:3990-3998
- Lee, S.W. et al., 1986: Impedance Formulation of the Fast Field Program for Acoustic Wave Propagation in the Atmosphere, *J. Acoust. Soc. Am.*, 79:628-634
- Pierce, A.D., 1989: Acoustics, An Introduction to It's Physical Principles and Applications, Acoustical Society of America, Woodbury, NY
- Tappert, F.D., 1977: The Parabolic Approximation Method, in Wave Propagation and Underwater Acoustics, edited by J.B. Keller and J.S. Papadakis, Springer-Verlag, New York, NY
- Thompson, D.J. and N.R. Chapman, 1983: A Wide-Angle Split-Step Algorithm for the Parabolic Equation. *J. Acoust. Soc. Am.*, 74:1848-1854

# MODELING THE OPTICAL AND MECHANICAL PROPERTIES OF EXOTIC BATTLEFIELD OBSCURANTS

by

Robert A. Sutherland  
U.S. Army Research Laboratory  
White Sands Missile Range, NM 88002-5501

James D. Klett  
PAR Associates  
Las Cruces, NM 88003

## ABSTRACT

Theoretical and semi-empirical methods for modeling the mechanical and optical properties of non-spherical battlefield aerosols are presented. Methods for treating mechanical properties include semi-empirical expressions to calculate stable mode terminal velocities of cylindrical and disc shaped particles and a theoretical model for estimating particle orientation valid in the inertial subrange of turbulence. Methods for treating optical properties include the effect of particle orientation on the extinction and backscatter efficiencies for the two polarization modes. Results for thin, long, cylindrical shapes, characteristic of developmental MMW obscuring agents, indicate a transition region, based upon particle diameter, above which particles remain in the stable fall mode and below which particles assume random tumbling depending also upon the ambient turbulence level and the particle Reynolds Number. Also, for long cylindrical shaped particles, both the extinction and backscatter efficiencies are a strong function of the polarization state with the transverse magnetic (TM) modes being dominant over the transverse electric (TE) modes to a degree depending upon particle diameter and particle refractive indices.

## 1. INTRODUCTION

Most existing obscuration effectiveness models, including those in EOSAEL, assume spherical symmetry to describe the optical properties of the underlying aerosol. Whereas this is a reasonable assumption for the older conventional obscuring agents such as fog oil and white phosphorus, the approximation breaks down when considering the newer developmental obscuring agents designed to be most effective at the longer wavelengths. In particular, most of the newer MMW (millimeter wave) obscuring agents are highly non-spherical, requiring alternate, and usually more involved, mathematical modelling techniques. In this paper we examine different methods for modeling the optical and mechanical behavior of these highly non-spherical, or "exotic", battlefield obscuring agents. Two major issues are considered; one involving electromagnetic properties such as extinction, absorption, and scattering and the other involving mechanical properties such as fall velocity and angular orientation as influenced by atmospheric turbulence.

## 2. MECHANICAL EFFECTS

It is an observed fact that under certain conditions, non spherical particles tend to adopt a preferred orientation when falling through the atmosphere. For both long cylindrical-like shapes used to approximate MMW obscurants (carbon fibers) and disk-like shapes used to approximate IR obscurants (brass flakes) the stable mode occurs when the particle is oriented with long axis horizontal. It is furthermore observed that the fall velocity of a non-spherical particle is usually significantly lower than that for an equivalent spherical particle of the same mass. The governing equation for describing the motion of particles falling under the influence of gravity in either a quiescent or turbulent atmosphere is the Navier-Stokes equation which is written here in simplified notation as (Pruppacher and Klett, 1978):

$$\frac{\partial \mathbf{u}}{\partial t} + \mathbf{u} \cdot \nabla \mathbf{u} = - \frac{\nabla p}{\rho} + \nu \nabla^2 \mathbf{u} + \mathbf{g} \quad (1)$$

where  $\mathbf{u}$  is velocity,  $t$  is time, and  $\nu$  is the kinematic viscosity of air. In general, due to the non-linear nature of the inertial term,  $\mathbf{u} \cdot \nabla \mathbf{u}$ , the equation does not lend itself to closed analytical solutions; however, there are reasonable approximations valid for various flow regimes. The most well known parameter to describe the flow regime is the Reynolds Number,  $R_e$ , which is defined as the ratio of the inertial to viscous forces, that is, from Eq. (1);

$$R_e = \frac{|\mathbf{u} \cdot \nabla \mathbf{u}|}{|\nu \nabla^2 \mathbf{u}|} \sim \frac{Ud}{\nu} \quad (2)$$

where the approximate form follows from dimensional analysis with the characteristic dimension,  $d$ , taken to be the particle diameter. For a particle freely falling in the atmosphere,  $U$  is taken as the fall velocity. For spherical particles and low Reynolds numbers, the Navier Stokes equation can be solved to yield the familiar Stokes Law; however, for more complex shapes there are no known analytical solutions and one must rely on reasonable theoretical approximations or empirical parameterizations. One such parameterization involves the Davis, or Best, Number,  $B_c$ , defined for cylinders and discs as:

$$B_c = C_d^2 R^2 = \frac{2mg}{L\eta^2} \quad \text{Cylinders} \quad (3)$$

$$B_d = \frac{8mg}{\pi\eta^2} \quad \text{Discs}$$

where  $C_d$  is the drag coefficient,  $m$  is the mass of the particle, and  $\eta$  is the dynamic viscosity of air. The particle Reynolds Number is then found from the following empirical expression:

$$\log R_e = B_0 + B_1 X + B_2 X^2 + B_3 X^3 ; X = \log B_c \quad (4)$$

where the  $B$  coefficients depend upon particle type and aspect ratio (Pruppacher and Klett, 1978).

In Fig. 1 we show a plot of  $R_e$  as a function of the particle maximum dimension using both discs and cylinders and an aspect ratio of 1/10 and 1/600 (5/3000). These are reasonable values for carbon fibers (Bruce, et. al., 1989) and for brass flakes (Embury, 1982), respectively.

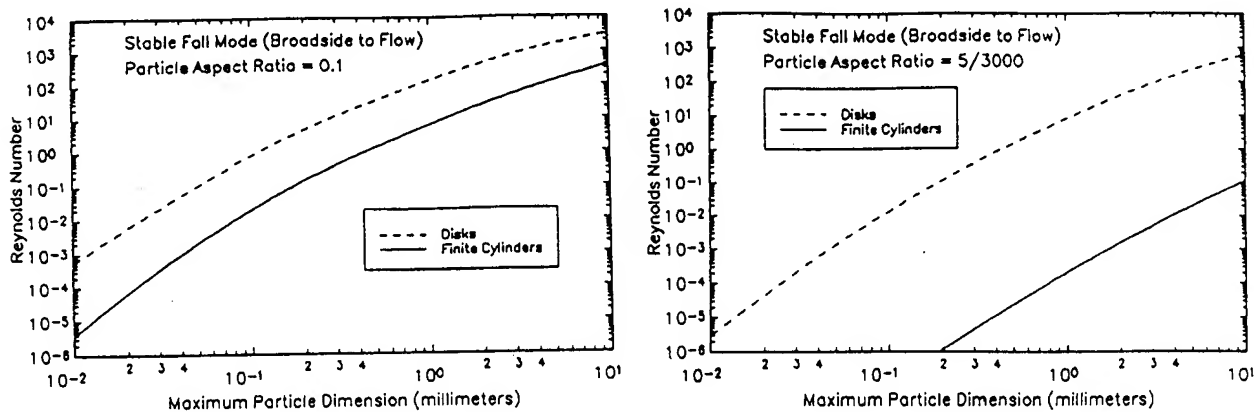


Figure 1. Plot of Reynolds Number as a function of particle maximum dimension for cylindrical and disc shaped particles in the stable fall mode; (a)  $d/L = 1/10$ , (b)  $d/L = 5/3000$ .

The results of Fig. 1 demonstrate the strong dependence of  $R_e$  on particle dimension; that is for given particle size and aspect ratio, the value for cylinders is lower compared to discs, with the difference being greater for greater aspect ratio.

TABLE 1. TERMINAL VELOCITIES FOR SPHERES AND CYLINDERS

TERMINAL VELOCITY (CM/SEC)					
Diam. ( $\mu\text{m}$ )	Re (Sphere)	D/L = 0.00	D/L = 0.10	D/L = 1.00	SPHERE
.25	3.09E-08	9.26E-04	3.59E-06	8.33E-06	1.87E-04
.50	2.47E-07	5.06E-03	8.45E-05	8.76E-05	7.49E-04
1.00	2.31E-06	2.47E-02	1.34E-03	7.86E-04	3.49E-03
2.00	1.71E-05	1.07E-01	1.47E-02	6.01E-03	1.30E-02
4.00	1.32E-04	4.16E-01	1.15E-01	3.92E-02	4.99E-02
5.00	2.56E-04	6.29E-01	2.09E-01	6.93E-02	7.74E-02
8.00	1.03E-03	1.44E+00	6.66E-01	2.18E-01	1.96E-01
10.00	2.01E-03	2.09E+00	1.10E+00	3.67E-01	3.04E-01
16.00	8.19E-03	4.44E+00	2.92E+00	1.04E+00	7.75E-01
32.00	6.41E-02	1.22E+01	1.01E+01	4.19E+00	3.03E+00
64.00	4.85E-01	2.99E+01	2.79E+01	1.45E+01	1.15E+01
128.00	3.12E+00	6.54E+01	6.46E+01	4.26E+01	3.69E+01
256.00	1.61E+01	1.27E+02	1.28E+02	1.07E+02	9.49E+01
512.00	7.01E+01	2.22E+02	2.25E+02	2.29E+02	2.07E+02
1024.00	2.77E+02	3.43E+02	3.60E+02	4.18E+02	4.10E+02

With  $R_e$  so determined and for given particle size the particle fall velocity can be calculated from Eq. (2). Results for the case of long cylindrical shaped particles are shown in Table 1 where we



have include three aspect ratios and, for reference, have included the spherical particle Reynolds Number and terminal velocity for spheres of the same radius.

From Table 1 it can be seen that the terminal fall velocity is a strong function of the particle diameter and is usually smaller for cylinders than for equivalent spheres. All values tend to merge to a terminal velocity of about 500 cm/sec at a particle diameter of 1000  $\mu\text{m}$ , however, at the smaller diameters which are of interest here there is a significant difference for the various aspect ratios with the higher fall velocity corresponding to the higher aspect ratios. For an aspect ratio of zero (infinite cylinder) and a particle diameter of 5-10  $\mu\text{m}$  the data of Table 1 yields a value of about 2-4 cm/sec which is near the values measured for carbon fibers by Newsom and Bruce (1992).

The above discussion is applicable to particles falling in the stable mode under quiescent conditions. In the real atmosphere, effects of turbulence can cause significant changes in the fall characteristics. This is particularly true for smaller particles that can easily be entrained by turbulent eddies and hence will experience random tumbling with no preferred orientation. On the other hand, larger particles may tend to maintain an overall stable fall mode but may nevertheless experience random forces by the various multi-scaled eddies that will cause a wobbling motion superimposed on the quasi-steady fall. In the work here we seek a model to estimate the degree of orientation of various sized particles falling in turbulent atmosphere. The problem is difficult, and, like most problems involving the real atmosphere, is intractable in the exact sense and hence we seek reasonable approximations.

It is possible to obtain some reasonable estimates of particle orientation by considering only the inertial subrange of turbulence where there is a reasonable understanding of the turbulence structure and approximate expressions for various quantities are available (cf. Lumley & Panofski, 1964). The most critical aspect of turbulence that is relevant here is the turbulent eddy size spectrum where we are particularly interested in the smallest scale, also referred to as the microscale length. The microscale length,  $\lambda_k$ , and two other quantities of interest, the microscales of time,  $t_k$ , and velocity,  $v_k$ , are defined here for later reference as:

$$\begin{aligned}\lambda_k &= (\nu^3/\epsilon)^{1/4} \\ t_k &= (\nu/\epsilon)^{1/2} \\ v_k &= (\nu\epsilon)^{1/4}\end{aligned}\tag{5}$$

where  $\nu$  is, as before, the kinematic viscosity of air and  $\epsilon$  is the turbulent energy dissipation rate per unit mass. A plot of the microscale length as a function of  $\epsilon$  is shown in Fig. 2.

In interpreting the results of Fig. 2, we define conditions of strong turbulence to correspond to values on the order of  $10^3$  for the dissipation rate ( $\text{cm}^2 \text{s}^{-3}$ ), and similarly for moderate, and mild turbulence the appropriate estimates are  $10^2$ , and 10, respectively. From Fig. 2 we see that the corresponding microscale lengths for these conditions varies from about 0.50 to 2.5 mm which is near the range of particle sizes of interest in MMW obscuration.

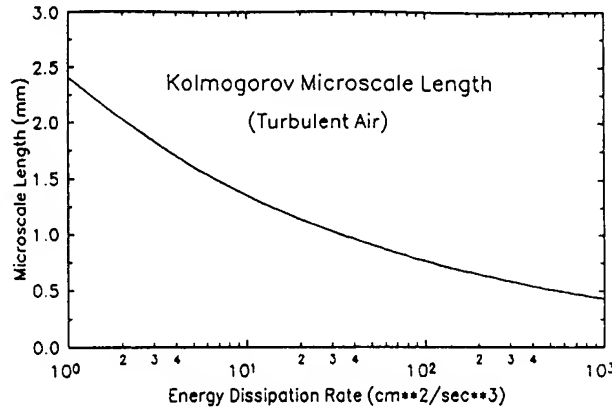


Figure 2. Plot of turbulence microscale length as a function of eddy dissipation rate.

With the aid of the above formulation it is possible to estimate the effect of turbulence on particle orientation by assuming the root mean square tilt angle to be derived from a balance between the stresses due to turbulent fluctuations and the stresses due to the mean flow. The derivation depends also upon  $R_e$  as well as  $\lambda_k$  and this, in turn, leads to different formulations depending upon the particular combinations considered. Nevertheless it is possible to develop interpolation formulas that cover the range of conditions of interest. The interpolation parameters needed to bridge the gap between various regions are defined as:

$$\alpha = \frac{2R_e + 1}{R_e + 1} \quad ; \quad \beta \left( \frac{d_{\max}}{\lambda_k} \right) = \frac{1}{3} + \frac{5}{6 \left[ 1 + \left( \frac{d_{\max}}{\lambda_k} - \frac{1}{2} \right)^2 \right]} \quad (6)$$

where  $d_{\max}$  is the maximum particle dimension. The tilt angle as estimated from the pressure stress ratios is then given by the following simple expression:

$$\delta \approx \gamma \left[ \frac{v_k \left( \frac{d_{\max}}{\lambda_k} \right)^\beta}{U} \right]^\alpha \quad (7)$$

where  $\gamma$  is a dimensionless parameter on the order of unity. Some results generated for carbon assuming either cylinders or discs and either mild or moderate turbulence are plotted in Fig. 3. The plots show tilt angle, in degrees from the stable orientation, as a function of particle size. Values near zero indicate stable orientation and values near 90 indicate random tumbling.

The most marked feature of the plots of Fig. 3 is the sharp increase at a particular threshold. The picture is one of a very sharp transition region from stable orientation to complete random tumbling. All curves show a shift toward the larger particles with increased turbulence indicating a higher threshold. The curves for discs show a marked shift to lower thresholds indicating a more stable fall for discs as opposed to cylinders.

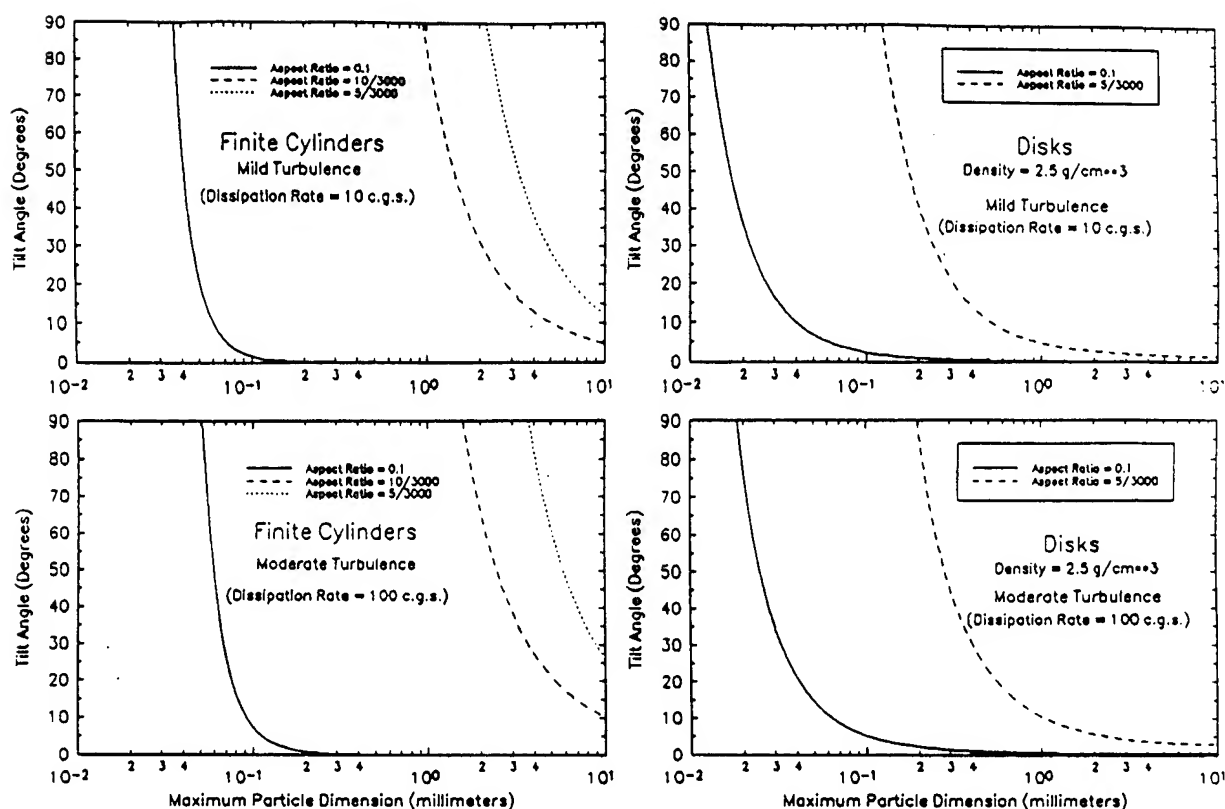


Figure 3. Plots of estimated root mean square tilt angle as a function of particle maximum dimension for several aspect ratios; (a) cylinders, mild turbulence, (b) discs, mild turbulence, (c) cylinders, moderate turbulence, (d) discs, moderate turbulence.

The results of Fig. 3 are difficult to verify quantitatively; however the general trends do seem to be compatible with intuition and at least not opposed to anecdotal observations made in the field. For example the transition region for carbon fibers 3 mm in length appears to occur for a particle diameter of between 5 and 10  $\mu\text{m}$ . This result is in qualitative agreement with general observations made in both the laboratory and field for MMW obscuring (Farmer, 1991; Bruce, 1992) and RADAR chaff (Silverman, 1978).

### 3. OPTICAL EFFECTS

A suitable starting point for a discussion of the optical effects is the far field scattering solution to Maxwell's Equations. The appropriate expression, assuming a plane wave of wave vector  $\mathbf{k}$ , and electric vector,  $\mathbf{E}_0$ , incident upon an arbitrarily shaped particle of refractive index,  $m$ , can be written in terms of a scattering amplitude,  $A(\mathbf{k}, \mathbf{r})$ , superimposed on an outgoing spherical wave as:

$$E_s(r) = E_0 A(k, r) \frac{e^{ikr}}{r},$$

$$A(k, r) = k^2 [1 - \hat{r}(\hat{r} \cdot)] I, \quad (8)$$

$$I = \frac{(m^2 - 1)}{4\pi} \int_V \frac{E(r')}{E_0} e^{(-i\hat{r} \cdot \hat{r}') d^3 r'}$$

where  $E(r)$  is the electric vector of the scattered wave at a distance  $r$  from some suitable origin and  $k$  is the wave vector. Eq. (8) is an integro-differential equation that cannot be solved in analytical form except for certain specialized cases, one being for a spherical particle and the other being for an infinite cylinder. These solutions form the basis of the well known Mie theory which is described in the textbooks (cf. Bohren and Huffman, 1978) and used in most EOSAEL models. In other cases various approximations are used based upon any number of semi-analytical and numerical approaches (cf. Klett and Sutherland, 1992). A most relevant aspect of the effects of cylindrical scatterers as opposed to spherical scatterers is the effect on the polarization and de-polarization of the scattered wave. This is demonstrated in the plots of Fig. (4) where we present several plots of the extinction and backscatter efficiency of infinite cylinders as a function of the phase parameter  $\rho = kd(m_r - 1)$ , where  $m_r$  is the real component of the complex index of refraction and other quantities are as defined previously. In the plots of Fig. 4 the efficiency is defined as the optical cross section (either backscatter or extinction) divided by the geometrical cross section per unit length projected normal to the incident beam.

In each of the four sub-plots of Fig. (4) we show two cases; one assuming the incident electric field polarized parallel to the cylinder axis (the transverse magnetic, or TM mode) and the other assuming the electric field polarized perpendicular to the cylinder axis (the transverse electric, or TE mode). In general, all curves show differences in extinction and backscatter efficiencies between the two polarization modes with the TM component being dominant. This effect could be important in military applications, especially at the longer wavelengths where systems are sensitive to signal polarization. For high values of the refractive indices which are characteristic of the MMW regime (Fig. 4a) the differences between the two polarization modes are very large especially at the lower values of the phase parameter; however, for lower values of the refractive indices which are characteristic of the optical regions (Fig. 4c) the differences are insignificant. Similar observations are evident for backscatter cases although the results are further complicated by the periodic resonances occurring at various values of the phase parameter. In practice the backscatter coefficient is difficult to determine experimentally because of the oscillations which are most rapid at the lower values of refractive index. The results of Fig. (4) were generated by assuming an infinite length cylinder and normal incidence. In the real world, involving finite length cylinders and random angles, the situation is more complex. For finite cylinders the presence of boundaries at the ends cause resonance effects that are difficult to model (Waterman and Pederson, 1992); however, extended calculations showed only small sensitivity to the incident angle.

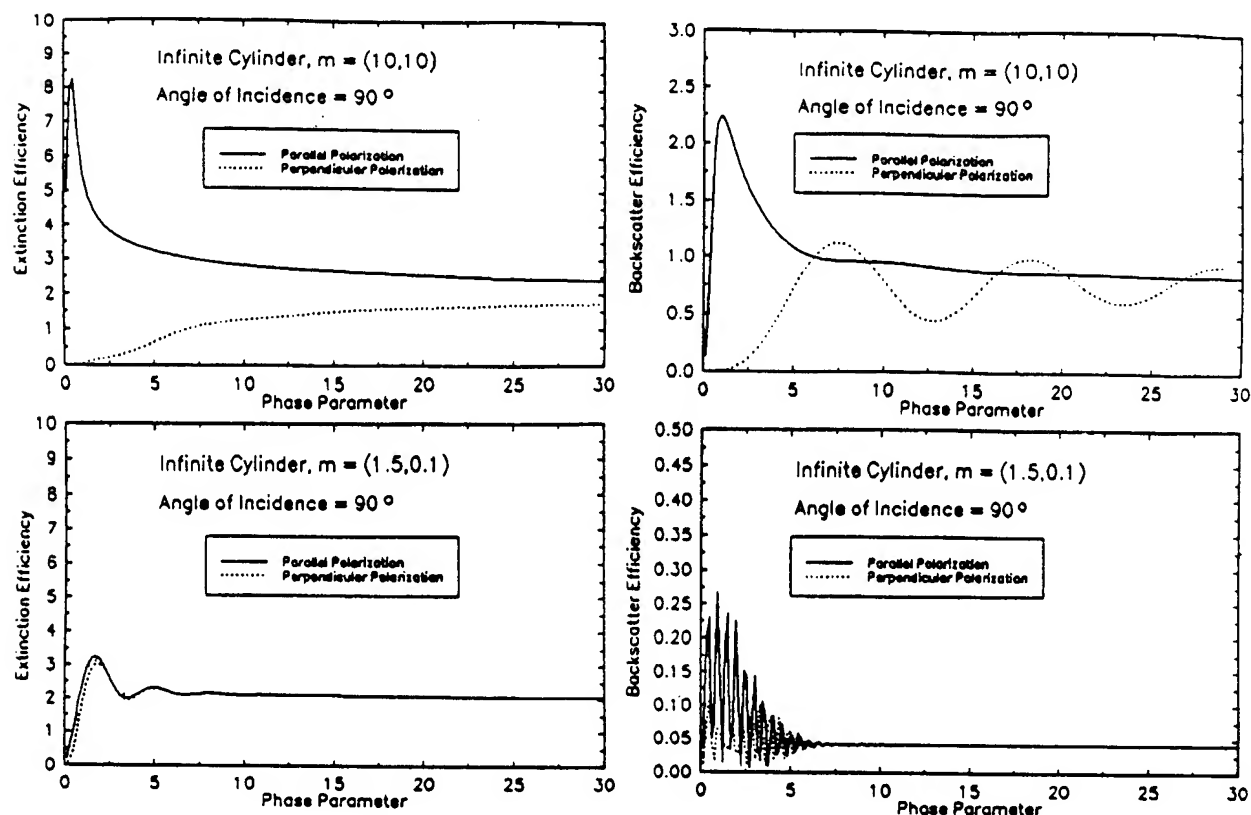


Figure 4. Plots of extinction and backscatter efficiency at normal incidence for the two polarization modes of long cylindrical shaped particles as a function of phase parameter; (a) extinction,  $m=(10,10)$ , (b) backscatter,  $m=(10,10)$ , (c) extinction,  $m=(1.5,0.10)$ , (d) backscatter,  $m=(1.5,0.10)$ .

The trend in the effect of the refractive indices is shown in the three dimensional plots of Fig. (5) which show extinction efficiency as a function of both phase parameter and refractive index. The leftmost plots were calculated using a very small value for the imaginary component of the index of refraction ( $m_i = 0.01$ ) which is representative of a very weak absorber. In this case the plots show an extreme sensitivity to the magnitude of the real index which becomes more intense with increasing magnitude. It is also evident from Fig. (5) that the TM component is dominant and that the positions of the relative maxima and minima are not the same for the two polarization types but do tend to approach coincidence at lower values of the index.

The rightmost plots of Fig. (5) show the effects of increased absorption which tend to damp out the resonances exhibited for the weakly absorbing case. Here we have assumed the real and imaginary components to be equal (typical of conductors at long wavelengths). Here it is clear that the effect of the increased imaginary index, and hence absorption within the particle, is to damp the resonances; however the dominance of the TM component is still evident.

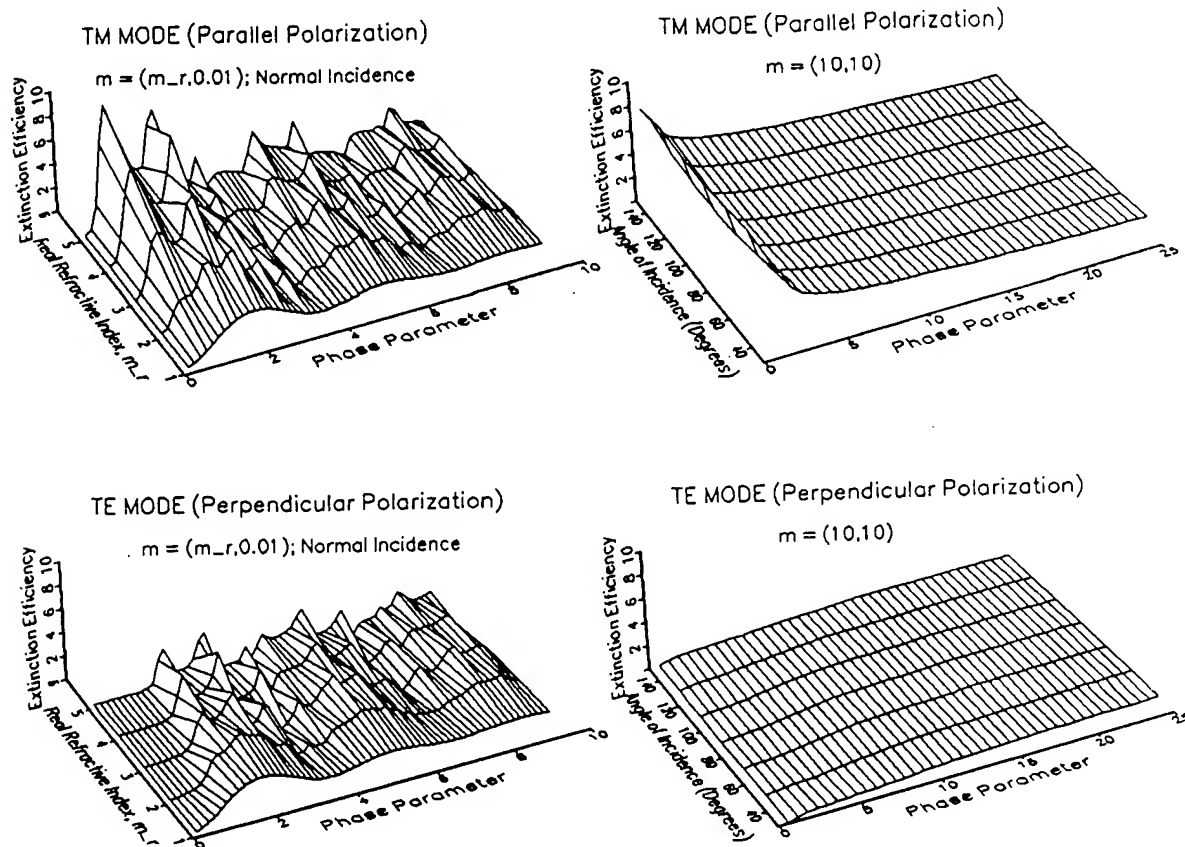


Figure 5. Extinction efficiency at normal incidence of cylindrical shaped particles as a function of both phase parameter and refractive index; (a) TM mode, optical region, (b) TM mode, MMW region, (c) TE mode, optical region, (d) TE mode, MMW region.

#### 4. SUMMARY AND CONCLUSIONS

Results of our modeling effort show that effects of particle shape and orientation are important when modeling the behavior of realistic battlefield aerosols. Under some conditions, depending upon the level of turbulence and the  $R_e$ , particles tend to undergo random tumbling with no particular preferred orientation; however, for lower levels of turbulence particles tend to fall in the stable mode, usually with the broadest dimension horizontal. For carbon fibers tailored to the MMW regime the threshold between stable and random fall lies somewhere in the 5 to 10  $\mu\text{m}$  diameter range for moderate levels of turbulence. For higher turbulence levels the fall is best approximated as uniform random for smaller particles.

For cylindrical shaped particles both the extinction and backscatter efficiencies are dependent upon the polarization state of the incident radiation with the transverse magnetic mode being most affected. Differences are strongly dependent upon the magnitude of the complex indices of refraction, being quite large for indices characteristic of the MMW region but almost negligible for the optical regions.

## ACKNOWLEDGEMENTS

The authors wish to acknowledge the assistance of Mr. Liam McDaid, New Mexico State University for helping with the calculations and manuscript.

## REFERENCES

Bohren, C.F., and D.R. Huffman, 1983: Absorption and Scattering of Light by Small Particles, Wiley, New York.

Bruce, C.W., Jelinek, A.V., Halonen, R.M. and M.J. Stehling, 1990: Millimeter Wavelength Attenuation Efficiencies of Fibrous Aerosols, Technical Report CRDEC-CR-092, Proceedings of the Smoke/Obscurants Symposium XIV Volume 1, Chemical Research Development & Engineering Center, Aberdeen Proving Ground Maryland, November 1990.

Embury, J.F., 1982: Extinction by Aerosol Clouds of Non-spherical Particles at Arbitrary Wavelengths, U.S. Army Chemical Systems Laboratory Special Publication, ARCSL-SP-81021, Aberdeen Proving Ground, Maryland.

Evans, B.T.N., 1991: An Interactive Program for Estimating Extinction and Scattering Properties of Most Particulate Clouds, Commonwealth of Australia Department of Defense Materials Research Laboratory Technical Report MRL-R-1123, Ascot Vale, Victoria 3032, Australia.

Klett, J.D., and R.A. Sutherland, 1992: Approximate Methods for Modeling the Scattering Properties of Non-spherical Particles: Evaluation of the Wentzel-Kramers-Brillouin Method, Applied Optics, 31(3):373-386.

Lumley, J.L. and H.A. Panofsky, 1964: The Structure of Atmospheric Turbulence, John Wiley & Sons, New York, New York.

Newsom, R.K. and C.W. Bruce, 1992: Orientation Properties of Fibrous Aerosols in Free Fall Through a Quiescent Atmosphere, draft manuscript, U.S. Army Atmospheric Sciences Laboratory, White Sands Missile Range, NM.

Pruppacher, H.R. and J.D. Klett, 1978: Microphysics of Clouds and Precipitation, D. Reidel Publishing Company, Dordrecht, Holland.

Silverman, G., 1978: Chaff Dispersion and Polarization, Electronic Defense, 39-52, November/December 1978.

Waterman, P.C. and J.C. Pederson, 1992: Scattering by Finite Wires, J. Appl. Phys. 72(2):349-359.

# PROGRESS IN ATMOSPHERIC PROPAGATION MODELING

## AT FREQUENCIES BELOW 1000 GHz

H. J. Liebe, G. A. Hufford, and M. G. Cotton  
National Telecommunications and Information Administration  
Institute for Telecommunication Sciences, ITS.S3  
Boulder, CO 80303, U.S.A.

### ABSTRACT

Millimeter-wave propagation through the nonprecipitating atmosphere is modeled for frequencies below 1000 GHz. Complex refractivities represent the spectral properties of four natural absorbers; that is, oxygen, water-vapor, suspended droplets and ice particles. The *dry-air* model is supported by new, extensive 60-GHz laboratory absorption measurements of the pressure-broadened O<sub>2</sub> spectrum. The *water-vapor* model considers contributions of 30 local H<sub>2</sub>O lines, which are supplemented by an empirical continuum term based on laboratory measurements in the 138- to 213-GHz range. Revised formulations for the complex permittivities of water and ice are employed in the *suspended-particle* model which, due to the Rayleigh approximation, provides only minimum estimates above 300 GHz.

### 1. INTRODUCTION

The natural atmospheric absorber of oxygen, water vapor, and suspended water or ice particles must be treated collectively in order to evaluate the effects of adverse weather on millimeter-wave system performance. A physical model is described here that predicts from meteorological variables the spectral characteristics of the absorbers up to 1000 GHz, taking into account recent advances in experimental and theoretical work. This paper presents formulations suitable for updates of the Near-Millimeter-Wave module of EOSAEL (Brown, 1987), as well as the analytical and numerical details.

In atmospheric radio-wave propagation the interaction of radiation with the medium is expressed by a complex refractivity,  $N = N_0 + N' + iN''$  ppm. The real part addresses changes in the propagation velocity (refraction) and the imaginary part quantifies the loss of radiation energy (absorption). The real part consists of a frequency-independent term,  $N_0$ , and of the dispersive refraction  $N'(\nu)$ . Both amplitude and phase response of a plane radio wave propagating a distance  $z$  at frequency  $\nu$  through the atmosphere can be described by a complex field strength,

$$E(z) = \exp[i k z (1 + N \times 10^{-6})] E(0), \quad (1)$$

where  $E(0)$  is the initial value,  $k = 2\pi\nu/c$  is the free space wave number, and  $c$  is the speed of light in vacuum. For a homogeneous medium, refractivity  $N$  defines the path-specific quantities of power attenuation  $\alpha$  and propagation delay  $\tau$  as (frequency  $\nu$  is in GHz throughout)

$$\alpha = 0.1820 \nu N''(\nu) \text{ dB/km} \quad \text{and} \quad \tau = 3.336 [(N_0 + N'(\nu))] \text{ ps/km.} \quad (2)$$



## 2. REFRACTIVITY SPECTRA OF THE GASEOUS ATMOSPHERE

### 2.1 MODELING SCHEME

Complex refractivity  $N$  is the key quantity computed by the Millimeter-wave Propagation Model "MPM" (Liebe, 1989). The practical  $N$  model consists of 44  $O_2$  and 30  $H_2O$  local (centered below 1000 GHz) lines, of nonresonant spectra for dry air, and of an empirical water vapor continuum which reconciles experimental discrepancies. The model formulations for dry air and water vapor spectra follow closely the theory of absorption by atmospheric gases that is discussed in detail by Rosenkranz (1992). The Rayleigh absorption approximation is used for the refractivity of suspended water and ice particles (Liebe et al., 1989). The physical condition for a volume element of air is specified by

■	barometric pressure	$p$	( 0 to 1200 mb)
■	ambient temperature	$t$	(- 100 to 50 °C)
■	relative humidity	$u$	( 0 to 100 %)
■	suspended particle density	$w$	( 0 to > 5 g/m <sup>3</sup> ).

For modeling purposes, a reciprocal temperature variable  $\theta = 300/(t + 273.15)$  is introduced, and the total pressure,  $p = p_d + e$  mb (1 mb = 100 Pa), is separated into partial pressures for dry air and water vapor. Water vapor pressure  $e = (u/100) e_s$  is computed from the relative humidity  $u$  and the saturation pressure over water (-40 to 80°C) or ice (-100 to 0°C) at the temperature  $t$  by means of the Goff-Gratch (1946) formulations. Absolute humidity follows from  $q = 0.7223 e \theta$  g/m<sup>3</sup>. An adequate approximations for saturation pressure over water is given by

$$e_s = 2.408 \times 10^{11} \theta^5 \exp(-22.644 \theta) (\approx 35 \times \theta^{-18}) \text{ mb.} \quad (3)$$

### 2.3 OXYGEN SPECTRUM

Refractivity by atmospheric oxygen is expressed by

$$N_D = N_1 + \sum_k S_k F_k + S_o F_o + i S_n F_n'' \text{ ppm,} \quad (4)$$

where the nondispersive term is given by  $N_1 = 0.2588 p_d \theta$  ppm, and line refractivity results from 44  $O_2$  resonances ( $k$  = line index). Each line strength,

$$S_k = a_1 10^{-6} p_d \theta^3 \exp[a_2(1 - \theta)] \text{ kHz,} \quad (5)$$

is multiplied by the complex spectral shape function,

$$F(\nu) = \frac{\nu}{\nu_k} \left[ \frac{1 - i\delta_k}{\nu_k - \nu - i\gamma_k} - \frac{1 + i\delta_k}{\nu_k + \nu + i\gamma_k} \right] \text{ GHz}^{-1}. \quad (6)$$

The Van Vleck-Weisskopf function  $F(\nu)$  was modified by Rosenkranz (1988) to include line overlap effects. Width ( $\gamma$ ) and overlap ( $\delta$ ) parameters of pressure-broadened  $O_2$  lines in air are given by

$$\gamma_k = \{ [a_3 10^{-3} (p_d \theta^{0.8} - a_4 + 1.10 e \theta)]^2 + \gamma_z^2 \}^{1/2} \text{ GHz} \quad (7)$$

$$\delta_k = (a_5 + a_6 \theta) 10^{-3} p \theta^{0.8}. \quad (8)$$

Center frequencies  $\nu_k$  and spectroscopic coefficients  $a_1$  to  $a_6$  are listed in Table 1. While only of interest below 10 mb ( $h \geq 30$  km), Zeeman-splitting of  $O_2$  lines is approximated in Eq. (7) by a single linewidth,  $\gamma_Z \approx 0.001$  GHz. A better approximation,  $\gamma_Z \approx 25 B_0$ , takes into account the geomagnetic field  $B_0$  with values from  $(22 \text{ to } 65) \times 10^{-6}$  Tesla. Anisotropic effects due to the *anomalous Zeeman effect* of mesospheric  $O_2$ -lines have been detailed by Hufford and Liebe (1990).

Nonresonant refractivity arises below 10 GHz from the  $O_2$  relaxation spectrum  $S_o F_o$ . Additionally, pressure-induced  $N_2$  absorption  $S_n F_n''$  makes a small contribution above 100 GHz. The associated strengths and shape factors are

$$\begin{aligned} S_o &= 6.14 \times 10^{-5} p_d \theta^2 & \text{and} & & F_o(\nu) &= -\nu(\nu + i\gamma_o)^{-1}, \\ S_n &= 1.40 \times 10^{-12} p_d^2 \theta^{3.5} & \text{and} & & F_n''(\nu) &\approx \nu(1.9 \times 10^{-5} \nu^{1.5} + 1)^{-1}, \end{aligned} \quad (9)$$

where the relaxation frequency is  $\gamma_o = 0.56 \times 10^{-3} p \theta^{0.8}$  GHz.

Absorption of dry air ( $e = 0$ ) has been measured extensively in the laboratory (Liebe et al., 1990). Based on a best fit to these data (Liebe et al., 1992), the coefficients  $a_5$  and  $a_6$  have been revised. Further adjustments were made to the values for  $a_3$  and  $a_{5,6}$  listed in Table 1; that is, all  $\gamma_k$  were multiplied by 1.05 and all  $\delta_k$  by 1.15. This correction reduced, on the average by 7 percent, the r.m.s. error of the residuals for all 5400 data points. An example of predicted attenuation rates and measured data points is depicted in Fig. 1.

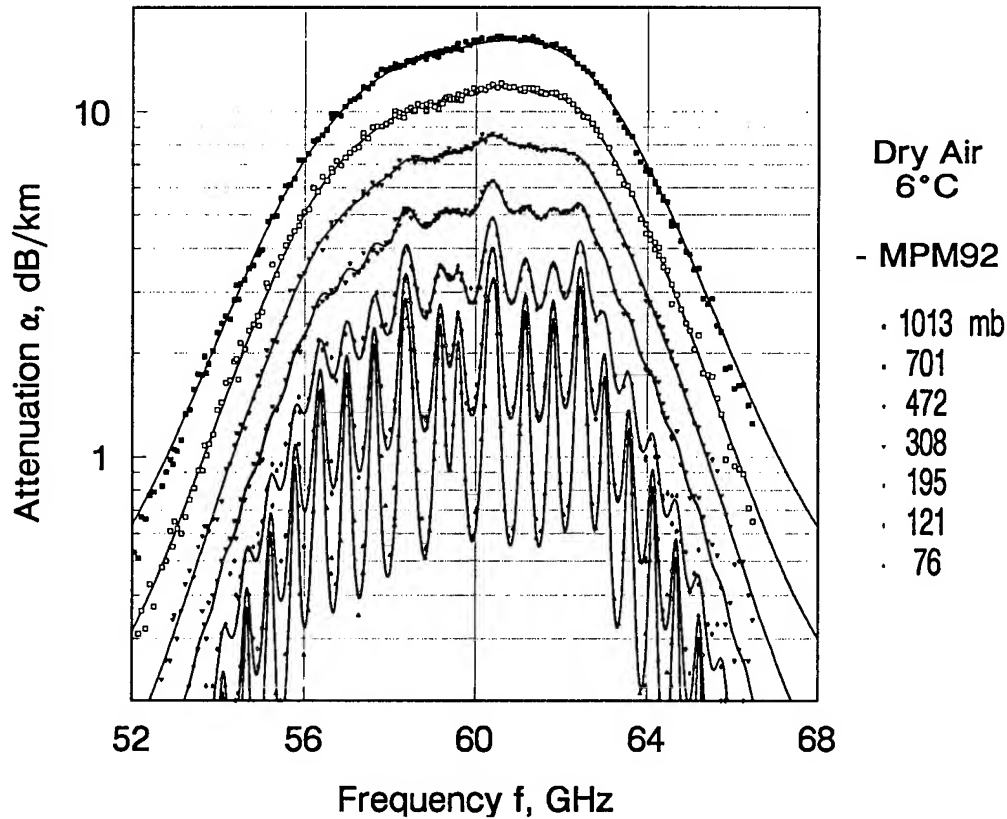


Figure 1. Dry air attenuation rates  $\alpha(\nu)$  between 50 and 68 GHz at 6°C and pressures between 76 and 1013 mb: MPM predictions (solid lines) versus measured data (symbols).

TABLE 1. Spectroscopic Coefficients of O<sub>2</sub> Lines in Air

Line Center $\nu_k$	Strength		Width		Overlap	
	$a_1$	$a_2$	$a_3$	$a_4$	$a_5$	$a_6$
GHz	(kHz/mb)10 <sup>6</sup>		(GHz/mb)10 <sup>3</sup>		10 <sup>3</sup> /mb	
50.474238	0.094	9.694	0.89	0	0.240	0.790
50.987749	0.25	8.694	0.91	0	0.220	0.780
51.503350	0.61	7.744	0.94	0	0.197	0.774
52.021410	1.41	6.844	0.97	0	0.166	0.764
52.542394	3.10	6.004	0.99	0	0.136	0.751
53.066907	6.41	5.224	1.02	0	0.131	0.714
53.595749	12.47	4.484	1.05	0	0.230	0.584
54.130000	22.80	3.814	1.07	0	0.335	0.431
54.671159	39.18	3.194	1.10	0	0.374	0.305
55.221367	63.16	2.624	1.13	0	0.258	0.339
55.783802	95.35	2.119	1.17	0	-0.166	0.705
56.264775	54.89	0.015	1.73	0	0.390	-0.113
56.363389	134.40	1.660	1.20	0	-0.297	0.753
56.968206	176.30	1.260	1.24	0	-0.416	0.742
57.612484	214.10	0.915	1.28	0	-0.613	0.697
58.323877	238.60	0.626	1.33	0	-0.205	0.051
58.446590	145.70	0.084	1.52	0	0.748	-0.146
59.164207	240.40	0.391	1.39	0	-0.722	0.266
59.590983	211.20	0.212	1.43	0	0.765	-0.090
60.306061	212.40	0.212	1.45	0	-0.705	0.081
60.434776	246.10	0.391	1.36	0	0.697	-0.324
61.150560	250.40	0.626	1.31	0	0.104	-0.067
61.800154	229.80	0.915	1.27	0	0.570	-0.761
62.411215	193.30	1.260	1.23	0	0.360	-0.777
62.486260	151.70	0.083	1.54	0	-0.498	0.097
62.997977	150.30	1.665	1.20	0	0.239	-0.768
63.568518	108.70	2.115	1.17	0	0.108	-0.706
64.127767	73.35	2.620	1.13	0	-0.311	-0.332
64.678903	46.35	3.195	1.10	0	-0.421	-0.298
65.224071	27.48	3.815	1.07	0	-0.375	-0.423
65.764772	15.30	4.485	1.05	0	-0.267	-0.575
66.302091	8.01	5.225	1.02	0	-0.168	-0.700
66.836830	3.95	6.005	0.99	0	-0.169	-0.735
67.369598	1.83	6.845	0.97	0	-0.200	-0.744
67.900867	0.80	7.745	0.94	0	-0.228	-0.753
68.431005	0.33	8.695	0.92	0	-0.240	-0.760
68.960311	0.13	9.695	0.90	0	-0.250	-0.765
118.750343	94.50	0.009	1.63	0	-0.036	0.009
368.498350	6.79	0.049	1.92	0.6	0	0
424.763124	63.80	0.044	1.93	0.6	0	0
487.249370	23.50	0.049	1.92	0.6	0	0
715.393150	9.96	0.145	1.81	0.6	0	0
773.839675	67.10	0.130	1.81	0.6	0	0
834.145330	18.00	0.147	1.81	0.6	0	0

## 2.4 WATER VAPOR SPECTRUM

Refractivity of atmospheric water vapor is represented by

$$N_V = N_2 + \sum_{\ell} S_{\ell} F_{\ell} + N_C \text{ ppm}, \quad (10)$$

where nondispersive refractivity is given by  $N_2 = (4.163 \theta + 0.239) e \theta$  ppm, and line refractivity results from 30 local H<sub>2</sub>O-resonances ( $\ell$  = line index). The line strength,

$$S_{\ell} = b_1 e \theta^{3.5} \exp [b_2 (1 - \theta)] \text{ kHz}, \quad (11)$$

is multiplied by the shape function, Eq. (6). The width of a pressure-broadened H<sub>2</sub>O line follows the formulation given by Bauer et al. (1989),

$$\gamma_{\ell} = b_3 10^{-3} (p_d \theta^{b_5} + b_4 e \theta^{b_6}) \text{ GHz}. \quad (12)$$

Line overlap is neglected; i.e.,  $\delta_{\ell} = 0$ . Table 2 lists for the center frequencies  $\nu_{\ell}$  the spectroscopic coefficients  $b_1$  to  $b_6$ . Doppler-broadening of the lines is taken into account at pressures below 0.7 mb ( $h \geq 60$  km) by the approximation  $\gamma_{\ell}^* = 0.535 \gamma_{\ell} + (0.217 \gamma_{\ell}^2 + \gamma_D^2)^{1/2}$ , where the Doppler width is  $\gamma_D = 1.46 \times 10^{-6} \nu_{\ell} \theta^{-1/2}$  GHz.

Continuum refractivity,

$$N_C = \nu e [0.998 \nu (1 - 0.20 \theta) \theta^{2.7} + i (0.357 e \theta^x + 0.0113 p_d \theta^{3.0})] 10^{-6} \text{ ppm}, \quad (13)$$

addresses contributions to Eq. (10) that are in excess over the 30 local lines listed in Table 2. The real part is a first-order approximation to analytical results reported by Hill (1988). This part is small and insensitive to either a specific shape function or to dry-air pressure.

The imaginary part accounts empirically for absorption in excess of line contributions computed with the VanVleck-Weisskopf shape, Eq. (6). The strong negative temperature dependence of the  $e^2$ -term (exponent  $x$ ) is still a source of controversy. Experimental and theoretical evidence for  $x$  are not in full agreement, as shown below:

$\nu$ , GHz	$x(\text{Exp.})$	$\nu$ , GHz	$x(\text{Theory})^d$
137.8 <sup>a)</sup>	10.5	30	6.5
190.3 <sup>b)</sup>	8.4	120	6.7
213.5 <sup>c)</sup>	7.5	360	10.2

<sup>a)</sup> Liebe, 1889; <sup>b)</sup> Bauer et al., 1991; <sup>c)</sup> Godon et al., 1992; <sup>d)</sup> Ma and Tipping, 1990.

Equation (13) is by and large supported by absolute absorption results from laboratory experiments on pure water vapor, and on mixtures with air <sup>a)</sup> and nitrogen <sup>b,c)</sup>. The current choice is  $x = 10.5$ ; but an analysis is under way with the purpose of modifying Eq. (13), so that the reported evidence is more accurately reflected. The unusual temperature dependence has found a plausible interpretation by Ma and Tipping (1990). Their continuum theory relies only on far-wing contributions by the allowed rotational H<sub>2</sub>O transitions (over 500 lines). Frequency and temperature are interwoven and the negative temperature dependence is predicted to become stronger as frequency increases.

TABLE 2. Spectroscopic Coefficients of H<sub>2</sub>O Lines in Air

Line Center $\nu_t$	Strength		Width			
	$b_1$	$b_2$	$b_3$	$b_4$	$b_5$	$b_6$
GHz	kHz/mb		(GHz/mb) $10^3$			
22.235080	0.0114	2.143	2.811	4.80	0.69	1.00
67.813960	0.00011	8.735	2.858	4.93	0.69	0.82
119.995940	0.00007	8.356	2.948	4.78	0.70	0.79
183.310074	0.230	0.668	2.813	5.30	0.64	0.85
321.225644	0.0046	6.181	2.303	4.69	0.67	0.54
325.152919	0.154	1.540	2.783	4.85	0.68	0.74
336.187000	0.0001	9.829	2.693	4.74	0.69	0.61
380.197372	1.1900	1.048	2.873	5.38	0.54	0.89
390.134508	0.0004	7.350	2.152	4.81	0.63	0.55
437.346667	0.0064	5.050	1.845	4.23	0.60	0.48
439.150812	0.0921	3.596	2.100	4.29	0.63	0.52
443.018295	0.0194	5.050	1.860	4.23	0.60	0.50
448.001075	1.060	1.405	2.632	4.84	0.66	0.67
470.888947	0.033	3.599	2.152	4.57	0.66	0.65
474.689127	0.128	2.381	2.355	4.65	0.65	0.64
488.491133	0.0253	2.853	2.602	5.04	0.69	0.72
503.568532	0.0037	6.733	1.612	3.98	0.61	0.43
504.482692	0.0013	6.733	1.612	4.01	0.61	0.45
556.936002	51.0	0.159	3.210	4.11	0.69	1.00
620.700807	0.509	2.200	2.438	4.68	0.71	0.68
658.006500	0.0274	7.820	3.210	4.14	0.69	1.00
752.033227	25.0	0.396	3.060	4.09	0.68	0.84
841.073593	0.0013	8.180	1.590	5.76	0.33	0.45
859.865000	0.0133	7.989	3.060	4.09	0.68	0.84
899.407000	0.0055	7.917	2.985	4.53	0.68	0.90
902.555000	0.0038	8.432	2.865	5.10	0.70	0.95
906.205524	0.0183	5.111	2.408	4.70	0.70	0.53
916.171582	0.856	1.442	2.670	4.78	0.70	0.78
970.315022	0.916	1.920	2.550	4.94	0.64	0.67
987.926764	13.8	0.258	2.985	4.55	0.68	0.90

Using a ground-based, zenith-viewing radiometer, Westwater et al. (1990) measured thermal emission at frequencies of 20.6, 31.7, and 90 GHz looking at identical air volumes. A radiosonde provided height profiles of  $p$ ,  $t$ , and  $u$ . More than 100 data sets for clear air were converted to path attenuations and compared with MPM-predictions. Good agreement was obtained at 31.7 GHz and 90 GHz; whereas the 20.6-GHz data prompted us to raise the  $b_1$  coefficient of the 22.2-GHz line by 5 percent.

Figure 2 displays the attenuation rate  $\alpha(\nu)$  of moist air for a standard, sea-level condition. One notices more or less transparent window ranges (minimum absorption) centered around 35, 90, 140, 220 GHz. Measurement data reported by Furashov et al. (1988) for the 180- to 930-GHz range generally agree with MPM predictions.

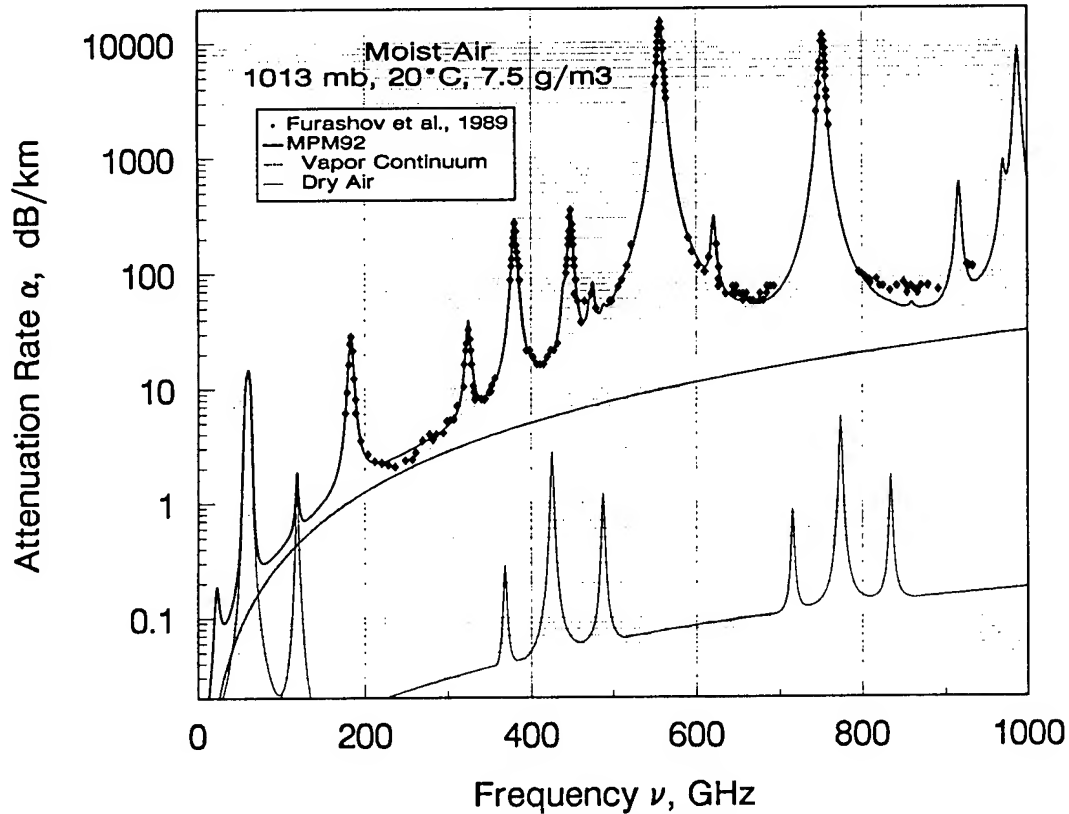


Figure 2. Predicted attenuation rate  $\alpha$  of moist ( $q = 7.5 \text{ g/m}^3$ ) and dry air up to 1000 GHz for a standard sea-level condition.

### 3. SUSPENDED WATER/ICE PARTICLE SPECTRA

#### 3.1 RAYLEIGH APPROXIMATION

The interaction of suspended water droplets and ice particles with radio waves is treated with the Rayleigh absorption approximation ( $c/\nu \gg 2r$ ),

$$N_{w,i} = 1.5 (w / m_{w,i}) [(\epsilon_{w,i} - 1) / (\epsilon_{w,i} + 2)], \quad (14)$$

where  $m_{w,i} = 1.000$  and  $0.916 \text{ (g/cm}^3\text{)}$  are specific weights, and  $\epsilon_{w,i}$  are complex permittivities of water and ice, respectively (Liebe et al., 1989). For the size spectra (radii  $r \leq 50 \mu\text{m}$ ) of suspended water droplets, Eq. (14) is valid up to 300 GHz and, disregarding scattering, provides minimum estimates up to 1000 GHz. Fog or cloud conditions are modeled with the mass density of suspended particles,  $w$  ( $0$  to  $\geq 5 \text{ g/m}^3$ ). Above freezing ( $t \geq 0^\circ\text{C}$ ), water droplets form when the relative humidity exceeds saturation slightly; that is,  $u = 100$  to  $101 \%$ .

#### 3.2 COMPLEX PERMITTIVITY OF WATER AND ICE

Complex permittivity of Water may be approximated by a double-Debye model (Liebe et al., 1991),

$$\epsilon_w = \epsilon_0 - \nu [(\epsilon_0 - \epsilon_1) / (\nu + i\gamma_1) + (\epsilon_1 - \epsilon_2) / (\nu + i\gamma_2)], \quad (15)$$

which realizes a best fit to measured values with the following coefficients:

$$\begin{aligned} \text{Static } (\nu = 0) \text{ permittivity } \epsilon_0 &= 77.66 + 103.3 (\theta - 1), \\ \text{high-frequency permittivities } \epsilon_1 &= 0.0671 \epsilon_0, & \epsilon_2 &= 3.52; \\ \text{relaxation frequencies } \gamma_1 &= 20.20 - 146 (\theta - 1) + 316 (\theta - 1)^2, & \gamma_2 &= 39.8 \gamma_1 \text{ GHz}. \end{aligned}$$

The temperature dependence of  $\epsilon_2$  was eliminated to avoid for super-cooled (-20 to -40°C) water nonphysical behavior at frequencies above 100 GHz.

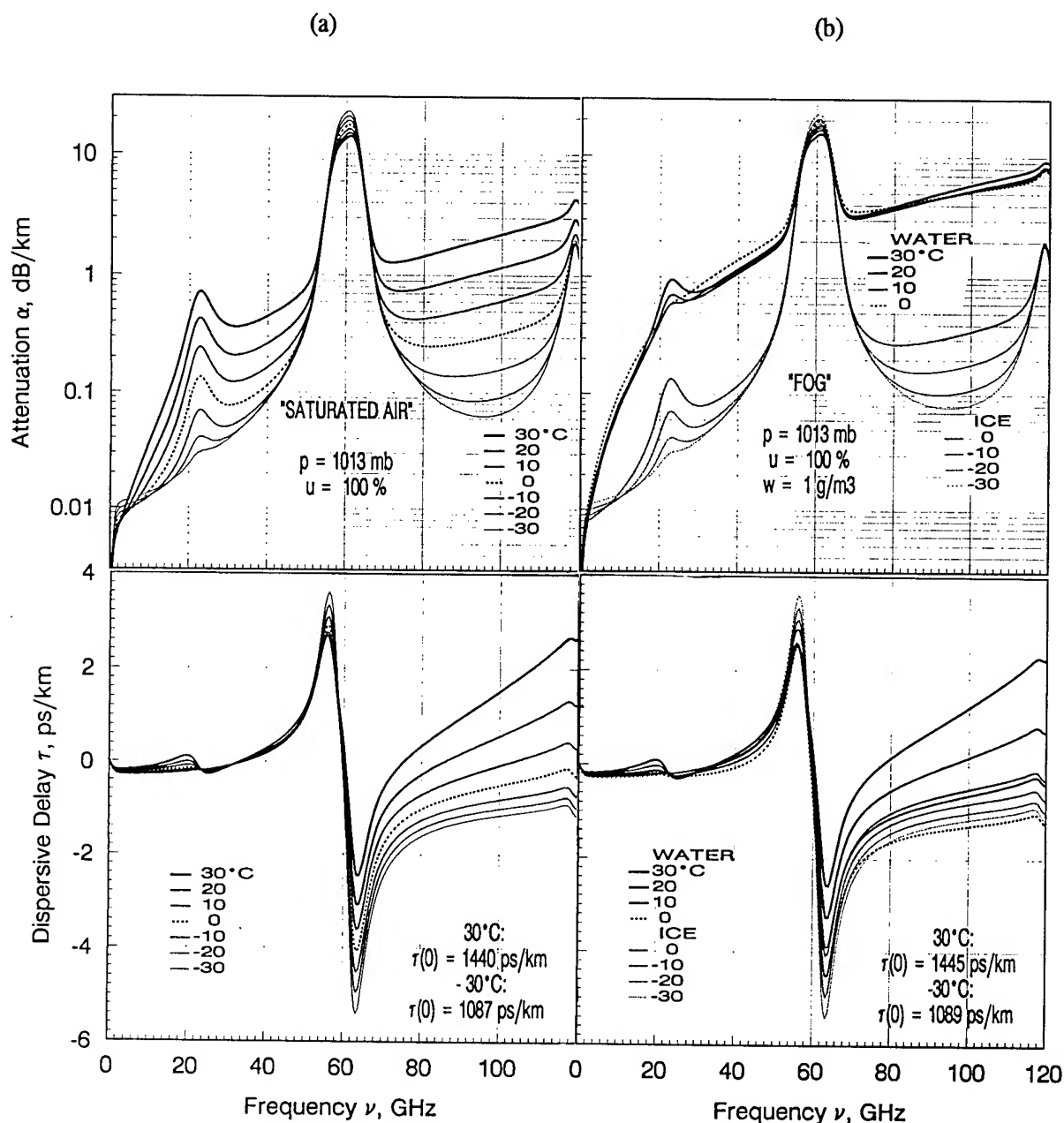


Figure 3. Attenuation and Delay Spectra between 0 and 120 GHz at Temperatures  $\pm 30^\circ\text{C}$ :  
(a) Saturated Air at Sea-Level,  $u = 100\%$ , (b) Water and Ice Fog,  $w = 1 \text{ g/m}^3$ .

Figure 3 gives examples of predicted attenuation and delay spectra for saturated, sea-level air with a normalized density of  $w = 1 \text{ g/m}^3$  (heavy fog, about 50 m visibility). One notices that from 1 to 100 GHz the overall attenuation behavior is between 0 and 30°C almost independent of temperature. The refractive delay is given by  $\tau(0) = 3.336 (N_1 + N_2 + N_3)$ , where  $N_3 = 1.5 w [1 - 3/(\epsilon_0 - 1)]$ .

A permittivity model for ICE was reported by Hufford (1991),

$$\epsilon_i = 3.15 + i(a_i/\nu + b_i \nu), \quad (16)$$

where  $a_i(\theta) = (\theta - 0.171) \exp(17.0 - 22.1 \theta) \text{ GHz}$ , and  
 $b_i(\theta) = \{0.0542 [\theta / (\theta - 0.993)]^2 + (6.33 / \theta) - 1.31\} 10^{-5} \text{ GHz}^{-1}$ .

Equation (16) is valid for  $t \leq 0^\circ\text{C}$  ( $\theta \geq 1.099$ ) over the frequency range from 1 MHz to 1000 GHz. Propagation effects caused by suspended ice crystals (needles and plates) are primarily depolarizing in nature. Ice attenuation and delay rates (see Fig. 3) were estimated with Eq. (14).

## 5. SUMMARY

Systems that operate at millimeter-wave frequencies offer much improved performance over infra-red/optical systems under fog or cloud conditions. Propagation characteristics of the nonprecipitating atmosphere are predicted by the refractivity model,  $N = N_D + N_V + N_{W,I}$  [Eqs. (4), (10), (14)]. Transmission and emission properties of the inhomogeneous atmosphere (e.g., opacity, path delay, brightness temperature) can be modeled when the path distributions of pressure, temperature, and humidity are known. The suspended particle density  $w$  might be estimated from databases for the extinction of visible light.

Uncertainties of MPM predictions may be evaluated by comparison with data for which the true values of  $p$ ,  $t$ ,  $u$ , and  $w$  are known. However, such measurements cannot be made reliably under "real" atmospheric conditions. Under "controlled" laboratory conditions, the dry-air absorption has been measured between 49 and 67 GHz. The extensive experimental data set agrees with MPM predictions to within 1 percent (Liebe et al., 1992). The errors of model predictions involving  $\text{H}_2\text{O}$  vapor and water droplets are estimated to lie in the 10 percent range. Validation and error checking of predictions, as well as incorporating new research results into MPM, will continue to be critical and time-consuming tasks.

## ACKNOWLEDGMENT

This work was supported in part by the U. S. Army Atmospheric Sciences Laboratory, ARL, SLCAS-BA under Reference No. ASL 92-8058.

## REFERENCES

- Bauer, A., M. Godon, M. Kheddar, and J. M. Hartmann, 1989: Temperature and Perturber Dependences of Water Vapor Line-Broadening: Experiments at 183 GHz, Calculations Below 1000 GHz. *J. Quant. Spectr. Radiat. Transf.*, **41**(1):49-54.
- Bauer, A., and M. Godon, 1991: Temperature Dependence of Water Vapour Absorption in Line-wings at 190 GHz. *J. Quant. Spectr. Rad. Transf.*, **46**(3):211-220.



- Brown, D. R., 1987: Near Millimeter Wave Module, NMMW, ASL-TR-0221-6, U.S. Army Atmospheric Sciences Laboratory, White Sands Missile Range, NM 88002-5501.
- Furashov, N. I., V. Yu. Katkov, and B. A. Svertlov, 1989: Submillimetre Spectrum of the Atmospheric Water Vapor Absorption - Some Experimental Results. ICAP 89, IEE Conf. Publ., No. 301:310-311.
- Godon, M., J. Carlier, and A. Bauer, 1992: Laboratory Studies of Water Vapor Absorption in the Atmospheric Window at 213 GHz. J. Quant. Spectr. Radiat. Transf., 47(4):275-285.
- Goff, J. A., and S. Gratch, 1946: Low-Pressure Properties of Water from -160 to 212°F. Trans. Amer. Soc. Heat. Vent. Eng., 52:95-121 (also List, R. J., Smithsonian Meteorological Tables. Washington D.C., Smithsonian Inst., Sixth Ed., 1966).
- Hill, R. J., 1988: Dispersion by Atmospheric Water Vapor at Frequencies Less Than 1 THz. IEEE Trans. Antennas Propag., AP-36(3):423-430.
- Hufford G. A., and H. J. Liebe, 1989: Millimeter-Wave Propagation In The Mesosphere. NTIA-Report 89-249, U.S. Dept. Com., Boulder, CO; NTIS Order No. PB 90-119868/AF (1989).
- Hufford, G. A., 1991: A Model for the Complex Permittivity of Ice at Frequencies Below 1 THz. Int. J. Infrared and Millimeter Waves, 12(7): 677-680.
- Liebe, H. J., 1989: MPM - An Atmospheric Millimeter-Wave Propagation Model. Int. J. Infrared and Millimeter Waves, 10(6): 631-650.
- Liebe, H. J., T. Manabe, and G. A. Hufford, 1989: Millimeter-Wave Attenuation and Delay Rates Due to Fog/Cloud Conditions. IEEE Trans. Antennas Propag., AP-37(12):1617-1623.
- Liebe, H. J., G. A. Hufford, and T. Manabe, 1991: A Model for the Complex Permittivity of Water at Frequencies Below 1 THz. Int. J. Infrared and Millimeter Waves, 12(7):659-675.
- Liebe, H. J., P. W. Rosenkranz, and G. A. Hufford, 1992: Atmospheric 60-GHz Oxygen Spectrum: New Measurements and Line Parameters. J. Quant. Spectr. Radiat. Transf., 48(5): in press.
- Ma, Q., and R. H. Tipping, 1990: Water Vapor Continuum in the Millimeter Spectral Region. J. Chem. Phys., 93(9):6127-6139.
- Rosenkranz, P. W., 1988: Interference Coefficients for Overlapping Oxygen Lines in Air. J. Quant. Spectr. Radiat. Transf., 39(4):287-297.
- Rosenkranz, P. W., 1992: Absorption of Microwaves by Atmospheric Gases. In Atmospheric Remote Sensing By Microwave Radiometry, Chap. 2; M. A. Janssen, ed., Wiley and Sons, N.Y., N.Y. (in press).
- Westwater, Ed. R., J. B. Snider, and M. J. Falls, 1990: Ground-Based Radiometric Observations of Atmospheric Emission and Attenuation at 20.6, 31.65, and 90.0 GHz: A Comparison of Measurements and Theory. IEEE Trans. Antennas Propag., AP-38(10):1569-1580.

# **RADAR BACKSCATTER FROM SNOW SURFACE (VERIFICATION OF MODEL AND PREDICTION)**

by

Dr. Oskar Essenwanger  
University of Alabama in Huntsville  
c/o Atmospheric Science Program, RI-A11  
Huntsville, Alabama, 35899

## **ABSTRACT**

It is well known that the condition of the surface of a snowfield may lead to reflectivity affecting the radar signal. For operational use a model based on standard meteorological conditions was developed which provides criteria when high reflectivity exists. The new model was verified by associating meteorological data and radar signals from tests at Fort Drum (NY) and Germany.

A regression equation was established to predict high reflectivity for 7 snowclasses. As a first result the prediction was successful in over 90% of the cases for dry snow surface. However, the regression model's weakness was the poor performance in correctly specifying the change to a wet snow surface. Hence the precipitation expectancy 3 hours later was incorporated into the regression model. This inclusion considerably improved the predictability.

## **1. INTRODUCTION**

For operational purposes it is important whether radar clutter from the snow surface can be expected. Snow surface conditions are described by CRREL (see Fisk, et al., 1991) for 32 different classes of snow grains and water content. In our study these classes have been reduced to 4 major types, with subdivision to a total of 7 types of surface. A computer model has been developed to permit the calculations of climatological probabilities by an objective and efficient data processing method (see Essenwanger, 1989).

The boundaries were earlier determined by discussions between the author and radar engineers. It was intended, however, to check the validity of the class boundaries by simultaneous meteorological observations and radar signals during test flights. Some data have now become available and have been used in this study (see Table 2). They confirmed the validity of the boundaries although some uncertainty is still valid for dry snow surfaces.

After the snow classes for daily records at 3 hourly intervals were determined for the time from 1 November through 30 April during the years 1973 - 1989 for several stations in Germany a prediction scheme was established. These details are presented in part 3.

## **2. VALIDITY OF PREVIOUSLY ESTABLISHED BOUNDARIES IN THE SNOW MODEL COMPUTER CODE**

### **2.1. Clutter Data, Meteorological Observations, and Snow Code.**

Radar clutter information became available in the later part of 1991 from test flights at Fort Drum in January - February 1991. The meteorological and snow surface observations were made by CRREL (Cold Region Research and Engineering Laboratory, Hanover, NH), (see Fisk, et al., 1991). Unfortunately the meteorological observations were not made on a continuous daily basis but only for days when flights were performed. Thus the author could not include the history of previous days, and had to rely on the snow surface characterization by CRREL and the interpretation in terms of the computer model. It is reasonable that the

computer code is limited to 4 main types: 0 = now snow, W = wet snow, D = dry snow, and MF is frozen snow after melting (see Table 1).

The categories are further subdivided by temperature ranges. This subdivision is of no interest for no snow hours. Since wet snow (W) occurs at  $T \geq 0^{\circ}\text{C}$  except for solar loading at first no subdivision was considered necessary for W. The frequency of wet snow due to solar loading during daytime proved to be about 30% (see Table 3), thus, it appeared appropriate to subdivide wet snow. This leaves 7 classes (see Table 1).

As previously reported (FARMY112.FIN) the class code as shown in Table 1 is based on several entries into the computer modeling. This can be an actual observation of the snow surface reported in the synoptic surface weather code by an observer, or when frozen precipitation is reported. The computer model is also including the snow surface condition of the previous hour as well as the melting of the snow, so that snow cover is not perpetuated. This formula for reducing the snow height may need some further refinement.

The codes  $\geq 4$  in Table 1 are classes where radar clutter may be expected.

## 2.2. Test Flights at Fort Drum.

Table 2 lists the results of the test flight for 7 missions at Fort Drum as they apply to the snow model computer code. The first two columns show the mission date and flight, the third column the time of day (local time). It can be deduced that in 4 cases clutter was observed for melt-freeze conditions, with the snow model codes 4 through 6. The data agree with the snow model code. The three columns on temperature delineate some differences between the temperature measured during the test, for the air (6 m height), and for the snow surface. These temperature differences are small and could be expected. The computer model for the classification of the snow surface is based on the standard meteorological observation of the air temperature as made by CRREL during the test. The data of Table 2, although limited, do not contradict the snow surface classification by the computer model.

Let us inspect the 7 cases where the computer model placed the snow surface into code 1, wet snow. No clutter was observed during the test flights. Consequently there is no contradiction.

The only uncertainty was found on day 33A. According to the snow surface observation by CRREL dry snow surface existed during that test flight. The first line of day 33A shows an air temperature of  $-6^{\circ}\text{C}$ . Since a boundary of  $-5^{\circ}\text{C}$  was assumed in the computer model the code of 5 is obtained. This would indicate radar clutter which is confirmed by the test flight.

The second line of day 33A the air temperature is  $-4^{\circ}\text{C}$ , and the snow code is 3, which is not a clutter category. Careful inspection of the test data reveals that this may be a borderline where clutter could have occurred. The data are somewhat inconclusive but weak clutter could have been present.

The two cases of the flight test on dry snow surface are not sufficient to make any final decision whether the clutter boundary for dry snow should be changed. According to data from the European community the boundary lies around  $-5^{\circ}\text{C}$ . Thus this boundary is not changed by the author at the present time for the calculation of the climatological frequency, or the prediction investigation.

An interesting case is found on day 49A,B. Two test flights were made (49A) about 20 minutes apart (7:28 and 7:48 AM). The first flight (Figure 1a, provided by MDTT) shows cluttering, and the model correctly places the snow surface into the clutter category (code 6). Then 20 minutes later the sun came up and caused solar loading, and the clutter disappeared (wet snow, code 2, Figure 1b). At 10:30 AM the sky was covered about 90% (see last column, skycover in Table 2). By the low temperature the snow surface apparently refroze (code 4). At 11:15 AM solar loading started again, and the clutter faded. Although this indicates that at Fort Drum solar loading in February 91 started already at  $-10$  to  $-12^{\circ}\text{C}$  the solar angle at  $50^{\circ}$  North latitude is different from Fort Drum, NY. Consequently a boundary of  $-5^{\circ}\text{C}$  appears to be reasonable for Germany. The only change could be that solar loading

Table 1 Snow Code of Snow Surface Conditions and Temperature

Code	Letter Code	Snow Condition	Temperature
0	0	no snow	--
1	W	wet snow	$T \geq 0^{\circ}\text{C}$
2	W <sub>s</sub>	wet snow, solar loading	$T \geq -5^{\circ}\text{C}$
3	D <sub>1</sub>	dry snow	$T \geq -5^{\circ}\text{C}$
4	MF <sub>1</sub>	melt-freeze snow	$T \geq -5^{\circ}\text{C}$
5	D <sub>2</sub>	dry snow	$T < -5^{\circ}\text{C}$
6	MF <sub>2</sub>	melt-freeze snow	$T < -5^{\circ}\text{C}$

Table 2 Test Data, Fort Drum, Temperature, Snow Code

Day	Mission	Time	Signal	TM	TA	TS	Sky-cover	Code
19A	MD10	11.05-12.30	Y	-4	-4	-4	100%	4
19B	MD11	13.40-15.10	N	0	0	0	100%	1
33A	MD14	7.25-8.21	Y	-6	-6	-6	80%	5
33A	MD14	8.25-9.31	(Y)	-5	-4	-6	80%	3
33B	MD23	11.29-12.18	N	0	2	0	00	1
33B	MD23	12.22-13.36	N	1	3	0	00	1
34	MD13	7.50-9.30	Y	0	1	-1.5	60%	4
35	MD12	7.00-7.45	N	0	0	3	60%	1
35	MD12	7.48-8.56	N	0	0	6	20%	1
49A	MD23	7.28	YY	-15	-12	-14	20%	6
49A	MD23	7.46	N	-10	-10	-10	20%	2
49B	MD21	10.30	Y	-5	-5	-5	90%	4
49B	MD21	11.15	N	0	-2	-1	50%	2

Temperature: TM measured by test, TA air (6m height), TS snow surface (CRREL).

Table 3 Solar Loading and Wet Snow Frequency  
(1 Nov - 30 Apr, 1973 - 1989, Germany)

	Stuttgart	Hof	
Wet snow	11.2%	14.1%	of <u>all</u> hours
Wet during daytime	51.8%	54.3%	of wet snow hours
Solar Loading	30.7%	33.7%	of wet snow hours
Solar Loading	1.8%	2.6%	of <u>all</u> hours

would take place already at 50% of skycover instead of 30% as originally assumed. The effect of this change on the climatological frequency of high reflecting snow in German data is minimal. Analysis of data from German sites is continuing.

### 2.3. Solar loading Occurrence for German Stations.

Table 3 discloses the frequency of encountering wet snow, and the percentages how much of it is attributed to solar loading. Stuttgart was chosen because it represents about average snow frequency in Southern Germany, and Hof has high number of hours with snowcover during winter. We deduce that wet snow (non-reflecting) can be found in about 11-14% of the hours (November - April). Of these about 50% were observed during daylight hours (9 - 15 hours GMT). Of these 1/3 was caused by solar loading. However, the total number of hours with solar loading was 1.8 and 2.6% for Stuttgart and Hof, respectively. It is evident that the boundary change from 30 to 50% of skycover has little effect on climatological probabilities.

### 2.4. Boundaries Derived from the Present Data.

The data available for verification of the computer model are limited. However, they indicate that the assumptions in the computer code classifying the snow surface with reference to clutter (high reflectivity) appear correct for codes 1,2 (wet snow), and 4,6 (frozen snow surface from melt freeze, see also FARMY138.FIN, FARMY153.FIN). The boundary between 3 and 5 needs more analysis.

Solar loading occurred at Fort Drum around an air temperature of about - 10° C. Since in Germany the average latitude is 50° N, i.e. about 10° higher than at Fort Drum, US, the boundary of - 5° C for Germany for solar loading appears reasonable. The skycover has been changed from 30 to 50%, below which solar loading can already be assumed. Probably it may be more realistic to keep 30% for lower solar angles, and use 50% during the noon hours. However, this sophistication does not reduce the climatological frequencies of high reflectivity in Germany during the wintertime by more than a small fraction of a percentage.

## 3. PREDICTION OF BACKSCATTER FROM STANDARD METEOROLOGICAL DATA

### 3.1. Persistence.

Table 4 reflects the chances for correctly forecasting the condition of the snowsurface by assuming persistence. An extended table can be found in Essenwanger (1991). We learn that the only high persistence suitable for use in a forecast is the "no snow" class. In all other snow surface types persistence is very low, only D<sub>2</sub> has some reasonable persistence. However, even there some improvement is desirable.

### 3.2. Prediction by a Regression Model.

The regression model is base on the relationship between predictand and predictors such as

$$y = a_0 + a_1x_1 + a_2x_2 \dots\dots + a_nx_n$$

where y is the predictand, and x are suitable predictors, the a<sub>n</sub> are calculated coefficients. The weather elements at time 0 hour serve as predictors except that the temperature 3 hours later and the anticipated possibility of precipitation was included into the new model.

An earlier attempt was presented (Essenwanger, 1990) with a uniform model for all hours (see later Table 6a). Although this model provided some improvement over

Table 4 Persistence of Snow Condition  
(Code see Table 1)  
(Dec - March, 1973 - 1989, Germany)

Code		STU	HOF	BER	HAN	PRED*
0	0	95	94	96	96%	--
1	W	52	64	58	61%	90%
2	Ws	22	24	32	27%	90%
3	D <sub>1</sub>	72	79	74	74%	93%
4	MF <sub>1</sub>	57	65	61	62%	99%
5	D <sub>2</sub>	85	88	87	85%	98%
6	MF <sub>2</sub>	68	71	68	67%	99%

\* New regression model, STU = Stuttgart, BER = Berlin, HAN = Hannover.

Table 5 Incorrect predictions (earlier regression model)

Hours:	0	3	6	9	12	15	18	21	GMT
	7.1	15.4	12.6	9.2	7.8	19.3	12.7	7.9%	

Table 6 Matrix for 3 Hour Prediction (all hours)  
(Stuttgart, Germany, Dec - March, 1973 - 1989)

(A) Early Regression Model

Code	1,2,3	4	5,6
1,2,3	90.1	66.4	1.0%
4,5,6	9.9	33.6	99.0%
N	27.1	5.2	9.7% of 14519

Remark: 9.9, 66.4 and 1.0 are incorrect predictions.  
It adds up to a total of 6.3% incorrect predictions.

(B) New Regression Model

Code	1,2,3	4	5,6
1,2,3	91.7	0.7	1.3%
4,5,6	8.3	99.3	98.7%

Remark: 8.3, 0.7, and 1.3 are incorrect predictions.  
It adds up to 2.4%

For codes 1,2,3 the discontinuity by precipitation is not included into the new model.

Table 7 Standardized Coefficients for Regression Model

Hour										
GMT	A <sub>o</sub>	SNO	TTO	DTO	VISO	WW0	CEILO	NHO	WSPO	TT3
0	0.835	1.436	0.558	0.005	0.038	0.011	0.092	0.055	0.027	0.952
3	1.976	1.087	0.279	0.107	0.117	0.011	0.016	0.061	0.075	0.484
6	2.003	0.512	0.031	0.092	0.093	0.066	0.442	0.016	0.068	1.380
9	1.395	0.200	0.266	0.121	0.055	0.095	0.025	0.343	0.066	1.610
12	2.447	0.505	0.317	0.112	0.062	0.092	0.300	0.189	0.075	1.474
15	2.589	0.067	0.329	0.228	0.162	0.084	0.111	0.074	0.098	1.481
18	1.346	1.131	0.472	0.072	0.059	0.024	0.015	0.022	0.087	1.209
21	1.531	1.388	0.898	0.318	0.088	0.030	0.221	0.169	0.006	1.418

ALL 1.310 0.430 0.234 0.062 0.009 0.007 0.002 0.042 0.010 0.947

SN = snow, TT = temperature, DT = dewpoint, VIS = visibility  
 WW = weather, CEIL = ceiling height, NH = skycover,  
 WSP = windspeed

Table 8 Ranking of Coefficients

Hour	GMT	SNO	TTO	DTO	VISO	WW0	CEILO	NHO	WSPO	TT3
0	1	3	9	6	8	4	5	7	2	
3	1	3	5	4	9	8	7	6	2	
6	2	8	5	4	7	3	9	6	1	
9	4	3	5	8	6	9	2	7	1	
12	2	3	6	9	7	4	5	8	1	
15	9	2	3	4	7	5	8	6	1	
18	2	3	5	6	7	9	8	4	1	
21	2	3	4	7	8	5	6	9	1	
Σ/8	2.9	3.5	5.3	6.0	7.4	5.9	6.3	6.6	1.2	
ALL	2	3	4	7	8	9	5	6	1	

0 behind means at time of prediction, 3 = three hours later

persistence, the changes for type 4 were not properly predicted. Thus the predictability of high reflecting snow was attempted by a breakdown into individual hours.

The result is disclosed in Table 5. We deduce that predictability ranges from 7 to 19%, an obvious improvement. However, especially the figure of 19% is not satisfactory. Thus a different approach was taken.

This new regression model is separated into three groups: wet snow, (1,2) dry snow (3), (5) and (6), i.e. dry snow and melt-freeze, and melt-freeze (4).

The result for Stuttgart is listed in the last column of Table 4, and in Table 6b. By comparing the correct predictions (percentages) of the former model with the present percentages this is a considerable improvement. In the types 1,2 the anticipated precipitation 3 hours later was not included. Thus there is still room for improvement.

### 3.3. Importance of Predictors.

Table 7 lists the individual coefficients of the regression model for standardized parameters (i.e. the predictor is divided by its standard deviation). The coefficients in Table 7 are presented for the earlier model by hours. However, the result is the same for the new model. The ranking of the coefficients is delineated in Table 8.

It is comforting to see that the first 4 important predictors are the same for all hours. The zero behind the parameter symbol indicates that these predictors would be available at the time of prediction. Only TT3, the temperature 3 hours later, would be needed as a forecast. As it proves, this is a most important predictor. This result is no surprise. Therefore, this predictor was included into the regression model.

During the hours 6 through 15 (i.e. 7 through 16 local time) the importance of the temperature is obvious because it determines whether the snow surface melts or refreezes.

During the night (0 and 3 hour GMT) the condition of the snow surface is ranking first. This is logical because the snow surface would not change during the night except probably to freeze towards the morning hours after it is wet, or when precipitation changes the surface.

For the hours 18 and 21 GMT (i.e. 19 and 22 local time) the snow surface condition and the temperature exert about equal effects.

The temperature and dew point at prediction time are next in importance. Visibility, weather, cloud ceiling and skycover vary in ranking for the individual hours. Surprisingly, the weather condition is last in the average for the hours and next to last for the combined hours. This may be somewhat misleading. It must be reiterated that the regression model is based on continuity, and the changes by precipitation is a discontinuity. This change was incorporated into the new regression model through an additional criteria. Since this change does not occur frequently enough it does not have a significant impact as a term in the old regression model. The inclusion improved the probability of correct forecasts considerably (see Table 6b).

## 4. CONCLUSION.

A limited set of data was made available to the author to verify the boundaries in the computer model which determines the conditions of the snow surface for 7 types, indicating reflection or non-reflection.

Solar loading occurred at Fort Drum, NY, around  $-10^{\circ}$  C. Under consideration that the latitude in Germany is 10 degrees higher to the North, the present threshold for Germany of  $-5^{\circ}$  C was kept. It was discovered, however, that solar loading may already occur when the sky is still 50% covered by clouds. Thus the present 30% boundary has been changed but it affected the climatological probabilities of reflecting snow by less than 0.2%.

The boundary when dry snow begins reflecting could not be completely firmed up. However, no contradictory observation of reflection could be found. At the present time the analysis of the boundary between code 3 and code 5 (see Table 1) is continuing.



The prediction by a regression model for individual hours showed improvement in reducing the incorrect prediction which range from 1 to 10%. This is better than the magnitude as expected for present weather prediction.

#### REFERENCES

- Essenwanger, O. M., 1989, FARMY112.FIN  
Final Report on Contract DAAH01 - 87 - D - 0021, D) # 112  
Army Missile Command.
- Essenwanger, O.M., 1990, FARMY138.FIN  
Final Report on Contract DAAH01 - 87 - D - 0021, DO # 138  
Army Missile Command.
- Essenwager, O.M., 1990, On Short Term Prediction of High Reflectivity  
Snow in Central Europe. Proceedings of the 11th Annual  
EOSEAL/TWI Conference, Las Cruces, NM. p.
- Essenwanger, O.M., 1991, FARMY153.FIN  
Final Report on Contract DAAH01 - 87 - D - 0021, DO # 153  
Army Missile Command
- Fisk, D.J., and G.E. Lemieux, 1991, Snow Conditions During MLRS-TGW BBU1  
Captive Flight Program, Fort Drum, N.Y., January-February  
January-February 1991.  
US Army Cold Regions Research and Engineering Laboratory,  
Hanover, NH 03755.

#### ACKNOWLEDGEMENT

The principal investigator wishes to acknowledge the assistance of Mr. David Watson in the tedious task of preparing the data from magnetic tape furnished by ETAC of the National Weather Records Center, Asheville, NC for usage on a PC. Ms. Taylor must be thanked for preparation of the manuscript on the stencil. Finally, the principal investigator is grateful to Mr. Francois Naussac for his discussion of high reflectivity data furnished by MDTT. This research was performed under contract DAAH01-91-D-R002, D.O. # 28.

Figure 1a

# BBU1 SNOW CLUTTER Ft. Drum, NY - 18 Feb. 1991

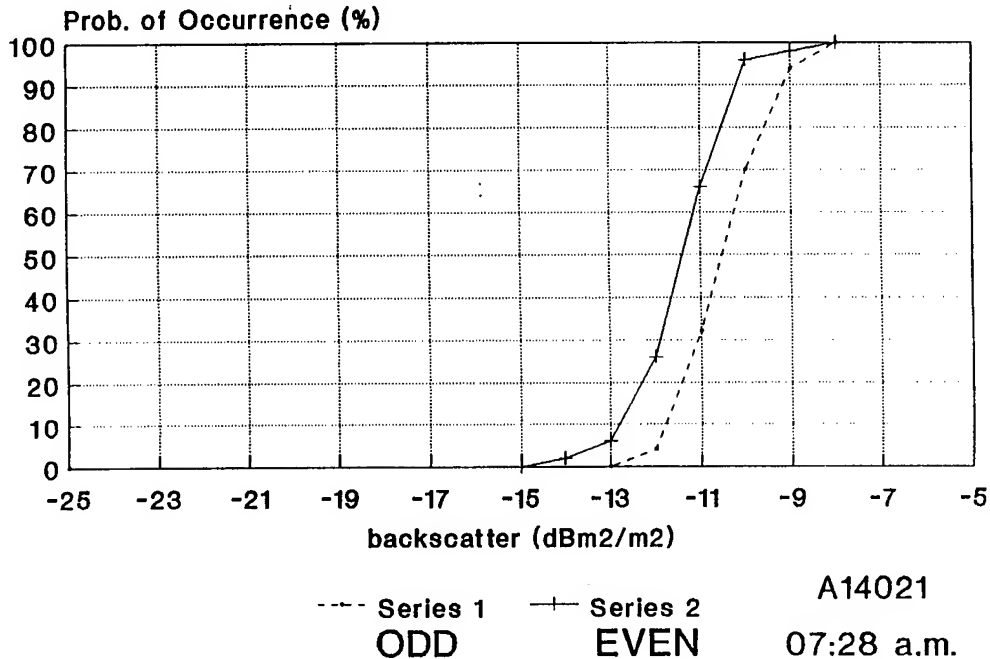
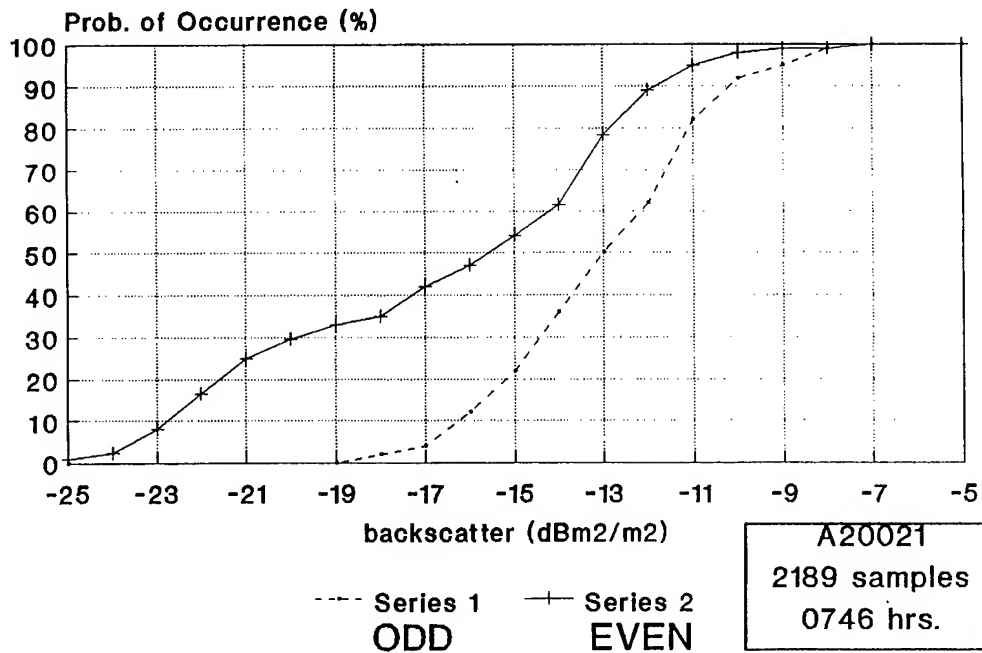


Figure 1b

# BBU1 SNOW CLUTTER Ft. Drum, NY - 18 Feb. 1991







## THE IMPORTANCE OF DUCTING IN ATMOSPHERIC ACOUSTICS

by

John M. Noble  
Battlefield Environment Directorate\*  
U.S. Army Research Laboratory  
White Sands Missile Range, New Mexico 88002-5501

### ABSTRACT

The state of the atmosphere is very important for determining how well sound will propagate. As the atmosphere changes during the diurnal cycle, the temperature and wind speed profiles with height can vary significantly. Examining just the diurnal variations in the temperature profile would show that the best acoustic propagation occurs at night after an inversion has been established and daytime propagation will be poor. However when experiments are performed, the results show that propagation in the daytime can be as good as if not better than at night. Including the wind speed profile in the examination shows that a phenomenon called ducting can result. The duct formed by including wind effects can be just as effective as ducts formed by temperature inversions. Knowing when this phenomenon is occurring during the daytime is the key to predicting good acoustic propagation conditions.

### 1. DEFINING AN ACOUSTIC DUCT

Before an explanation of acoustic ducting can be presented, the definition of an acoustic duct must be given. A general definition of an acoustic duct is a region of the atmosphere where a layer that causes downward refraction resides on top of a layer that causes upward refraction as shown in fig. 1. In layer 1, the speed of sound decreases with height, causing upward refraction. In layer 2, the speed of sound increases with height, causing downward refraction. This definition does not seem to apply to surface ducts as in fig. 2. This case appears to contradict the definition of an acoustic duct. However, the reflection of sound by the ground leads to the concept of image sources and image atmospheres in the ground. Figure 3 shows the result of applying this concept to the case in question. If the image atmosphere is included in the problem, the slope of the speed of sound profile must be

---

\* formerly U.S. Army Atmospheric Sciences Laboratory

changed so the reflection of a downward refractive layer in the atmosphere now becomes an upward refractive layer. Therefore, the definition given previously for an acoustic duct still applies.

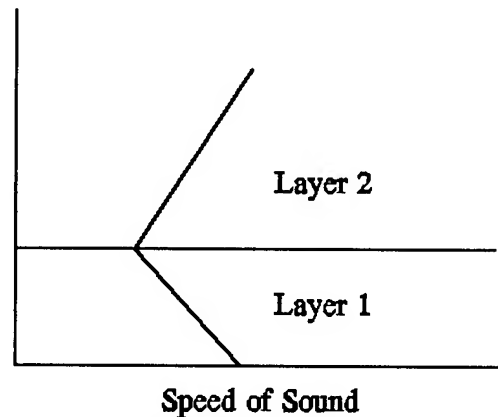


Figure 1. Idealized shape of an acoustic duct.

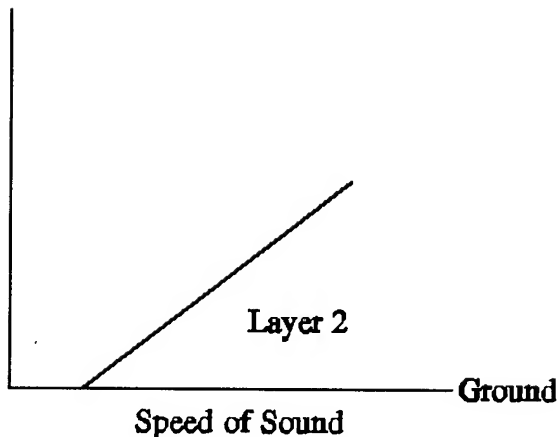


Figure 2. Idealized shape of a surface duct.

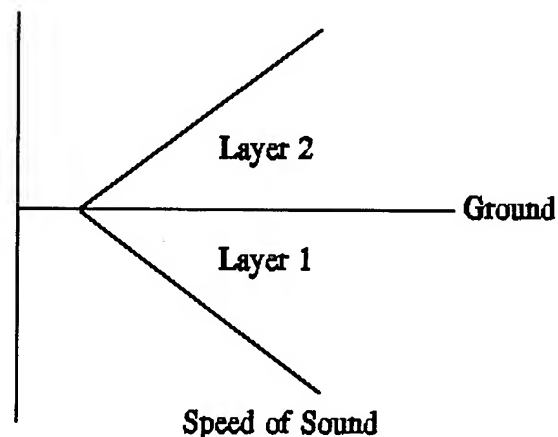


Figure 3. Idealized shape of a surface duct and its image.

The effectiveness of an acoustic duct to propagate sound is a function of the thickness, frequency of the sound, and strength within the duct. A thicker acoustic duct will be able to refract more of the acoustic wave back towards the surface, resulting in more trapped acoustic energy within the duct. The frequency of the sound is important because acoustic ducts of a certain size will support propagation of certain frequencies better than others, just as in a waveguide. The strength of an acoustic duct is a function of speed of sound gradient, which is related to the thickness of the duct and the change of the speed of sound profile within the duct. There is a limit to strength of an acoustic duct. The speed of sound gradient will eventually reach a point where any benefit of additional downward refraction is offset by a loss of acoustic energy from the acoustic wave undergoing diffraction by the strong speed of sound gradient. This effect contributes to a property of acoustic ducts known as the "leakiness" of the duct.

## 2. METEOROLOGICAL EFFECTS ON SPEED OF SOUND

The meteorological variables that affect the speed of sound in the air are pressure, temperature, vector wind speed, and humidity. To observe the effect of each meteorological variable, considering each independently, one can examine the equation for the speed of sound in air. The value of  $c$ , according to Laplace's adiabatic assumption for air as an ideal gas, is

$$c(T) = \sqrt{\gamma RT/M}, \quad (1)$$

where  $\gamma$  is the ratio of specific heats,  $R$  is the universal gas constant that is equal to 8314.16 J/(kg K), and  $M$  is the molecular weight. The dependence of the speed of sound on pressure and humidity is found in the ratio of specific heats and molecular weight of moist air. However, these dependencies are not very strong and can be ignored when confining the problem to the lower 1 to 2 km of the atmosphere.

The consideration of the wind speed to the speed of sound is a vector relation. The effective speed of sound is calculated using

$$c_{eff} = c(T) + u \cdot \cos(\theta_w - \pi - \theta_R), \quad (2)$$

where  $c(T)$  is the speed of sound in the absence of wind at temperature  $T$ ,  $u$  is the magnitude of the horizontal wind speed,  $\theta_R$  is the bearing of the receiver from the target,  $\theta_w$  is the direction from which the wind blows, and  $\theta_w - \pi$  is the direction the wind is blowing to relative to north. Typically in acoustics, the term "effective" is dropped when referring to the speed of sound profile including the vector wind speed. This terminology will be used in this paper.

## 3. ATMOSPHERIC CAUSES OF ACOUSTIC DUCTS

Since the speed of sound is dependent on the temperature and vector wind speed, the creation of an acoustic duct will depend on the profile of these properties. Before examining both atmospheric properties at once, one can begin by examining the temperature contribution to the speed of sound profile and how the temperature profile varies diurnally. The daytime temperature profile shows, in the planetary boundary layer, the highest temperature occurring at the surface with the temperature decreasing with height. The speed of sound profile based solely on the temperature would show the same trend as in the temperature profile. Using this information alone, the daytime temperature profile would cause sound propagating in the atmosphere to be refracted upwards. This effect would result in poor acoustic propagation conditions. At night, the ground can cool more rapidly than the surrounding air. This leads to an atmospheric condition called a nocturnal inversion. This condition means that the temperature at the ground is not the hottest, but the air above the ground increases in temperature until a height is reached where the air temperature begins to cool again with height (see fig. 4). This atmospheric condition would lead to the presence of an acoustic duct (fig. 5) resulting

in excellent propagation of sound in the atmosphere. Considering only the temperature profile alone, one could only conclude that the best acoustic propagation would only occur at night. However, the next discussion will show that using the temperature profile alone does not adequately indicate the true type of acoustic propagation occurring in the atmosphere.

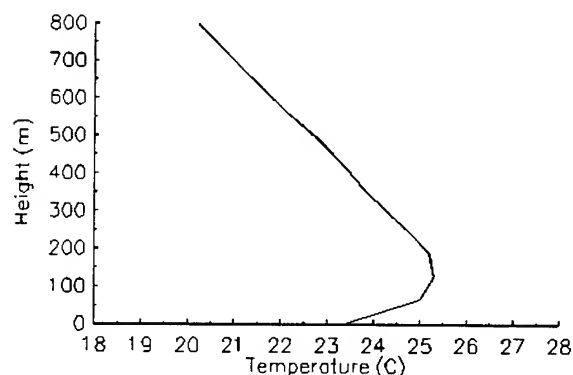


Figure 4. Temperature profile showing a nocturnal inversion.

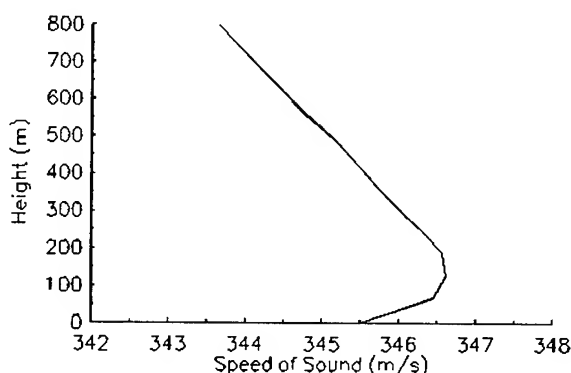


Figure 5. Speed of sound profile using only temperature.

As eq. (2) shows, the speed of sound profile is directly related to the vector wind speed profile. Since the vector wind speed is a direct relationship to the speed of sound, a small variation in the vector wind speed with height has a larger effect on the speed of sound profile than does the same magnitude of change in the temperature. A case will be examined where a vector wind speed profile increases the size and strength of an acoustic duct formed by the presence of a nocturnal inversion. Figure 6 shows a sound speed profile obtained from using just the temperature profile. The nocturnal inversion causes a formation of an acoustic duct about 150 m thick and a change in the speed of sound within the duct of about 2 m/s. Now the speed of sound profile that incorporates the vector wind speed as well as the temperature will be examined. As fig. 7 shows, the thickness of the duct has now been increased twice the original thickness with a change in the effective speed of sound within the duct of 4 m/s. Even though the sound speed gradient is the same in both cases, the increased thickness of the duct will cause more sound to be trapped within it.

Since the relationship of the speed of sound is a vector relationship to the wind speed, the addition of the vector wind speed does not always help the effectiveness of an acoustic duct. Figure 8 shows an actual case where the wind speed profile prevented the formation of an acoustic duct in certain directions. The solid line is the speed of sound profile including only the temperature. As the no-wind case shows, there is a nocturnal inversion present. The downwind case shows that the incorporation of the vector wind speed profile in the direction of wind flow increases both the thickness and strength of the duct. For the upwind case, instead of the presence of an acoustic duct

in that direction, there is a region of all upward refraction. This means in the direction of propagation that is against the flow of the wind, the sound will be refracted up away from the ground, resulting in poor propagation.

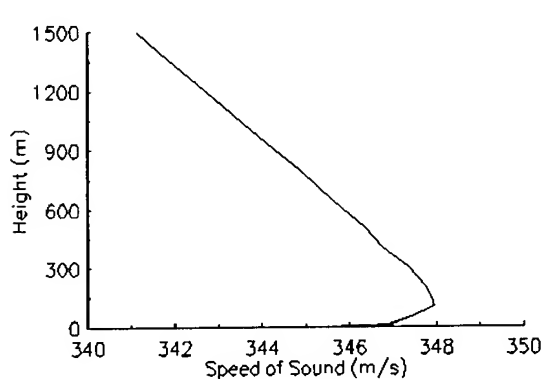


Figure 8. Speed of sound profile including temperature only.

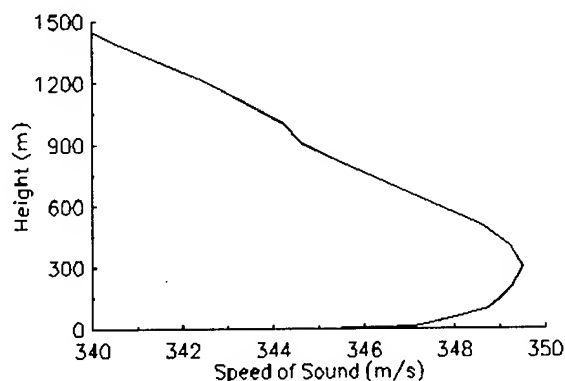


Figure 7. Speed of sound profile showing enhancement of the duct due to the vector wind speed.

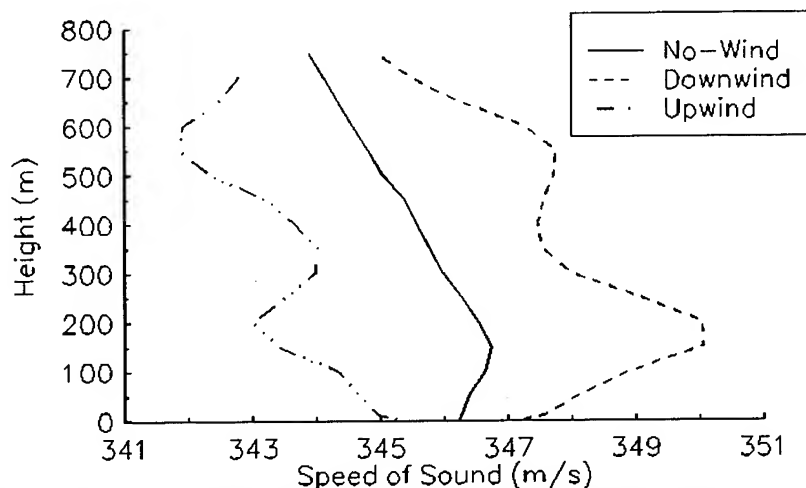


Figure 6. Speed of sound profiles showing the effect of vector wind speed on a nocturnal inversion.

#### 4. ACOUSTIC DUCTS DURING THE DAY

The examples given so far have dealt with enhancement or destruction of acoustic ducts from nocturnal inversions. The following text concentrates on what occurs to the speed of sound profile when the vector wind is included. As mentioned previously, the temperature profile during the day leads to an upward refractive speed of sound profile indicating poor acoustic propagation conditions.



However, incorporating the vector wind speed profile will lead to dramatically different conclusions. Figure 9 shows the speed of sound profiles calculated from meteorological data taken at White Sands Missile Range in the spring of 1989. The data was collected in mid-morning after the nocturnal inversion was gone. The solid line shows the speed of sound profile using only the temperature indicating the absence of a temperature inversion. Incorporating the vector wind speed profile into the speed of sound profile shows in the downwind case a formation of an extremely large acoustic duct. This means in that direction the propagation of sound will be excellent. In the opposite direction, the vector wind speed contribution resulted in an increase in the degree of upward refraction causing very poor propagation conditions.

The effect of the vector wind speed on the speed of sound profile during the day can cause other variations of acoustic ducts other than surface ducts. Figure 10 shows speed of sound profiles calculated from data taken at White Sands Missile Range in late summer of 1991. Again, the solid line is the speed of sound profile using just the temperature profile. As in fig. 9, the downwind direction shows the formation of an acoustic duct. In the upwind direction, the degree of upward refraction is increased, causing poor acoustic propagation conditions next to the ground. In the upwind case a very large acoustic duct is formed at a height of 600 m. This acoustic duct is an elevated acoustic duct, but it will trap sound as well as a surface duct. So even though the propagation conditions at the surface are poor, there are excellent acoustic propagation conditions a few hundred meters above the ground.

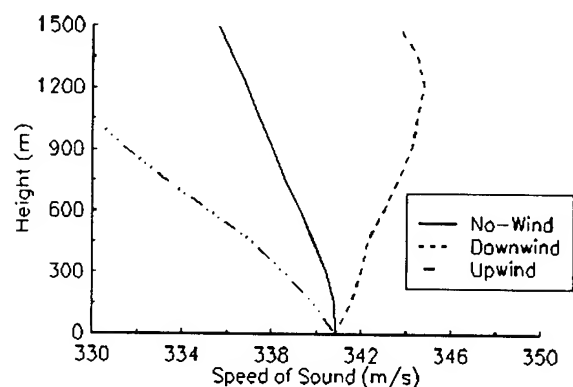


Figure 9. Speed of sound profiles showing creation of a surface duct during the day.

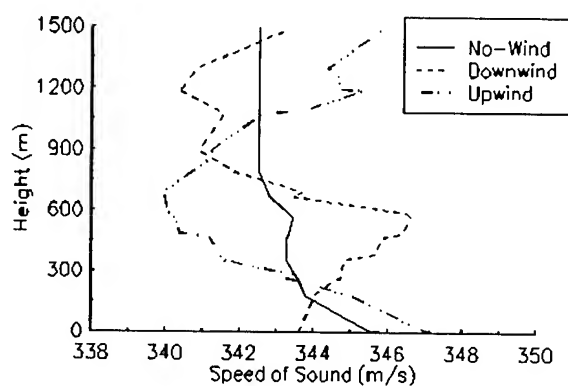


Figure 10. Speed of sound profiles showing the creation of a surface and elevated duct.

## 5. SUMMARY

The best acoustic propagation in the atmosphere occurs when an acoustic duct is present. The acoustic duct traps sound within, creating a waveguide effect. This means that the attenuation of sound due to geometrical spreading will be closer to cylindrical spreading (3 dB/doubling distance) as opposed to the normal spherical spreading (6 dB/doubling distance). Formation of acoustic ducts is controlled by the combination of the temperature and vector wind speed profiles. At night with no wind, a nocturnal inversion can be formed that leads to an acoustic duct in all directions since there is not a vector relationship between the speed of sound and the temperature. If wind is present, the wind will typically enhance the effect of the duct in some directions and reduce or totally eliminate the duct in other directions. During the day with no wind, the temperature profile will result in upward refraction of the sound meaning poor acoustic propagation. Including the wind, acoustic ducts can be formed that provide good acoustic propagation in certain directions. Knowing when and in which direction an acoustic duct is present is the key to being able to predict good acoustic propagation conditions.

## REFERENCES

- Pierce, Allen D., 1981: Acoustics: An Introduction to Its Physical Principles and Applications. McGraw-Hill Book Company, New York, 678 pp.
- Stull, Roland B., 1988: An Introduction to Boundary Layer Meteorology. Kluwer Academic Publishers, Boston, 666 pp.
- Tolstoy, Ivan, and C.S. Clay, 1987: Ocean Acoustics: Theory and Experiment in Underwater Sound. American Institute of Physics, Inc., New York, 381 pp.



**Session V**

## **WEATHER DECISION AIDS**

**Session Chair**

**Mr. Gary Clayton  
U.S. Army Missile Command**

## IR VISIBILITY

C. N. Touart  
Hughes STX Corporation  
Lexington, MA 02172

### ABSTRACT

In response to demand from field users, the current release of the Air Force Phillips Lab EOTDA (Electro-Optical Tactical Decision Aid) outputs values of an 8-12  $\mu\text{m}$  "visibility" that is denoted IRVIS. It is defined as the MRT detection range for an "average" FLIR viewing a target of "standard" size and inherent contrast. The rationale for this definition and how IRVIS behaves in various weather conditions are described.

### 1. BACKGROUND

Over the past decade, the Battlefield Weather Observation and Forecast System managed by the Geophysics Directorate of the Air Force Phillips Laboratory has fielded a succession of Electro-Optical Tactical Decision Aids (EOTDAs) (Hodges et al., 1984; Higgins et al., 1987; Higgins et al., 1990; and Hilton et al., 1991). Version 3.0 of the Mark III EOTDA was beta-released in June of 1992.

The EOTDA is a software system that predicts performance parameters of electro-optical weapons and detection systems. Three classes of systems are presently supported: a) television (TV), low-light-level television, and night-vision goggles; b) laser-guided weapons (1.06  $\mu\text{m}$ ); and c) imaging infrared (IR) systems (approximately 8-12  $\mu\text{m}$ ). It is designed for hosting on a PC.

The performance of electro-optical (EO) weapons systems is typically dependent on weather conditions and other environmental factors. For passive imaging systems (TV or IR) this sensitivity derives from two sources. The inherent (zero-range) strength of target signature is strongly influenced by environmental parameters, and the degradation of this signature as it propagates from target to weapon sensor is determined by weather conditions.

The EOTDA predicts system performance in terms of maximum detection range, maximum lock-on range, maximum ranging range,

and the like. Performance for IR systems depends on many facets of target weather and other particulars of the target scenario, notably the following: geographical location, date, and time of day; the specific target, its operating state and speed (if applicable), and its orientation; the particular background against which the target will be viewed; the sensor, its altitude, and heading; and clutter level of the target scene.

Depending on the computer that hosts the EOTDA and the length of time over which output is desired, a prediction for any one such scenario may require up to several minutes to generate. Given this overhead of the full-fledged EOTDA, it is no surprise that field users of the IR EOTDA have campaigned at length for a more generalized output, particularly for use in the planning mode where multiple targets, multiple sensors, and multiple locations may well be under consideration. They call this desired new output "IR visibility." It is visualized as a generic index of the suitability of a particular time and place for the use of IR systems, regardless of specific target, sensor, etc.

Meanwhile, a parallel and, perhaps, interrelated practice has sprung up among aircrews who fly IR sensor systems. Reportedly, "IR visibility" is a common term of reference among them. No particulars are available as to how they define IR visibility, but, presumably, it is evaluated subjectively and qualitatively. Also unknown, is how well operators of different IR sensors agree on the state of IR visibility in any given instance.

While the underlying problem in the field is quite understandable, the requested solution cannot be a panacea. FLIRs (forward-looking infrared sensors) vary significantly in sensitivity. No single index can accurately characterize the performance of all FLIRs. Worse yet, no measure of IR transmissivity through the atmosphere can, alone, serve as a dependable index of the operational suitability of any given target scenario. Target-background thermal contrast, which is totally independent of transmissivity, is an equally important factor.

Notwithstanding these intrinsic limitations of the concept, Version 3 of the EOTDA does output a measure of IR visibility denoted IRVIS. The algorithm used for this purpose and some examples of the behavior of IRVIS will be discussed in the remainder of this report.

## 2. DEFINITION OF IRVIS

An obvious way to define IRVIS is to identify it with the detection range of a FLIR. Since FLIRs vary considerably in

sensitivity, the minimum resolvable temperature (MRT) was averaged for the 14 narrow field-of-view FLIRs in the current EOTDA menu. The resulting average, namely, 0.153 K at 1 cy/mr, is one parameter in the definition of IRVIS. (The units of spatial frequency, cy/mr, refer to the inverse of the angular spacing of lines on the bar chart used to measure MRT in the laboratory. Later in this report spatial frequency will be related to field parameters.)

Inherent target-background thermal contrast is the other parameter that must be specified. The value for this parameter was taken to be 2 K.

It will be seen later that the quasi-arbitrary choices made for these two parameters are not particularly critical.

In the customary formulation of the range equation,  $\Delta T$  (thermal contrast) suffers exponential decay with range (R) from the target:

$$\Delta T(R) = \Delta T(0) e^{-\beta(IR) R} \quad (1)$$

where  $\beta(IR)$  is the mean coefficient of volume extinction for the 8-12  $\mu\text{m}$  band. (Assuming a constant extinction coefficient for the band and applying Beer's law to thermal contrast, as opposed to radiance, are both approximations. However, they can be shown to be acceptably accurate in normal circumstances.)

The range at which  $\Delta T$  becomes equal to MRT is the maximum MRT detection range (DR), i.e.,

$$R = DR \quad \text{when} \quad \Delta T(R) = MRT$$

IRVIS is defined to be this detection range for the chosen values of inherent contrast and MRT, i.e.,

$$IRVIS = DR \quad \text{for} \quad \Delta T(0) = 2 \text{ K} \quad \text{and} \quad MRT = 0.153 \text{ K}$$

With these values inserted in eq. (1), it can be inverted to yield

$$IRVIS = 2.570 / \beta(IR) \quad (2)$$

### 3. BEHAVIOR OF IRVIS

It goes without saying that for any definition of IRVIS to be acceptable, it must produce reasonable values. Tables 1-5 suggest that IRVIS does, indeed, pass this test. These tables were computed with the EOTDA transmission model (Higgins et al., 1989), which approximates LOWTRAN.

Table 1 compares VIS, which is meteorological range, and IRVIS for the LOWTRAN URBAN aerosol. The relative humidity is 50%, and the dew point is 0°C. Absorption by water vapor, as well as scattering by the aerosol, is taken into account for IRVIS. IRVIS is substantially greater than VIS. This is consistent with the common knowledge that IR sensors see through haze better than sensors operating at visible wavelengths.

**TABLE 1. IRVIS IN AN URBAN AEROSOL**

<b>VIS (km)</b>	<b>IRVIS (km)</b>
1	6
2	10
5	15
10	18
15	25

The opposite is true for LOWTRAN ADVECTION FOG where IRVIS is generally less than VIS, as is shown in table 2.

**TABLE 2. IRVIS IN AN ADVECTION FOG**

<b>VIS (km)</b>	<b>IRVIS (km)</b>
0.1	0.1
0.2	0.1
0.4	0.2
0.6	0.3
0.8	0.5
1.0	0.6



Table 3 shows that IRVIS is significantly reduced by RAIN, except for the very lightest intensity. Comparable values for VIS cannot be cited because it does not scale with rainrate.

**TABLE 3. IRVIS IN RAIN**

<b>Rainrate (in/hr)</b>	<b>IRVIS (km)</b>
0.01	17
0.1	3.9
0.2	2.5
0.5	1.4
1.0	0.9

Table 4 reveals that SNOW is a more effective impediment to IR than to visible wavelengths.

**TABLE 4. IRVIS IN SNOW**

<b>VIS (km)</b>	<b>IRVIS (km)</b>
0.2	0.1
0.5	0.3
1.0	0.5
2.0	1.1
5.0	2.6
10.0	5.3

Absorption of IR by WATER VAPOR is quite significant, as table 5 illustrates. (Relative humidity is taken to be 100%.) The only related sensitivity of VIS derives from the dependence on relative humidity of the extinction coefficient for a hygroscopic aerosol.

**TABLE 5. IRVIS IN WATER VAPOR**

Dew Point Temp (°C)	IRVIS (km)
-10	48
0	28
10	15
20	7
30	3

To summarize, IRVIS appears to be a well-behaved function of weather, and its magnitude is intuitively reasonable in comparison with ordinary visibility.

#### **4. SENSITIVITY OF IRVIS TO ITS PARAMETERS**

Two parameters were arbitrarily specified in defining IRVIS: the target-background inherent contrast and the minimum resolvable temperature for the hypothetical FLIR. Tables 6 and 7 suggest that neither choice is critical.

In table 6, IRVIS is compared with the values that would ensue from two other choices for  $\Delta T(0)$ ; namely, 1 and 3 K. These alternatives form the columns flanking the value of 2 K that is actually used in the definition. The rows are for decreasing values of transmissivity at 4 km (TRANS4). (TRANS4 is an index of IR turbidity that is routinely used in the IR EOTDA.) As would be expected, IRVIS increases with  $\Delta T(0)$ .

**TABLE 6. SENSITIVITY OF IRVIS TO  $\Delta T(0)$**

	IRVIS (km)		
$\Delta T(0)$ (K) =	1	2	3
<b>TRANS4</b>			
0.9	91	98	113
0.7	21	29	33
0.5	11	15	17
0.3	6	9	10
0.1	3	4	5

Table 7 compares IRVIS for different values of MRT; namely, 0.1, 0.15, and 0.2 K. Again, the center column is for the value actually used in the definition of IRVIS.

**TABLE 7. SENSITIVITY OF IRVIS TO MRT**

	IRVIS (km)		
MRT (K) =	0.1	0.15	0.2
<b>TRANS4</b>			
0.9	114	98	88
0.7	34	29	26
0.5	17	15	13
0.3	10	9	8
0.1	5	5	4

The point of these two comparisons is not that IRVIS is insensitive to its parameters. Instead, the message is that with somewhat different choices for the parameters, the resulting values of IRVIS would still be physically reasonable. Besides, the absolute magnitude of IRVIS is not expected to be

particularly meaningful, only its differences from one weather scenario to another.

## 5. SIGNIFICANCE OF SPATIAL FREQUENCY

As previously mentioned, MRT is measured in the laboratory as a function of spatial frequency of a bar chart. MRT increases as this frequency increases. This is intuitively reasonable. As the angular separation of the bars decreases (increasing spatial frequency), you would expect that stronger contrast would be required to resolve the bars (higher MRT).

When the MRT methodology is used to compute a detection range, the appropriate value of spatial frequency must be related to target geometry in the given scenario in order to establish the applicable value of MRT. This is done via the Johnson criterion (Johnson, 1958) which defines the probability of detection in terms of the number of bar-chart cycles that can be resolved across the target's critical dimension, which is taken to be the target's vertical extent in the EOTDA. In particular, for detection at the 50% level of probability in a moderately cluttered target scene, the Johnson criterion prescribes that one cycle be resolvable across the target's critical dimension.

Thus, when the angular subtense of target height is 1 mr at its MRT detection range and the clutter level is moderate, the corresponding spatial frequency is 1 cy/mr. Conversely, when spatial frequency is fixed at this value, as is done in the prescription for IRVIS, it implies that the computed detection range is valid for a target whose height subtends 1 mr.

(A feeling for the size of 1 mr can be gained by unbending a common paper clip and holding it at arm's length. The diameter of the wire subtends about 1 mr.)

## 6. SIMILARITY TO METEOROLOGICAL RANGE

The similarity in structure is obvious between the definition of IRVIS and Koschmieder's definition of Meteorological Range (VIS) (Middleton, 1952):

$$\begin{aligned} \text{IRVIS} &= 2.570 / \beta(\text{IR}) \\ \text{VIS} &= 3.912 / \beta(0.55 \mu\text{m}) \end{aligned}$$

where  $\beta(0.55 \mu\text{m})$  is the atmospheric volume extinction coefficient at  $0.55 \mu\text{m}$ .

At first sight, this similarity is surprising, seeing that there is a major difference between the two concepts in terms of underlying mechanism. Contrast reduction in VIS is caused

primarily by path radiance; contrast reduction in IRVIS is caused entirely by extinction.

However, on second thought, the reason for the similarity is obvious. If any function of atmospheric transmissivity is to be measured in units of length, then it follows simply from dimensional analysis that this function must be proportional to the reciprocal of the volume extinction coefficient, whose units are 1/length.

## 7. SUMMARY

The newly released Version 3.0 of the Mark III EOTDA computes an index of 8-12  $\mu\text{m}$  transmissivity called IRVIS. IRVIS is the 50% probable MRT detection range of an average EOTDA FLIR under the following conditions.

- a. The FLIR is in narrow-field mode.
- b. Target inherent contrast is 2 K.
- c. Clutter in the target scene is moderate.
- d. Target height subtends 1 mr.

The User's Manual for the EOTDA strongly emphasizes that IRVIS is not the detection range of any real sensor for any real target under any real weather conditions. Instead, it is merely an index of IR transmissivity that is measured in distance units. Correlation between IRVIS and the performance of any real FLIR can be established only from actual experience with that FLIR.

## ACKNOWLEDGMENTS

This work was supported by the Air Force Phillips Laboratory under contract F19628-90-C-0183. I am indebted to Maj. James K. Hancock, TDA Technical Director, AFPL, for many long and stimulating discussions during the evolution of IRVIS and for his critical review of the drafts of this report. Any residual deficiencies are certainly not for want of his trying.

## REFERENCES

Higgins, G. J., P. F. Hilton, D. B. Hodges, R. Shapiro, C. N. Touart, and R. F. Wachtmann, 1987: Operational Tactical Decision Aids (OTDA) Final Report, Volume I. STX Scientific Report No. 37. AFGL-TR-87-0300. Phillips Laboratory, Hanscom AFB, MA 01731-5000. ADB119842L.

Higgins, G. J., P. F. Hilton, R. Shapiro, C. N. Touart, and R. F. Wachtmann, 1989: Operational Tactical Decision Aids (OTDAs). STX Scientific Report No. 39. GL-TR-89-0095, Phillips Laboratory, Hanscom AFB, MA 01731-5000. ADB145289L.

- Higgins, G. J., D. A. DeBenedictis, M. J. Gouveia, P. F. Hilton, D. B. Hodges, D. M. Hoppes, and C. N. Touart, 1990: Electro-Optical Tactical Decision Aid (EOTDA) - Final Report. STX Scientific Report No. 44 (I). GL-TR-90-0251 (I), Phillips Laboratory, Hanscom AFB, MA 01731-5000. ADB153311L.
- Hilton, P. G., D. A. DeBenedictis, M. J. Gouveia, I. Halberstam, D. B. Hodges, D. M. Hoppes, and C. N. Touart, 1991: Electro-Optical Tactical Decision Aid (EOTDA). Hughes STX Scientific Report No. 45. PL-TR-92-2007, Phillips Laboratory, Hanscom AFB, MA 01731-5000. ADB153311.
- Hodges, D. B., G. J. Higgins, M. A. Mickelson, R. Shapiro, and C. N. Touart, 1984: Operational Tactical Decision Aids (OATDA) for Infrared (8-12 micrometer) Systems - Final Report - SASC Scientific Report No. 19. AFGL-TR-84-0191, Phillips Laboratory, Hanscom AFB, MA 01731-5000. ADB087503L.
- Johnson, J., 1958: Analysis of Image Forming Systems. In Proceedings of Image Intensifier Symposium, Fort Belvoir, Virginia.
- Middleton, W. F. K., 1952: Vision through the Atmosphere. University of Toronto Press, 250 pp.

## THE NEXT GENERATION OF FORECASTER DECISION AIDS

Jeffrey E. Passner  
Battlefield Environment Directorate\*  
U.S. Army Research Laboratory  
White Sands Missile Range, New Mexico 88002-5501, USA

### ABSTRACT

In recent years the Battlefield Environment Directorate (BED) has made much progress in developing technology for the Integrated Meteorological System (IMETS). IMETS is a mobile, tactical, automated system (now being developed) that furnishes weather support for Army operations. Currently there are numerous forecaster decision aids (FDAs) ready for transition to IMETS to assist the staff weather officer (SWO). However, in light of recent advances in modern weapon systems and expanding computer technology, there is a need to develop the "next generation" of FDAs. Currently such efforts are taking place at BED where the concept of single-station weather forecasting has been expanded to include aviation hazards such as turbulence and icing. In addition, technology from the evolution of mesoscale forecasting models will be synthesized with the FDAs to generate more timely, accurate, and detailed products for the SWO.

### 1. INTRODUCTION

The Integrated Meteorological System (IMETS) will be a transportable, automated weather data receiving, processing, and disseminating system operated by Air Force weather forecasters in support of Army operations. To expedite the progress of IMETS, the Battlefield Environment Directorate (BED) has assembled the technology exploitation weather testbed (TEWTB). The objective of the TEWTB is to support a platform for BED to develop, evaluate, and demonstrate software products before they are actually transitioned to IMETS. For more information on IMETS and TEWTB, see Harris (1992).

This paper will emphasize some of the advancements made in forecasting techniques. Currently there are numerous tactical decision aids (TDAs) and forecaster decision aids (FDAs) on the TEWTB that are ready for transition to IMETS; however, as advances in computers and forecasting techniques continue, there is a need to supply the staff weather officer (SWO) with state-of-the-art, practical, and accurate decision aids to enhance the performance of military troops and weapon systems in military conflict.

---

\*formerly U.S. Army Atmospheric Sciences Laboratory

## 2. FORECASTER DECISION AIDS TODAY

Much of the data used to formulate the TDAs and FDAs consists of large-scale and sporadic synoptic data reports. Data being utilized by the TWETB currently consists of Air Force automated weather distribution system (AWDS) data and data supplied by a commercial system called Zephyr. This large-scale data incorporates both surface and upper air data and is used to develop the FDAs.

As a first step, the forecaster can set this data to a gridded field, chosen by the user, over a map background in an effort to provide more detailed information at locations on the battlefield.

Once the data has been gridded, the information is manipulated to develop the FDAs. Such meteorological variables as air temperature, surface pressure, relative humidity, visibility, wind speed, and precipitation amounts and rates can be displayed in an assortment of contour plots over the data field. These data can be employed into regions of favorable, marginal, or unfavorable areas on the battlefield based on limits set by the system user. Also, surface winds can be plotted by using streamline plots, velocity vector plots, and wind speed contour plots.

The upper air Skew T - log P or Stüve diagram presents the temperature, moisture, wind, and heights of the atmosphere from the surface to a level typically around 50,000 ft. This provides a vertical evaluation of the main atmospheric conditions and presents the SWO with information that can assist in assembling a weather forecast. Also, contour plots, streamline plots, and velocity vector plots of the mandatory upper air levels can be drawn in the atmosphere.

Another FDA currently being used is called historical climatology, which contains a large data base of weather information for a variety of regions around the world. The historical climatology records assist in studying weather elements at many stations in preparation for long-term military plans.

The FDAs, while of great help to the SWO, provide only general information to the SWO to resolve detailed weather analysis on the mesoscale or battlefield scale. The current array of FDAs is generalized graphs, plots, and charts that produce some of the primary meteorological variables and data that are needed by the SWO to assist the battlefield commander. These FDAs are also based on current weather data and there has been no effort to make these true "forecasting" decision aids.

## 3. LIMITED DATA FORECASTING

Over the past several years, BED has developed an FDA that utilizes only a single-station upper atmospheric sounding to assist the SWO in making predictions for some weather hazards, thunderstorms, and severe weather events that might degrade the performance of weapons systems and troops in the field. This single-station program, called the single-station nowcast analysis program (SSNAP), has been fairly successful in making forecasts of thunderstorms and severe weather (Passner and Lee, 1990). The SSNAP program also displays icing layers, upper-level winds, temperature data, and moisture



information at the station. Additionally, SSNAP uses the single-station data to illustrate D-values and numerous meteorological variables. Finally, the program calls an expert system to forecast thunderstorms and severe weather. The SSNAP program uses artificial intelligence (AI) techniques by initiating a program that creates a knowledge-based set of rules to forecast thunderstorms. The goal-oriented pattern detection (GOPAD) expert system is another example of an FDA that takes the AI approach by developing a set of rules using a neural network and historical data base. It is a most useful FDA in that it makes a prediction of precipitation probability over a region.

#### 4. MESOSCALE FORECASTING

More information with improved temporal and spatial resolution is needed to advance the FDAs to meet the needs of the modern battlefield commander. Data sources will incorporate AWDS data, the automated weather network (AWN), meteorological satellites, remote surface sensors, unmanned aerial vehicles (UAVS), artillery upper-air systems, and high-frequency radio intercept.

Over the last 20 years, there has been significant progress in what is called mesoscale meteorology. According to McGinley (1986) mesoscale weather typically alludes to weather systems that influence approximately 100 km, move at 10 m/s, and persist for about 3 h. Often mesoscale data is needed to detect and analyze the atmosphere between meteorological stations.

IMETS will provide mesoscale four-dimensional (x,y,z,t) gridded meteorological data for use in battlefield planning and in generating weather effects decision aids. Harris and Meyers (1992) describe some of the desired features for a mesoscale model in the battlefield environment. At the current time, BED is deciding which mesoscale model will be incorporated into IMETS. Regardless of this choice, the highly dense grid patterns based on weather data and terrain will be manipulated to develop more accurate FDAs. The model will be able to "nest" to a scale perhaps as small as 5 km by 5 km.

In addition, hemispheric model data provided by Air Force Global Weather Central will be used to initialize the mesoscale model and provide weather data input for an extended forecast period. This would enable the SWO to run meteorological forecast parameters to allow the commander more timely and accurate forecasts for the military operations beyond a few hours. As an example, the SWO will be able to forecast visibility on the battlefield 48 h in advance. Forecasts of temperature, moisture, pressure, and wind fields will be possible on much smaller scales than are currently available. There will be an effort to depict meteorological parameters to forecast both the horizontal and vertical scales and display these products to improve the caliber of weather forecasts. AI techniques will be used in forecasting hazard layers, thunderstorms, and severe weather well in advance by having a sounding at each grid point from the derived models available from the Air Force. There will also be forecasts for clouds, ceiling heights, jet maxima or minima, and any weather that might influence military operations. With a diversity of weather scales to work on, the SWO will have the most contemporary and modernized techniques that are evolving in the field of meteorology as well as several products that are currently not available for military planning.

The future battlefield weather forecast will become an interaction between forecasting on the larger scale and on the mesoscale, and the products being currently developed and tested will greatly assist the SWO in producing more accurate and dependable forecasts that are needed on the battlefield.

#### REFERENCES

- Harris, J. E., 1992: A Technology Exploitation Weather Testbed For Army Applications, Preprint of the Eighth International Conference on Interactive Information and Processing Systems for Meteorology, Oceanography and Hydrology, Atlanta, Georgia, American Meteorological Society, Boston, MA.
- Harris, J. E., and R. Meyers, 1992: Adaptation of the Navy's Limited Area Dynamical Weather Prediction Model for Army Applications. Preprint of the Fifth Conference on Mesoscale Processes, and Preprint of the Symposium on Weather Forecasting, Atlanta, Georgia, American Meteorological Society, Boston, MA.
- McGinley, J., 1986: Nowcast Mesoscale Phenomena. Mesoscale Meteorology and Forecasting. Ed. Peter S. Ray, American Meteorological Society, Boston, MA, 657-688.
- Passner, J. E., and R. R. Lee, 1991: Use of an Expert System to Predict Thunderstorms and Severe Weather, in Proceedings of Applications of Artificial Intelligence IX, International Society for Optical Engineering, Orlando, Florida.

# FORECASTING USING A HYBRID STATISTICAL-NEURAL NET METHOD

Jerrold S. Foster  
Command Control, Inc. (CCI)  
Atlanta, Georgia 30350 USA

Kenneth C. Young  
University of Arizona  
Tucson, Arizona 85721 USA

## ABSTRACT

Goal Oriented PAttern Detection (GOPAD) is a hybrid statistical-neural net software program which analyzes data collected from past events and extracts patterns that permit an optimal matching between predictor variables and predictands that derive from those variables. The result is a model capable of using selected variables to forecast the probability of similar future events. GOPAD creates a data base of variables using NGM Model Gridded Data and routine weather observations. These variables are optimally separated and optimally selected to model the non-linearity in the data. This paper discusses the key features of GOPAD, which has been expanded to include many different variables; i.e., temperature, humidity, wind speed, and direction. GOPAD can be used to forecast variables from any other historical data bases. Using a data base of historical weather parameters, the system analyzes the data to select a small subset of the potential set of predictor variables. Several thousand potential predictor variables are analyzed, but only 10-30, are chosen. These predictor variables then make up the set of data used to make forecasts. Finally, a set of analogs that constitutes the forecast is determined, relying on current values of the predictor variables.

## 1. INTRODUCTION

### 1.1 UNDERSTANDING OF THE PROBLEM

Weather prediction is necessary for many different military and civilian operations. History is full of military operations that pivoted around weather and its effects on the terrain, people, equipment, and missions. In today's military, the Army and Air Force collaborate in the process known as Intelligence Preparation of the Battlefield (IPB),

where weather prediction and its potential effects on various aspects of the AirLand Battle are anticipated and provided to the operational planners.

Toward this objective, a local, short-range forecasting capability is needed. Such a capability will make use of local, as well as global, weather parameter sensing capabilities; provide as much automation as reasonable to reduce the degree of manual sifting and analysis of data; and provide a consistent and acceptable degree of accuracy for meteorologists making the forecast.

## 1.2 BACKGROUND INFORMATION

CCI is a small business research and development firm which is involved in the application of artificial intelligence (AI) technology. Among the AI technologies CCI is using is a proprietary hybrid algorithm called Goal-Oriented PAttern Detection (GOPAD), which is being used to detect weather parameter patterns relevant to several types of weather forecasts, including temperature, relative humidity, precipitation, and winds. GOPAD is a hybrid statistical neural net model capable of the prediction of parameters from most any historical database. GOPAD has outperformed National Weather Service forecasters, numerical models, and other forms of artificial neural systems (neural nets) in weather forecasting. GOPAD is innovative in that it surpasses the skill of the human weather expert, discovering relationships previously unknown in the input data. In contrast, expert systems can at best duplicate a human expert. GOPAD is trained, rather than programmed, by providing a large number of input data examples of the associated ground truth data. The result of the training session is a model that is used to make forecasts when used with real-time data input.

### 1.2.1 Expert Systems for Weather Forecasting

Rule-based expert systems have been proposed for a number of meteorological applications. WILLARD, one of the first weather forecasting expert systems, was designed to predict severe thunderstorms in the Great Plains region of the United States.<sup>1</sup> Campbell and Olson demonstrated a nowcaster for conditions of strong wind shear and microbursts at major airports based on Doppler radar input.<sup>2</sup> McArthur et al. outlined plans for a scenario-driven nowcaster for thunderstorms at the Kennedy Space Center.<sup>3</sup>

Each of these rule-based expert systems was created through a knowledge engineering process designed to transform heuristics or rules of thumb into a comprehensive rule set. The objective of an expert system is to mimic the decision-making process of the best

---

<sup>1</sup> Zuberick, S.M., and C.E. Riese, "An Expert System to Aid Severe Thunderstorm Forecasting," presented at the 14th Conference on Severe Local Storms, 1985 American Meteorological Society, November 1985.

<sup>2</sup> Campbell, S.D., and S.H. Olson, "Recognizing Low-Altitude Wind Shear Hazards from Doppler Weather Radar: An Artificial Intelligence Approach," *J. Atmos. Oceanic Technology*, 1987, Vol. 4, pp. 5-18.

<sup>3</sup> McArthur, R.C., J. R. Davis, and D. Reynolds, "Scenario-driven Automatic Pattern Recognition in Nowcasting," *J. Atmos. Oceanic Technology*, 1987, Vol. 4, pp. 29-35.

human experts. Such human-derived knowledge bases are useful in systems where there is a limited set of precise decisions that need to be made when given a discrete input data set. These rule-based systems are designed to represent and apply factual knowledge about specific areas of expertise and to solve problems. Appropriate problem domains for expert systems include diagnostics for machinery and human diseases, configuring computer systems, and prospecting for minerals.

However, there are other problem domains where a complexity of interaction between elements or parameters in the process is more than an expert system can adequately be programmed to manage. In these domains, a relatively new approach is available that has the potential to outperform rule-based weather forecasting expert systems, as well as the traditional statistical models. Based on the results of CCI's weather forecasting research and previous experience with WILLARD, it is apparent that weather forecasting, and possibly environmental forecasting in general, is a problem domain that may be too extensive for the construction and/or maintenance of rule-based weather forecasting expert systems.

### 1.2.2 Neural Nets for Weather Forecasting

A superior approach to the development of weather forecasting software appears to be the use of an Artificial Neural System (ANS), or "neural net". A neural net is often defined as a number of nodes with vectors of weights interconnecting the nodes and the variables of the input data vector. A neural net is trained, rather than programmed, by providing a very large number of input data examples of the associated ground truth. The result of the training session is a model that is used to make forecasts with real-time data input. When historical input data is fed into the learning algorithm, each node's contribution to the answer is evaluated. If the node is correct in its classification of the data point, no action is taken. If the node is incorrect, it is adjusted so as to correct the classification. When the neural net has been trained, the resultant network is the forecast model.

### 1.2.3 Comparison Between Expert Systems and Neural Nets

The accuracy of ANS for forecasting weather events is limited by the number of years of meteorological data available and the accuracy of this historical data. In contrast, the accuracy of a rule-based expert forecasting system is dependent upon the expertise of the meteorologist and the ability of a knowledge engineering process to extract and incorporate heuristic knowledge into a rule base, as well as the limitations upon the input data. Placed in this perspective, the dependence of an ANS upon the availability of historically accurate meteorological data is not a significant disadvantage as compared with the knowledge engineering problem associated with the construction of a rule-based expert system.

An ANS program has the potential to exceed the skill level of expert forecasters; whereas an expert system, based on human-derived knowledge, cannot exceed the skill of the expert used to construct the rule base. There are several reasons for this important phenomenon. During the learning process, an ANS creates its own set of associations

based upon input data, whereas a rule-based expert system must represent and integrate the known physical relationships and human-derived heuristics. When ANS-derived associations are analyzed, a researcher may discover facts that were not previously recognized.<sup>4</sup> Cottrell et al. documented many examples in which their back propagation network found solutions that were not known in advance.<sup>5</sup> In expert systems construction, this integration process (i.e., knowledge engineering) is error prone, difficult, and time-consuming, and may not extract all the knowledge needed to achieve a domain expert's skill level, resulting in lower than optimal performance.

An ANS algorithm can be programmed to automatically learn and/or modify itself, thereby improving its performance over time by self-adaptation as new data is introduced. This capability is clearly superior to the manual tinkering that must be performed on the rule base in an expert system.

An ANS is able to function with missing or incomplete data more robustly than can an expert system. An expert system depends on the presence of exactly-specified facts to trigger its rules, while an ANS can generalize its training examples to nearby regions in the data space. Thus, an ANS model will degrade gracefully in the presence of incomplete or inaccurate data, whereas an expert system is fragile in this regard.

### 1.3 GOPAD

The GOPAD forecast model is an optimized analog forecasting system based upon multiple discriminant analysis. The method follows the approach used by Miller<sup>6</sup>, but is extended to provide non-linear discrimination. Non-linear responses up to the third order are included in the present system.

Using a historical data base of available weather parameters, the system analyzes the data to select a relatively small subset of the potential set of predictor variables. Typically, several hundred potential predictor variables are analyzed but only a few (10 to 30) are chosen. These "N" predictor variables may then be viewed as representing an n-dimensional hyper-space with a set of historical data representing points in this hyper-space (fig 1).

For a given forecast, a set of analogs is determined from the nearest neighbors. The values of the predictor variables for the forecast situation represent a point in this n-dimensional hyper-space. The analogs represent those points in the historical data set that are closest geometrically to the forecast situation. The set of analogs then constitutes the forecast.

---

<sup>4</sup> Young, K.C., and Dumais, R.E. Jr., "The Role of the Westerlies South of Australia in Triggering Strong El Nino Episodes," 1990, pending publication Mon. Wea. Rev., pp. 15-17.

<sup>5</sup> Cottrell, G.W., P. Munro, and D. Zipser, "Image Compression by Back Propagation: An Example of Extensional Programming," UCSD Institute for Cognitive Sciences.

<sup>6</sup> Miller, R.G., "Statistical Prediction by Discriminant Analyses," Meteorol. Monogr., 1962, Vol. 4, p. 54.

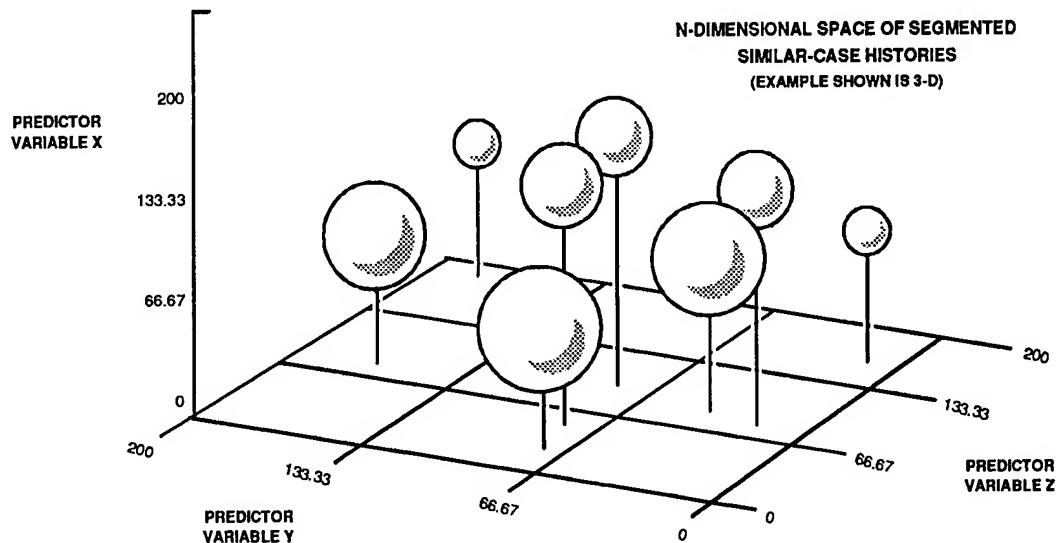


Figure 1. GOPAD Description

The first version of GOPAD used 32 predictor variables to produce a probability of precipitation that exceeded the predictions of the National Weather Service (NWS) in Atlanta by 32 percent and the Limited Fine Mesh Model (LFM) computer-based predictions by 69 percent. This forecast was executed on an IBM PC/AT microcomputer in a matter of seconds and required approximately 125K bytes of memory for each month in the forecast model.

GOPAD consists of three modules. The first two modules are derived from multiple discriminant analysis (MDA) (Miller, 1962), and employ both straightforward linear MDA and a proprietary, non-linear MDA. The second module provides a set of "predictor variables" (PVs) which defines the parameters of the n-dimensional hyperspace. The third module orthogonalizes the data space formed by the predictor variables with another proprietary algorithm and optimizes the selection of analogs from the PVs to form diagnoses or predictions.

## 2. WEATHER FORECASTS FOR USE IN UTILITY LOAD FORECASTING

CCI is currently working on a contract with the Electric Power Research Institute (EPRI) to create forecast models for six cities throughout the United States. These models will include forecasts for temperature, relative humidity, wind speed, and wind direction. Using an IBM RS-6000 Reduced Instruction Set Computer (RISC), CCI built data sets of historical surface weather observations and Nested Grid Model (NGM) numerical prediction data to train and create the forecast models.

### 2.1 PROCEDURES

The first step was to take the Local Climatological Data (LCD) for 1948-1991, obtained from the National Climatic Data Center in Asheville, North Carolina, and the archived

Nested Grid Model (NGM) data for 1985-1991, obtained from the National Center for Atmospheric Research (NCAR) in Boulder, Colorado, and transfer these data from 9-Track Tapes to Optical Disks for use by the GOPAD model.

The data was checked for homogeneity. Non-standard or Co-op Station temperature data was used to fill in for missing data and then was used to check the homogeneity of the entire set of temperature data. An interpolation program read the temperature data from both the LCD and Co-op stations and created separate temperature files for each month and hour. This program also created an interpolated temperature for every observed temperature to be used by the homogeneity checking program. The homogeneity of all temperature data was analyzed. Inhomogeneities were located in the three-hourly temperature data. Only those inhomogeneities appearing in three or more of the eight three-hourly time series were corrected. A harmonic analysis then determined the annual and diurnal cycles in the temperature data. This analysis was used to convert temperatures after the homogeneity check to temperature anomalies used by GOPAD. Finally, the GOPAD models for each of the six cities were created.

## 2.2 PRELIMINARY RESULTS

The forecast models were developed using data from 1986 through 1990. The data for 1991 was used for an independent evaluation of the forecast skill of the models. Since no other corresponding set of forecasts was available for comparison, forecasts were evaluated viz. climatology, i.e., a simple forecast of the average expected conditions for that hour and that month for the given station. Figure 2 shows that for forecasts out to 72 hours in advance, the mean absolute forecast error at Denver during the winter is substantially smaller than the corresponding mean absolute error using a climatological forecast. Similarly, the mean absolute forecast error is smaller than the mean climatological forecast error for all hours for the summer months (fig. 3), although the fractional reduction in the mean absolute error is smaller than for the winter months.

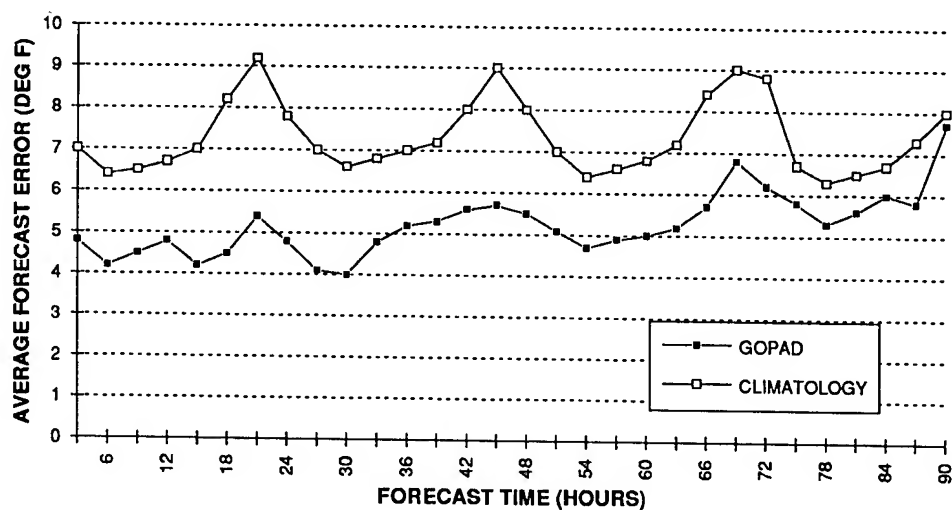


Figure 2. Denver - Temperature (Dec-Jan-Feb 00Z)



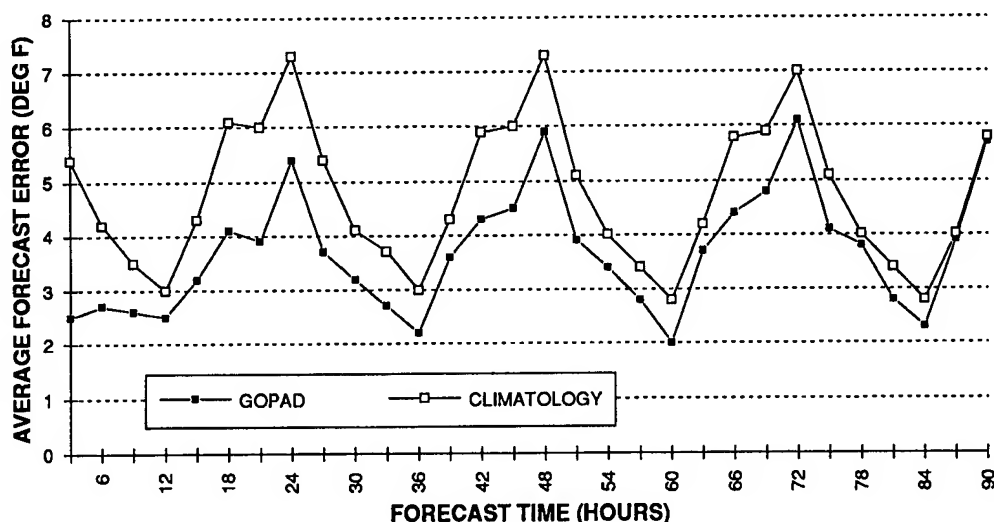


Figure 3. Denver - Temperature (Jun-Jul-Aug 00Z)

Both the mean absolute error (MAE) and root mean squared error (RMSE) were evaluated. The forecast skill is defined as the reduction in error viz. climatology provided by the forecast model, divided by the climatology forecast error. Forecast skills of 30% or greater were found for the temperature forecasts out to 36 hours in advance, dropping to 20% after 72 hours. All six stations exhibited similar temperature forecast skills.

Relative humidity forecasts exhibited lower skill levels for Sacramento and Miami than for the other four cities. Atlanta exhibited a humidity forecast skill above 40% out to 36 hours, dropping to less than 20% beyond only 84 hours in advance. The humidity forecast skills for Sacramento and Miami averaged near 20% out to 48 hours, dropping to 10% beyond 72 hours in advance.

The ability of the forecast model to predict the trend in temperature may be expressed in the fraction of the time the correct trend (increasing or decreasing) was predicted. Figure 4 shows that the forecasts provided the correct sign of the 24-hour temperature change at Denver more than 60% of the time, even when starting 36 hours in advance. The 48- and 72-hour trends were correctly predicted 70% of the time. This result is significant for load forecasting by utility companies, since utilities are very concerned with the short-term changes in temperature, almost as much as with the actual hourly temperature forecasts.

The final phase of this project will be an operational test using real-time data as input. These results will be compared with the forecasts the utilities currently receive. The test will provide a four-month period to assess savings which may accrue as a result of improved weather forecasts.

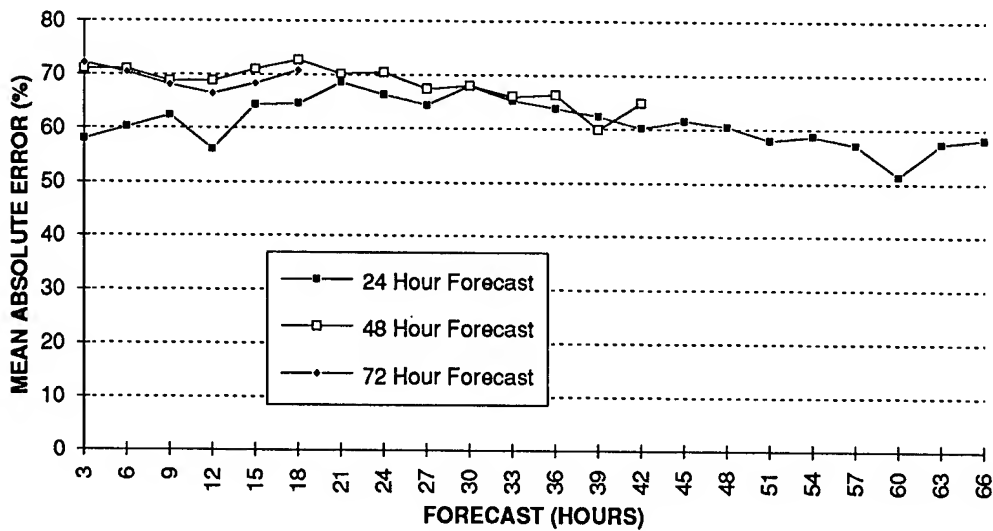


Figure 4. Denver Forecast Hits - Annual (00Z)

### 3. FUTURE PLANS

#### 3.1 PROPOSED PROJECTS

1. Use of Rawindsonde data to create forecast models and compare results to those obtained using NGM data.
2. Create forecast models for the entire forecast area of one of the participating utilities. This will truly determine if complete and more accurate weather input can produce more accurate load forecasts.
3. Create forecast models for use in the Tactical Military Environment.
4. Use GOPAD for support to aviation flight planning for optimum route planning.

**Session I Posters**

**ATMOSPHERIC MODELING**

# SOUP—A Battlefield Atmosphere

Robert E. De Kinder, Jr.\*

Chairman-JTCG/ME Smoke and Aerosol Working Group

U.S. Army Research Laboratory

Battlefield Atmospheric Simulation Division

White Sands Missile Range, NM 88002-5501.

## Abstract

Smoke Operations in Urban Places (SOUP) has been recently considered by a knowledgeable senior military officer, as the most important area of consideration for future conflicts, in particular those of more limited scales.

A brief introduction to SOUP will be given with its connection to other more familiar combat genre. For example, a "meeting engagement" in an urban environment has several aspects quite different from those in an open or rural environment. And while a "forest engagement" has some of the "shortness of range" features of the urban situation, the potential for "thermal clutter" is markedly different. Military Operations on Urbanized Terrain (MOUT) is what limited operations are really about. Most limited military "objectives" are where people are. And people are, for the most part, where urbanized terrain is.

The problems of simulating smoke and weather impacts in urban environments are compounded by recent environmental restrictions/interpretations on the use of smokes and obscurants at many of our military test sites. Unless relief is obtained from these overly restrictive "regulations", our ability to "validate and verify" our combat simulations through proper field trials will be drastically limited, if not actually impossible. Our computer simulations, no matter how sophisticated, must be compared with reality at least once in a while.

Examples of urban scenarios, their data bases, and potential algorithms for depicting urban obscurants will be postulated, time permitting.

## 1 Introduction

Smoke Operations in Urban Places (SOUP) has been recently considered by a knowledgeable senior military officer, as the most important area of consideration for future conflicts, in particular those of more limited scales. A brief introduction to SOUP will be given with its connection to other more familiar combat genre.

### 1.1 Engagements

For example, a "meeting engagement" in an urban environment has several aspects quite different from those in an open or rural environment. And while a "forest engagement" has some of the "shortness of range" features of the urban situation, the potential for "thermal clutter" is markedly different. Military Operations on Urbanized Terrain (MOUT) is what limited operations are really about. Most limited military "objectives" are where people are. And people are on urbanized terrain.

\*Secretary of the Army Research and Study Fellow Los Alamos National Laboratory '88-'89

## 1.2 Range

One marked difference as pointed out previously is the "shortness of range" for the urban environment vs. the "normal" combat distances. For European terrain, 667 meters is the nominal range; for the Mid-east, 1100 meters; BUT for urban villages, 67 meters—an order of magnitude shorter.

This order of magnitude difference will probably impact the scheme needed to model the effects of obscurants used in MOUT operations. Instead of using the "sandia" opaque ellipsoids, or the "onion-skin" model, it most likely will require a modified form of COMBIC[1], or at least some form of exponential attenuation out through the "onion-skin" clouds.

## 1.3 Thermal Clutter

Also, the urbanized *thermal clutter* will be markedly different from that seen in the "open" or "forested" terrain. This must also be accounted for in improving the target acquisition models for MOUT.

# 2 MOUT Village—Fort McClellan

A DRAFT Test Plan for an Urban Smoke Week has been prepared[2]. The need for an Urban Smoke Week is very apparent to those working in military obscurants. The various urban environmental pollution models have not been tested at the concentration levels of tactical importance. Figure 1 gives the plan for the MOUT Village at Fort McClellan, Alabama. This is representative of several MOUT facilities that might be suitable for an Urban Smoke Week.

## 2.1 Environmental Considerations

The problems of simulating smoke and weather impacts in urban environments are compounded by recent environmental restrictions/interpretations on the use of smokes and obscurants at many of our military test sites. Unless relief is obtained from these overly restrictive "regulations", our ability to "validate and verify" our combat simulations through proper field trials will be drastically limited. The environmental considerations for MOUT facilities are NOT insurmountable, but must be approached from the fact that the tests must be done, and the local command's cooperation and local environmentalists "good will" must be sought early on.

## 2.2 Smoke Clouds

The modeling of the obscurant clouds as opaque solid geometrical shapes may not prove fruitful for MOUT cases, since the lines-of-sight are so much shorter than on more open terrain. Thus we may be back to doing a path integration to determine the *Target Acquisition* probabilities.

$$T_r = T_0 e^{-\int_0^r \int_0^\lambda \alpha_\lambda C(r) d\lambda dr}$$

## References

- [1] D.W. Hooek, R.A. Sutherland, and D. Clayton. *Combined Obscuration Model for Battlefield-Induced Contaminants (COMBIC)*, TR-0221-11, U.S. Army Atmospheric Sciences Laboratory, White Sands Missile Range, New Mexico 88002-5501 (1987).
- [2] LTC S.J. Smaczniak. *Project SOUP, Smoke Operations—Urban Places, A Proposed MOUT Smoke Test Plan*. Prepared for: Battlefield Atmospheric Simulation Division, ASL, White Sands Missile Range, NM 88002-5501.





**SOME FLOW CHARACTERISTICS OF SURFACE LAYER MICROMETEOROLOGY  
OVER COMPLEX TERRAIN USING FIELD MEASUREMENTS**

Brian L. Orndorff  
Battlefield Environment Directorate\*  
U.S. Army Research Laboratory  
White Sands Missile Range, New Mexico 88002-5501, USA

**ABSTRACT**

Evaluation of microscale models for Army battlefield use requires knowledge of the meteorological data, terrain, and land use over the modeled region. Characterization and analysis of the data used in model evaluations provide such an understanding of the micrometeorological environment. These data are available from Project WIND (wind in nonuniform domains) Phase I, which was a multiple scale meteorological field study performed over northern California during the summer of 1985. The WIND micrometeorological data base was collected in two major high-resolution 5 km by 5 km domains. For this study, data collected over complex terrain in a randomly spaced evergreen forest is used. Characterization and analysis of the horizontal fields and the vertical structure of the surface layer are performed for two daytime periods and two nighttime periods. Vertical characterization and meteorological analysis include surface layer cross sections of micrometeorological wind speed, wind direction, temperature, and relative humidity. Horizontal characterization includes wind speed gradient analysis, isotach analysis, and temperature gradient analysis. Vertical cross sections are constructed from three 32 m high micrometeorological towers with eight measurement levels, and horizontal fields and contours are constructed from six 10 m high meteorological towers. Composite fields and average profiles are produced to define average daytime and nighttime conditions during these time periods.

**1. INTRODUCTION**

Micrometeorological data taken during Project WIND (wind in nonuniform domains) (Cionco, 1989a and 1989b) has provided a large database for the analyses of surface boundary layer characteristics over northern California. Micrometeorological measurements were obtained over two 5 km by 5 km domains. One site (Orchard) was located over relatively smooth terrain with uniformly spaced almond trees (Orndorff and Cionco, 1991). The second site (Forest) was located over complex terrain with nonuniform trees and low-level vegetation. This paper will characterize and analyze data over the Forest.

---

\*formerly U.S. Army Atmospheric Sciences Laboratory



Three 8-level micrometeorological towers, called Forest Towers (FTs), were used to record the vertical structure of the surface layer. Tower FT-1 was located in a large clearing about 20 tree heights (586 m) from the forest edge. Tower FT-2 was located just within the forest edge, and tower FT-3 was located about 450 m inside the forest. Vertical profiles of wind speed, wind direction, temperature, relative humidity with singular levels of solar and net radiation, soil heat flux, and pressure were recorded at the three tower locations.

[illegible]

306

The micrometeorological data were analyzed for one daytime period, one nighttime period, and one 24-h period. Characterization was performed for daytime conditions from 0900 to 1600 Pacific Standard Time (PST) on 24 June 1985, nighttime conditions from 2100 to 0400 PST on 25-26 June, and conditions during one diurnal period from 0900 on 27 June to 0900 on 28 June. Horizontal analyses over the Forest include 10 m level data from stations BC-1 through BC-6, and vertical analyses include 2 m through 32 m level data at 8 levels from stations FT-1 through FT-3. Methods used for characterization of the horizontal wind speed, wind direction, and temperature were wind speed gradient analysis, isotach analysis, and temperature gradient analysis. Characterization of the vertical winds, temperature, and relative humidity was performed using vertical cross section analysis of the parameters.

Horizontal composite averages of winds and temperature were computed for two daytime periods and two nighttime periods to characterize average meteorological conditions for those time intervals. Also, composite average vertical profiles of the wind speed, wind direction, temperature, and relative humidity were provided for daytime and nighttime conditions.

## 2. CHARACTERIZATION

Figure 2a shows a composite of horizontal wind speed and wind direction fields over the Forest during the day in the summer of 1985. The streamlines with arrows show the wind direction, and the contours indicate the wind speed. The wind direction was primarily from the northwest this day, which was different than a typical summer day. This different wind direction was caused by an upper level trough that moved through the region during the morning. The west-central portion of this figure shows that the wind direction changed slightly upon reaching a large clearing where stations BC-5 and BC-6 were located. This is probably due to the relaxing gradient over the open field. The wind speed increased over the open field due to the wind moving over the trees and then flowing along near the ground surface over the field. This descending air brought the higher wind speeds from above the forest down near the surface. As the air again traveled over the forested areas, there was a slight gradual turning of the wind direction and a slight divergence. Of greater significance was the change in wind speed. Over the large clearings in the western half of the domain, wind speeds were about 6 to 7 m/s. However, over the eastern half of the domain, the wind speeds were 3 to 4 m/s. This significant difference was probably caused by several factors. The primary reason was likely that the sizes of the clearings over the western portion were much greater than over the eastern side. These larger clearings allowed the frictional effects of the forest to subside in the western regions. Also, in general, the trees averaged about 14 m high over the northwestern portion of the Forest domain where measurements were taken, but over the eastern half the trees were generally 24 m to 30 m high.

Figure 2b shows a composite horizontal temperature field over the Forest domain for the same time period as in fig. 2a. This figure indicates that during the daytime in the summer, the temperature differences across the Forest domain are small. The slight differences that did occur this day appear to have been caused by stronger winds over the large clearings causing more mixing of the higher level air that brought cooler air down



Figure 4a shows a nighttime composite of wind speed and wind direction for 26-27 June over the Forest domain. As expected, the winds are generally from the east with downslope flow. Wind speeds are light over the eastern portion of the domain, but high wind speeds of about 7 m/s in the clearing is somewhat surprising. Also of interest is that the winds over the southern third of the Forest domain appear to curve and follow along the valley, which would be expected for nighttime drainage flow.

This colder drainage flow is also evident in the composite temperature plot of fig. 4b during the same night as in fig. 4a. This plot indicates that the temperature is 1 to 2 °C colder in the more heavily forested valley region of the southern third of the Forest domain than in the larger clearings of the western half of the Forest. This difference is due partly to the relatively cold drainage flow that occurs preferentially along the valley. Also, the significantly stronger winds in the large clearings induce mechanical mixing near the surface, which greatly modifies the effect of radiational cooling. Evidence from the micrometeorological towers suggests that the temperature differences were primarily caused by the differences in wind speed and mixing.

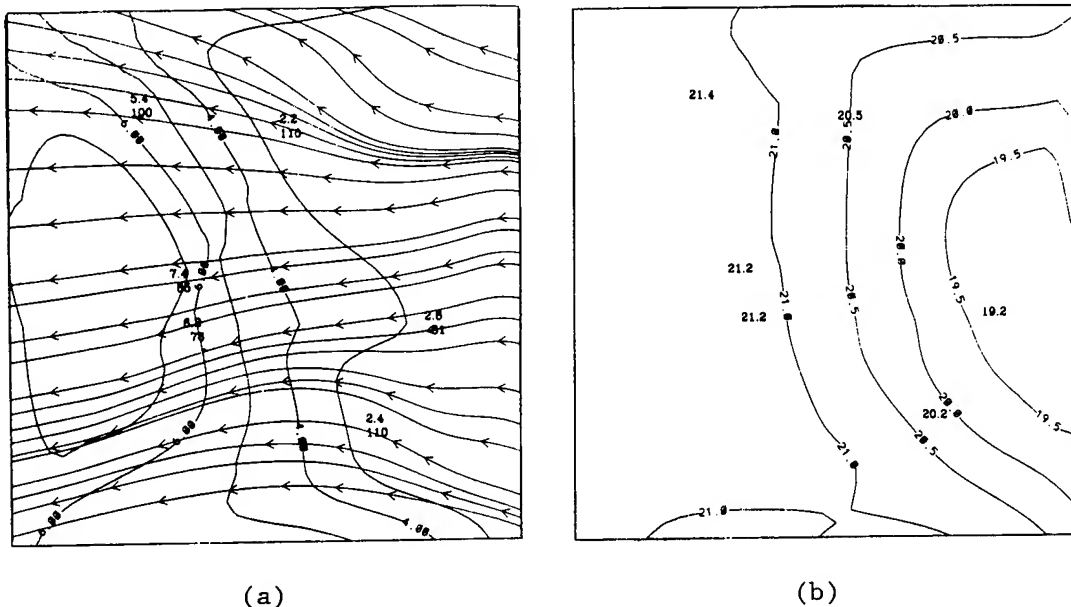


Figure 4. Composite horizontal (a) streamlines and isotachs (m/s) and (b) horizontal temperature (°C) fields over the Forest domain for 25-26 June at 2100 to 0400 PST.

Figure 5 is a plot of the 5-min average wind speed and wind direction over the Forest during the morning transition of 28 June. This figure shows southerly winds from upvalley flow developing over the southwest two thirds of the domain. However, the northeast third of the Forest domain shows easterly drainage flow coming from the Sierra Nevada mountains to the east. These two wind flow regimes meet and merge near the center of the domain and form a narrow area of convergence. This type of flow lasted for less than an hour and shows evidence of the shifting winds from downslope to upslope as the valley land surface warms.

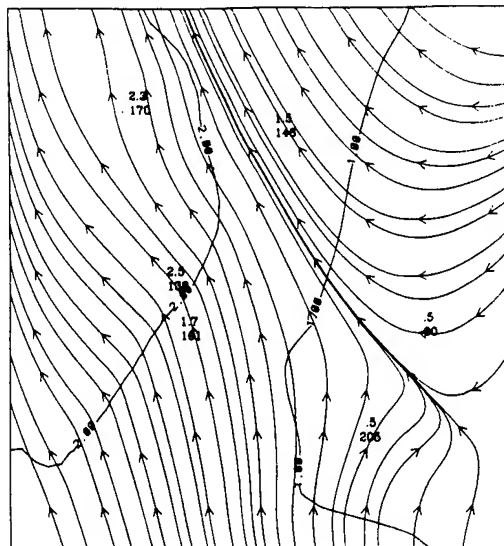
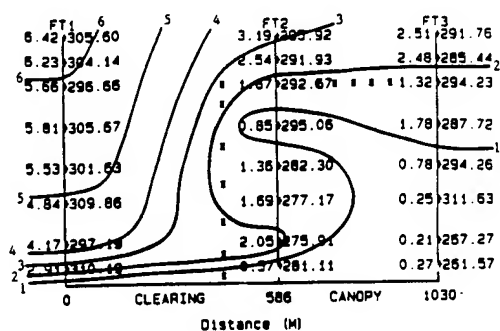


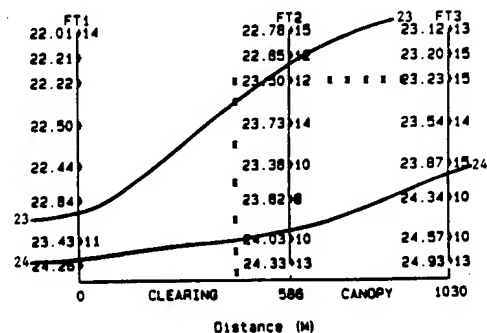
Figure 5. Analyzed horizontal streamlines and isotachs (m/s) over the Forest domain for 28 June at 0800 PST.

Figure 6a shows a composite cross section of vertical profiles of wind speed and wind direction from 32 m high micrometeorological stations FT-1, FT-2, and FT-3. This plot in conjunction with fig. 1 shows that the wind traveled at about a  $30^\circ$  angle from normal to the forest edge during this day. However, the wind traveled from FT-1 (which was in a large clearing toward FT-2, which was at the forest edge) toward FT-3 (which was deep within the Forest). This cross section shows generally increased wind speed with height for FT-1, but FT-2 has increased wind speed at level 2 and levels 6 and above. The relatively higher wind speed at tower FT-2 at level 2 is due to the trunk space of the trees in the Forest, and the marked minimum wind speed at level 5 is due to the forest canopy. By the time the wind reaches tower FT-3, it again shows a gradual increase with height except at level 6. By this time the tree trunks and canopy have extracted much of the wind energy. The wind speed minimum at level 6 is believed to be due to the wind moving up and over the forest edge and then later moving down into the forest canopy like a jet, which occurs at level 5 at FT-3. This explanation indicates that level 5 is really a maximum rather than level 6 being a minimum.

Figure 6b is a composite cross section of vertical profiles of temperature and relative humidity for the same time period as figure 6a. This plot shows that there was a small positive temperature gradient from the clearing at FT-1 to the forest at FT-3. The daytime temperature in the clearing was slightly cooler than in the forest because wind speeds were significantly greater, causing more mixing down of the cooler air from above. The relative humidity, as expected, was greater within the forest canopy than within the trunk space, but overall it was very dry.



(a)

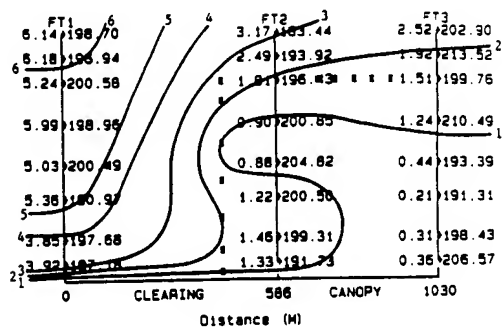


(b)

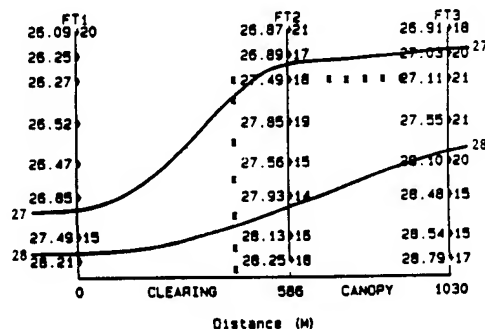
Figure 6. Composite (a) isotach and (b) temperature and relative humidity cross sections through the forest edge using FT-1, FT-2, and FT-3 data for 24 June at 1000 to 1600 PST.

Figure 7a is a composite plot of wind speed and wind direction during the day on 27 June. The wind speed values for all three towers were very similar to those of fig. 6a, but the wind direction values were significantly different. On this day, the wind was from the south-southwest and was nearly parallel to the forest edge that ran north-south. There were still greater wind speeds along the forest edge in the trunk space region than the canopy as in fig. 6a; however, the wind speed maximum at FT-3 at level 5 was not there in fig. 7a. This difference is probably due to the wind direction being nearly perpendicular to the forest edge in fig. 6a, and nearly parallel to the forest edge in fig. 7a.

Figure 7b shows a very similar temperature cross section as in fig. 6b but it is during a different day. The temperature continued to be warmer within and above the forest, probably due to the increased mixing of the air in the clearing.



(a)



(b)

Figure 7. Composite (a) isotach and (b) temperature and relative humidity cross sections through the forest edge using FT-1, FT-2, and FT-3 data for 27 June at 1000 to 1600 PST.

Figure 8a is a composite cross section of wind speed and wind direction for nighttime hours. This plot appears very different from fig. 6a and 7a since in this case the wind was nearly perpendicular to the forest edge, but more importantly it came from the east from within the forest and exited into the clearing. This plot indicates a much smoother and uniformly changing wind flow since the effects of the travel through the forest have been balanced and an established wind flow through the forest has occurred. Another difference between fig. 8a and daytime cases is that from about level 4, the height of the canopy, to the top of tower FT-2, the wind speed is greater exiting the canopy than entering even though winds are about the same speed in the clearing. This indicates that much of the wind flows above the forest rather than through the forest when it first encounters the forest edge.

Figure 8b is a nighttime temperature and relative humidity composite plot for 26-27 June. This figure shows inversion conditions at all towers, but the tower within the forest (FT-3) has a much stronger inversion due to significantly colder temperatures. The colder forest temperatures were probably due to less mixing within the forest because the wind speeds were significantly less. Except for slightly higher relative humidity within the forest canopy as compared to the trunk space, the relative humidity overall was relatively uniform.

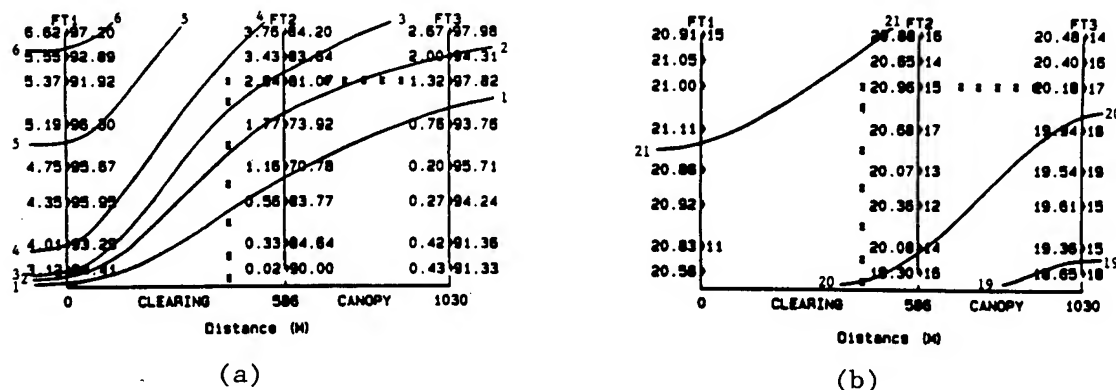


Figure 8. Composite (a) isotach and (b) temperature and relative humidity cross sections through the forest edge using FT-1, FT-2, and FT-3 data for 25-26 June at 2100 to 0400 PST.

Figure 9a shows a nighttime composite cross section of wind speed and wind direction for 27-28 June. The wind for this time period is close to a southeasterly direction as opposed to an easterly direction in fig. 8a. This difference did not seem to affect the way the winds react when traveling from the forest to the clearing. Another difference between these two figures is the wind speed. The wind speed was significantly lower in fig. 9a than in fig. 8a. This also appeared to produce lower wind speeds within the canopy and the trunk space, and at tower FT-3 (deep within the forest) the winds were nearly calm.

Figure 9b shows the temperature and relative humidity cross section for the same nighttime hours as in fig. 9a. The main difference seen in this figure is the nearly 3 °C temperature difference between tower FT-1 and FT-3. This

also shows a strong inversion at FT-3. Although the temperature in the clearing at FT-1 is warmer than the temperature at FT-1 in fig. 8a, the temperature near the surface at FT-3 in fig. 9a is nearly 1 °C lower than near the surface at FT-3 in fig. 8a. This difference is believed to be due to the very low wind speeds in the forest in fig. 9a, and slightly higher wind speeds in the forest in fig. 8a. Again, mixing from the stronger wind speeds appears to have played a major role in the temperature differences at night between different time periods and between the forest and clearings. Also, the relative humidity was greater within the forest primarily because of the lower temperatures there.

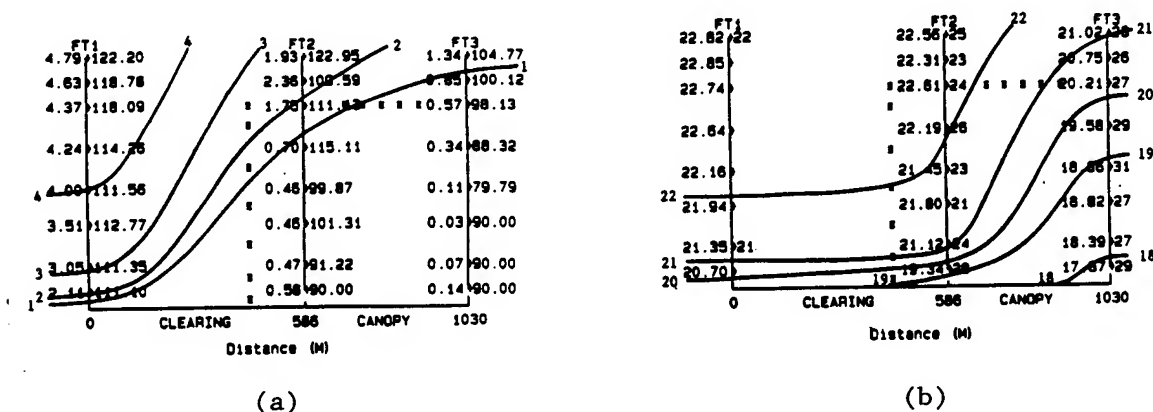


Figure 9. Composite (a) isotach and (b) temperature and relative humidity cross sections through the forest edge using FT-1, FT-2, and FT-3 data for 27-28 June at 2100 to 0400 PST.

### 3. SUMMARY

The horizontal plots from the summer of 1985 showed that the winds over the Forest domain generally exhibited a bimodal distribution, changing from a southwesterly direction during the daytime to an easterly direction at night. During the daytime the southerly component of the wind flow was primarily produced by the upvalley flow from the Sacramento River Valley to the west, and the westerly component of the wind flow was produced by upslope flow from the valley toward the Sierra Nevada mountains. There was little change in temperature over the entire Forest domain during daytime hours. However, the clearings were slightly cooler than the forest because of the stronger winds and greater downward mixing of air above the clearings.

During the nighttime hours, the winds tended to be from an easterly direction, indicating downslope drainage winds. This drainage flow was surprisingly strong in the clearings and appeared to conform and flow along the valley over the southern part of the Forest domain. The temperature was also colder within this valley, and there were temperature inversion conditions throughout the nights. The temperature was also colder within the forest than in the clearings, probably because of the greater mixing of the air above the clearings due to the significantly stronger wind speeds.



Evidence from the forest towers indicates the winds flowing from the forest to the clearing did react somewhat differently than the air flowing from the clearing to the forest. Much of the wind flowing into the forest ascended up the forest edge and then flowed back into the forest like a wind jet. The wind that did flow through the forest edge was slowed significantly faster by the canopy region than by the trunk space region. The wind flowing out of the forest and into the clearing appeared to uniformly increase in speed as it flowed beyond the forest edge, and the wind speeds above level four in tower FT-2 were greater upon exiting the forest than entering.

#### REFERENCES

- Cionco, R. M., 1989a: Design and Execution of Project WIND. In Proceedings of the 19th Conference of Agricultural and Forest Meteorology, Charleston, SC, American Meteorological Society, Boston, MA.
- Cionco, R. M., 1989b: Micrometeorological Measurements of Canopy Domains During Project WIND. In Proceedings of the 19th Conference of Agricultural and Forest Meteorology, Charleston, SC, American Meteorological Society, Boston, MA.
- Orndorff, B. L., and R. M. Cionco, 1991: On The Characterization of Army-Scale Surface Layer Micrometeorology Using Field Measurements. In Proceedings of the 1991 Battlefield Atmospherics Conference, Fort Bliss, Texas, U.S. Army Atmospheric Sciences Laboratory, White Sands Missile Range, NM.

# A MESOSCALE NUMERICAL SIMULATION OF THE PERSIAN GULF WIND FIELDS:

CASE STUDY OF 28-29 MARCH 1991

Robert E. Dumais, Jr., and Teizi Henmi

Battlefield Environment Directorate\*

U.S. Army Research Laboratory

White Sands Missile Range, New Mexico 88002-5501, USA

John Barnes

Computer Sciences Corporation

White Sands Missile Range, New Mexico 88002-5501, USA

## ABSTRACT

The Battlefield Environment Directorate is currently evaluating candidate mesoscale meteorological models for operational use in the future Integrated Meteorological System. One of these models, the Yamada Higher Order Turbulence Model for Atmospheric Circulations (HOTMAC), is examined for its ability to simulate the Persian Gulf wind fields of 28-29 March 1991. The model was tested over a 1500- by 1500-km domain on Cray-XMP architecture and incorporated a finer scale nested grid in the vicinity of the gulf. In this paper, emphasis is placed upon the evaluation of the HOTMAC prognostic wind fields simulated from 1200 Universal Time Coordinated (UTC), 28 March through 1200 UTC of 29 March 1991.

## 1. INTRODUCTION

### 1.1 MODEL EQUATIONS

Developed by Yamada (1982), Yamada Higher Order Turbulence Model for Atmospheric Circulations (HOTMAC) is a hydrodynamical meteorological computer code that uses the level two closure model for parameterizing turbulence and subgrid-scale mixing. The model equations for mean wind, mixing ratio of water vapor, turbulence kinetic energy, turbulence length scale, and deviation of the horizontally averaged potential temperature are solved prognostically, using the alternating direction implicit numerical scheme to integrate, and staggered on the Arakawa C-grid. Forward differences are used for time derivatives, and centered differences are used for advection and diffusion terms. The alternating direction implicit technique allows for larger time stepping such as the 600-s step used in this study. Additionally, the model is hydrostatic Boussinesq and uses a terrain following coordinate system. The vertical coordinate transformation is given by eq. (1) as

$$Z^* = H^* [(Z - Z_g)/(H - Z_g)], \quad (1)$$

\*formerly U.S. Army Atmospheric Sciences Laboratory

where  $Z^*$  and  $Z$  are transformed and Cartesian vertical coordinates, respectively;  $Z_g$  is ground elevation;  $H^*$  is the material surface top of the model in the  $Z^*$ -coordinate; and  $H$  is the corresponding height in the  $Z$ -coordinate. For simplicity, in this study  $H$  is described as

$$H = H^* + Z_{gmax}, \quad (2)$$

with  $H^* = 5000$  m and  $Z_{gmax} = 2601.1$  m. Refer to Yamada (1982) and Yamada and Bunker (1989) for the complete listings and derivations of the model equations. For simplicity, this study ignores the effects of vegetative canopies and sets the initial value of surface roughness length,  $Z_0$ , equal to a constant of 0.01 at all grid points. Additionally, a soil eddy conductivity value of  $4.44 \times 10^{-7}$  m<sup>2</sup>/s and soil density of 1500 kg/m<sup>3</sup> are assumed at all grid points. A stable precipitation scheme is not provided by the model at this time, and cumulus parameterization consists of a second-order turbulence closure (including moisture) coupled with a Gaussian cloud model.

## 1.2 TREATMENT OF BOUNDARY CONDITIONS

The boundary conditions used in this simulation will be discussed briefly in this section. The lateral boundary values for the prognostic variables are obtained by solving the one-dimensional vertical equations (that is, variations of the variables in the horizontal direction are set to zero). The model top is treated as a rigid boundary, with mean values of the prognostic variables left unchanged from their initial values and turbulence variables vanishing completely.

Surface boundary conditions for the mean momentum, deviation potential temperature, and mean water vapor mixing ratio equations are constructed from the empirically derived formulas for wind, temperature, and water vapor in the surface layer discussed by Yamada (1982). There are four soil layers, and the temperature of the soil is obtained from numerically integrating a heat conduction equation. The boundary conditions for this conduction equation are the heat energy balance at the surface and a specified soil temperature value at 50 cm below the surface. The treatment of the long-wave radiation flux at the surface is reviewed in Yamada (1982).

## 1.3 FOUR-DIMENSIONAL DATA ASSIMILATION

The technique of Newtonian nudging, similar to the approach reviewed by Yamada and Bunker (1989), was applied to the equation of motion to guide the model winds in the layers well above the surface (in this study, at or above 395 m) toward the observed winds. Under a horizontally homogeneous condition, an analytical expression may be obtained for the relationship between the nudging and Coriolis parameters. Yamada and Bunker (1989), using a series of one-dimensional simulations, found that a ratio of 5 between the nudging coefficient and the Coriolis parameter could handle cases of directional shear up to as much as 180°. In this study, the value of the nudging coefficient was somewhat subjectively set at 0.0005, due to this value's apparent ability in past simulations to assimilate environmental wind flows that were well sheared directionally and largely decoupled from the near-surface wind flow. Although nudging of other prognostic variables such as specific humidity and potential temperature can be accomplished in the same fashion, it was not undertaken for this study. Observed data was assimilated every hour during the simulation.

## 2. SIMULATION DESIGN

### 2.1 DESCRIPTION OF GRIDDED DOMAIN

HOTMAC model calculations were conducted over an area 1500 by 1500 km, centered at latitude  $29.5^{\circ}\text{N}$  and longitude  $47.5^{\circ}\text{E}$ , almost directly over the Persian Gulf. This area was covered by a total of  $49 \times 49 \times 16$  grid points, with a unit horizontal grid distance of 30 km (grid 1). However, since the HOTMAC model equations require terrain gradients, wind vectors are calculated at every other horizontal grid point. Vertical grids are staggered so that more resolution can be obtained near the surface.

The model uses a linear universal transverse mercator (UTM) grid, which is best suited for small domains where the effects of the earth's sphericity can be safely neglected. Admittedly, one major weakness of our Persian Gulf simulation is the large size of the grid domain that reduces the validity of using the UTM system.

To better resolve the sometimes complex wind field about the Persian Gulf, a nested grid (grid 2) was incorporated centered on latitude  $28.4^{\circ}\text{N}$  and longitude  $50.2^{\circ}\text{E}$ . This nested region was covered by  $31 \times 31 \times 16$  grid points, with a horizontal resolution of 15 km. The southwest corner of the nested grid is located roughly at grid point coordinate (27.5,13.5) of the coarse grid domain.

The nested grid is designed to provide exactly twice the resolution provided by the coarse grid. Variables for the coarse grid are first advanced in time by one integration time step, where the lateral boundary conditions are obtained through integration of the governing equations while neglecting variations in the horizontal directions. However, the coarse grid values at the boundaries of the nested area provide the lateral boundary conditions for the nested grid. The additional lateral boundary values between the coarse points are obtained by linear interpolation. Using these boundary values, the variables for the nested grid area are advanced by one coarse grid time step in two steps, each step equal to one-half the coarse grid time step.

Since HOTMAC output from this simulation was designed to be later used as input into a Lagrangian particle model (which requires input at discrete time steps of around 10 min), the time interval for each time step was explicitly set at a fixed value of 600 s. However, this value is such that the Courant-Friedrich-Lewy criteria will not be left unsatisfied regarding this particular simulation. Normally, the time interval for each individual time step is computed implicitly to satisfy this criteria, which is based on the actual winds and the propagation speed of fast gravity waves for both the coarse and nested grids. The prognostic variables are smoothed at each time step using the values at four neighboring points, except at the lateral boundaries where only three points are used.

### 2.2 MODEL TERRAIN

The terrain data set for the coarse gridded region was supplied by Dr. Robert Walko of Colorado State University. In the case of the nested grid domain, the terrain set was generated by applying a simple bilinear interpolation to

the coarser grid set. Although interpolation will tend to smooth out the finer scale terrain features, this was deemed a suitable (although not the most desirable) approach due to the lack of finer scale terrain data that was readily available to the modelers at the Battlefield Environment Directorate. The potential adverse effects introduced from using the smoothed nested terrain data can be expected to be most pronounced in the northeast portion of the grid, where the relief is highest and most complex. However, we hoped that the nested grid might provide enough additional horizontal resolution so that solenoidal circulations such as the diurnal land-sea breeze might be simulated by the model in the region of the gulf.

The highest relief over the 1500- by 1500-km coarse grid domain is that of the Zagros Mountain chain that spans northwest to southeast across western Iran. The highest point in this area is Zard Kuh, at an elevation of 4548.0 m above sea level. By comparison, the maximum elevation (for this same area) that is contained in the coarse terrain data set is 2706.1 m. Obviously, the coarse terrain resolution of 30 km is not capable of accurately representing the highest peaks, due to the very large terrain gradients in the Zagros. Since HOTMAC is capable of forecasting terrain-induced wind flows such as daytime upsloping and nocturnal valley draining, it can be expected that excessive smoothing of the terrain data will adversely affect model results. This effect may be greater than that introduced by ignoring the vegetation and simplifying many of the region's surface characteristics in the model physics. Ballard and Barnes (1991) ran several transport simulations over a similar area around the Persian Gulf for March 1991 using the United Kingdom Meteorological Office's mesoscale model. In their research, they report that use of an interpolated terrain set including steeper and higher orography actually caused one case with very strong southwesterly flow to blow up over the Zagros (the northeast corner of their grid).

### 3. OBJECTIVE ANALYSIS AND INITIALIZATION

#### 3.1 MODEL INITIALIZATION

HOTMAC model initialization was based on the 1200 UTC, 28 March sounding taken at Dhahran, Saudi Arabia (26.3°N, 50.2°E, 18.3 m). An initial wind profile at this site (values assigned to the nearest gridpoint) was constructed by assuming a logarithmic variation from the ground up to the level where the wind speed reaches an ambient value (6.5 m/s). Initial wind profiles at other grid locations were obtained by satisfying the principle of mass continuity. Wind directions below model level 8 (395 m) were initially set to northerly at all grid points. Above level 8, the wind directions were nudged towards the "observed" data derived by the National Center for Atmospheric Research (NCAR).

The vertical profile for potential temperature is based on the Dhahran sounding, and initial potential temperatures are assumed to be uniform horizontally. Initial values for water vapor were constructed by using the initial potential temperatures, the pressure at the model top, and an assumed value of relative humidity.

### 3.2 OBJECTIVE ANALYSIS USED FOR NUDGING

Gridded, analyzed wind fields were constructed at intervals of 1 h throughout the simulation period so that "observed" data was available for model nudging. From NCAR, gridded 2.5° by 2.5° data sets were provided for the region of interest and at all mandatory levels up to and including 400 mbar. From this data set, winds were interpolated vertically from the mandatory levels to the model levels by using a cubic spline polynomial method. Once accomplished, the wind values were then interpolated horizontally from the NCAR grid point space to the model grid point space by using a Barnes (1973) objective analysis scheme. Since the NCAR data was provided at 12-h intervals, analyzed model wind fields were generated for 1200 UTC on 28 March and 0000 and 1200 UTC on 29 March. To create hourly sets, a simple linear interpolation in time was done using the three original analyzed sets.

### 4. MODEL RESULTS

Generally, the flow over the grid 1 region was cyclonic between 1200 UTC of 28 March and 0000 UTC of 29 March, reflecting an upper level trough of low pressure centered north of the grid over the Soviet Union. However, a hint of a cyclonic circulation is noted in the southwestern corner of grid 1 at 1200 UTC of 28 March. By 1200 UTC of 29 March, anticyclonic flow dominates most of the grid 1 southern sector, and this is verified by 850 and 700 mbar analyses of the region. Additionally, no large scale precipitation or frontal passages occurred, and only a very weak diurnal land-sea solenoidal circulation was evident (Walko and Pielke, 1991). This type of weak synoptic regime allows the surface wind field to be largely forced by diurnal variations in surface heating over complex terrain. It is precisely this type of flow that HOTMAC is best suited to simulate, particularly during the day.

Figure 1 shows the vertical profile of wind and potential temperature at Dhahran, Saudi Arabia, at 1200 UTC on 28 March. Note the predominately westerly flow above the surface. It was from this profile that the model's first guess wind and temperature fields were developed. Figures 2 through 4 show the analyzed wind fields for each of the 12-h periods, derived from the NCAR 2.5 by 2.5 degree pressure level data using a Barnes objective analysis. These figures indicate both the cyclonic flow over the eastern sector of grid 1 and the increasingly anticyclonic flow with time over the southern sector of the same grid. These figures refer to model level 12, located at 1767 m above ground.

Figures 5 through 12 show the model results for both grids 1 and 2 at 12 h and 24 h after the initial time. The model winds are shown at the levels 10 m and 3000 m above ground. Most evident from these figures is the development of daytime upsloping and nighttime downsloping flows near the surface, starting from the gulf eastward to the Zagros Mountains in Iran. However, very little resolution was obtained from the second grid, apparently because a pronounced solenoidal circulation did not develop over the gulf on this day. The prevailing ambient flow is also represented well in the figures referring to the 3000-m level, indicating that the nudging was working satisfactorily in the model's upper levels.

Tables 1 through 3 summarize some of the model results in statistical form, although these numbers should be taken cautiously due to the very small sample size. These statistics were derived by comparing the model wind values to those observed at up to six possible raob sites around the gulf. These sites were in Saudi Arabia: Dhahran, Hafr Al-Batin, Hail, and Riyadh; in Qatar: Doha; and in the United Arab Emirates: Abu Dhabi. The three levels compared were at 10, 861, and 3739 m. The observed values for each raob station were obtained by linearly interpolating vertically to the desired level from the nearest levels in the respective sounding. The model values were obtained by computing the median value of the four grid points nearest the station in question and from the model level desired. Since none of the six raob stations were located within the nested grid, all of the statistics shown below were taken from the coarse grid.

The HOTMAC simulation assumed many simplifications within the surface layer, such as spatially constant initial values of roughness length and friction velocity. In addition, the initial temperature structure over the entire coarse grid was based on a single atmospheric sounding, that is unrealistic when the grid area is so large. Also, because of the grid's large size, the model's UTM grid scheme was stretched beyond its truly valid limits, due to sphericity considerations. Finally, the terrain resolution was relatively coarse, being 30 km for grid 1.

Considering all this, the results below show that the model still did a reasonable job of simulating the diurnal wind flow around the gulf between 28-29 March 1991. The only truly bad model wind forecasts appear to be at night near the surface, and these were due to poorly forecast wind directions. The errors were largest at Hafr Al-Batin and Riyadh, both located just west of the gulf where forecast winds had a westerly rather than easterly component. This indicates that the model underestimated the extent of the downslope flow, possibly due to the low terrain resolution. Typically, mesoscale models tend to have difficulty forecasting wind direction at night, probably due to localized complexities in the terrain that create unique shallow drainage patterns. Other modeling difficulties such as the correct parameterization of the nocturnal boundary layer and the surface radiation budget add to this problem. In the upper levels, the nudging approach seems to have allowed the model winds to simulate the ambient wind quite well, with only a bit of underestimation of the wind speeds.

## 5. CONCLUSION

The HOTMAC was designed initially to interact with a three-dimensional particle model, providing the wind data over the grid 1 domain that would be used as input into the particle model. Since at that time the model had not developed the capability to nudge temperature and moisture, these fields were initially assigned very homogeneously and simplistically. Because of these limitations, and due to the fact that the model's UTM gridding scheme was not truly valid considering the size of the grid area, the expectations of this model were to provide prognostic wind forecasts that correctly depicted the general regional flow, in particular the diurnal upsloping and downsloping flows near the surface and in the vicinity of the gulf. It was believed that this could be accomplished, even with the shortfalls described, due to the very quiet synoptic regime that was present.

Overall, although there were some rather large deviant wind values simulated by the model near the surface at night, the majority of the prognostic forecasts that were examined compared quite reasonably with the values observed. Typically, root-mean-square errors were less than 2.5 m/s for wind speeds and less than 30° for wind direction. Taking into account that the model was really applied to a grid domain much larger than it is really designed for, the results are fairly acceptable. Given a finer terrain resolution and a more realistic initial temperature and moisture field, the results shown here would probably be improved upon quite considerably. As mentioned previously, although the results show that HOTMAC did fairly well in this simulation when one considers the limitations, it is to be made clear that the model is really designed to run over a much smaller grid area. Additionally, although the model results are probably better than could be expected in reality due to nudging towards observed data, in real time the model would nudge to the output generated from a larger scale atmospheric model. Hence, nudging will work best if the output from the larger scale model is acceptable.

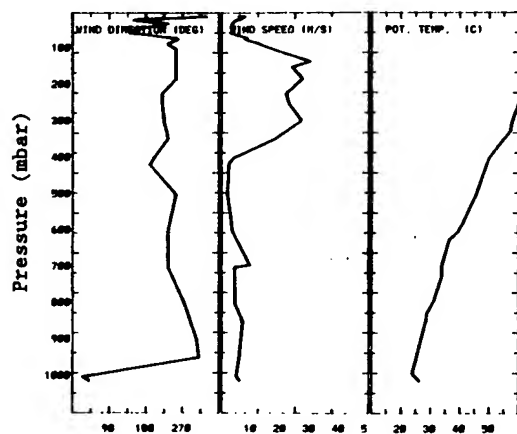
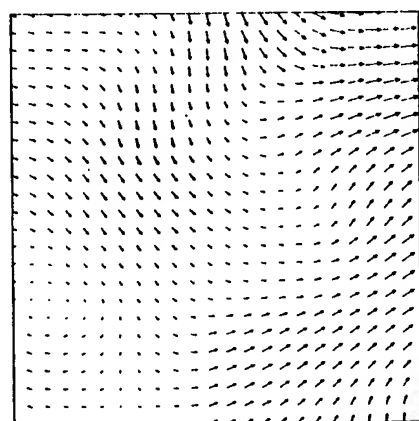
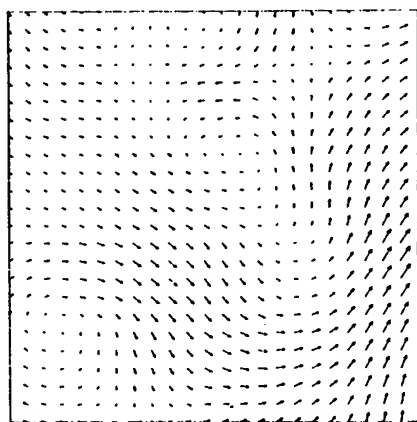


Fig. 1. 28 Mar 91, 1200 UTC sounding, Dhahran, Saudi Arabia.



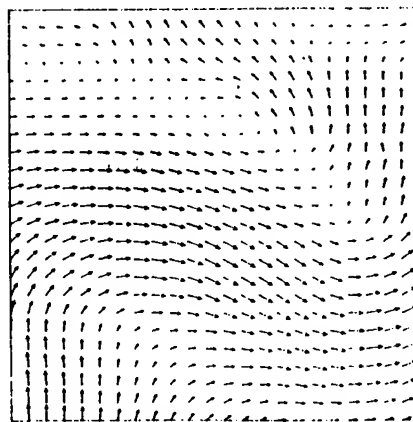
Max wind = 11.8 m/s

Fig. 2. 28 Mar 91, 1200 UTC 1767 m, analyzed winds for grid 1.



Max wind = 13.1 m/s

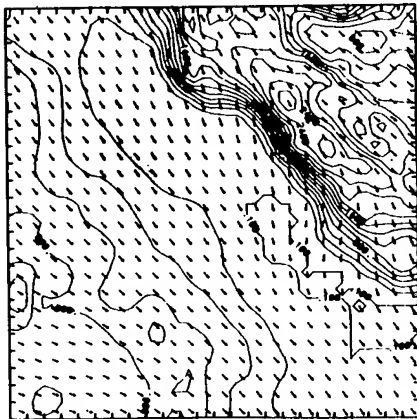
Fig. 3. 29 Mar 91, 0000 UTC 1767 m, analyzed winds for grid 1.



Max wind = 8.82 m/s

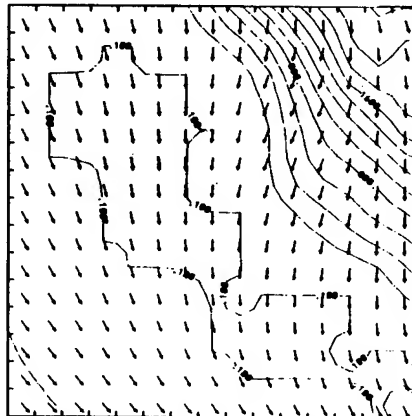
Fig. 4. 29 Mar 91, 1200 UTC 1767 m, analyzed winds for grid 1.





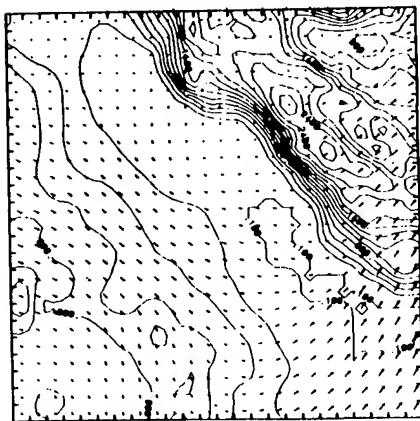
Max wind = 4.19 m/s

Fig. 5. 29 Mar 91, 0000 UTC 10 m, model winds (grid 1) after 12 h.



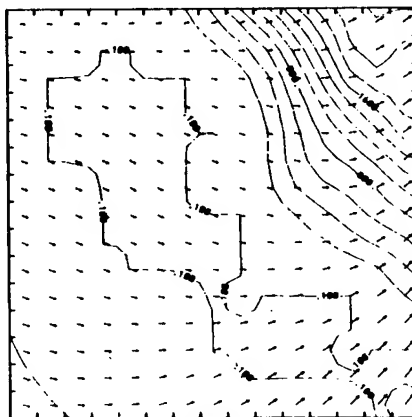
Max wind = 3.54 m/s

Fig. 6. 29 Mar 91, 0000 UTC 10 m, model winds (grid 2) after 12 h.



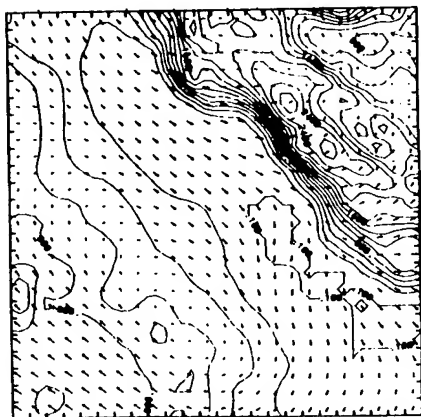
Max wind = 14.0 m/s

Fig. 7. 29 Mar 91, 0000 UTC 3000 m, model winds (grid 1) after 12 h.



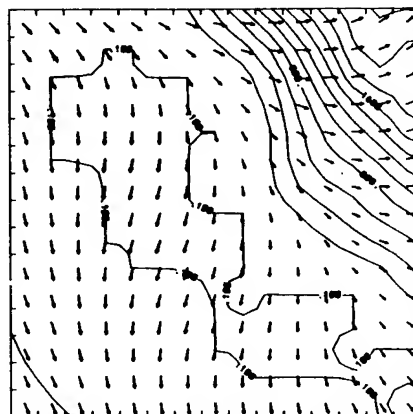
Max wind = 10.7 m/s

Fig. 8. 29 Mar 91, 0000 UTC 3000 m, model winds (grid 2) after 12 h.



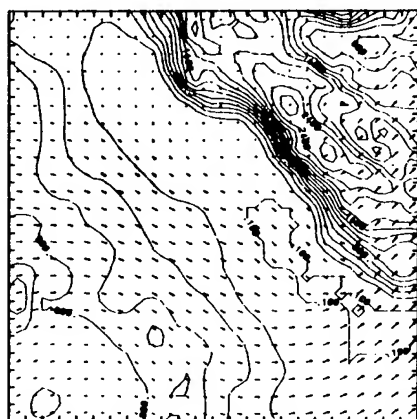
Max wind = 3.70 m/s

Fig. 9. 29 Mar 91, 1200 UTC 10 m, model winds (grid 1) after 24 h.



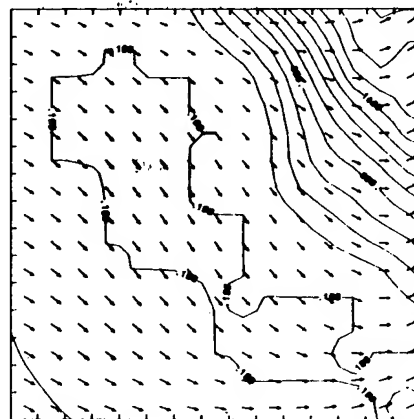
Max wind = 2.70 m/s

Fig. 10. 29 Mar 91, 1200 UTC 10 m, model winds (grid 2) after 24 h.



Max wind = 11.7 m/s

Fig. 11. 29 Mar 91, 1200 UTC 3000 m,  
model winds (grid 1) after  
24 h.



Max wind = 8.36 m/s

Fig. 12. 29 Mar 91, 1200 UTC 3000 m,  
model winds (grid 2) after  
24 h.

TABLE 1. MEAN AND MEDIAN DIFFERENCES

Model Value - Observed Value					
0000 UTC, 29 March 1991					
Mean Values					
HT (AGL) (m)	U	V	WS	WD	No. OBS.
10	2.26	-2.58	1.53	92.73	4
861	-0.82	1.17	-0.48	11.00	5
3739	1.12	-0.46	1.61	32.83	6
Median Values					
10	2.38	-2.39	1.56	84.93	4
861	-1.04	1.11	0.45	4.03	5
3739	1.01	-0.95	1.01	36.31	6
1200 UTC, 29 March 1991					
Mean Values					
10	-0.19	0.02	-1.79	21.95	4
861	-2.57	-0.14	-1.10	26.53	4
3739	1.01	-0.60	1.37	18.74	5
Median Values					
10	-0.47	0.27	-2.66	18.18	4
861	-2.06	0.16	-2.01	17.24	4
3739	1.50	-0.26	2.22	13.10	5

TABLE 2. RMSE (m/s) AT 0000 UTC, 29 MARCH 1991 AFTER 12 h OF SIMULATION

HT (AGL) (m)	U	V	WS	WD	No. OBS.
10	2.78	2.85	1.74	107.63	4
861	0.93	1.54	1.68	17.42	5
3739	3.92	3.77	2.88	41.38	6

TABLE 3. RMSE (m/s) AT 1200 UTC, 29 MARCH 1991 AFTER 24 h OF SIMULATION

HT (AGL) (m)	U	V	WS	WD	No. OBS.
10	1.62	2.46	2.73	22.79	4
861	2.78	1.68	2.16	35.47	4
3739	2.67	2.16	2.23	24.18	5

#### ACKNOWLEDGMENTS

The authors extend a big thank you to Mr. Dennis Joseph of NCAR for his most able efforts in providing a suitable meteorological database for our study and Drs. L. Luces and H. Holt and Mr. Jeff Passner for their suggestions and input. In addition thanks to the Army High Performance Computing Resource Center for the use of their resources.

#### REFERENCES

- Ballard, S. P., and R. T. H. Barnes, 1991: Mesoscale Model Simulations of Smoke Transport: Notes on Forecasts-ARATS Project. Technical Report for the Short Range Forecasting Division, United Kingdom Meteorological Office, London, England, 22 pp.
- Barnes, S. L., 1973: Mesoscale Objective Map Analysis Using Weighted Time-Series Observations. NOAA Technical Memorandum ERL NSSL-62, National Severe Storms Laboratory, Norman, Oklahoma, 60 pp.
- Walko, R. L., and R. A. Pielke, 1991: Transport Simulations of Smoke Particles from the Kuwait Oil Fires. Report prepared for the U.S. Army Research Office, Research Triangle Park, NC 27709, Contract NO. DAAL03-86-0-0001, 80 pp.
- Yamada, T., 1982: A Numerical Model Study of Turbulent Airflow in and above a Forest Canopy. J. Meteorol. Soc. Japan, 60:439-454.
- Yamada, T., and S. Bunker, 1989: A Numerical Model Study of Nocturnal Drainage Flows with Strong Wind and Temperature Gradients. J. Appl. Meteorol., 28:545-553.

## SURFACE WIND SPEED DISTRIBUTIONS

Elton P. Avara and Bruce T. Miers  
Battlefield Environment Directorate\*  
U.S. Army Research Laboratory  
White Sands Missile Range, New Mexico 88002-5501, USA

### ABSTRACT

Some weapon systems are sensitive to winds in the lowest layers of the atmosphere. Wind speed distributions and random wind speeds derived from the distributions are often required to help determine the operational capabilities of these systems. A literature survey revealed that investigators usually used either a lognormal or a Weibull distribution as the model for the distribution of wind speeds independent of direction. In addition to these two distributions, a gamma distribution was also evaluated in this study. Wind speeds observed in three different geographical regions during nine selected meteorological conditions (weather classes), three diurnal time periods, and five seasonal time periods were evaluated. This presentation contains the results of the wind speed analysis for some of the combinations of weather classes, diurnal time periods, and seasonal time periods for each of the three geographical regions--European Lowlands, European Highlands, and Mideast Desert. The observed wind speed distributions were adequately represented by the analytical distributions except in a few cases. For those exceptions, the observed empirical wind speed distributions should be used rather than the analytical distributions to generate random wind speeds in simulation studies.

### 1. INTRODUCTION

The Program Manager (PM) for BAT (PM-BAT) and his associated contractors (CAS, Incorporated, and Dynetics, Incorporated) have a requirement to find analytical distributions to adequately represent the observed wind speed distributions obtained under different meteorological conditions, at different time periods, and at different geographical regions of the world. These distributions are required to test the operational capabilities of the BAT system. The U.S. Army Atmospheric Sciences Laboratory (ASL) (now the Battlefield Environment Directorate (BED)) was requested to perform the task.

Dramatic changes in the atmosphere occur each day on the average as the sun rises and sets. Although diurnal variations are most prominent in the atmosphere's lower layers, changes in boundary layer winds have been documented also for other atmospheric variables (Holton, 1967). Frequency of occurrence

---

\*formerly U.S. Army Atmospheric Sciences Laboratory

of low wind speeds have important applications in air pollution analysis or for nuclear-biological-chemical (NBC) predictions for military applications. The predictions of frequencies of high wind speeds also have important applications in the areas of structural design and assessment of potential output from wind-powered generators.

Most wind speed data used in this analysis are from measurements made by rotary cup anemometers. For low wind speed measurements, two errors are inherent in using cup anemometers—static friction and dynamic friction. A starting wind speed must be sufficient to overcome static friction and cause the cups to turn. Dynamic friction becomes a factor as the wind decreases from a speed above the starting threshold until the cups stop turning. Higher wind speed measurements are also subject to an error known as overspeeding. Overspeeding occurs because the anemometer responds more quickly to an increase in speed than to a decrease in speed. In a turbulent wind field the mean value of the anemometer reading will be higher than the true mean. Also, an error caused by vertical wind fluctuations is of the same sign as the overspeeding error. The additive effect of these errors can cause measurements to be greater than the true wind speed by as much as 10 percent (Mage, 1980).

Investigators have examined various statistical models for wind speed frequency distributions that range from calm to the maximum observed wind speed. A Planck distribution was investigated by Dinkelacker (1949) and Wentink (1974). A Rayleigh distribution (a chi-square distribution with 2 degrees of freedom) has been used by Narovlyanskii (1968) and Baynes (1974). Crutcher and Baer (1962) showed that the bivariate normal distribution is adequate for most wind samples. The Pearson Type III (gamma) was used by Putnam (1948) and Sherlock (1951) to describe wind speed distributions. The Weibull distribution was used to fit both upper air data (Baynes and Davenport, 1975) and surface wind speed data (Wentink, 1976). Justus et al. (1976) were successful in fitting the Weibull distribution to data from 135 sites. The Weibull model has been an especially useful tool for wind power analysis (Hennessey, 1974). Stewart and Essenwanger (1978) examined the Weibull distribution, and Luna and Church (1974) the lognormal distribution as models for the distribution of wind speeds independent of direction.

## 2. CLIMATOLOGY DATA BASE AVAILABLE

The ASL maintains a climatology data base containing historical weather observations from over 1000 locations in North, Central, and South America; Northern, Central, and Southern Europe; Mideast and North Africa; Southwest, Southern, and Southeast Asia; and Korea. These data were obtained over a period of years from the U.S. Air Force Environmental Technical Applications Center (USAFETAC) at Scott Air Force Base, Illinois. The period of record for the data from each station is generally 11 years or less and may be anywhere from 1966-76 to 1976-86, depending upon which year the data were obtained from the USAFETAC.

The regions of interest were the European Lowlands, European Highlands, and the Mideast Desert geographical areas (Miers et al., 1985a; Miers et al., 1985b). The list of stations used in the analysis for each region is available in Avara and Miers (1992). The period of record for the data from most of the stations in these regions is 1966-76.

For the two European regions winter and annual wind speed distributions were obtained by grouping the observations from all hours of the day. Winter for these regions is defined to be November, December, January, and February. For the Mideast Desert region, summer and annual wind speed distributions were obtained by grouping the observations taken at night into one group and the observations taken during the daytime into another group. Summer for the Mideast Desert region is defined to be June, July, and August.

The 3-hourly observations (0000, 0300, ..., 2100 GMT) in the data base tend to be more reliable and consistent over time than the observations taken at the other hours of the day. Therefore, the 3-hourly observations were the only observations included in the analysis for any region, season, or period of the day.

### 3. WEATHER CLASSES

There was interest in the wind speed distributions derived from observations taken in different weather conditions or classes. A weather class is a specific configuration of cloud cover and cloud base height, visibility, and obscuration type. The specific classes are defined in table 1 as WXCL-1 through WXCL-6, WXCL-8, and WXCL-9. The analysis was performed for the wind speed information for WXCL-1 to WXCL-6 for the European regions and WXCL-1, WXCL-8, and WXCL-9 for the Mideast region. The class WXCL-7 was added by the authors for the European regions to allow one to see the results of fitting analytical distributions to wind speeds observed during fog conditions without regard to the type of fog.

TABLE 1. DEFINITIONS OF THE NINE OBSERVATION WEATHER CLASSES IN TERMS OF CLOUD COVER, CLOUD BASE HEIGHT, OBSCURATION TYPE, AND VISIBILITY

LABEL	DEFINITION
WXCL-1	No Clouds (either no clouds or no clouds with bases $\leq 3000$ m)
WXCL-2	Clouds with bases $\leq 3000$ m
WXCL-3	Clouds with bases $\leq 3000$ m and Precipitation
WXCL-4	Clouds with bases $\leq 3000$ m and Advective Fog
WXCL-5	Clouds with bases $\leq 3000$ m and Precipitation and Advective Fog
WXCL-6	Radiative Fog
WXCL-7	Fog
WXCL-8	Sandstorms and Dust
WXCL-9	Low Visibility ( $3 \leq \text{visibility} \leq 10$ km)

By World Meteorological Organization (WMO) standards a fog can be reported only when the visibility is not more than 1000 m. There is a distinction between radiative and advective fog conditions. Observations in the BED climatology data base contain fog reports, but they do not contain information about the type of fog reported. To account for the difference between fog types, definitions of radiative and advective fogs were taken from the USAFETAC Electro-Optical Climatology software (USAFETAC, 1991). A reported fog was classified as radiative fog if the wind speed was less than 3.5 m/s (7 kn). Similarly, a reported fog was classified as advective fog if the wind speed was at least 3.5 m/s.

#### 4. ANALYTICAL DISTRIBUTIONS

Three analytical distributions were selected for potential use in representing the observed wind speed distributions. They were chosen based upon the work of the researchers referred to in section 1. These three candidate distributions were the gamma, lognormal, and Weibull. Each of these distributions performed reasonably well at representing the observed wind speed distributions for most of the weather classes.

The gamma probability distribution is defined by

$$f(x; \alpha, \beta) = \frac{\left(\frac{x}{\beta}\right)^{(\alpha-1)} \exp\left[-\left(\frac{x}{\beta}\right)\right]}{\beta \Gamma(\alpha)}, \quad (1)$$

where  $\Gamma(\alpha)$  is the gamma function with argument  $\alpha$ ,  $x > 0$ ,  $\alpha > 0$ , and  $\beta > 0$ .

The lognormal probability distribution is defined by

$$f(x; \mu, \sigma) = \frac{\exp\left[-\frac{1}{2}\left(\frac{\ln(x) - \mu}{\sigma}\right)^2\right]}{x\sigma\sqrt{2\pi}}, \quad (2)$$

where  $\mu$  is the expected value and  $\sigma$  is the standard deviation of  $\ln(x)$  and  $x > 0$ .

The Weibull probability distribution is defined by

$$f(x; \alpha, \beta) = \left(\frac{\alpha}{\beta}\right)\left(\frac{x}{\beta}\right)^{\alpha-1} \exp\left[-\left(\frac{x}{\beta}\right)^\alpha\right], \quad (3)$$

where  $x > 0$ ,  $\alpha > 0$ , and  $\beta > 0$ .

In this report  $\mu$  and  $\beta$  are called scale parameters because changing their values tends to either move the center or skew the distribution toward higher or lower values.  $\sigma$  and  $\alpha$  are called shape parameters because changing their values tends to change the shape of the distribution to either a more peaked or a flatter form.

Three procedures for computing values for  $\alpha$  and  $\beta$  or  $\mu$  and  $\sigma$  were considered for fitting the analytical distributions to the observed wind speed distributions (histograms). These procedures are the method of moments, maximum likelihood, and nonlinear least squares fit to the observed cumulative probability distribution. For each observed wind speed distribution, the best of the three analytical distributions and the associated parameter values were determined. Once the name of the best analytical distribution and the

distribution parameter values are known, the estimation of the tail probability of the wind speed is possible.

The "goodness-of-fit" of the analytical distributions was compared by computing both the mean absolute difference and the root-mean-square (rms) difference between the observed and each of the three analytical cumulative distributions. After thoroughly comparing the analytical distributions by using both criteria, we decided to use the minimum rms difference to make the final selection.

When this criterion is used, the method of moments generally yields parameter estimates that do not perform as well as the other two procedures. The maximum likelihood procedure tends to yield better estimates of the parameters than the method of moments. The nonlinear least squares fit gives the best parameter estimates, as expected by the selection criterion. Specific details about these three methods are contained in Avara and Miers (1992).

## 5. WIND SPEED DISTRIBUTIONS

All three of the analytical distributions considered in this analysis have zero probability of occurrence at  $x = 0$ . The observed wind speed, however, may be calm or zero. To account for this phenomenon in all weather classes except WXCL-4 and WXCL-5 (advective fog cases), the wind speed cumulative distribution is defined by the equation

$$W(X; p_0, \alpha, \beta) = p_0 \delta(0) + (1 - p_0) F(X; \alpha, \beta), \quad (4)$$

where  $X$  is the wind speed,  $\delta(0)$  is the Dirac Delta Function,  $p_0$  is the probability of calm wind speeds, and  $F(X; \alpha, \beta)$  is the appropriate analytical cumulative distribution function.

For weather classes WXCL-4 and WXCL-5, the wind speed cumulative distribution is defined by a modification of the previous equation to give

$$W(X; p_0, \alpha, \beta) = (1 - p_0) F(X - 3; \alpha, \beta), \quad (5)$$

where the wind speed,  $X$ , is at least 3.5 ms. The probabilities of calm wind speeds for each region, time period, and weather class combination are listed in table 2.

The observed probability distribution was obtained by forming histograms of frequency of occurrence of observed wind speed with all histogram interval widths being 0.5 m/s. The histogram frequencies of occurrence were converted to probabilities and assigned to the wind speeds at the midpoints of the intervals. The corresponding analytical probability distribution was obtained by evaluating the analytical cumulative probability distribution at the wind speeds corresponding to the beginning and end of each histogram interval and using the difference between the two values assigned to the wind speed at the midpoint of the interval.

The rms deviation between the observed and analytical cumulative distributions for each region, time period, and weather class combination is listed in table 3. Generally, the rms deviations are small, indicating that the



analytical distributions adequately represent the observed wind speed distributions. The names of the corresponding best distribution are listed in table 4. Two additional tables containing the number of noncalm wind speed observations used in the analysis and the mean absolute deviation between the observed and analytical cumulative distributions for each region, time period, and weather class combination are contained in Avara and Miers (1992).

TABLE 2. PROBABILITIES OF CALM WIND SPEEDS FOR ALL WIND SPEED DISTRIBUTION CASES

Region	Season	Time Period	WX Class	Probability (%)
European Lowlands	Winter	All hours	WXCL-1	5.33310
			WXCL-2	3.33883
			WXCL-3	1.82471
			WXCL-4	0.00000
			WXCL-6	19.41515
			WXCL-7	15.16001
European Lowlands	Annual	All hours	WXCL-1	6.81479
			WXCL-2	3.60214
			WXCL-3	1.90912
			WXCL-4	0.00000
			WXCL-6	20.65096
			WXCL-7	17.10452
European Highlands	Winter	All hours	WXCL-1	16.06559
			WXCL-2	8.78897
			WXCL-3	4.84744
			WXCL-4	0.00000
			WXCL-5	0.00000
			WXCL-6	29.69938
European Highlands	Annual	All hours	WXCL-1	17.58078
			WXCL-2	8.42896
			WXCL-3	4.43246
			WXCL-4	0.00000
			WXCL-5	0.00000
			WXCL-6	35.54087
Mideast Desert	Summer	Night	WXCL-1	14.88957
			WXCL-8	8.10640
			WXCL-9	15.84338
Mideast Desert	Summer	Day	WXCL-1	13.15426
			WXCL-8	6.31811
			WXCL-9	12.18719
Mideast Desert	Annual	Night	WXCL-1	21.29619
			WXCL-8	7.62053
			WXCL-9	21.73497
Mideast Desert	Annual	Day	WXCL-1	17.75504
			WXCL-8	6.83641
			WXCL-9	16.04527

TABLE 3. THE ROOT-MEAN-SQUARE DEVIATION BETWEEN THE OBSERVED AND ANALYTICAL CUMULATIVE DISTRIBUTIONS

Region	Season	Time Period	WX Class	rms Dev (%)
European Lowlands	Winter	All hours	WXCL-1	0.58660
			WXCL-2	0.54364
			WXCL-3	0.51059
			WXCL-4	0.95719
			WXCL-6	3.81003
			WXCL-7	0.96541
European Lowlands	Annual	All hours	WXCL-1	0.76201
			WXCL-2	0.78650
			WXCL-3	0.57538
			WXCL-4	0.86317
			WXCL-6	3.55605
			WXCL-7	0.80706
European Highlands	Winter	All hours	WXCL-1	0.59869
			WXCL-2	0.78476
			WXCL-3	1.05942
			WXCL-4	4.25872
			WXCL-5	2.37126
			WXCL-6	3.48083
			WXCL-7	3.15858
European Highlands	Annual	All hours	WXCL-1	0.64867
			WXCL-2	0.73165
			WXCL-3	0.89949
			WXCL-4	3.24614
			WXCL-5	2.02381
			WXCL-6	3.48151
			WXCL-7	2.92015
Mideast Desert	Summer	Night	WXCL-1	0.88549
			WXCL-8	0.95012
			WXCL-9	0.774849
Mideast Desert	Summer	Day	WXCL-1	0.85728
			WXCL-8	1.78054
			WXCL-9	0.67480
Mideast Desert	Annual	Night	WXCL-1	0.81240
			WXCL-8	0.66669
			WXCL-9	0.72328
Mideast Desert	Annual	Day	WXCL-1	0.91409
			WXCL-8	1.22850
			WXCL-9	0.71903

TABLE 4. THE NAMES OF THE BEST ANALYTICAL DISTRIBUTIONS TO REPRESENT THE OBSERVED WIND SPEED DISTRIBUTIONS

Region	Season	Time Period	WX Class	Distribution
European Lowlands	Winter	All hours	WXCL-1	Gamma
			WXCL-2	Gamma
			WXCL-3	Weibull
			WXCL-4	Lognormal
			WXCL-6	Weibull
			WXCL-7	Gamma
European Lowlands	Annual	All hours	WXCL-1	Weibull
			WXCL-2	Weibull
			WXCL-3	Weibull
			WXCL-4	Lognormal
			WXCL-6	Weibull
			WXCL-7	Lognormal
European Highlands	Winter	All hours	WXCL-1	Lognormal
			WXCL-2	Lognormal
			WXCL-3	Lognormal
			WXCL-4	Weibull
			WXCL-5	Gamma
			WXCL-6	Gamma
			WXCL-7	Lognormal
European Highlands	Annual	All hours	WXCL-1	Lognormal
			WXCL-2	Lognormal
			WXCL-3	Lognormal
			WXCL-4	Weibull
			WXCL-5	Lognormal
			WXCL-6	Lognormal
			WXCL-7	Lognormal
Mideast Desert	Summer	Night	WXCL-1	Weibull
			WXCL-8	Weibull
			WXCL-9	Weibull
Mideast Desert	Summer	Day	WXCL-1	Weibull
			WXCL-8	Weibull
			WXCL-9	Weibull
Mideast Desert	Annual	Night	WXCL-1	Gamma
			WXCL-8	Weibull
			WXCL-9	Gamma
Mideast Desert	Annual	Day	WXCL-1	Weibull
			WXCL-8	Weibull
			WXCL-9	Weibull

## 6. ANALYSIS RESULTS

For the European Lowlands, the weather class WXCL-5 had insufficient noncalm wind speed observations to be analyzed. Of the 12 different weather class and season combinations where the gamma distribution was best for three cases, the lognormal for three cases, and the Weibull for six cases (reference table 4). The lognormal distribution was the best for weather class WXCL-4 (advective fog case) and the annual wind speed distribution for WXCL-7 (fog). The gamma distribution was the best for the winter wind speed distributions for WXCL-1, WXCL-2, and WXCL-7. Overall, the analytical distributions perform well at describing the observed wind speed distributions. The worst performance was for the weather classes involving fog. Even for those cases the analytical distributions perform fairly well for the European Lowlands.

For the European Highlands, the weather class WXCL-5 had enough noncalm wind speed observations to be analyzed. Of the 14 different weather class and season combinations the gamma distribution was best for 2 cases, the lognormal for 10 cases, and the Weibull for 2 cases (reference table 4). The gamma distribution was best for the winter wind speed distributions for WXCL-5 (advective fog and precipitation) and WXCL-6 (radiative fog). The Weibull distribution was the best for weather class WXCL-4 (advective fog). Overall, the analytical distributions performed fairly well for all cases except WXCL-4 and WXCL-7. Again, the analytical distributions for weather classes involving fog proved to have the worst performance, with WXCL-4 and WXCL-7 being unsuited for analytical distribution representation for the European Highlands.

For the Mideast Desert, of the 12 different weather class and time period combinations the gamma distribution was the best for 2 cases and the Weibull for 10 cases (reference table 4). The gamma distribution was the best during the annual night period for WXCL-1 (no clouds) and WXCL-9 (low visibility). For the Mideast the observed wind speed distributions were more "lumpy" than those for the European regions. However, the analytical distributions appear to adequately represent the observed distributions. The worst representations occur for the daytime duststorm conditions (WXCL-8) when the wind speeds tend to be greater and more variable.

Plots of the observed empirical wind speed distribution along with the corresponding analytical distribution and the difference between the observed and analytical distributions for each of the geographical region, time period, and weather class combinations are contained in Avara and Miers (1992). Both the probability distributions and cumulative probability distributions are plotted. The individual plots give more details and provide considerably more information than the resultant rms or mean absolute deviation concerning the quality of the distribution fit over the range of wind speeds.

## 7. CONCLUSIONS

The observed wind speed distributions are adequately represented by the analytical distributions except in a few cases. For these exceptions, weather classes WXCL-4 and WXCL-7 for the European Highlands, the observed wind speed distributions do not lend themselves to analytical representation with enough accuracy to be useful. One might use the analytical distributions to

generate wind speeds by pseudorandom numbers. For the two exception cases, the observed wind speed empirical distributions should be used rather than the analytical distributions to generate random wind speeds. In all cases, whether analytical or empirical distributions are used, generated wind speeds in excess of 40 m/s should be discarded. Furthermore, occurrences of such large values of wind speed may indicate a problem with the pseudorandom number generator.

#### REFERENCES

- Avara, E. P., and B. T. Miers, 1992: Surface Wind Speed Distributions. ASL-TR-0313, U.S. Army Atmospheric Sciences Laboratory, White Sands Missile Range, NM 88002-5501.
- Baynes, C. J., 1974: The statistics of strong winds for engineering applications. Research Report, BLWT-4-1974, Engineering Science Department, University of Western Ontario, Canada, 265 pp.
- Baynes, C. J., and A. G. Davenport, 1975: Some statistical models for wind climate prediction. Preprints 4th Conference on Probability and Statistics in the Atmospheric Sciences, Tallahassee, Florida, American Meteorological Society, Boston, MA, pp. 1-7.
- Crutcher, H. L., and L. Baer, 1962: Computations from elliptical wind distribution statistics. J Appl Meteorol, 14:1512-1520.
- Dinkelacker, O., 1949: Uber spezielle windverteilungsfunktionen. Wetter Klima, 2:129-138.
- Hennessey, J. P., 1977: Some Aspects of Wind Power Statistics. J Appl Meteorol, 16:119-128.
- Holton, J. R., 1967: The diurnal boundary layer wind oscillation above sloping terrain. Tellus, 19:199-205.
- Justus, C. G., W. R. Hargraves, and A. Yalcin, 1976: Nationwide assessment of potential output from wind powered generators. J Appl Meteorol, 15:673-678.
- Luna, R. E., and H. W. Church, 1974: Estimation of long-term concentrations using a 'universal' wind speed distribution. J Appl Meteorol, 13:910-916.
- Mage, D. T., 1980: Frequency distributions of hourly wind speed measurements. Atmospheric Environment, 14:367-374.
- Miers, B. T., E. P. Avara, and L. D. Duncan, 1985a: Global Electro-Optical Systems Environmental Matrix (GEOSEM) Climatology for Mideast Southwest Asia. ASL-TR-0172, U.S. Army Atmospheric Sciences Laboratory, White Sands Missile Range, NM 88002-5501.

- Miers, B. T., E. P. Avara, and L. D. Duncan, 1985b: Global Electro-Optical Systems Environmental Matrix (GEOSEM) Climatology for Central and Northern Europe. ASL-TR-0177, U.S. Army Atmospheric Sciences Laboratory, White Sands Missile Range, NM 88002-5501.
- Narovlyanskii, G. Y., 1968: Aviation Climatology, TT-69-55100, National Technical Information Service, Atlanta, GA.
- Putnam, P. C., 1948: Power from the Wind, Von Nostrand Publications, 224 pp.
- Sherlock, R. H., 1951: Analyzing winds for frequency and duration. Meteorol Monogr, 4:72-79., American Meteorological Society, Boston, MA.
- Stewart, D. A., and O. M. Essenwanger, 1978: Frequency distributions of wind speed near the surface. J Appl Meteorol, 17:1633-1642.
- U.S. Air Force Environmental Technical Applications Center (USAFETAC), 1991: EO Climatology Version 2.0 Microcomputer Program. U.S. Air Force Environmental Technical Applications Center, Scott Air Force Base, IL 62225-5438.
- Wentink, T., 1974: Wind power potential of Alaska; Part I. PB 238-507, National Technical Information Service, Atlanta, GA.
- Wentink, T., 1976: Study of Alaskan wind power and its possible applications. PB 253-339, National Technical Information Service, Atlanta, GA.

## **AN EXAMINATION OF THE EVOLUTION OF RADIATION AND ADVECTION FOGS**

Montie M. Orgill  
Science and Technology Corporation  
White Sands Missile Range, New Mexico 88002

Robert Sutherland  
U.S. Army Research Laboratory  
White Sands Missile Range, New Mexico 88002

### **ABSTRACT**

Past field and numerical model studies have been reviewed with respect to the five stages of radiation fog evolution. The five identified stages are: (1) sundown, (2) conditioning, (3) mature phase, (4) sunrise, and (5) dissipation. These are analyzed and described on the basis of past radiation fog models and field programs. Afternoon temperature and dewpoint; the nighttime temperature decrease; wind, soil properties, and moisture; dew formation; and topography are important factors in initial fog development. Fog onset time is also affected by the radiative absorption of aerosols and by turbulence levels. Turbulence may also determine the type of fog, surface or elevated, that will form. During the mature phase the fog interface, the effects of absorption and scattering of infrared radiation, fog droplet settling, and turbulence have been shown to be very important in the maintenance of the fog. The role of solar radiation, aerosols, evaporation of fog droplets, and cloudiness in the dissipation of radiation fog has been well demonstrated by various fog models. A precursor sixth stage is under investigation. Future work may be directed toward the development of a prognostic fog evolution model incorporating multiple scattering and absorption of infrared radiation and the linking of the boundary-layer fog model with a larger-scale mesoscale/synoptic model. Possible applications of the model will be in assessing visibility, optical turbulence, and obscuration for U.S. Army sensitive operations.

### **1. INTRODUCTION**

Fog, a cloud forming and persisting near the ground for up to several hours, can be a problem for many U.S. Army operations. Visibility may be diminished, making low-level flight operations and conventional aircraft flight operations hazardous. Electro-optical targeting devices may also be hampered by the absorption and scattering of radiation by fog droplets. Thus it is important to know how fog forms, persists, and dissipates in order to use this information in the most effective manner, both defensively and offensively.

We have investigated the evolution of two common fog types: radiation and advection. Radiation fog is basically a fair-weather fog formed by radiative cooling and mixing of moist air. Advection fog is common near coastlines, where moist air is transported over cooler water or land; however, other

processes such as radiative cooling, mesoscale convergence, and turbulent mixing also help in the formation processes.

The question of how radiation and advection fogs form and evolve has been under investigation for many years. Radiation and advection fog field programs have supplied important information on many aspects of the problem, and numerical fog models have developed in sophistication so that they can reproduce reasonably accurate simulations of fog formation, variability, and dissipation in a one- or two-dimensional manner. However, no model has adequately simulated all the four-dimensional observational aspects of radiation and advection fogs. The apparent failure of models to simulate "reality" may be traced to shortcomings in measuring, understanding, and modeling the temporal and spatial variability of boundary-layer processes.

The purpose of this study is to examine in detail the evolution of radiation and advection fogs. The objective is to identify strengths and weaknesses of current models and field programs so that improvements can be made in our knowledge of how to predict radiation and advection fog behavior. This paper is a condensation of a more extensive ASL Technical Report on the subject to be published in the near future (Orgill, in preparation).

## 2. RADIATION FOG EVOLUTION

The evolution of radiation fog has been divided into five distinct stages by Jiusto and Lala (1983). These are: (1) sundown, (2) conditioning, (3) mature, (4) sunrise, and (5) dissipation. These stages have been identified by field measurements (Pillie et al., 1975; Low, 1975; Jiusto and Lala, 1983) and by model studies (Welch et al., 1986).

The results from the field program FOG-82 (Meyer et al., 1986) suggests a sixth stage. This stage will be called the "precursor" or "initial conditions" stage. Fitzjarrald and Lala (1989) and Meyer and Lala (1990) stressed the importance of initial conditions on the possibility of fog development in the evening and early morning.

Figure 1 shows a schematic illustrating some of the different physical mechanisms and processes involved in a radiation fog. The following paragraphs discuss each stage in the process individually. The symbols used in the following discussion refer to those used in Fig. 1.

### 2.1 PRECURSOR STAGE

The initial condition or precursor stage depends on season, location, synoptic weather patterns, and boundary-layer conditions. The location of a site can be an important determining factor because of terrain, vegetation, and presence of aerosols or cloud condensation nuclei (CCN). CCN are usually sparse in maritime air ( $\sim 100 \text{ cm}^{-3}$ ), more plentiful in continental air ( $\sim 1000 \text{ cm}^{-3}$ ), and abundant in urban or industrialized areas ( $> 5000 \text{ cm}^{-3}$ ). The chemical nature of CCN also depends on location, with industrialized areas providing various aerosol particles through photochemical reactions (Hung and Liaw, 1981).

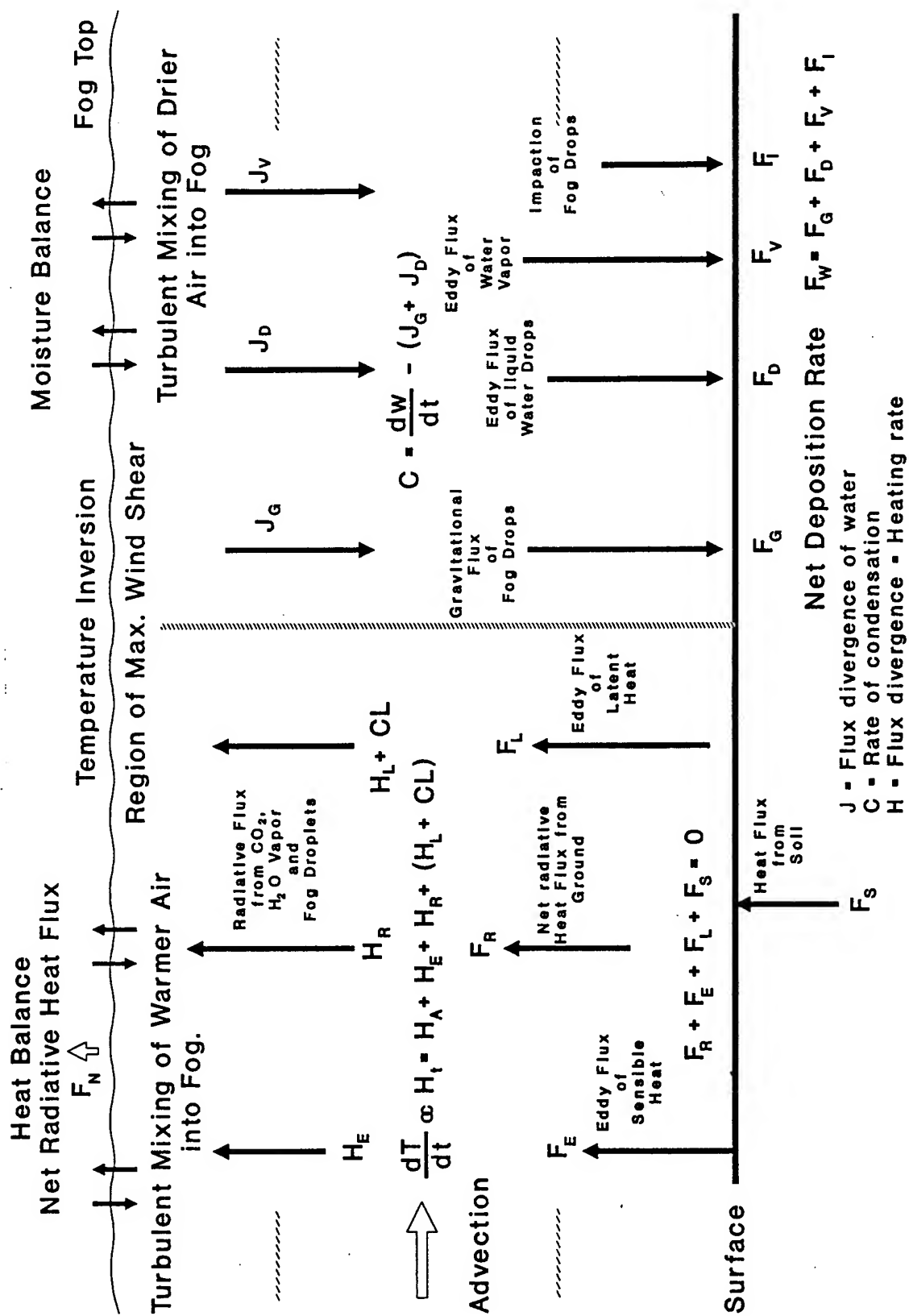


Figure 1. Factors and variables involved in the formation and growth of radiation fog.



## 2.2 SUNDOWN PERIOD

The sundown period, if clear, allows the radiative cooling ( $F_n$  in Fig. 1) to cool the lower atmosphere and change the vertical temperature profile from lapse to inversion. An increase in relative humidity is accompanied by haze formation. Jiusto and Lala (1983) indicate that at a visual range of about 10 km the liquid water content (LWC) of the air is about  $3 \times 10^{-3} \text{ g m}^{-3}$ , and there is a steady increase in the number concentration of haze aerosols in the  $1\text{-}\mu\text{m}$  size range as the relative humidity approaches 95%.

## 2.3 CONDITIONING STAGE

The conditioning stage may last from 4 to 10 hr depending on the radiation cooling, wind and turbulence, stability of the lower atmosphere, CCN, and relative humidity. Initial fog development may take place either as ground fog or as fog aloft.

Fog onset time (FOT) has been estimated by Fitzjarrald and Lala (1989) by

$$FOT \approx \ln(RH_0) \left[ \left[ \frac{\epsilon L_v}{R \bar{T}^2} \right] \frac{\partial T}{\partial z} \right]^{-1} \quad (1)$$

where  $RH_0$  is the initial relative humidity,  $\epsilon$  is 0.622,  $L_v$  is the latent heat of vaporization,  $R$  is the gas constant,  $\bar{T}$  is the estimated average temperature during the evening, and  $\partial T/\partial z$  is the estimated local nighttime temperature change. When  $FOT > LON$  (length of night), fog is unlikely; when  $FOT < LON$ , fog is likely. These investigators found that the expression for FOT is only partially successful because it neglects important processes such as dew formation, winds, turbulence, and the effects of CCN on condensation.

Lala et al. (1975), Brown and Roach (1976), and Pickering and Jiusto (1978) view dew deposition as a "governor" on fog formation ( $F_d$  and  $F_v$  in Fig. 1). For a given rate of radiative cooling, fog formation may be inhibited if the dew deposition rate and accompanying downward transport of moisture is large. However, if the dew deposition at the surface is somewhat less, radiative cooling may be sufficient to initiate fog formation.

Many studies show that fog formation depends upon the balance between radiative cooling ( $F_n$  in Fig. 1), leading to saturation of air, and turbulent diffusion of moisture ( $F_v$ ) to the surface, which dries and warms the air. Turbulence may act either to promote or to prevent fog formation depending on its occurrence during the fog formation process (Jiusto and Lala, 1980; Welch et al., 1986; Roach et al., 1976). Smolarkiewicz and Fitzjarrald (1988), however, suggest from their model study that fog evolution is a Benard convection problem and does not depend so much on surface layer turbulence but on the fog top interface, infrared radiative transfer, stability, wind shear, and water phase exchange.

During the conditioning stage, three modes of aerosol or droplets may form. Jiusto and Lala (1983) indicate that for a visual range of around 1 km and LWC of  $0.03 \text{ g m}^{-3}$  that the haze size mode around  $1 \mu\text{m}$  (radius) becomes more pronounced and persists, while a second size mode of 5 to  $7 \mu\text{m}$  appears. A larger fog droplet size mode between 10 and  $35 \mu\text{m}$  appears with supersaturated conditions.

## 2.4 MATURE STAGE

Once dense fog (visual range  $< 0.4$  km) is formed, the time variation in visual range becomes highly damped. Generally, other distinct changes are slightly stronger surface winds, very low Richardson numbers, a lapse rate below the inversion that may vary from isothermal to superadiabatic, much higher droplet concentrations, and a shift to larger droplet sizes.

The processes important in a mature fog are the effects of supersaturation on fog drop size ( $C$ ), radiative cooling of fog droplets in the upper part of the fog ( $H_r$ ), effect of radiative cooling on droplet growth, droplet settling ( $F_g$ ), and deposition ( $F_d$ ).

During the mature fog stage, a series of fog dissipation and redevelopment episodes can occur, which can result in quasi-periodic oscillations in fog variables such as net radiation, surface temperature, wind, LWC, and visibility. These variations have been observed in the field (Roach et al., 1976; Choularton et al., 1981; Duynkerke, 1991) and in models (Welch et al., 1986). These oscillations vary from 31 to 40 min. The balance among radiative cooling and turbulent mixing, gravity waves propagating at the top of the fog layer, and the advection of convective cells within the fog layer has been suggested as providing possible mechanisms for the oscillations.

## 2.5 SUNRISE PERIOD

At sunrise, an additional variable, solar short-wave radiation, enters into the fog equation. In many cases, the heating of the surface is sufficient to modify an existing radiation fog, but in some cases the fog may be well established or in equilibrium so that the solar radiation is not sufficient to break the fog's persistence. In other cases, solar radiation may actually assist in the persistence or formation of morning fog by evaporating water deposited by dew, precipitation, and impaction ( $F_w$ ). Thus factors of importance at sunrise are the water budget of fog, deposition or impaction on vegetation, and morning fog formation and persistence.

## 2.6 DISSIPATION STAGE

Fog can be dissipated by (1) solar radiation heating the ground and convective warming from below, (2) direct absorption of the radiation by fog droplets, (3) evaporation or sedimentation of the larger fog droplets, (4) the advection of a low-level cloud layer over the fog, (5) increase in wind speed or greater turbulence, and (6) eroding of the fog edges by convective motions. Dissipation may be detected during the last hour of the fog's life cycle with a dramatic decrease in droplet concentration, LWC, and supersaturation, and with appreciable improvement in visibility, greater broadening of the drop-size spectrum, and a rapid increase in CCN concentration (Low, 1975).

The effects of different physico-chemical properties of urban, rural, and maritime aerosols on fog dissipation have been studied by Bott (1991) and Forkel et al. (1987). Numerical sensitivity studies using these three different aerosol distributions show that the fog events are completely different, especially for LWC, supersaturation, and fog dissipation.

### 3. THE EVOLUTION OF ADVECTION FOG

The evolution of advection fog has not been divided into different stages in the literature, but this study arbitrarily divides the evolution process into four stages: (1) precursor, (2) initiation, (3) mature, and (4) dissipation. Figure 2 illustrates the different physical mechanisms and processes involved in an advection fog formed by warm, moist air moving over a colder surface.

#### 3.1 PRECURSOR STAGE

Factors important in the precursor stage are (1) the trajectory of the air mass, (2) chemical nature of CCN, and (3) upstream conditioning of the boundary layer. Studies by Rogers et al. (1975) and Mack and Rogers (1976) indicate that for fog to form after it has been advected over a temperature change of about 4 to 8 °C, the prefog air mass should have a significant trajectory over a water surface and the dew-point depression near the surface should be about 0.5 °C.

The chemical nature of CCN for advection fogs has been studied by Hung and Liaw (1980). The major contribution of combustion-related pollutants as CCN comes from aerosols with species of SO<sub>x</sub> and NO<sub>x</sub>. CCN associated with a polluted atmosphere can grow into droplets and produce dense fog without having the air attain supersaturation. The more favorable conditions for fog formation are produced by (1) hygroscopic chemicals with a higher value of the Van't Hoff factor (ratio of mole number of solution to molecular weight), (2) a higher number density of CCN, (3) heavier mass nuclei aerosol particles, and (4) CCN with larger radii.

#### 3.2 INITIATION STAGE

For the advection of a conditioned air mass over a cooler surface, model and observations do not produce similar fog results (Rogers et al., 1975). The apparent discrepancy between model and observation arises from the absence of two important factors not included in the models used by these researchers: mesoscale convergence and the difference in heat and water vapor transfer rates between ocean and atmosphere. Fukuta and Saxena (1973) suggest that the greater rate of molecular diffusion of water vapor than heat in the laminar sublayer at the water surface aids fog formation over warmer water and inhibits fog formation over colder water.

Saxena and Fukuta (1982) indicate that the evolution of fog supersaturation is inherently time and space dependent. In the case of advection fog, a cold surface contributes to the formation of fog in the warm moist air and the nominal supersaturation reaches a maximum in the middle of the fog layer. The true supersaturation level is much lower, however, because the fog droplet growth reduces the availability of water vapor. The maximum supersaturation occurs close to the upwind fog boundary but not near the water surface because of wind shear and the eventual drying effect (evaporation) of the cool water surface. As the fog life cycle advances, the turbulent mixing and vapor depletion by growing droplets and the water surface reduce the fog supersaturation. Thus zones of droplet evaporation and growth may occur simultaneously in different parts of the fog.

## STAGES IN THE EVOLUTION OF ADVECTION FOG

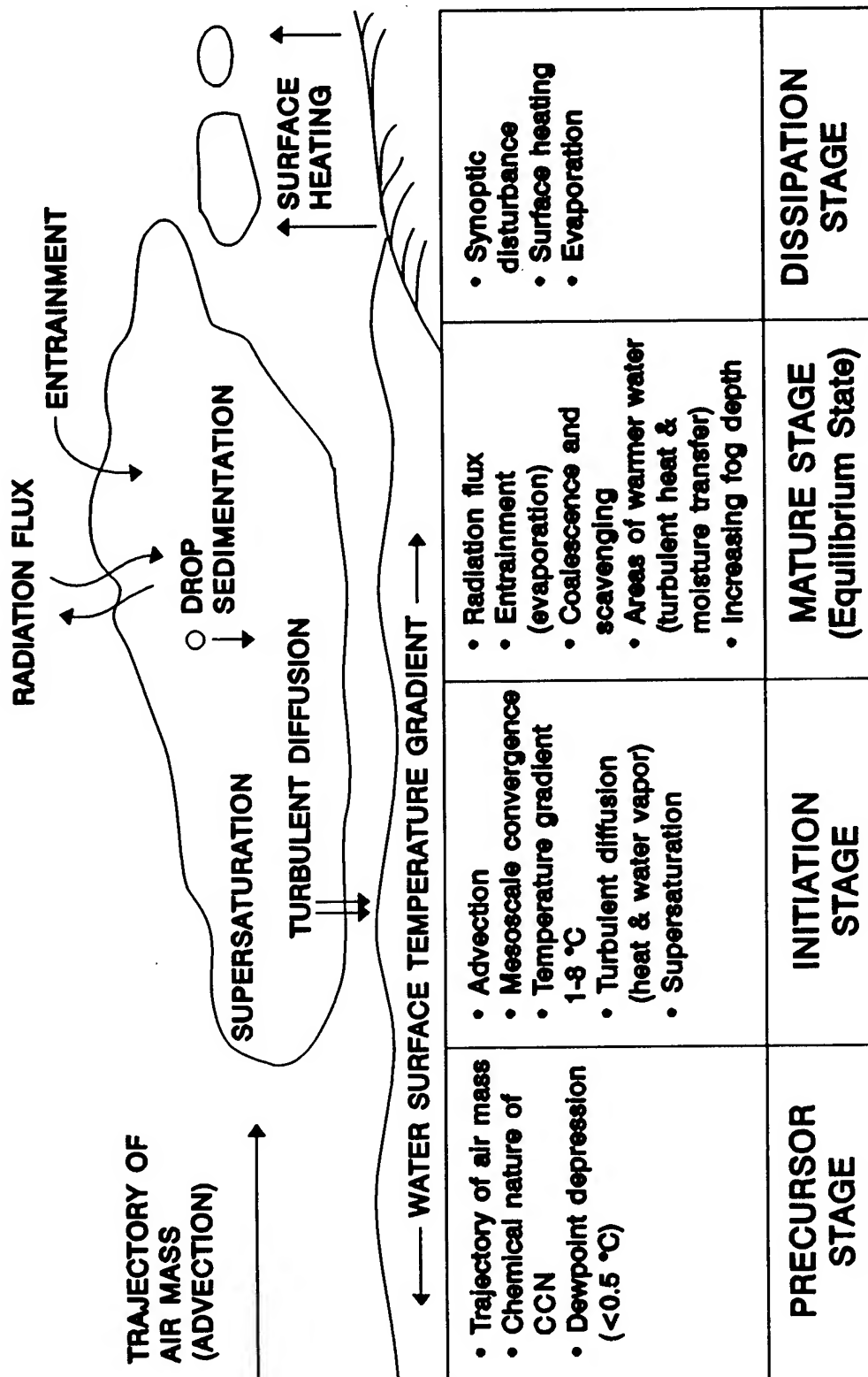


Figure 2. Evolution of advection fog.

### 3.3 MATURE STAGE

As an advection fog reaches maturity, additional physical mechanisms such as coalescence, scavenging, droplet sedimentation, evaporation, and entrainment will play a role in determining whether the fog will reach an equilibrium status, vacillate between development and dissipation, or dissipate entirely.

In the case of a warm, moist air mass being transported over cool water, fog may reach an equilibrium state once it forms. According to Findlater et al. (1989), long-wave radiation from large-scale advection fogs gradually takes over the cooling of the air mass and eventually depresses the fog temperature below the sea surface temperature. This process initiates convective and radiative heating from the sea surface and entrainment of warm air at the fog top, eventually balancing the radiative loss. The radiative loss also leads to increasing LWC due to condensation and increasing evaporation from the sea surface until it is balanced by increasing precipitation (drizzle) reaching the surface. This equilibrium state is then diurnally modulated by the direct absorption of solar radiation within the fog. Once established, it appears that this equilibrium state could persist almost indefinitely in the absence of major synoptic-scale disturbances.

### 3.4 DISSIPATION STAGE

One mechanism for dissipating advection fogs near coastlines is the advection over warmer surfaces heated either by solar radiation or artificially. Model studies by Mack et al. (1973) indicate that a 200-m-deep fog with LWC in the range 0.25 to 0.30 g m<sup>-3</sup> will completely dissipate in slightly more than 8 km when advected over a temperature rise of 5 °C in the surface. They found, however, that fog movement over a warmer surface is not necessarily sufficient for complete dissipation unless the heat from the surface is distributed throughout the fog layer.

The diurnal nature of coastal advection fog has been documented by several studies such as Skupniewiez et al. (1991). Synoptic disturbances such as fronts also dissipate advection fogs by changing the environmental conditions.

## 4. CONCLUSIONS

Several field studies and numerical models have made considerable progress in understanding and modeling radiation and advection fog evolution and behavior. The evolution of these fogs has been described by different stages or phases. Many of these aspects need further study, especially in order to understand and predict the intermittency and the spatial and temporal variability of these types of fogs. For example, future studies could be directed toward examining the required initial conditions for radiation and advection fog formation, the role that convection may play in the formation or dissipation of fogs, the linking of boundary-layer fog models to larger-scale models, and the different physical processes that dissipate fogs.

## REFERENCES

- Bott, A., 1991: On the influence of the physico-chemical properties of aerosols on the life cycle of radiation fogs. *Bound.-Layer Meteor.*, **56**, 1-31.
- Brown, R., and W.T. Roach, 1976: The physics of radiation fog. II. A numerical study. *Q. J. R. Meteorol. Soc.*, **102**, 335-354.
- Choularton, T.W., G. Fullerton, J. Latham, C.S. Mill, M.H. Smith, and I.M. Strombert, 1981: A field study of radiation fog in Meppen, West Germany. *Q. J. R. Meteorol. Soc.*, **107**, 381-394.
- Duynkerke, P.G., 1991: Observation of a quasi-periodic oscillation due to gravity waves in a shallow radiation fog. *Q. J. R. Meteorol. Soc.*, **117**(502), 1207-1224.
- Findlater, J., W.T. Roach, and B.C. McHugh, 1989: The haar of north-east Scotland. *Q.J.R. Meteorol. Soc.*, **115**, 581-608.
- Fitzjarrald, D.R., and G.G. Lala, 1989: Hudson valley fog experiments. *J. Appl. Meteor.*, **28**(12), 1303-1328.
- Forkel, R., and W. Zdunkowski, 1983: The influence of atmospheric aerosol on the life cycle of radiation fog. *Meteorol. Rundschau*, **36**, 158-161.
- Forkel, R., U Sievers, and W. Zdunkowski, 1987: Fog modeling with a new treatment of the chemical equilibrium condition. *Beitr. Phys. Atmos.*, **60**, 340-360.
- Fukuta, N., and V.K. Saxena, 1973: Kinetic threshold conditions for fog formation in cloud chambers and marine environment. *J. Atmos. Sci.*, **30**, 1638-1644.
- Hung, R.J., and G.S. Liaw, 1980: Advection fog formation associated with atmospheric aerosols due to combustion-related pollutants. *Water, Air and Soil Pollution*, **14**, 267-285.
- Hung, R.J., and G.S. Liaw, 1981: *Numerical simulation of advection fog formation on multi-disperse aerosols due to combustion-related pollutants*. UAH Research Report No. 248, University of Alabama in Huntsville, Huntsville, Alabama, 118 pp.
- Jiusto, J.E., and G.G. Lala, 1983: *Radiation fog field programs: recent studies*. Pub. No. 869, ASRC-SUNY, Atmos. Sci. Res. Center, New York State Univ., Albany, New York, 67 pp.
- Jiusto, J.E., and G.G. Lala, 1980: Radiation fog formation and dissipation. A case study. *J. de Rech. Atmos.*, **14**(3-4), 391-397.
- Lala, G.G., E. Mandel, and J.E. Jiusto, 1975: A numerical evaluation of radiation fog variables. *J. Atmos. Sci.*, **32**(Apr), 720-728.
- Low, R.D.H., 1975: Microphysical evolution of fog. *J. de Rech. Atmos.*, **12**, 23-32.

- Mack, E.J., and C.W. Rogers, 1976: *Simulation of marine advection fog with the CALSPAN advection fog model using prognostic equations for turbulent energy*. CALSPAN Report No. CJ-5756-M-2, Project Sea Fog, Part 2, CALSPAN Corp., Buffalo, New York, 26 pp.
- Mack, E.J., W.J. Eadie, C.W. Rogers, W.C. Kocmond, and R.J. Pilie, 1973: *A field investigation and numerical simulation of coastal fog*. NASA CR-2201, Cornell Aeronautical Lab. Inc., Buffalo, NY, 145 pp.
- Meyer, M.B., and G.G. Lala, 1990: Climatological aspects of radiation fog occurrence at Albany, New York. *J. Climate*, **3**(5), 577-586.
- Meyer, M.B., G.G. Lala, and J.E. Jiusto, 1986: FOG-82: A cooperative field study of radiation fog. *Bull. Amer. Meteorol. Soc.*, **67**(7), 825-832.
- Orgill, M.M., in preparation: *An examination of the evolution of radiation and advection fogs*. ASL Technical Report (in preparation), U.S. Army Atmospheric Sciences Laboratory, White Sands Missile Range, NM.
- Pickering, K.E., and J.E. Jiusto, 1978: Observations of the relationship between dew and radiation fog. *J. Geophys. Res.*, **83** (C5), 2430-2436.
- Pilie, R.J., E.J. Mack, W.C. Kocmond, W.J. Eadie, and C.W. Rogers, 1975: The life cycle of valley fog. I. Micrometeorological characteristics. *J. Appl. Meteor.*, **14**(3), 347-363.
- Roach, W.T., R. Brown, S.J. Caughey, J.A. Garland, and C.J. Readings, 1976: The physics of radiation fog: I-a. Field Study. *Q.J.R. Meteorol. Soc.*, **102**, 355-359.
- Rogers, C.W., W.J. Eadie, U. Katz, and W.C. Kocmond, 1975: *Project Fog Drops V--Task I: A numerical model of advection fog, Task II: Recommendations for simplified individual zero-gravity cloud physics experiments*. NASA CR-2633, CALSPAN Corp., Buffalo, NY, 79 pp.
- Saxena, V.K., and N. Fukuta, 1982: The supersaturation in fogs. *J. Rech. Atmos.*, **16**(4), 327-335.
- Skupniewicz, C.E., J.W. Glendening, and R.F. Kamada, 1991: Boundary layer transition across a stratocumulus cloud edge in a coastal zone. *Mon. Wea. Rev.*, **119**(10), 2337-2357.
- Smolarkiewicz, P.K., and D. Fitzjarrald, 1988: Small scale structure of a radiative fog. A numerical study. *Annalen der Meteorol.*, **25** (10th International Cloud Physics Conference), Vol.2, 493-495.
- Welch, R.M., M.G. Ravichandran, and S.K. Cox, 1986: Prediction of quasi-periodic oscillations in radiation fogs, Pt. 1, Comparison of simple similarity approaches. *J. Atmos. Sci.*, **43**(7), 633-651.

# QUANTITATIVE DETERMINATION OF HOW SMOKE OBSCURATION VARIES WITH OBSERVER HEIGHT

Scarlett D. Ayres  
U.S. Army Research Laboratory  
Battlefield Environment Directorate\*  
White Sands Missile Range, New Mexico 88002-5501, USA

## ABSTRACT

The Combined Obscuration Model for Battlefield Induced Contaminants (COMBIC) predicts time and spatial variations in transmission through dust and debris raised by high-energy explosives and vehicular movement, through smoke from phosphorus and hexachloroethane munitions, through smoke from diesel oil fires, through generator disseminated fog oil and diesel fuel oil, and other sources. COMBIC has been designed primarily for large scenarios where many obscuration sources are present and where many observer-target lines of sight (LOS) must be treated simultaneously. Aerial observers in COMBIC are the focus of this study. After each study of battlefield obscuration, the question almost inevitably arises of how does obscuration change with different viewing heights as might be encountered from helicopters. The usual response is a qualitative "it depends upon the meteorological (met) conditions." The objective of this study is to quantitatively determine the differences in the amount of obscuration that is measured by viewing from different heights for varying met conditions.

## 1. THE COMBIC MODEL

As explained by Hooek, Sutherland, and Clayton (1987), the purpose of COMBIC is to predict transmittance through battlefield obscurants such as high explosive (HE) and white phosphorus (WP). Transmittance is the quantity that defines the fraction of the original energy that is left in a beam of electromagnetic energy after the beam has passed along the optical path, which is the "line of sight" (LOS). In COMBIC, LOS is a geometric

---

\*formerly U.S. Army Atmospheric Sciences Laboratory (ASL)



term meaning a straight line between some initial point (the observer) and a final point (the target). COMBIC does not determine if terrain intercepts an optical path. COMBIC includes the transmission reductions only by obscurant aerosols and does not have any implications concerning the ability of a person on the observer line to see something at the target line, nor does it include natural phenomena, such as gasses, haze, and rain.

Energy is removed from a propagating beam through scattering of the energy out of the LOS and by absorption of energy along the LOS. The combination of both processes is called extinction. COMBIC uses a "mass extinction coefficient," which is a single number that describes the extinction encountered in traversing 1 m of an aerosol cloud that has a concentration of 1 g/m<sup>3</sup>. The mass extinction coefficient is wavelength dependent and is different for each type of aerosol. Transmittance is determined by the Beer-Lambert law:  $T = \exp(-\alpha CL)$ , where  $T$  is the transmittance;  $\alpha$  is the mass extinction coefficient in units of square meters per gram; and  $CL$  is the concentration length (the combined product, or more accurately the integral, of the aerosol concentration in grams per cubic meter over the optical path length in meters). Thus, the term in the exponent in the transmittance function,  $\alpha CL$ , is dimensionless and is called the "optical depth" or "optical thickness" of the path through the aerosol.  $T$  is a fraction between 0 and 1 and has no physical units. Thus, a  $T$  of 0.35 means that 35 percent of the original energy will remain after passing along that particular optical path.

The purpose of COMBIC is to compute the  $CL$  for each point in time on the LOS, and then, using the above equation, find the transmission for that point and the appropriate value of  $\alpha$ . The objective of this project was to compare the transmission values for observers of different heights with the  $CL$  for an observer at a great enough height that all the smoke lies between the observer and the ground. However, since the value of  $\alpha$  is constant for a given set of conditions, this comparison was made by using the  $CL$  values in place of the transmittance values.

## 2. THE EXPERIMENTAL DESIGN

Measures of effectiveness must be defined to compare the  $CL$  values of LOS with observers at different heights above ground. For a given aerosol cloud and a given point of time, the aerosol cloud is not homogeneous. Thus, for a given point of time, a  $CL$  value for one LOS will have a  $CL$  that is most likely different from the  $CL$  for another LOS at the same point of time. In addition, because the aerosol cloud can be blown by the wind, the  $CL$  value for a given LOS at one point of time can be quite different from the  $CL$  value for that LOS at another point of time. Thus,  $CL$  is a function of the LOS and of the time; that is,  $CL$  is a continuous function of two variables, LOS and time. The objective of the study was to compare the  $CL$  values for the LOS originating at different heights.

To obtain comparisons between the two models, four summary measures were defined over all LOS for each point of time with each model. These measures were the mean  $CL$

value, the standard deviation of the CL values, the proportion of CL values above a given threshold, and the maximum CL value. The mean indicates a central tendency for the CL values over the LOS; the standard deviation measures how much the CL values vary over the LOS; the proportion above a threshold is comparable to an observer not being able to see through the aerosol cloud when the CL value is above a given threshold; and the maximum is the largest CL value over all LOS.

Since LOS is essentially a continuous variable, a discrete approximation was used in this study. The printer-plot option was used in COMBIC. This defines 10000 LOS. All LOS are defined by an observer location and a target location. The observer varies in height from 10 m to 1000 m. The target is directly below the observer at ground level. All the LOS are vertical and parallel to each other. The printer plots are computed for a specified observer height. The summary measures (mean, standard deviation, proportion, and maximum) were computed over these LOS values for each point of time. These summary measures form a basis for comparing the effects of observer height on obscuration levels.

In this study, we decided to examine the effects of observer height on the CL produced by viewing from different heights for buoyant smoke, slightly buoyant smoke, and HE dust. Various computer programs are available for generating the locations of the impact points of the rounds of munitions. One volley of six rounds produced the clouds in this study. The program recommended for this study specifies for the rounds to fall randomly according to the following two-dimensional distribution—uniform along the target line and normal perpendicular to the target line. The rounds fall randomly in an ellipse approximately 200 m by 40 m. Since the rounds are falling randomly, the results of one run can be different from those of another run. To remove the bias that can result from a single run, five runs were made for each scenario, where each run had different random locations for the rounds. Then, four measures for each point of time—mean, standard deviation, percent above a threshold, and maximum—were averaged over the five runs. This averaging over the five runs had the effect of smoothing the data. Thus, for each time point there is a vector of average values, one for each of the above measures. These vectors are a function of time and are used to determine if there is a difference in the CL measures of two models.

Two statistical tools were used to compare the CL values for the different observer heights. The first was the correlation coefficient. This coefficient provides a measure of the similarity of two time profiles, such as the time profiles of the average maxima at 10 m and the average maxima at 1000 m. The correlation coefficient varies between -1 and +1. Since we did not expect the results for the two models to be negatively correlated, we made a one-tailed statistical test of the correlation coefficient and listed the p-value. Under the standard 5-percent level of significance, we assume that the corresponding correlation is significantly different from 0, if its p-value is under 0.05. If the p-value is greater than 0.05, then the corresponding correlation coefficient is not statistically different from 0.

The second statistical tool used in this analysis is Hotellings  $T^2$  test (Johnson and Wichern, 1988), which was used to test the hypothesis of no difference in the mean vectors.

Using the 5-percent level of significance, we conclude that a difference in mean vectors does exist if the corresponding p-value is less than 0.05. To determine which differences are statistically different from 0, and which statistically significant differences are of practical importance, we also measured the 95-percent simultaneous confidence intervals. Note that the true 95-percent confidence region is an ellipse rather than a rectangle. Thus, the 95-percent simultaneous confidence intervals given in the computer output may not always be consistent with the Hotelling's  $T^2$  test results.

Normally, the correlations are examined first. If any are not significantly different from zero, we can conclude that the corresponding profiles are not the same. Furthermore, even if a correlation is significantly different from zero, it still may not signify a real similarity in profiles. The magnitude of the correlation coefficient indicates the degree of similarity between each of the pairs of time profiles. In fact, the square of the correlation coefficient, the coefficient of determination, is the proportion of variability explained by the linear regression line between the two profiles. Thus, even if the correlation coefficient is significantly different from zero, it could be too small to be of practical significance. For the purposes of this study, the following heuristic rule was used: a correlation of 0.90 or above was considered to be high enough to indicate a real similarity in profiles between the two LOS. If the correlation was 0.70 or below, we concluded that there was not much similarity in the profiles. A correlation between 0.70 and 0.90 indicated a questionable similarity of profiles. If the correlations were all 0.90 and above, indicating a real similarity in profiles, we continued to the next test, namely the test on the averages. If the correlations were all below 0.70, there was no point in continuing. The profiles did not pass the similarity test. If some correlations were above and some in the 0.70 to 0.90 range, one might consider continuation to the next test.

Even if the LOS passes the correlation tests, the profiles still may not be the same. They can be similar, but far apart. The coincidence of similar profiles is tested by using the Hotelling's  $T^2$  test.

Eighteen different scenarios were generated for this study. There were six Pasquill categories (PC)-A, B, C, D, E, and F, and three types of munitions used-M328 4.2-in WP, fougol, and HE dust. Each scenario was run for an observer height of 10 m, 20 m, 40 m, 80 m, and 160 m. Due to time restrictions caused by long computer runs, the number of COMBIC runs per scenario and per observer height was restricted to only five for a total of 900 COMBIC runs.

### 3. THE NUMERICAL OUTPUT

The results of the 18 scenarios for the 5 different observer heights as compared to an observer at 1000 m are presented in tables 1 and 2. Table 1 lists the correlation and p-values for a buoyant smoke - 4.2-in M328 WP. Similarly, table 2 lists the statistics for 155-mm HE dust. Observer height is column one and the Pasquill stability is column two.

Each line represents 10 runs—5 for observer at height 1000 m and 5 for observer at the height specified in column one. As discussed above, a larger number may be desirable, but the COMBIC time requirements limited the number of runs that could be made. However, even with this small sample size, several important conclusions can be made in comparing the different observing heights of LOS. Furthermore, the robustness of this small sample size was examined through the running of the same scenario twice with different seeds for the random number generator. This was done for several different scenarios. The results were very close, and in no case were different conclusions reached. Column five gives the proportion above threshold (indicates the fraction of time the CL value is above  $3 \text{ g/m}^3$ .)

In all cases, observations began at time 1 s and finished at time 191 s. Since there were 10 s between observations, there was a maximum of 20 observations in the 191 s. However, the statistical algorithm program provides for a termination of the computations whenever the mean and standard deviation of the CL values both become less than 0.01. Thus, the number of time points in the first section of statistical results can be considerably less than the maximum given above.

Figures 1 and 2 show the profiles for the difference in mean values across time. Each figure profiles the difference in mean CL for the five different observer heights. The profiles were derived by computing the mean CL for each time step for an observer height of 1000 m and the lower observer height, then taking the difference.

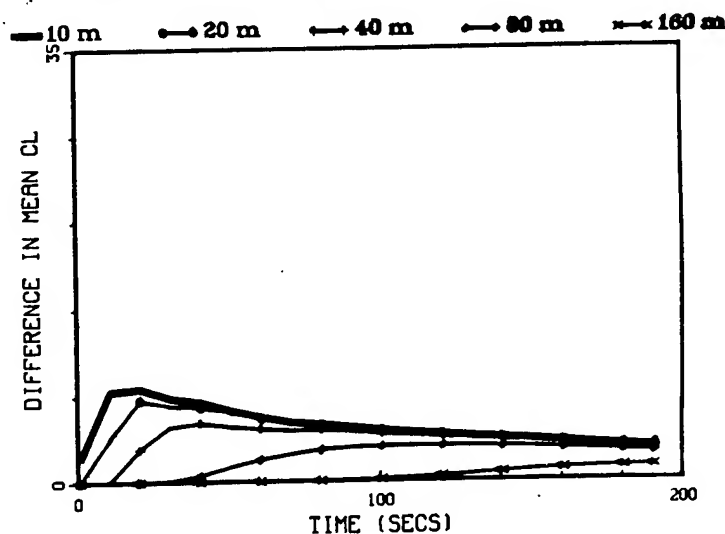


Figure 1. Difference in mean CL for the 4.2-in M328 WP cartridge for Pasquill stability A.

#### 4. CONCLUSIONS

In table 1, correlations are shown for 4.2-in M328 WP. The correlations are low for low observer heights for unstable and stable atmospheres for each of the measures of

TABLE 1. STATISTICAL RESULTS  
COMPARISON OF CL FOR DIFFERENT  
OBSERVER HEIGHTS  
4.2-in M328 WP

OBS HT	PASQ STAB	Correlation Coefficients and Associated P-Values							
		Mean Values		Standard Deviations		Proportion Above Threshold		Maxima	
		corr.	p-value	corr.	p-value	corr.	p-value	corr.	p-value
10 m	A	.702	.000	.570	.004	.664	.000	.103	.000
20 m	A	.811	.000	.723	.000	.803	.000	.444	.025
40 m	A	.922	.000	.838	.000	.950	.000	.556	.005
80 m	A	.989	.000	.958	.000	.988	.000	.737	.000
160 m	A	.997	.000	.997	.000	.983	.000	.999	.000
10 m	B	.798	.000	.702	.000	.787	.000	.608	.002
20 m	B	.889	.000	.819	.000	.892	.000	.689	.000
40 m	B	.969	.000	.928	.000	.940	.000	.802	.000
80 m	B	.996	.000	.994	.000	.921	.000	.979	.000
160 m	B	.999	.000	.999	.000	.994	.000	.999	.000
10 m	C	.786	.000	.707	.000	.789	.000	.600	.002
20 m	C	.874	.000	.815	.000	.678	.000	.675	.000
40 m	C	.977	.000	.947	.000	.972	.000	.879	.000
80 m	C	.997	.000	.997	.000	.955	.000	.991	.000
160 m	C	.999	.000	1.000	.000	.989	.000	.999	.000
10 m	D	.823	.000	.748	.000	.690	.000	.645	.001
20 m	D	.912	.000	.877	.000	.837	.000	.833	.000
40 m	D	.974	.000	.963	.000	.931	.000	.952	.000
80 m	D	.998	.000	.997	.000	.996	.000	.997	.000
160 m	D	1.000	.000	1.000	.000	1.000	.000	1.000	.000
10 m	E	.777	.000	.806	.000	.646	.000	.844	.000
20 m	E	.868	.000	.903	.000	.823	.000	.864	.000
40 m	E	.959	.000	.968	.000	.862	.000	.933	.000
80 m	E	.998	.000	.997	.000	.986	.000	.981	.000
160 m	E	1.000	.000	1.000	.000	1.000	.000	1.000	.000
10 m	F	.664	.000	.714	.000	.604	.000	.794	.000
20 m	F	.794	.000	.891	.000	.794	.000	.885	.000
40 m	F	.957	.000	.968	.000	.797	.000	.991	.000
80 m	F	1.000	.000	1.000	.000	1.000	.000	.999	.000
160 m	F	1.000	.000	1.000	.000	1.000	.000	1.000	.000

**TABLE 2. STATISTICAL RESULTS  
COMPARISON OF CL FOR DIFFERENT  
OBSERVER HEIGHTS  
155-mm HE DUST**

OBS HT	PASQ STAB	Correlation Coefficients and Associated P-Values							
		Mean Values		Standard Deviations		Proportion Above Threshold		Maxima	
		corr.	p-value	corr.	p-value	corr.	p-value	corr.	p-value
10 m	A	.986	.000	1.000	.004	.986	.000	1.000	.000
20 m	A	.996	.000	1.000	.000	.959	.000	1.000	.000
40 m	A	1.000	.000	1.000	.000	.995	.000	1.000	.000
80 m	A	1.000	.000	1.000	.000	1.000	.000	.999	.000
160 m	A	1.000	.000	1.000	.000	1.000	.000	1.000	.000
10 m	B	.992	.000	1.000	.000	.967	.000	1.000	.000
20 m	B	.999	.000	1.000	.000	1.000	.000	1.000	.000
40 m	B	1.000	.000	1.000	.000	1.000	.000	1.000	.000
80 m	B	1.000	.000	1.000	.000	1.000	.000	1.000	.000
160 m	B	1.000	.000	1.000	.000	1.000	.000	1.000	.000
10 m	C	.995	.000	.988	.000	.994	.000	1.000	.000
20 m	C	.998	.000	.999	.000	1.000	.000	1.000	.000
40 m	C	1.000	.000	1.000	.000	1.000	.000	1.000	.000
80 m	C	1.000	.000	1.000	.000	1.000	.000	1.000	.000
160 m	C	1.000	.000	1.000	.000	1.000	.000	1.000	.000
10 m	D	.990	.000	.994	.000	.955	.000	.985	.000
20 m	D	.998	.000	.999	.000	.987	.000	.998	.000
40 m	D	1.000	.000	1.000	.000	.999	.000	1.000	.000
80 m	D	1.000	.000	.998	.000	.963	.000	.998	.000
160 m	D	1.000	.000	1.000	.000	1.000	.000	1.000	.000
10 m	E	.991	.000	.995	.000	.960	.000	.993	.000
20 m	E	.997	.000	.999	.000	.977	.000	.999	.000
40 m	E	1.000	.000	1.000	.000	.998	.000	1.000	.000
80 m	E	1.000	.000	1.000	.000	1.000	.000	1.000	.000
160 m	E	1.000	.000	1.000	.000	1.000	.000	1.000	.000
10 m	F	.993	.000	.996	.000	.954	.000	.996	.000
20 m	F	.998	.000	.999	.000	.975	.000	1.000	.000
40 m	F	1.000	.000	1.000	.000	1.000	.000	1.000	.000
80 m	F	1.000	.000	1.000	.000	1.000	.000	1.000	.000
160 m	F	1.000	.000	1.000	.000	1.000	.000	1.000	.000

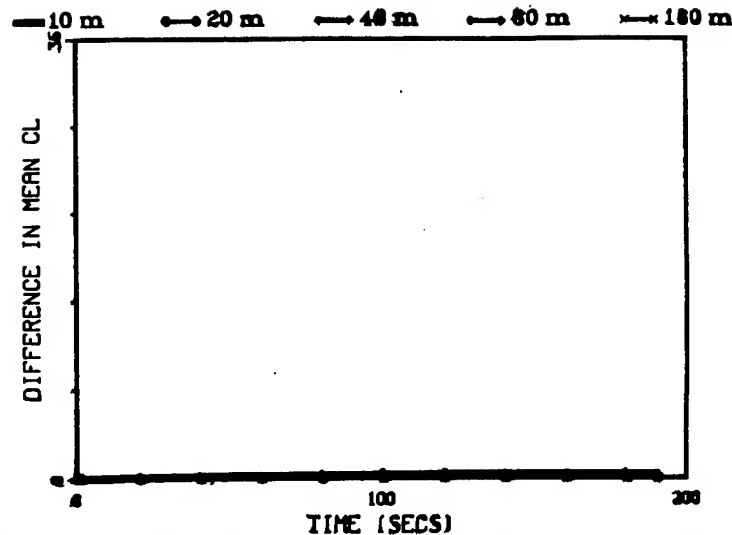


Figure 2. Difference in mean CL for the 4.2-in M328 WP cartridge for Pasquill stability A.

effectiveness threshold and maxima, indicating a lack of similarity of profiles. This lack of similarity of profiles is illustrated by fig. 1. Figure 1 shows the difference in mean CL for the 4.2-in M328 WP for an unstable atmosphere. It is clear that real differences exist in comparing the CL from observers of heights 10 m and 20 m to the CL produced by an observer viewing from 1000 m. Also, the hypothesis tests of the profiles for WP indicate a significant difference in the profiles.

It is clear from the correlation for a nonbuoyant fogoil (table not shown) that most of the fogoil stays below 10 m. Little difference is seen whether the observer is viewing from 10 m height or 1000 m. Figure 2 illustrates the differences in CL for fogoil for PC = E. Hardly any differences are seen.

Table 2 lists the correlations for HE dust. Most of the dust does not rise to great heights. Little difference is seen whether the observer is viewing from 10 m height or 1000 m. One would intuitively expect that HE dust should show the same trends as the M328 WP since both are buoyant sources and will rise. However, HE dust is modeled by COMBIC as a combination of five subclouds. Only two of the subclouds exhibit buoyant rise. Of the two subclouds, one is composed of large particles and settle out rapidly with time. The only subcloud that is buoyant and composed of small particles contains less than 2 percent of the mass.

So far we have tested the effect of Pasquill stability and the relationship it has with determining CL for different observer's heights. In table 1, we have demonstrated that differences exist for the M328 WP for stable and unstable atmospheres, but almost no differences exist for neutral atmospheres. In these scenarios the wind speed is 1 m/s for PC = A, F; 2 m/s for PC = B, E; 3 m/s for PC = C; and 5 m/s for PC = D. This implies a relationship between wind speed and the correlations. To test this, we

compute the statistics for one Pasquill stability and vary the wind speed. Table 3 show the correlations of M328 WP for PC = D with the windspeed varying from 1 m/s to 6 m/s. There is a general trend of low correlations with low windspeeds. The cause of this trend is that increasing windspeed promotes mixing (mechanical turbulence). This turbulence produces a local eddy diffusivity that will tend to break up and can halt warm, rising columns of air.

**TABLE 3. STATISTICAL RESULTS**  
**4.2-in M328 WP**  
**COMPARISON OF CL FOR PC = C**  
**FOR DIFFERENT OBSERVER HEIGHTS**  
**AND WINDSPEEDS**

OBS HT	WSP m/s	Correlation Coefficients and Associated P-Values							
		Mean Values		Standard Deviations		Proportion Above Threshold		Maxima	
		corr.	p-value	corr.	p-value	corr.	p-value	corr.	p-value
10 m	1	.716	.000	.620	.001	.709	.000	.426	.030
10 m	2	.793	.000	.719	.000	.811	.000	.666	.000
10 m	3	.755	.000	.706	.000	.568	.004	.623	.001
10 m	4	.798	.000	.732	.000	.650	.000	.638	.001
10 m	5	.823	.000	.748	.000	.690	.000	.645	.001
10 m	6	.836	.000	.754	.000	.722	.000	.667	.000
20 m	1	.806	.000	.742	.000	.856	.000	.556	.005
20 m	2	.885	.000	.836	.000	.921	.000	.731	.000
20 m	3	.864	.000	.833	.000	.697	.000	.720	.000
20 m	4	.895	.000	.866	.000	.804	.000	.794	.000
20 m	5	.912	.000	.877	.000	.837	.000	.833	.000
20 m	6	.922	.000	.886	.000	.862	.000	.844	.000
40 m	1	.926	.000	.873	.000	.966	.000	.698	.000
40 m	2	.966	.000	.937	.000	.962	.000	.841	.000
40 m	3	.949	.000	.934	.000	.952	.000	.889	.000
40 m	4	.965	.000	.956	.000	.904	.000	.939	.000
40 m	5	.974	.000	.963	.000	.931	.000	.952	.000
40 m	6	.980	.000	.967	.000	.951	.000	.9663	.000

The conclusions can be summarized by the following:

- Strong differences in CL of buoyant WP can occur for different observer heights depending upon the Pasquill stability, wind speeds, and the time after the munition start time.



- Most of the fogoil and HE dust remain below 10 m, causing little differences in viewing from any greater height.
- In general, the greatest differences in CL for observers of buoyant smoke at the same observing height occur for low wind speeds.
- In general, viewing from a height greater than 40 m shows little difference from viewing from a height of 1000 m (neglecting atmospheric effects) for the typical buoyant and nonbuoyant smoke in COMBIC.
- In general, viewing from a height less than 40 m can be greatly different than viewing from a height of 1000 m for buoyant smokes at low windspeeds.

Users of COMBIC must analyze their scenarios to determine if a COMBIC run at a particular height can be equated to viewing at another height.

## 5. REFERENCES

- Hoock, D. W., R. A. Sutherland, and D. Clayton, 1987: Combined Obscuration Model for Battlefield-Induced Contaminants, ASL-TR-0221-11, U.S. Army Atmospheric Sciences Laboratory, White Sands Missile Range, NM.
- Johnson, R. A., and D. W. Wichern, 1988: Applied Multivariate Statistical Analysis, Prentice Hall, Englewood Cliffs, New Jersey.
- Joint Technical Coordinating Group for Munitions Effectiveness: Handbook of Operational Testing of Electro-Optical Systems in Battlefield Obscurants, Smoke and Aerosol Working Group, JTCG/ME-87-10

**Session II Posters**

**SENSORS AND SYSTEMS**

**THE U.S. ARMY ATMOSPHERIC PROFILER RESEARCH FACILITY:  
OVERVIEW AND PRELIMINARY INTERCOMPARISON**

John R. Hines, Frank D. Eaton, Scott A. McLaughlin, and William H. Hatch  
U.S. Army Research Laboratory  
Battlefield Environment Directorate\*  
White Sands Missile Range, New Mexico 88002-5501 USA

**ABSTRACT**

The U.S. Army Research Laboratory's Battlefield Environment Directorate has established a unique atmospheric profiler research facility (APRF) at White Sands Missile Range, New Mexico. The facility features high performance remote sensing components to monitor in high resolution three primary atmospheric parameters: refractive index structure parameter  $C_n^2$ , wind (speed and direction) and ambient temperature. The APRF component mix permits coverage up to ~19 km with emphasis on boundary layer and upper-air regions. Specialized and standard surface, tower and balloon-borne instrumentation are deployed to provide local base line, comparison and calibration data. The APRF supports research applications including testbed analyses, electro-optical and electro-magnetic imaging and propagation system design and testing, meteorological and earth-observation satellite ground comparison and system cal/val, and environmental forecasting.

An overview of the APRF capabilities is described. Preliminary measured atmospheric parameters as well as initial intercomparisons are shown. Synopses of various ongoing studies at the APRF are presented.

**1. INTRODUCTION**

The U.S. Army Research Laboratory's Battlefield Environment Directorate (ARL-BED) at White Sands Missile Range (WSMR), New Mexico, has studied atmospheric effects on electro-optical systems for a number of years. Our mission was enhanced in 1986 to include a better understanding of high resolution vertical and slant-range profile measurements and interactions of certain atmospheric parameters for boundary layer and upper-air studies. In turn, the atmospheric measurements needed for the new mission required development of a specialized remote sensing measurement and analysis facility. The facility, unique within the U.S. Army and known locally as the **Atmospheric Profiler Research Facility (APRF)**, incorporates recently developed atmospheric remote sensing equipment that provides high resolution vertical profiles of turbulence ( $C_n^2$ ), wind speed, wind direction and ambient temperature. These parameters, supported by sufficient comparison and/or calibration data, are considered the minimum required for the current mission.

The APRF was designed and developed in close coordination with the National Oceanic Atmospheric Administration (NOAA) Wave Propagation Laboratory (WPL). Construction of the APRF site commenced in 1988 and was completed in late 1990. A series of integration, verification and validation tests are currently in progress.

**2. FACILITY DESCRIPTION**

A primary design criterion used in the development of the APRF required that it be possible to measure the selected atmospheric parameters continuously and in various resolutions from the surface up through ~19 km above ground level (AGL). The APRF systems include: (1) two high performance

---

\* formerly U.S. Army LABCOM Atmospheric Sciences Laboratory

clear-air atmospheric profilers (49.25 and 2900 MHz), (2) a specialized independent optical turbulence measurement system, (3) a suite of three supporting standard atmospheric profilers (404.37 MHz, 924 MHz, and 1850 Hz), and (4) an array of specialized tower and surface-mounted point and integrated-path instrumentation, and selected tethered and free-flight balloon soundings. Figure 1 depicts the current Facility layout. Tables 1 and 2 summarize the Facility's high performance characteristics.

## 2.1 HIGH PERFORMANCE CLEAR-AIR PROFILERS

Conventional weather radars were designed to detect reflections from objects (hydrometeors) in the air rather than from the air itself. As these radars became more sensitive, other reflections not associated with hydrometeors were observed. These "clear-air" reflections can only be detected with radars exhibiting very high receiver sensitivity and significant data processing gains. These radars evolved into a new class of radars called radar profilers which operate in a near vertical pointing angle configuration.

Clear-air profilers (Chadwick, 1986) calculate a structure parameter for the index of refraction,  $C_n^2$ , from the raw backscattered power received by the profiler. The profiler receives the strongest reflections from the turbulent cells that are one-half the transmitted wavelength, thus the need for several frequencies to aid in characterizing the desired atmospheric height coverage. The sensed power, therefore the higher frequency profilers obtain measurements closer to the ground. The profiler backscattered signals are also characterized by their Doppler-frequency shift and spectral width. Radial wind velocities are determined for each profiler using Doppler analysis procedures. The spectral width parameter is useful in determining the quality of the data as well as calculating the dissipation energy of turbulence.

Augmenting the radar profilers with radio acoustic sounding systems (RASS) permits the derivation of a temperature profile at the radar's inherent resolution, but at a somewhat lower height coverage (Moran et al., 1990).

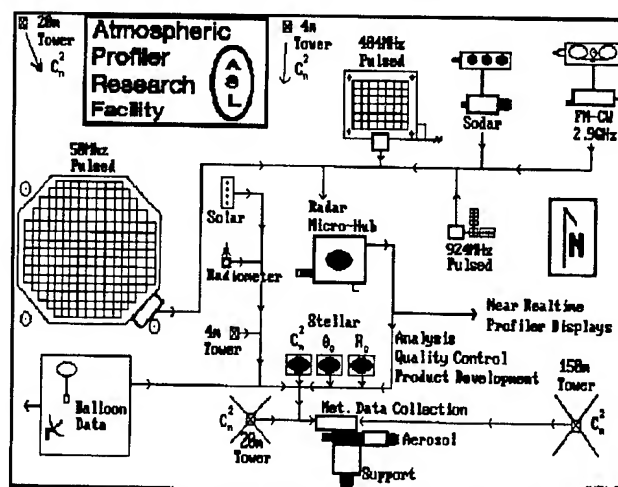


Figure 1. U.S. Army Atmospheric Profiler Research Facility Layout.

### 2.1.1 49.25 MHz Profiler

The ARL-BED is operating a new pulsed, multi-beam 49.25 MHz radar profiler for specialized upper-air atmospheric studies. The profiler, developed and manufactured by Tycho Technology, Incorporated, is one of two high performance research-quality VHF profiler systems deployed in the United States. The second system is deployed at the National Aeronautics And Space Administration's Kennedy Space Center in support of space shuttle missions.

The WSMR 49.25 MHz profiler provides high-resolution calibrated  $C_n^2$ , winds and ambient temperature through use of a high-gain, large-aperture phased-array antenna. Pertinent system characteristics are shown in Table 1. Specialized spectral processing quantifies the total received power into calibrated  $C_n^2$  at the 150-m resolution. Calibrated  $C_n^2$ , based on a first principles calibration approach (Eaton et al., 1988a), is obtained for both the 49.25 and 2900 MHz radar profilers. The 49.25 MHz profiler system is augmented with a RASS capability. 49.25 MHz profiler measurements are applied to tropospheric scintillation, storm convection and slant-path propagation studies.

An example of high resolution 49.25 MHz profiler wind barb data is shown in Figure 2. The two missing barb columns represent RASS acquisition periods. An example of 49.25 MHz profiler radar  $C_n^2$  data is shown in Figure 3. An example of 49.25 MHz profiler temperature data is shown in Figure 4.

TABLE 1. RELEVANT PROFILER CHARACTERISTICS

Characteristics	49.25 MHz	404.37 MHz	924 MHz	2900 MHz
<u>Min / Max Height (AGL)</u>				
Wind	2-4 km / ~20 km	.5-1 km / ~16 km	.12 km / ~6 km	50 m / ~2 km
$C_n^2$	2-4 km / ~20 km	N/A	N/A	50 m / ~2 km
Temperature	4-5 km / ~12 km	.5-1 km / ~6 km	.13 km / ~1 km	50 m / ~.5 km
<u>Spatial Resolution</u>				
Wind	150 m	375 m or 1 km	100 m or 200 m	32 or 64 m
$C_n^2$	150 m	N/A	N/A	~2 m
Temperature	150 m	375 m or 1 km	100 m or 200 m	32 m
<u>Temporal Resolution</u>				
Wind	3, 30 & 60 min	6 & 60 min	1, 15 - 30 min	~15-30 min
$C_n^2$	3, 30 & 60 min	N/A	N/A	~10 sec
Temperature	6, 30 & 60 min	6 & 60 min	3 - 15 min	~15 min
<u>Antenna</u>				
Physical ant. aperture	15,657 m <sup>2</sup>	170 m <sup>2</sup>	4.0 m <sup>2</sup>	7.3 m <sup>2</sup> x 2
Beams / Pointing angle	3 / Zenith and 15° off vertical S & W	3 / Zenith and 16.1° off vertical N & E	3 / Zenith and 20° off vertical N & E	1 / Zenith or 0-90° off vertical
Type	phased array of coaxial-collinear elements, fixed	phased array of coaxial-collinear elements, fixed	phased array of microstrip elements, fixed	parabolic reflector, 2 ea
Beam width	3.3°	4.0°	10.0°	2.7°
Power aperture product	$1.8 \times 10^8 \text{ W m}^2$	$5 \times 10^4 \text{ W m}^2$	$2 \times 10^2 \text{ W m}^2$	$1.6 \times 10^3 \text{ W m}^2$
<u>Transmitter</u>				
Wavelength	600 cm	74 cm	32 cm	10 cm
Maximum Transmitter Power	250 kW	7 and 12 kW	1 kW	0.22 kW
Duty Cycle	5%	5%	5%	100%
<u>Performance</u>				
Measured parameters	$C_n^2$ , wind, temperature	wind, temperature	wind, temperature	$C_n^2$ , wind, temperature
Number of gates	112	72	24	1000 ( $C_n^2$ ), 32 (wind and temp)

TABLE 2. RELEVANT SUPPORT EQUIPMENT CHARACTERISTICS

	SODAR	Optical	Surface	Towers <sup>+</sup>	Balloon <sup>+</sup>
Measurements	Wind, $C_n^2$	$r_o$ ( $C_n^2$ )	Solar radiation	152 m-W,T, $C_n^2$ ,U 20 m-W,T, $C_n^2$ ,U 4 m-W,T,U	T-W,T,U, $C_n^2$ R-W,T,U
Averaging Time	15 min	2.5 min	15 min	15 min	1 min
Levels/Heights	50-525 m (W) 20-650 m ( $C_n^2$ )	earth-to-space path; horiz. path	1 m	152 m- 7,23,38, 53,68,91,121, 152 m 20 m- 4, 20 m 4 m- 0.5,1,2,4 m + 0 to -1.0 m (T only)	T- 0- 2000 m R- 0-30000 m

<sup>+</sup> W = wind, T = temperature, U = relative humidity; <sup>+</sup> R = radiosonde, T = tethered sonde

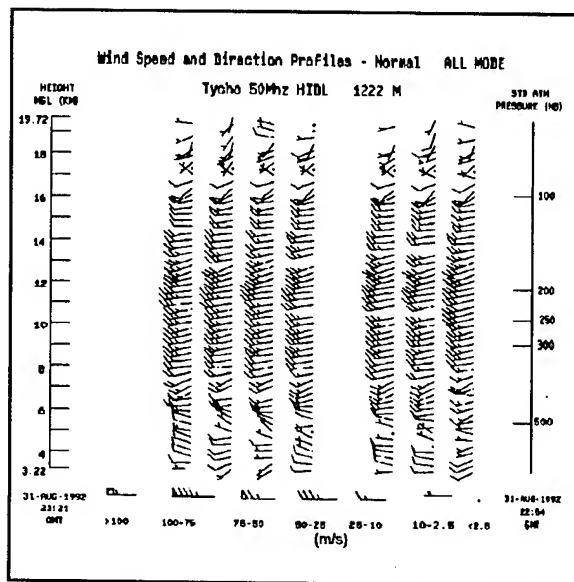


Figure 2. 49.25 MHz profiler wind barb profile data.

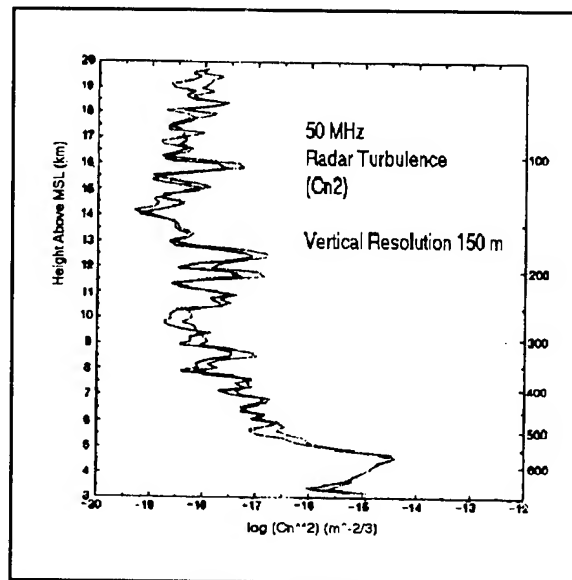


Figure 3. 49.25 MHz profiler  $C_n^2$  profiler data.

### 2.1.2 2900 MHz Radar

The ARL-BED is operating a unique frequency modulated-continuous wave (FM-CW) radar for unique boundary layer (BL) studies. Representing a third generation FM-CW radar, the 2900 MHz radar was manufactured by Radian Corporation and modified extensively by ARL-BED to customize the delivered system software and presentation techniques.

The 2900 MHz radar obtains continuous ultra-high resolution (1-2 m) measurements of radar power return by sensing clear-air turbulent backscattered power from Bragg scattered 5-cm turbulent cells above the radar from 50 m to 2200 m AGL. When observing hydrometeor type backscatter, radar hardware gains can be adjusted to also obtain similar resolution of power return from Rayleigh scattered precipitation. FM-CW radar measurements are applied to BL dynamic theory, hydrometeor observations, radio wave propagation, insect interference, and studies of imaging and laser propagation. Slow rate azimuth scans can be made for velocity azimuth display (VAD) low resolution wind profiling, or the antennas can be directed vertically (or lower, e.g. slant path measurements) for low resolution temperature (radar is equipped with a RASS capability) or high resolution backscatter profiling (McLaughlin, 1992). The radar is used predominately for high resolution  $C_n^2$  profiling. In this mode the antennas are directed vertically, and typically, the data is averaged over 6-10 seconds, with a 2.15 meter resolution from 0 to 2200 m AGL.

An example of Kelvin-Helmholtz instability induced waves, observed by the FM-CW radar on 5 December 1991, is shown in Figure 5. The lighter shades indicate the strongest reflectivity. The vertical scale is from 325 m to 1355 m. Time increases from right to left and represents about 25 minutes with 14 second averaging. An example of hydrometeor backscatter from an early morning light winter rain is shown in Figure 6. Time increases from right to left and represents approximately 17 minutes with similar averaging. Height ranges from 64 m to 1120 m. Notice the apparent size of the melting layer as seen by the radar (the lighter shaded band).

## 2.2 SPECIALIZED OPTICAL TURBULENCE MEASUREMENT SYSTEM

The ARL-BED is operating a unique stellar or laser-source optical measurement system for independent integrated path measurements of atmospheric "seeing ( $C_n^2$ )" (Eaton et al., 1988b). Developed by ASL and Lockheed Engineering and Sciences Company, the portable Atmospheric Turbulence Measurement and Observation System (ATMOS) is designed to produce consistent and accurate atmospheric characterization. The ATMOS uses a differential image motion analysis technique to provide transverse coherence length ( $r_0$ ) measurements while minimizing telescope vibration and focus errors. Ideal for

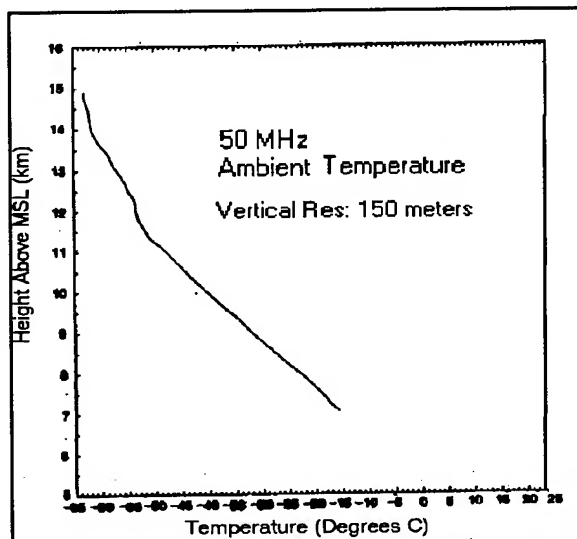


Figure 4. 49.25 MHz profiler temperature profile data.

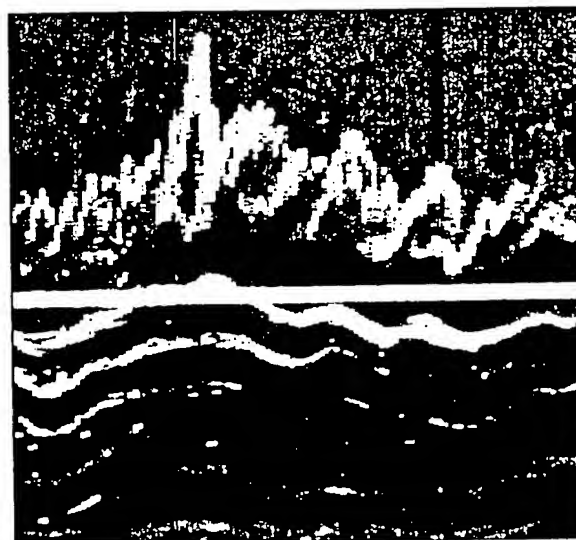


Figure 5. Kelvin-Helmholtz induced wave structure.

atmospheric seeing site evaluation studies, the ATMOS operates during both dark and daylight conditions. ATMOS measurements are applied to first-order adaptive optics implementation and verification studies (Qualtrough et al., 1992), aperture size influence on horizontal path angle-of-arrival measurement studies (Drexler et al., 1992) and independent  $C_n^2$  calibration/validation data sets. An example of ATMOS measurements used for adaptive optics image correction is shown in Figure 7. The plot shows two time series of x and y image positions on the detector plane which were observed on two consecutive data sets using the side port camera.

Research studies involving isoplanatic angle ( $\theta_0$ ), power spectral densities (PSDs), image centroid motion (wavefront tilt), phase structure function, and scintillation index have been performed with the ATMOS. Additional ATMOS applications include optical instrument site surveys, atmospheric research, laser propagation studies, telescope performance measurements, and horizontal path characterization.

## 2.3 STANDARD ATMOSPHERIC PROFILERS

A standard remote sensing profiling capability is provided by three atmospheric Doppler profilers: (1) a 404.37 MHz, (2) a 924 MHz, and (3) a specialized 1850 Hz acoustic sounder. These systems provide comparison and calibration data for Facility use.

### 2.3.1 404.37 MHz Profiler

The 404.37 MHz wind profiler, manufactured by Paramax (formerly UNISYS), is one of 31 identical profilers deployed about the central part of the United States to assess the effectiveness of a network of wind profilers in improving synoptic and mesoscale weather forecasts (Law, 1991). All but two of the profilers (WSMR and Hanscom Air Force Base) are owned and operated by the NOAA National Weather Service.

The 404.37 MHz profiler provides medium resolution winds and temperature through use of a high-gain, medium-aperture phased-array antenna.

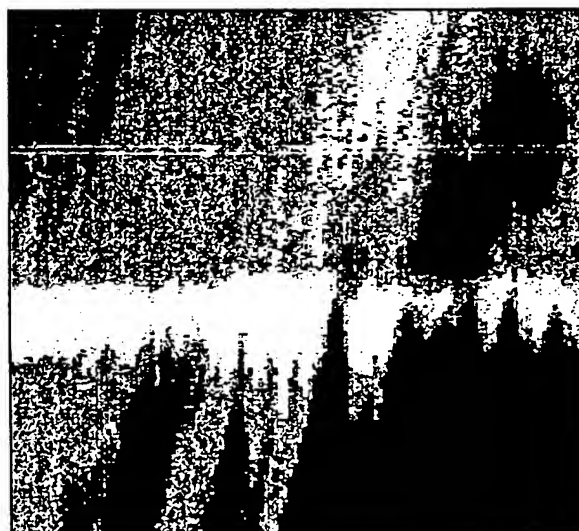


Figure 6. Light winter rain as observed by the FM-CW radar.

Relevant system characteristics are shown in Table 1. Radar  $C_n^2$  is not directly derived. It has been shown that the radar power measured by the 404.37 MHz radar can be related to  $C_n^2$  by comparison with other accepted  $C_n^2$  profiles (Eaton et al., 1992). The horizontal wind data are presented in graphic visualizations such as a wind barb display. The WSMR system is augmented with a RASS capability and a NOAA National Data Buoy Center developed automated surface meteorological station.

### 2.3.2 924 MHz Profiler

The 924 MHz profiler, manufactured by NOAA-WPL and Radian Corporation (normally at 915 MHz), is a portable profiler developed by the NOAA Aeronomy Laboratory (AL). The WSMR 924 MHz system is only the second 924 MHz profiler developed by the AL to utilize a phased-array antenna. The 924 MHz profiler is currently under test at the APRF for possible permanent installation. Relevant system specifications are shown in Table 1. The system is augmented with a RASS capability.

### 2.3.3 1850 Hz Profiler

A monostatic acoustic sounder profiler, manufactured by Radian Corporation and calibrated (first principles approach) by ARL-BED, is installed at the APRF to provide near surface comparison data as well as to supplement the lower portion of the Facility's continuous  $C_n^2$  and wind profiles.

The acoustic sounder uses a three-beam configuration to provide high-resolution  $C_n^2$  and winds. The sounder is a pulsed, unattended, moderately sensitive Doppler system operating at 1850 Hz with a  $\pm 130$  Hz bandwidth. The sounder has a physical antenna aperture of 4.8 m<sup>2</sup> (for each of three separate antennas, collocated on a trailer) and a power aperture product of  $\sim 1 \times 10^3$ .

Two  $\sim 15$ -s beam cycles are averaged to achieve a backscatter profile. An example of the acoustic sounder time series backscatter intensity, observed on 19 August 1992, is shown as a black and white FAX (normal output is in 15 colors) in Figure 8. The lighter shades indicate the strongest backscatter. Time increases from left to right and represents approximately 4 hours centered about the morning neutral period. The vertical scale ranges from 20 m to 655 m.

## 2.4 TOWER, SURFACE AND BALLOON INSTRUMENTATION

An array of specialized tower-mounted instrumentation, a surface-based radiation station, and selected tethered and free-flight balloon systems provide independent baseline comparison and calibration data at the APRF.

There are three towers: a 152-m steel triangular

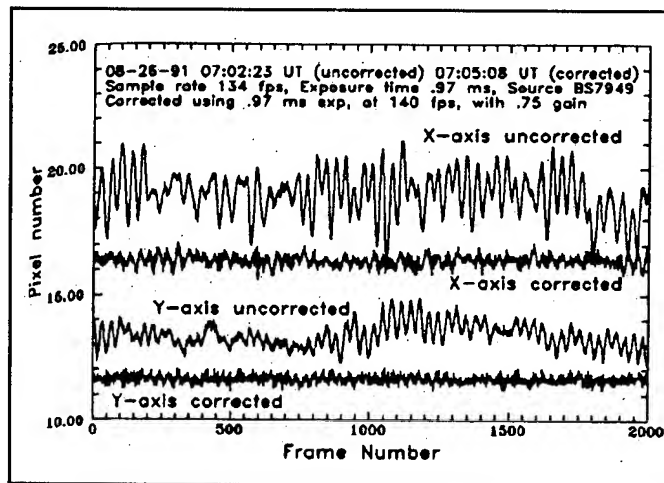


Figure 7. Comparison of open loop ("uncorrected") and closed loop ("corrected") operation of the Kitt Peak National Observatory 2.1 m telescope.



Figure 8. Acoustic sounder backscatter intensity data.



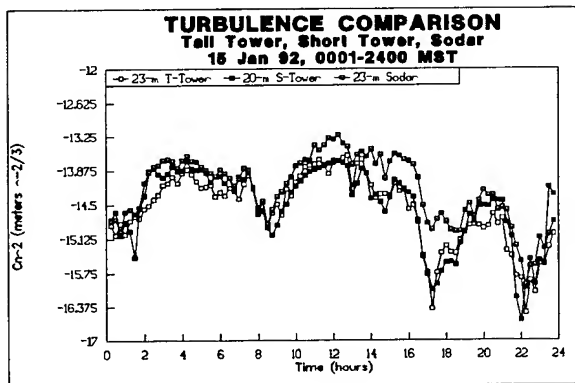


Figure 9. Diurnal variability of wind at a fixed height as measured by the sodar and the 152 m tower.

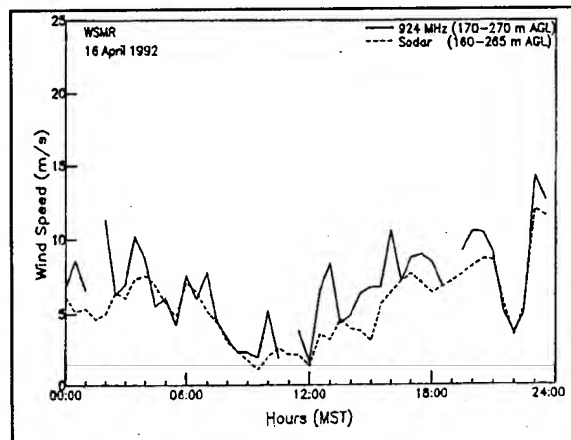


Figure 10. Diurnal variation of wind speed as measured with a 924 MHz profiler and a sodar.

mast and a 20-m and a 4-m scaffold type. The 4-m tower is a complete micrometeorological tower. Relevant specifications are shown in Table 2. Four examples of preliminary APRF system comparisons are shown in Figures 9, 10, 11 and 12. Figure 9 depicts the diurnal variability of  $C_n^2$  at a fixed height as measured by the acoustic sounder (sodar), the 152-m tower and the 20-m tower. The plot shows a 24-h period beginning 0001 and ending 2400 on 15 January 1992. The sodar and the 23-m and 20-m tower levels agree reasonably well during the period. Figure 10 depicts the diurnal variability of wind at a fixed height as measured by the 924 MHz profiler (volume averaged) and sodar (volume averaged). The plot shows a 24-h period beginning 0001 and ending 2400 on 16 April 1992. The 924 MHz profiler and sodar agree reasonably well during the period. Figure 11 depicts a comparison of horizontal wind measurement profiles from the sodar and 924 MHz profiler. The plots show a 12-h period beginning 1200 and ending 2400 on 18 June 1992. The data points are displayed as wind barbs and represent 30-min averages. The sodar and 924 MHz profiler winds agree reasonably well during the period. Figure 12 depicts the diurnal variability of wind at a second fixed height as measured by the sodar (volume averaged) and the 152-m tower (point). The plot shows a 24-h period beginning 0001 and ending 2400 on 15 April 1992. The sodar and 91.4-m tower level agree reasonably well during the period.

The radiation station consists of an albedometer, a long-wave/short-wave net radiation probe, a four-wavelength pyranometer set, a three-band normal-incidence-pyrheliometer solar tracking set, a shadow

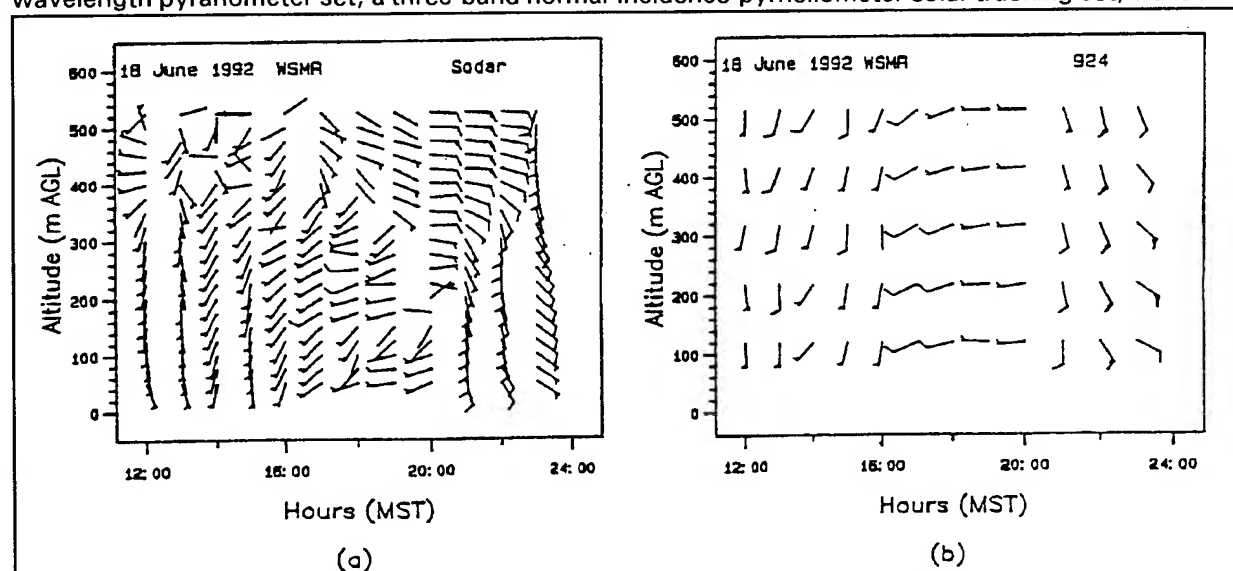


Figure 11. Comparative horizontal wind measurements from the (a) sodar and (b) 924 MHz profiler.

band with pyranometer, and a Linke Feussner actinometer. Data from these sensors is used for comparison purposes and to derive surface heat exchange parameters.

A tethered balloonsonde system (A.I.R.) provides profiles of wind, ambient temperature, relative humidity, and  $C_n^2$  (derived from point  $C_t^2$  measurements) from the air space above a site located ~2 km north of the Facility. These data are compared with remote sensing profiles derived from the sodar and the 924 MHz and 2900 MHz radars.

Free-flight radiosonde balloon observations (RAOB) provide standard profiles of wind, ambient temperature and relative humidity above the Facility. The balloons are released from a site approximately 8 km south of the APRF. Figures 13, 14 and 15 depict comparisons between profilers and RAOB observations.

Figure 13 depicts a comparison of wind speed profiles derived from the 49.25 MHz and 404.37 MHz profilers, and a nearby RAOB flight on 1 April 1991 at 1700 GMT (Flowers et al., 1992). The 49.25 and 404.37 MHz profiles represent the minimum quality-controlled hour-averaged output for each system, respectively. The RAOB profile represents the portion of its flight completed during the profiler's sensing period. The  $r^2$  correlation values for the comparisons are provided. The 49.25 MHz profiler and RAOB wind speeds compare very well. Figure 14 depicts a comparison of 6-min wind speed profiles from the 49.25 MHz profiler and a corresponding RAOB flight on 1 April 1991 at 1700 GMT, after eliminating noise contaminated samples below 4000 m MSL and samples for which wind speeds from the 49.25 MHz profiler and RAOB differed by more than 15 m/s for a given height. The

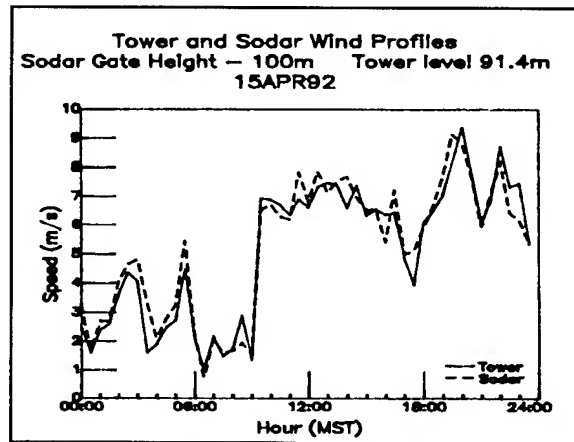


Figure 12. Diurnal variation of  $C_n^2$

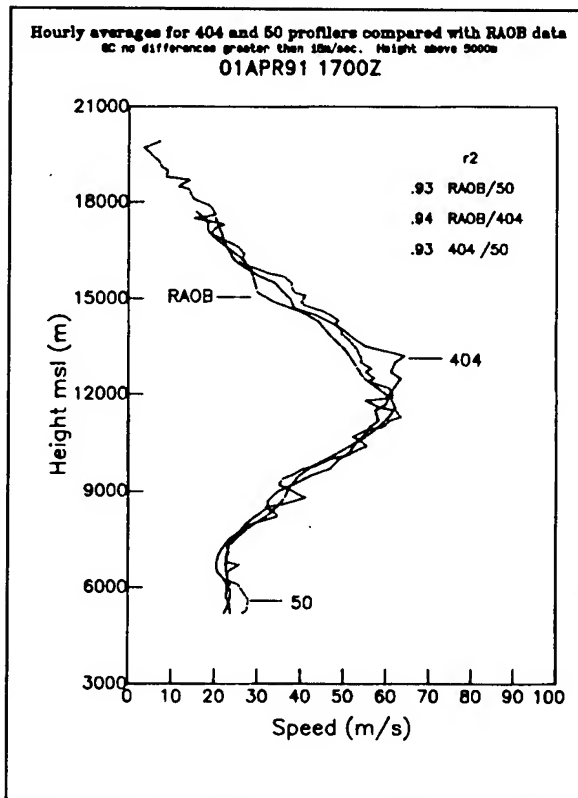


Figure 13. Comparison of a vertical wind profile as measured by a 49.25 MHz profiler, a 404.37 MHz profiler and a RAOB.

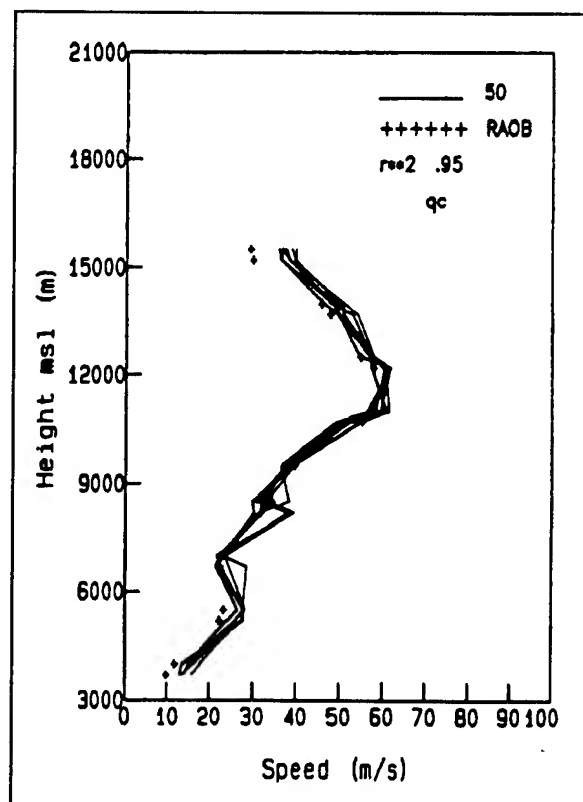


Figure 14. Wind speed 6-min data from the 49.25 MHz profiler compared with corresponding RAOB observations with quality control applied.

49.25 MHz profiler and RAOB wind speeds compare very well. Figure 15 depicts a comparison of 6-min wind speed profiles from the 404.37 MHz profiler and a corresponding RAOB flight on 1 April 1991 at 1700 GMT, after eliminating noise contaminated samples below 4000 m MSL and samples for which wind speeds from the 404.37 MHz profiler and RAOB differed by more than 15 m/s for a given height. The 404.37 MHz profiler and RAOB wind speeds compare reasonably well.

Figure 16 depicts a composite wind barb plot using the tower, sodar, 924 MHz, and 404.37 MHz profiler data. The data represent hourly means, selected because of their higher reliability. The plot shows a 12-h period beginning 0001 and ending 1200 on 21 June 1992. Tower data were used for winds from the surface to 150 m AGL. Sodar measurements were used from 150 m to 350 m AGL. 924 MHz profiler data were used from 350 m to 2500 m AGL. 404.37 MHz profiler data were used from 2500 m to 16000 m AGL. All data are reported as 1-h averages, with a given data point representing the start of a given hour. This effort is being extended to add data from the 49.25 MHz profiler into the composite wind profile and to provide similar composite  $C_n^2$  and temperature profiles. Additionally, efforts are underway to: (1) automate the data selection procedure within the regions of overlap, and (2) shorten the temporal resolution.

### 3. CONCLUSIONS

The APRF provides high resolution (spatial/temporal)  $C_n^2$ , wind speed, wind direction and ambient temperature measurements needed for micrometeorological, boundary layer, and upper atmospheric research, optical sensor evaluations, transport and diffusion studies, scintillation studies, satellite ground truth, and propagation studies as well as providing excellent detail for weather forecasting. New features in the atmosphere including insect migrations in the New Mexico Tularosa basin and the different backscatter return signatures derived from the different operating frequencies of the various radar profilers have stimulated new research interests.

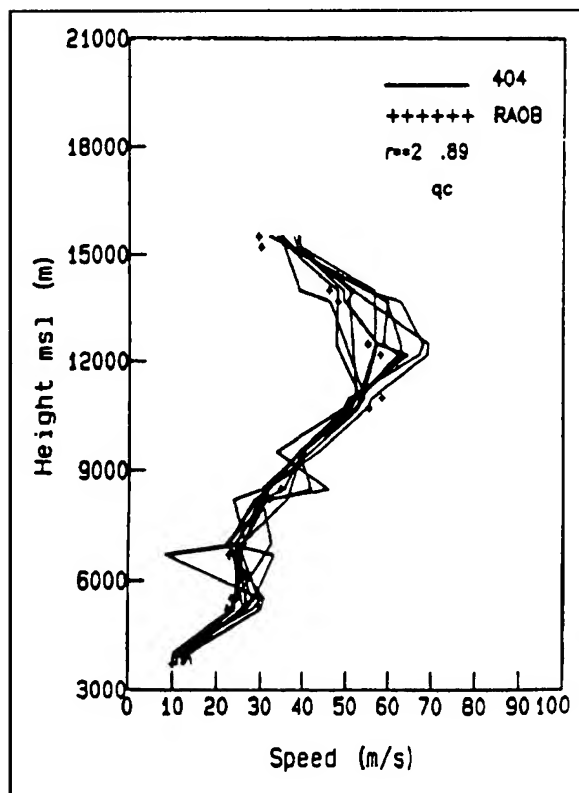


Figure 15. Wind speed 6-min data from the 404.37 MHz profiler compared with corresponding RAOB observations with quality control applied.

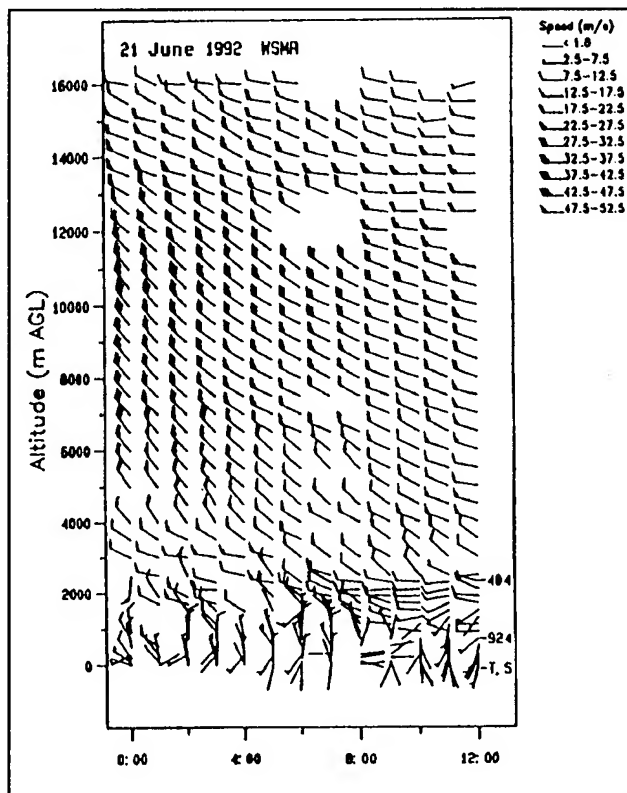


Figure 16. Composite vertical profile of horizontal wind derived from various sources at the APRF. The presented data represent hourly means.

Performance verification techniques are being developed, and improvements in profiler data processing algorithms are expected to continue in the near future. With the increased reporting intervals available from the profilers, atmospheric transient features such as wind shears, downbursts, microbursts, gravity waves and tropospheric scintillation can be detected. Doppler spectra taken with the 49.25 MHz radar were used to study the coupling of gravity waves and turbulence at WSMR (Nastrom and Eaton, 1992). Mean winds, wind shears,  $C_n^2$ , spectral widths, and static stabilities were examined.

#### 4. REFERENCES

- Chadwick, R. B., and E. E. Gossard, 1986: Radar Probing and Measurement of the Planetary Boundary Layer, from Probing the Atmospheric Boundary Layer, Lenschow, D. editor, AMS, pp. 163-182.
- Drexler, J. J., D. B. Soules, J. A. Qualtrough, F. D. Eaton, and J. R. Hines: Aperture Size Influence on Horizontal Path Angle-of-Arrival Measurements, Submitted for publication in *Journal of Waves in Random Media*.
- Eaton, F. D., W. A. Peterson, J. R. Hines, K. R. Peterman, R. E. Goode, R. R. Beland, and J. H. Brown, 1988a: Comparisons of VHF Radar, Optical, and Temperature Fluctuation Measurements of  $C_n^2$ ,  $r_0$ , and  $\theta_0$ , *Theoretical and Applied Climatology*, vol 39, pp. 17-29.
- Eaton, F. D., W. A. Peterson, J. R. Hines, J. J. Drexler, A. H. Waldie, and D. B. Soules, 1988b: Comparison of Two Techniques for Determining Atmospheric Seeing, In *Proceedings of the SPIE meeting, Orlando, FL*, vol 926, pp. 319-334.
- Eaton, F. D., W. H. Hatch, J. R. Hines, J. O. Johnson, W. L. Flowers, G. B. Hoidale, and E. Santantonio, 1992: Intercomparison of  $C_n^2$  Data Derived From VHF and UHF Radars, In *Proceedings of the SPIE meeting, Orlando, FL*, vol 1688, pp. 178-184.
- Flowers, W., E. Santantonio, G. Hoidale, F. Eaton, W. Hatch, J. Hines, and J. Johnson, 1992: Wind Measurements From Doppler Radar Profilers and Rawinsondes: A Comparison of 50-MHz and 404-MHz Profilers and Rawinsonde Data at White Sands Missile Range, In *Proceedings of the SPIE meeting, Orlando, FL*, vol 1688, pp. 199-309.
- Law, D. C., 1991: Interpretation of Wind Profiler Spectral Moment Data, In *Proceedings of the AMS meeting, New Orleans, LA*, vol 7SMOI, pp. 389-392.
- McLaughlin, S. A., 1992: The U.S. Army Ultra-High Resolution Turbulence Profiling FM-CW Radar: Description and Data, In *Proceedings of the SPIE meeting, Orlando, FL*, vol 1688, pp. 294-298.
- Moran, K. P., D. B. Wuertz, R. G. Strauch, N. L. Abshire, and D. C. Law, 1990: Temperature Sounding with Wind Profiler Radars, In *Journal of Atmospheric and Oceanic Technology*, vol 8, pp. 606-608.
- Nastrom, G. D., and F. D. Eaton: The Coupling of Gravity Waves and Turbulence at White Sands, NM, from VHF Radar Observations, Accepted for publication in *Journal of Applied Meteorology*.
- Qualtrough, J. A., J. J. Drexler, D. B. Soules, F. D. Eaton, and J. R. Hines, 1992: Development and Implementation of First Order Adaptive Optics Algorithms, In *Proceedings of the SPIE meeting, Orlando, FL*, vol 1688, pp. 520-526.

#### DISCLAIMERS

The citation of trade names and names of manufacturers in this paper is not to be construed as official Government endorsement or approval of commercial products referenced herein.

## **AN ACOUSTIC METEOROLOGICAL TEST BED USES AND APPLICATIONS**

J. Fox and R. Olsen  
Battlefield Environment Directorate\*  
U.S. Army Research Laboratory  
White Sands Missile Range, NM 88002-5501, USA

R. Okrasinski and P. Chintawongvanich  
Physical Science Laboratory  
New Mexico State University  
Las Cruces, NM 88003, USA

### **ABSTRACT**

An Acoustic Meteorological Test Bed has been installed at White Sands Missile Range to investigate atmospheric effects on acoustic propagation and verify the performance of acoustic and meteorological models. It consists of two 30-meter walkup towers, a 30-meter met tower, a sodar, a UHF wind profiler and RASS, and radiosonde and tethersonde systems. The walkup towers are placed 1 kilometer apart along an approximate north-south line. Each has a complement of loudspeakers and microphones at the 2-meter and 30-meter levels for generating and receiving sound over the path. Atmospheric turbulence is measured by sonic anemometer/thermometers and hot-film anemometers installed on each tower. The 30-meter met tower is instrumented with standard meteorological sensors which measure wind, temperature, humidity, pressure, and solar radiation. Upper-air data are provided by the remote and balloon sensors. The test bed was utilized during the Joint Acoustic Propagation Experiment to obtain data for acoustic model verification and to investigate turbulence effects on sonic booms.

### **1. INTRODUCTION**

The purpose of the Acoustic Meteorological Test Bed is to investigate atmospheric effects on acoustic propagation to determine the performance and utility of acoustic and meteorological models. The prime area of interest is the lower frequencies below 2000 Hz which can

---

\*Formerly U.S. Army Atmospheric Sciences Laboratory.

propagate relatively long distances during specific atmospheric conditions. There have been a number of studies involving outdoor propagation. Most of them, however, have been confined to distances of less than several hundred meters.

The test bed consists of controlled acoustic sources and receivers and an array of meteorological sensors to measure the state of the atmosphere. Standard atmospheric measurements of the vertical profiles of temperature, winds, and humidity and surface measurements of wind, temperature, humidity, pressure, and solar radiation are collected. In addition, non-standard measurements are made of the turbulence structure parameters,  $C_T^2$  and  $C_V^2$ , which are used to calculate the acoustic refractive index parameter.

This complement of in situ and remote sensors permit the state and variation of the boundary layer, which undergoes significant diurnal changes, to be continually monitored throughout the day. The test bed instrumentation is capable of defining the spatial sound structure of this area of the atmosphere.

To date, two field programs, Phase I and II of the Joint Acoustic Propagation Experiment, have utilized the Acoustic Meteorological Test Bed. Phase I was primarily concerned with the assessment of acoustic model performance, and Phase II was conducted to determine turbulence effects on sonic booms. The latter was accomplished by having aircraft generate sonic booms over the site during specific measurement periods.

Late this year (1992), an Acoustic Source Generation System will be added to the test bed. This will permit the spatial area of interest to be increased from one kilometer to ten kilometers by setting the sound generating system at various distances from the acoustic meteorological test bed. The Acoustic Source Generation System is a transportable pneumatic loudspeaker which is designed to operate at low frequencies and transmit up to 20,000 acoustical watts (163 dB).

## **2. TEST BED SITE DESCRIPTION**

The Acoustic Meteorological Test Bed was installed at Dirt Site, located in the extreme southeast portion of White Sands Missile Range (WSMR), New Mexico about 5 kilometers west of the Jarilla mountains near Orogrande, New Mexico. The area slopes from an elevation of 1275 to 1254 meters above sea level from south to north. Properties and parameters that affect acoustic propagation including acoustic ground impedance, soil porosity, moisture content, and vegetation type, size, and density were determined and documented for the location. In addition, site geology was documented through seismic refraction tests, and surface soil properties were documented with soil classification and cone penetrometer tests.

## **3. INSTRUMENTATION**

Figure 1 is a schematic of the Acoustic Meteorological Test Bed and depicts all the instrumentation except the Acoustic Source Generation System. The most critical elements

of the test bed are the two 30-meter walkup towers which are one kilometer apart. A total of four loudspeakers, with the capability of outputting 115 dB over a frequency range of 30-20000 Hz, are placed at the top and bottom of each tower. The speakers are driven by tape recorders, on which sounds may be recorded for propagation over the test bed path. For impulse sounds, a propane cannon is used, and in most cases, the cannon has sufficient energy to propagate over the one-kilometer path.

Each of the towers is instrumented with microphones at various levels, and the capability exists to deploy microphones on the ground between the towers. The acoustic data is recorded on 16 channel digital audio (DAT) tape recorders with the capability of recording up to two hours of continuous acoustic data.

Also located on each walkup tower are two 3-axis sonic anemometer/thermometers. In addition, a hot-film anemometer is mounted on one of them. A listing of the performance characteristics of these sensors is given in Table 1. These high performance meteorological sensors are specifically designed to measure turbulence parameters. The sonics consist of paired transmitters and receivers placed 15 cm apart that alternately transmit and receive at the rate of 100 Hz. The sensors detect the wind speed along the path by subtracting the travel times of the two paths and assuming that the speed of sound does not change during the sampling interval. If the travel times are added rather than subtracted, the speed of sound and virtual temperature can be determined. The latter is a function of both the ambient temperature and moisture.

The hot-film anemometers consist of a fused quartz substrate with a platinum film bonded to the surface. The winds are determined by the heat dissipation rate of the heated film. These sensors are sampled at a rate of 1000 Hz.

**Table 1**  
**Meteorological Sensors Specifications (High Performance)**

<u>Sensor Type</u>	<u>Parameter Measured</u>	<u>Rate Sampled (<math>s^{-1}</math>)</u>	<u>Resolution</u>	<u>Accuracy</u>
Sonic anemometer /thermometer (3-axis)	Wind	10	$.01 \text{ m s}^{-1}$	$> 1.0\%$ or $> 1.0 \text{ cm s}^{-1}$
	Temperature	10	$.01^{\circ}\text{C}$	$0.05^{\circ}\text{C}$
Hot-film anemometer	Wind	1000	$\sim .002 \text{ m s}^{-1}$	$0.05^{\circ}\text{C}$

In close proximity to the north walkup tower is a 30-meter meteorological tower on which standard meteorological sensors are mounted at 2, 4, 8, 16, and 30 meters. This additional tower is required because the propeller anemometers induce bearing noise into the microphones. Temperature, wind, humidity, pressure, and solar radiation are measured. A listing of these sensors and their operating specifications is shown in Table 2.

**Table 2**  
**Meteorological Sensors Specifications (Standard)**

<u>Sensor Type</u>	<u>Parameter Measured</u>	<u>Rate Sampled (s<sup>-1</sup>)</u>	<u>Response Characteristic</u>	<u>Accuracy</u>
Propeller-vane anemometer	Wind speed/ direction	1	1 minute distant constant	~ 3.0%
Thermistor	Temperature	1	1 minute time constant	0.3%
Hygristor	Humidity	1	1 minute time constant	3.0%
Absolute pressure	Ambient pressure	1	3 minute time constant	1.0%
Pyroheliometer	Solar radiation	1	~ 5 minute	3.0%

Winds and temperature are measured remotely by a 924 MHz wind profiler with Radio Acoustic Sounding System (RASS). The UHF wind profiler measures winds by detecting Doppler shifts in electromagnetic energy that has been backscattered from turbulence. It has three antennas which are oriented along three radials, one in the vertical and the others 15° from the vertical. The two off-vertical antennas are oriented along north-south and east-west directions, respectively. Doppler shifts measured along each of the radials are used to compute the radial wind velocities which are then resolved into horizontal wind speed and direction. Operating in conjunction with the profiler is the RASS which is able to remotely measure vertical temperatures by utilizing a acoustic source matched for Bragg resonance to the collocated UHF profiler. The acoustic pulse is tracked by the radar, and the speed of sound is determined from the frequency Doppler shift off the propagating wave front. Virtual temperature, which is proportional to the measured speed of sound, can be converted to ambient temperature if the humidity is known.



The sodar operates much like the UHF profiler with the exception that acoustic energy is used. The acoustic signal is backscattered due to changes in the acoustic refractive index caused by temperature variations. Winds are determined from Doppler shifts in the backscattered energy. Remote measurements of  $C_T^2$  can be obtained from the acoustic power intensity by extrapolating an in situ measurement of  $C_T^2$  to the first sodar measurement level and then calculating the ratio between  $C_T^2$  and the power intensity. Table 3 provides a summary of the remote sensors and their specific characteristics. Upper-air measurements are also obtained from radiosondes and tether sondes. The former utilizes a radiosonde tied to a free flight balloon to provide vertical profiles of wind, temperature, humidity, and pressure from the surface to 5 kilometers. This system is capable of making measurements to greater altitudes, but they are not usually needed for acoustic propagation programs. To complement these and other vertical profile measurements, a tether sonde balloon can be deployed to provide more detailed measurements of temperature and winds up to 500 meters, depending on wind conditions. The tether sonde consists of a tethered balloon and a tetherline with attached sonde for measurement of temperature, wind, pressure, and humidity.

**Table 3**  
Remote Sensors Specifications

<u>Sensor Type</u>	<u>Parameter Measured</u>	<u>Measurement Range</u>	<u>Temporal/Spatial Resolution</u>	<u>Accuracy</u>
924 MHz wind profiler	Winds	100-3000 m	100 m/15 min	1 m s <sup>-1</sup>
Radio Acoustic Sounding System (RASS)	Temperature	100-600 m	20 m/5 min	1°C
Acoustic Doppler Sodar	Winds	50-600 m	50 m/5 min	.5 m s <sup>-1</sup>
	Turbulence ( $C_T^2$ )	50-600 m	50 m/5 min	> 1 %

#### 4. TEST BED DATA

The Acoustic Meteorological Test Bed was made operational to support the Joint Acoustic Propagation Experiment, conducted at Dirt Site during July/August 1991. One of the objectives was to provide data for evaluating the performance of existing sound propagation models under different atmospheric conditions. An example of some of the data collected is shown in Figure 2 where 1000 Hz longitudinal wind speeds measured by the hot-film anemometer are plotted versus time. Notice the relatively large amount of wind variation that occurs in a 9-second time span. Time series plots of the sonic anemometer/thermometer wind data (Figure 3) and temperature data (Figure 4) also show large short-term variations. Good agreement between the sonic and hot-film sensors is indicated by Figure 5 where the wind speed spectra from the two sensors fall on top of each other in the region of overlap. The only difference is that the hot-film is extended out to 500 Hz while the sonic frequency is cutoff at 5 Hz. Figure 6 shows the power spectra of both the temperature and the longitudinal component of the winds. This information is used to calculate  $C_T^2$  and  $C_V^2$  for a 15-minute period. Data from the test bed was also used to develop new techniques for measuring  $C_T^2$  and  $C_V^2$  and to investigate the variations of the structure parameters with height.

#### 5. SUMMARY

The Acoustic Meteorological Test Bed is a unique system for obtaining data to verify the performance of acoustic propagation models and meteorological models of the atmospheric boundary layer. It has the capability of supporting investigations of the effects of atmospheric interactions, such as turbulence, on acoustic propagation. A new time-domain method for computing turbulence structure parameters was developed for the test bed utilizing time varying wind and temperature sonic anemometer/thermometer data. This method requires less processing than the more complex method using spectral techniques. Later, with the addition of the Acoustic Source Generation System, the propagation distances can be extended from one kilometer to ten kilometers providing the capability to verify the performances of acoustic propagation models at longer ranges.

# ACOUSTIC METEOROLOGICAL TEST BED

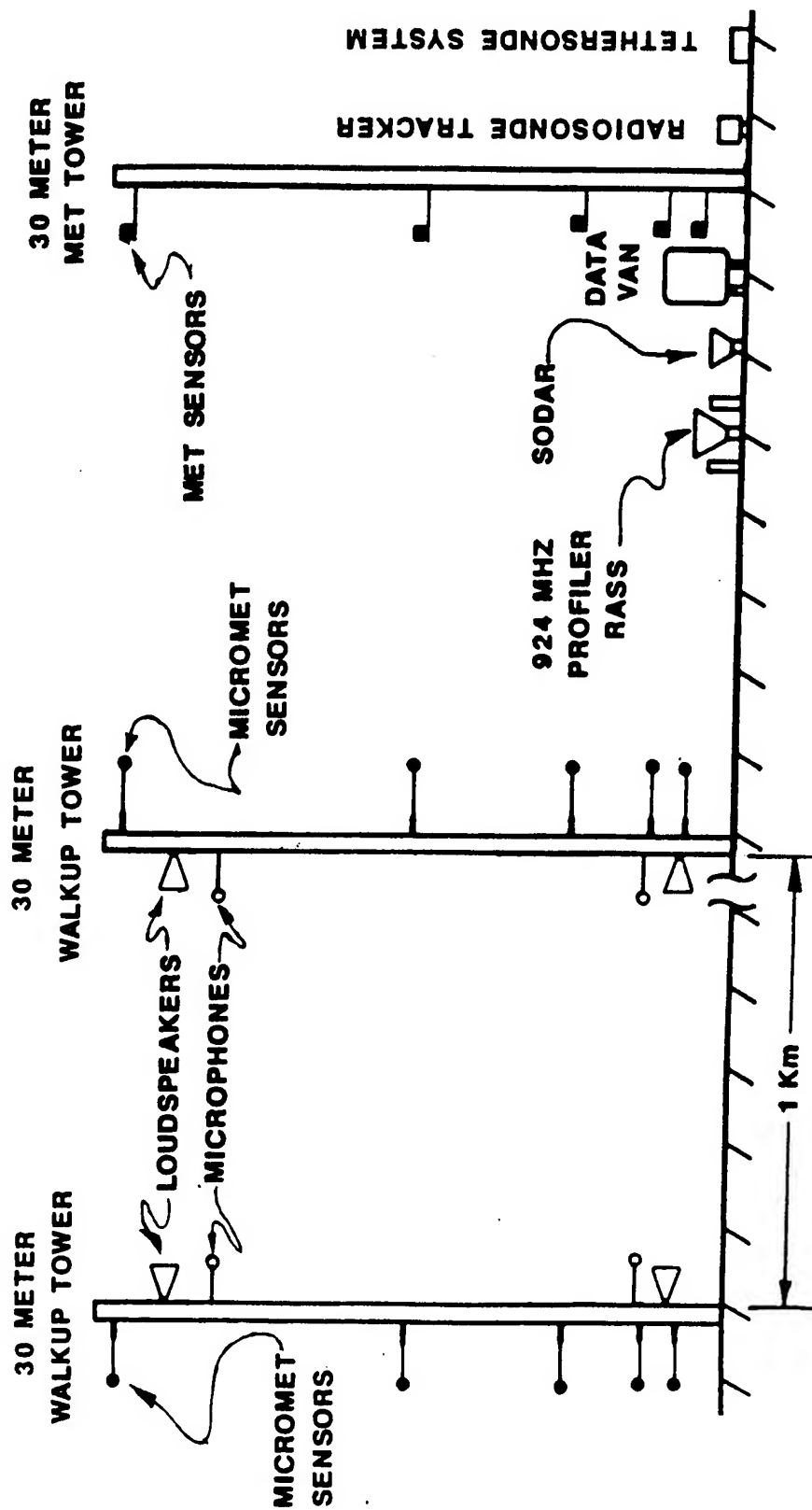


Figure 1. Schematic of Acoustic Meteorological Test Bed.

Hot-film u-Component Velocity at 16 m  
28 Aug 1991, DIRT Site, WSMR

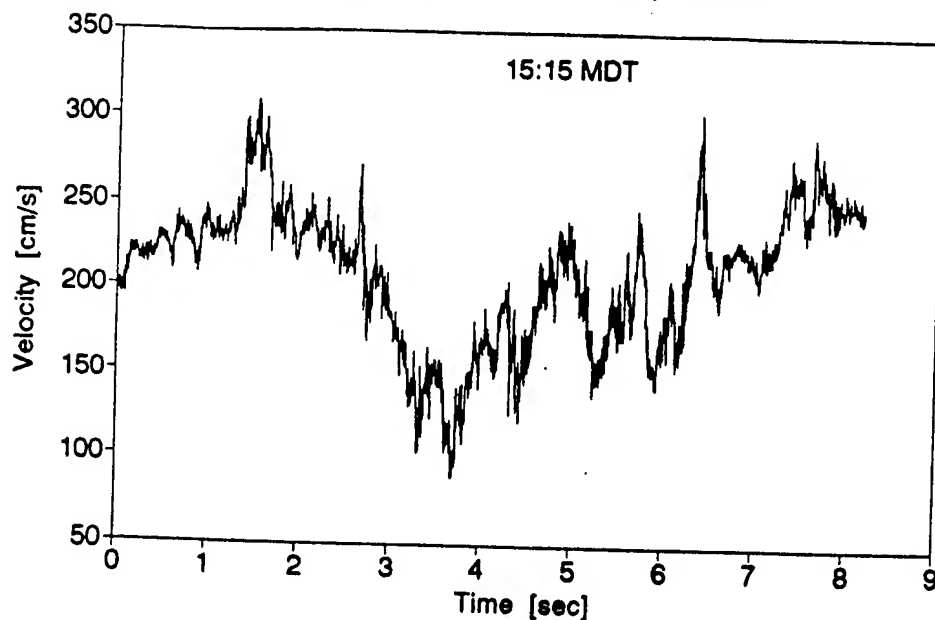


Figure 2. Wind data obtained from hot-film anemometer.

Sonic u & v Wind Components at 16 m  
28 Aug 1991, DIRT Site, WSMR

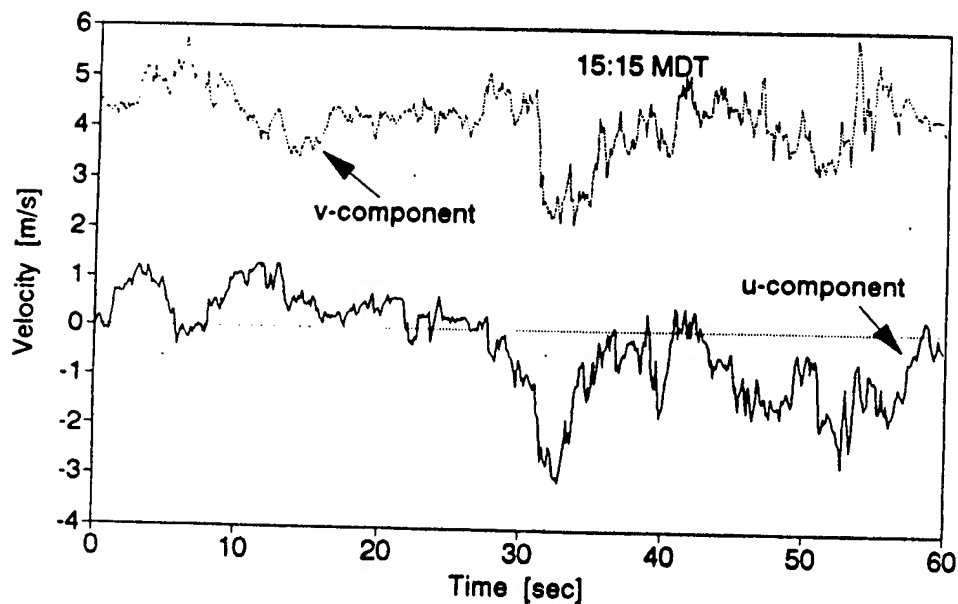


Figure 3. Wind data obtained from sonic anemometer.

# Virtual Temperature from Sonic at 16 m

28 Aug 1991, DIRT Site, WSMR

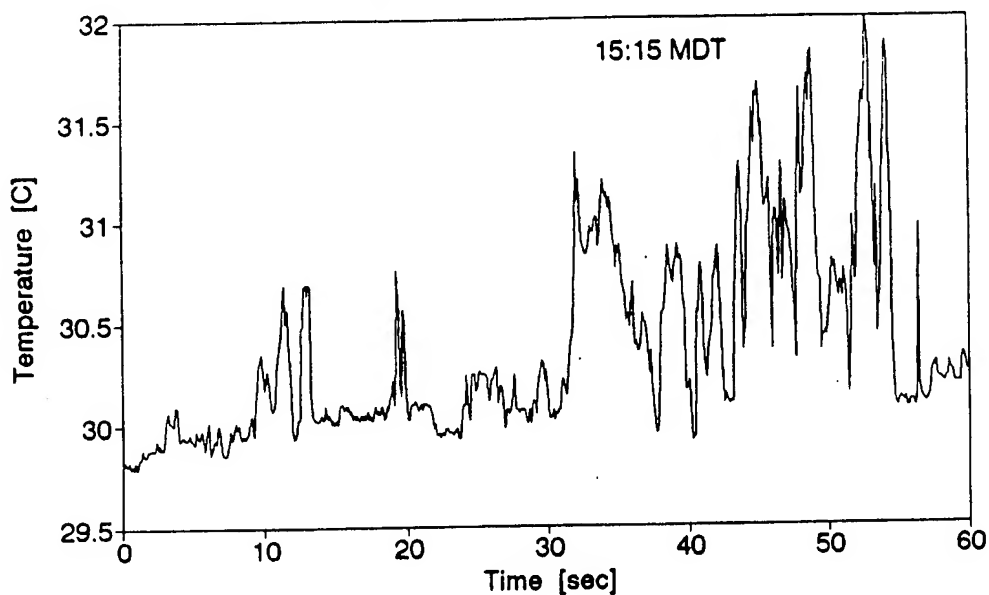
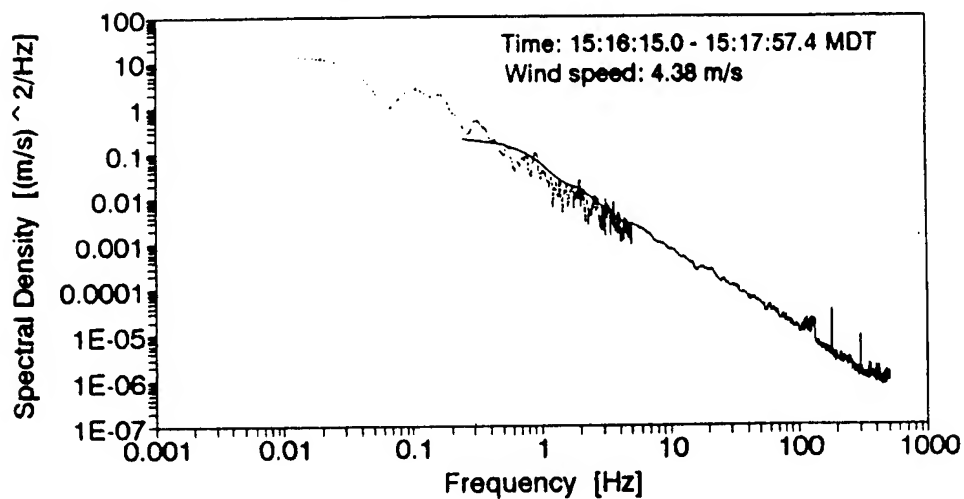


Figure 4. Temperature data obtained from sonic thermometer.

## u-Spectrum: Sonic vs. Hot-film at 4 m

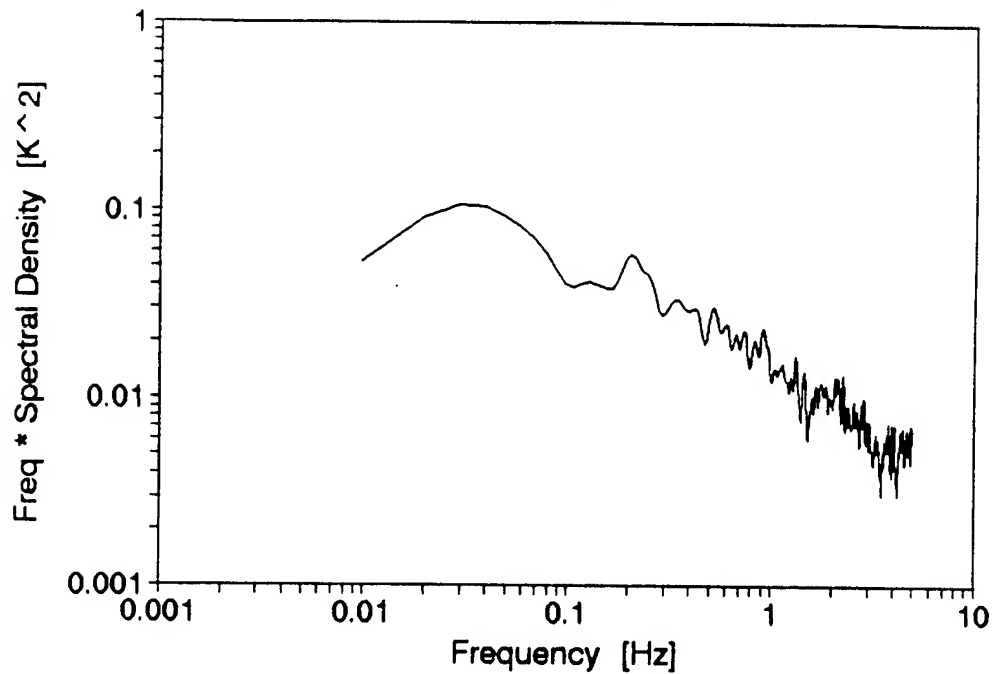
28 Aug 1991, DITR Site, WSMR



--- Sonic (10 Hz)      — Hot-film (1000 Hz)

Figure 5. Comparison plot of wind data obtained from sonic anemometer and hot-film anemometer.

15-Min Averaged T-Spectrum at 16 m AGL  
28 Aug 91, 15:15 MDT, Speed = 3.76 m/s



15-Min Averaged u-Spectrum at 16 m AGL  
28 Aug 91, 15:15 MDT, Speed = 3.76 m/s

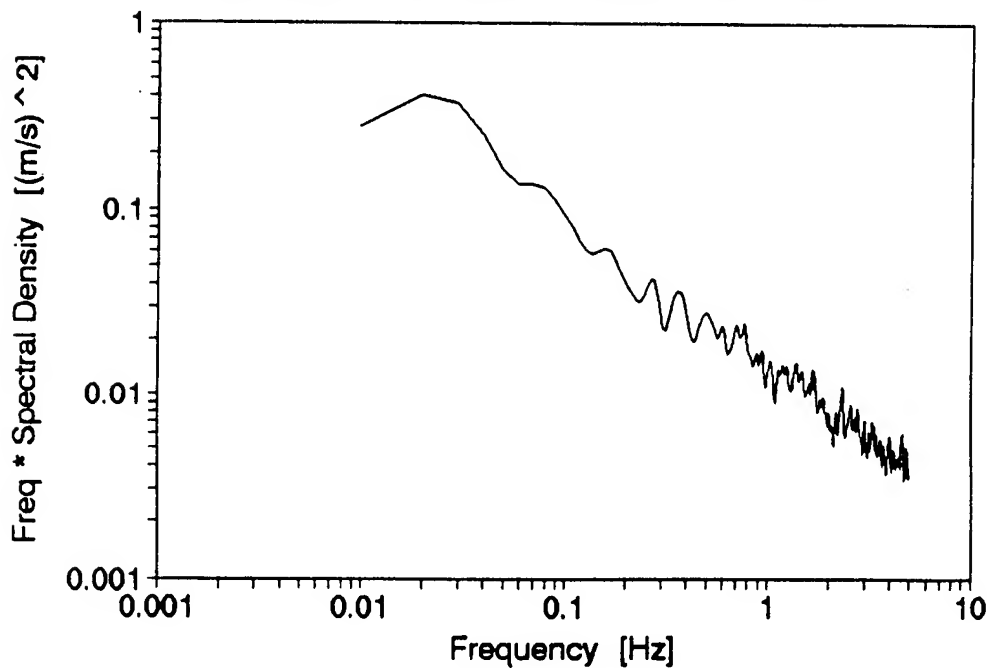


Figure 6. Temperature and wind spectrum for turbulence calculations.

A REVIEW OF SELECTED REMOTE SENSOR MEASUREMENTS OF TEMPERATURE,  
WIND AND MOISTURE, AND COMPARISON TO RAWINSONDE MEASUREMENTS

Bruce T. Miers, James L. Cogan and Richard J. Szyrmer  
Battlefield Environment Directorate\*  
U.S. Army Research Laboratory  
White Sands Missile Range, New Mexico 88002-5501, USA

ABSTRACT

Reliable, accurate atmospheric temperature, moisture, density, and wind profile measurements over specified areas have significant military importance. Rawinsonde, radar wind profilers, radio acoustic sounding systems (RASS), microwave profilers, sodar systems, and satellite-borne instruments were reviewed. Each of these systems can provide certain types of useful data; and when properly combined, complementary remote sensing systems can equal or at times exceed certain army requirements for meteorological data. All data used in this review was extracted from the cited literature. For timely temperature, moisture, and wind vertical profiles, a combination of ground-based and satellite instruments is suggested. Such a system could consist of a 924-MHz radar wind profiler with RASS, a 5-KHz Doppler sodar, a microwave radiometer, and sounding data from military and civilian satellites.

1. INTRODUCTION

The accurate measurement of meteorological variables, especially temperature, moisture, and wind, over large areas with reasonably high spatial and temporal resolution has been a goal of meteorologists providing support to the army products for many decades. Both military and civilian activities would benefit from accurate profiles and surface values of the aforementioned variables. Military and civilian forecasters would welcome the resultant improvement in atmospheric analysis, and modelers would have the benefit of better initialization and verification data. One important military need concerns the improvement in timeliness, coverage, and accuracy of meteorological data for increased accuracy of artillery fires, both tube and rocket launched, especially as munitions become more sophisticated and consequently increasingly subject to atmospheric effects.

Numerous studies (e.g. Arnold and Bellucci, 1957; Swingle, 1976; Blanco, 1988) over the past 30 years or more have examined the effect of winds, temperature, humidity and pressure on artillery fires. Usually, there has been an emphasis on attaining the ability to achieve first round fire-for-effect (a hit on a target). There are two types of errors that cause artillery inaccuracy, precision error and bias error. Precision error is thought to be small while the bias error is significant and includes

---

\*formerly U.S. Army Atmospheric Sciences Laboratory (ASL)

meteorological variability. Artillery units compensate for the meteorological variability by first measuring wind speed and direction, temperature, humidity, and pressure through a vertical profile of the atmosphere via a rawinsonde and providing these parameters to the firing units by way of a meteorological message. The effective utilization of future smart munitions may require data on cloud height, precipitation, wind speed and direction, visibility, and other conditions in the target area.

## 2. MEASUREMENT OF METEOROLOGICAL PARAMETERS USING RAWINSONDES (RAWINS)

### 2.1 WINDS FROM RAWINSONDES

The rawinsonde gives measurements (Lagrangian) that are time averaged over the balloon's trajectory, corresponding normally to layers 300-400 m thick in the troposphere (WMO 1983), with the observation point being assigned to the center of the layer. In strong winds, the rawinsonde is carried many kilometers from the point of release, and the measurements at different heights are not made directly above one another and are far from the location of the release point. A tracking system on the ground follows the balloon, and its horizontal displacement per unit time is converted into an estimate of the wind.

An alternate method of tracking a balloon is to use a conventional rawinsonde that receives and retransmits LORAN signals to a ground based receiver and computer system. Winds are then determined by the change in position of the balloon; independent wind estimates can be obtained every 30 s. State variables (temperature, pressure, and humidity) are received approximately every 3 s utilizing the RF signal from the rawinsonde. State variable data is smoothed over 20 s using a least squares solution. Wind data are computed from time of arrival of three or more LORAN-C station signals. These data are smoothed over 30 s using a least squares fit. (Smith et al., 1990)

Hoehe (1980) reports that RMS vector speed errors may vary from 1 m/s near the surface to 4 m/s at 12 km altitude. Also, the average functional precision (surface to 30 km) of wind speed measurements by rawinsonde is considered to be 3.1 m/s.

Barnes et al. (1971) reported results of winds derived from paired soundings over Oklahoma. Two sets of seven paired (5 min separation) rawinsondes were tracked independently, yielding standard deviations in speed of 1.43 m/s and 2.55 m/s respectively. The directional differences were 6.0 and 7.7 deg. (Note: Due to page limitations of these proceedings, the reader is referred to ASL TR-0315 [see references] where an extensive set of tables can be referenced that pertain to this paper.)

### 2.2 TEMPERATURES FROM RAWINSONDE FLIGHTS

Temperature profiles derived from rawinsondes are subject to errors from several sources. These include errors due to the thermal lag of the temperature sensor as well as errors due to differences in energy between the incoming and outgoing radiation. Radiation errors are caused by the difference between energy absorbed by the instrument from incoming radiation and energy emitted as outgoing radiation. Despite all of these potential



error sources, the rawinsonde's capability for resolving details of the thermodynamic structure in the vertical has yet to be duplicated by any of the new remote sensing systems.

### 3. RADAR WIND PROFILERS

Radar wind profilers are doppler radars designed primarily for measuring winds in the clear atmosphere. These profilers are able to sense atmospheric motions by detecting signals backscattered from refractive index perturbations created by turbulence on scales of half of the radar wavelength. These eddies drift with the mean wind speed and their translational velocity therefore provides a direct measure of the wind. Wind profiling radars typically operate near 915/924, 405 or 50 MHz.

#### 3.1 BASIC PRINCIPLES

Wind profilers make Eulerian measurements by sensing the radial component of turbulent eddies passing through the antenna beams, while the individual sample volume of the wind profiler increases with height for a given antenna beam width. The profiler samples a large volume because of the time integration involved in an individual sample averaged over time, while the rawinsonde effectively provides a series of point measurements.

#### 3.2 RADAR WIND PROFILER PERFORMANCE WITH RASS

A Radio Acoustic Sounding System (RASS) combines acoustic sources with wind profilers to obtain measurements of the profile of virtual temperature. The wind profiler's doppler radar measures the speed of refractive index perturbations induced by acoustic waves as they ascend at the local speed of sound, which is directly related to the virtual temperature at each height. There is a resonant condition for enhanced backscatter when the radar wavelength is twice the acoustic wavelength (known as Bragg match). Bragg-matching techniques have enabled considerably greater height coverage for temperature. The enhanced return at the Bragg-match appears as a peak on the wind profiler Doppler spectrum at the speed of sound. Virtual temperature can be determined in each profiler range gate from the measured speed of sound and the vertical wind speed. Height coverage is determined primarily by the horizontal winds (which advect the acoustic waves away from the antenna), the size of the vertically pointing radar antenna, attenuation of the signal, and the placement of the acoustic sources. Typical virtual temperature ranges of 50, 404, 924, and 915 MHz radars with RASS capabilities vary from 0.13 km to 1.0 km for the 924 MHz and up to 10 km for the 50 MHz profiler, while the vertical resolution varies from 130 m for the 924 MHz profiler to 250 m for the 404 MHz system.

RASS operations are generally limited by atmospheric attenuation of the acoustic signal. The attenuation, being frequency sensitive, provides nominal RASS altitude operating ranges of 1 to 2 km for 900 MHz radars and a 2 to 10 km range for 400 MHz radars. For the 50 MHz system, coverage starts about 2.1 km AGL and extends above 6 km. Lower radar frequencies provide higher RASS operating ranges, however advection of the acoustic wave fronts by the wind and the corresponding loss of the backscattered energy from the acoustic signal becomes the dominant limiting range factor.

### 3.3 RADAR WIND PROFILER COMPARISONS

Kaimal(1990) reports differences in similar wind profiler measurements of horizontal wind components with a standard deviation of about 2.2 m/s. This is somewhat larger than the 1.3 m/s observed in side-by-side comparisons of identical UHF wind profilers in clear air when correction for the vertical component of the wind was made, but it is similar to the standard deviation in those same side-by-side comparisons when the correction was not made(Strauch et al.,1987). It was less than the standard deviation of 2-4 m/s observed during precipitation (Wuertz et al. 1988). Failure to correct for vertical motion dramatically increases the variance in the horizontal wind component measurements during precipitation, but it can also increase the variance of the measurements in clear air.

### 3.4 RADAR WIND PROFILER,LIDAR/RAWINSONDE AND LIDAR/PROFILER COMPARISONS

Lawerence (et al.,1986), lists comparison values for doppler lidar, rawinsonde, and 915-MHz UHF wind profiler measurements of tropospheric winds. The data suggest that the lidar and profiler are measuring the same winds while spatial and temporal variability could account for the larger values in the lidar/Rawinsonde comparisons.

## 4. SODAR-SONIC ANEMOMETER COMPARISONS

Okrasinski and Olsen(1991) reported the results of a test on the comparison of wind data derived from two sodars, a 924 MHz wind profiling radar, tower mounted anemometers and rawinsondes. One sodar consisted of three acoustic antennas(two tilted 18 deg from vertical) and operated at 1600 Hz with an acoustic power of 60 W. The other sodar used a single phased array antenna with three electronically steered beams, two of which are directed 30 deg from the vertical and 90 deg from each other and operates at 2100 Hz with an acoustic power of 140 W. Tower mounted anemometers(propeller type) were located about 3 km from the sodar and recorded data at eight different levels. Rawinsondes were AIR, Inc. instruments and were tracked by an automatic radio theodolite and a wind finding radar.

## 5. MOISTURE AND TEMPERATURE PROFILING

A radiometric atmospheric profiler operated by ASL consists of two passive instruments utilizing six frequencies(57.45, 55.29, 53.88, 51.07, 31.4, 20.4 GHz; with nominal bandwidths of 200 MHz) to measure brightness temperatures of the atmosphere. Temperature is derived mainly by using the channels in the 50 GHz range and total path integrated water vapor is obtained by using the 31.4 and 20.4 GHz channels. All channels are used to some extent in the retrieval process for both temperature and water vapor. Brightness temperatures can be measured along any upward looking path. Inferred temperature profiles and moisture overburdens are measured directly above the instrument. The field of view of the radiometers is approximately 5 deg and vertical resolutions of temperature profiles are best near the surface with the initial temperature level being about 30 meters above the surface. The microwave radiometer is most accurate up to the 500 hPa level(e.g. 1 K lower levels to 3 K rms upper levels) and provides useful information to about 5 hPa. Moisture measurements are unresolved with height(total column).

## 5.1 TEMPERATURE AND MOISTURE PROFILES FROM SATELLITE INSTRUMENTS

### 5.1.1 Basic Physical Principles

The atmosphere is partially or totally opaque for most of the spectrum of radiation emitted by the earth's surface. Water vapor, carbon dioxide, ozone, and other gases absorb the surface radiation and re-emit it at temperatures prevailing in the atmosphere. The amount of radiation absorbed depends on the absorbing characteristics as a function of wavelength and the amount of the gases in the atmosphere. At wavelengths of weak absorption, the surface radiation is absorbed in the atmospheric layers close to the surface and re-emitted to space from these low layers. At wavelengths of strong absorption, the surface radiation goes through a process of absorption and re-emission as it is transferred through the atmosphere and is essentially emitted to space from the higher atmospheric layers. At wavelengths of moderate absorption, the effective emission levels are at intermediate altitudes of the atmosphere. The spectrum of radiation measured by a instrument observing across such an absorption band would thus furnish information on thermal conditions at the respective effective levels of emission. Hence, the possibility exists of deducing vertical temperature profiles from remote spectral observations.

### 5.1.2 Effects of Clouds on IR Soundings

Most low and middle clouds(liquid) behave almost as black bodies for IR radiation, i.e. their transmittances are close to zero. IR remote sounding instruments in this case provide information about the atmosphere only at and above the cloud top. If the sky is partially covered with clouds, the contributions from the clear and cloudy portions of the atmosphere can be weighted, but the percentage of cloud cover must be estimated. Cirrus clouds (ice crystals) not only do not behave as black bodies but transmit IR radiation with considerable variability. Since the heights, amounts, and transmittances of cirrus clouds are difficult to estimate and since they can obscure so much of the lower atmosphere from the satellite view, their presence severely hampers remote IR sensing schemes (this is especially relevant for thin or sub-visible cirrus).

### 5.1.3 Microwave Observations

Because the longer wavelengths of microwave(MW) radiation can penetrate most cloud systems, observations of thermal emission in the MV region can yield temperatures below clouds, providing for an almost "all weather" capability. Interpretation of MV observations are hampered by surface emissivity effects and sensitivity to precipitation. But these mechanisms also open possibilities for sensing surface properties(e.g. snow, sea ice, soil moisture) and precipitation.

### 5.1.4 Operational Use

The main tropospheric, sounding instrument is the 20 channel High-resolution Infrared Sounder (HIRS), which consists of seven temperature sounding channels in the 15  $\mu\text{m}$  region, five more temperature sounding channels in the 4.3  $\mu\text{m}$  region, one ozone channel at 9.7  $\mu\text{m}$ , three window channels at 11.1, 4.0, and 3.7  $\mu\text{m}$ , three water vapor channels at 8.3, 7.3, and 6.7  $\mu\text{m}$ , and one

visible channel. This instrument is supplemented in the stratosphere with the Stratospheric Sounding Unit(SSU), a three channel instrument that uses a pressure modulation to measure the upper atmosphere. The HIRS is also supplemented by a Microwave Sounding Unit(MSU) to help eliminate the effects of clouds and to provide a limited sounding capability in overcast regions. The MSU is a four channel instrument consisting of a window channel and three atmospheric channels. These instruments comprise the TOVS (TIROS-N Operational Vertical Sounder).

Complex data processing algorithms are required for soundings under cloudy conditions. Because radiation in the infrared region does not penetrate clouds, the radiation in a cloudy area is not representative of the region below the clouds. The algorithm first attempts to determine which areas are clear by using various tests such as those based on known clear-air statistical relationships between channels. If cloud free areas are not found, an attempt is made to extract clear radiances from partly cloudy values. In this process, the fact that microwave radiances are relatively unaffected by most clouds is used. If clear radiances cannot be extracted, an attempt is made to produce a retrieval using only the microwave radiances. Finally, no retrievals are made if the tests for good retrievals fail. Once cloud free radiances are obtained, they are converted to brightness temperatures from which temperature profiles are determined by using the eigenvector regression described by Smith and Woolf(1976).

#### 5.1.5 Moisture Measurements from Geostationary Satellites

The retrieval of moisture parameters from satellite measurements is generally more difficult than the retrieval of temperature because water vapor is a highly variable absorbing and emitting constituent which causes strong changes in  $H_2O$  channel weighting functions(Hilger,1984). In the case of temperature retrievals the absorbing constituent,  $CO_2$  or  $O_2$ , has a relatively constant mixing ratio throughout the atmosphere. Temperature is merely a characteristic of the absorber, so temperature variations leave the weighting functions largely unchanged. However, the effect which moisture variations have on the weighting functions must be considered in every step in the retrieval process. Another degree of difficulty in retrieving moisture information from satellite measurements arises because the moisture lies largely near the surface, and meteorological parameters near the surface are typically harder to retrieve than those in the middle levels. Much of the difficulty occurs because of the strong effect of the boundary or surface temperature upon the satellite radiances. To determine moisture the surface skin temperature must be either known or retrieved independently of the atmospheric channels. The retrieval scheme(Gruber and Watkins,1979), therefore, allows the surface skin temperature to be determined from satellite window channels alone. However, an inherent drawback of infrared measurements is their inability to sound below clouds.

#### 5.1.6 Temperature Soundings from the DMSP Microwave Sounder

The Special Sensor Microwave Temperature (SSM/T) Sounder on the polar orbiting Defense Meteorological Satellite Program (DMSP) satellites obtains temperature soundings through the use of a seven channel instrument operating in the oxygen band (50-60 GHz). Temperature profiles are retrieved by using a minimum variance approach whose covariance matrices are

constructed from a fixed set of simulated SSM/T data and corresponding temperature profiles (Grody, et al., 1985). This method is in contrast to non-physical methods, which depend on antecedent satellite and rawinsonde data for generating the first guess for the retrieval algorithm. The SSM/T algorithm relies only on a-priori data.

#### 5.1.7 WATER VAPOR MEASUREMENTS FROM SATELLITE INSTRUMENTS

The major source of surface data for the validation of the SSM/I determination of total precipitable water was the international rawinsonde network. The pressure, temperature, and humidity data from the rawinsondes were integrated numerically to give values which were compared to SSM/I values (Alishouse et al., 1990). Water vapor values can also be derived from the SSM/T-2 and TOVS instruments.

#### 5.2 SATELLITE INSTRUMENTS - RAWINSONDE COMPARISONS

Both operational and research processing of TOVS radiances data has indicated that the TOVS instrument is capable of providing soundings with RMS differences near 2 K compared to computer model analyses and rawinsonde data from 850 hPa to the tropopause region. Differences between retrieval level temperatures and computer model analyses or rawinsonde data were found to be near 2 K through much of the troposphere and near 3 to 4 K around the tropopause (Le Marshall, 1988 and Reale, 1990).

Grody et al. (1985), have shown samples of brightness temperature measurements and temperature retrievals compared against rawinsonde data. Matchups were between the satellite and rawinsonde data based on a  $\pm 3$  hr,  $\pm 1$  deg lat.-lon. window. The differences were generally between 2 to 3 K (rms) for pressures between 700 and 20 hPa. These results were independent of cloud cover and were generally more accurate than the retrievals obtained from TOVS data, particularly for cloudy conditions. TOVS - SSM/T differences approached 1 K with smaller differences between the two satellite systems occurring for partly cloudy and clear regions.

#### 5.3 SATELLITE INSTRUMENTS - PROFILER COMPARISONS

Schroeder et al. (1991) combined TOVS soundings with temperature profiles measured by a ground based 915 MHz/2 kHz RASS system. Temperature inversions were resolved by the RASS which the TOVS alone could not determine and conversely the TOVS data extended the RASS coverage much above its nominal altitude range. Westwater et al. (1984) compared the RMS differences in geopotential height between rawinsonde and profiler, TOVS data, and combined retrievals. RMS differences ranged from 5 to 32 m for the profilers and 21 to 49 m for the TOVS data. Rawin precision is 6 to 25 m.

#### 5.4 WINDS DERIVED FROM SATELLITE DATA

The best satellite derived winds on constant pressure surfaces is a geostrophic wind derived from highly smoothed fields of geopotential height. Geopotential height fields are computed from gridded satellite data by integrating the hydrostatic equation from the surface upward. In the integration process, mean virtual temperature for each layer is defined as the arithmetic average of the values at the top and bottom of the layer.

Initial surface temperature, dew point temperature and pressure are usually obtained from hourly synoptic data.

Magnitudes of the average and standard deviation of the differences between satellite derived geostrophic and rawinsonde wind speeds are decreased when satellite height fields are smoothed. Also, differences in wind direction are decreased by the smoothing process.

Scoggins et al.(1979) determined that differences in geopotential heights ranged from 8 m at 850 hPa to 16 m at 100 hPa in the Caribbean area, 12 to 56 m in central US, 18 to 50 m in western US, and 28 to 60 m in Canada with maximum values near 250 hPa. Also, differences between geostrophic wind computed from rawinsonde and satellite geopotential heights were small in the lower layers, with values near 5 to 7 m/s near the tropopause. Standard deviations of differences in wind speed were found to increase with altitude, with values between 5 and 15 m/s. Large differences between satellite and rawinsonde derived fields may be due to the poor quality of the satellite sounding data and the use of a limited number of satellite data levels.

Scoggins et al.(1979) also found that mean differences ranged from about 5 to 15 m/s and were smallest in areas of low wind speeds. Magnitudes of the standard deviation of the differences in wind speed generally increased with altitude until the level of the maximum rawinsonde wind speed was reached. At this level, magnitudes of the standard deviation ranged from 5 to 12 m/s.

#### 6. VISSR ATMOSPHERIC SOUNDER (VAS):

The VAS is a passive infrared radiometer which senses radiation emitted by the atmosphere and the earth's surface in 12 spectral bands from 3.7 to 15.0  $\mu\text{m}$ (Clark,1983). VAS data is collected in scan lines as the GOES satellite spins in a west to east direction. The resolution of each field of view along a scan line is 7 or 14 km at nadir depending on whether small or large detectors are used. Only with the large detectors(14 km) can the atmosphere be sampled in all 12 channels.

Weldon and Holmes (1991), took as a measure of error in the VAS retrievals, the standard deviations of the difference between the satellite and the ground truth values. In most cases the standard deviations were largest in the upper levels. Values ranged from 1 to 2 K for temperature and 3 to 5 K for dew point(Weldon & Holmes,1991). Derived parameters from VAS soundings reflected the biases in the original temperature and moisture profiles to a large extent. Geopotential height profiles were generally good, especially for the modified physical retrievals. For the regression and physical retrievals, heights became too large in the upper levels. Standard deviations for heights range from 20 to 30 meters above 600 hPa but were somewhat smaller below.

#### 7. COMBINED SYSTEM

A number of investigators have looked into the idea of combining data from ground based and/or airborne systems with data from satellite sensors to derive a more accurate sounding through the entire troposphere and above

(Schroeder et al., 1991; Cogan, 1990; Westwater, 1984). Schroeder et al., (1991) and Westwater et al., (1984) developed a relatively complex statistical method for combining temperatures from TOVS and RASS that required considerable a priori information. Over four hundred rawinsonde soundings for a particular site were used to derive coefficients for an inversion technique that involved large (41 X 41) matrices. The difference between the resultant soundings and rawinsonde profiles were about  $\pm 2$  K at most levels, greater near the tropopause. Schroeder et al., (1991) also discussed a much simpler "blending" method that did not require a priori information, but did assume a moist adiabatic lapse above the highest RASS level. The accuracy of the method relative to rawinsonde profiles was about the same as the statistical method, except for some degradation above the highest RASS level. Cogan (1990), presented a more general "merging" technique that can combine data from a dropsonde or ground based system (including RASS), an airborne system (manned or unmanned), and a satellite sounder. The aforementioned "blending" method represents a "special case" of the more general technique. Neither one assumed a priori information, but the generalized method made no assumptions on lapse rate, and included a scheme for spatial and temporal weighting. Based on results from a limited set of real data the "merging" method seemed to yield accuracies relative to rawinsondes of about  $\pm 1$  K at aircraft and dropsonde levels, increasing to  $\pm 2$  to 4 K near the tropopause or where the satellite profile was significantly distant in space or time from the rawinsonde.

## 8. Summary

Each system described in this paper can provide certain types of useful data. For example, profiler accuracy is better in the lower atmosphere and the satellite is better in the upper atmosphere, with the accuracy crossover point at about 400 hPa. Also, from 500 to 300 hPa, the accuracy of the two systems is almost the same. A combined system would exhibit an accuracy everywhere better than the best of the two individual systems, with a rms error of 2 to 3 K below 50 hPa except near the tropopause. Below 300 hPa, rms errors of a composite system may be less than 2.0 K.

A combination of radar profilers with RASS, under optimum conditions, can provide temperature profiles from 80 meters to 10 km AGL with 80 to 300 m vertical resolution. Wind profiles can be obtained up to 16.5 km.

Numerous studies were cited that compared winds derived from rawinsondes with radar wind profilers. Winds derived using a 915 MHz system showed a standard deviation of 2.63 m/s to 4.67 m/s. RMS differences between two LORAN systems tracking the same instrument were 1.2 m/s in wind speed and 1.9 degrees in direction. Another comparison of profiler to rawinsonde yielded RMS differences of 3.31 m/s in speed and 4.61 degrees in direction. When a 924 MHz system was compared to rawinsondes the RMS differences ranged from 2.4 to 3.7 m/s in speed and 9.1 to 23.3 degrees in direction. Lidar comparisons to rawinsondes found RMS differences of 3.3 m/s in speed and 12.13 degrees in direction. Lidar to profiler comparisons yielded an RMS difference of less than 1 m/s. sodar comparisons to tower mounted anemometers showed RMS differences of 1.6 to 1.8 m/s in wind speed and 24.9 to 31.0 degrees in direction. When 924 MHz profiler derived winds were compared to sodar derived winds the RMS differences ranged from 1.8 to 2.8 m/s for speed and 11.8 to 20.1 degrees for direction.

Winds derived from satellite data are geostrophic winds derived from highly smoothed fields of geopotential heights. Standard deviation of differences (from rawinsondes) in component winds ranged from 4 to 14 m/s with the largest differences being near the tropopause. Wind speeds derived from TOVS computed height fields were on the average larger than those derived from rawinsondes derived height fields. The values ranged from 3.5 m/s at 850 hPa to 13.0 m/s at 250 hPa. Magnitudes of average differences in wind direction ranged from 16 to 28 degrees.

For vertical profiles of temperature, moisture and wind on a timely basis a combination of ground based and geostationary satellite instruments is suggested. An example of such a system would consist of a 924 MHz wind profiler with RASS, a 5 kHz Doppler sodar, a microwave profiler and military and civilian satellite data.

#### REFERENCES

- Alishouse, J.C., et. al., 1990: Determination of Oceanic Total PW from SSM/I., IEEE Trans. on Geos. & Remote Sensing, 28:811-816.
- Arnold, A. & R. Bellucci, 1957: Variability of Ballistic Met. Parameters, TM M-1913, U.S. Army Signal Eng. Lab. Ft. Monmouth, NJ.
- Barnes, S., J. Henderson, R. Ketchum, 1971: Rawinsonde observation & processing at NSSL, NOAA Tech. Memo ERL-NSSL-53, 244-246.
- Blanco, A., 1988: Methodology for estimating wind variability, U.S. Army, ASL, TR-0225, WSMR, NM 88002-5501.
- Clark, J.D., Editor, 1983, The GOES User's Guide, U.S. Dept. of Commerce, NOAA, NESDIS, Washington, D.C.
- Cogan, J.L., 1990: A preliminary method for obtaining remote area soundings in real time. Preprints of the 5th Conf. on Satellite Meteor. and Ocean., London, UK, pp. 98-103.
- Grody, N.C., D.G. Gray, C.S. Novak, J.S. Prasad, M. Piepgrass and C.A. Dean, 1985: Temperature Soundings from the DMSP Microwave Sounder, Advances in Remote Sensing Retrieval Methods, pp. 249-265, A. Deepak, H.E. Fleming and M.T. Chahine (Editors), A. Deepak Publishing.
- Gruber, A. and C.D. Watkins, 1979, Preliminary evaluation of initial atmospheric moisture from the TOVS-N sounding system., Satellite Hydrology, Proc. Fifth Ann. Symp. Remote Sensing, Minneapolis, MN, Amer. Water Resour. Assoc., pp. 115-123.
- Hoehne, W.E., 1980: Precision of National Weather Service upper air measurements. NOAA Tech Memo. NWS T&ED-16, Sterling, VA, 23 pp.
- Kaimal, J.C. (Editor), 1990: Remote Atmospheric Profiling Systems for Tropospheric Monitoring, NOAA Tech. Memo. ERL WPL-175, 72p.
- Lawrence, T.R., et al., 1986: A comparison of Doppler Lidar, Rawinsonde, and 915 MHz UHF wind profiler measurements of tropospheric winds, NOAA Tec. Memo. ERL WPL-130, 36p.
- Le Marshall, J.F., 1988: An Intercomparison of Temperature and Moisture Fields Derived from TIROS Operational Vertical Sounder Data by Different Retrieval Techniques. Part I: Basic Statistics, J. Appl. Meteor., 27:1282-1293.
- Miers, B.T., J.L. Cogan, R.J. Szymler, 1992: Review of selected remote sensor measurements of temperature, wind, and moisture, and comparison to rawinsonde measurements. ASL-TR-0315, U.S. Army, ASL, WSMR, NM 88002-5501.
- Okrasinski, R.J., and R.O. Olsen, 1991, Intercomparison of Wind Measurements from Two Doppler SODARs, a UHF Profiling Radar, Rawinsondes, and in situ Tower Sensors. Conf. on Lower Trop. Profiling: Needs and Technologies, pp. 123-122, NCAR & NOAA/WPL sponsored with Amer. Meteor. Soc., September 10-13, 1991, Boulder, CO.
- Reale, A.L., 1990: Baseline Upper Air Network (BAUN) Final Report; NOAA Tech. Rpt. NESDIS 52, 57 pp.; NOAA/NESDIS, Washington, D.C.
- Schroeder, J.A., E.R. Westwater, P.T. May and L.M. McMillin, 1991: Prospects for Temperature Sounding with Satellite and Ground-based RASS Measurements, J. Atmos. & Oceanic Tech. 8:506-513.
- Scoggins, J.R., et. al., 1979: Comparative Analysis of Rawinsonde and Nimbus-6 and TIROS-N Satellite Profile Data, ARO, Durham, NC.
- Smith, W.L., and H.M. Woolf, 1976: The use of eigenvectors of statistical covariance matrices for interpreting satellite sounding radiometer observations. J. Atmos. Sci. 33:1127-1140.
- Smith, W.L., 1990: GAPEX: A Ground-based Atmospheric Profiling Experiment, B. Amer. Meteor. Soc., 71:310-318.
- Strauch, R.G., et. al., 1987: The precision and relative accuracy of Profiler wind measurements. J. Atm. Ocean. Tech., 4:563-571.
- Swingle, D., 1976: Meteorological Data Input for FAMAS COEA, U.S. Army, ASL, WSMR, NM 88002-5501.
- Weldon, R. and S. Holmes, 1991: Water Vapor Imagery: Interpretation and Applications to Weather Forecasting, NOAA Tech. Rpt. NESDIS 57
- Westwater, E.R., W.B. Sweeney, L.M. McMillin and C. Dean, 1984: Determination of Atmospheric Temperature Profiles from a Statistical Combination of Ground-Based Profiler and Operational NOAA 6/7 Satellite Retrievals, J. Clim. Appl. Meteor., 23:689-703.
- WMO 1983: Guide to Meteorological Instruments and Methods of Observation. 5th Ed., WMO, Geneva, Switzerland.
- Wuertz, D.B., et. al., 1988: Effects of precipitation on UHF Wind Profiler measurements. J. Atm. Ocean. Tech., 5:450-465.



# A FRESH LOOK AT THE PLANETARY BOUNDARY LAYER: HIGH RESOLUTION PROFILING WITH THE U.S. ARMY RESEARCH LABORATORY FM-CW RADAR

Scott A. McLaughlin  
U.S. Army Research Laboratory  
Battlefield Environment Directorate\*  
White Sands Missile Range, New Mexico 88002, USA

## ABSTRACT

A new high resolution atmospheric turbulence profiling radar has been operating for nearly a year in the Tularosa Basin of south-central New Mexico at White Sands Missile Range. The frequency-modulated continuous-wave (FM-CW) radar obtains 1-20 meter spatial resolution turbulence induced backscatter every 5-10 seconds up to 20 kilometers above ground level. The transmitted power is reflected back toward the radar by irregularities in the index of refraction. This returned power is calibrated and presented as the structure parameter of the index of refraction  $C_n^2$ . The data is plotted in a time versus height format in real-time using a sixteen color high resolution printer. Over the last year the radar has seen classical Kelvin-Helmholtz wave instability, high reflecting thin stationary layers, nocturnal boundary layer events, rising and falling daytime mixing layer signatures, and various hydrometeor events. The radar is integrated into the Atmospheric Profiling Research Facility which operates several types of in situ and remote sensing systems. The Facility has several other remote sensing profilers as well as a unique suite of meteorologic sensors. The FM-CW radar data is important for boundary layer modeling, electromagnetic propagation, and in aiding scientists to better understand this highly variable portion of the atmosphere. High resolution color data and a short system description will be shown.

## 1. INTRODUCTION AND BACKGROUND

Since the earliest observations, the use of ground-based radar has provided remarkable insight to aid in understanding the atmosphere. Starting out as slightly modified military tracking radars, weather radars came into their own in the 1950's and were extensively used for forecasting severe weather and for basic atmospheric studies of hydrometeor targets. Later in the 1960's it became patently apparent that there was much to be learned from the optically clear air as well. It was during this time that a new class of weather radars originated which use clear-air turbulence to reflect radar transmitted power back to the antenna.

Early on, much interest was generated about the nature of radar reflections from an optically clear atmosphere (see Atlas, 1990, editor-in-chief, for an excellent history of weather radars). Reflections were not only thought to originate from turbulence in the atmosphere, but also from insects and birds. Because of the confounding nature of these non-hydrometeor targets (often called dot angels or pixies), theories regarding the turbulent backscatter were difficult to validate with radar measurements. Standard pulse radars were highly sensitive and high power, but did not have the necessary spatial resolution to quantify and separate returns from insects, birds, and thin atmospheric layers. To fill this need a new application of an older concept in radar design was used, a frequency-modulated continuous-wave (FM-CW) radar.

The first ultra-high resolution meteorological FM-CW radar constructed was operated near San Diego in 1969 by Richter (1969). The radar was originally designed to study electromagnetic propagation for

---

\*formerly U.S. Army Atmospheric Sciences Laboratory

the Navy. But the radar proved itself crucial in observing fine scale atmospheric events such as marine/dry air interactions, Kelvin-Helmholtz (K-H) wave structures, and the infamous dot angels. The radar exhibited such a high level of spatial and temporal resolution that atmospheric layers were found to be only a few meters thick. Pulse radars at the time had resolutions closer to 100 meters, and it was known that these size range cells under-sampled the layer thicknesses (studied in the Wallops Island multiwavelength radar experiments; Hardy, 1966, and Richter, 1974). With the Navy FM-CW radar individual insects were distinguishable from the atmospheric backscatter and K-H instability-produced "cat's eyes" were seen in spectacular detail (Gossard, 1971).

In the 1970's the National Oceanic and Atmospheric Administration (NOAA), Wave Propagation Laboratory, in Boulder, Colorado, built an FM-CW radar of their own. Doppler processing was added to allow for wind profiling (Chadwick, 1976), and the radar was calibrated for  $C_n^2$  measurements. This FM-CW radar also had extraordinary success seeing the tremendous variety of atmospheric structure present in the planetary boundary layer (PBL).

In the mid-1980's the U.S. Army Research Laboratory (ARL) Battlefield Environment Directorate (previously designated the Atmospheric Sciences Laboratory), contracted to have built an FM-CW Doppler radar for PBL research and directed energy weapons support. The radar was delivered August

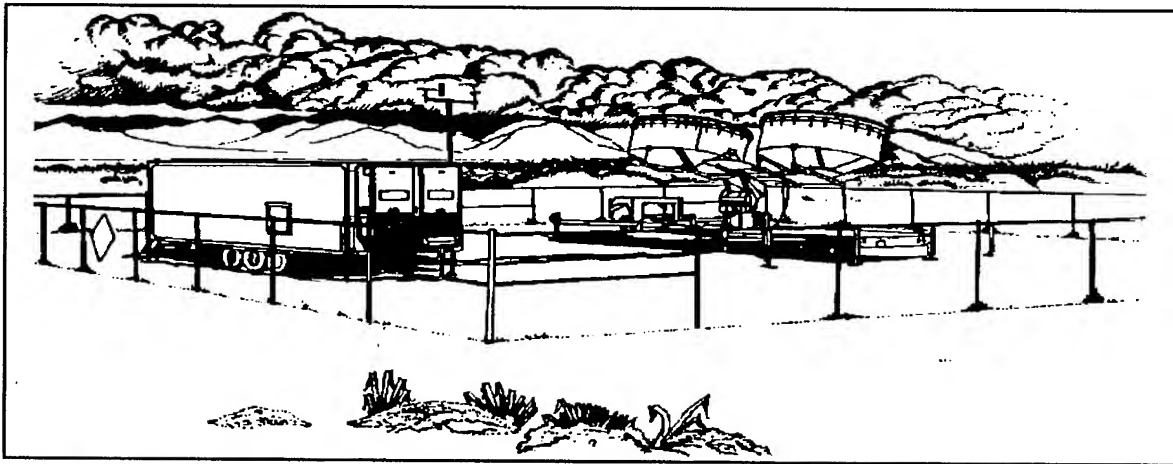


Figure 1. Artist sketch of ARL FM-CW.

1990 and began full scale data collection eighteen months later. This FM-CW radar is thought to be the third used for clear-air lower atmosphere studies. The radar is now operating as part of the Atmospheric Profiler Research Facility (APRF) (Hines, 1992, this conference) at WSMR and will be used for long and short term PBL observation studies, comparison with other PBL observation techniques, cloud and other hydrometeor observations, computer model verification, and various other research studies. Following is a system description and sample data obtained from the radar thus far.

## 2. SYSTEM DESCRIPTION

From the outside, the ARL FM-CW Atmospheric Doppler Radar System (FADRS) consists of two trailers, one for the data processing and electronics equipment, the other for the two antennas and the supporting elevation and azimuth mount (see Figure 1).

The FADRS uses a phase-locked-loop digital frequency synthesizer to obtain a very linear, very low noise 200 MHz swept signal centered at 2.9 GHz. Final amplification is through a traveling-wave-tube (TWT) amplifier with a continuous 220 Watt output. The backscattered signal is gathered by the receive antenna, amplified and sent to the electronics trailer. The signal is then homodyned, amplified again, filtered, and sampled by a 16-bit analog-to-digital converter. The radar transmits and receives

simultaneously, processing all data real-time using an array processor combined with a real-time minicomputer. Data is then written to tape or disk, graphically to screen, and in color to a high resolution inkjet type printer (see Table I for pertinent radar specifications).

Standard pulse weather radars (hydrometeor or clear-air) use time as a range coding/decoding modulation, where as an FM-CW radar uses frequency. The FADRS simultaneously makes use of two antennas (side-by-side, pointed straight up), one for transmitting and one for receiving. This technique allows for the high resolution and for an increased average transmitted power over a pulse system. After being scattered by atmospheric turbulence, gathered by the receive antenna and processed, the return signal will consist of frequencies from 0 to 25 kHz, where frequency is directly proportional to distance (range). After digitizing it is then a simple matter of performing a Fast-Fourier-Transform (FFT) to "decode" the modulation and calculate the magnitude of backscatter per FFT point or range cell.

One familiar with radar would probably note that this FFT application on a pulse system yields the Doppler information (speed) of a target, which would now seem to be ambiguous on a swept system. It was found by Strauch (1976) that this information is still present in FM-CW radar data as a change of phase from sweep to sweep. Chadwick (Chadwick et al., 1976) found that Strauch's technique could be used and clear-air winds were calculated on the NOAA FM-CW radar. The ARL FM-CW radar can obtain winds, but since this requires a degradation of the range resolution, it is not normally used. This phase information is used for another very important purpose though, that is to blank out ground clutter from the received signals. This is done by essentially subtracting the amplitudes of signals in the spectra which do not change phase sweep to sweep. This technique allows for an exceptionally clean spectra.

### 3. DATA CALIBRATION

Clear-air radars (see Chadwick and Gossard, 1986, for further discussion) quantify the turbulence induced backscattered power reflected by refractivity fluctuations in the atmosphere by using Tatarskii's (1973) and Hardy's (1966) theory to calculate a structure parameter for the index of refraction,  $C_n^2$ . In an optically clear atmosphere with no point targets (insects, birds, etc.) the strongest radar-returns will consist of reflections from turbulent cells that are one-half the transmitted radar wavelength. To obtain true  $C_n^2$  values using a calibrated system, these eddies must fall within the inertial sub-range on the Kolmogorov scale.

Table I. Key Specifications of the ARL FM-CW Radar.

ARL FM-CW Radar Characteristics	Value
Operating Frequency / Wavelength	2.9 GHz $\pm$ 100 MHz / 10 cm
Spatial Resolution / Height coverage	1 to 20 m / 1 to 20 km
Temporal Resolution	6 to 12 s
Number of Gates	1024
Antenna Type Antenna 3 dB Beamwidth	parabolic 2.7°
Transmitter Type Transmitter Power	traveling-wave-tube 220 Watts continuous
Minimum Detectable Signal	less than -170 dBm

A standard form of the radar range equation is used,

$$P_r = \frac{P_t R_G \left(\frac{D}{R}\right) G^2 \lambda^2 \theta^2 \Delta}{2^9 \ln 2 \pi^2 R^2} \eta$$

from Hardy,

$$\eta = 0.38 C_n^2 \lambda^{-1/3}$$

simplifying,

$$C_n^2 = 4.061 \frac{P_r R^2}{P_t R_G \left(\frac{D}{R}\right)}$$

where (in SI units)  $P_r$  is the received power,  $P_t$  the transmitted power,  $G$  the antenna gain,  $\lambda$  the radar wavelength,  $\theta$  the antenna 3-dB half-power beamwidth,  $\Delta$  the radar range resolution,  $R$  the radar range,  $R_G(D/R)$  the antenna autocorrelation function (after Chadwick, 1978), and  $\eta$  the radar cross section per unit volume. An additional term, not included here, is used to convert  $P_r$  in Watts to "FFT units." This term must be applied to take into account the significant amount of computer processing gains (approximately 40 dB). A similar derivation is applied to calibrate in the cases of hydrometeor backscatter to obtain dBZ units.

A  $C_n^2$  value is calculated for each of the 1024 range cells every acquisition cycle and immediately plotted as a color pixel on the high resolution color printer. The range gates are plotted one on top of another to give a continuously flowing, high resolution, sixteen-color picture of the atmospheric turbulence flowing directly over the radar.

#### 4. DISCUSSION OF DATA

Two slides were selected to show the resolution of the radar and the enormous variability of atmospheric structure. [Author's note: these grey-scale images do not do the radar justice and much is lost in the color-to-grey translation]. Rather than attempt to duplicate the color scale in grey (so that dark shades would be proportional to low backscatter and lighter shades to high backscatter), the color slides were converted so that the grey shades are "wrapped around" the color scale. This provided for a much more detailed, if not quantitative picture for this proceeding. (Please view the data at the poster session or contact the authors to see the calibrated color data).

Figure 1 shows a now often seen turbulent daytime mixed layer. Time runs right to left and represents about forty minutes starting at 14:51 MDT August 26, 1992. The data starts at ground level on the vertical axis extending to 2200 meters in two meter resolution. The smoother looking layered patterns are atmospheric structure while the single streaks and points are insects. The top atmospheric layer is believed to be the capping inversion.

Figure 2 shows a Kelvin-Helmholtz structure. The "braid" like event can occur during wind shear and represents the shear and interplay of energies from two different air masses. The time is also right to left representing about twenty-five minutes. Height is again represented vertically running from 1700 to 2200 meters, once again in two meter resolution.



Figure 2. Daytime planetary boundary layer as seen by the ARL FM-CW radar.

## 5. DATA APPLICATIONS

The ARL FM-CW radar owes its existence to the directed energy effort of a few years ago where this data would of been a requirement for high energy weapons research. Current applications have focused on basic planetary boundary layer research. Future uses of the data include use for communications research (detection of ducting layers, forward propagation studies), target detection (also ducting layers, use of the FM-CW radar high sensitivity), diffusion/dispersion (mixed-layer depth and other PBL capping structures), the effect of  $C_n^2$  on other high resolution target detection radars,  $C_n^2$  quantification for laser and other electro-optical applications, possible use for studying CAT, microburst, wind shear and other aviation applications including unmanned fixed wing reconnaissance vehicles, support for other PBL instrumentation, validation of PBL models, and research into hydrometeor events (icing, hail, rain, clouds etc).



Figure 3. Kelvin-Helmholtz waves seen by the ARL FM-CW radar.

## REFERENCES

- Atlas, D. editor, 1990: Radar in Meteorology: Battan Memorial and 40th Anniversary Radar Meteorology Conference, AMS, Boston, MA.
- Chadwick, R. B., Moran, K. P., Morrison, G. E., 1978: "Measurements Toward a  $C_n^2$  Climatology," *18th Conference on Radar Meteorology*, AMS, Atlanta, March 28-31.
- Chadwick, R. B., Moran, K. P., Strauch, R. G., Morrison, G. E., Campbell, W. C., 1976: "A New Radar for Measuring Winds," *Bull. of the AMS*, 57, 9, 1120-1125.
- Chadwick, R. B., Gossard, E. E., 1986: "Radar Probing and Measurement of the Planetary Boundary Layer," from Probing the Atmospheric Boundary Layer, Lenschow, D. editor, AMS, pp 163-182.
- Gossard, E. E., Jensen, D. R., Richter, J. H., 1971: "An Analytical Study of Tropospheric Structure as Seen by High-Resolution Radar," *J. Atmos. Sci.*, 28, 794-807.
- Hardy, K. R., Atlas, D., Glover, K. H., 1966: "Multiwavelength Backscatter from the Clear Atmosphere," *J. of Geoph. Res.*, 71, 6, 1537-1552.
- Hines, J. R., Eaton, F. D., McLaughlin, S. A., Hatch, W., 1992: "The U.S. Army Atmospheric Profiler Research Facility: Overview and Preliminary Intercomparison," in *Proceedings of the Battlefield Atmospherics Conference*, Army Research Laboratory, Battlefield Environment Directorate, White Sands Missile Range, New Mexico, 88002-5501.
- Richter, J. H., Jensen, D. R., Noonkester, V. R., Konrad, T. G., Arnold, A., Rowland, J. R., 1974: "Clear air convection: A close look at its evolution and structure," *Geophys. Res. Lett.*, 1, 173-176.
- Richter, J. H., 1969: "High Resolution Tropospheric Radar Sounding," *Radio Science*, 4, 12, 1261-1268.
- Strauch, R. G., 1976: "Theory and Application of the FM-CW Doppler Radar," *Phd thesis, Univ. of Colorado*.
- Tatarskii, V. I., 1971: "The Effects of the Turbulent Atmosphere on Wave Propagation," *NTIS TT-68-50464*, Natl. Tech. Inf. Serv., Springfield, Va.

## TACTICAL WEATHER SUPPORT CONCEPT FOR AUSTERE FIELD OPERATIONS

John R. Elrick  
Battlefield Environment Directorate\*  
U.S. Army Research Laboratory  
White Sands Missile Range, New Mexico 88002-5501, USA

Phillip R. Raihl  
New Mexico State University  
Las Cruces, New Mexico 88003-0002, USA

MSgt Timothy J. Smith  
Operating Location N, Headquarters Air Weather Service  
White Sands Missile Range, New Mexico 88002-5501, USA

### ABSTRACT

The U.S. Army continually needs accurate, real-time weather support to its operations forces in peacetime and in times of conflict in austere locations worldwide. Highly mobile forces must be able to react to changing weather conditions and, if possible, use the weather as a force multiplier. The rapid mobility capabilities of the modern Army were clearly demonstrated in the Persian Gulf Operation Desert Shield and subsequent Operation Desert Storm. Modern advances in satellite meteorology, meteorological sensors, and electronics have made this real-time or near real-time weather support a reality. The portable weather workstation demonstrated here, designated the Portable Weather Testbed (PWTB), has the potential to satisfy Army needs now and in the future. The PWTB can be carried by two soldiers in a backpack configuration and is small enough to be easily loaded aboard a tactical transport aircraft occupying less than 25 ft<sup>3</sup>. The unit consists of two distinct subsystems: an antenna assembly and a computer workstation. The antenna assembly can receive several forms of imagery and information from automatic picture transmission to processed weather facsimile products to high-frequency radio transmission of weather text and analyzed chart data. The system operates under a multitasking PC multi-operational system environment. A dedicated weather sensor is with the system to collect local weather conditions. The system can transfer information to other locations via a dedicated transceiver system. Peacetime applications include field data collection for research or forecasting activities and agricultural meteorology.

---

\*formerly U.S. Army Atmospheric Sciences Laboratory

## 1. INTRODUCTION

The U.S. Army Research Laboratory, Battlefield Environment Directorate, has procured a second-generation, portable weather workstation that has the potential for real-time support to highly mobile military forces in peacetime and in times of conflict. The system was engineered and developed by Lone Eagle Systems Company of Omaha, Nebraska. It will receive and process automatic picture transmission (APT) imagery, weather facsimile (WEFAX) products, and high-frequency (HF) radio transmissions from regional broadcasting stations. The system is designated the Portable Weather Testbed (PWTB). The PWTB consists of two main systems: the antenna assembly and the computer workstation. Timely weather information, used properly, can be used for effective mission planning as well as a force multiplier.

## 2. HARDWARE

### 2.1 ANTENNA ASSEMBLY

The antenna assembly consists of three antenna groups that are collocated and integrated to receive weather data. The first group is composed of two separate antennas for receipt of APT imagery from polar-orbiting satellites: one antenna is a Quadrifilar used for garrison or semifixed operations and the other is a more portable, rugged sierra plane antenna for tactical use. The second antenna group is a dual-boom loop Yagi antenna consisting of two 6-ft rods with focusing elements along their length for receipt of processed weather facsimile data in the form of weather charts and satellite pictures from geosynchronous satellites. The last antenna is a long-wire, inverted "V" copper wire antenna for receipt of HF data, including plain text bulletins and advisories as well as current weather observations and forecasts. This weather information provides qualified meteorologists with the information to make limited forecasts of the weather in a given area of interest. After receipt, data are transferred to a computer workstation for processing and viewing.

### 2.2 WORKSTATION UNIT

The PWTB computer workstation is made up of several components. The basic unit is a 386-based IBM compatible computer with a 387-mathematics coprocessor. The system is primarily mouse driven in a PC-MOS multitasking operating environment. The display terminal for garrison use or research purposes is a super video graphics array (SVGA) with a 1024- by 768-pixel resolution on a Mitsubishi 12-in monitor; a 5-in television monitor is included with the system for the rapid-deployment mode of tactical operations. Satellite data collection is accomplished by redundant Quorum receiver units. An HF transceiver collects and transmits data from indigenous sources and local sensors and provides WWV information for accurate system timing.

### 2.3 OTHER HARDWARE

The PWTB has a dedicated weather sensor to measure temperature, relative humidity, pressure, wind direction and windspeed, and rainfall accumulation. The HF radio can send locally collected data to other locations automatically.



or on demand. The total system weight is about 200 lb packaged in rugged shipping cases. The "tactical" version of the system occupies about 25 ft<sup>3</sup> of space. The system can be loaded on two backpack frames and easily carried for short distances. The primary mode of transport, however, will be by U.S. Army utility vehicles or tactical transport aircraft. A solid-state cooling system is used to maintain system temperature integrity in austere environments. The PWTB can automatically operate on commercial power worldwide or on system solar cells. A Kodak Diconic 150 inkjet printer allows limited hard copy printout capabilities.

### 3. SUMMARY

The Battlefield Environment Directorate continues to exploit emerging computer and electronic technology in its research and development efforts to provide viable weather support to highly mobile forces. The need for mobility has been shown in the effective execution of recent operations in the Persian Gulf where superior U.S. technology was instrumental in the swift defeat of the Iraqi Army. In addition to its obvious military application, the PWTB could be used by operational and research meteorologists in any number of disciplines where portability and reliability are important in an austere environment. There are many potential applications for the use of this system in peacetime.



# ACOUSTIC SOURCE GENERATION SYSTEM

by

Jeff Balding and John M. Noble  
Battlefield Environment Directorate\*  
U.S. Army Research Laboratory  
White Sands Missile Range, NM 88002-5501

## ABSTRACT

U.S. Army Atmospheric Sciences Laboratory is currently building a pneumatic loudspeaker system. The Acoustic Source Generation System (ASGS) is an air-driven horn capable of the production of sound in a frequency range of 10 to 630 Hz with a maximum output ability of 20,000 acoustic watts or 163 decibels. The ASGS will be able to generate sufficient sound levels for the testing of the atmospheric effects on the acoustic propagation of sources up to 10 km away. This will greatly exceed the propagation ability of any previous stable outdoor sound source in the United States. This capability will allow the validation of acoustic propagation models used in creating accurate acoustic decision aids for tactically important ranges.

## 1. INTRODUCTION

The horn that has been developed is a very large horn capable of producing intense, low frequency sounds. Among the horn's physical dimensions are an overall length of 56 ft., a throat diameter of 4 inches and mouth diameter of 8 ft. Its ability to produce sound is equally as large; 20 acoustic kilowatts of power in the 10 Hz to 630 Hz frequency range. To produce the energy needed to drive the horn, a six-cylinder diesel engine turns a rotary compression blower. The air mass is then stabilized and cooled before being modulated at the horn's throat.

## 2. SYSTEM DESCRIPTION

### 2.1 DESIGN CONSIDERATIONS

Several design criteria were specified before the full design was calculated. One such criteria was that the horn needed to have a flat frequency response down to 10 Hz and up to 500 Hz.

---

\* Formerly U.S. Army Atmospheric Sciences Laboratory.

Another criteria was that the horn need not have permits to be transported between locations on a flatbed trailer. The horn was also specified to operate up to 163 dB. These factors alone almost completely specified the design.

The frequency range being flat from 10 Hz to 500 Hz dictated that the horn be an exponential one. A conical horn rolls off at low frequencies very rapidly. The largest possible mouth diameter would also be the choice since the flattest frequency response is obtained from the larger mouth diameters. The 10 Hz low frequency specification dictated how long the horn needed to be; the longer the horn is; the lower the frequency response is. The longest possible flatbed trailer was located and found to be 65 ft. long. Enough room was needed for the horn driver section and electronics. Nine feet were determined to be all that was necessary. That left a length of 56 ft. for the horn.

In order to not need permits on the highways the mouth diameter was set at 8 ft. This would allow the horn to sit on a flatbed trailer with no side overhang.

The air modulator chosen was determined because of its low frequency response and the acoustical power required. The throughput diameter of the modulator that could do this is four inches.

This set the throat diameter at four inches, the mouth diameter at eight feet, and the horn length at 56 ft. These three dimensions in an exponential horn format determine the exact dimensions of the entire horn.

To produce enough acoustical power at the modulator, a certain air flow at a certain pressure was needed. An air storage system was ruled out of the possibility because the storage tank necessary to hold enough air to operate the system for more than a minute wouldn't fit on a flatbed trailer. So a system that generated its own air as it needed was the alternative. An air compressor powered by a motor was chosen as the driver system. Since the air flow and pressure was known, this determined what size the compressor needed to be. The size of motor needed to power the compressor was also known now since each compressor has its own horsepower curve. In this case a 150 horsepower motor was needed.

Two choices of motors exist to power the compressor; a piston engine or an electrical motor. The electrical motor was ruled out because the cost of the controller to vary the speed, the electrical generator and the motor was too much. Thus the piston engine was chosen.

## **2.2 SYSTEM COMPONENTS**

Once the overall design scheme was chosen and calculated, the detailed components were determined and engineered. The following sections detail the various subsystems.

### **2.2.1 Air Supply System**

The first component in the system provides the major energy supply. As is the case of the musical instrument type of horn, a moving, compressed air mass is used to "blow" the horn.

But in order to make sounds with this horn something larger than a set of lungs is necessary. The solution used is a rotary lobed blower powered by a diesel piston engine.

The air supply system's diesel motor and rotary blower are mounted side-by-side next to each other and attached by a 2 inch rubber belt. The diesel motor is a standard six-cylinder John Deere 150 horsepower model that has been used in farm applications for years. The German built blower/compressor is also a standard AERZEN model that produces 2250 scfm of air at 11.5 psig.

### **2.2.2 Stabilization and Cooling**

The air exiting the supply system is a modulated or pulsed stream that is very hot due to the increased pressure. Both the modulation and the increased temperature have a negative effect on the system components that follow in the system chain. The modulated air tends to vibrate and thus wear out the heat exchanger and voice modulator. The vibrations also make unwanted sound. The increased air temperature destroys the epoxy glue and graphite lubricant on the modulator. Therefore these effects need to be reduced.

To reduce the modulation, or pressure waves in the air stream, a baffled muffler system is used. This component has the effect that a capacitor does in an electrical system. That is, to reduce the higher frequency energy pulses; in this case, the pressure waves. It is quite effective in reducing these pulses from the system.

To decrease the temperature of the air stream requires an air-to-air heat exchanger. This heat exchanger reduces the air temperature from around 280°F to 180°F. This decrease in temperature is enough to stay below the critical point that the modulator can operate at.

In the event of an air flow blockage at some point in the system, an emergency pressure relief valve is opened. The valve is set to open at 40 psig which is the maximum that the modulator can possibly survive. This valve is located between the baffled muffler and the heat exchanger.

### **2.2.3 Modulation System**

Once the air supply is generated, stabilized and cooled, pressure modulation of the air stream is needed to produce audible frequencies. In a typical horn system this is accomplished by a magnet/voice coil arrangement. This system is no different functionally; only the size of the magnet and voice coil are larger. One difference, though, is that the pressure fluctuations aren't generated by a vibrating membrane as in the standard electrical horn. In this system the air stream is pulsed by opening and closing a valve that in effect interrupts the air stream at the required frequency.

The actual modulating device is designed and made by Wyle. Their WAS-3000 air-stream modulator is a commercially available pneumatic valve. This modulator has the capability to produce 30,000 acoustic watts; though only 20,000 acoustic watts will be used for this system. And since it is most efficient at producing lower frequencies, this is a good component for the system.

But since this modulator is used in a higher temperature environment than it was designed to be operated at, it has been modified. The modification to the modulator incorporates a CO<sub>2</sub> injection scheme that will further reduce the temperature of the modulator's internal components. This will reduce heat expansion inside the modulator and, in effect, lengthen the life of the modulator.

To supply the CO<sub>2</sub> a rack which accommodates eight bottles of the gas is used. These bottles are connected to a 40 psig regulator. 6,000 pound insulated lines are connected from the regulator to the modulator to flow the gas into the voice coil area.

#### **2.2.4 Acoustic Horn**

The acoustic horn efficiently couples the modulated internal air stream to the outside environment. Because of the immense proportions of the horn, it is made of fiberglass at least 1 inch thick throughout its body. The total weight of the horn and its mounting hardware is approximately 3 tons (6000 pounds).

The horn is fairly efficient at coupling to the atmosphere. Its frequency response is flat to within 3 dB in its normal frequencies of operation. While this is not good compared to typical speakers, it is good considering how loud the system is.

The fiberglass horn is supported at critical points along the horn's axis to reduce modal oscillations. Such oscillations could destroy the horn if not properly dampened. At these points the fiberglass is about 6 inches thick and there is metal support sheets imbedded into the fiberglass.

#### **2.2.5 System Controller**

Due to the very high sound levels that the system is capable of producing, remote operation of the system is a required option. To control the horn remotely, two computers linked by modem communicate with each other. One computer is located on the trailer near the horn; the other is located remotely away from the system. Functions such as diesel motor engine speed, tape recorder control and modulator power regulation are controlled via computer.

In addition, temperature and pressure sensors are monitored via the computer. These sensors help in determining system degradation and maximum performance limiting conditions.

The acoustic signals that can be made by the horn are varied. Numerous waveforms and tones can be produced from the computer and output through the horn. Pre-recorded sounds can also be played through the horn to simulate various acoustic signals. This allows maximum flexibility of the system.

#### **2.2.6 Operation and Transportation Platform**

The entire system is physically located on the top of a flatbed trailer. The flatbed trailer is a special one that is telescopic. That is, it can be stretched out from its 40 ft. compressed length

to 65 ft. expanded length. This expanded version of the flatbed trailer allows the horn to be entirely placed on the trailer. The horn is located to the rear of the trailer and leaves enough of trailer for the air supply, cooling, modulation and electronic systems. These components are located at the front end of the trailer.

This system is designed to travel the U.S. highways without getting any special permits. So to make it legal during transportation, the trailer must be in its compressed state. To accommodate this requirement, the horn was broken into two 28 ft. sections. The large mouth end of the horn is placed at the rear of the trailer and is permanently attached to the trailer. The smaller throat end of the horn is made to be detached from larger horn section during transportation. During transportation the smaller section is placed side-by-side next to the larger section. A small one ton crane is permanently mounted on the trailer to aid in moving this small section of horn from its transportation position to its operation position and vice versa.

Along with the air stream generation and modulation components, an electrical generator and thermally isolated electronics rack is located on the front of the trailer. All system control electronics are located in the rack. The generator is capable of providing enough power to drive all the electronic components, the air-to-air heat exchanger and the diesel motor.

### **3. SYSTEM OPERATION**

#### **3.1 POTENTIAL USES FOR THE HORN**

This horn has several unique advantages to make it a very useful research tool. One factor is that its acoustic output is very high. Another is that it is a mobile system. And the last one is that it can reproduce sounds from 10 Hz to 630 Hz.

The study of atmospheric effects on sound propagation is a very likely candidate. Long path lengths between the horn and a microphone are possible because the horn is very loud. The source signal is very well characterized and any degradation of the signal at a distance is due to atmospheric effects. Propagation models can then be fine tuned using the data acquired from these studies. From this fine tuning, better acoustic tactical decision aids can be provided.

Simulation of various military and civilian noise sources can be simulated. This use of this horn for extremely low frequency operation is very useful in reproduction of helicopters and other very low frequency signals.

#### **3.2 SAFETY AND ENVIRONMENTAL CONSIDERATIONS**

The use of this horn at its maximum levels creates some safety and environmental concerns. Safe operation of the horn requires the use of hearing protection and erection of safety zones. In these zones various hearing protection combinations are required. The environmental concerns are being addressed at this time; though no restrictions are expected.

#### 4. SUMMARY

In summary, a 56 ft. long horn has been acquired by the Battlefield Environment Directorate. The horn is located on a mobile flatbed trailer. It is powered by a diesel motor and rotary blower. The air-stream is stabilized and cooled. The air is directed through a pneumatic air-stream valve modulator which generates sound levels at 140 dB and above and frequencies from 10 Hz to 630 Hz. The horn will be used for field tests studying acoustic signal propagation. This will in turn provide better acoustic decision aids.

#### ACKNOWLEDGEMENTS

The authors would like to thank the following for each contributing to the procurement of this impressive system: Mike White and the people at U.S. Army CERL without whom the money would never have found its destination, Jim Sabatier and Hank Bass of the University of Mississippi's National Center for Physical Acoustics (along with all the others there) for creation of this monster, and Bob McPeck of the U.S. Army Research Laboratory BED for getting the ball rolling.

#### REFERENCES

- Noble, John M., 1991: Acoustic Propagation in the Atmosphere using the Scanning Fast Field Program. In Proceedings of the 1991 Battlefield Atmospheric Conference, U.S. Army Atmospheric Sciences Laboratory, White Sands Missile Range, NM 88002-5501.
- Sabatier, James M., 1991: Pneumatic Loudspeaker Acoustic Generation System. NCPA Report JMS91-01, National Center for Physical Acoustics, University, MS 38677.



THE MOBILE ATMOSPHERIC SPECTROMETER: ENHANCEMENTS IN DATA

ACQUISITION AND ANALYSIS FOR SMOKE WEEK XIV

Frank T. Kantrowitz  
Battlefield Environment Directorate\*  
U.S. Army Research Laboratory  
White Sands Missile Range, New Mexico 88002-5501, USA

William M. Gutman, Troy D. Gammill  
Physical Science Laboratory  
New Mexico State University  
Las Cruces, New Mexico 88003, USA

Jerry V. B. Rice  
Science and Technology Corporation  
Las Cruces, New Mexico 88001, USA

ABSTRACT

Since the completion of SMOKE Week XIII in May 1991, significant enhancements have been incorporated into the Battlefield Environment Directorate's Mobile Atmospheric Spectrometer. In preparation for SMOKE Week XIV, a high-speed parallel spectrometer-to-computer interface was installed. Although this interface arrived too late to optimize fully, the increase in spectrometer performance was impressive. Rather than slewing on-source and off-source to separate blackbody radiance from path radiance (as was done at SMOKE Week XIII), a mechanically chopped source was used to increase the data acquisition rate and maintain the same line of sight. With these two enhancements, the number of spectra collected at SMOKE Week XIV increased by a factor of 6.

With more than 9,000 spectra collected, the next significant task was data reduction and analysis. In the past, the only means a researcher had to view the data were commercial plot packages where a few spectra could be observed. A decision was made that with such a large volume of data, a new approach was required. This requirement evolved into a three-dimensional (3-D) spectral movie that displays transmittance (or radiance) versus spatial frequency as a function of time. In this manner, complete trials incorporating hundreds of spectra may be viewed. Use of this technique will be demonstrated in a short time-series movie, "Obscurants Through the Eye of a Spectrometer," at the 1992 Battlefield Atmospheric Conference.

---

\*formerly U.S. Army Atmospheric Sciences Laboratory

## 1. BACKGROUND

Obscurant tests have traditionally placed a heavy emphasis on the use of broadband transmissometers in the characterization of optical properties of test materials. Broadband transmissometry has many attractive features, including high temporal resolution, relatively simple instrumentation, and relatively small data storage requirements.

Unfortunately, it is impossible to match a transmissometer response function to the multitude of electro-optical systems that must contend with optically obscured battlefield environments. The inherent broadband nature of many transmissometers, therefore, severely limits the usefulness of such data. Researchers using such data are at a risk of formulating erroneous results.

Transmittance measurements made with the Battlefield Environment Directorate's (BED) Mobile Atmospheric Spectrometer (MAS) overcome this shortcoming of the broadband instruments (Gutman et al., 1991). While the traditional transmissometer can obtain only one transmittance data point per spectral window per time interval, a Fourier transform spectrometer (FTS) can provide hundreds of transmittance data points per spectral window per time interval. High-resolution FTS obscurant transmittance spectra can be convolved with ANY system response function desired and thereby remove the uncertainty that accompanies the comparison of transmissometers with different response functions. The result can be a more accurate prediction of the system performance.

The primary goal of the MAS support of Smoke Week XIV was to demonstrate the utility of spectrally resolved measurements in the obscurant test setting. The transmittance and radiance spectra of the obscurants and munitions have been made available to the scientific community through the Atmospheric Aerosols and Optics Data Library (AAODL). Figure 1 depicts the MAS.

## 2. ENHANCEMENTS IN DATA ACQUISITION

Significant enhancements were employed at Smoke Week XIV (Kantrowitz et al., in preparation). At Smoke Week XIII the spectrometer and host computer communicated via a serial interface. Before the system was shipped to Eglin Air Force Base for Smoke Week XIV, a high-speed parallel interface was installed. Due to the lack of time to become familiar with this upgrade, the system was not optimized to its fullest extent. Even so, the increase in data acquisition rates was exceptional. With familiarization to this upgrade, higher data rates are anticipated at future tests.

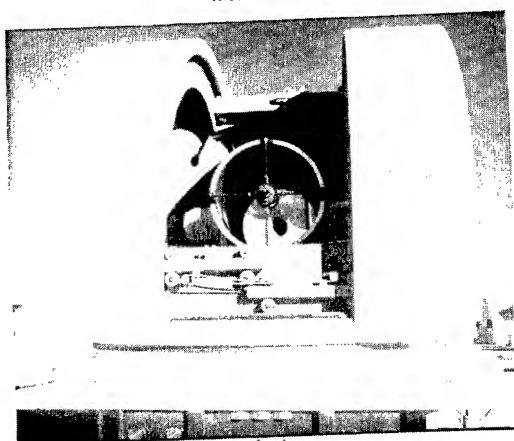
A second enhancement dealt with the method for obtaining source and path radiance spectra. During Smoke Week XIII the telescope had to cycle from on-source to 0.5 degree off-source repeatedly. This not only changed the background, but it also required a relatively great period of time. For Smoke Week XIV a source chopper was employed. Communications from the host computer to the chopper were accomplished via communications wire.

While transmittance measurements of obscurants were obtained at both Smoke Weeks XIII and XIV, no munition radiance measurements were made at Smoke Week III. Because of the higher data acquisition rates at Smoke Week XIV,

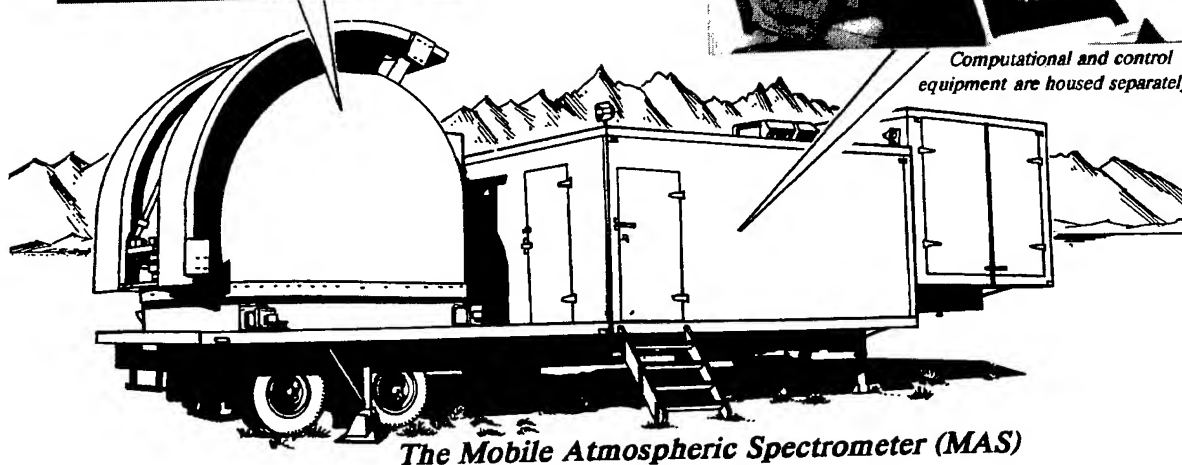
radiance measurements of munition detonations were, to some extent, successful.

Rather than employing the multipath transmissometer sources as was done at Smoke Week XIII, a 60-in searchlight with a 1000 °C blackbody source was used.

*The dome contains the Fourier spectrometer, telescope, and other optical instruments.*



*Computational and control equipment are housed separately.*



*The Mobile Atmospheric Spectrometer (MAS)*

Figure 1. Mobile Atmospheric Spectrometer (MAS).

TABLE 1. A COMPARISON OF SMOKE WEEK XIII AND XIV DATA		
	Smoke Week XIII	Smoke Week XIV
Approx. raw data (megabytes):	50	450
Spectral data acquisition (seconds):	11	3.0 (1)
S/N ratio (2 - 2.5 $\mu\text{m}$ ):	+/- 8 %	+/- 3 %
S/N ratio (3 - 5 $\mu\text{m}$ ):	+/- 3 %	+/- 1 %
S/N ratio (8 - 12 $\mu\text{m}$ ):	+/- 2 %	+/- 0.5 - 0.8 %
Number of trials (participation)	111	141
Number of transmittance spectra:	1471	7369
Number of radiance spectra:	0	1649 (2)
Total spectra:	1471	9018

(1) Without optimization of spectrometer upgrade.

(2) For transient event trials, only 1 or 2 spectra contain data.

### 3. METHODOLOGY

The transmittance of a sample of material at radiation frequency  $\vartheta$  is defined to be the ratio of the radiant power at frequency  $\vartheta$  exiting the material to the radiant power at that frequency incident upon the material

$$T(\vartheta) = \frac{I(\vartheta)}{I_o(\vartheta)}$$

For an obscurant measurement, what is usually required is not the absolute transmittance of the entire path but rather the transmittance through the path with the obscurant relative to the clear air path. The spreading factors and the instrument response function remain unchanged when comparing the path with the obscurant to the path without the obscurant, and so a simpler measurement methodology can be applied. Without path radiance and background effects, the relative transmittance of the obscurant is the point-by-point ratio of the obscurant spectrum to the clear air spectrum. Path radiance and background radiation may contaminate the raw signals and thus must be removed.

$$I_o(\vartheta) = S_{\text{clear}} - S_{\text{bkg}}$$

and

$$I(\vartheta) = S_{\text{obs}} - S_{\text{path}};$$

therefore,

$$T(\theta) = \frac{S_{\text{obs}} - S_{\text{path}}}{S_{\text{clear}} - S_{\text{bkg}}}. \quad (1)$$

All the quantities on the right side of eq. (1) are functions of  $\theta$ .

An effective measurement methodology is to measure these four quantities over as short an interval as practical. It is especially important for the obscurant and path radiance data to be close together in time because of the transient nature of the typical obscurant cloud. Clear air data may be acquired either before or after the obscurant is present; but, in general, pretrial clear air data are less likely to be contaminated by residual obscurant that may not be obvious to an observer. In repetitive, alternating sequence, obscurant spectra and path radiance spectra are collected. Path radiance spectra can be obtained either by blocking the source or by pointing the collecting telescope slightly off the source. The latter alternative was used at Smoke Week XIII. To enhance the data acquisition rates, a source chopper was incorporated into the system for Smoke Week XIV.

#### 4. INSTRUMENTATION

The key components of the MAS for support of the activities at Smoke Week XIV were the FTS and the 31-in Coudé telescope.

##### 4.1 FOURIER TRANSFORM SPECTROMETER CONFIGURATION

The MAS FTS consists of a scanning Michelson interferometer with associated optics and control electronics and a dedicated computer system. Depending upon the detector, beamsplitter, and source that are in use, the spectrometer can cover a segment of the spectral region from about 700 to 20,000  $\text{cm}^{-1}$  (0.5 to 14  $\mu\text{m}$ ).

Although the instrument is capable of spectral resolution as high as 0.04  $\text{cm}^{-1}$ , a resolution of 4  $\text{cm}^{-1}$  was used during Smoke Week XIV. Very high resolution is not needed, and indeed not practical, for most obscurant transmittance measurements because of time resolution considerations.

The Fourier spectrometer was configured with a potassium bromide (KBr) substrate beamsplitter with a mercury-cadmium telluride (MCT) detector. The useful spectral coverage was about 800 to 5000  $\text{cm}^{-1}$  (2 to 12.5  $\mu\text{m}$ ). The instrument was operated at a spectral resolution of 4  $\text{cm}^{-1}$ , so the point spacing in the spectra was 2  $\text{cm}^{-1}$ .

There are 234 data points in the 800- to 1250- $\text{cm}^{-1}$  spectral region, 114 points in the 2020- to 2240- $\text{cm}^{-1}$  region, 316 points in the 2390- to 3000- $\text{cm}^{-1}$  region, and 492 points in the 4050- to 5000- $\text{cm}^{-1}$  spectral region.

A factor in choosing the instrument configuration was that a KBr beamsplitter was clearly the best choice for most mid-infrared work, but KBr is hygroscopic. Great care must be exercised to avoid damage during humid weather and especially during periods of precipitation. Since a KBr

beamsplitter was damaged beyond use during a period of high humidity during Smoke Week XIII, both a replacement KBr beamsplitter and a moisture-insensitive ZnSe beamsplitter were in the MAS inventory for Smoke Week XIV. The KBr beamsplitter was used during all tests because the test site experienced good weather and we noted that the ZnSe beamsplitter was insensitive to radiation shorter than 3  $\mu\text{m}$ .

Whenever the time between trials permitted, the data acquisition sequence for each trial included high signal-to-noise ratio clear air source and clear air background data. For all clear air data, 100 instrument scans were coadded. Each interferogram required about 35 s to acquire, with another 2.3 s required for transfer and storage. For most trials, clear air data acquisition was initiated at about T - 3 min, and two complete cycles were performed. Whenever time permitted, a similar posttest clear air acquisition sequence was carried out.

Obscurant and path radiance interferograms were obtained by coaddition of two scans. Coaddition of two scans required 0.7 s. Transfer and storage again required about 2.3 s per interferogram. Each interferogram, therefore, required 3 s to acquire and store. Each complete measurement cycle of obscurant and path radiance interferograms required 6 s.

Coaddition of multiple instrument scans serves two important functions:

1. It improves the signal-to-noise ratio of the interferograms and the resulting spectra (the signal-to-noise ratio increases proportionally with the square root of the number of instrument scans coadded).
2. It reduces the signal variation that results from atmospheric turbulence. In some cases, as much as  $\pm 10$  percent variation in the clear air signal was observed over a short period as a result of turbulence.

The usual MAS sources are a quartz-halogen lamp and a temperature controlled blackbody that can reach 1000  $^{\circ}\text{C}$ . In either case, the radiation is collimated with a modified searchlight. The blackbody is the source of choice for most of the mid-infrared region, while the lamp provides better performance for wavelengths shorter than 2  $\mu\text{m}$ . Therefore, the near-infrared and mid-infrared regions require different sources, and only one region can be optimized at a time.

#### 4.2 COUDÉ TELESCOPE

The MAS Coudé-mounted telescope is a classical Cassegrain telescope consisting of a 31-in diameter parabolic primary and a 6-in diameter hyperbolic secondary mirror. Segments of the optical path are coaxial with the elevation and azimuth rotational axes of the telescope so the beam position on the optical bench is invariant with respect to the pointing.

The telescope uses a sophisticated servo loop control system. The angular resolution is 1.24 arc-s. A desktop computer provides the user interface. A control program has been written to translate simplified commands into

valid telescope instructions. The telescope control program provides the capability to fine-tune the pointing to optimize the signal. Once the correct coordinates have been found, it is very easy to return to a given position with high precision.

## 5. DATA REDUCTION

All data reduction was performed using programs written in Fortran, and MS-DOS-based computers acted as hosts. Before departure for Smoke Week XIV, batch-oriented data analysis programs were produced and fine-tuned.

Because data acquisition required only 0.7 s, a data file can be thought of as a snapshot of the changing spectrum at the time listed in the file header. Those spectral intervals in which atmospheric opacity significantly impaired the ability to retrieve the obscurant transmittance are not included in the files, and breaks in the listings are used to delineate the resulting discontinuities in the spectral coverage.

## 6. ANALYSIS ENHANCEMENTS: THREE-DIMENSIONAL SPECTROSCOPIC MOVIE

With more than 9,000 spectra collected, the next significant task was data analysis. In the past, the only means a researcher had to view the data were commercial plot packages where a few spectra could be displayed. A decision was made that with such a large volume of data a new approach was required. This requirement evolved into a three-dimensional (3-D) spectral movie that displays transmittance (or radiance) versus spatial frequency as a function of time. In this manner, complete trials incorporating hundreds of spectra may be viewed. Use of this technique will be demonstrated in a short time-series movie, "Obscurants Through the Eye of a Spectrometer," at the 1992 Battlefield Atmospherics Conference. Preliminary 3-D displays exhibit a wealth of detail. But, more importantly, they give the researcher an appreciation of the spectral dynamics of obscurants.

A version of the program under development will permit the aspect angle to change by using a mouse. The movie may be paused at any time and reversed, or a particular 3-D spectrum may be selected and displayed as a two-dimensional (2-D) plot. From this 2-D mode, the user may use a zoom feature.

## 7. EXAMPLE SPECTRA

MAS spectra provide useful insight into the behavior of the obscurant materials. Frequency dependence of the smoke transmittance that cannot be observed with broadband transmissometers is readily apparent in the spectra.

In general, in the mid-infrared, some materials exhibit only a smooth fall-off with increasing frequency. Others, however, exhibit a wealth of interesting detail. Among the more interesting materials are silica, kaolin, and red and white phosphorus. Note the dynamics of the strong silica absorption feature in fig. 2. Some of the fog oil spectra also exhibit the well-known C-H stretch vibrational-rotational band at about  $2800\text{ cm}^{-1}$ .

Radiance spectra of munitions and a flare were taken at Smoke Week XIV. In fig. 3 note the rapid decay of a small emission feature near  $1110\text{ cm}^{-1}$ . Also

note red spike ( $2240\text{ cm}^{-1}$ ) and blue spike ( $2390\text{ cm}^{-1}$ ) due to heated atmospheric  $\text{CO}_2$ . The development of two small emission features at  $4275$  and  $4530\text{ cm}^{-1}$  is also of interest, though not understood at this time. These data have twice the temporal resolution since the blackbody source was only observed before and after a trial.

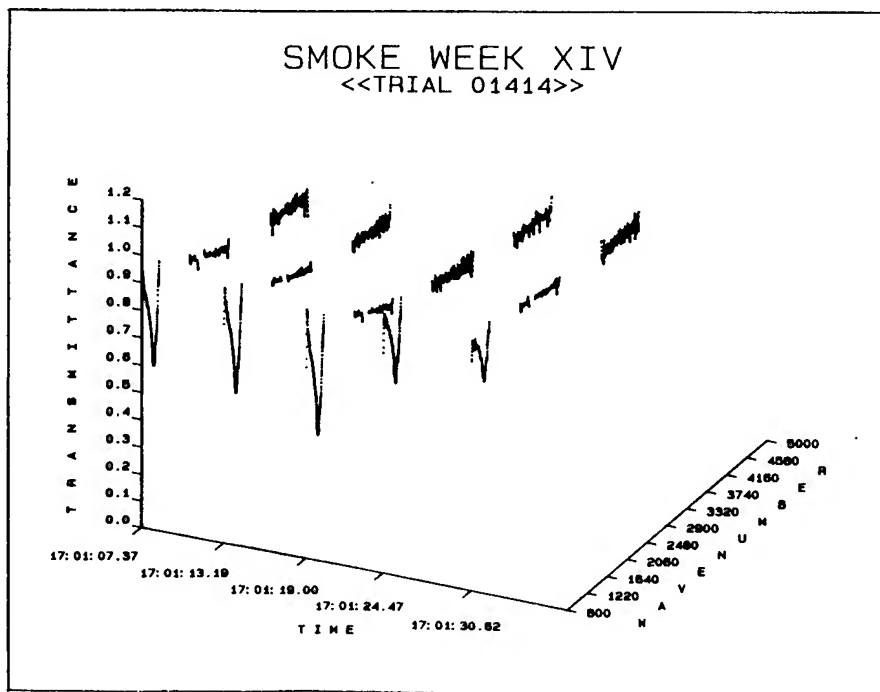


Figure 2. Silica spectra as a function of time.

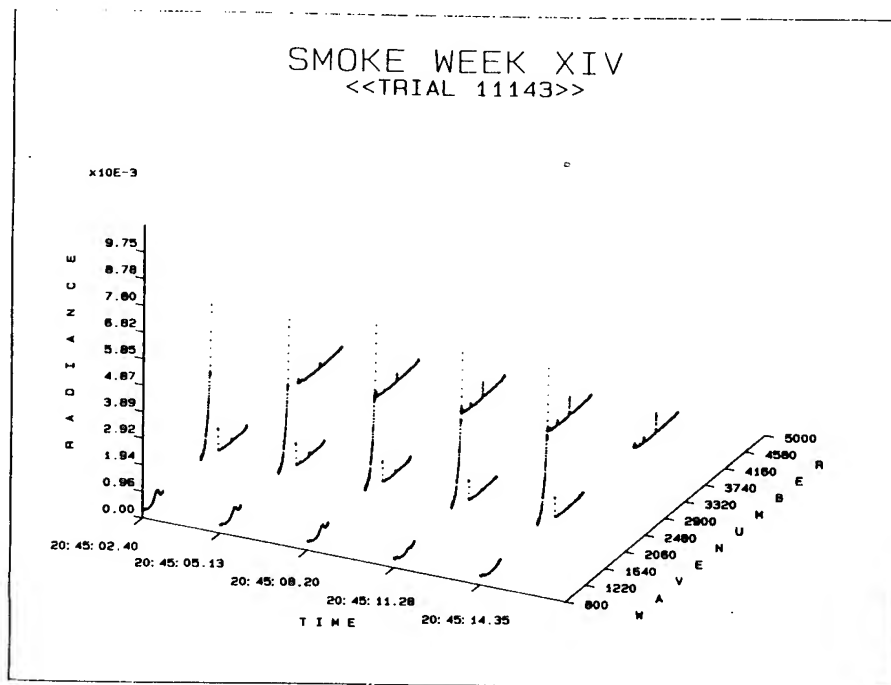


Figure 3. Radiance spectra of a flare.



## 8. ERRORS AND UNCERTAINTIES

Several observations should be made about the uncertainty in the transmittance values and the noise in the spectra. Often, the level of the baseline of the spectra is uncertain to as high as  $\pm 0.1$  in transmittance. This uncertainty resulted from atmospheric turbulence. Turbulence caused beam spread and wander that were observed as fluctuations in the intensity of the radiation from the source. There was a clear correlation between the interferogram centerburst amplitude and the turbulence level. For diagnostic purposes, the interferogram was frequently displayed in real time during test preparations, and the turbulence could be assessed by observing the source downrange.

The signal-to-noise ratio of the spectra varies over a wide range. Within a given spectrum, the signal-to-noise ratio changes across the bandwidth. For the mid-infrared spectra, the lowest noise occurs from 800 to 1200  $\text{cm}^{-1}$ . The regions of lowest noise correspond to the best response regions of the particular spectrometer configuration (beamsplitter and detector). In all but the lowest noise intervals of the spectra, a small degree of smoothing was applied to the data. A five-point quadratic least squares technique was used. Each point was replaced by the value of a second degree least squares polynomial fit to a subset of the points consisting of itself and two points on either side. Smoothing reduces high frequency noise, but it also reduces the spectral resolution somewhat. The smoothing applied here reduced the spectral resolution by about 8 percent, and so did not significantly degrade the spectra. Compared with other common smoothing techniques, the least squares method has minimal detrimental effects on the shape of spectral features.

Near the boundaries of the recognized atmospheric transmittance windows, the signal-to-noise ratio tends to deteriorate. The reason for the deterioration is that as the atmosphere becomes opaque because of absorption by water vapor or carbon dioxide, the right side of eq. (1) approaches indeterminacy, and a small change in the value in going from one point to the next may result in a large change in the apparent transmittance. The limits on the useful regions were determined by examining the noise in the plot of a full spectrum. On a day with high absolute atmospheric water content, the useful region bordering a water absorption band will be smaller compared with a drier day. Likewise, spectra collected over a longer atmospheric path will provide smaller useful intervals. There are spectra in the full data set in which the signal-to-noise ratio still deteriorates at the ends of some of the plotted intervals. Likewise, the plotted intervals could undoubtedly have been expanded in other spectra. The spectral intervals that were included in the reduced mid-infrared data files were:

800	-	1250 $\text{cm}^{-1}$	(8.000	-	12.500 $\mu\text{m}$ )
2020	-	2240 $\text{cm}^{-1}$	(4.464	-	4.950 $\mu\text{m}$ )
2390	-	3000 $\text{cm}^{-1}$	(3.333	-	4.184 $\mu\text{m}$ )
4050	-	5000 $\text{cm}^{-1}$	(2.000	-	2.469 $\mu\text{m}$ )

## 9. RESULTS

All of the reduced spectra have been provided to the managers of the AAODL database. Each spectrum was provided in two column, comma delimited, ASCII format. The first column is the spatial frequency (wave number) in centimeters<sup>-1</sup> of each point, and the second column is the transmittance (%) or radiance (watts/cm<sup>2</sup>/steradian/cm<sup>-1</sup>).

Among the enhancements employed at Smoke Week XIV were a high-speed parallel spectrometer-to-computer interface and a mechanical chopper at the blackbody source. While these enhancements were not fully optimized, they accounted for a dramatic increase in data acquisition rate and the total number of spectra obtained.

With more than 9,000 spectra collected, analysis is a significant task. Typically, a researcher uses commercial plot packages with which only a few spectra can be displayed. Because of the large volume of data a new approach was required. This requirement evolved into a 3-D spectral movie that displays transmittance (or radiance) versus spatial frequency as a function of time. In this manner, complete trials incorporating hundreds of spectra may be viewed.

Work continues toward the goal of fully optimizing the high-speed spectrometer interface. We hope that there will be a second spectrometer in the MAS inventory by Smoke Week XV. This capability will provide transmittance characterization of obscurants over two lines of sight. During munition trials, one spectrometer will obtain munition source radiance while the other monitors cloud transmittance.

## REFERENCES

- Gutman, W. M., et al., 1991: Spectrally Resolved Transmittance Measurements at SMOKE Week XIII. In Proceedings of the 1991 Battlefield Atmospherics Conference, U.S. Army Atmospheric Sciences Laboratory, White Sands Missile Range, New Mexico 88002-5001.
- Kantrowitz, F. T., W. M. Gutman, T. D. Gammill, R. F. Soto, J. V. Rice, and R. Douglass, SMOKE Week XIV Test Support, Mobile Atmospheric Spectrometer. (Technical Report in preparation) U.S. Army Research Laboratory, White Sands Missile Range, New Mexico 88002-5501.

## OWN THE WEATHER: A VISION FOR ARMY METEOROLOGY

James Cogan, Richard Szymber, and Robert McPeck  
Battlefield Environment Directorate\*  
U.S. Army Research Laboratory  
White Sands Missile Range, NM 88002-5501, USA

### ABSTRACT

The phrase "own the weather" refers to the use of knowledge of the weather and environment to gain an advantage over enemy forces. An effective "all weather" capability may be achievable through the selection of the appropriate mix of sensors and systems that give friendly forces the ability to maneuver, see, and fight in adverse weather. This paper provides an insight of how the use of data from space platforms combined with data from ground-based systems, and airborne systems as needed, can make a major contribution to the goal of being able to "own the weather."

### 1. INTRODUCTION

The phrase "own the weather" refers to the use of knowledge of the weather and environment to gain an advantage over enemy forces. An effective "all weather" capability may be achievable through the selection of the appropriate mix of sensors and systems that give friendly forces the ability to maneuver, see, and fight in adverse weather. To make this selection possible, an accurate and timely knowledge of the current weather/environment, as well as accurate and timely forecasts, must be available for processing into the necessary atmospheric intelligence. Atmospheric intelligence is the processed data that provides information for operational users and planners. This type of intelligence is essential for effective employment in adverse weather conditions of both offensive and defensive weapon systems being developed to satisfy DoD Science and Technology (S&T) Thrust Areas. Specific S&T Thrust Area weapon families include precision strike, advanced land combat vehicles, and air defense. Also, the Global Surveillance S&T Thrust Area requires good atmospheric intelligence. This paper provides an insight of how the use of data from space platforms combined with data from ground-based systems complemented with airborne and other systems can make a major contribution to the goal of being able to "own the weather." It presents a research plan that has the potential to greatly improve the ability of current and planned Army and DoD environmental data gathering and analysis systems to provide atmospheric intelligence. The paper references directly or indirectly Army operations and doctrine to show the potential value of the research. Such references are not meant to state or imply recommendations for change to Army doctrine.

---

\*formerly U.S. Army Atmospheric Sciences Laboratory

## 2. CURRENT SITUATION

The imagers and sounders carried by current Defense Meteorological Satellite Program (DMSP) and operational civilian satellites are passive, and consequently cannot directly measure many needed parameters such as wind speed and wind direction or obscuration. Present analysis techniques available to the Army include methods such as remapping, looping, and color enhancement. Interpretation of the resultant satellite products remains in the hands of highly skilled personnel. Planned terminals will improve data collection (high resolution real-time data (RTD) from the DMSP and high resolution picture transmission (HRPT) data from the National Oceanic Atmospheric Administration (NOAA) satellites). Improved analysis and enhancement techniques will help the operator or forecaster interpret the much greater amount of incoming data. However, the requirement for highly trained personnel will continue and the need for good atmospheric intelligence will remain only partially fulfilled.

The Battlefield Environment Directorate (BED) (formerly the U.S. Army Atmospheric Sciences Laboratory) of the U.S. Army Research Laboratory (ARL) has initiated efforts to improve both data collection by satellite and ground-based systems and data analysis and interpretation, while reducing the need for skilled personnel. The Army Space Technology and Research Office (ASTRO) and the Program Manager Electronic Warfare Reconnaissance Surveillance and Target Acquisition (PM EW/RSTA) are partially funding these research efforts. These research programs along with other related work at BED can form the "seed" for a program to collect atmospheric data and convert those data via advanced processing methods into atmospheric intelligence on spatial and temporal scales appropriate to Army user needs.

## 3. DATA TYPES AND USES

Some primary Army tactical applications (TA) affected by weather and environment include intelligence and electronic warfare (IEW); fire support (FS); air defense (AD); aviation (AVN); maneuver (M); nuclear, biological, chemical defense (NBC); combat service support (CSS); special operations forces (SOF); and engineering (ENG). Part of the intelligence process is to know friendly and enemy capabilities. The environment will affect reconnaissance and surveillance, target acquisition, electronic warfare, or weapon systems differently, thereby directly affecting the relative capabilities of the opposing forces. Wind and temperature directly affect artillery accuracy, and a variety of parameters such as visibility and cloud cover impact effectiveness in the target area as well as ability to defend against airborne threats. Wind, clouds, precipitation, pressure, and other variables are of concern for aviation and become critical for nap of the earth flight. The combination of weather and terrain directly affects the ability of maneuver elements to move (mobility) and fight, and have a major effect on combat support and engineering. Effective defense from NBC agents requires that friendly forces know where the agents are going, how fast they will get there, and the extent of their dispersion. Although wind has the major effect, temperature and humidity also may significantly affect dispersion. Special forces need atmospheric intelligence to plan and execute operations such as parachute drops and amphibious landings.

Table 1 relates satellite data type with TA through the type of weather/environmental application.

TABLE 1. RELATION OF SATELLITE DATA TO TA AND MET APPLICATION

Satellite Date	Tactical Application	Meteorological Application
VIS imagery	ADA, M, AVN, FS, IEW, SOF	Clouds, precipitation, visibility, severe weather, snow/ice cover
NIR imagery	ADA, M, AVN, IEW	Clouds, precipitation, severe weather, snow/ice cover, visibility, vegetation index
MIR imagery	ADA, AVN	Clouds, snow/ice cover
TIR imagery	ADA, M, AVN, ENG, FS, IEW, NBC, SOF	Clouds, surface temperature, precipitation, severe weather
MW imagery	M, AVN, ENG, IEW, INF, SOF	Precipitation, soil moisture, snow/ice cover, surface temperature
H2O sounding	FS, IEW, NBC	Water vapor profile, surface humidity, precipitable water
Temp sounding	AVN, FS, IEW, INF, NBC, SOF	Temperature profile, wind profile, surface temperature, atmospheric stability

VIS = visible

NIR = near infrared

MIR = mid-infrared

TIR = thermal infrared

MW = microwave

#### 4. RESEARCH AND DEVELOPMENT PLAN

Knowledge of the atmosphere in the area of operations requires the capability to acquire accurate and timely data and to process those data to produce atmospheric intelligence. Satellite sensors combined with ground-based sounding systems and complemented with unmanned air vehicles, automatic meteorological (met) ground stations, and conventional systems will form the baseline met data collection system. A three-dimensional (3-D) data base derived from the collected data can provide input for real-time operational decisions as well as for 4-D (three space dimensions and time) forecasting models. This combination of data and the means to process them will provide the essential baseline capability to begin to approach an effective "all weather" capability. Research underway at ARL/BED addresses data gathering systems and generation and analysis of derived atmospheric parameters.

The primary goal of the research plan is to develop an efficient, accurate, and user friendly means to process the data and get output products to the user. Figure 1 outlines the flow from data ingest to user. The met data base is the initial form that will evolve into the processed met data base. The met data base and the processed met data base are shown separately to

emphasize the differences between the initial and later status and the additional processing required. This figure presents information on the research plan, and is not meant to state or imply changes to Army doctrine. Atm refers to atmosphere or atmospheric.

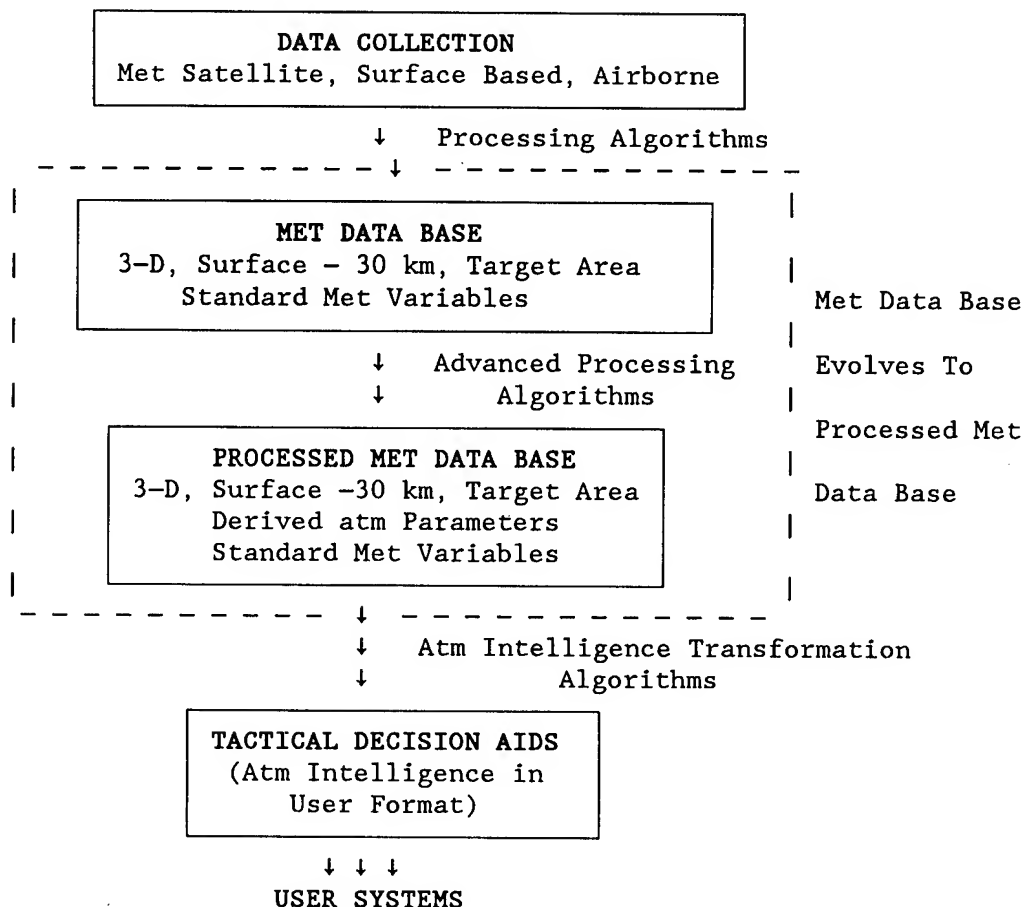


Figure 1. Overview of the process of converting met data to atmospheric intelligence and the flow from collection to user.

Current processing methods will be modified, and new ones will be developed to generate three-dimensional (3-D) data bases covering the target area from the surface to 30 km (more if required). This initial data base will contain the standard meteorological variables of wind speed, wind direction, temperature, pressure, and humidity. Others, such as total liquid water content in a column through a specified layer, may be added as required. This data base will evolve into one containing both standard met variables and processed met data (derived atm parameters). Derived atm parameters are variables such as visibility, infrared, and millimeter wave transmittances at appropriate frequencies, obscurant concentrations, cloud top and base heights, cloud type, precipitation type and rate, and others for entry into tactical decision aids (TDA) for specific systems or classes of systems. Both the standard and processed met data bases can be used to provide input to 4-D

battlescale forecast models and TDA's on systems such as the planned IMETS and on Army Tactical Command and Control System (ATCCS) common hardware software (CHS).

The research and development program for meeting the primary goal consists of several main thrusts for both standard and processed met data. Plans for obtaining input for the standard met data base include the following:

- a. Develop a proof of concept MPS.
- b. Employ user friendly software to combine satellite and ground-based systems and to combine satellite and other complementary data such as unmanned aerial vehicle (UAV) data.
- c. Determine the accuracy, spatial and temporal resolution, and other required data characteristics through determination of space and temporal variation of the atmosphere.
- d. Participate in the calibration and validation of DMSP 5D3 and block 6 sensors.
- e. Develop the target area (up to 500 by 500 km), surface to 30 km, 3-D data base for standard met variables.

Plans for developing the processed met data base include the following:

- a. User friendly software for small portable terminals that use smoothed satellite data.
- b. Methods to combine satellite and complementary data.
- c. Processing methods for high-resolution data from DMSP (block 5D2, 5D3, 6) and operational civilian satellites.
- d. Algorithms and software to process data from future sensors of the Earth Observing System (EOS) satellites and combine those data with data from future ground-based and airborne systems.

Plans for application of the standard met and processed data bases include the following:

- a. Test and evaluate the developed algorithms on the ARL BED Technology Exploitation Weather Testbed (TEWTB), a prototype IMETS designed to emulate the future IMETS and battlefield weather support concept.
- b. Develop 4-D battlescale forecast models to predict the atmosphere over the target area using input from the 3-D data base.
- c. Develop forecaster aids and weather effects decision aids using the Directorate's TEWTB.

The type of sensors planned for EOS may fly on post block 6 DMSP satellites. The software for portable terminals using low resolution data (APT and WEFAX

imagery) is a low risk, low cost item suitable for current and near future small terminals. The processing software for high resolution data will involve the use of advanced techniques including artificial intelligence (neural nets and knowledge-based systems) and will include multispectral input data.

Software is being developed that will combine data from satellite and ground-based systems complemented with data from airborne platforms to produce atmospheric soundings for the entire battlefield from the surface to 30 km. The methods to be developed for the EOS data will provide a means to use data from future active, space-based instruments such as the laser atmospheric wind sounder (LAWS) and a synthetic aperture radar (SAR). The package will include processing of data from future passive sensors such as a hyperspectral sounder and much improved multispectral and hyperspectral imagers. Simulated data will be used when real data are not available. However, actual EOS data for the passive EOS instruments are expected to become available starting in 1998, even though initial work will involve simulations. Except for the near term software for low resolution satellite data, each work area contains a mix of low and moderate risk items with an overall low cost relative to many remote sensing efforts. The goal of these efforts is to provide software packages that satisfy high priority Army requirements for weather/environmental data as defined by users and stated in official Army documents. The outcome of these demonstration packages may lead to further efforts for development of Army-influenced satellite and complementary sensors.

These packages will be developed to run on standard Army processors (ATCCS CHS) and fit into prototype IMETS and MPS (for artillery) processing systems. Evaluation of the software on these test and evaluation systems may lead to adoption of the software for operational versions of IMETS, MPS, or equivalent systems. These systems will interconnect with users of atmospheric intelligence within most tactical application areas. For example, the IMETS will connect with Division and Corps All Source Analysis Systems and Digital Topographical Support Systems, and the MPS will connect with the artillery TACFIRE system through the data interface. Therefore, through the chain of sensor, data receiver, data processor/data base, and connection to functional area, the software developed at ARL/BED can provide atmospheric intelligence that can start the process of enabling the Army to "own the weather."

#### 4. BENEFIT, COST, AND RISK BY FUNCTIONAL AREA

Knowledge of the atmosphere and ability to accurately forecast atmospheric conditions for periods related to Army operations can be used to select the most appropriate asset or combination of assets to accomplish the mission. In addition this knowledge can reduce the need for material and personnel.

In the intelligence area less costly sensors operating in the visible and infrared can perform adequately most of the time; but in adverse weather such as cloud cover and precipitation, occasional use of a more costly sensor such as a synthetic aperture radar (SAR) may be necessary. However, an SAR is not required all the time everywhere. The same type of sensor substitution applies to the target area, especially with regard to critical mobile targets. A helicopter operation may succeed through selection of an



alternate route to reach the target area when the original avenue of approach is "closed" by adverse weather. Knowledge of the environment can enable armor to avoid terrain made impassible or difficult by weather effects. Even in good terrain, friendly forces may be able to shoot and destroy in certain atmospheric conditions that degrade enemy seekers and therefore their ability to hit their targets (or vice versa!). NBC defense can be far more effective if the weather is known and useful forecasts are available. Efficient deployment of forces and use of mission-oriented protective posture (MOPP) gear depends on weather knowledge; fewer forces would require full MOPP and would be less subject to heat stress. Special operations can be planned with the weather in mind to assure maximum effectiveness and probability of success.

Attainment of the goal of providing atmospheric intelligence for TA's involves cost and technical risk. Benefit, cost, and technical risk need to be evaluated to efficiently develop the most cost effective research and development (R&D) effort. In tables 2 and 3 these factors are estimated in a relative sense (high, moderate, low) for each block of the "flowchart" in fig. 1, and for a representative list of atmospheric intelligence parameters. Benefit values are subjective indicators derived by the authors based on their own knowledge and conversations and written materials from personnel at Army schools and other agencies. Other individuals may assign a different value for a given parameter. A high benefit suggests a potential for a significant improvement in the ability of the user to accomplish a TA. Moderate indicates some useful enhancement, and low suggests minimal improvement. High risk indicates a high degree of difficulty in achieving the goal, moderate risk suggests the goal has a reasonable probability of completion, and low risk goals almost certainly can be completed. Data collection has a high benefit because it is essential for subsequent blocks. Artillery met message profiles of wind, virtual temperature and pressure assume new/planned systems in place (for example, MPS, UAV).

Table 4 lists the same atmospheric intelligence parameters as in the previous table along with relevant TA's and an indication of the relative ratio of potential benefit to a combination of cost and technical risk (high, moderate, low).

TABLE 2. BENEFIT, COST, AND TECHNICAL RISK BY FLOWCHART BLOCK

Parameter	Benefit	Cost	Technical Risk
Data collection	High	Mod	Low
Met data base	High	Low	Low
Processed met data base	Very high	Mod	Mod
TDA	Very high	Mod	Mod

TABLE 3. BENEFIT, COST, AND TECHNICAL RISK BY DERIVED ATM PARAMETERS

Parameter	Benefit	Cost	Technical Risk
Cloud type	High	Low	Low
Cloud top	Mod	Low	Low
Cloud base	High	Low	Mod
Visibility (lower Atm)	High	Low	Mod/high
IR transmittance (lower Atm)	High	Low	Mod
Precip area	High	Low	Low
Precip rate	High	Low	Mod
Obscurant concentration	High	Low/Mod	Mod
Artillery met message	High	Low	Low

TABLE 4. DERIVED ATMOSPHERIC PARAMETERS RELATED TO TA AND TO RATIO OF BENEFIT TO COST AND TECHNICAL RISK

Parameter	TA	Ratio
Cloud type	IEW, AVN, AD, NBC, SOF	High
Cloud top	IEW, AVN, AD	Mod
Cloud base	IEW, AVN, FS, AD, NBC	High
Visibility (lower atm)	IEW, AVN, FS, AD	High/mod
IR transmittance (lower atm)	IEW, AVN, AD, FS, SOF	High
Precip area	IEW, M, AVN, FS, NBC, SOF, AD, CSS	High
Precip rate	IEW, M, AVN, FS, NBC, SOF, AD, CSS	High/mod
Obscurant concentration	IEW, FS, AVN, AD, NBC	Mod
Artillery met message profiles	IEW, FS, NBC, SOF	High

All but one of the relative costs were low (obscurant concentration cost is estimated to be low to moderate). Cloud base has a high ratio, even though the risk is considered moderate, because of the very high benefit to many TA's. The same holds for infrared transmittance. Visibility has a high to moderate ratio because of the moderate to high risk. In the case of visibility, the benefit for the lower atmosphere is probably so high that the relatively high risk is worth taking.

A qualitative listing (table 5) of the estimated relative benefit, cost, and technical risk (high, moderate, low) of the aforementioned research plan activities to the TA's most affected can provide an indication of the payoff of the overall effort. The cost and risk for intelligence, fire support, and air defense are somewhat higher because they are the first functional areas to be addressed. Following areas will take advantage of previous work. The maneuver area shows moderate cost and risk because of the increased emphasis on soil moisture. Payoffs in the intelligence area are expected to appear first.

TABLE 5. BENEFIT, COST, AND TECHNICAL RISK BY TA

Tactical Application	Benefit	Cost	Risk
Intelligence	High	Moderate	Low to mod
Fire support	High	Low to mod	Low to mod
Air defense	High	Low to mod	Low to mod
Aviation	High	Low	Low
Maneuver	High	Moderate	Moderate
NBC defense	High	Low	Low
Special ops forces	High	Low	Low
Combat Svc Support	Moderate	Low	Low

## 5. CONCLUSION

Current systems have only a very limited capability to provide needed atmospheric intelligence. The first phase of the planned research will enable the Army to significantly upgrade that capability with systems and software that use passive satellite sensors. The advent of active satellite sensors after the year 2000 will lead to the ability to fully meet the research goals.

These atmospheric sensing capabilities, exploitation techniques, and software that will be developed will enable the Army to establish a baseline capability to use weather and environmental knowledge to gain a decisive advantage over enemy forces. The atmospheric sensing capabilities developed under the research plan will be used to build the met data bases that will feed the TEWTB 4-D battlescale forecast models and software developed by this research. The software products of the R&D effort, particularly the satellite data exploitation techniques and system specific applications packages, mounted on ATCCS CHS systems at battlefield functional area nodes will enable the Army to "own the weather" and ultimately "own the enemy."

#### ACKNOWLEDGMENT

The authors acknowledge Mr. Edmund Westcott, Assistant Chief of Staff, Research, Development, and Engineering, U.S. Army Materiel Command, who originally coined the phrase "own the weather" to describe the concept presented in this paper.

**Session III Posters**

**DATA BASES AND ANALYSES**

# **DIGITAL SIGNAL PROCESSING TECHNIQUES USED TO REDUCE ACOUSTICS DATA FROM THE JAPE TEST**

**Thelma Chenault, Rene' Klein, and Ascencion Acosta, Jr.  
Battlefield Environment Directorate\*  
WSMR, New Mexico, USA**

## **ABSTRACT**

During the Joint Acoustics Propagation Experiment in July 1991, acoustic data was collected and processed from long/short range propagation tests, terrain masking tests, and military vehicle classification tests. This paper will go into great detail on the methods used to collect, process, and analyze this acoustics data.

## **1. INTRODUCTION**

During July 1991, the acoustic team participated in the Joint Acoustic Propagation Experiment (JAPE) at Dirt Site, WSMR. Each participant had responsibility for his special acoustic tests and part of the joint test. The test consisted of three separate phases: 1) long/short range propagation, 2) terrain masking, and 3) military vehicle characterization and detection. The Atmospheric Sciences Laboratory (ASL) acoustics team had responsibility for collecting and reducing acoustics data from the north tower microphones and operating the four source speakers located on that tower for the long/short range propagation phase and the military vehicle characterization phase.

## **2. FIELD SETUP**

The acoustical meteorological test bed located at Dirt Site consists of two thirty-three meter walkup towers that are instrumented at five levels with various meteorological sensors. The towers are placed approximately on a north south line with a one kilometer spacing between them. Each tower has a complement of loudspeakers at the two meter and thirty meter levels for generating sound over the one kilometer range and microphones located at the zero, one, two, four, eight, sixteen, thirty-two meter levels and in front of the source speakers (figure 1).

The microphones used by the acoustic team were Bruel & Kjaer 4155, 4165, and 4176 acoustics sensors, 2642 preamplifiers and 2810 power supplies. The sensors were individually calibrated at least twice per day using a Quest Sound Calibrator which produced a 94dB, 250Hz calibration tone. One calibration was done previous to the first trial of the day. Another calibration was done after the last trial of the day was completed. If groups of trials were spaced more than an hour apart, intermediate calibrations were done.

\*formerly U.S. Army Atmospheric Laboratory

## JAPE Field Test, 1991 Dirt Site, White Sands Missile Range

- ASL had microphones on the north tower at the 0, 1, 2, 4, 8, 16, and 32 meter level.
- ASL also had microphones on both towers in front of the four source speakers.

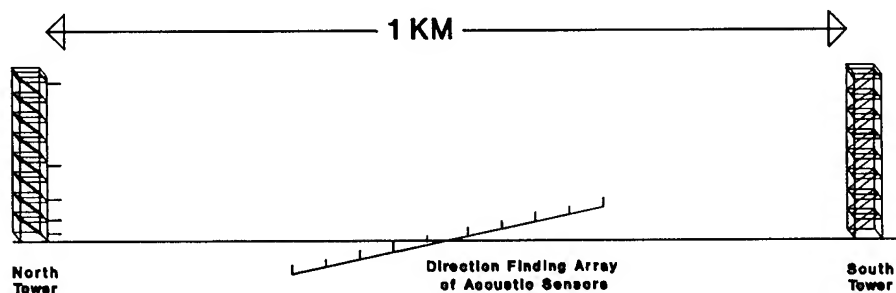


figure 1.

During the long/short range sound propagation phase the microphone configuration consists of four source microphones, three arrays, one longitudinal array, one transverse array, and one direction finding array. A vertical array of microphones is placed on each of the two thirty-three meter towers. The eleven microphones that make up the longitudinal array are placed on the ground one hundred meters apart along a line between the two towers. The transverse array was placed perpendicular to the longitudinal array midway between the towers.

Microphones in the transverse array were placed both on the ground and one meter above ground at one, three, seven and fifteen meters east of the center microphone pair and thirty-one meters west of the center pair. The direction finding array consists of eight elements: one in the center surrounded by seven evenly spaced on a circle with a 1.85 meter radius. This array is located about fifty meters west of the midway point between the two towers. Source microphones were positioned approximately two meters in front of the source. The acoustic team was responsible for sensors on the north tower, in front of the four source speakers, and IRIG-B timing.

The acoustics source for the long range moving trials was a UH-1 "Huey". The helicopter followed a predefined flight pattern and flew at a constant speed of eighty knots and an altitude of two hundred feet. During the pre-dawn testing period two trials were made with the helicopter flying above the thermal inversion and two trials were made flying below the inversion.

The acoustics sources for the short range trials were speaker and propane cannons mounted at two meters and thirty meters on each of the thirty-two meter towers. The propane cannon trials consisted of eleven shots fired at thirty seconds intervals. Each speaker was

driven by pre-recorded signals played from audio tape. Tones of thirty second duration were broadcasted at 25, 50, 100, 200, 300, 400, 500, 650, 850, 1000, 2000, and 3000 Hz in sequence. This sequence was followed by an eight minute signal consisting of a superimposed 80, 200, and 500 Hz tones. The eight minute signal were recorded at thirty minute intervals during the transition period, the pre-dawn, and late afternoon sessions.

During the military vehicle characterization and detection trials M1, M60 (tanks), M113 (armored personal carrier) and the UH1-A helicopter were used to acquire acoustic signatures. The test provided well documented atmospheric conditions. Ground truth data for the vehicles' position were provided by global positioning equipment.

## 2. DATA RECORDING

Data from the acoustic sensors were recorded on a Teac RD-200T PCM data recorder in the sixteen channel mode during the calibration and test trials. The RD-200T data recorder is a state-of-the-art data recorder. This data recorder provides analog-digital data conversion before the data is recorded to digital audio tape (DAT). The sixteen channel mode provides recording of a frequency band from dc to 2.5 KHz at a 6 KHz sample rate. Other features of the recorder are built in 2.5 KHz anti-aliasing filter, identification (ID) code recording, and optional control by an external computer via a GPIB interface board. The recording of ID codes facilitated data search and filing. Using this feature software was written to search and retrieve data from specific test trials. One channel was used to record IRIG-B timing.

Two dedicated personnel computers and an HP9000-827 computer were used (figure 2), to provide efficient extraction, storage and processing of the acoustics data collected during the JAPE test.

Data were extracted from the TEAC audio data recorder directly to the HP9000-827 computer via the PC Lan using a dedicated personal computer equipped with a AT-GPIB (IEEE488) interface board, and IRIG timing board. Specialized software was used to read and calibrate the digitized data.

### Data Reduction System Schematic ASL Acoustic Team

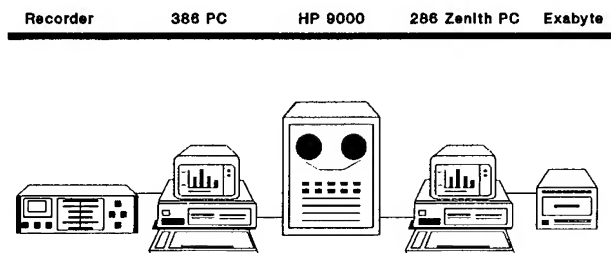


figure 2



### 3. DATA CALIBRATION

The digitized data were recorded as voltage variations. The calibration data from the individual microphones were used to convert the voltage variations into pascal. Each microphone was calibrated before and after the daily trials using a 94 dB, 250 Hz calibration tone.

To convert the time series to pascal, begin with the formula for the sound pressure level (SPL):

$$SPL = 20 \log \left( \frac{P}{P_o} \right) \text{ dB} \quad (1)$$

where  $P$  is the root mean square (rms) pressure, and  $P_o$  is the effective standard reference pressure. For atmospheric acoustics the standard reference pressure is  $20 \mu \text{ Pa}$ . Substitution now yields:

$$SPL = 20 \log P - 20 \log (20 \times 10^{-6}) \quad (2)$$

$$SPL = 20 \log P + 94 \quad (3)$$

The calibrator used produced a SPL of 94 dB:

$$SPL = 94 = 20 \log P + 94 \quad (4)$$

$$0 = 20 \log P \quad (5)$$

So the rms pressure of the calibrator is:

$$P = 1 \quad (6)$$

Solving for some constant,  $c$ , so that when it is applied to the calibration time series a root mean square (rms) pressure of 1 is obtained:

$$P = \sqrt{\frac{\sum_{i=1}^N (x_i - \mu)^2}{N}} \quad (7)$$

where  $\mu$  is the mean value of the time series,  $x_i$  is the  $i^{\text{th}}$  point in the time series, and  $N$  is the number of points in the time series. When  $P$  equals 1, the inverse of our rms pressure can be used to convert our time series to pascal.

$$\sqrt{\frac{\sum_{i=1}^N [c(x_i - \mu)]^2}{N}} = 1 \quad (8)$$

$$\sqrt{\frac{c^2 \sum_{i=1}^N (x_i - \mu)^2}{N}} = 1 \quad (9)$$

$$c \sqrt{\frac{\sum_{i=1}^N (x_i - \mu)^2}{N}} = 1 \quad (10)$$

$$c = \frac{1}{\sqrt{\frac{\sum_{i=1}^N (x_i - \mu)^2}{N}}} \quad (11)$$

To find this constant  $c$ , the rms pressure for our calibration time series must be calculated. To calculate the rms pressure the following steps are required:

1. calculate the mean of the time series
2. subtract out the mean from each element of the time series
3. calculate the sum of squares of the elements calculated in step 2
4. divided by the number of elements in the time series
5. take the square root of this value.

The inverse of our calculated rms pressure is our conversion factor  $c$  specific to our 94 dB calibration tone. This conversion factor is only good for the test day of the calibrations, and the microphone which produced the data. Our conversion factor will not always be the inverse of our rms pressure. The general case for evaluating the conversion factor shows that the 94 dB calibration tone simplified our task. For the general case, let us suppose our SPL is set at a value of  $Y$  dB. Then the equation for our SPL will be:

$$Y = 20 \log P - 20 \log P_o \quad (12)$$

If our reference pressure is  $20 \mu$  Pa, then from Equation (3):

$$20 \log P = Y - 94 \quad (13)$$

$$\log P = \frac{Y - 94}{20} \quad (14)$$

$$P = 10^{\frac{Y - 94}{20}} \quad (15)$$

Equation (15) is the theoretical rms pressure of our calibrator. Calculating  $P$  from our time series by:

$$P = \sqrt{\frac{\sum_{i=1}^N (x_i - \mu)^2}{N}} \quad (16)$$

Solve for the conversion factor  $c$ :

$$\sqrt{\frac{\sum_{i=1}^N [c(x_i - \mu)]^2}{N}} = 10^{\frac{Y - 94}{20}} \quad (17)$$

Multiplying the time series by our conversion factor,  $c$ , will now yield the data in pascal. To verify the special case where a 94 dB calibration tone was used:

$$c = \frac{10^{\frac{Y-94}{20}}}{\sqrt{\frac{\sum_{i=1}^N (x_i - \mu)^2}{N}}} \quad (18)$$

$$c = \frac{10^{\frac{Y-94}{20}}}{\sqrt{\frac{\sum_{i=1}^N (x_i - \mu)^2}{N}}} = \frac{1}{\sqrt{\frac{\sum_{i=1}^N (x_i - \mu)^2}{N}}} = \frac{1}{P} \quad (19)$$

Thus the specific and general cases for converting acoustic signals into pressure units.

#### Quality Checking The Results

A quality check for the conversion factor calculated can be made by using the definition:

$$P = \frac{A_{\max}}{\sqrt{2}} \quad (20)$$

where P is the rms pressure of our calibration time series and  $A_{\max}$  is the peak value of the sinusoidal signal. From this definition, a theoretical value for the peak value of the sinusoidal signal can be found:

$$A_{\max} = P\sqrt{2} \quad (21)$$

Determining the theoretical value for P in the same way as in Equation (15):

$$A_{\max} = 10^{\frac{Y-94}{20}} \sqrt{2} \quad (22)$$

where Y is the SPL of our calibrator, referenced to 20  $\mu$  pascal. Thus, after the conversion factor has been applied to the calibration time series, the peak value of the sinusoidal signal of the calibration time series should be Equation (22). This can be verified by graphing the resulting time series or using a program to scan for maximum and minimum values. In the case of our 94 dB calibration tone, P was equal to 1, leaving our  $A_{\max}$  equal to  $\sqrt{2}$ .

#### 4. DATA ANALYSIS

To lower our sampling rate from 6 KHz to 2 KHz and avoid aliasing of our acoustics data, a digital finite impulse response (EQFIR) filter was developed and applied to our data. This ninety point digital filter passed frequencies from 0 - 670 Hz and stopped frequencies from 1000 - 3000 Hz. The simplest way to apply a digital filter to data is by direct evaluation of the convolution sum which defines the filter:

$$y(n) = \sum_{k=0}^{\frac{N}{2}-1} h(k)[x(n-k) + (n-N+1+k)] \quad (23)$$

Where:

N is the filter length

h(k) is the k th filter element and

n is the n th element of the data set

Since our filter contained an even number of points and decimation of the data was being done at the same time the filter was implemented:

$$y(n) = \sum_{k=0}^{(\frac{N}{2})-1} h(k)[x(n-k) + x(n-N+1+k)] \quad (24)$$

Where:

N is an even filter length

h(k) is the k th filter element and

n is the n th element of the data set

Since our data was decimated by a factor of 3 to change from a sampling rate of 6 KHz to a sampling rate of 2 KHz (n = 1, 4, 7, 10, ...).

Traditional fast fourier transform analysis methods were used to obtain military vehicle signatures. This information will be used together with our meteorological and global positioning data to determine acoustic detection ranges for various military vehicles. Also our terrain masking experiments allow for nonlinear-of-sight analysis.

The HP9000 computer was used for digital filtering, data decimation and analysis of the acoustic data because it provided the required computational speeds and large intermediate data storage capabilities.

A second dedicated personnel computer was used to archive data via the LAN to an Exabyte Tape Drive. The Exabyte Tape Drive is a eight millimeter tape unit capable of storing up to five gigabytes of data per tape. Because of present software limitations, the full potential

of this drive has not been achieved.

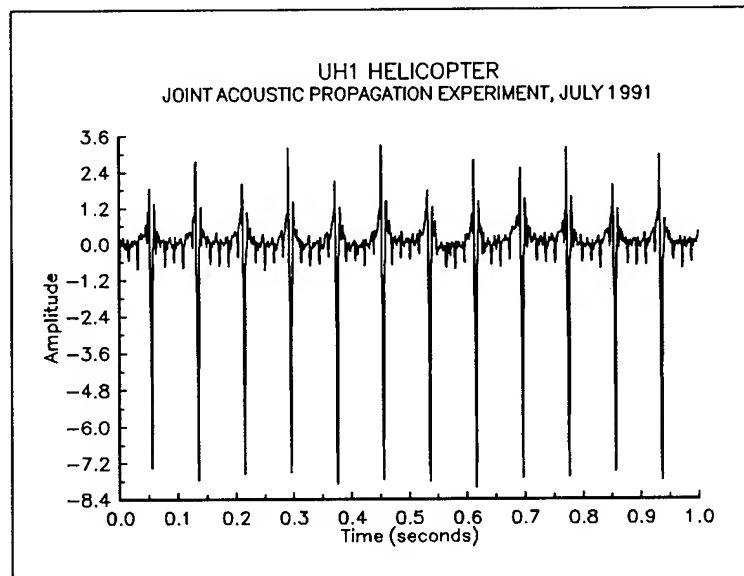


figure 3

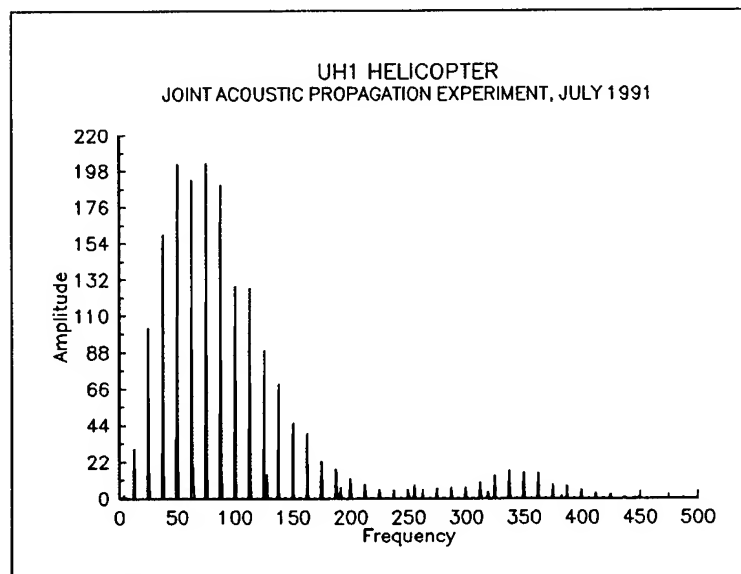


figure 4

## 5. CONCLUSIONS

Because of the massive amount of data collected during this test, it is believed that every effort must be made to expedite the data processing. Some suggestions to speed up this effort are:

1. Use high quality analog filters and a workstation with analog-to-digital conversion boards to collect data at the proper sampling rate.
2. Use this workstation to do quick-look analysis in the field.
3. Use this workstation in-house as a data processing computer so that data doesn't have to be moved between computer systems.

## REFERENCES

Cappelline, V., Constantinides, A.G., Emiliani, P., 1981. Digital Filters and Their Applications.

Ludeman, Lonnie C., 1986. Fundamentals of Digital Signal Processing.

# PYROLYSIS-MASS SPECTRA OF BIOLOGICAL AEROSOLS INTERPRETED

## BY FACTOR ANALYSIS-RANK ANNIHILATION

David Rosen  
Battlefield Environment Directorate\*  
U.S. Army Research Laboratory  
White Sands Missile Range, New Mexico 88002-5501, USA

Alice Harper  
U.S. Army Edgewood Research, Development, and Engineering Center  
Aberdeen Proving Ground, Maryland 21010-5423, USA

### ABSTRACT

Mass spectroscopy is a method of chemical analysis that has potential use for detecting and identifying biological aerosols. Mass spectroscopy is more sensitive and faster than most methods of analysis although it is not a remote sensing technique. However, interpreting mass spectra in mixtures of substances is difficult because the mass spectra of many compounds overlap. Pyrolysis-mass spectroscopy is a method where the sample is pyrolyzed. The resulting time evolution of the mass spectrum is used to distinguish between background components. This paper shows how factor analysis-rank annihilation (FARA) can be used to interpret pyrolysis-mass spectra. The paper focuses on the background produced by contaminants in the sensor. FARA can also be used to eliminate the background caused by substances that are normally in the troposphere.

### 1. INTRODUCTION

Mass spectroscopy is a method of chemical analysis that has potential use for detecting and identifying microbes and other organic materials. Scientists usually use other methods such as fluorescence and microbiology techniques. However, mass spectroscopy is more sensitive and faster than these other techniques. Certain fundamental problems limit the accuracy and specificity of mass spectroscopy. If these problems are solved, mass spectroscopy could become an important detection tool for chemical-biological warfare.

Mass spectroscopy is a very sensitive and specific method for chemical analysis where the sample is not a mixture. However, real world data usually comes from mixtures of substances. The measurement of mass spectra, described in section 2.1, produces a series of line spectra that overlap each other. Experimenters often introduce a second variable besides mass number to add

---

\*formerly U.S. Army Atmospheric Sciences Laboratory



specificity to the measurement. Pyrolysis is a technique, described below, that adds the dimension of time to the mass spectroscopy data. Factor analysis-rank annihilation (FARA) methods are often necessary to interpret two-dimensional data.

Pyrolysis-mass spectroscopy (PMS) is a type of mass spectroscopy where time has been added to mass number as an independent variable. The experimenter places a sample in a pyrolysis chamber that heats the sample. The molecules decompose into various ions and neutral species. A gas flow carries these products to a membrane. Some of these products diffuse through the membrane. The ions pass through a velocity selector and a magnetic field. The magnetic field separates the different ions according to mass number. Mass number for neutral species is called the molecular weight.

A detector measures the number of ions as a function of time and mass number. Without hysteresis, the temporal profile at a particular mass number would be a convolution of the temporal profile of the pyrolyzer temperature and a response function of the sample. The data comes as data matrices, where the row vectors correspond to mass spectra and the column vectors correspond to temporal profiles.

Atmospheric constituents can create a background that changes from experiment to experiment. The detector counts some ions even when the pyrolyzer is off. The ions come from contaminants in the atmosphere. When the pyrolyzer is on, compounds other than the ones of interest decompose by the heat and create a nonconstant background. Although atmospheric constituents are not the focus of this paper, they may be a severe problem in the future.

A hysteresis effect also complicates the temporal profiles, so the temporal profiles change from run to run. Hysteresis means that the apparatus does not return entirely to its original state after ions have passed through it. For example, sometimes mass spectra from previous experiments are superimposed on the mass spectra of the sample. Contamination of the mass spectrometer itself causes part of the hysteresis background.

Adsorbed contaminants reside in the surface of tubing, the membrane, or anywhere else in the mass spectrometer. Although most of this effect can be reduced by cleaning the apparatus, PMS is so sensitive that a measurable background always remains. Contamination is present even in a new instrument. Analytical corrections for this correction would greatly extend the applications of PMS.

The authors have made the following initial assumptions about the contaminants that cause hysteresis. First, the mass spectrum for a short time near the beginning of an experiment is entirely from the contaminant and does not change during this time. Second, the normalized mass spectrum from the contaminant does not change at any time during the experiment. Although the intensity at any mass number may change as a function of time, the ratio between peaks will remain constant. Third, the mass spectrum of the contaminant adds linearly to the mass spectrum of the sample.

The authors know that the second assumption is only approximate. However, this assumption may be close enough to reality to allow background subtraction.

## 2. EXPERIMENT

This section describes the measurements of mass spectra and the conditions of these experiments. The following subsections discuss the experimental data and the mathematics of the analysis.

### 2.1 MEASUREMENTS AND DATA

The data provided for analysis in the project came from a pyrolysis-mass spectrometer developed by Brucker-Franzen, GMBH. Brucker via Teledyne provided data to the Chemical Research and Development Laboratory. A similar experiment has been described by Brown (1991). The experimenters examined 19 samples by slow pyrolysis. Slow pyrolysis means that the pyrolyzer was on during the measurements, which took 70 to 80 s. A rapid-scan mass spectrometer averaged 25 raw-mass spectra for each mass spectrum included in a data matrix. The mass spectral responses showed responses only over mass numbers from 40 to 250. The temporal measurements started from zero, when the pyrolyzer was turned on, to either 70 or 80 s. The data matrices consist of rows that are mass spectra and columns that are temporal profiles. Every row corresponds to 1 s of the experiment's run. The matrices are either 70 by 210 or 80 by 210.

The authors analyzed the five sets of data matrices. This paper describes only the analysis of the ALDO set, which contained data matrices from samples of a protein called aldolase.

### 2.2 MATHEMATICAL ANALYSIS

The mathematical analysis of the data matrices consisted of three parts: standard factor analysis (FA), evolving factor analysis (EFA), and rank annihilation (RA). This study attempted to identify the hysteresis component by EFA and remove it from the rest of the data matrix by RA. Standard FA is an eigenanalysis technique for decomposing an entire matrix to identify the independent components of the data. The EFA is a technique where one estimates the number of principal components in a submatrix of a data matrix to identify interesting regions. The RA is a technique where one calculates the concentration of a particular component in the sample and subtracts the contributions of this component.

In standard FA, singular value decomposition decomposes a data matrix,  $M$ , into singular values, temporal eigenvectors, and mass eigenvectors. A singular value of  $M$  is the square root of the eigenvalue of  $MM^t$ , where the superscript  $t$  means transpose. The singular values correspond to the contribution of each independent component to  $M$ . The  $i$ th singular value of  $M$  is designated  $\lambda_i$ , where the singular values are ordered so that if  $i > j$ , then  $\lambda_i > \lambda_j$ .  $M$  is a data matrix where the rows are mass spectra and the columns are temporal profiles. The eigenvectors of  $MM^t$  are called temporal eigenvectors because they generate the temporal profiles, while the eigenvectors of  $M^tM$  are called mass eigenvectors because they generate the mass spectra. A set of

eigenvectors generates a set of data vectors if every data vector is a linear combination of those eigenvectors. This paper later shows a plot of a corrected mass spectrum to compare with an actual mass spectrum. Single value decomposition (SVD) computes the eigenvectors and singular values. SVD decomposes the data matrix  $M$  as follows:

$$M^t = USV^t, \quad (1)$$

where  $U$  contains the orthonormal temporal eigenvectors;  $S$  is a diagonal matrix containing the singular values; and  $V$  contains the orthonormal mass eigenvectors.

The authors applied the following EFA technique to each data matrix (Maeder, 1987). Each data matrix,  $M$ , extended between times 0 and  $t_f$ .  $M$  was subdivided into two submatrices at a cutoff time,  $t_c$ . The investigators included the entire mass spectra in the submatrices because the mass spectra contain the most chemical information. The programs for EFA truncated only the temporal profiles. The matrix for times between 0 and  $t_c$  inclusive are designated  $M_f(t_c)$ , and the matrix for times  $t_c$  to  $t_f$  inclusive are designated  $M_b(t_c)$ . SVD calculated between 8 and 12 of the largest singular values of  $M_f$  and  $M_b$  as a function of  $t_c$ .

The singular values all increased with the size of the submatrix, even when the amplitude of the noise or the background was constant (that is, independent of time or mass number). Therefore, the authors divided the singular values by a size factor as a correction for the size of the submatrix. The size factor used in this analysis is the square root of the number of rows in the submatrix.

This study assumed that the region of pure background started from time zero and extended over the region where the first singular value, divided by the size factor, was flat. However, another algorithm was necessary to calculate the number of bilinear components in that background. This study used a variation of the eigenvalue ratio test (Hirsch et al., 1987), which will not be described in this paper.

The rank annihilation method consists of four parts. First, the border and number of components in the background are determined as described earlier. Second, SVD decomposes the submatrix,  $M_b$ , consisting of background alone by the following equation, analogous to eq. (1)

$$M_b^t = U_b S_b V_b^t. \quad (2)$$

Third, a program truncates the noise eigenvectors from the matrix of mass eigenvectors,  $U_b$ . Fourth, the projection of the data matrix on the mass eigenvectors of the background is calculated and subtracted from the data matrix to form a residual matrix. The following equation defines the residual matrix,  $M_R$ , as

$$M_R = M - MU_b U_b^t. \quad (3)$$

### 3. RESULTS AND DISCUSSION

This paper discusses the analysis of the data in three parts. First, the authors show how EFA was used to determine the regions of constant background in a data matrix designated ALD03. Second, the authors show a typical mass spectrum of ALD03. Third, the authors show the corresponding mass spectrum after subtraction of background.

#### 3.1 EFA ON ALD03

The authors applied EFA on ALD03 to find out more about this background. Figure 1 shows an EFA curve for the first 12 singular values of ALD03. The curve for the first singular value corrected by size factor is flat for the first 38 s, indicating a constant background for the first 38 s. The authors found the region of pure background in other samples using EFA. The EFA curves of the residual data matrices show no obvious anomalies. Brown (1991) describes an EFA analysis of a similar experiment, but does not include a size factor.

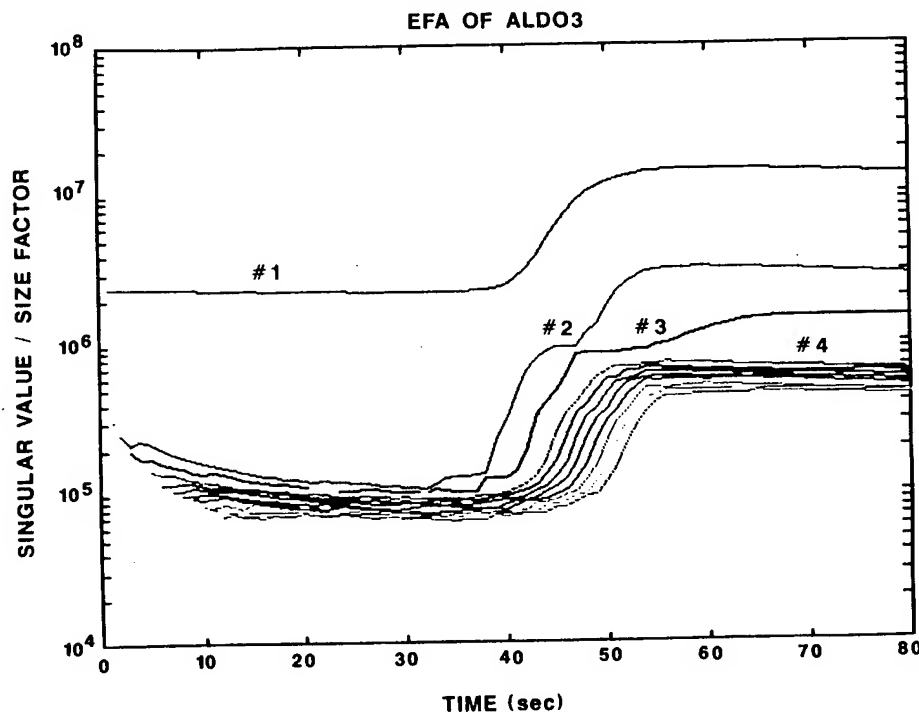


Figure 1. Evolving factor analysis curve for the first 12 singular values of ALD03.

### 3.2 RANK ANNIHILATION

The investigators applied rank annihilation to ALDO3. Figure 2 shows the original mass spectrum of ALDO3 at 53 s after starting the experiment. Figure 3 shows the residual mass spectrum of ALDO3 at 53 s after starting the experiment.

The residual mass spectrum has negative values at many peaks. Negative values for ion count are unphysical. Therefore, these negative peaks must be artifacts of the authors' rank annihilation method. Mass 208 and 194 represent some contaminant that depletes during pyrolysis. Other negative peaks can be explained by the different temporal profiles of the individual ions. Researchers may be able to eliminate these negative peaks by using knowledge of the temporal dynamics. Some peaks such as mass 68 are greatly reduced by rank annihilation without becoming negative. Many of these reduced peaks may be from contaminants that cause the hysteresis effect. The authors believe that an improved version of FARA, using eigenvector rotation, may successfully interpret spectra.

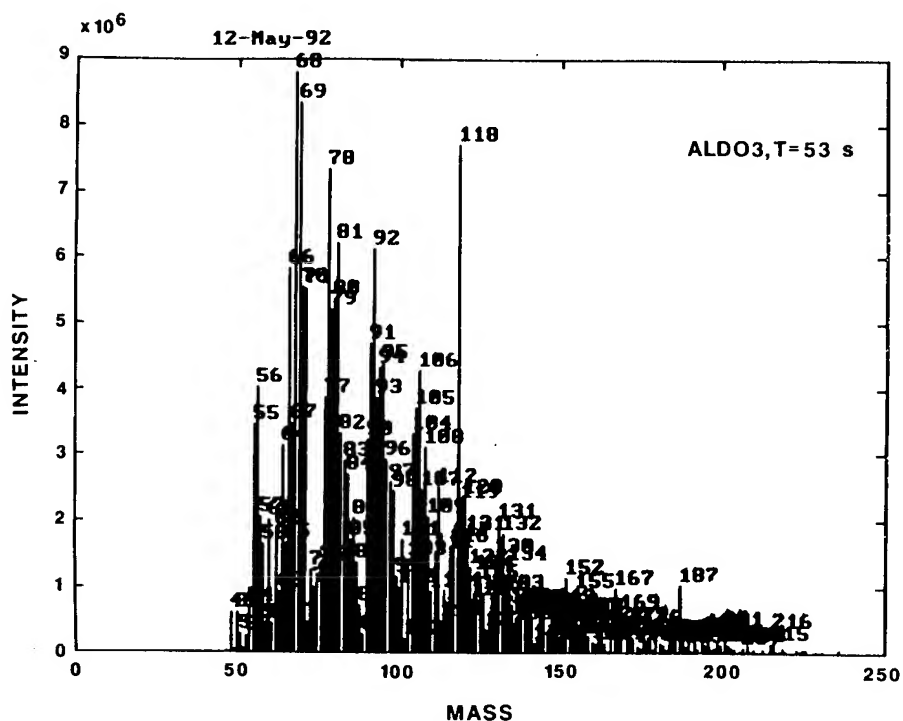


Figure 2. Mass spectrum of ALDO3 after 53 s.

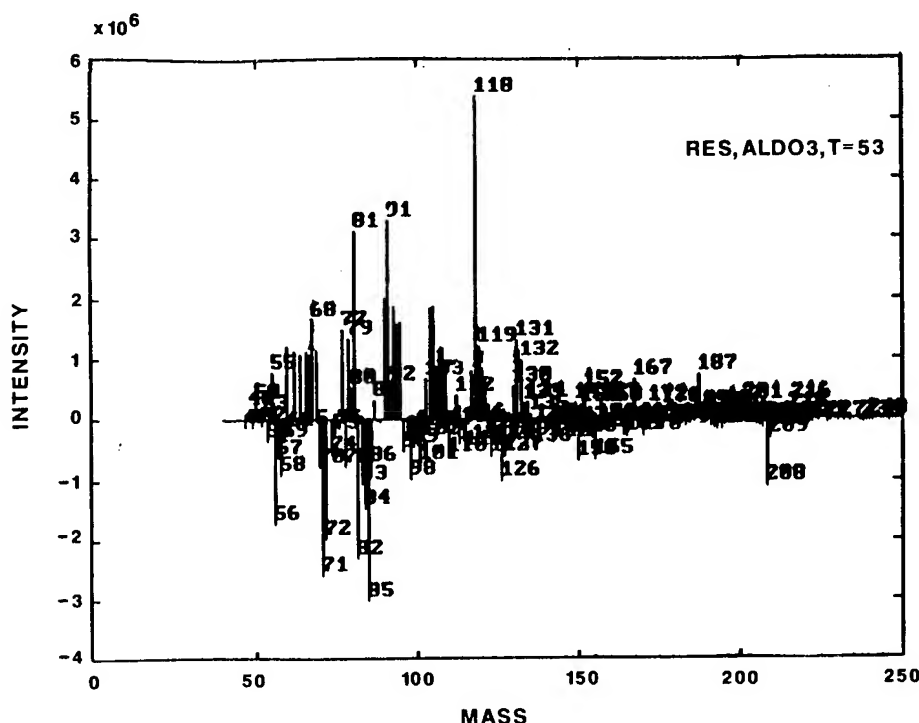


Figure 3. Residual mass spectrum of ALDO 3 after 53 s. Rank annihilation has removed the background.

#### 4. CONCLUSIONS

This study suggests the following. First, the EFA technique is useful for finding and evaluating constant backgrounds. Second, rank annihilation using the assumptions of this paper eliminates too much important information with the background. Third, scientists need a better set of assumptions to analyze pyrolysis-mass spectra.

The assumption of constant mass spectrum of contaminants may be the most important flaw in the analysis in this paper. Inspection of the temporal profiles of the strongest background peaks shows that the temporal profiles of each mass number evolve differently. Only a few physical processes can produce such behavior in ions. A more detailed model of the temporal dynamics of a contaminant, including correlations between mass numbers, must be included in the RA algorithm. However, rank annihilation should give a clear and unambiguous interpretation of pyrolysis-mass spectra once the dynamics of the contaminant are understood.

#### REFERENCES

- Brown, Steven D., 1991: Multivariate Analysis of Pyrolysis Mass Spectral Responses from Several Bacteria and Common Interferents. Contractor Report DAAL03-86-D-0001, U.S. Army Research Office, Research Triangle Park, NC.
- Hirsch, Roland H., Grace Lam Wu, and Patricia C. Tway, 1987: Reliability of Factor Analysis in the Presence of Random Noise or Outlying Data. Chemometrics and Intell. Lab. Sys., 1:265-272.
- Maeder, Marcel, 1987: Evolving Factor Analysis for Resolution of Overlapping Chromatographic Peaks. Anal. Chem., 59:527-530.

# A COMPARISON OF LOW LEVEL WIND AND TEMPERATURE PROFILES FROM A RADIOSONDE, SODAR AND MESOSCALE MODEL

Ian D. Todd and Jonathan D. Turton  
Meteorological Office  
Bracknell, U.K.

## ABSTRACT

Noise assessment is an important task for the met office at the Proof and Experimental Establishment, Shoeburyness. Work is being conducted to improve on the accuracy of acoustic predictions provided to the range. Part of this work concerns assessing the usefulness of low level wind and temperature profiles from several different sources - radiosonde, sodar and a Mesoscale Model. This paper presents some results from a comparison of these data with particular emphasis on their relevance for making acoustic predictions.

## 1. INTRODUCTION

One of the most important tasks for the met office at the Proof and Experimental Establishment (P&EE) Shoeburyness is the provision of noise predictions for the range. At Shoeburyness, range activities include the proof and testing of service stocks and production samples of weapons and ammunition, and trials associated with the development of new weapon systems and munitions. These activities create a significant amount of impulsive blast noise from firings and detonations. The range lies near to a number of populated areas which could, on occasions, be subjected to high noise levels. If this happens complaints of noise nuisance, or even structural damage to buildings, can arise. Noise predictions are made by the met office to assist the range in minimising noise nuisance, whilst still enabling the optimum use of range facilities.

There is an ongoing program of work to improve on the quality of noise predictions provided to the range. This consists of work to improve on the acoustic modelling, since the current operational model (the so-called Larkhill MkII model; Turton et al, 1988) is limited by its semi-empirical nature. However, whatever type of model is used, the results will only be as good as the meteorological data used as input to the model.

The meteorological data required to make acoustic predictions are the low level (up to a km height or so) profiles of wind (speed and direction) and (virtual) temperature. This paper focuses on the accuracy, usefulness and limitations of low level meteorological profiles available from an on-site radiosonde system, a doppler sodar, and a Mesoscale Model.



## 2. SOURCES OF METEOROLOGICAL PROFILE DATA

From October 1991 through to September 1992 meteorological profile data for Shoeburyness were archived. Shoeburyness is a flat coastal site so that there are no topographic effects, but coastal effects (e.g. sea breezes) do occur. The data include profiles measured by the on-site radiosonde system and a doppler sodar, together with profiles extracted from operational runs of the Met Office Mesoscale Model for the grid point corresponding to Shoeburyness.

### 2.1 RADIOSONDE DATA

The current acoustic model uses data from the on-site radiosonde system and takes, as input, winds and temperatures at 150 m intervals up to 3 km (150 m, 300 m, ... , 3 km). These data are supplemented by the 10 m wind and screen temperature measured at the range met office site.

In 1990 all Meteorological Office upper air sounding stations and range stations were equipped with the Vaisala PC-Cora radiosonde system, which replaced the older Met Office RS3 system. The PC-Cora system has been described by Nash (1991) and uses the standard Vaisala RS80 sonde for temperature and humidity measurements. At Shoeburyness winds are currently determined by tracking a radar target using a Cossor 353C wind-finding radar.

At Shoeburyness soundings are usually made several times a day (typically around 0700 and 1100), with additional ascents as required. Such soundings provide a snap-shot of the atmosphere at the time of flight. The temperature and humidity sensors have an accuracy of  $\pm 0.2$  °C and  $\pm 2$  %, and give measurements every 2 s ( $\approx 10$  m) from launch. One of the disadvantages of using sonde ascents for acoustic predictions is that radar lock-on does not occur until about 200 m height, so radar derived winds can not be obtained below this. The low level wind structure is critical in the propagation of sound and so this may be an important limitation. The derived winds are 150 m layer ( $\approx 30$  s) averages centred on the designated 150 m levels. Since the profiles are near instantaneous samples, they may contain irregularities as a result of the balloon rising through turbulent eddies in the boundary layer, and may not be representative of the mean wind. The 150 m wind (speed and direction) produced by the system is based on a Vaisala algorithm which interpolates between the input 10 m wind and the first radar derived winds, and may be less reliable.

### 2.2 DOPPLER SODAR

The sodar used was a Remtech PA2 (phased array) device which operates at 2100 Hz and has a maximum vertical range of 1.5 km. The device has an electronically steered antenna which emits acoustic pulses sequentially in three different directions. The pulses are back-scattered by turbulent variations in the acoustic refractive index; these variations being primarily due to small scale ( $\approx 16$  cm) fluctuations in temperature. The doppler shift of the detected return signals gives information on the motion of the fluctuations causing the scattering and it is assumed that these are moving with the velocity of the mean wind. By measuring the delay of the return signals the height of the scatterer can be determined. Sequences of pulses are emitted periodically and (the three components of) the mean wind at selected heights are determined over a specified integration period.

In this study the sodar was set up to produce horizontal wind data at 50 m intervals to a maximum of 1 km height with an integration period of 30 minutes. Since October 1991 the sodar has operated almost continuously with just a few breaks in the data. Whilst the sodar can give "time-averaged" winds over the sampling period at lower levels (down to 50 m) and better vertical resolution than the PC-Cora system its performance (range and accuracy) is affected by the weather conditions (e.g. strong winds and precipitation) and stability.

Fig. 1 gives the maximum ranges which were available from the sodar over the whole period, nearly one year, and shows that 750 m was reached on 25% , 500 m on 50% and 300 m on 75% of occasions. There was, as expected, slightly better range performance during the day, which is due to the fact that at night reduced levels of turbulence occur aloft, in spite of the lower level of ambient noise. This range behaviour is consistent with that found previously with other sodars e.g. Beljaars (1985), Nash and Bond (1989). However at Shoeburyness the difference in range performance between daytime and night-time was relatively small, and is probably due to a reduced diurnal variation because of the coastal location.

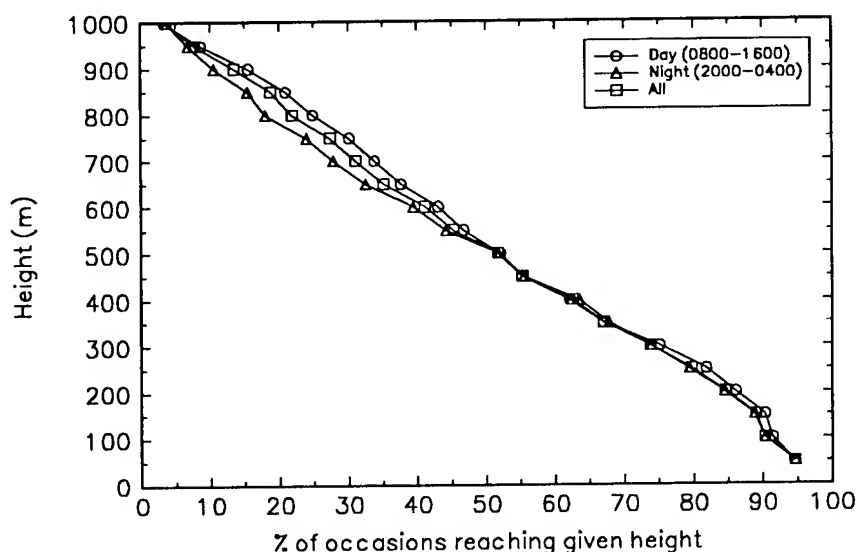


Figure 1. Maximum height available from the sodar.

### 2.3 MESOSCALE MODEL

The Meteorological Office Mesoscale Model (MM) is a short period forecasting model covering the British Isles and is described in detail by Golding (1990). The version of the MM run during this study had a horizontal resolution of 15 km and 32 vertical levels, 14 of which are below 1 km (i.e. at 1.25, 2.5, 5, 10, 20, 40, 70, 115, 175, 255, 355, 480, 630 and 810 m). The MM was run operationally to produce forecasts twice daily; at 00Z out to 18 hours and at 06Z out to 30 hours. The potential of the MM is that it could be used to give an indication of acoustic conditions for the day ahead for trials planning; also it would be possible to make acoustic predictions for locations (e.g. bombing ranges) where there is no on-site meteorological support.

In the results presented here, the model data from the 00Z forecast run were used since these are the data that would be available to the forecaster in the early morning in time for trials planning. The MM profiles for  $t+8$ ,  $t+11$  and  $t+14$  from the 00Z forecast run were extracted and compared against the on-site measurements (radiosonde and sodar).

### 3. WIND COMPARISONS

Comparisons were made between the PC-Cora, sodar and MM winds at various heights up to 600 m. However, it should be noted that there are significant differences in the way the winds are produced. For the PC-Cora the winds are nearly instantaneous, the 300 m and 600 m winds are 150 m layer ( $\approx 30$  s) averages, whilst the 150 m wind is derived from an algorithm. The sodar the winds are 30 minute "averages" with a 30 m resolution centred on the specified height. The MM winds are numerical forecasts. Whilst the PC-Cora and the sodar actually gave winds at the specified levels, the MM winds were determined by linear interpolation between adjacent grid levels (as given in section 2.3).

An example of one of the comparisons is given in Fig. 2 which shows how the sodar wind speeds and directions related to those produced by the PC-Cora system; the data are for 300 m height. All sodar winds "validated" by the software were included in the figure and the subsequent analysis; no additional quality control was made, so some dubious winds will inevitably have been included.

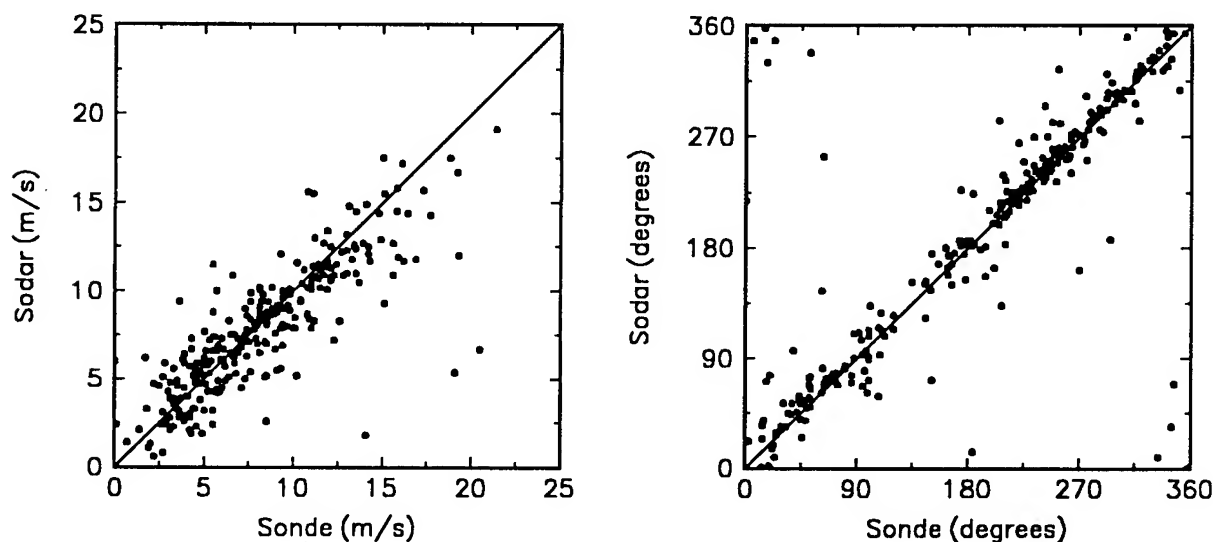


Figure 2. Comparison of sodar and PC-Cora (radar derived) wind speed and direction at 300 m height.

The results are summarised in Tables 1 to 3, which show the comparisons between each source of wind data. The mean differences give the "bias", whilst the rms differences give the "comparability".

TABLE 1. MEAN AND RMS WIND DIFFERENCES (SODAR-SONDE)

Height (m)	no samples	Wind Speed (m/s)		Wind Direction (deg)	
		mean diff	rms diff	mean diff	rms diff
150	328	0.16	2.14	4.43	31.16
300	265	-0.42	2.41	0.64	28.33
600	132	-0.08	2.80	1.28	37.75

TABLE 2. MEAN AND RMS WIND DIFFERENCES (MM-SONDE)

Height (m)	no samples	Wind Speed (m/s)		Wind Direction (deg)	
		mean diff	rms diff	mean diff	rms diff
10*	285	1.21	1.96	4.84	41.47
150	285	0.83	2.40	-1.76	38.91
300	285	0.07	2.45	-6.79	35.85
600	284	0.10	2.52	-3.73	35.80

\* from 10 m anemometer, as input to the PC-Cora system

TABLE 3. MEAN AND RMS WIND DIFFERENCES (MM-SODAR)

Height (m)	no samples	Wind Speed (m/s)		Wind Direction (deg)	
		mean diff	rms diff	mean diff	rms diff
50	385	0.09	2.74	-8.68	45.07
100	355	0.36	2.22	-6.64	41.57
150	373	0.53	2.51	-4.49	39.83
300	296	0.48	2.83	-6.26	39.66
600	160	0.32	2.73	-6.10	43.94

As the data are from three different sources it is reasonable to assume that the errors in the winds for each source are independent. Then

$$\begin{aligned}\sigma_{\text{sodar-sonde}} &= (\sigma_{\text{sodar}}^2 + \sigma_{\text{sonde}}^2)^{1/2} \\ \sigma_{\text{MM-sonde}} &= (\sigma_{\text{MM}}^2 + \sigma_{\text{sonde}}^2)^{1/2} \\ \sigma_{\text{MM-sodar}} &= (\sigma_{\text{MM}}^2 + \sigma_{\text{sodar}}^2)^{1/2}\end{aligned}$$

where  $\sigma$  denotes the standard deviation, which is given by

$$\sigma = ((\text{rms diff})^2 - (\text{mean diff})^2)^{1/2},$$

and  $\sigma_{\text{sonde}}$ ,  $\sigma_{\text{sodar}}$  and  $\sigma_{\text{MM}}$  can be calculated. These estimates give an indication of the error in the winds for those heights where data was available from all three sources. The error estimates are given in Table 4.

TABLE 4. ESTIMATED ERRORS (1 SD) IN THE WINDS

Height (m)	Sonde		Sodar		Mesoscale Model	
	speed (m/s)	dirn (deg)	speed (m/s)	dirn (deg)	speed (m/s)	dirn (deg)
150m	1.34	21.2	1.66	22.4	1.80	32.6
300m	1.39	15.9	1.93	23.4	2.01	31.4
600m	1.85	20.0	2.10	32.0	1.71	29.5

These results can be compared with a number of previous studies. Beljaars (1985) found that the rms differences between a (Remtech AO) sodar (for 30 minute samples) measurements from a 200 m tower were typically  $\approx 1$  m/s for wind speed and  $\approx 10$ -20 degrees in direction; the differences (errors) increasing with height. Similar results for two Remtech AO sodars were also obtained against tower measurements (20 minute samples) by Chintawongvanich et al (1989) at heights of 100 m, 200 m and 300 m, who also found an increase in error with height. Studies by the UK Met Office comparing the Cardington (a Remtech AO) sodar with instrumentation on a tethered balloon cable also show similar characteristics (Hopwood, 1991). These studies also found that the rms differences (scatter) appeared to be smaller under stable conditions than in neutral or unstable conditions. In a trial of several sodars at Larkhill, during April 1988, Nash and Bond (1989) obtained similar differences between the Cardington sodar (30 minute samples) and balloon winds (tracked using high precision kine-theodolites) with sd differences of  $\approx 1.3$  m/s and 25 degrees below 600 m height.

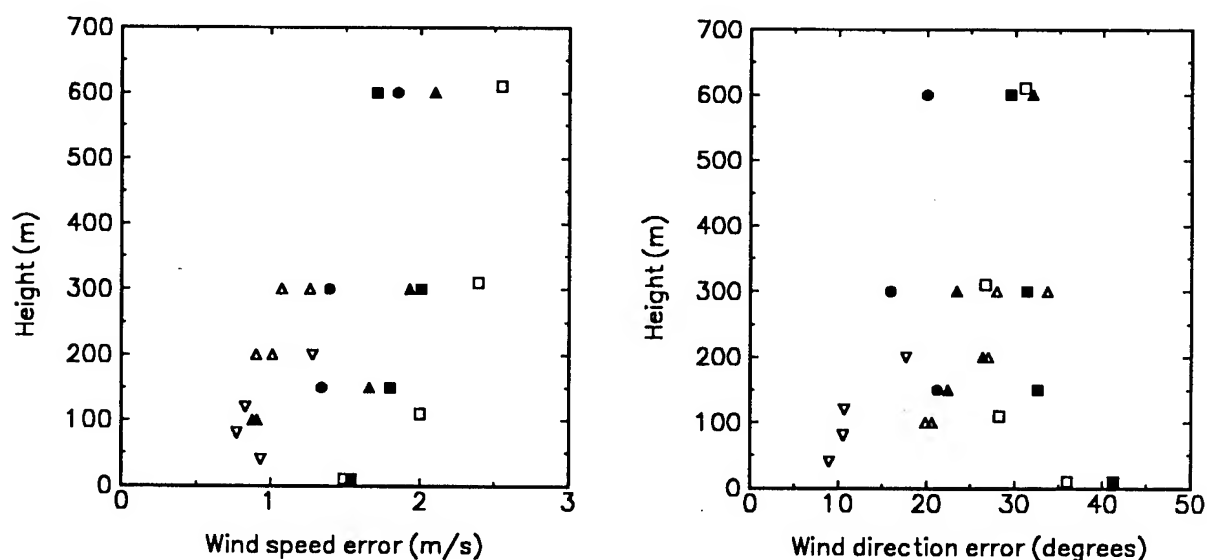


Figure 3. Errors (1 sd) of wind speed and direction from the PC-Cora (●); doppler sodar - Shoeburyness (▲), Chintawongvanich et al (Δ), Beljaars (▽); and Mesoscale Model - Shoeburyness (■), Galinski and Thomson (□).

The wind errors, together with those found in the other studies, are shown in Fig. 3. However, at Shoeburyness the sodar and balloon data were collected over an extended period (nearly a year)

under all weather conditions, thus the results obtained here are representative of the operational performance of such a device. Consequently, the estimated sodar wind errors are a little greater than those found in the other studies, and suggest typical errors for the sodar measurements up to 600 m of  $\approx 1.6$ -2.1 m/s and 22-32 degrees; the errors increasing with height. As noted earlier all sodar winds "validated" by the software were used in the results presented here. However, experience with the Cardington sodar (Galinski and Thomson, 1990) has shown that the errors can be significantly reduced by smoothing the data in time and height.

Galinski and Thomson (1990) compared the winds predicted by the MM to those measured by the Cardington sodar. They found that the MM tended to give higher speeds (by  $\approx 1.1$  m/s at 110 m height,  $\approx 0.6$  m/s at 310 m and  $\approx 0.7$  m/s at 610 m) with rms differences of 2.3 m/s, 2.5 m/s and 2.6 m/s respectively. These figures are similar to those found at Shoeburyness (Table 3). For direction Galinski and Thomson found a relatively small mean directional difference of  $\approx 0.1$  degrees up to 600 m, with a rms difference of 31 degrees; the directional differences being somewhat less than those obtained at Shoeburyness. Estimated errors (1 sd) for the MM based on the Cardington figures together with those from Shoeburyness (Table 4) are also shown in Fig. 3.

The results given in Table 4 suggest that the sodar wind speeds are only slightly less accurate than those derived from the PC-Cora system, but that the sodar directional accuracy is rather poorer, particularly at greater heights. However, there is scope for some improvement in the sodar winds by applying some further data processing/smoothing as applied to the Cardington sodar data. The PC-Cora winds are still quite reasonable at 150 m, despite the fact that they are calculated from an algorithm, although the results suggest that the 150 m wind direction is less reliable than that measured at 300 m. The wind speeds from the MM appear to be of comparable quality to the sodar measurements, but the directions are less reliable than the measurements with a (1 sd) error of  $\approx 30$  deg. However, at 600 m they are no poorer than the sodar directions. Near the ground (at 10 m) the MM wind speed error decreases, whilst the directional error is greater; this behaviour was also found by Galinski and Thomson (1990).

#### 4. TEMPERATURE COMPARISONS

A comparison was also made between the virtual temperatures predicted by the MM and those measured in the screen (1.3 m) and by the radiosonde at 150 m, 300 m and 600 m height. The accuracy of the radiosonde temperature measurements is believed to be about  $\pm 0.2$  °C. The results are given in Table 5.

TABLE 5. MEAN AND RMS TEMPERATURE DIFFERENCES (MM-SONDE)

Height (m)	no samples	Virtual Temperature (°C)		
		mean diff	rms diff	sd
1.3	286	0.40	1.56	1.51
150	238	0.50	1.58	1.28
300	238	0.53	1.35	1.24
600	238	0.27	1.29	1.26

The table shows over the period the MM had a small warm bias and that the rms differences actually reduced slightly with height. Typically the rms temperature differences were  $\approx 1.3$ - $1.6$  °C with errors of  $\approx 1.2$ - $1.5$  °C for the MM.

## 5. DISCUSSION AND CONCLUSIONS

The results discussed above give an indication of the errors in winds and temperatures derived from the different sources. In modelling the propagation of sound these parameters are used to calculate the profile of sound speed ( $c$ ) in a given direction,

$$c(z) = 20.05 T_v(z)^{1/2} + v(z) \cos[\alpha(z)-D]$$

where  $\alpha$  is the wind direction (here the direction the wind is blowing towards) and  $D$  is the direction of interest. Therefore the accuracy of the derived sound speed values will depend upon the errors in the wind speed, direction and virtual temperature. The error in  $c$  ( $\delta c$ ) is given by

$$\delta c = [(10.025 \delta T_v / T_v^{1/2})^2 + (\cos^2(\alpha-D) \delta v^2 + v^2 \sin^2(\alpha-D) \delta \alpha^2)]^{1/2}.$$

Substituting typical values for the (MM) errors, i.e.  $\delta v = 2$  m/s,  $\delta \alpha = 30$  degrees,  $\delta T_v = 1.3$  °C,  $v = 10$  m/s and  $T_v = 10$  °C (283 K) gives (i) along the wind direction

$$\delta c = [(0.77)^2 + (2)^2]^{1/2} = 2.1 \text{ m/s},$$

and (ii) across the wind

$$\delta c = [(0.77)^2 + (5.24)^2]^{1/2} = 5.3 \text{ m/s}.$$

In both cases the contribution of the temperature error is small compared to the errors in the winds. All the directionality in the noise propagation is due to the wind profile and this highlights the fact that for acoustic modelling it is essential to have reliable wind profile data, but is less critical to have accurate temperature data. The estimated  $\delta c$  values also show that the effect of wind errors is least in the down/up wind directions and greatest across the wind. This implies that the predictions in the across wind direction will be subject to the greatest error; this is not surprising since the across wind direction is usually associated with the transition region between downwind sound enhancement (high noise levels) and upwind sound shadow (low noise levels) zones and is a region where the noise levels change rapidly. However, in practice it is predicting the regions of enhancement and focusing that are associated with high noise levels that is the critical aspect of acoustic forecasting. Whilst the results suggest that predictions for the enhancement region should be fairly reliable, it is more difficult to draw any conclusions on predictions of focusing.

From the data presented in this paper it is possible to draw some conclusions on the usefulness of the different sources of wind measurements. The results suggest that the accuracy of winds derived from the PC-Cora radiosonde system are better than those from the sodar, even down to 150 m height. However, below this height the sodar winds would be expected to be better, although acceptable winds below 150 m could probably be obtained from the PC-Cora system using an improved algorithm. It is likely that the accuracy of the sodar winds could be improved by some further data processing/smoothing.

Given the availability of both radiosonde and sodar winds the results suggest that the PC-Cora winds should be better. However, this will only be true if the measurements pertain to the time that the acoustic prediction is required for. Nash and Bond (1989) estimated the (1 sd) vector wind change, up to 600 m height, due to atmospheric variability as  $\approx 1$  m/s for 30 minutes separation and  $\approx 2$  m/s for 2 hours separation. This indicates that, at low levels, the winds may quickly become "stale". The advantage of the doppler sodar is that it can provide continuous wind data throughout the day such that the wind profile can be regularly updated. This suggests that there should be a benefit from using sodar wind data for acoustic modelling if predictions are required at more regular intervals. Also, if noise hindcasts are required for the analysis of specific events then the availability of sodar data for those occasions should permit more accurate hindcasts to be made.

The availability of doppler sodar data would have little impact on providing noise forecasts for several hours ahead. At present the forecaster subjectively modifies the available radiosonde data, to account for the expected diurnal and synoptic changes, and uses the adjusted profiles to generate a noise forecast. For this application it is suggested that the MM winds and temperatures look sufficiently accurate to allow reasonably reliable noise predictions to be generated. The directional errors are only  $\approx 10$ -15 degrees poorer than the measurements, which should not have a major detrimental impact on the noise predictions, other than in the across wind direction. However, the quality of any noise forecasts would be expected to be the best, if the forecaster was able to assess and modify, as necessary, the MM winds and temperatures.

Although the results presented here suggest that using MM data should allow useful noise forecasts to be made, this hypothesis can only be properly tested by validating such predictions against noise measurements under a wide range of meteorological conditions. Since May 1992 a program to collect noise level data from various firings/detonations at P&EE Shoeburyness has been underway; these data are being used to assess and validate the various acoustic models available and will also permit the accuracy of noise forecasts generated using MM data to be quantified.

#### REFERENCES

- Beljaars, A.C.M., 1985: Verification of doppler sodar measurements. KNMI Scientific Report W.R. 85-2, KNMI, De Bilt, Netherlands.
- Chintawongvanich, P., Olsen, R. and Biloft, C.A., 1989: Intercomparison of wind measurements from two acoustic doppler sodars, a laser doppler lidar, and in situ sensors. J.Atmos.Oceanic Technol., **5**, 785-797.
- Galinski, A.E. and Thomson, D. J., 1990: Intercomparison between the Mesoscale and Fine-Mesh Model winds and observations at Cardington, Hemsby and Crawley. Met.O.(P) Special Investigations Technical memorandum No. 4, Met Office, Bracknell, UK.
- Golding, B., 1990: The Meteorological Office Mesoscale Model. Meteorol. Mag., **119**, 81-96.
- Hopwood, W.P. 1991: Principles, accuracy and performance of a doppler acoustic sodar. (Unpublished report, Met. Office Research Unit, Cardington, UK.)
- Nash, J. and Bond, F., 1989: An operational evaluation of wind measurements by two doppler sodars. WMO/TD No. 35, 407-212.
- Nash, J., 1991: Implementation of the Vaisala PC-Cora upper air sounding system at operational radiosonde stations and test ranges in the United Kingdom. In Proceedings of the 7th Symposium on Meteorological Observations and Instrumentation, New Orleans, LA, US.
- Turton, J.D., Bennetts, D.A. and Nazer, D.J.W., 1988: The Larkhill noise assessment model. Part 1: theory and formulation. Meteorol. Mag., **117**, 169-179.





## ERRORS IN SKY-COVER OBSERVATION BY GROUND-BASED OBSERVERS

Donald L. Reinke, Thomas H. Vonder Haar, Kenneth E. Eis, and D. Neil Allen  
Cooperative Institute for Research in the Atmosphere (CIIRA)  
Colorado State University, Foothills Campus  
Fort Collins, Colorado 80521, USA

and

METSAT Inc.  
Fort Collins, Colorado 80521, USA

Paper in conjunction with poster for  
1992 Battlefield Atmospheric Conference

### ABSTRACT

DoD planning and simulation activities are highly dependent upon the Air Weather Service's Real Time Nephanalysis (RTNEPH) for cloud climatologies. The RTNEPH is predominantly driven by surface observations to produce its 43 x 43 nm gridded data base. A recent study suggests that the surface observations, in certain circumstances such as coastal, high haze, and mountain valley regions, may not be accurate because of the ground observer's limited view of the sky dome over the station. In this recent study, detailed GOES composite climatologies were compared to cloud climatologies from ground-based observing sites. The two methods of cloud measurement were generally in good agreement. The exceptions were at locations where persistent cloud cover gradients occurred within the sky dome of the ground observer. These exceptions cause significant local biases in the observed sky condition and subsequently, in the RTNEPH. The biases discussed in this preliminary analysis have significant impacts on specific locations of high military interest such as coastal regions (amphibious and naval operations) where fog or coastal stratus are dominate features and regions of persistent haze or smoke (like SE Asia where seasonal crop burn off can cause a serious overestimate of cloud occurrence). In a more general sense, this bias demonstrates another source of error in the RTNEPH process. Fortunately, a possible solution or correction is also within reach. The AFGWC cloud analysis and forecast process when studied "ex post facto" has always had a pessimistic bias when predicting no-cloud or little-cloud conditions and an optimistic bias on the overcast and mostly cloudy end of the cloudiness spectrum. Fortunately, the cloud frequency comparisons of surface stations and GOES composite climatologies show this same behavior. As a result, further study of many individual RTNEPH boxes using our new satellite product

could improve the RTNEPH analysis and future cloud forecast products.

## 1. INTRODUCTION

Cloud cover analyses have been made from satellite and surface-based observations for over two decades and until recently the ground-based observer's values have been used to ground-truth the satellite analysis. Consequently, military planners have used ground-observer dominated data as the basis for many of their decisions. The Real-Time Nephanalysis, (RTNEPH) produced at the Air Force Global Weather Central (AFGWC) and archived and used by the USAF Environmental Technical Applications Center (USAFETAC) to produce planning cloud climatologies for all three services, has its roots in a ground-based cloud analysis (Kiess and Cox, 1988). It is time to reexamine the "truth" of "ground-truth".

## 3. SOURCES OF ERROR

Ground-based cloud observation has two primary sources of error, obstructions to visibility, and the perspective error associated with the observer's point of view, the so-called sky dome vs surface cloud coverage. The sky dome issue has been well treated in the observing literature.

The coupling of visibility to cloud observation has not had as thorough a treatment. Figure 1 illustrates the error, as a function of distance from the observer, intrinsic in a visibility limited case, as a linear cloud deck (or clearing) moves toward an observer. Figure 2 shows the geometry and equation used to compute fig. 1. The error is computed by taking the segment of a circle within the radius of influence and dividing by half the area of the radius of influence. Beyond the radius of influence the error is defined as zero. The error is again zero when the cloud boundary is directly over the observer because the observer sees half of his sky cloud covered, regardless of visibility. Typically, a nephanalysis, including the RTNEPH, uses a radius of influence of 25 to 50 kilometers for each surface observation. The simple geometry of fig. 2 and the analysis in fig. 1 shows that during dynamic movement of clouds over an observer where the visibility is less than the nephanalysis's radius of influence errors in excess of 80 percent result.

High resolution satellite cloud analyses have been compared to surface observations (Reinke et al., 1992). This study has shown other sources of error associated with obstructions to visibility. Figure 3 shows the 25 km radius of influence for a surface station, as viewed by the GOES satellite. The pixels are 2.5 km resolution. The color represents the probability of sky with a ceiling at each pixel. Note that within the observation's 25 km radius of influence the GOES image gives over 300 cloud probability values for the observer's one. The left circle in fig. 3, the area over San Diego, shows a persistent gradient in cloud probability due to marine stratus off the Pacific coast. Figure 4 shows circles depicting surface observing locations in the western United States. The grey shades represents the difference between the mean surface observed cloud ceiling probability and the cloud ceiling probability as computed from monthly mean GOES composites for the same locations. The most disagreement occurs along the coast where persistent marine stratus is beyond the view of the surface observer.

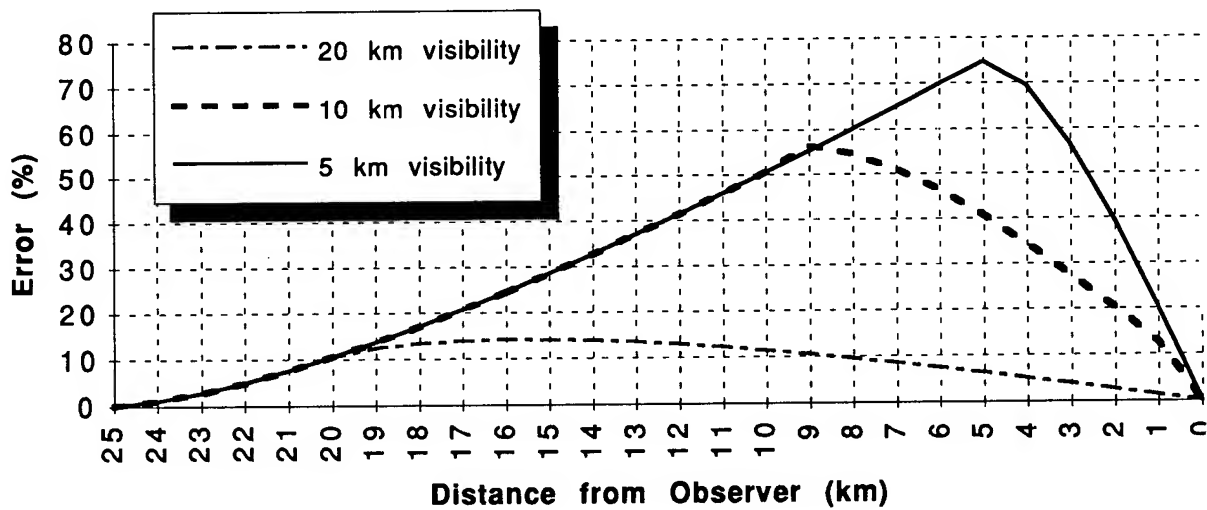


Figure 1. Observed Cloud Cover Error as Function of Visibility (25 km)

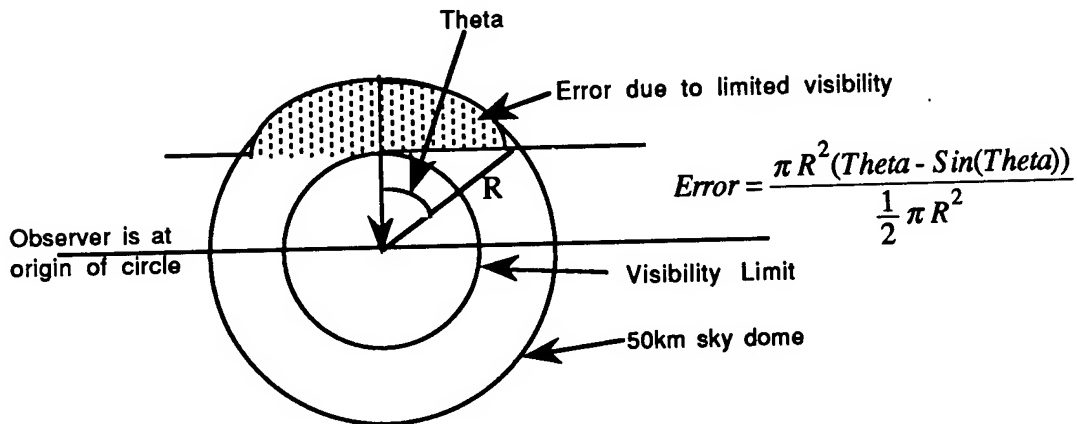


Figure 2. Geometry and Equation Used to Compute Figure 1.

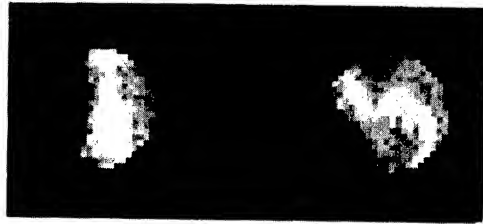


Figure 3. 50 km diameter circle from GOES cloud composite climatology showing gradient across the station circle. The circles are centered on San Diego, CA and San Luis Obispo, CA.



Figure 4. Circles represent a 50 km diameter area around surface reporting stations. Grey-shades show difference between surface observations of cloud and satellite-derived cloud cover.

### 3. IMPACTS ON MILITARY METEOROLOGY

These errors will propagate into the RTNEPH which is used to initialize cloud forecasts at AFGWC for a variety of DoD customers. The RTNEPH itself is used to produce a variety of products including cloud statistics for weapons systems simulations and as a seed for statistically based cloud simulators. As fig. 4 indicates, significant errors occur along land/sea boundaries, in mountain valleys, and other areas where large gradients occur in cloud climatology. It appears that amphibious and mountain operations planning would benefit from a satellite-based cloud climatology which detects these gradients.

#### ACKNOWLEDGEMENTS

This paper was supported by METSAT Inc.'s internal R&D program.

#### REFERENCES

- Kiess, R.B. and W.M. Cox, 1988: The AFGWC Automated Real-Time Analysis Model. AFGWC/TN-88/001, AFGWC, Air Weather Service (MAC), Offutt AFB, NE, 82 pp.
- Reinke, D.L., C.L. Combs, S.Q. Kidder, T.H. Vonder Haar, 1992: Satellite Cloud Composite Climatologies: A New High-Resolution Tool in Atmospheric Research and Forecasting, Bull. Am. Meteor. Soc., 73, No. 3, 278-285.



# **THE MIDAS/ATLAS VIDEO IMAGERY DATABASE: AN ADVANCED SYSTEM FOR STORING AND ACCESSING DIGITALLY COMPRESSED VIDEO IMAGERY**

Michael Rollins  
Science and Technology Corporation  
Las Cruces, New Mexico 88001

Max P. Bleiweiss  
U.S. Army Research Laboratory  
White Sands Missile Range, New Mexico 88002

Rebecca Tipton  
New Mexico State University  
Las Cruces, New Mexico 88003

## **ABSTRACT**

For the past 14 years, the MIDAS/ATLAS work unit of the Atmospheric Sciences Laboratory (ASL) has participated in nearly 60 field tests. This work has resulted in the acquisition of several thousand videotapes of multispectral imagery, creating storage and accessibility problems whose solutions are described in this paper. Solving these problems involves three main efforts: (1) inventory and cataloging of existing tapes (2) development of a digitally compressed image database system, and (3) implementation of that system. Under ASL sponsorship, Science and Technology Corp. (STC) is currently conducting an inventory of the MIDAS/ATLAS tapes and is preparing a catalog of the tape data, which will aid in the implementation of the database system. The inventory is now nearly complete, with the exception of newly acquired data, and development has begun on the hardware/software system that will reduce the thousands of tapes to several hundred optical disks. This system uses image compression techniques, primarily frame averaging and the JPEG algorithm, to reduce storage requirements while maintaining data fidelity. The library of optical disks produced with this system will allow random and rapid access to any image in the inventory. In the coming year, this database system will be integrated into the AAODL as the process of conversion to optical storage begins. Future efforts will address the addition of image processing capabilities to the database system. This paper presents construction details of the system, along with examples of implementation.

## **1. INTRODUCTION**

During the past 14 years, the MIDAS/ATLAS work unit of the U.S. Army Atmospheric Sciences Laboratory (ASL) has participated in nearly 60 field tests. This participation has resulted in the acquisition of several thousand videotapes of multispectral imagery, creating storage and accessibility problems whose solutions are described in this paper. The large quantity of tapes and estimated



6000 hours of video content provides a thorough but inconvenient record of field tests. The inconvenience lies in the lack of easily accessed storage space, the limited amount of video on each tape, and the awkwardness of searching through individual tapes for a desired scene. The task of solving these problems involves three main efforts: (1) inventory and cataloging of existing tapes, (2) development of a digitally compressed image database system, and (3) implementation of that system.

For the past two years, Science and Technology Corp. (STC) has been creating an inventory of these tapes and preparing a catalog of tape information to aid in the automation of video digitization and compression procedures. With the exception of newly acquired data, the inventory is nearly complete. Also during this period, a hardware/software system has been under development. This system will reduce the thousands of tapes to several hundred optical disks through image compression techniques. The image compression techniques use frame averaging and the Joint Photographic Experts' Group (JPEG) algorithm to reduce storage requirements while maintaining data fidelity. This library of optical disks will allow random and rapid access to any scene in the inventory. Through the JPEG algorithm, a 20:1 compression of 10 grey-scale frames per second, for instance, will result in 691 GB of stored data. This figure assumes an equivalent 320 x 200 input resolution suitable for VHS picture quality. These data would likely be stored on about 110 12-in, 6.4-GB optical disks. Proportionally more disks would be required for higher spatial or temporal resolution. At any rate, storage problems and access time would be greatly reduced.

In the coming year, this system will be integrated into the Atmospheric Aerosols and Optics Data Library (AAODL) as the process of conversion to optical storage begins. Future efforts will address the addition of image processing capabilities to the database system. Hardware needed to construct the compression and storage system is described in this paper, along with examples of implementation.

## **2. INVENTORY AND CATALOGING**

The inventory process consists of acquiring videotapes of smoke tests, obtaining corresponding field notes, and entering tape and testing information into a paper tape log. Copies of pages of the log are placed with the boxes in which the tapes are stored. The information is also entered into a database using the test name, tape number, and trial number to uniquely specify a particular video sequence. The sequence length, spectral band, and other test condition information are also entered. A listing of all processed tapes can be generated in alphabetical and chronological order. To date, 2849 tapes have been logged and an estimated 600 more await processing. For further information on the tape log, see Rivas (1992). Information in the database will be used in the compression and storage process so that an efficient and convenient ordering of optically stored video sequences results.

## **3. COMPRESSION AND STORAGE SYSTEM DEVELOPMENT**

The key components of the image compression system under development include a real-time JPEG-based image compression board and a multifunction optical disk drive (see Fig. 1). A frame grabber provides a default 720 x 480 image to the compression board at 30 frames (60 fields) per second. The image compression board then performs the required discrete cosine transformation of contiguous 8 x 8 image blocks, the quantization, and the Huffman coding as prescribed in the JPEG algorithm. The output bit stream is sent through the ISA bus to an SCSI card, which sends the data to an external cacheing unit. This unit, which can currently cache up to 64 kB, makes transfer to the optical disk drive more efficient by decreasing the number of individual disk accesses and providing a continuous

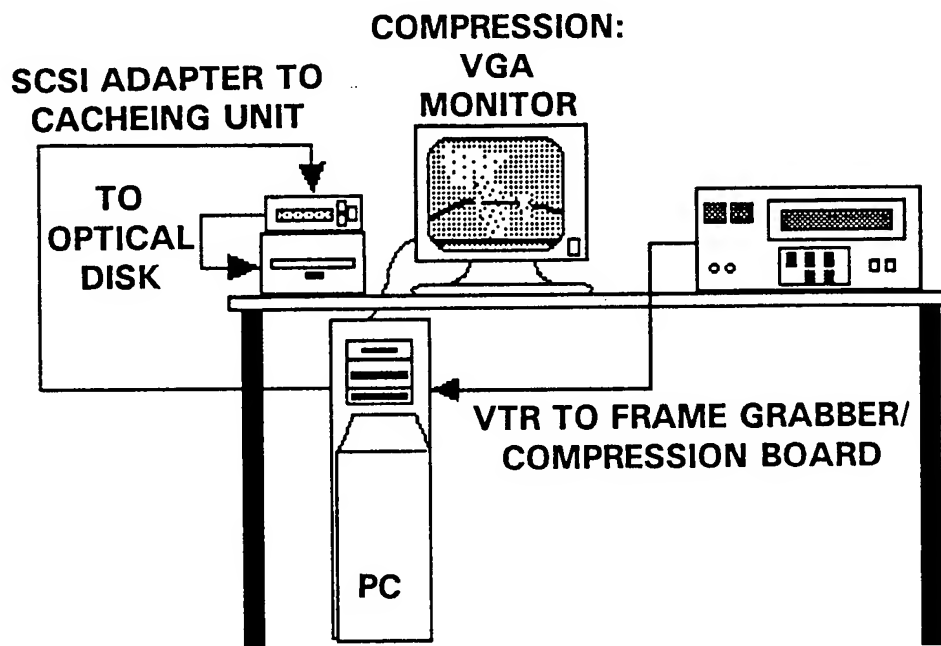


Figure 1. The current ATLAS/MIDAS compression and storage developmental system.

stream of data. The cacheing unit is also designed to provide further compression through a lossless algorithm.

The optical drive, which receives data via the cacheing unit, is designed to operate with either rewritable or WORM ("write once, read many times") media. Writing to rewritable media has been sustainable at about 440 kB per second using an assembly language routine based on Interrupt 13. When code is substituted that performs the write operation using a C-language file handle function, the observed sustained data rate is somewhat slower, although the optimal use of such code, which essentially performs Interrupt 13 writes, should approach the speed of the assembly code as well as providing convenient file handling capability. With the higher transfer rate, grey-scale images at default dimensions require a compression ratio of about 23:1.

Permanently retrievable storage of the file information requires a means of reinitializing variables and registers to restore the environment in which the image was saved. A program module to record the environment as a header or regenerate the environment by simulating the save procedure is under development. Another module is being written to retrieve IRIG timing information (where present) and include it with the stored image data.

The performance of the JPEG algorithm at various compression levels for a typical smoke image can be seen in Figs. 2 through 7. Two performance measures have been used to rate the quality of the compressed/decompressed images as compared to the original: the square root of the mean square error (SQRTMSE), and the mean absolute error (an L1 metric). The L1 metric has recently been suggested (DeVore et al., 1992) to be superior to the mean-square error in terms of human visual judgement. Comparison of quality over the sequence of images shows a more dramatic degradation using the L1 metric (25.97%) from the fifth to the sixth image, than with the SQRTMSE (24.52%). The opposite is true for the other samples.

#### 4. IMPLEMENTATION

The system under development as described in the previous section will continue to evolve with improvements in software and hardware. The model currently operating can store about two hours of grey-scale video on a WORM or rewritable optical disk at 10 frames per second and 20:1 compression. Ten frames per second is seen as an acceptable sampling rate in view of slowly changing smoke cloud dimensions. The input video signal may first undergo a frame averaging if it is necessary to remove periodic visual effects that occur at more than 5 Hz.

The decompressed video will show timing information referenced to the beginning of the sequence. If IRIG timing was originally recorded in the audio channel of the tape, it will also appear in a predesignated spot in the decompressed frames. The nature of optical storage with all recorded information exposed on the surface at once allows for rapid random access of a prespecified frame within milliseconds. With this in mind, an ASCII file containing the tapelog and disklog information will be available to the user in a window-oriented environment. The user will search by alphabetical field test listing for a desired image sequence. When the user selects the sequence, certain information will be passed to the image decompression program such as the starting and ending times and disk sectors for the sequence. When the user then enters the decompression window, a specified frame time could be entered and the program will calculate and quickly access an appropriate sector very close to the location of the desired frame. Fast-forward and reverse control will be available.

Key components of the current model may be changed or upgraded as technology becomes available. For instance, a manufacturer of a JPEG chip has been developing another encoding/decoding compression chip that will implement the Moving Picture Experts' Group (MPEG) algorithm, which uses JPEG-type intraframe compression as well as predictive interframe compression. Interframe compression, which capitalizes on temporal redundancy, can give a three-fold increase in compression ratios for the same level of quality generated by JPEG intraframe compression. In addition, the storage and hardware media could eventually be replaced by equipment such as a currently available mixed-media jukebox, which can store as much as 74 TB (Neilson, 1992).

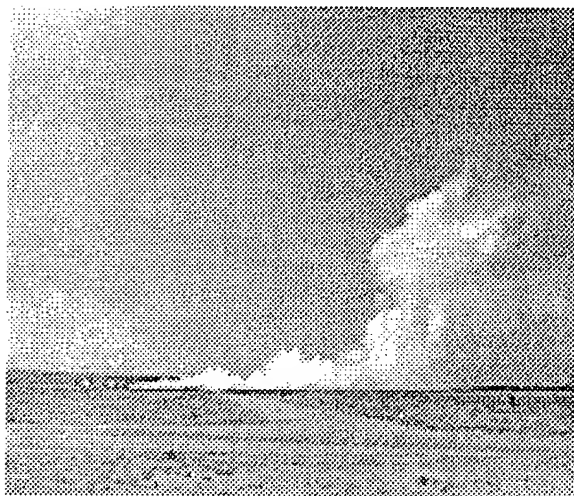


**Figure 2.** Original image.

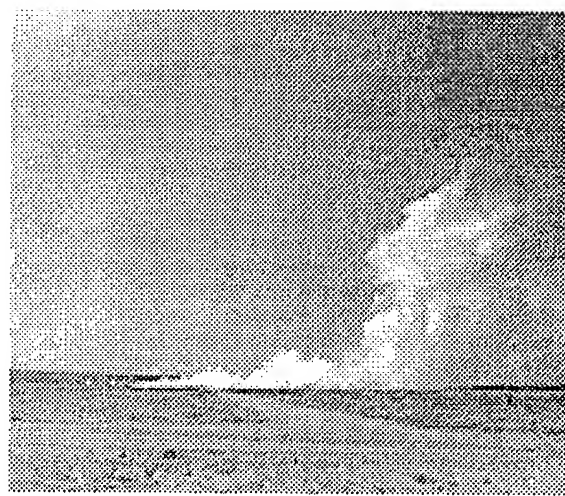


**Figure 3.** 6.55:1 compression;  
SQRTMSE=5.045, L1=3.829.

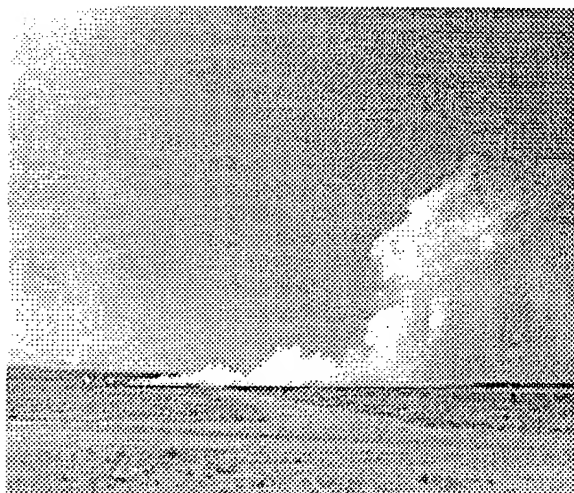


**Figure 4.** 10.86:1 compression;  
SQRTMSE=5.905, L1=4.439.

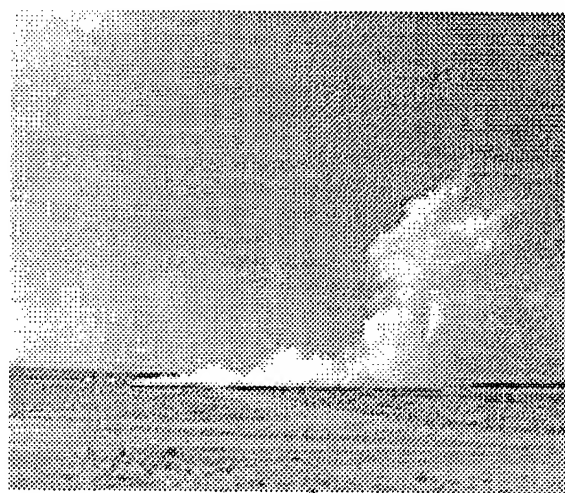


**Figure 5.** 19.59:1 compression;  
SQRTMSE=6.801, L1=5.046.

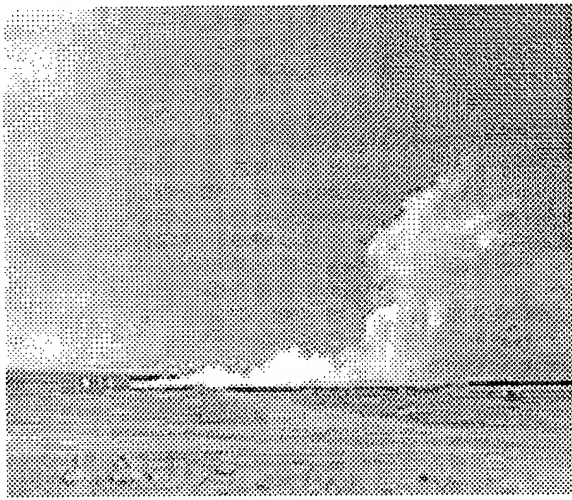


**Figure 6.** 29.67:1 compression;  
SQRTMSE=7.974, L1=5.875.

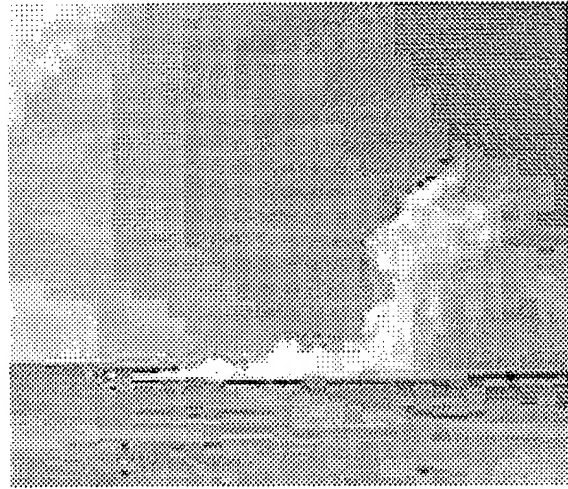


**Figure 7.** 39.77:1 compression;  
SQRTMSE=9.929, L1=7.401.

#### REFERENCES

- DeVore, R.A., B. Jawerth, and J.L. Bradley, 1992: Image compression through wavelet transform coding. *IEEE Trans. Information Theory*, 38(2), 719-746.
- Rivas, J.J., 1992: *Archiving of the MIDAS/ATLAS Work Unit*, Science and Technology Corp. Technical Report #6230(A), Hampton, Virginia (in press).
- Neilson, M., 1992: A Mixed Media Robot. *Imaging Magazine*, Sept., 16.

## MODERNIZED GRAPHICS CODES FOR USE WITH PROJECT WIND DATA

John D. Kincheloe  
New Mexico State University  
Las Cruces, NM 88003

### Abstract

A graphics program, titled MGCgraf, was created to assist in quality control error flagging(QCEF) and analysis of the data acquired by Project WIND. Written in Pascal, the program specifications required the display of over forty different graphs of various meteorological parameters such as air temperature, relative humidity, wind speed, wind direction, solar radiation, etc., in the form of time histories, cross-sections, time sections, vertical profiles, and horizontal spacial fields customized for computer assisted QCEF of the Project WIND data set. A DOS environment was specified as were output capabilities for EGA & VGA graphics monitors, HP LaserJet, HP DeskJet, dot matrix printers and HPGL compatible plotters. The program is currently implemented on an AST486 work station with Oracle interfacing capabilities and on a Zenith 386 personal computer. The application's main focus was to aid in analysis of the data on the monitor, allowing quick access to large amounts of data without generating an abundance of hard copy output.

### 1. INTRODUCTION

Project WIND (Cionco 1989) gathered well over 2 billion points of data when averaged using one minute intervals. One second interval data was recorded, and is still available, but converted to one minute averages for QCEF applications and analysis. Strict quality control of the data was desired and the intense work of error flagging began. Hard copy output of the first phase of data, taken during a period of two weeks in the summer of 1985, was created for this purpose. Eventually more than 14,000 plots, of the 40 different graphs, were generated for the Phase 1 data set of Project WIND. It was apparent that the resources required for both generating and storing the plots were expensive. Thus, the concept of creating a user friendly interactive plotting program tailored to the Project WIND data base, which utilized the monitor as its main output media, was conceived.

The Modernized Graphics Codes (MGC) allow for graphical data analysis on site eliminating second party dependency and increasing turn around time and overall productivity while decreasing end user cost.

The graphs desired were initially proposed and defined by ASL Project WIND scientists who also proposed a screen oriented input system, designed to allow users to get started quickly and be able to focus on data analysis instead of learning a complex graphics program. Another specification for the program was that it must support a variety of output devices, these are: standard EGA and VGA monitors, HP LaserJet printers, HP DeskJet printers, standard (Epson) dot matrix printers and HP plotters. This was done with complete transparency to the user who need only specify which device is desired for output.

The program was written in the Turbo Pascal, version 6.0, programming language because of its availability and the author's familiarity with it. Also, Turbo Pascal supported the application quite well due to its variety of complex data structures and a built-in fundamental graphics library.

## 2. PROJECT WIND

Project WIND was conducted as a cooperative field study between U.S. Army Laboratories and the U.S. Department of Agriculture Forest Service (Cionco 1989). The design was based on the multi-scale data requirements of the Atmospheric Sciences Laboratory's (ASL) hierarchical system of nested meso- and micrometeorological models (Cionco 1987). Project WIND obtained data within three domains: 200km x 200km, 80km x 80km and 5km x 5km. Data was gathered by thirty Surface Automated Meteorological Stations (SAMS), fourteen Campbells Stations (CAMS), six Micrometeorology (Micromet) Towers, five upper air sites, two to four tetheredsonde sites (depending on the Phase) and thirty three miscellaneous surface stations (hereafter referred to as "other" sites). The other sites data was gathered from both external sources, such as the U. S. Air Force, California Air Research Board, etc., and internal sources, i.e. Project WIND personnel. Four phases of data were gathered, each to obtain data for a different meteorological physics aspect: marine inversion, cyclonic events, shallow convection and subsidence.

During the task of error flagging of the first phase of data from hard copy output, produced by the Science and Technology Corporation (STC), it was realized that this format occupied too much space and was not very versatile. Thus the idea of the MGCGraf program was conceived, allowing computer assisted analysis of data on screen with the added capability to zoom into "interesting" data.



### 3. SCREEN ORIENTED INPUT

A general screen-oriented user interface library was created for the MGCGraf program. It was developed to allow users immediate access to the data without spending a lot of time learning to use the program. When started, the program offers a menu at the top of the screen for the user to choose a class of data to be displayed, along with a utility choice for setting up certain system defaults for the graphs and an editor to look at the actual ASCII data files of data involved. The classes of data to choose from are: SAMS/CAMS, Micromet Tower, Upper Air, Others and Maps. Once a data class is chosen, a sub-menu appears prompting for the particular format in which to display the data. As an example, if Micromet is chosen then a sub-menu offers the following: Micromet Measurements, Micromet vs. Time, Micromet Cross Sections, Micromet Single Params., and Micromet 1-Second Data. When this subsequent choice is made, a large detailed window appears on the screen which allows the user to input more information of details for the graph to be produced.

Figure 1 shows the screen if "Micromet vs Time" is chosen from the Micromet sub-menu. The user can input which of the six micromet towers to plot, the meteorological parameter to graph against time, the graph format, which tower levels to display and the particular day of data to use. Once choices are made the user selects the "Plot" button and the graph is displayed. "Cancel" is used to leave this menu, either before or after plotting, and the "Same" button automatically re-displays the last graph shown.

e	Sams/Cams	Micromet	UpperAir	Others	Maps	PE2
Micromet Measurements						
Micromet Single Level Parameters						
Tower:			Variable to Plot:			
<input type="checkbox"/> Forest 1			<input checked="" type="checkbox"/> Temperature vs Time			
<input type="checkbox"/> Forest 2			<input type="checkbox"/> Relative Humidity vs Time			
<input type="checkbox"/> Forest 3			<input type="checkbox"/> Rho Temperature vs Time			
<input checked="" type="checkbox"/> Orchard 1			<input type="checkbox"/> Intensity of Turb. vs Time			
<input type="checkbox"/> Orchard 2			<input type="checkbox"/> Wind Speed vs Time			
<input type="checkbox"/> Orchard 3			<input type="checkbox"/> Wind Direction vs Time			
Data Presentations:			<input type="checkbox"/> U-Component vs Time			
<input checked="" type="checkbox"/> Tiered			<input type="checkbox"/> V-Component vs Time			
<input type="checkbox"/> Overlay			<input type="checkbox"/> W-Component vs Time			
<input type="checkbox"/> Bar Graph			<input type="checkbox"/> Wind Vectors vs Time			
Output Type:			Levels to Plot:			
<input checked="" type="checkbox"/> Monitor			<input checked="" type="checkbox"/> Level 1		<input checked="" type="checkbox"/> Level 5	
<input type="checkbox"/> Hard Copy			<input type="checkbox"/> Level 2		<input type="checkbox"/> Level 6	
Data: 1 Minute Ave			<input checked="" type="checkbox"/> Level 3		<input checked="" type="checkbox"/> Level 7	
Day: 33			<input type="checkbox"/> Level 4		<input type="checkbox"/> Level 8	
<input type="button" value="Plot"/>			<input type="button" value="Cancel"/>		<input type="button" value="Same"/>	

Figure 1. The monitor screen after choosing "Micromet"/"Micromet vs Time" options.



The input system uses the cursor keys and tab keys to move about the different choices, input strings and buttons. Short-cut keys are also available for quick jumps to areas of the input screens by using the highlighted letter (i.e. P for Plot).

#### 4. GRAPHS

##### 4.1 SAM AND CAM DATA GRAPHS

The main purpose of the MGCGraf program is the display of the data gathered during Project WIND. Once the user has performed the necessary input for defining the graph to be produced, the program then displays it on the monitor or outputs a hard copy at the user's discretion. Each of the different types of graphs available will be discussed in association with its data class.

The first data class discussed is the SAMS and CAMS data. The first two graphs are the single site parameter plots which show the different available temperatures (soil, 2 meter height and 10 meter height) and the wind variables (speed, direction and standard deviation of the wind) of a single station versus time (Figure 2) and the relative humidity and pressure of the station versus time (Figure 3).

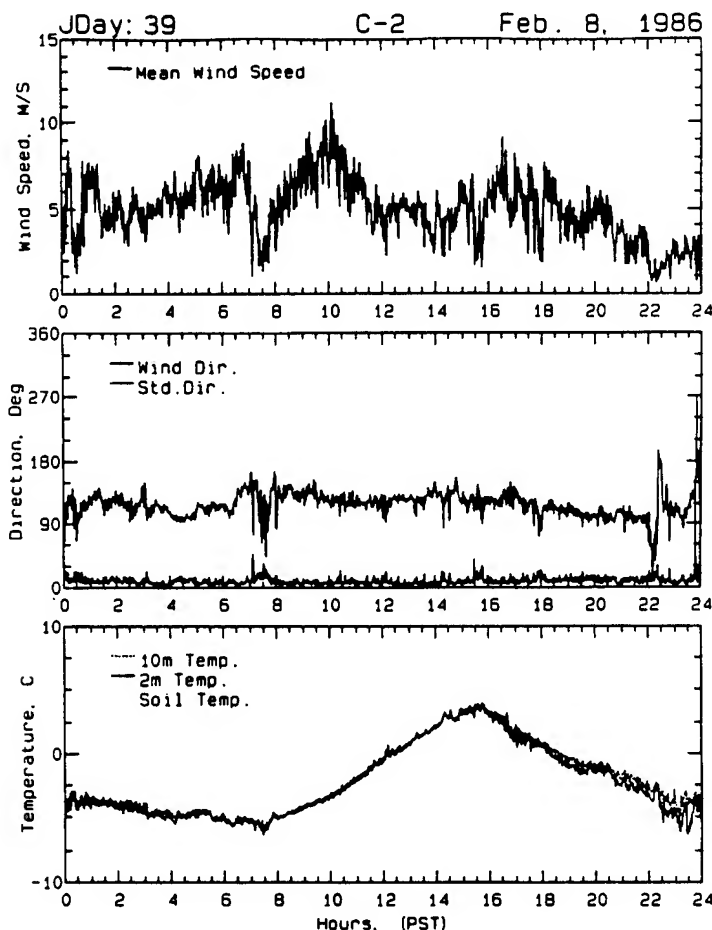


Figure 2. CAMS Site 2 Temperature and Wind Data for Feb 8, 1986.

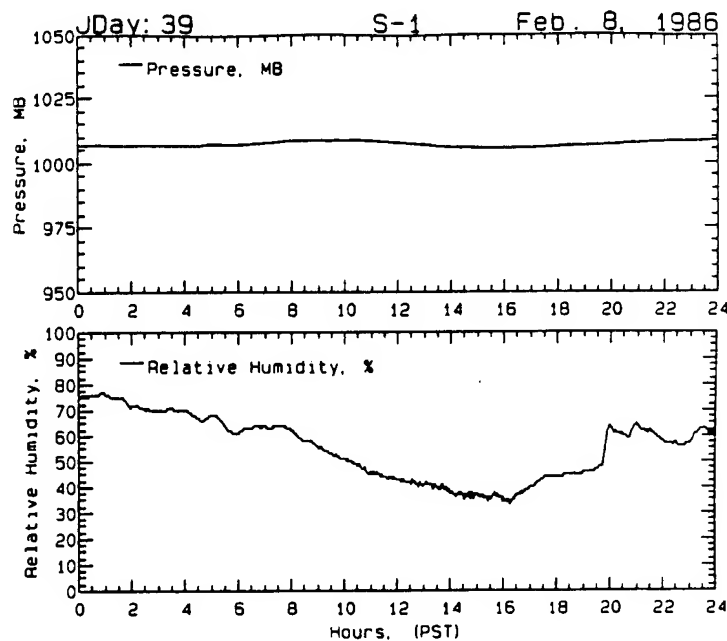


Figure 3. SAMS Site 1 Relative Humidity and Pressure Data for Feb 8, 1986.

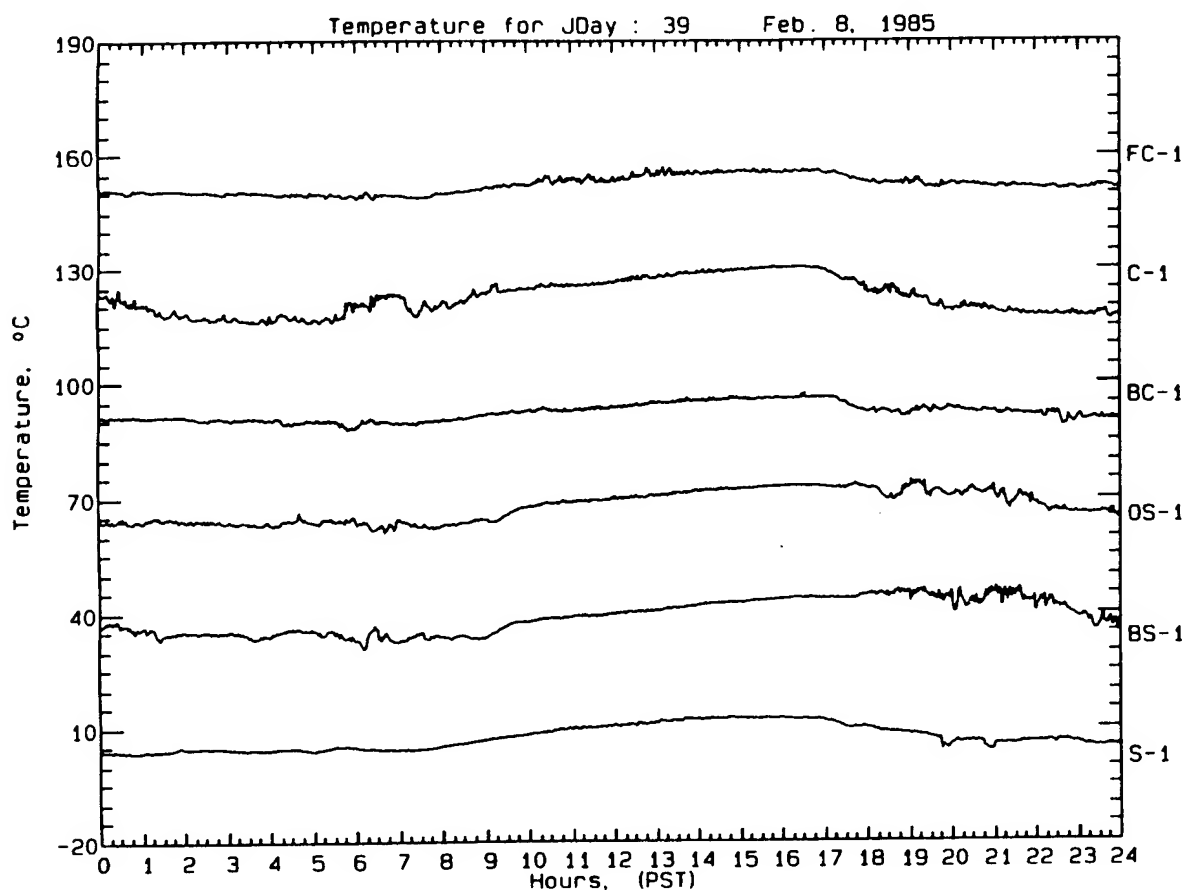


Figure 4. Time history graph of several SAMS and CAMS sites.

The next graph displaying SAMS and CAMS data is the time history graph (Figure 4) which allows the comparison of data between stations. The example given shows the first station of each SAMS and CAMS type comparing temperature. An option was created allowing the data to be overlaid instead of offset as it is in figure 4. The final graph of this data type is the single site parameter graph that display solar radiation or tipping bucket precipitation versus time (Figure 5), which was recorded only at the SAMS stations.

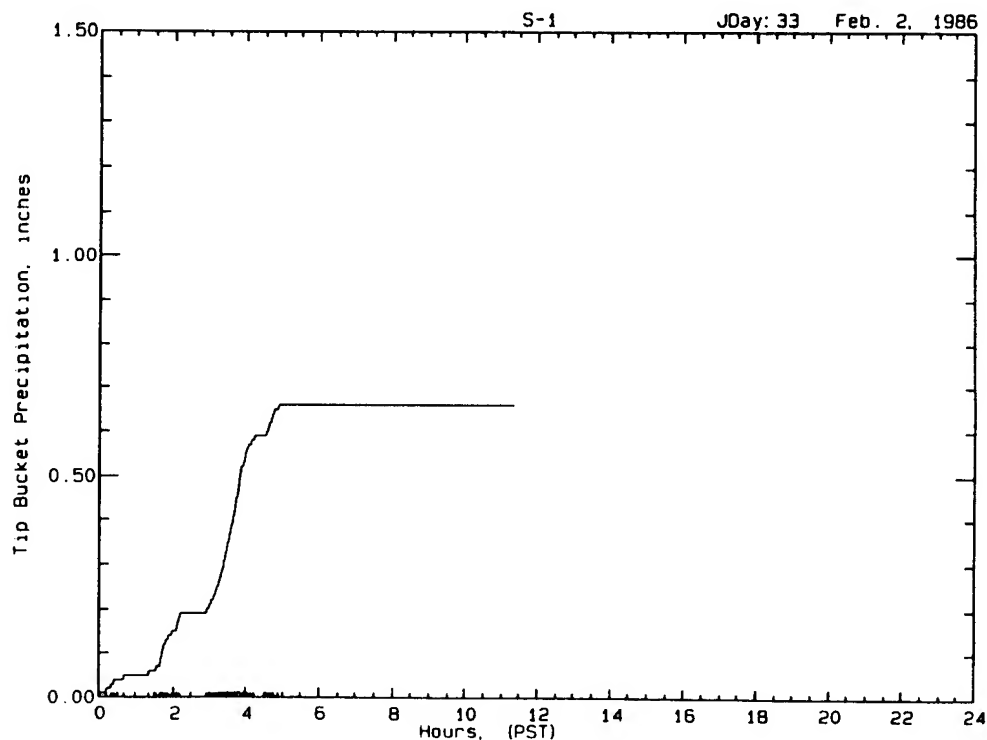


Figure 5. Tip bucket precipitation for at SAMS site 1 for Feb. 2, 1986.

#### 4.2 MICROMET TOWER DATA GRAPHS

The micromet tower data has four basic graph forms available for use. The first is the profile graph which displays a vertical profile of a micromet tower data at several different times (Figure 6). The times are offset by a constant amount so each profile does not interfere with the others. The time difference between each profile is chosen by the user who has the option of one or five minute intervals.

Similar to the time history of the SAMS and CAMS data is the time section of micromet data (Figure 7), but the different plots represent the eight levels of the same tower instead of comparing different sites. Any of the nine different parameters recorded at the eight levels may be plotted in this format.

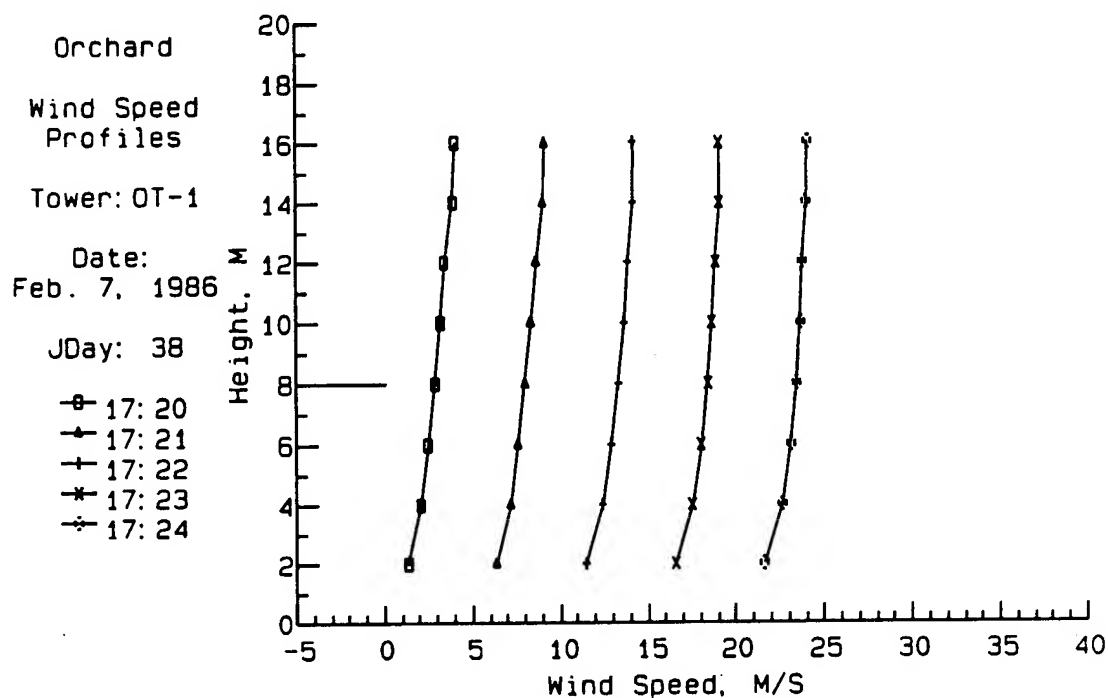


Figure 6. Micromet profiles graph of wind speed.

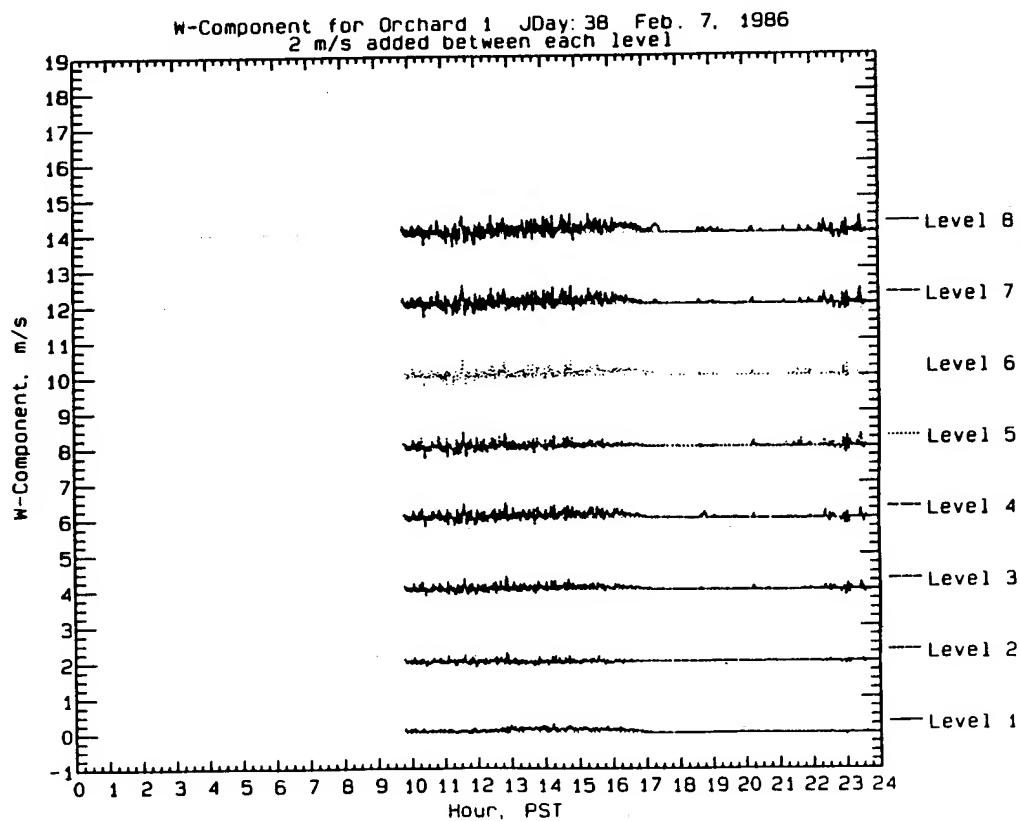


Figure 7. Time history of vertical wind component at micromet tower 1 for Feb. 2, 1986.

A micromet cross section graph is also available which allows the user to plot the data in a spacial display. It shows the three towers for the chosen site, either orchard or forest areas, with the data values for wind speed and direction in one set and temperature and relative humidity for the other displayed at each of the eight instrument levels (Figure 8).

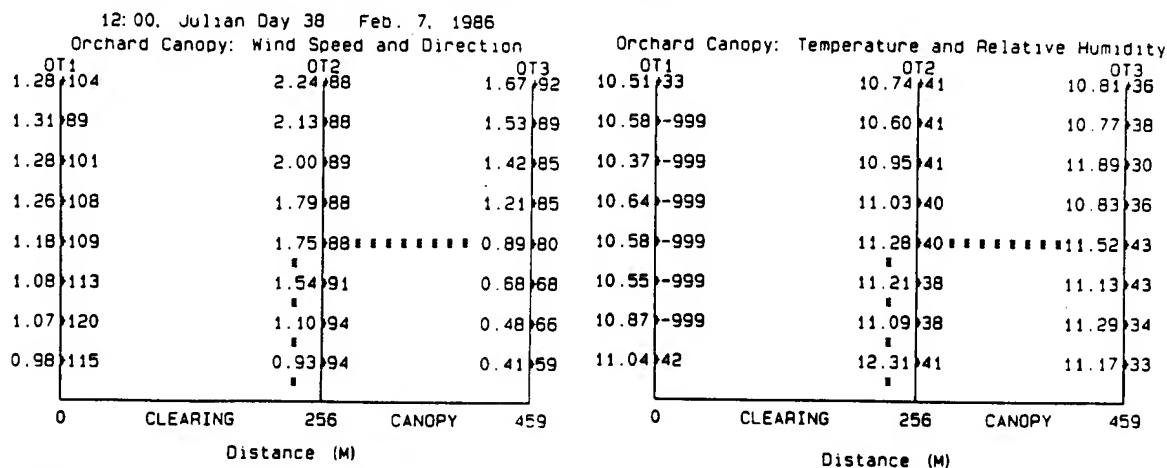


Figure 8. Micromet cross-section graphs showing wind speed, wind direction, temperature and relative humidity at the different orchard towers for february 7, 1986.

The other two graph formats for the micromet data are for single level parameters and one second interval data. The single level parameters have the same format as the SAMS and CAMS single site parameters as shown in figure 5, offering the choice of tipping bucket precipitation, net radiation, heat flux, air pressure or solar radiation versus time. The one second interval data graph is the same as the multi-line time history of micromet data as in figure 7, offering the plot of any of the multi-level parameters recorded at the micromet towers.

#### 4.3 UPPER AIR GRAPHS.

The MCGraf program also provides graphs for two of the upper air soundings taken during Project WIND. The first shows the wind speed and direction taken by the GMD upper air soundings. This gives a plot of the wind speed and by each data point shows the wind direction in degrees (Figure 9). The other parameters taken by these soundings were graphed by STC on standard DOD USAF Skew T, Log P plotting paper.

During the test periods of Project WIND tethersondes were taken at two to four sites, depending on the phase, approximately every two hours. Graphs are available for this data showing either average wind speed, wind direction, relative humidity, air temperature, wet bulb temperature or pressure for a given level versus height of the balloon (Figure 10). Values by each data point indicate the average time, also brackets can be displayed to indicate either the maximum or minimum values of the data during the averaging period or the standard deviation of the data about the average point.

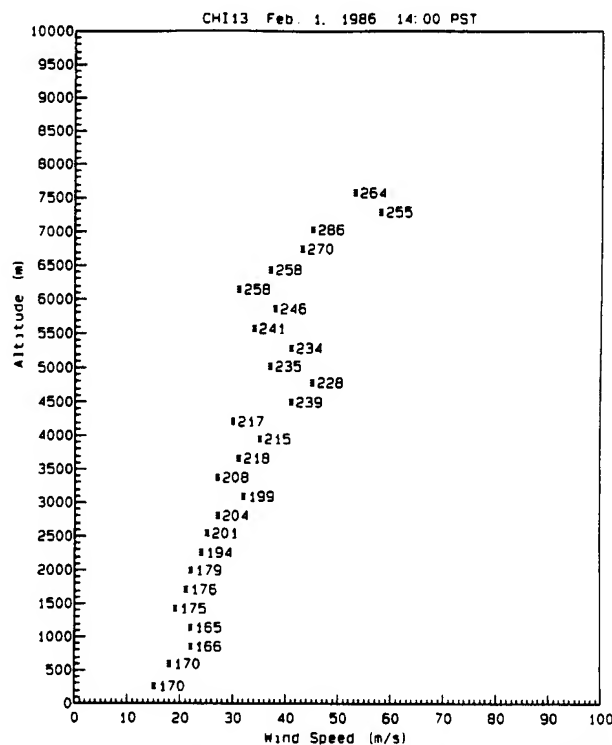


Figure 9. GMD Sounding profile of wind speed and direction for Chico.

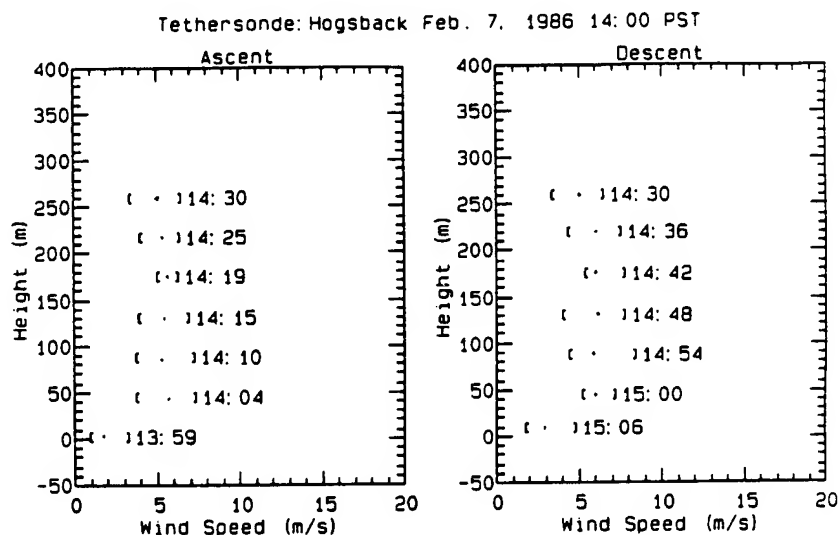


Figure 10. Tethersonde for Hogsback on Feb. 7, 1986 as 14:00 PST showing wind speed versus height with minimum and maximum value brackets.

#### 4.4 OTHER SURFACE STATIONS

As described above, the data gathered during Project WIND was also supplemented with other surface stations from the region operated by both Project WIND personnel and outside sources. This data was recorded less frequently, having data points every hour, with

different sets of parameters being recorded by the different site types. The graphical display of this data is similar to the SAMS and CAMS time history plot. It shows a given parameter for all of the stations of a single type versus time. Options allow for overlay comparisons of the parameters and wind vectors with respect to time.

#### 4.5 TERRAIN DATA

Terrain data of the area utilized by Project WIND is also available and contour maps have been generated also showing the station locations within the regions. Three different terrain plots are currently produced. The first is of the 80km x 80km fine mesoscale area indicating primary stations while the second and third plots are of the 5km x 5km areas of the orchard and forest micromet data collection areas. Figure 11 shows the complex terrain of the forest area.

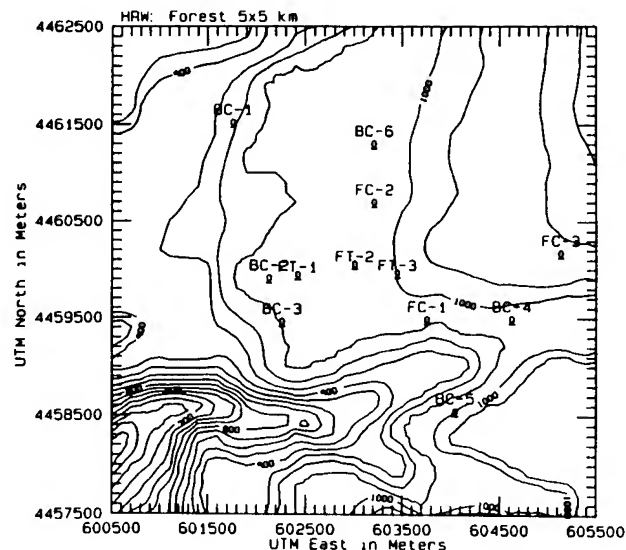


Figure 11. 25m contour map of the forest 5km x 5km area.

#### CONCLUSIONS

The MGCgraf program has been fully implemented in conjunction with and Oracle data base management system and is used daily in support of QCEF of the Project WIND data. Expansion of the system is proposed for further data and model analysis.

#### REFERENCES

Cionco, R. M., 1989: Design and Execution of Project WIND, 19th Conference on Agriculture and Forest Meteorology, American Meteorology Society, Boston, Massachusetts, pp. 156-159.

Cionco, R. M., 1987: Windfield Simulations from a Hierarchy of Nested Meso- and Micrometeorological Models. In Symposium on Mesoscale Analysis and Forecasting, IUGG Proceedings, Vancouver, Canada.

# The CASTFOREM Graphics Postprocessor's Smoke Display Demonstration

Robert E. De Kinder, Jr.\*  
U.S. Army Research Laboratory  
Battlefield Atmospheric Simulation Division  
White Sands Missile Range, NM 88002-5501.

Steven J. LaMotte  
Physical Science Laboratory  
New Mexico State University  
Las Cruces, New Mexico 88003

Thomas C. Loncarich†  
Joseph F. Bebb, Jr.  
US Army TRADOC Analysis Command  
White Sands Missile Range, New Mexico 88002-5502

## Abstract

Smoke Operations in TRADOC Analysis Command's Combined Arms and Support Task Force Evaluation Model (CASTFOREM) have been played almost since its inception via EOSAEL's COMBIC module. Within the past several months, TRAC-WSMR has been developing with the PV WAVE software a Graphics Postprocessor for the display and playback of CASTFOREM runs of their many scenarios. Since this past July, we at ASL in concert with PSL have been developing the additional routines to display the various smoke and obscurant areas on the display for use in TRAC-WSMR analyses and results briefings.

A brief introduction to the PV WAVE software and its application to the display of obscurant clouds within the CASTFOREM Playbacks will be given. Descriptions of the obscurant algorithms used to drive the Sun SPARC station displays for various cloud types will be posted. Variations in the possible displays (e.g. 2-D, 3-D) will be postulated.

Various obscurant cloud types known to be of interest to the military analyst/wargamer/trainer will be demonstrated on the Sun SPARCstation from a series of selected CASTFOREM Outcome files.

## 1 Introduction

Smoke Operations in TRADOC Analysis Command's Combined Arms and Support Task Force Evaluation Model (CASTFOREM)[1] have been played almost since its inception via EOSAEL's COMBIC module[2]. Within the past several months, TRAC-WSMR has been developing with the PV WAVE software Graphics Postprocessor for the display and playback of CASTFOREM runs of their many scenarios[3]. Since

---

\*Secretary of the Army Research and Study Fellow Los Alamos National Laboratory '88-'89

†Current address U.S. Army Missile Command, Redstone Arsenal, AL



this past July, we at ASL in concert with PSL have been developing the additional routines to display the various smoke and obscurant areas on the display for use in TRAC-WSMR analyses and results briefings.

## 2 PV~Wave

The use of PV~Wave software facilitates the display and playback of various war game results. PV~Wave has the capability of displaying 2-D and 3-D data from many different data sets. These will be shown for various scenario trial runs.

## 3 Smoke Clouds

The smoke clouds used in the CASTFOREM combat simulation have traditionally been generated using COMBIC, but more recently an option has been incorporated using curve fitting methods to the COMBIC module, which also incorporate nominal performance factors for the various EO systems used in the simulation. This technique, Sutherland's Aerosol Notional Detection Impact Algorithms ("sandia" <sup>1</sup>), generates *opaque* ellipsoids that are assumed to *totally block* the specific lines-of-sight (LOS). The nominal levels are:

- The visible (0.4-0.7  $\mu$ ) : 2% Transmission,
- The far infrared (8-12  $\mu$ ) : 12% Transmission.

Recent requests have been made to increase the levels slightly upward to more closely match cloud durations seen in several artillery firing tables:

- The visible (0.4-0.7  $\mu$ ) : 5% Transmission,
- The far infrared (8-12  $\mu$ ) : 18% Transmission.

## 4 DEMONSTRATION

Various obscurant cloud types known to be of interest to the military analyst/wargamer/trainer will be demonstrated on the Sun SPARCstation from a series of selected CASTFOREM Outcome files.

## References

- [1] TRAC-WSMR-TD-4-88, 1988: *Combined Arms and Support Task Force Evaluation Model (CASTFOREM) METHODOLOGIES*, U.S. Army TRADOC Analysis Command-WSMR, White Sands Missile Range, New Mexico 88002-5501.
- [2] D.W. Hooch, R.A. Sutherland, and D. Clayton. *Combined Obscuration Model for Battlefield-Induced Contaminants (COMBIC)*, TR-0221-11, U.S. Army Atmospheric Sciences Laboratory, White Sands Missile Range, New Mexico 88002-5501 (1987).
- [3] M.E. Lee and S.J. LaMotte. *Loss Exchange Ratio Sensitivity to Variations of Sky-To-Ground Radiance in a Combat Simulation*, Proceedings of the Eleventh Annual EOSAEL/TWI Conference, NMSU/PSL, Las Cruces, NM 88003 (Nov 1989).

---

<sup>1</sup> "sandia" is Navajo for "watermelon", not the Corporation

**Session IV Posters**

**ATMOSPHERIC EFFECTS**

# SIMULATING ATMOSPHERIC EFFECTS ON INFRARED IMAGES USED AT THE NIGHT VISION ELECTRO-OPTICS DIRECTORATE

James Williams, David Tofsted, and Alan Wetmore  
U.S. Army Battlefield Environment Directorate\*  
White Sands Missile Range, New Mexico 88002-5501, USA

Richard Dutro  
New Mexico State University  
Las Cruces, New Mexico 88003

## ABSTRACT

The U.S. Army Night Vision Electro-Optics Directorate (NVEOD) develops images stored in Another Raster Format (ARF) that are displayable on a variety of UNIX platforms. Some of these images are designed to represent scenes as viewed by an infrared camera engaged in target detection. Each image is accompanied by an ARF range file that maps the distance from the detector to each pixel in the image.

Our investigation has centered on simulating atmospheric effects on 256-level grayscale ARF images for a band-averaged 8- to 12- $\mu\text{m}$  sensor. An atmospherics file was created from a series of LOWTRAN 7 runs that maps range along the line of sight to transmission and path radiance effects. We have developed an algorithm that will convert each pixel in the original image to a new gray-level using the transmission and path radiance associated with the range for that pixel.

The introduction of these atmospheric effects results in a degraded image which is more representative of the scene as viewed by an infrared imager. For the ARF image studied, the range values vary between 4.4 and 6.2 km, yielding similar transmittance and path radiance results for each pixel. Application of our algorithm to the image reduced the dynamic range of pixel values, drawing them toward the limiting path radiance. This effect has produced an overall darkening of the image.

---

\*formerly U.S. Army Atmospheric Sciences Laboratory

## 1. INTRODUCTION

The Battlefield Environment (BE) Directorate of the U.S. Army Research Laboratory has recently provided an algorithm to the U.S. Army Night Vision Electro-Optics Directorate (NVEOD) of the Communications Electronic Command. This algorithm simulates the atmospheric degradation effects on the contrast in simulated infrared imagery. The algorithm contains the basics of radiative transfer theory sufficient to simulate characteristic atmospheric effects for a typical mid-latitude summer day.

This model was developed in response to a request from NVEOD for assistance in obtaining more realistic infrared image simulations from their physical terrain board images. This enhancement of image formation techniques will aid in a research effort by NVEOD to improve the criteria controlling the estimation of target detection probabilities in such models as the NVEOD ACQUIRE and FLIR92.

## 2. NVEOD IMAGE PACKAGE

The focus of this study involved a package supplied by NVEOD consisting of a weather scenario specifying "typical" low-observable conditions, an infrared ARF (Another Raster Format) image, and an ARF range map. ARF is a special image format supporting multiple frames and eleven image types, and uses the XDR (eXternal Data Representation) standard to represent data [Smith, 1992]. Although designed as a universal format, ARF is used primarily on UNIX systems. A rather extensive library of utility software to interface with the images has been written for NVEOD for use on SUN Microsystems workstations.

The ARF image received by BE for use in this study is shown in fig. 1. The resolution is 640 horizontal by 480 vertical pixels. The image was designed to depict a scene taken by an infrared camera. The range map stores the range values (in centimeters) corresponding to each pixel in the image, thereby mapping each pixel to a certain distance from the detector. Figure 2 is a contour plot in meters of the range map. The range values vary from approximately 4.4 km in the foreground to 6.2 km in the upper right portion of the image.

## 3. LINE-OF-SIGHT RADIATIVE TRANSFER

The BE contrast reduction model deals with the transport of radiation from a source to a detector in the presence of an atmosphere. There are several ways that the atmosphere interferes with the ability to observe the world. Our model deals with two of them: transmittance and path radiance.

Transmittance is the measure of the amount of energy that arrives at an observer location compared to the amount that started toward the observer from a source. It is a measure of the reduction in energy available for detection. Path radiance is energy that arrives at the detector that did not originate at the source. It is similar to background noise and thus carries no information about the source.

Path radiance can arise when energy from the sky that should pass through the line of sight on its way toward the ground is instead scattered into the direction of the detector. At infrared wavelengths, the gases and aerosols in the line of sight can emit blackbody (thermal) radiation, some of which will travel along the line of sight to the detector.

From this description, we can write the effect of the atmosphere on the propagation of an image pixel as

$$B'(r) = T(r)B(r) + P(r) \quad , \quad (1)$$



Figure 1. Original NVEOD infrared ARF image

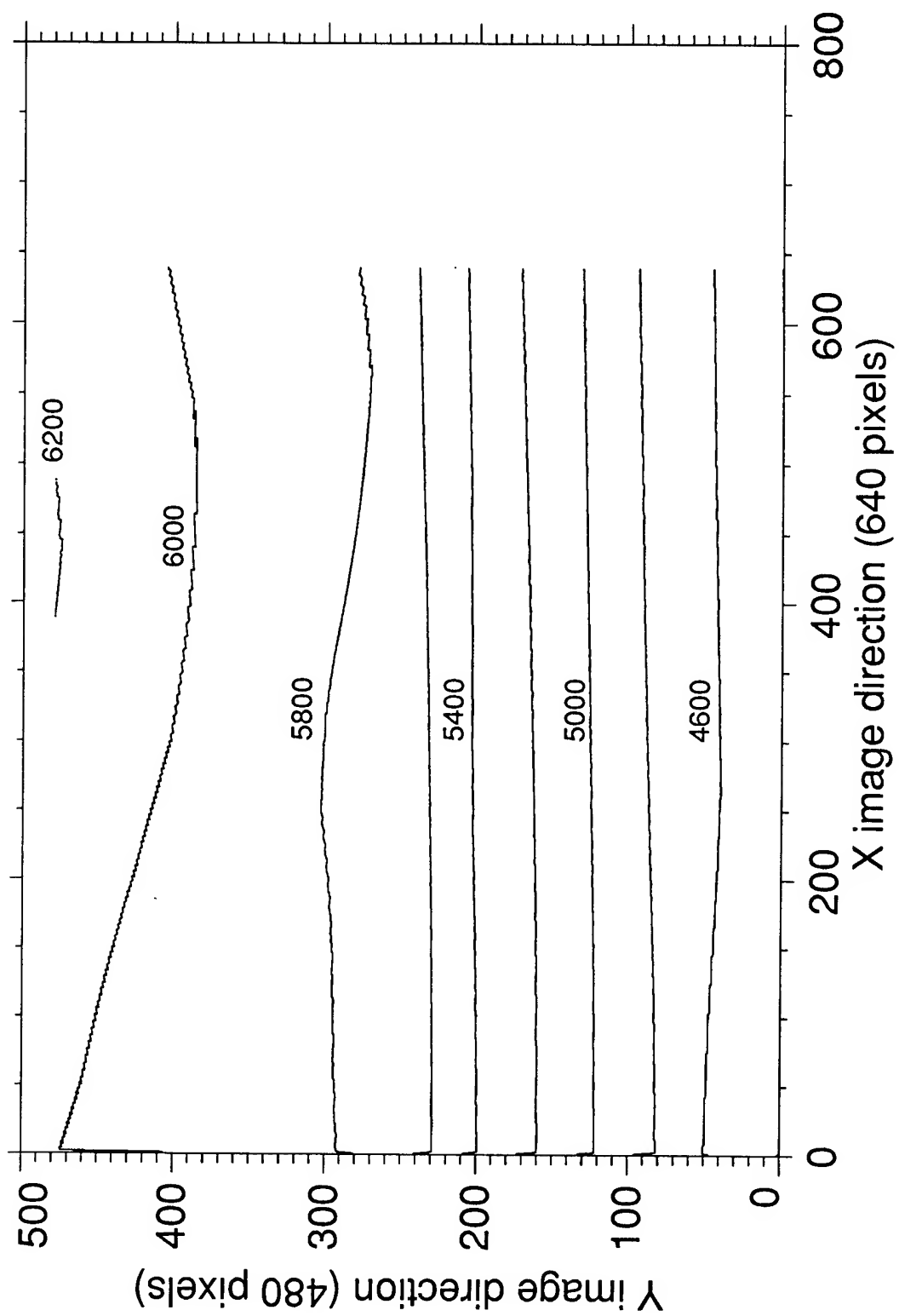


Figure 2. Contour plot of NVEOD range map  
(contour interval 200 m)

where, for a specified range,  $r$ , the brightness (gray-level) of the original pixel,  $B$ , is modified by the range-dependent transmittance,  $T$ , and path radiance,  $P$ , producing the new  $B'$  value for that pixel. Both  $T$  and  $P$  are nonlinear functions of the weather conditions, location viewing geometry, and range. Because of the range dependence, we use eq. (1) to calculate the effect of the atmosphere on a pixel-by-pixel basis.

For this work we have adopted the technique of providing tabulated functions of range for  $T$  and  $P$  (see Table 1). Each pair of functions,  $T(r)$  and  $P(r)$ , can represent a single weather scenario and viewing orientation. To produce these functions for a given scenario, the LOWTRAN 7 computer program [Kneizys et al., 1989] can be used to generate the tabulated results at a set of ranges. These tabulated functions can be used for transforming images that have the same observer orientation, weather conditions, and range map.

#### 4. LOWTRAN SCENARIO AND METHODOLOGY

The scenario developed for use on the image was a 5-km visibility, mid-latitude summer day in Fulda Gap, FRG. The specifics of this scenario are as follows:

- date: 10 July 1992
- time: 1100 GMT
- latitude: 50 degrees north
- longitude: 15 degrees east
- surface altitude: 500 m above MSL (mean sea level)
- observer altitude: 174.5 m AGL (above ground level)
- observer view direction: due west
- field of view: 2.2 degrees
- initial observer depression angle: 2 degrees

A clear air LOWTRAN 7 run was initially made to determine the surface radiance at the detector site. For a grassy patch with an infrared emissivity of 0.94 and a blackbody temperature of 291.86 K, this radiance was found to be 31.957477 W/m<sup>2</sup>-sr. This value may be used to match the uncalibrated grayscale values in the images to the quantitative values provided by the BE model.

LOWTRAN 7 runs of variable path lengths were then performed to calculate the transmittance and path radiance in the 8- to 12- $\mu$ m wave band. These runs were made every 100 m for ranges between 0 and 2 km, every 250 m between 2 and 6 km, and every 1 km thereafter to a maximum range of 12 km. These results were stored in tabulated form in which transmittance and path radiance were mapped to range for later use by the BE model. Table 1 lists the BE atmospheric file.

The starting point for the runs was a 5-km slant path with a 2° depression angle that corresponds to an observer height of 174.5 m AGL. For all ranges greater than this, the depression angle was decreased to allow a longer line of sight. For shorter ranges, the depression angle was increased until it reached 3°, corresponding to a range of 3.3 km. For ranges less than this, the observer location was moved along the line of sight toward the surface.

This methodology is an approximation to the geometry that would be required for individual images. All lines of sight will be approximately correct and have consistent orientation, transmittance, and path radiance effects.

TABLE 1. ATMOSPHERICS FILE DERIVED FROM LOWTRAN 7 RUNS

RANGE (m)	TRANSMITTANCE	PATH RADIANCE (W/m <sup>2</sup> -sr)
0.0	1.0000	0.0
97.0	0.9498	1.6768
204.0	0.9153	2.8393
296.0	0.8893	3.7202
410.0	0.8598	4.7230
508.0	0.8363	5.5140
608.0	0.8136	6.2894
708.0	0.7920	7.0197
800.0	0.7731	7.6637
900.0	0.7534	8.3232
1007.0	0.7332	9.0088
1100.0	0.7164	9.5757
1214.0	0.6965	10.2516
1311.0	0.6800	10.8089
1412.0	0.6637	11.3598
1504.0	0.6491	11.8464
1602.0	0.6342	12.3526
1705.0	0.6190	12.8683
1804.0	0.6048	13.3421
1904.0	0.5909	13.8163
1996.0	0.5785	14.2326
2243.0	0.5469	15.2925
2500.0	0.5162	16.3236
2755.0	0.4879	17.2779
3001.0	0.4624	18.1329
3239.0	0.4392	18.9043
3494.0	0.4153	19.7081
3757.0	0.3919	20.5059
4007.0	0.3710	21.2038
4245.0	0.3522	21.8446
4502.0	0.3330	22.4882
4742.0	0.3162	23.0650
4995.0	0.2994	23.6319
5266.0	0.2825	24.2020
5509.0	0.2682	24.6790
5747.0	0.2548	25.1372
5987.0	0.2422	25.5599
7009.0	0.1950	27.1583
8015.0	0.1580	28.4107
9016.0	0.1283	29.4199
10035.0	0.1039	30.2396
11022.0	0.0849	30.8868
12000.0	0.0695	31.4090



## 5. CONTRAST REDUCTION PROGRAM

The contrast reduction program operates in the following manner. The program first reads the ARF image, the range map, and the BE atmospheric file. It then cycles through each pixel in the image, applying the effects of atmosphere by means of eq. (1). The transmittance is calculated for the pixel's range by linearly interpolating between the transmittance points in the atmospheric file. This value is multiplied by the brightness (gray-level) of the pixel. The path radiance is calculated for the pixel's range by linearly interpolating between the path radiance points in the atmospheric file. This path radiance value is added to the new brightness, and the result is saved to the output ARF image.

Figures 3 and 4 confirm that with increasing range the transmission decreases and path radiance increases as calculated by the model. Note that the scenario in this study involved ranges between 4.4 and 6.2 km, producing similar transmittances and path radiances for all image pixels. In scenes with greater range variations, there would be correspondingly greater variations in transmittance and path radiance results, yielding a larger dynamic range of pixel values in the final image.

A user-interface incorporating the BE model has been designed on SUN workstations based on the X Window System and utilizing SUN's Open Look and Xview libraries. By means of buttons and menus, users may display the original ARF image and the atmospheric-adjusted image as well as echoing the location, grayscale, and range associated with each pixel as the mouse is moved over the image window. Additionally, the effects due solely to transmission or path radiance may be shown as gray-level images.

## 6. DISCUSSION

Application of the BE atmospheric algorithm to the NVEOD image resulted in an expected degradation of contrast in the image (see fig. 5). However, the image was darkened nearly uniformly such that degradation did not visibly increase with range. This seemingly erroneous effect was due entirely to the small dynamic range of detector-to-pixel distances contained in the range map. The pixel values produced by the BE model for the entire image were not substantially different because the mean transmittance for the image was relatively low. The model did, in fact, calculate greater reductions in gray-level with distance, but this effect is quite subtle and best observed by displaying only the transmission or path radiance gray-levels.

The approach used for this work is not without problems. Some of these are:

- The model does not perform any of the steps associated with an Automatic Gain Control (AGC) circuit that would modify the image in a hardware system. Ideally, atmospheric effects should be applied before digitization of the image. Thereafter, detector noise and system gain would be applied. Because this study was attempted on a previously optimized image in which noise was added by NVEOD in an unspecified manner, we did not attempt to rescale the image. This contributed to the darkening shown in the output image. The expertise and knowledge concerning the operation of AGC systems reside at NVEOD, and we did not implement any corrections. In our opinion an AGC processing stage will be required for any use of the BE atmospheric effects simulation.
- Assumptions were necessarily made with respect to the minimum and maximum radiances (in watts per square meter per steradian) contained in the image.
- The NVEOD images are not absolutely free of atmospheric effects. They contain some influences due to atmospheric gases and path radiance caused by the physical terrain board system in use.

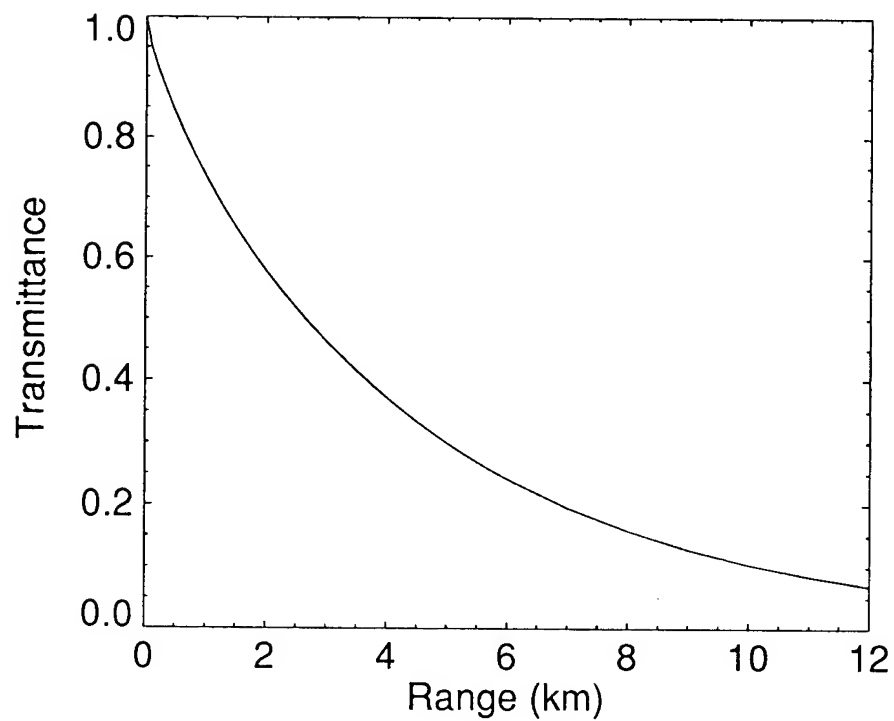


Figure 3. Transmittance as a function of range

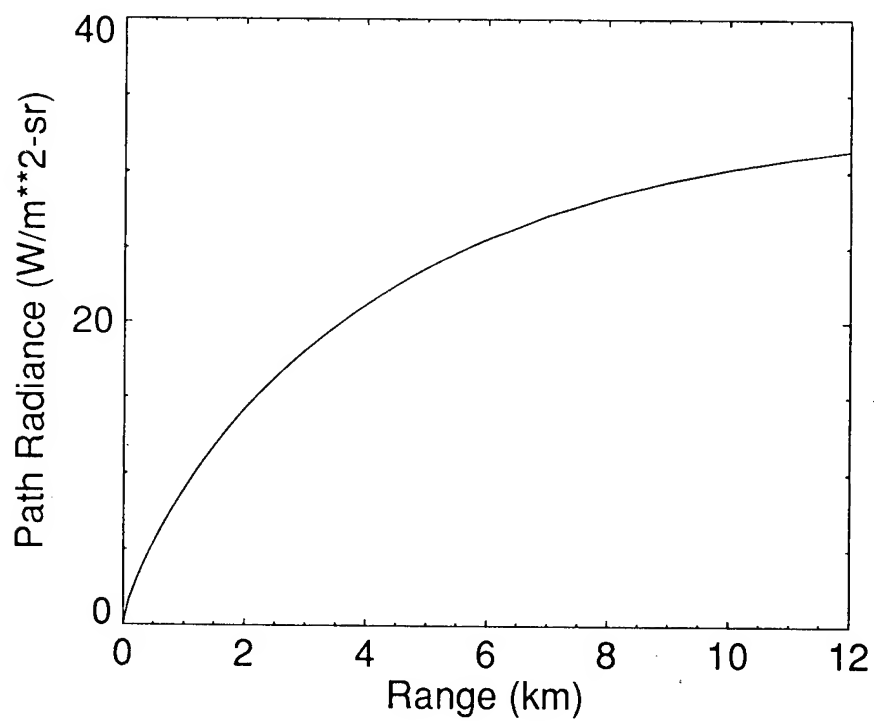


Figure 4. Path radiance as a function of range

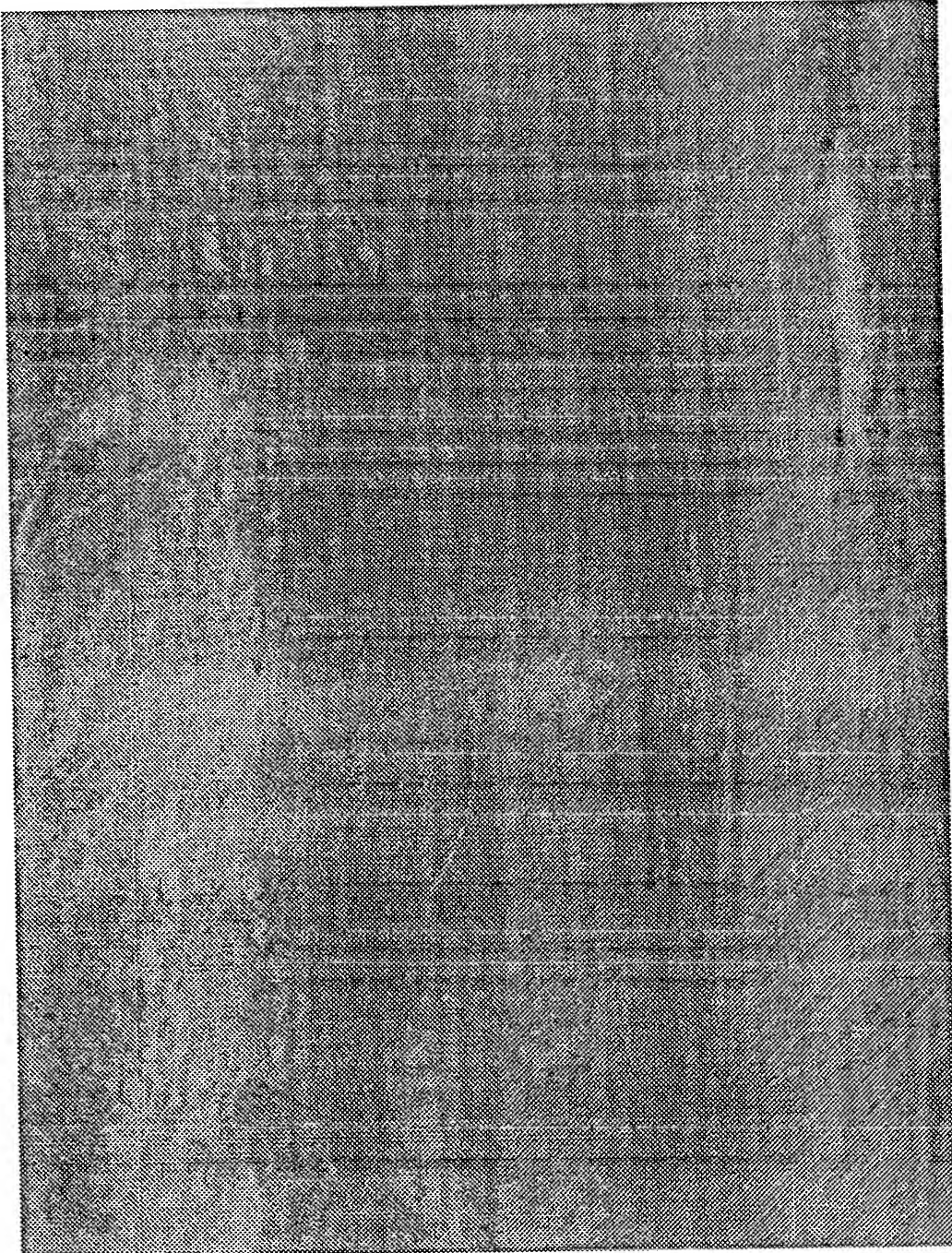


Figure 5. NVEOD infrared ARF image with simulated atmospheric effects (without automatic gain control for path radiance)

at NVEOD. Time constraints did not permit us to back out all atmospheric effects to produce a "truly" pristine image and then apply the atmosphere in a controlled fashion.

- Another limiting factor was that this study did not consider the degradation due to atmospheric scattering into the line of sight of an image pixel from nearby scene elements.

These problems will be addressed in the future.

As a first approximation, the BE contrast reduction model provides a more realistic depiction of ARF imagery. It may be successfully used on arbitrary infrared ARF images and easily modified to include enhancements.

## REFERENCES

Kneizys, F. X., E. P. Shettle, L. W. Abreu, G. P. Anderson, J. H. Chetwynd, W. O. Gallery, J. E. A. Selby, and S. A. Clough, 1989: *Users Guide to LOWTRAN 7*. AFGL-TR-88-0177, Air Force Geophysics Laboratory, Hanscom Air Force Base, MA, USA.

Smith, Mark, 1992: *ARF Specification (DRAFT)*. E-OIR Measurements, Inc., Developed under contract to U.S. Army Night Vision Electro-Optics Directorate, Fort Belvoir, VA, USA.

## CORRELATION OF $C_n^2$ WITH IMAGE DISTORTION AT THE REBAL TEST

Fernando R. Palacios, Wendell R. Watkins, Samuel B. Crow  
and Daniel R. Billingsley  
U.S. Army Battlefield Environment Directorate  
White Sands Missile Range New Mexico 88002-5501, USA

### ABSTRACT

The degrading effects of optical turbulence on far-infrared (IR) imagery were characterized in 1990 for horizontal path observations, but without accurate measures of the turbulence structure parameter,  $C_n^2$ . This deficiency was corrected at the 1992 Radiation and Energy Balance test in Bushland, Texas. With values of  $C_n^2$  ranging from  $10^{-16}$  to  $10^{-12}$  collected at a 2-Hz rate, the corresponding optical distortion of the Mobile Imaging Spectroscopy Laboratory (MISL) large-area target board at a range of 473 m was recorded by an Inframetrics, Inc., IR imager with a 30-Hz frame rate. Also data were collected for vertical and horizontal thermal bar pattern configurations that allow characterization of the peculiarities of the single detector imager during times of minimum optical turbulence. This new database of image distortion will be used for model validation and improvements of the MISL image restoration techniques.

### 1. INTRODUCTION

The Target Contrast Characterizer (TCC) of the Mobil Imaging Spectroscopy Laboratory (MISL) was used to perform the image characterization measurements at the 1992 Radiation and Energy Balance (REBAL) test. The TCC was used to collect simultaneous sets of infrared (IR) and visible imagery from two locations. An image acquired close to the target (near field) provided a measure of the spatial radiance distribution inherent to the target and its background, while the corresponding image acquired far from the target (far field) provided a measure of the spatial radiance distribution after propagation through the intervening atmosphere (Crow et al., 1991). At REBAL a large-area thermal target board with bar patterns and a shielded plywood sheet were used as targets. Optical turbulence and meteorological measurements were made using a Lockheed Engineering and Meteorological IV-L scintillometer and a surface automated meteorological system (SAMS).

Measurement of the short and long exposure far-IR image distortions due to optical turbulence along horizontal paths near the ground was presented at last year's Battlefield Atmospherics Conference (Watkins et al., 1991). Although very useful in illustrating the magnitude and temporal behavior of optical turbulence induced image distortion, the corresponding terrain and meteorological conditions were not appropriately characterized for model validation. Hence, the REBAL test was conducted over flat, well characterized terrain; and the test site was appropriately instrumented with meteorological sensors to characterize the turbulence structure parameter,  $C_n^2$ , as well as the vertical temperature and humidity gradients that cause optical turbulence. Also at the REBAL test, the MISL target board was used for the first time with horizontal bar patterns and resulted in characterizing a hysteresis phenomenon in the Inframetrics, Inc., model 610 imager that must be corrected prior to using techniques for two-dimensional partial restoration of optical turbulence distorted or blurred images. Preliminary results in these areas from the REBAL test are presented here.

## 2. EXPERIMENTAL SETUP

The TCC imagers have dual 3 to 5  $\mu\text{m}$  and 8 to 12  $\mu\text{m}$  wavelength response; although, analysis was performed for only the far-IR (8 to 12  $\mu\text{m}$ ) imagery collected at the REBAL test in May and July 1992. Characterization of the temporal changes in the inherent spatial radiant distribution of the IR scene is accomplished using an imager located near the target. An optically matched second imager located far from the target (far field) is used to isolate the changes in propagated target contrast by comparing far field and near-field imagery (Watkins et al., 1988). These changes that include optical turbulence effects can then be correlated to changes in meteorological conditions and scintillometer readings.

The imager located near the target is referred to as the "near-field" imager, while the imager located far from the target is referred to as the "far-field" imager. The imagers share a common line of sight (LOS) to the target. Near-field images, met data, and scintillometer data are transmitted over a fiber optics data cable to the far-field position. When the TCC was used at REBAL, the near-field imager was placed 48 to 51 m from the targets, while the far-field imager was placed at a distance of 473 m, approximately 10 times the near-field distances. The images collected share a common dimensional field of view because the far-field imager uses a 10X telescope. Pixel to pixel frame registration is accomplished through the use of remote control of the near-field camera platform and a real-time image processing system. The TCC is conceptually depicted in fig. 1.

The target board with two interchangeable bar pattern configurations (that can be displayed either in a vertical or horizontal position) was observed during varying meteorological conditions. Atmospheric turbulence induced bar pattern fluctuations were observed on the target board with the pattern being periodically switched between the vertical and horizontal orientation. After analyses of the far-IR (8 to 12  $\mu\text{m}$ ) data, one of the driving parameters for turbulence fluctuations was determined to be varying solar irradiance. Also noted on the horizontal bar pattern were certain camera anomalies that caused image blurring between bars, both on the near-field and far-field images. These were analyzed for image restoration purposes.

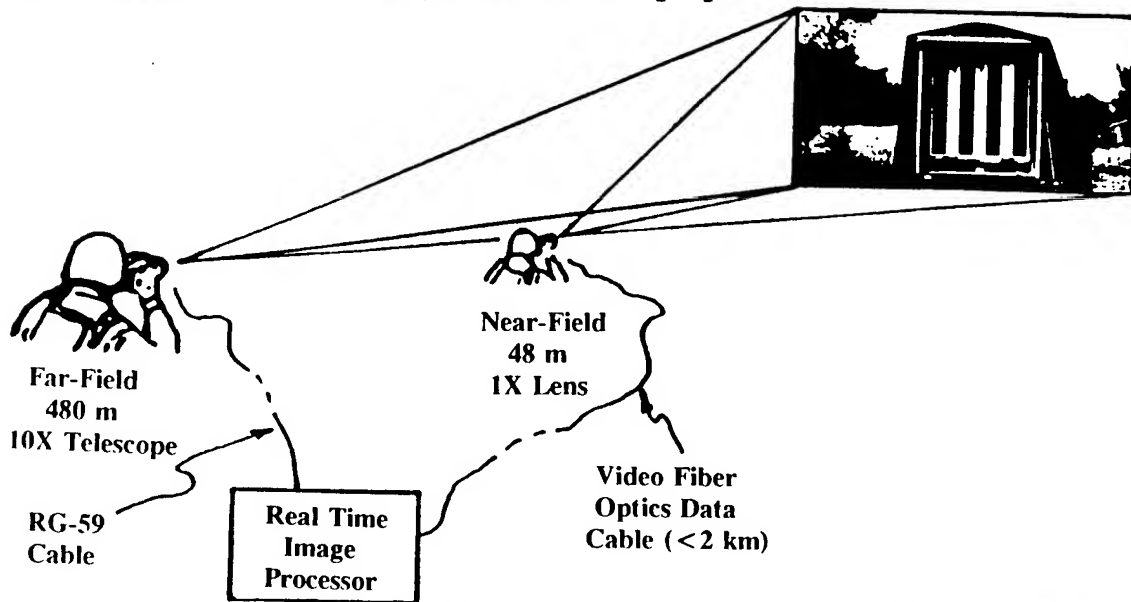


Figure 1. Conceptual use of the Target Contrast Characterizer.

### 3. MEASUREMENTS AND ANALYSES

The MISL instrumentation van that houses the far-field imagers was set up at the REBAL site at the center of the north side of a 500-m by 500-m plowed field. To the right of the MISL van was the scintillometer transmitter at a height of 2 m, as shown in fig. 2. A target area was situated at the center of the south end of the field at a range of 473 m from the MISL instrumentation van. The target area contained a large-area target board that was used for characterization of the atmospheric degradation between the near-field and far-field TCC imagery. To the left of the target board was the scintillometer receiver and the SAMS, as shown in fig. 3. To the right of the target board was the source van with a plywood board to establish a vertical background in the target plane because the flat back ground surfaces at Bushland could not be registered due to parallax. Measurements were made by the MISL van over four 48 h periods, under dry (not irrigated) surface conditions and, under wet (irrigated) surface conditions. Correlations of  $C_n^2$  with image distortion were accomplished by setting the target board scintillometer and met station on the same LOS as the IR and visible imagers (situated 2 m above the ground).

The analysis of the TCC measurements of degrading effect of optical turbulence on IR imagery will begin with changes in  $C_n^2$  caused by solar irradiance. On May 1992, there was scattered, but dense, cloud cover at the REBAL test site that caused fluctuation in the scintillometer readings. Every time there was cloud cover between the near field (NF) and far field (FF), we observed that image distortion on the target board bar pattern was reduced. Referring to Figs. 4 through 7, a segment of the pyrometer, scintillometer, temperature, and 2-to-5 m elevation temperature gradient readings for that day is displayed to determine the correlation between image distortion changes and occurrence of meteorological events. The meteorological data were collected at a 2-Hz sample rate and were then compressed to 1 min averages for analytical purposes. Referring to fig. 4, we noted that at 1420 there was no cloud cover between the NF and the FF for about 20 min. Then around 1440 there was dense cloud cover moving from south to north from the target area toward the MISL van. Figure 5 shows that once there was sufficient cloud cover between the NF and FF, the  $C_n^2$  value began to drop around 1445 and remained low until the cloud cover dissipated. There was a 48 percent drop of  $C_n^2$  between the maximum of  $1.105\text{E-}12$  and minimum of  $5.323\text{E-}13$ . Note that the wind direction came from the south at 2.5 m/s, while relative humidity was 45 percent with no changes in vertical gradient. The met station had two temperature probe readings: one at 2 m and the other at 5 m, as shown in fig. 6. When the scintillometer reading dropped, the difference between the 2-m and 5-m temperatures dropped also as shown in fig. 7. The change in temperature gradient ( $\Delta T$ ) was the dominate contributing factor to the change in  $C_n^2$ . There was no corresponding drop in the humidity gradient, however. What happened to the imagery during no cloud cover and with cloud cover is displayed in Figs. 8 and 9, respectively. For reference fig. 10 shows an essentially undistorted image with a corresponding  $C_n^2$  value of  $5.0\text{E-}14$ . Figures 8, 9, and 10 are 10 frame averages with the bar pattern in the vertical position. These averages were done to highlight the slow response image blurring in target board image distortion due to atmospheric turbulence and also to reduce background noise. Figure 8 with no cloud cover shows that the vertical bar patterns are blurred with poorly defined transition between hot and cold bar patterns due to higher  $C_n^2$  values. When cloud cover moves in between the NF and FF there is better contrast, less blurring (between cold and hot bar on the target board) and better definition between the target and the background as shown in fig. 9. With a low  $C_n^2$  value of  $5.0\text{E-}14$ , fig. 10 is given as a reference of an undistorted IR imagery. Note the sharp transition between hot and cold bar and the good contrast of the individual bars. To be effective, models for predicting the degrading effects of optical turbulence must be able to track these types of intermediate temporal changes in meteorological parameters.



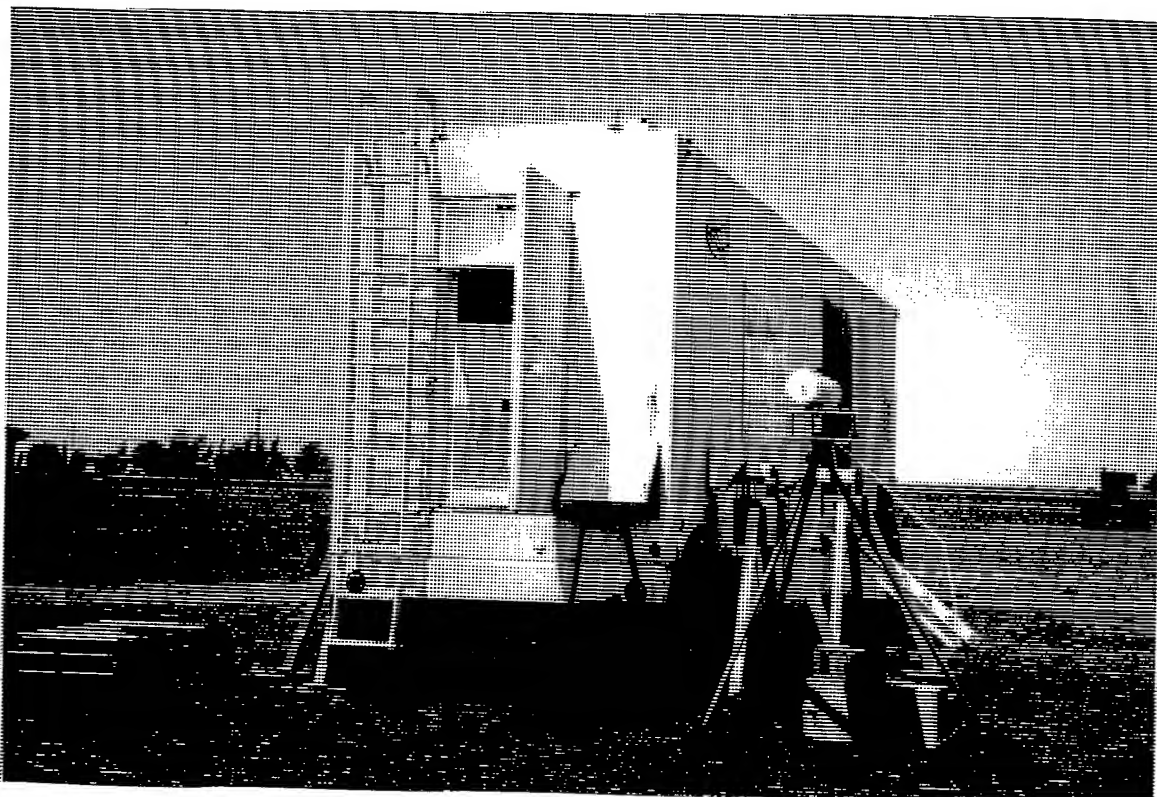


Figure 2. MISL van and scintillometer transmitter.



Figure 3. Target board, scintillometer receiver, and SAMS.



Figure 4. Pyronameter

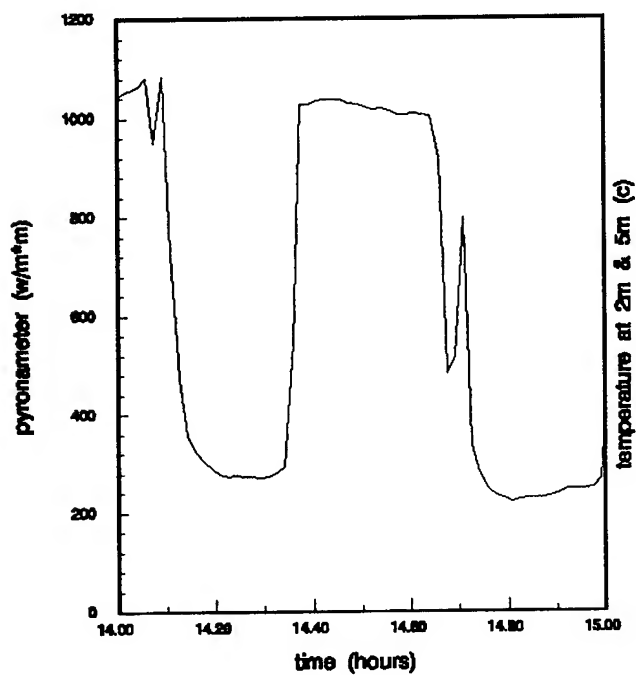


Figure 6. Temperature

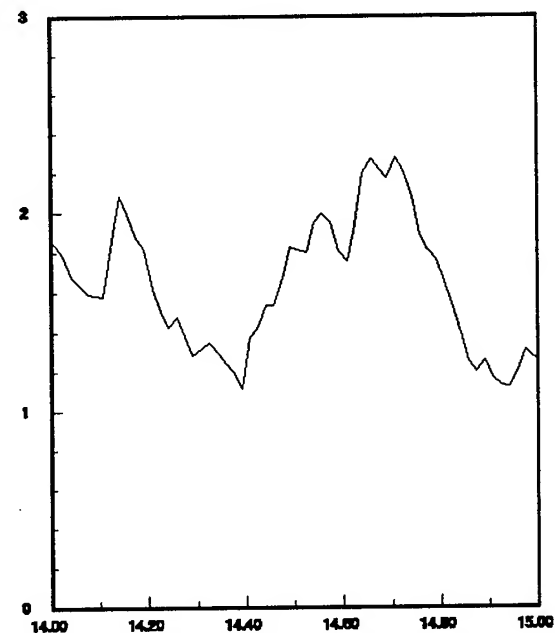
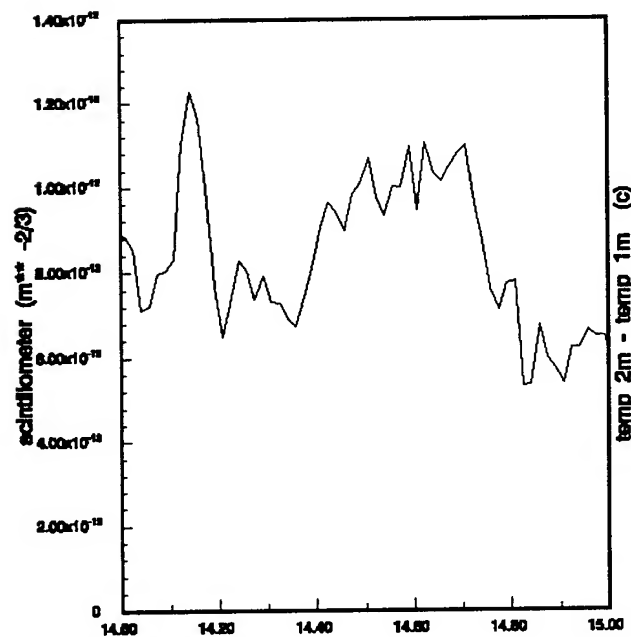
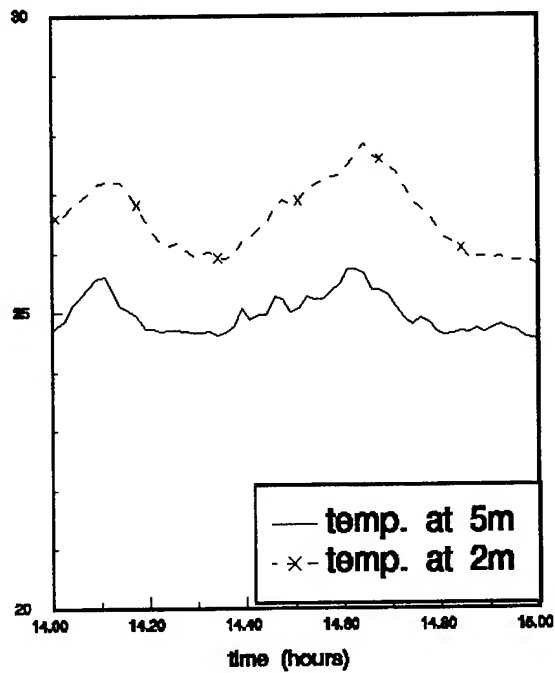


Figure 5. Scintillometer

Figure 7. Delta T

At the REBAL test the target board bar pattern configuration was placed in vertical and horizontal orientations. This allowed for peculiarities of the single detector scanning imager during times independent of optical turbulence to be characterized. On May 1992 at 1205, the target configuration was in the horizontal position. During this time, the NF target boards that do not exhibit optical distortion were blurred in the horizontal direction. By analyzing 30 consecutive frames, we discovered that the blurring was caused by camera scan anomalies. The pattern distortion showed hysteresis recycling every four frames. Figures 11 through 14 are four consecutive frames that show one complete cycle of the blurring between the bars of the target board pattern configuration. The blurring can be distinguished by noting the extent of blur between the bars in each frame shown in Figs. 11 through 14. Now to illustrate that the blurring is occurring in 4-frame cycles, Figs. 15 through 18 are 5, 9, 13 and 17 in the 30-frame sequence that was used. These frames represent the first repetitive blurred frame in the cycle of four. Thus figures 11, 15, 16, 17, and 18 all show the same camera peculiarities. Both the NF and FF imagers showed the same peculiarities to a different extent because of the difference between the optical transfer function of the NF with no lens and the FF with a 10X lens. To understand why the blurring is not consistent through all the frames, an understanding on how the imager captures and reconstructs a frame must be presented.

Inframetrics uses electro-mechanical servos (galvanometers) to perform horizontal and vertical scanning. Horizontal scanning is performed at a very high rate (4 KHz) in a resonant sinusoidal mode. For the vertical scan a magnetic field is used to rotate a mirror several degrees back and forth against a stiff spring shaft under closed-loop electrical control as shown in fig. 19. Vertical scanning is a saw tooth pattern commensurate with standard television format (Inframetrics Manual, 1983). The scan speed for the 610 imager is 1/60 of a second per field, and each field contains 50 lines of detected samples. Each field is then duplicated and combined with the next field and its duplicate to form a single frame. The field of view (FOV) for an imager without a telescope is 15° by 20°, with a resolution element size of 2 mrad by 2 mrad. There are 175 resolution elements and 256 digital samples per line, as shown in fig. 20. When the imager zoom feature is used the resolution element size remains the same but the FOV reduces, causing over-sampling of the scene.

The horizontal target board configuration was captured by the TCC imager with a 50 percent FOV. The height of hot and cold bars on the target board was 12.70 cm. The distance between the NF imager and the target board was 51 m; thus, at this range, there was just more than an instantaneous FOV on each hot and cold bar that was scanned back and forth in each field with almost exactly one-half bar height between scanned lines. The cycling of the blurring due to aliasing occurs because the vertical galvanometer does not sample at the same starting position each time. Instead it repeats a specific sampling pattern every four frames. It takes two individual fields that are scanned 1/60 of a second apart to produce a frame, and each is taken at a varying starting height position with different degrees of aliasing. These aliased fields are combined to produce a frame with blurred horizontal bars similar to those produced by vertical platform jitter. Because of the consistency of the pointing error in each imager field, there is a potential to correct this error in each field and eliminate the imager induced vertical blur. Although some assessment of meteorological impact on optically induced blurring of vertical bar patterns can be done as above, the vertical image induced blur must be removed before two-dimensional partial image restoration techniques are used to enhance the FF image contrast degraded by optical turbulence.

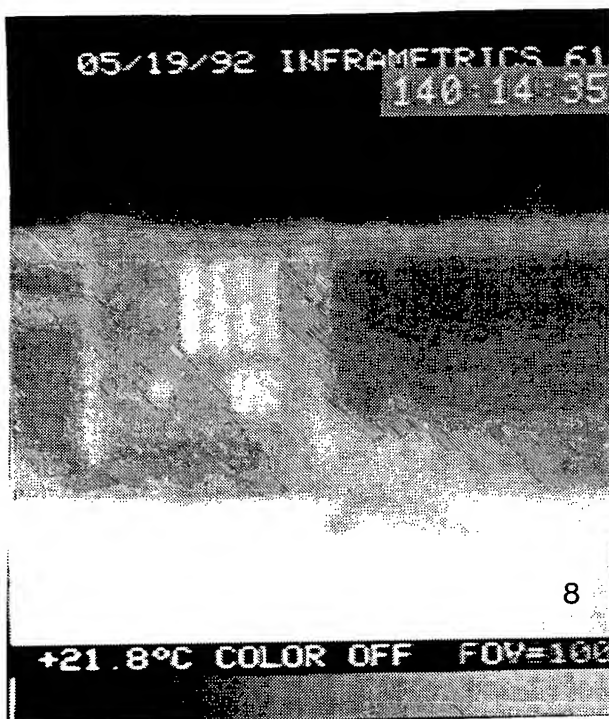


Figure 8. No cloud cover is present between the NF and FF station, moderate values of  $C_n^2$ .

Figure 9. Cloud cover is present between NF and FF stations, relatively low values of  $C_n^2$ .

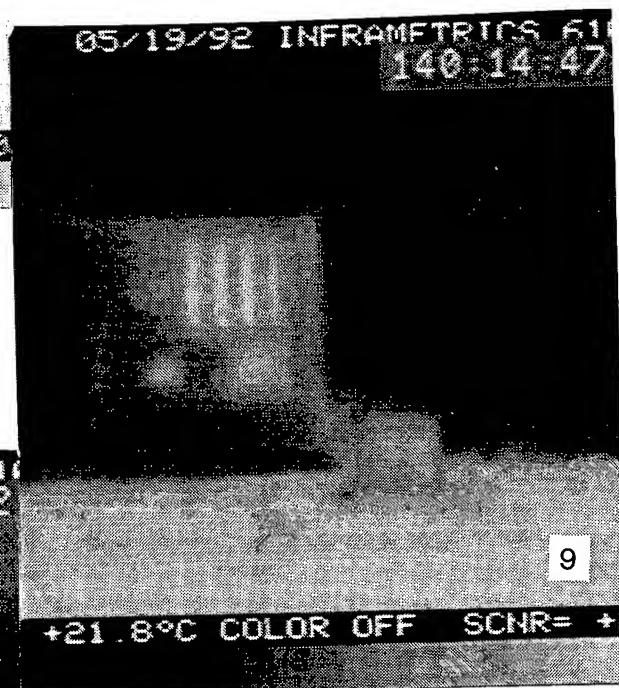
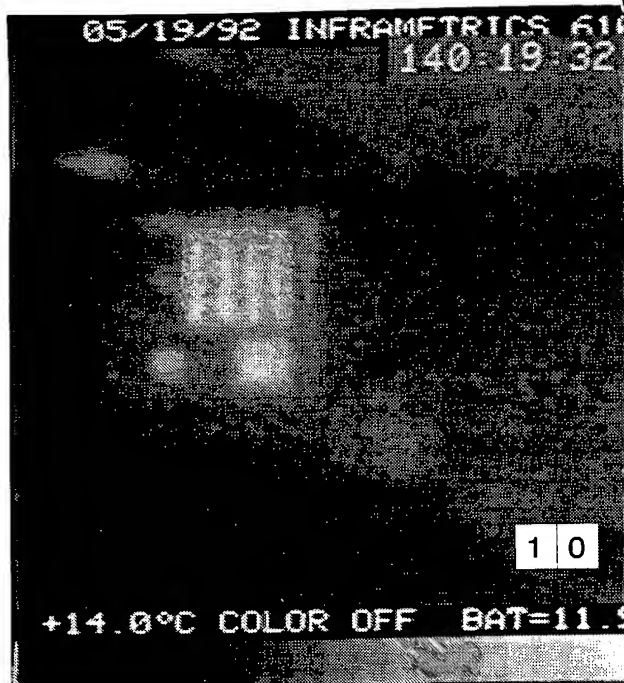
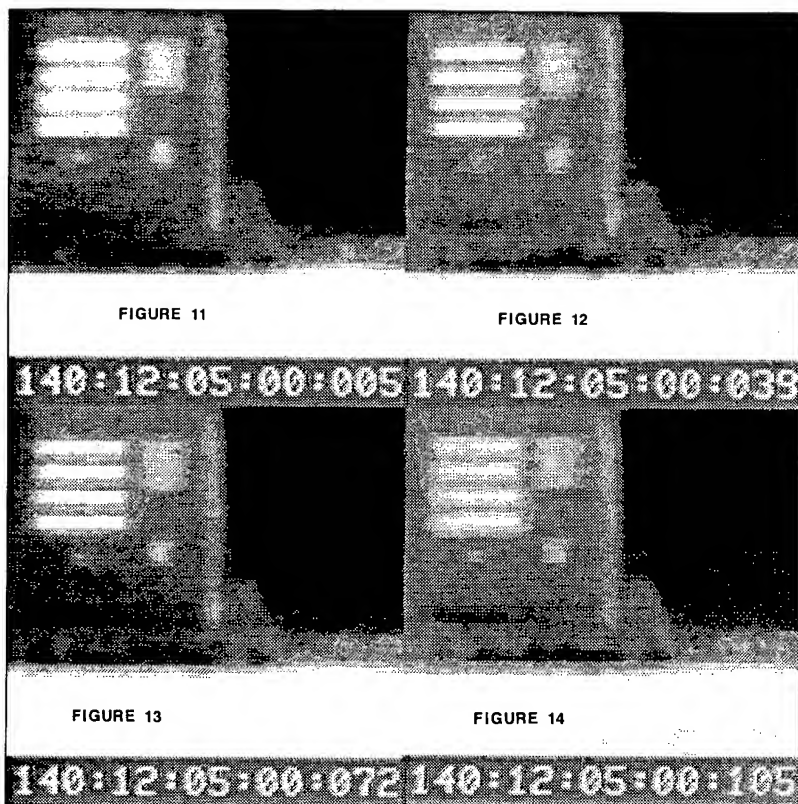


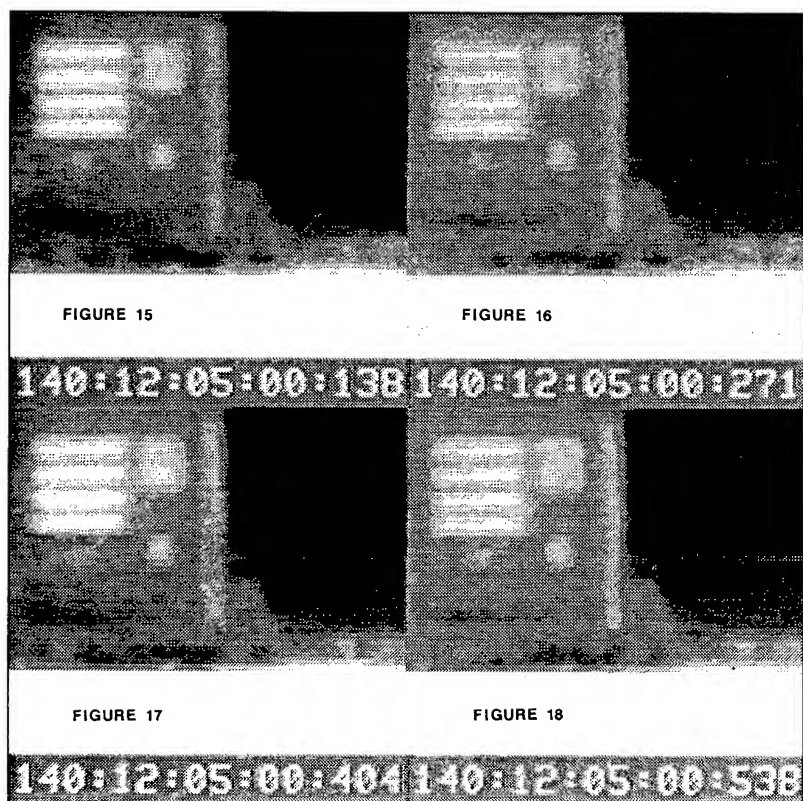
Figure 10. Reference is of an undistorted IR scene with a low  $C_n^2$  value.





Figures 11-14.

Here are 4 consecutive frames that show a complete cycle of bar blurring.



Figures 15-18.

This illustrates the same bar blurring occurring every 4th-frame.

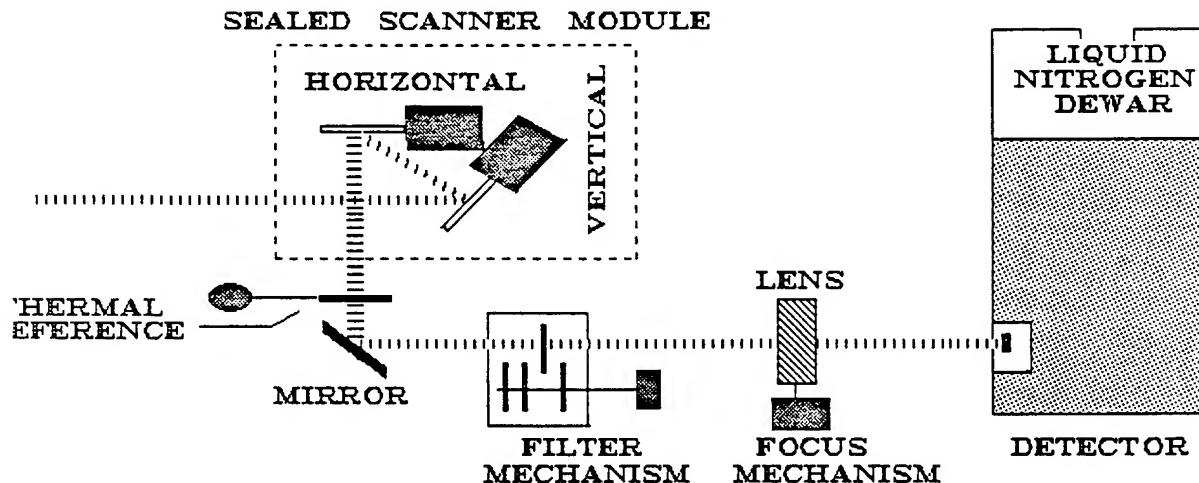


Figure 19. Imager scanner configuration.

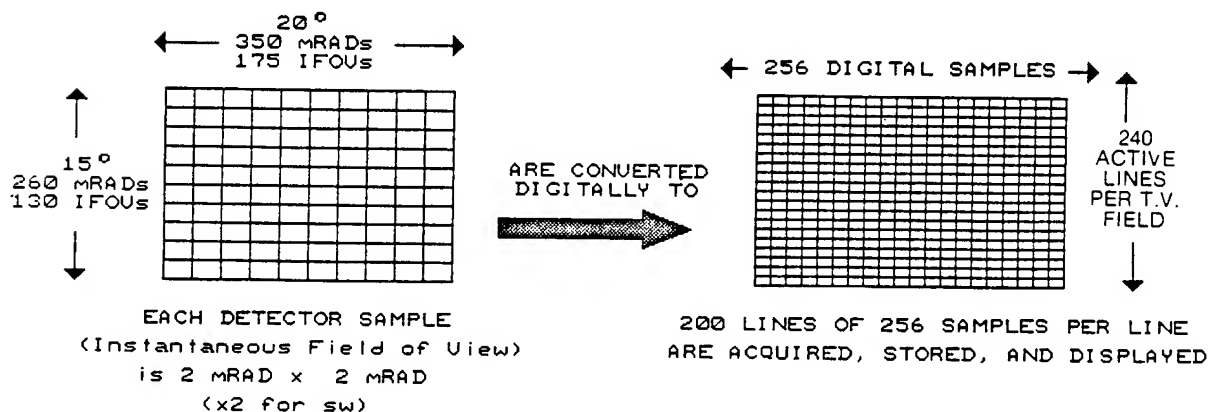


Figure 20. Imager detector and frame resolution.

#### 4. CONCLUSIONS

The TCC provides a means to separate changes in the spatial radiance distribution inherent to the target and its background from those changes in spatial radiance distribution caused by propagation through the atmosphere. This allows the effects of solar radiance variation on  $C_n^2$  and image distortions to be isolated. The large-area target board in the horizontal-bar configuration showed that there were imager anomalies that needed to be addressed to correct vertical imager induced blurring. Once done, image restoration of optical turbulence induced blurring is possible.

#### ACKNOWLEDGMENTS

We thank Dr. Jay B. Jordan of the New Mexico State University Department of Electrical and Computer Engineering for his great help in the analysis of these problems. We also extend our thanks to B.A. Stewart, Don Dusek, Karen Copeland, Arland Schneider, Steve Evett, and Joseph Serda of the USDA-ARS, Conservation and Production Research Laboratory. Additionally, we extend our thanks to Arnold Tunick, Robert Brown, John Fox, and Frank V. Hansen of the Battlefield Environment Directorate of the US Army Research Laboratory.

#### REFERENCES

- Inframetrics 610 operations manual. 1983.
- Jordan, J. B., private conversation Department of Electrical and Computer Engineering, New Mexico State University, Las Cruces N.M., March 1991.
- Kantrowitz, F. T., W. R. Watkins, D. R. Billingsley, and F. R. Palacios, 1990: Characterization and Optimization of Infrared Imager Detector Response for Long Path Research. In SPIE Conference Proceedings, 1311, Orlando, FL.
- Crow, S. B., W. R. Watkins, F. R. Palacios, and D. R. Billingsley, 1991: Technique for measuring atmospheric effects on image metrics. In SPIE Conference Proceedings, 1486, Orlando, FL.
- Watkins, W. R., F. T. Kantrowitz, and S. B. Crow, 1988: Characterization of atmospheric effects on target contrast. In SPIE Conference Proceedings, 926, Orlando, FL.
- Watkins, W. R., F. T. Kantrowitz, and S. B. Crow, 1989: Transmission measurements with the Target Contrast Characterizer. In SPIE Conference Proceedings, 1115, Orlando, FL.
- Watkins, W. R., S. B. Crow, D. R. Billingsley, and F. R. Palacios, 1991: MISL Measurements at the NATO Best Two. In Proceedings of the 1991 Battlefields Atmospherics Conference, U.S. Army Atmospherics Laboratory, White Sands Missile Range, NM.

**Session V Posters**

**WEATHER DECISION AIDS**



## THE INTEGRATED WEATHER EFFECTS DECISION AID: A NEW PLANNING TOOL

Robert R. Lee and Sue E. Bussells  
Battlefield Environment Directorate\*  
U.S. Army Research Laboratory  
White Sands Missile Range, New Mexico 88002-55012, USA

### ABSTRACT

Future C<sup>3</sup>I systems will harmonize operational and tactical planning of battlefield functional areas (BFA) by communicating on local and wide area networks. A new tactical decision aid (TDA) being developed will reside on these separate BFA nodes and will allow the commander and his staff to consider weather and its effects while planning operations and engagements.

The Integrated Weather Effects Decision Aid (IWEDA) program will identify and classify weather effects on equipment, operations, and personnel. The IWEDA displays initial weather effects assessments as color-coded cells, favorable-marginal-unfavorable, in a matrix of mission type versus time. Mission types and matrix times are definable by the user. The program provides information concerning the specific causes of weather effects via an explanation facility and generates maps of the area of interest to show which weather effects are present.

### 1. INTRODUCTION

The Battlefield Environment Directorate, in conjunction with Science and Technology Corporation, is developing an integrated weather effects decision aids (IWEDA) software program that will be used to assess the effects of environmental impacts.\*\* The responsibility and requirements for assessing environmental effects through weather decision aids (WDA) are contained in an Army/Air Force joint regulation. The regulation states that the Army is responsible for providing weather effects information to the Air Weather Service (including weather elements and their weather effects critical threshold values) and the Air Force is responsible for providing weather decision aid information in general formats such as favorable, marginal, or unfavorable. These WDAs (using green, amber, and red color codes, respectively) are based on operating limitations (critical values) provided by the Army. The time line to automate manually produced WDAs on Army operations, systems, and subsystems is fiscal year 1995.

---

\*Formerly U.S. Army Atmospheric Sciences Laboratory

\*\*Work completed under Contract No. N00014-90-D-0065, Delivery Order 0004.



To meet the 1995 time line the U.S. Army Atmospheric Sciences Laboratory (ASL) developed three separate and distinct modules: a Weather Effects Matrix (WEM), a Tactical Weather Effects Messages (TWEM), and a Consolidated Weather Effects Decision Aids (CWEDA). The WEM automatically compared a terminal airdrome forecast against critical parameters and then depicted the resultant weather impacts in a color-coded matrix against 10 types of fixed Army mission operations. The colors green, amber, and red correspond to the requirement of specifying favorable, marginal, and unfavorable conditions, respectively. The WEM served a very useful purpose by providing an overview of the forecast weather that may negatively impact future missions. The TWEM concept was to use weather impact messages to provide a reasonable amount of detail about weather and environmental effects on equipment, operations, and personnel. The user received a text only message that described detrimental weather impacts present in the outdoor environment. The CWEDA was very similar to the TWEM, except the CWEDA divided the weather impact messages into a hierarchical structure. The program calculated an overall equipment performance by considering separate weather impacts on each subelement of the piece of equipment being considered. The Science and Technology Corporation was asked to evaluate these three modules and concluded that the concepts used to develop them were sound and attempted to address user requirements; however, the implementation of these concepts was flawed. Based on this evaluation, STC was tasked to design the IWEDA software program using the concepts that were developed by ASL.

Weather has always impacted and will always impact operations, equipment, and personnel. However, the current weather support precludes planners from being informed of weather impacts *before* the adverse conditions appear. Problems exist in the definition and validation of critical values applied to various operations. Inasmuch as Army field manuals contain critical values for a number of mission operations without reference to systems, the basis of these critical values is not known. Hence, no obvious vertical connection exists between these published values and specific systems that might be related to the operations.

## 2. THE IWEDA CONCEPT

The primary use of IWEDA will be by Army users (commanders, staff principals/planners, and the Service Weather Officer (SWO)). The Integrated Meteorological System (IMETS) will perform the environmental data collection effort from various sources and provide the environmental data to drive IWEDA. The role of the SWO will be to ensure that the environmental database in IMETS is current and complete, to generate WDAs to determine the impacts that may occur if and when weather conditions change, and to brief the tactical commander on the WDAs. With IWEDA on the user's standard workstation (which contains a complete, Army-wide knowledge base), the program will serve to encourage the user to be more reactive to potential weather impacts and take the timely and necessary actions to minimize environmental effects on systems and/or operations.

The IWEDA software program can be considered a shell that consists of three distinct parts: weather decision aids, user interface, and data interaction. The WDA component can be further subdivided into traditional algorithmic aids and advanced intelligent aids, the latter being the *expert system* or IWEDA.

The design of IWEDA addresses only those interface issues relevant to the IWEDA expert system and does not address the interface needs for traditional algorithms or other interactions with the host hardware system. The data interaction requirements between the IWEDA software and other hardware systems containing IWEDA input data are also not explicitly addressed in this paper. The question of "push-pull" of environmental data between IMETS and IWEDA must be addressed in the IMETS concept of operation. This determination and whether IWEDA will automatically generate updated reports whenever new data are available must be addressed when the detailed design of IWEDA commences.

### 3. KEY DESIGN ATTRIBUTE

The vertical connectivity or linking between mission operations and systems/subsystems is the key factor that makes IWEDA an extremely useful and effective tool. The IWEDA, by taking three separate ASL modules (WEM, TWEM, and CWEDA) and vertically linking them, captures their individual strengths, thereby encapsulating the IWEDA expert system. Vertical connectivity allows the user to determine the basis or rationale of critical values and visualize how the effects impact the mission. Vertical connectivity also supports the WDA process by allowing the user to trace a weather impact on a mission or operation down to the contributing impact on an individual system or subsystem. The IWEDA program will permit the user to query the system and learn *where, what, when, and why* a mission operation and/or a system is or is not forecast to be degraded. This capability will be possible because IWEDA is based upon the vertical connectivity of systems and subsystems with simple defined battlefield mission operations.

### 4. ASSUMPTIONS

The following major assumptions were identified in developing IWEDA. It is envisioned that other Army hardware and/or software systems will provide the information needed.

- Four-dimensional, gridded environmental input data fields are available for observations, forecasts, and climatology.
- Terrain, mobility, and vegetation data are available.
- Gridded area of interest boundary, with geographical references (that is, rivers, cities, and north orientation), is available.

### 5. INDIVIDUAL SYSTEMS

The system level approach for developing WDAs is critical to the success of IWEDA. It allows the user to receive WDA information directly about a specific system (and its subsystems and components) based on available weather data (forecast and observed). The IWEDA program will provide WDAs on systems, subsystems, and components after the user selects a system and identifies the desired timeframe and location in the area of interest. Figure 1 is an example of two separate aviation systems. Because of the availability of a large number of systems within a tactical unit, this capability to obtain WDAs for specific systems will normally be used by the

staff principals and not by the commander. In many instances, this system level approach will provide the commander's staff with the answer or rationale to the question why a military mission is impacted by weather.

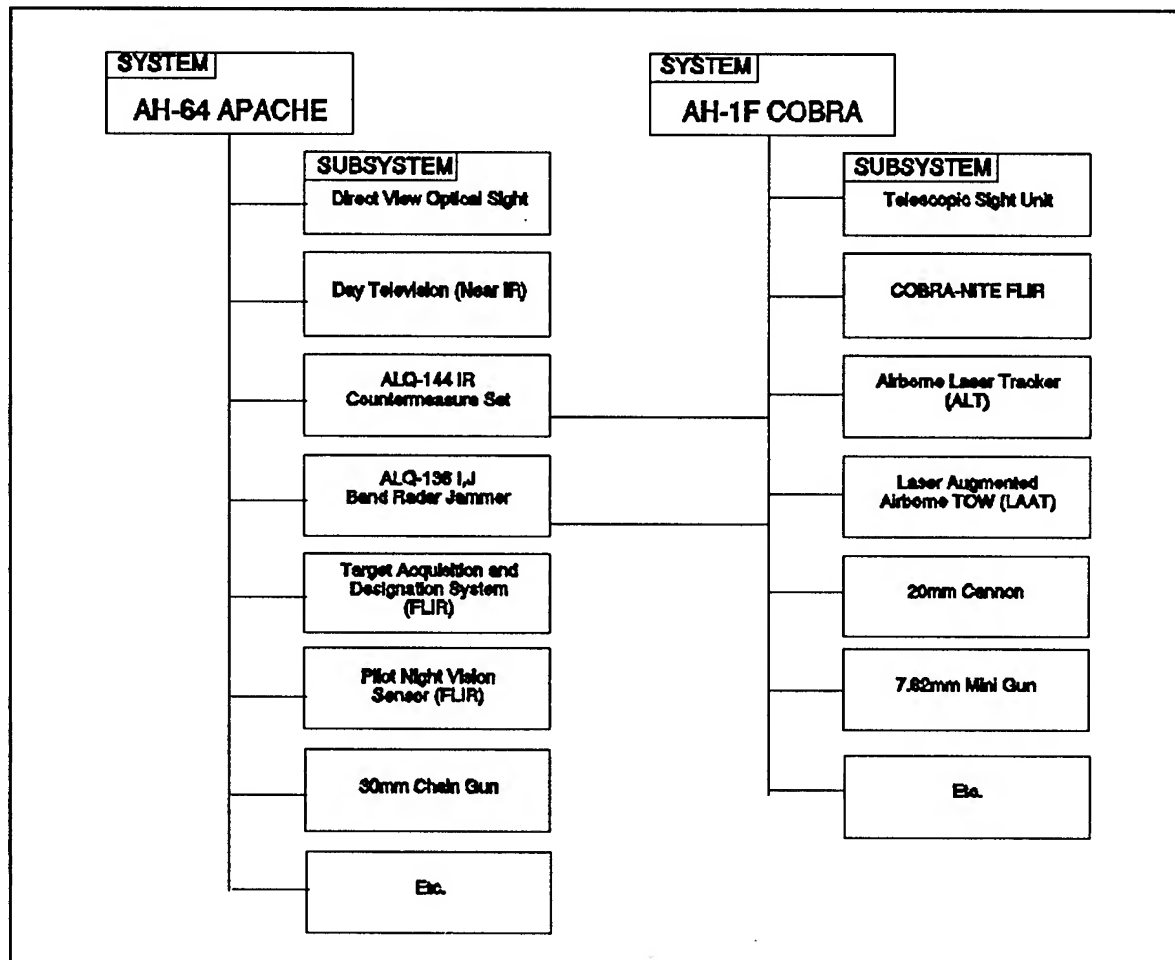


Figure 1. Example definition of two separate Army aviation systems.

## 6. MISSION OPERATIONS

Tactical commanders want, in a graphical presentation, a quick overview of the effects that weather will have on their operations. A green mission operation indicates favorable conditions and that no further elaboration on weather and its impact is needed. Conversely, if one or more than one mission operation is impacted, the commander will want additional information on only those affected missions. While graphical presentations may suffice for the tactical commander, textual presentations are required by staff principals/planners so that they can provide the commander with more detailed information on the possible weather effects. Therefore, in addition to providing WDAs on specific systems, IWEDA will also provide WDAs for mission operations in which the user has an interest.

The IWEDA software program will present weather impact information by using a color-coded matrix of operations versus time, similar to the current WEM. However, the basic difference between the WEM concept and the one proposed for IWEDA is that, in IWEDA, when *amber* or *red* impacts occur, the user may make a query to find out *why* and *where* the mission operation is degraded. Another feature of IWEDA is that it will allow the user to override the impact on a specific system, if desired. For example, if an operation is degraded because of the weather impact on a tube-launched, optically-tracked, wire-guided (TOW) system, but the user does not envision the use of TOWs, he can negate the TOW impact and have IWEDA reevaluate its WDAs to determine the revised impact.

To define mission operations, the commander can identify the operations and then define and group equipment that will constitute each operation. This provides the flexibility for each commander to tailor the operations according to specific needs and interests. The weather effects assessment will provide the commander and staff an overview of the impact that forecast weather will have on mission operations. The IWEDA generates and displays a color-coded matrix of mission operation versus time as shown in fig. 2.

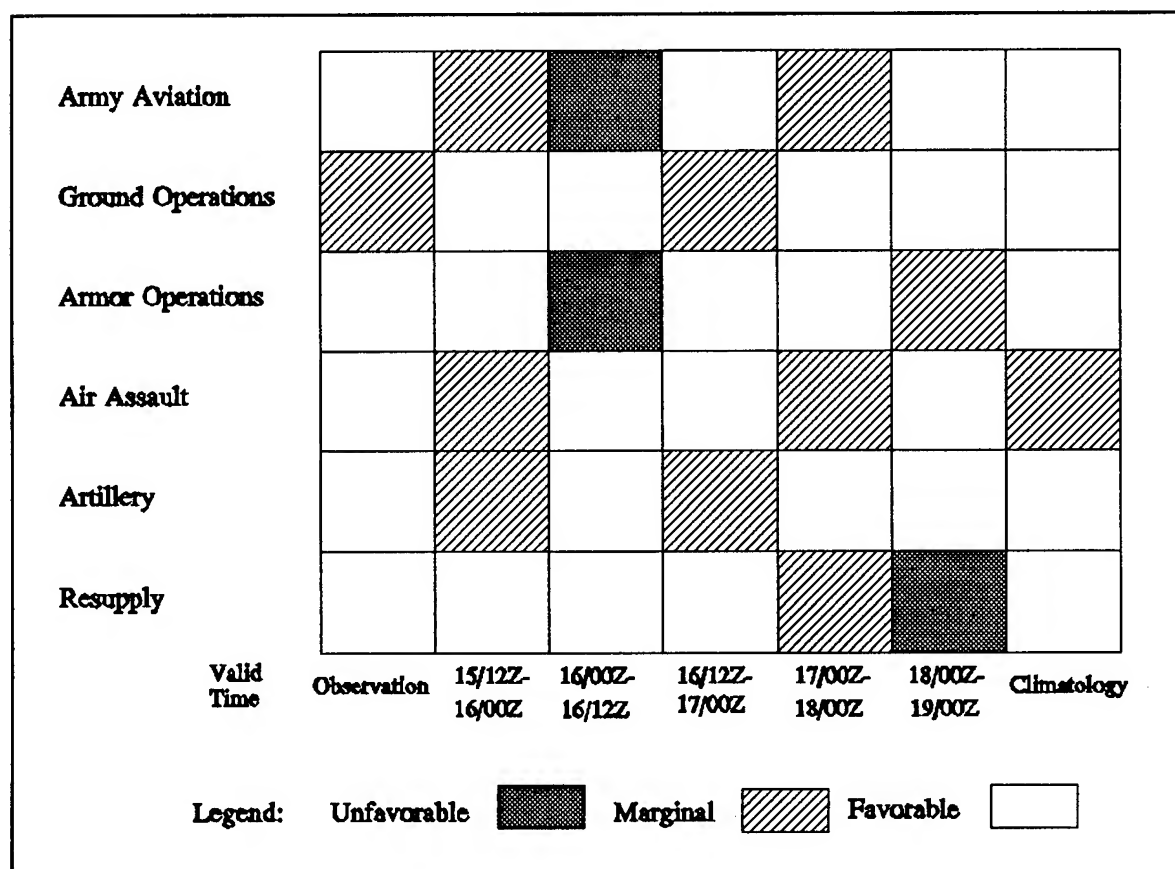


Figure 2. Sample mission operation weather effects matrix.

In the matrix, the mission operations displayed are determined and defined by the tactical commander, and the time period is a function of the user's tactical level or echelon. Because commanders are interested in what is happening beyond their immediate spheres of influence, the time period for the appropriate echelon or the period covered by the weather forecast will be used in conjunction with mission operations.

## 7. TAILORED MISSION OPERATIONS

The number and types of mission operations in IWEDA will be determined by the interests of the tactical commander and will be defined by grouping a subset of the unit's systems under a mission operation. For example, a commander may want to know the weather impact on Army aviation. This can be accomplished, as an example, by identifying and grouping the AH-64 and the AH-1 and their subsystems (see fig. 1) under the term "Army Aviation," as shown in fig. 3. To ensure uniformity and understanding of what systems comprise a mission operation, the tactical commander or representative (that is, G-3), would identify the military operations and their associated systems. Other users could define the same group heading differently on their individual workstations without changing the commanders definition by adding and/or deleting different systems, by using a "what if" capability. This flexibility of allowing the commander to tailor operations will enable the commander to obtain the weather advice in the context desired and to ensure that all staff principals obtain the same weather impacts briefed to the commander. It is important to remember that whatever definition the division commander uses to align systems with mission operations must be "pushed" up to corps and down to brigade so that the principals can also see the identical mission operation versus time matrix being run at division.

Although most of the systems that will be grouped under specific mission operations are tangible (such as tanks and aircraft), there are some intangible "systems" that may also be included (such as *personnel* and *trafficability*). Personnel and trafficability are impacted by weather and can be included (grouped) in several mission operations; or, if the commander desires, as stand-alone mission operations. This tailoring/defining capability provides the flexibility that a commander needs to readily see and understand weather impacts of extreme interest.

The IWEDA program uses the worst-case propagation to determine the weather impact. Using fig. 3 as an example, where the mission operation Army Aviation is defined as consisting of two systems each with its individual subsystems, the worst-case color in the subsystems influences the color code for the system. If the AH-64 day television subsystem was *amber* and the pilot night vision sensor (FLIR) was *red*, then the AH-64, as a system, was *red*. Conversely, if the AH-1F AN/PVS-6 was *amber*, then the AH-1F, as a system, was coded *amber*. And when a mission operation is defined as consisting of two or more systems, the worst-case system color influences the color code for the mission operation. In this example, Army Aviation is *red* because of the FLIR subsystem on the AH-64.

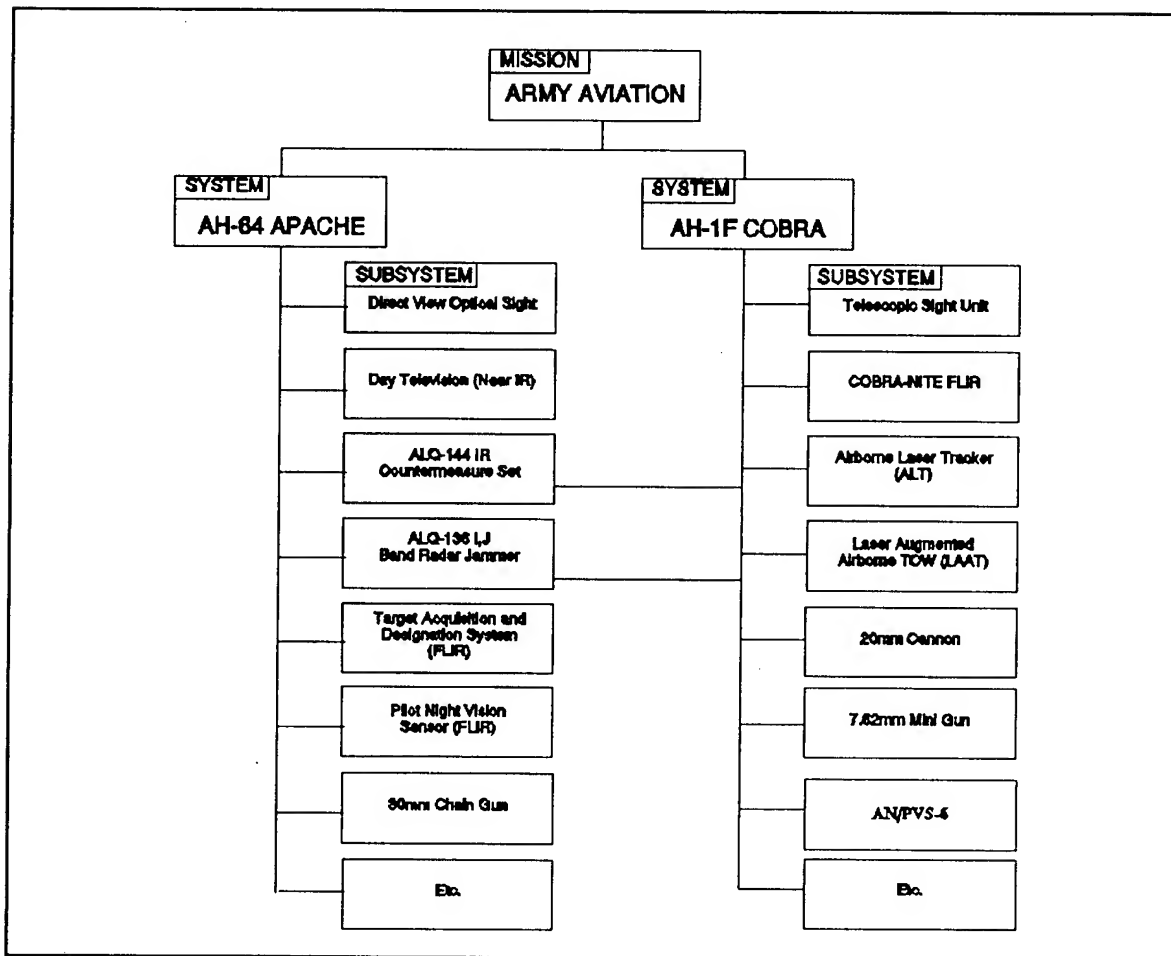


Figure 3. Example definition of Army Aviation tailored mission operation.

## 8. KNOWLEDGE BASE

The IWEDA knowledge base must contain the critical values for Army systems operating both in peacetime and wartime modes. Additionally, this rule base must be protected with a security classification sufficiently high that useful information can be obtained from the experts who will provide the meaningful operational limitations of the systems. Critical value information on systems should be collected for both peacetime and wartime conditions. During peacetime tactical exercises, a vast majority of critical values are based on unclassified or public knowledge information and on safety considerations because safety is paramount to mission accomplishment. The use of WDAs based on these values serves as an important and useful training tool for the commander and staff during peacetime tactical exercises. However, in wartime, safety considerations are significantly relaxed, whereas the classified operational limitations are more realistic to the operating environment and the systems capabilities. Therefore, different critical values should be used for the same system, in wartime versus peacetime.

## 9. SYSTEM INTEGRATION

The IWEDA software will reside in two primary locations: (1) the computers located on the ATCCS nodal points and (2) the IMETS computer. Placing the IWEDA software program in the user's computer will provide ready access to IWEDA products and allow the user to take advantage of WDAs to minimize the weather effects on systems and operations. Putting IWEDA in the IMETS with the SWO will help the SWO to identify key weather parameters rapidly and perform an improved "met watch" of these elements. The IWEDA program must be capable of residing on a multitude of ATCCS nodal point hardware systems, talking to and receiving environmental weather data field from IMETS through use of the ATCCS, and transmitting WDA information via ATCCS to other hardware systems (for example, the Digital Topographic Support System).

The preliminary IWEDA software program will be written in C/C++ for implementation in the MicroSoft Windows operating system. C/C++ was chosen to maximize portability to the final ATCCS platform. MicroSoft Windows is the target graphical user interface (GUI) because of its widespread use and acceptance as the leading GUI. The choice of MicroSoft Windows also maximizes exposure of the IWEDA preliminary model as a marketing tool.

## 10. OTHER CAPABILITIES

The next generation IWEDA program will also be capable of providing sensitivity information and selected outputs. Sensitivity statements report the user's proximity to crossing a critical value threshold, provide supplemental information needed for evaluating impacts, and inform the user "How red is red." The IWEDA outputs will consist of graphics that can be converted to text fields for facsimile transmission and text impact statements and explanations. To ensure that a workable next generation IWEDA program can be fielded in 1993, some of the IWEDA capabilities that cannot be implemented within this allotted time are weighing functions and uncertainty values.

Weighing functions have been frequently considered as the panacea for providing WDAs with a degree of intelligence or importance when compared with algorithmic WDAs. Numerous attempts have been made to quantify these weighing functions. If realistic weighing factors could be developed, they could provide the intelligence necessary for WDAs to make high-level recommendations to users (for example, alternative equipment suggestions).

Uncertainty values provide the user with a *confidence factor* on the goodness of environmental data and would be provided by either IMETS or the Air Force Global Weather Center, which is the primary producer of gridded data field products. This confidence value, which can be expressed as a percentage, can then be combined with other facts in the production of a WDA. The uncertainty value appended to the data that were used to generate the WDAs would provide the user the "confidence" needed to determine action based on the WDAs.

Finally, other outputs could be developed. Gridded impact data fields could be used by other computers and a natural language capability could provide text impact messages for translation into paragraphs for use in reports.

## 11. SUMMARY

The IWEDA concept is an expert software system that is feasible at the present time to provide weather effects or impacts to a variety of users so that timely corrective action can be taken. The IWEDA software program will be capable of giving the tactical commander the tailored information desired. A contract has been let with Science and Technology Corporation to develop the software and a very limited knowledge rule base to support the preliminary version of IWEDA well before FY 1995. The robustness of the IWEDA software program is only limited to the quality and completeness of the knowledge rule base on Army systems.





WEATHER AND TERRAIN ANALYSIS  
FOR AERIAL INTELLIGENCE PREPARATION OF THE BATTLEFIELD

Gary McWilliams and Steve Kirby  
Battlefield Environment Directorate\*  
U.S. Army Research Laboratory  
White Sands Missile Range, New Mexico 88002-5501, USA

ABSTRACT

The Army Research Laboratory (ARL) has embarked on a program to develop a prototype software system to automate a relatively new intelligence analyst function referred to as aerial intelligence preparation of the battlefield (AIPB). ARL's Battlefield Environment Directorate (BED), with support from the U.S. Army Topographic Engineering Center (TEC) and the U.S. Army Space Technology and Research Office (ASTRO), is responsible for developing the weather and terrain components of this prototype system. BED and TEC are using the software they previously developed for the more formally established ground intelligence preparation of the battlefield (IPB) as the foundation for the AIPB software. Adapting the ground IPB software to AIPB applications requires greater emphasis on air defense contingency threats such as fixed- and rotary-wing aircraft, missiles, and drones. The AIPB software is being designed to be compatible with both short-range air defense and high-to-medium-altitude air defense operations. This software, like the ground IPB software, will have a modular architecture, will make extensive use of artificial intelligence techniques, and will use both two-dimensional and three-dimensional graphics for displaying information.

1. INTRODUCTION

The Army Research Laboratory's (ARL) Battlefield Environment Directorate (BED), Weapons Technology Directorate (WTD), Advanced Computation and Information Sciences (ACIS) Directorate, Human Resource and Engineering (HRE) Directorate along with the U.S. Army Space Technology and Research Office (ASTRO) and the U.S. Army Topographic Engineering Center (TEC) are engaged in a cooperative effort to demonstrate the feasibility of automating aerial intelligence preparation of the battlefield (AIPB) procedures. These combined efforts are being pooled from experience and expertise that each organization has gained from work on related projects. BED's AIPB program responsibilities include developing the weather analysis/effects module and integrating this module with TEC's terrain effects module. This work is in support of the Army's efforts to greater utilize space resources and to automate tactical command, control, and intelligence (C2I) functions.

---

\*formerly U.S. Army Atmospheric Sciences Laboratory (ASL)

## 2. AERIAL INTELLIGENCE PREPARATION OF THE BATTLEFIELD

AIPB recognizes the third dimension of the battlefield--the airspace. Although presently not as formally developed as the more traditional ground level IPB, AIPB is rapidly growing in importance due to changes in warfighting technology and subsequent changes in military doctrine. Operationally neither air nor ground IPB can be performed as separate functions, but instead are best performed as a unified procedure.

AIPB greatly expands the battlefield area in terms of depth, width, airspace, and time. Usually the air defense areas of interest for friendly tactical units are the enemy's airfields and tactical ballistic missile launch sites from which the air threat can reach the friendly's units' areas of operation.

The most difficult and yet most important aspect of AIPB is the prediction of how enemy aircraft will approach a target. This prediction, which is usually graphically depicted as an air avenue of approach, is affected by many factors, including weather and terrain. Important weather factors are the temperature, humidity, winds, clouds, precipitation, light, and visibility. Some of the most important terrain issues are the observation and fields of fire, cover and concealment, obstacles, and key terrain (FM 44-100).

## 3. BASIC REQUIREMENTS

The basic AIPB operational requirements that we wish to demonstrate in our prototype system are the ability to address the threat contingencies associated with both short-range air defense (SHORAD) and high-to-medium-altitude air defense (HIMAD) threat contingencies, the ability to interface with other Army automated command and control systems, and the ability to use the most current environmental satellite information in near real time.

The SHORAD and HIMAD threat contingency is constituted by such assets as rotary- and fixed-wing aircraft, cruise missiles, tactical ballistic missiles, unmanned aerial vehicles, remotely piloted vehicles, and satellites. Examples of friendly systems typically associated with SHORAD activities are the Chaparral and Stinger. Examples of friendly systems associated with HIMAD activities include the Patriot and Hawk (FM 44-85).

Every effort is being made to achieve the highest level of automation possible and to facilitate the integration and configuration of our system software as a module in the larger C2I tactical systems environment. Thus we intend to ensure that our system appropriately interfaces with other Army automated C2I systems. As an integrated module, our system will need to receive and transmit various environmental and other relevant data and information. For example the AIPB module will need to receive weather data from the Integrated Meteorological System (IMETS) and terrain data from the Digital Terrain Support System (DTSS). It will then need to transmit its processed information to other battlefield systems needing IPB-related information.

Given the highly perishable nature of intelligence information, our system will make extensive use of the most currently available satellite data for updating its weather and terrain information data bases.

#### 4. USE OF EXISTING SOFTWARE

##### 4.1 THE WEATHER AND DOCTRINAL INFORMATION FUSION SOFTWARE SYSTEM

The Weather and Doctrinal Information Fusion Software System (WADIF) (Eskridge, 1992) currently produces asset performance templates for ground-based entities. A template can be produced for the asset as a whole or for a particular component of the asset. Three main factors are considered in producing these templates—weather, terrain, and enemy intentions. WADIF's knowledge base is a set of rules derived from the Consolidated Weather Effects Decision Aid (CWEDA). The rules outline how given weather and terrain conditions will impact an asset's performance. In WADIF's present form information such as 24/36 h precipitation totals, slope, visibility, and land use is reasoned over to derive these templates. As WADIF is expanded into the AIPB arena, new information types become critical. Among these are cloud types and locations and icing potential. To address these needs WADIF's meteorological server, Mercury, is being enhanced.

##### 4.2 THE MERCURY SOFTWARE SYSTEM

Mercury is an artificial intelligence (AI)-based software system under development at the BED (Army Research Laboratory) and is designed to produce a grid of meteorological data despite the complications of complex terrain and sparse data when pure objective analysis does poorly. Perhaps the most difficult task facing Mercury is providing gridded meteorological data within the boundary layer of the atmosphere. To do this Mercury uses surface reports and heuristics and will soon employ satellite information. The heuristics are intended to spread the data more intelligently than if only objective analysis were to be used. For example, given the knowledge of where significant terrain is, "representative" stations are found for "isolated" gridpoints (defined as gridpoints more than 1 grid length from a reporting station). Surface reports also aid in determining an appropriate lapse rate in the absence of upper-air soundings. Once representative stations are found for isolated grid points, their data are adjusted for differences in land-use and elevation. Finally, objective analysis is applied to the estimated values and the reporting stations, providing a grid of meteorological data to be fed into WADIF.

The typical weather parameters are very important to IPB, but a crucial one for AIPB is the accurate description of cloud fields. More often than not, surface and upper-air reports will be too sparse to describe all the cloud areas. Thus we must enlist an additional source: satellite data, in particular, Defense Meteorological Satellite Program (DMSP) data. DMSP data is the highest resolution data available (0.6 km). Also of potential use is Advanced Very High Resolution Radiometer data from the NOAA Polar Orbiter with a resolution of 1.1 km. A number of heuristics exist for identifying cloud types and heights using AVHRR channel data. Once identified the clouds need to be rendered. Numerous software packages exist for rendering clouds.

Among these packages are two (Meade, 1985; Owen, 1988) that were based on MOVIE.BYU (a software graphics system) as well as the highly popular McIDAS system (Hibbard and Santek, 1990). Our approach is not to adopt one of these large packages but to build a software module with the functionality needed to perform AIPB.

#### 4.3 TERRAIN ANALYSIS SOFTWARE

The software for terrain analysis is being written by the Topographic Engineering Center, Fort Belvoir, Virginia, and DBA, Incorporated, of McLean, Virginia. DBA is currently writing software that uses SPOT and LANDSAT imagery to update Interim Terrain Data (ITD). For example, roads may be washed out and/or reservoirs expanded, and a map reflecting these changes would be of great use to a G2/G3 officer. One can also pan and zoom on a particular area of interest. In addition, a number of software modules from the AirLand Battlefield Environment software suite will be applicable to this work. Among them are line of sight, helicopter landing zones, and aircraft icing zones.

#### 5. AIPB SOFTWARE ADDITIONS

To accommodate AIPB requirements within the general design of our existing IPB software, we will have to modify some of our existing software as well as implement totally new software functionality.

First, the weather and terrain effects rules will have to be expanded to include assets associated with the ADA threat contingency. Initially we intend to limit this expansion to include fixed- and rotary-wing aircraft. Eventually, as resources allow, the weather effects information will be further expanded to include assets such as remotely piloted vehicles and ballistic missiles.

Second, since the area of operations and especially the area of interest for AIPB usually have greater aerial dimensions than those for traditional ground IPB, our software will need to access and analyze considerably more weather and terrain data than with ground IPB. This need in turn requires the information to be displayed on map backgrounds covering a larger area and consequently having less resolution. Thus our system must be able to display map backgrounds with different scales of resolution.

Third, given that AIPB introduces the airspace dimension to the IPB, it becomes even more important to display the information in 3-D. The ability to display the information in 3-D requires many new graphic utilities and an understanding of the types of information best portrayed in 3-D.

Fourth, and perhaps most important, the system's reasoning engine must be able to generate products specific to AIPB needs. One of the prime AIPB products is the air avenues of approach. The ability to define the air avenues of approach must also be coupled with the ability to assign a probability rating to each selected avenue.

## 6. CONCLUSIONS

Development of the software for automating AIPB weather and terrain analysis requires a wide range of talents and expertise. This broad spectrum of required expertise is one of the primary reasons the software is being developed as a cooperative effort among several Army research organizations. As a cooperative program we will also be able to efficiently leverage the efforts of related research programs, which in many cases translates to the use of existing software.

The challenges presented by AIPB also present an important opportunity. This opportunity is to correctly recognize that the battlefield is truly 3-D and any properly performed analysis must give due reverence to each dimension.

## 7. REFERENCES

- Eskridge, Tom, 1992: WADIF: An Expert System for Fusing Weather and Doctrinal Information Used in the Intelligence Preparation of the Battlefield, CR-92-0034-1, U.S. Army Atmospheric Sciences Laboratory, White Sands Missile Range, New Mexico.
- FM 44-85 (final draft), 1992: Patriot Battalion and Battery Operations, U.S. Army Headquarters, Washington, D.C.
- FM 44-100, 1988: U.S. Army Air Defense Operations, U.S. Army Headquarters, Washington, D.C.
- Hibbard, W., and D. Santek, 1990: Visualizing Large Data Sets in Earth Sciences, Visualization in Scientific Computing, G. Nielson, B. Shriver, eds., and L. Rosenblum, Associate ed., 147-152.
- McWilliams, Gary, 1991: Research and Development Plan: Real-Time Weather/Terrain Exploitation. In Proceedings of the 2nd Workshop on IPB Weather and Terrain Templating, Computing Research Laboratory, New Mexico State University, Las Cruces, New Mexico.
- Meade, A., 1985: Applications for Three-Dimensional Computer Graphic Cloud Representations Produced from Satellite Imagery, Master's Thesis, Colorado State University, Fort Collins, Colorado.
- Owen, D., 1988: Three-Dimensional Analysis of Synoptic Satellite and Conventional Meteorological Observations, Master's Thesis, Naval Postgraduate School, Monterey, California.
- Raytheon Corporation, 1991: Software Requirements Specification for the Tactical Planner Workstation Build 1A of the Battalion Tactical Operations Center of the Patriot System (draft), Prepared for Patriot Project Office under contract number DAAH01-87C-A025.



## THE AIRLAND BATTLEFIELD ENVIRONMENT (ALBE) PROGRAM AT BED

David Sauter  
Battlefield Environment Directorate\*  
U.S. Army Research Laboratory  
White Sands Missile Range, New Mexico 88002-5501, USA

John B. Spalding and Danforth C. Weems  
Physical Science Laboratory  
New Mexico State University  
Las Cruces, New Mexico 88003, USA

### ABSTRACT

Airland Battlefield Environment (ALBE) is a technology demonstration program intended to provide the Army with the capability to assess and exploit battlefield environmental effects for tactical advantage. The U.S. Army Research Laboratory's Battlefield Environment Directorate (BED) is primarily responsible for weather-related effects while several Corps of Engineer Laboratories consider terrain effects. BED has produced several tactical decision aid (TDA) categories under which reside individual TDAs. These categories include meteorological analyses; Army aviation; nuclear, biological, and chemical; weapon system performance; and weather effects.

The ALBE program was presented at the 1991 Battlefield Atmospherics Conference. At that time the software was not nearly complete; thus the presentation focused on the ALBE concept and planned capabilities. The demonstration this year will provide attendees with a look at a more mature system in terms of an integrated package with respect to user interface, map display software, graphics, and TDA software.

### 1. INTRODUCTION

The Airland Battlefield Environment (ALBE) program includes participation by several Corps of Engineer Laboratories, one Army Materiel Command Laboratory, and associated contractors. Each of these entities is focusing primarily on software that will provide the Army with the capability to assess and exploit battlefield environmental effects for tactical advantage. The U.S. Army Research Laboratory's Battlefield Environment Directorate (BED) has been given primary responsibility to incorporate weather-related effects. As of early September 1992 BED had included five tactical decision aid (TDA) categories into ALBE. These TDAs will be discussed in more detail below. These five

---

\*formerly U.S. Army Atmospheric Sciences Laboratory



categories encompass approximately one dozen TDAs or utilities. Additional products are anticipated to be added in FY93. As part of the transition process of these TDAs to planned Army fielded systems, the BED is planning to participate and demonstrate the ALBE products during the 1992 REFORGER exercise.

## 2. ALBE TDA CATEGORIES

Terrain and weather affect combat more significantly than any other physical factors. With this in mind, the BED has incorporated into ALBE a number of TDAs to assist the commander in the field with the capability to assess and exploit battlefield environmental effects for tactical advantage. As stated in the ALBE Demonstration and Evaluation Program Draft of 1987, ALBE TDAs "enable the commander to evaluate weapon system effectiveness, determine the advantages of one system over another, and anticipate how operations will be degraded or improved during engagements. TDAs are not intended to make decisions by themselves, but rather to supplement the tactician's knowledge base and help guide him during the decision-making process by providing information useful in the formulation and execution of operations. The TDAs are based on a priori digital terrain data, both feature and elevation data; historical climatological data; and near real-time environmental sensor data. The TDAs enhance the ability to plan operations in a dynamic tactical situation, and let commanders use weather and terrain as force multipliers." (USATEC, 1987)

As previously mentioned, the BED has primary lead for weather-related TDAs. These products currently reside in five categories: meteorological analyses; Army aviation; nuclear, biological, and chemical (NBC); weapon system performance; and weather effects. Each of these five will now be addressed in further detail.

### 2.1 METEOROLOGICAL ANALYSES

This category is better referred to as forecaster decision aids (FDAs) as opposed to TDAs as they will be used primarily by the staff weather officer. This category addresses the management and analysis of meteorological data. It is critical because even the most sophisticated TDA will fail if its input weather data is out of date, incorrect, or not representative of the area where the TDA is being applied. Tools provided in this category include utilities for managing standard weather map displays and the surface and upper air weather data. A weather data ingest program will allow the staff weather officer to ingest the meteorological data necessary to drive the ALBE TDAs requiring this information. Also provided are a number of graphical products that aid the weather analyst in determining current surface and upper air weather conditions. Specific products include:

- manual surface meteorological data ingest
- surface contour plots over a digital map background
- surface wind analysis plots over a digital map background
- sounding analyses of upper air data

- historical climatology displays of a number of climatological variables for a number of worldwide locations. The display can be either alphanumeric or graphic.

## 2.2 ARMY AVIATION

These products provide information on and analyze conditions that affect aircraft performance, routes, and altitudes. The aircraft icing TDA estimates the severity of icing for either rotary-wing or fixed-wing aircraft. The user can specify whether to input cloud data manually or to use RTNEPH data (available only when automated ingest of this data is enabled). A flight path of up to five different locations can then be specified by the user with icing conditions displayed graphically and alphanumerically.

The night vision goggles (NVG) TDA provides the capability for determining the effects of the environment on the performance of the NVGs. This product assists the aviator and interested staff officers in determining optimal times for NVG use. Nocturnal illumination levels are predicted as a function of lunar position and phase as well as cloud type and amount. A number of alphanumeric and graphic products are available for displaying and analyzing this information.

## 2.3 NUCLEAR, BIOLOGICAL, AND CHEMICAL

These TDAs provide information on the location, extent, and persistence of NBC hazards and smoke. The ability to overlay chemical hazard areas on digital terrain map backgrounds is also provided. The mobile smoke TDA provides an automated capability to design a large area smoke screen to obscure radiation in the visible through far-infrared wavelengths using M3A3 and XM55 oil fog-generated smoke to provide concealment and deception and to prevent operational use of various threat electro-optical systems.

The tube-delivered smoke TDA aids in the efficient planning of the 105/155-mm howitzer (both hexachloroethane (HC) and white phosphorous (WP)), M825 155-mm howitzer (WP), 81-mm/4.2-in mortars (WP), and XM819 81-mm mortar red phosphorous (RP)-delivered smoke screens.

The three-dimensional chemical hazard model predicts the time-dependent horizontal as well as vertical dimensions of a chemical hazard. As such, it is of use to the aviation officer in determining the extent and duration of the vertical hazard posed to aviators and low-flying aircraft.

## 2.4 WEAPON SYSTEM PERFORMANCE

This TDA provides information on the effectiveness of electro-optical systems. Environmental effects considered are terrain, weather, and battlefield-induced contaminants such as smoke and fire products. Weapon systems' effective ranges will be provided in tabular form and in graphical displays such as video map overlays. The information is based on environmental data obtained from in situ measurements, forecasts, and terrain data bases. These capabilities will enable the battlefield commander to plan more effective tactical operations and to more effectively utilize his resources.

## 2.5 WEATHER EFFECTS

This product category includes three separate TDAs that allow the staff officers to assess the effects of the weather on equipment, operations, and personnel. A brief description of each is included below.

The weather effects matrix is a briefing tool that graphically depicts how present and forecast weather conditions will affect up to 13 types of battlefield military operations. The matrix is a table of colored blocks representing unfavorable (red), marginal (yellow), favorable (green), or unknown (gray) conditions for the various operations.

Tactical weather effects messages (TWEM) are tools for assessing environmental effects on combat resources. TWEM selects and displays messages that are dependent on critical values of weather parameters and current available weather data. At present there are four data bases--Blue Division/Brigade, Blue Artillery, Blue Armored Cavalry Regiment, and Red Forces. An example of a message would be a warning for Blue Artillery that if winds are greater than 16.0 kn then smoke operations will not be effective.

The consolidated weather effects decision aid is designed to estimate overall weapon system performance for a given environment, operation, and threat. These weapon systems are considered as a collection of subsystems that may be sensitive to the weather, terrain, and battlefield environment. A series of rules is used to determine favorable, marginal, and unfavorable subsystem status. The subsystem performance measures are then combined into an overall weapon system performance measure. Five weapon systems are currently available:

- AH-1F Cobra helicopter
- AH-64 Apache helicopter
- M1 Abrams main battle tank
- M60A3 main battle tank
- M2 and M3 Bradley fighting vehicle

## 3. SUMMARY

When this paper was written, plans were being finalized for demonstrating the ALBE weather-related TDAs to the V Corps and 3rd Infantry Division Staff Weather Officers in Germany as part of REFORGER. BED ALBE personnel supporting this exercise hope to obtain valuable information regarding the evaluation and critique of our software products from the corps and division staff officers using the ALBE programs. This in turn should result in the fine-tuning of our products in terms of inputs, outputs, and alphanumeric and graphic displays. As a result, transition of this software to fielded systems such as the Army Tactical Command and Control System's integrated meteorological system (IMETS) should be more mature and more efficient. Valuable information from previous ALBE demonstrations has been used to refine a number

of TDAs to date. Three of these products (night vision goggles, weather effects matrix, and tactical weather effects messages) are currently being transitioned to block one IMETS.

#### REFERENCE

U.S. Army Engineer Topographic Laboratory, 1987: AirLand Battlefield Environment Demonstration and Evaluation Program Master Plan FY 1987-1991, U.S. Army Engineer Topographic Laboratory, Fort Belvoir, VA 22060-5546.



# **LOCAL SPATIAL INFLUENCES ON TEMPERATURE AND RELATIVE HUMIDITY: PHOENIX, ARIZONA**

Bruce L. Gwilliam  
Department of Geography and Environmental Engineering  
United States Military Academy  
West Point, NY 10996

## **ABSTRACT**

Local spatial conditions affect temperature and relative humidity. Temporal scales were evaluated and daily frequency was selected providing the best agreement between the sites and the region. Spatial scales, using an areal correlation technique, defined distinct pattern for temperature and relative humidity. Remote sensing scales appear to validate the area of influence/agreement. Evaluation of the remote sensing values identified the influence of soil, vegetation, and moisture on the temperature and relative humidity variation observed. Land cover variations affect daily temperature and relative humidity, and provide a means of estimating inter-locational conditions knowing land cover alone.

## **1. INTRODUCTION**

Temperature and relative humidity can, and do vary spatially across large areas. These variations are the result of locational, semi-permanent attributes, and transient atmospheric conditions. Identification of these influences can improve our understanding and provide temporal and spatial definition. Prediction of inter-station atmospheric conditions, for military and civilian application, requires an identification of the cause and extent of their influence. The focus of this research is to determine the local spatial influences on temperature and relative humidity at three meteorological substations situated within the Phoenix metropolitan area.

## **2. BACKGROUND**

Review of the literature identifies several areas of concern for this study area and the temperature and relative humidity variables. Recent studies of the urban heat island effect [Kirby and Sellers 1987; and Balling and Lolk 1991] and for Phoenix in specific [Cayan and Douglas 1984; Hsu 1984; Balling and Brazel 1986; Brazel and Balling 1987] have defined the spatial variation and associated the cause with changes in land use. Studies of the spatial variation of temperature and relative humidity [Brazel and Johnson 1980; Pease, Lewis, and Outcalt 1976; Outcalt 1972] along with the influence of local land use [Balling and Lolk 1991; Balling and Brazel 1989; Cayan and Douglas 1984], elevation, and valley structure [Balling and Brazel 1989; Kirby and Sellers 1987] all provide insight into cause and variation. Direct causal attribution through spatial aggregation techniques and aerial instrumentation [Stoll 1990] and satellite imagery [Balling and Brazel 1988, 1989; Matson, McClain, McGinnis, and Pritchard 1978] provide for scalar measure of local conditions on temperature and relative humidity.

The three study sites define a cross section of the Salt River Valley from east to west. All sites are instrumented with temperature and relative humidity instruments and collect data at five minute intervals which are averaged daily. Alameda, the central station, is adjacent to a road intersection, surrounded by a large church parking lot, and within a large residential area. Alameda is an urban station selected to represent the city influences. Superstition, the desert station, is primarily open desert with limited vegetation and a low residential influence. Collier lies adjacent to a major highway which crosses the valley's irrigated, agricultural zone. These three sites readily represent the area and uses of the land within Phoenix, Arizona.

### 3. TEMPORAL VARIATION

An average of these three sites' temperatures and relative humidity provide an excellent thermal and moisture record of the valley as a whole. The variation between the instrument sites, as a function of local spatial conditions, first requires determination of the best time period for comparison. To accomplish this, simple correlation between each sites' temperature and relative humidity were made with the regional mean. Using moving averages the time periods were expanded over the 300 day period of record. Twelve concurrent months for all three sites were not available for this study.

For both temperature and relative humidity the form of the correlation equation between agreement -  $r^2$ , the coefficient of determination - and number of days was a power function.

$$\begin{array}{llll} \text{Tr}^2 = 0.995 - 1.092e-07 [\#days \wedge 2.137] & r^2 = 0.561 & F = 10 & [1] \\ \text{RHr}^2 = 1.132 - 0.115 [\#days \wedge 0.170] & r^2 = 0.170 & F = 1 & [2] \end{array}$$

Both equations show a rapid decrease with number of days. As an example temperature agreement between Superstition and the regional average decreases from over 0.99 at one day period down to a low of 0.91 at the 240 day moving average. Relative humidity shows even greater variability. Collier drops from 0.95 at one day averages down to 0.30 at the 240 day average. From review of the monthly temperature and relative humidity tables a transitional period, during March, occurs when the region warms and the westerlies move north. Regardless, the best time period for measuring agreement is daily.

### 4. SPATIAL VARIATION

This agreement between the sites and the regional mean, as shown by a simple linear equation, should also define the fixed differences between each site. The following tables show this agreement.

TABLE 1. TEMPERATURE AND SPATIAL AGREEMENT

Site	Temp. °F	a	b	$r^2$	F
Alameda	95.26	-14.39	1.167	0.969	8821
Collier	91.03	6.75	0.897	0.959	6514
Superstition	95.41	7.668	0.943	0.934	4193
PHOENIX	93.90				

Superstition, the desert site, is only slightly warmer than Alameda with its' urban locale. Collier with its' irrigation is several degrees cooler due to latent evaporation.

TABLE 2. RELATIVE HUMIDITY AND SPATIAL AGREEMENT

Site	RH %	a	b	r <sup>2</sup>	F
Alameda	22.61	-7.71	1.215	0.916	3028
Collier	31.63	3.563	1.144	0.807	1151
Superstition	19.30	3.614	0.639	0.829	1336
PHOENIX	24.51				

Collier shows the expected higher relative humidity. Alameda and Superstition show lower relative humidities as also expected for asphalt and desert surfaces. How well each stations' observations represents the local area is unknown.

To determine the spatial area of representation temperature and relative humidity observations were collected at .1, .3, and .5 mile intervals, on north-south and east west axes. Data were collected during three periods beginning at early evening through early morning to early afternoon successively at each of the sites. Daily averages for each distance group were compared with the average central site observation.

$$T_{\text{mean}} = 13.427 + 0.841 T_{\text{dispersed}} \quad r^2 = 0.928 \quad F = 1384 \quad [3]$$

$$RH_{\text{mean}} = 0.378 + 0.007 RH_{\text{dispersed}} \quad r^2 = 0.833 \quad F = 531 \quad [4]$$

The temperature measurements collected in the radial pattern, out to a half mile, show strong agreement. Relative humidity measurements show a lesser degree of agreement. Both temperature and relative humidity however do show decreased agreement from the center.

$$Tr^2 = 0.931 - 42.422 [\text{dist}^{12.953}] \quad r^2 = 0.743 \quad F = 1 \quad [5]$$

$$RHR^2 = 0.847 - 0.041 [\text{dist}^{0.746}] \quad r^2 = 1.000 \quad F = \text{Infinite} \quad [6]$$

In both cases the spatial correlation decreased following a power function. Temperature decreases from the central agreement of 0.928 down to an estimated zero at eight tenths of a mile. Relative humidity decreases slowly from 0.833 at the center. From these equations temperature follows the temperature variations of the immediate area. Relative humidity responds to point variations but also follows local variations out to a greater distance. Temperature and relative humidity appear to respond to variations within the immediate and local area respectively.

## 5. IMAGERY VARIATION

Sample inventories of each location are prohibitive. However, within the study period, a LANDSAT Thematic Mapper Image was taken of this area. Each of the study sites were identified on the image and pixel values for bands 1, 2, and 4 were recorded. Accepting that each pixel represents 30m<sup>2</sup>, grid squares of increasing size were selected and the average value for each band recorded. These values provide a means to measure spatial agreement and determine cause[s] of the variation.



TABLE 3. PIXEL VARIATION

<u>Band</u>	<u>Grid</u>	<u>Area</u>	<u>Alameda</u>	<u>Collier</u>	<u>Superstition</u>
1	1	30m2	65	80	73
1	3	90m2	68.2	74.7	73.3
1	5	150m2	69.9	73.6	74
1	7	210m2	71.9	71.8	74.9
2	1	30m2	30	37	36
2	3	90m2	31.6	35.4	35.6
2	5	150m2	32.4	35.6	35.8
2	7	210m2	33.3	34.6	36.6
4	1	30m2	57	42	51
4	3	90m2	52.1	45.1	49.7
4	5	150m2	52.8	51.9	49.5
4	7	210m2	50.6	54.9	50.6

The image was taken on 28 October 1992, the day after a one inch rainfall. Assuming that the temperature and relative humidity variation is relatively constant throughout the record the mean site observations were compared with the pixel variations. All pixel groups per band [B] were compared.

$$\begin{array}{llll} \text{Tsite} = 145.911 - 0.999 \text{ B47} & r^2 = 0.998 & F = 1124 & [7] \\ \text{RHsite} = 1.4603 + 0.965 \text{ B47} & r^2 = 0.999 & F = 15728 & [8] \end{array}$$

Both temperature and relative humidity show the greatest agreement with band 4 using the largest areal measure, 210m2. Band 4, reflected infrared, measures surface water and biomass. The 210m2 are is less then the predicted area of agreement. Further study is needed to determine the true limit of pixel agreement. The agreement is larger then predicted from the above spatial model also indicating a need to make closer and more frequent observations of temperature and relative humidity. Study of the individual sites' mean observations and the intercept and slope coefficients also vary.

$$\begin{array}{llll} \text{aTsite} = -189 + 0.999 \text{ B23} & r^2 = 0.999 & F = 15728 & [9] \\ \text{bTsite} = 2.329 - 0.999 \text{ B25} & r^2 = 0.999 & F = 22915 & [10] \end{array}$$

The mean site temperature intercept varies with band 2 within the 90m2 area. Band 2, representing plant vigor, appears to link vegetation extent with temperature. Alameda with the adjacent parking lot does have the least vegetation. Superstition, with it's xerophytic vegetation, responds rapidly to moisture would have the most vigorous vegetation within the 90m2 area. Slope coefficients for temperature also vary with band 2 out to 150 meters away from the instrument platform. The same pattern holds. Vegetation and its' health, immediately adjacent to the instruments, define the variation observed in mean site temperatures

$aRH_{site} = -94.25 + 0.999 B23$	$r^2 = 0.996$	$F = 616$	[11]
$bRH_{site} = 13.85 - 0.999 B17$	$r^2 = 0.960$	$F = 49$	[12]

The mean site relative humidity intercept follows the same pattern as for temperature with a slightly lesser measure of agreement. The slope, however, varies with band 1 which compares soil and vegetation within the 210m<sup>2</sup> area. Collier has the lowest reflective value indicating a greater extent of vegetation. Superstition with its' exposed reflective soil has the highest values. Interesting to note that the original spatial patterns of temperature having higher initial correlation and rapid decrease, and relative humidity having a rapid initial decrease and relatively constant agreement, is again evident in the pixel pattern.

## 6. CONCLUSIONS

The focus of this research is to determine the local spatial influences on temperature and relative humidity at three meteorological substations situated within the Phoenix metropolitan area. Study of the relationship between the regional average and the three sites showed the best temporal scale of comparison was on a daily basis. Longer studies out to a year and shorter studies of hourly variations should also be completed.

Spatial correlation between the station and the surrounding area indicates a high initial correlation for temperature followed by a predicted rapid decrease ending at approximately eight tenths of a mile. Relative humidity shows a spatial correlation pattern which has a large immediate decrease followed by a relatively constant correlation out beyond a mile. Further studies sampling temperature and relative humidity must be conducted on a grid pattern extending outward from immediate proximity to several miles.

Remote sensing provided the greatest insight into the local surface covering. Biomass and surface water variations, within the adjacent 210 meters of the sites, explain the temperature and relative humidity variations observed throughout the year. Plant vigor, within 150 meters of the platforms, provided further insight into the temperature variation. Near local conditions dominate. Relative humidity was described using plant cover, plant vigor, and soil exposure within 210 meters of the instruments. Further research relating other days of observation and comparison of greater pixel grids is necessary.

Local spatial conditions do affect temperature and relative humidity. Variations in soil, vegetation, and surface water, within the immediate area of the instruments, do affect the daily temperature and relative humidity observations. This linkage of land cover with temperature and relative humidity indicates the ability to predict inter-station conditions by associating temperature variations with land cover.

## REFERENCES

- Balling, R.C., and S.W. Brazel, 1987: Time and space characteristics of the Phoenix urban heat island. Journal of the Arizona-Nevada Academy of Science, 21: 75-81.
- Balling, R.C., and S.W. Brazel, 1989: High-Resolution nighttime temperature patterns in Phoenix. Journal of the Arizona-Nevada Academy of Science, 23: 49-53.
- Balling, R.C., and N.K. Lolk, 1991: A developing cool island in the Desert? the case of Palm Springs, California. Journal of the Arizona-Nevada Academy of Science, 23[2]: 93-96.
- Brazel, A.J., and D.M. Johnson, 1980: Land use effects on temperature and humidity in the Salt River Valley, Arizona. Journal of the Arizona-Nevada Academy of Science, 15: 54-61.
- Brazel, A.J., and R.C. Balling, 1986: Temporal analysis of long-term atmospheric moisture levels in Phoenix, Arizona. Journal of Climate and Applied Meteorology 25: 112-117.
- Cayan, D.R., and A.V. Douglas, 1984: Urban influences on surface temperatures in the southwestern United States during recent decades. Journal of Climate and Applied Meteorology 23: 112-117.
- Hsu, S.I., 1984: Variation of an urban heat island in Phoenix. Professional Geographer 36: 196-200.
- Kirby, S.F., and W.D. Sellers, 1987: Cold air drainage and urban heating in Tucson, Arizona. Journal of the Arizona-Nevada Academy of Science, 22[2]: 123-128.
- Matson, M., E.P. McClain, D.F. McGinnis, and J.A. Pritchard, 1978: Satellite detection of urban heat island. Monthly Weather Review 106: 1725-1734.
- Morgan, D., L. Mydrup, D. Rogers, and R. Baskett, 1977: Microclimates within an urban area. Annals of the Association of American Geographers 67: 55-65.
- Outcalt, S.I., 1972: A reconnaissance experiment in mapping and modeling the effect of land use on urban thermal regimes. Journal of Applied Meteorology 11: 1369-1373.
- Pease, R.W., J.E. Lewis, and S.I. Outcalt, 1976: Urban terrain climatology and remote sensing. Annals of the Association of American Geographers 66: 557-569.
- Stoll, M.J., 1990: Analysis of land use effects on surface to air temperature relationships in an urban environment. Masters Thesis, Arizona State University.

# **APPENDIXES**

**APPENDIX A: AGENDA**

**APPENDIX B: LIST OF ATTENDEES**

# **AUTHOR INDEX**

## APPENDIX A

### AGENDA

#### Tuesday, 1 December 1992

0730 **REGISTRATION**  
(Coffee and Donuts)

0830 Welcome  
Administrative Announcements  
Introduction of Keynote Speaker

0900 Keynote Address

1000 **BREAK**

<b>SESSION I: Atmospheric Modeling</b>
--

**Session Chair:** *Colonel Grant Aufderhaar, OUSD(A)ODDDR&E(R&AT)E&LS*

1030 Introduction

1040 A Multistream Radiative Transfer Model for Inhomogenous, Three-Dimensional Aerosol Clouds  
*Donald W. Hoock*, U.S. Army Research Laboratory; *Edward J. Burlbaw* and *John C. Giever*,  
New Mexico State University

1100 Visualization of Multiple Battlefield Obscurants  
*Geoffrey Y. Gardner*, Grumman Data Systems; *Michael Hardaway*, U.S. Army Topographic  
Engineering Center

1120 Modeling Chemical and Biological Agents and Chaff Transport and Diffusion Over Complex  
Structures  
*Ronald E. Meyers*, *Keith Deacon* and *Donald Durack*, U.S. Army Research Laboratory

1140 Meso-Scale Data Analysis Using a Meso-Scale Model  
*Kenneth E. Eis* and *Jan L. Behunek*, METSAT, Inc.; *Donald L. Reinke* and *Thomas H. Vonder  
Haar*, Colorado State University; *Craig J. Tremback*, ASTeR Inc.

1200 **LUNCH**

1340 An Optical Profile Function for Modeling Extinction and Backscatter Coefficients in Very Low  
Stratus Clouds and Subcloud Regions  
*Neal H. Kilmer*, New Mexico State University; *Henry Rachele*, U.S. Army Research Laboratory

1400 Acoustical Scattering From Atmospheric Turbulence  
*Harry J. Auvermann*, U.S. Army Research Laboratory; *George H. Goedecke*, New Mexico State  
University

**Tuesday, 1 December 1992**

- 1420 Modification of Atmospheric Aerosol  
*Austin W. Hogan*, USA CRREL RC
- 1440 Intermittency, Events, and Coherent Atmospheric Structure in Vegetative Canopies  
*Ronald M. Cionco*, U.S. Army Research Laboratory; *William D. Ohmstede*, WM Ohmstede, CCM
- 1500 The Zephyrus, Vaporus, Thermotics Connection  
*H. Rachele*, *A. Tunick*, and *F. Hansen*, U.S. Army Research Laboratory
- 1520 Poster Introductions
- 1545 **BREAK** (Refreshments)
- 1600 **POSTER SESSION**
- 1730 **ADJOURNMENT**

**Wednesday, 2 December 1992**

<b>SESSION II: Sensors and Systems</b>
--

**Session Chair:** *Mr. Chad George*, AMC Smart Weapons Management Office, Redstone Arsenal

- 0800 Introduction
- 0810 The MET Improvement Program: Key to Unlocking Target Area Meteorology  
*Mary Ann Seagraves* and *Robert E. McPeck*, U.S. Army Research Laboratory
- 0830 Mobile Profiler System (MPS): The Army's Future Target Area Meteorology Data Collection System  
*Robert E. McPeck* and *Mary Ann Seagraves*, U.S. Army Research Laboratory
- 0850 The Double Beam Interferometer Sounder (DBIS): A Device for the Passive Remote Sensing of Atmospheric Profiles  
*Jean-Marc Thériault*, DREV-Defence Research Establishment Valcartier, Canada; *Jean Giroux*, *Jacques Côté* and *Marc Fournier*, BOMEM Inc., Canada
- 0910 Battlefield Atmospheric Soundings in Near-Realtime Using Satellite and Ground-Based Remotely Sensed Data  
*James Cogan*, U.S. Army Research Laboratory
- 0930 **BREAK** (Refreshments)
- 1000 Use of SSM/I Data During Operation Desert Storm  
*Charles R. Holliday* and *Kenneth A. Nash*, Air Force Global Weather Central, Offutt Air Force Base

**Wednesday, 2 December 1992**

- 1020 A Comparison of Defense Meteorological Satellite Program Capabilities and U.S. Army Tactical Weather and Environmental Data Requirements  
*Richard J. Szymer* and *James Cogan*, U.S. Army Research Laboratory
- 1040 Radio Noise Effects on a Microwave Radiometer  
*T. L. Barber* and *E. M. Measure*, U.S. Army Research Laboratory; *R. J. Hulsey*, New Mexico State University
- 1100 Remote Sensors Comparison Analysis  
*Richard J. Okrasinski*, New Mexico State University; *Robert O. Olsen* and *Ted Barber*, U.S. Army Research Laboratory
- 1120 Characterization of Imager Spectral Response for Optimized Atmospheric Propagation  
*D. R. Billingsley*, *F. R. Palacios* and *W. R. Watkins*, U.S. Army Research Laboratory
- 1140 LUNCH

**SESSION III: Data Bases and Analyses**

**Session Chair:** *Mr. Anthony Van de Wal*, U.S. Army Research Laboratory

- 1300 Introduction
- 1310 Climatology of Cloud Statistics (C\_Cloud\_S)  
*Albert R. Boehm*, Hughes STX Corporation; *CPT Richard W. Hartman*, USAF Environmental Technical Applications Center
- 1330 High-Resolution Cloud Climatologies  
*Kenneth E. Eis*, METSAT, Inc.
- 1350 Cloud Information Reference Library and Archive  
*Ronald J. Nelson*, Science and Technology Corporation
- 1410 Rebal '92 - A Cooperative Radiation and Energy Balance Field Study for Imagery and E.M. Propagation  
*Arnold Tunick*, U.S. Army Research Laboratory; *Terry A. Howell* and *Jean L. Steiner*, U.S.D.A. - Agricultural Research Service Conservation and Production Research Laboratory
- 1430 VORTEX: A New Tool for Observing Vertical Structure of Smoke/Obscurant Clouds  
*Max P. Bleiweiss*, U.S. Army Research Laboratory; *Roger E. Davis*, Science and Technology Corporation; *Thomas A. King* and *Kenneth C. Payne*, New Mexico State University
- 1450 BREAK (Refreshments)
- 1500 POSTER SESSION
- 1700 ADJOURNMENT
- 1800 BANQUET - *Fort Bliss Officers' Club*  
*Mr. Sam Hoyle*, Curator, Fort Bliss Museum

Thursday, 3 December 1992

**SESSION IV: Atmospheric Effects**

**Session Chair: Mr. Don Grantham, Air Force Geophysics Laboratory**

- 0800 Introduction
- 0810 The Use of Analytic Approximation for Providing MET Guidance for Artillery  
*Fernando Caracena*, NOAA - Severe Storms Laboratory
- Impact of Atmospheric Sciences Laboratory (ASL) Recommended Changes to the Low-Energy Laser Weapon Simulation (LELAWS) - **PAPER WITHDRAWN**  
*John G. Thomas, Jr.*, U.S. Army Materiel Systems Analysis Activity
- 0830 Analysis of Simultaneous Scintillometer Measurements Over Four Unique Desert Terrain Paths  
*Gail Tirrel-Vaucher*, Science and Technology Corporation; *Robert W. Endlich* and *John W. Raby*, U.S. Army Research Laboratory
- 0850 The Three Faces of Clutter  
*Patti S. Gillespie*, U.S. Army Research Laboratory
- 0910 Mark III Electro-Optical Tactical Decision Aid Sensor Performance Model Evaluation  
*Kimberley Scasny* and *J. Michael Sierchio*, Naval Research Laboratory Monterey
- 0930 **BREAK** (Refreshments)
- 1000 The Green's-Function Parabolic Equation for Acoustic Propagation in the Atmosphere  
*David H. Marlin*, U.S. Army Research Laboratory
- 1020 Modeling the Optical and Mechanical Properties of Exotic Battlefield Obscurants  
*Robert A. Sutherland*, U.S. Army Research Laboratory; *James D. Klett*, PAR Associates
- 1040 Progress in Atmospheric Propagation Modeling at Frequencies up to 1000 GHz  
*Hans J. Liebe*, *George A. Hufford* and *Michael G. Cotton*, Institute for Telecommunication Sciences
- 1100 Radar Backscatter from Snow Surface (Verification of Model and Prediction)  
*Oskar Essenwanger*, University of Alabama in Huntsville
- 1120 The Importance of Ducting in Atmospheric Acoustics  
*John M. Noble*, U.S. Army Research Laboratory
- 1140 **LUNCH**



Thursday, 3 December 1992

**SESSION V: Weather Decision Aids**

Session Chair: *Mr. Gary Clayton*, U.S. Army Missile Command

1300 Introduction

1310 IR Visibility

*C. N. Touart*, Hughes STX Corporation

LASERX Modeling to Predict the Effects of Target Acquisition - **PAPER WITHDRAWN**  
*Alexander Akerman, III*, I-MATH Associates, Inc.; *Patti S. Gillispie*, U.S. Army Research Laboratory

1330 Comparison of Optical Turbulence Models for Forecast Applications

*Kenneth P. Freeman*, *Montie M. Orgill* and *Roger E. Davis*, Science and Technology Corporation; *Robert W. Endlich*, U.S. Army Research Laboratory

1350 The Next Generation of Forecaster Decision Aids

*Jeffery E. Passner*, U.S. Army Research Laboratory

1410 Forecasting Using a Hybrid Statistical-Neural Net Method

*Jerrold S. Foster*, Command Control, Inc.; *Dr. Kenneth C. Young*, University of Arizona

1430 Closing Remarks

Presentation of Awards

Photographs

1450 **ADJOURNMENT**

**SESSION I POSTERS:  
Atmospheric Modeling**

Operational Mesoscale Forecasting System: Preliminary Report

*Teizi Henmi*, U.S. Army Research Laboratory - **POSTER WITHDRAWN**

SOUP-A Battlefield Atmosphere

*Robert E. De Kinder, Jr.*, U.S. Army Research Laboratory

Some Flow Characteristics of Surface Layer Micrometeorology Over Complex Terrain Using Field Measurements

*Brian L. Orndorff*, U.S. Army Research Laboratory

Model of Atmospheric Chemical Hazards: MACH/MACH LT

*Ronald E. Meyers* and *Keith S. Deacon*, U.S. Army Research Laboratory

A Mesoscale Numerical Simulation of the Persian Gulf Wind Fields: Case Study of 28-29 March 1991  
**Robert E. Dumais, Jr.**, and **Teizi Henmi**, U.S. Army Research Laboratory; **John Barnes**, Computer Sciences Corporation

Surface Windspeed Distributions

**Elton P. Avara** and **Bruce T. Miers**, U.S. Army Research Laboratory

An Examination of the Five Stages of Radiation Fog Evolution

**Montie M. Orgill**, Science and Technology Corporation; **Robert A. Sutherland**, U.S. Army Research Laboratory

<b>SESSION II POSTERS: Sensors and Systems</b>
--

The U.S. Army Atmospheric Profiler Research Facility: Overview and Preliminary Intercomparison

**John R. Hines**, **Frank D. Eaton**, **Scott McLaughlin** and **William Hatch**, U.S. Army Research Laboratory

An Acoustic Meteorological Test Bed: Uses and Applications

**John Fox** and **Robert Olsen**, U.S. Army Research Laboratory

Tactical Weather Data Acquisition and Distribution Mechanisms Demonstrated During Fiscal 1992 on the ARL Technology Exploitation Weather Testbed

**Robert Dickenshied**, **Pat Laybe**, **Doug Shoop** and **Steve Huntwork**, U.S. Army Research Laboratory

A Review of Selected Remote Sensor Measurements of Wind, Moisture, and Temperature with Comparisons to Rawinsondes

**Bruce T. Miers**, **James L. Cogan** and **Richard J. Szymer**, U.S. Army Research Laboratory

A Fresh Look at the Planetary Boundary Layer: High Resolution Profiling with an FM-CW Radar

**Scott A. McLaughlin**, U.S. Army Research Laboratory

Tactical Weather Support Concept for Austere Field Operations

**John R. Elrick**, U.S. Army Research Laboratory; **Phillip R. Raihl**, New Mexico State University; **MSgt Timothy J. Smith**, Headquarters Air Weather Service, White Sands Missile Range

Automation of the Tactical Meteorological Observing Set

**Edward Vidal, Jr.**, and **Richard Wade**, U.S. Army Research Laboratory

Acoustic Source Generation System

**Jeffrey Balding** and **John M. Noble**, U.S. Army Research Laboratory

Capability for Calibration and Validation of Space and Ground Based Remote Sensors at White Sands Missile Range

**Richard J. Szymer** and **Robert E. McPeck**, U.S. Army Research Laboratory

The Mobile Atmospheric Spectrometer: Enhancements in Data Acquisition and Analysis at Smoke Week XIV

**Frank T. Kantrowitz**, U.S. Army Research Laboratory; **William M. Gutman** and **Troy D. Gummell**, New Mexico State University; **Jerry V. B. Rice**, Science and Technology Corporation

Own the Weather: A Vision for Army Meteorology

*James Cogan, Richard Szymber and Robert McPeck, White Sands Missile Range*

<b>SESSION III POSTERS:</b> <b>Data Bases and Analyses</b>
---

Digital Signal Processing Techniques Used to Reduce Acoustics Data from the JAPE Test

*Thelma Chenault, René Klein and Ascencion Acosta, U.S. Army Research Laboratory*

Pyrolysis-Mass Spectra of Biological Aerosols Interpreted by Factor Analysis-Rank Annihilation

*David Rosen, U.S. Army Research Laboratory; Alice Harper, U.S. Army Chemical Research and Development Laboratory*

A Comparison of Low Level Wind and Temperature Profiles from a Radiosonde, Sodar and Mesoscale Model

*Ian D. Todd and Jonathan D. Turton, Meteorological Office, U.K.*

Errors in Sky-Cover Observation by Ground-Based Observers

*Dr. Thomas H. Vonder Haar, Neil Allen and Donald L. Reinke, Colorado State University Foothills Campus, and METSAT Inc.*

Demonstration of Weather Data Dissemination by Using a Very Small Aperture Terminal Satellite Network

*Douglas Shoop, Patrick Laybe and Robert Dickenshied, U.S. Army Research Laboratory*

The MIDAS/ATLAS Video Imagery Database: An Advanced System for Storing and Accessing Digitally Compressed Video Imagery

*Michael Rollins, Science and Technology Corporation; Max P. Bleiweiss and Rebecca Tipton, U.S. Army Research Laboratory*

Remote Dial-In Access of the Atmospheric Aerosols and Optics Data Library (AAODL)

*John N. Crain, Science and Technology Corporation; Fidel Tibuni, U.S. Army Atmospheric Sciences Laboratory*

Modernized Graphics Codes for Use with Project Wind Data

*John D. Kincheloe, New Mexico State University*

The CASTFOREM Graphics Postprocessor's Smoke Display

*Robert E. De Kinder, Jr., U.S. Army Research Laboratory; Steven J. LaMotte, New Mexico State University; Thomas C. Loncarich and Joseph F. Babbs, Jr., U.S. Army TRADOC Analysis Command*

The FAUST Atmospheric Database

*Frank O. Clark, Phillips Laboratory*

**SESSION IV POSTERS:  
Atmospheric Effects**

An Interactive Model for Evaluating Color Contrast Propagation Through Haze Aerosols  
*David H. Tofsted*, U.S. Army Research Laboratory

The Effect of Relative Humidity, Wind, and Atmospheric Stability on Smoke Munitions  
*Edward D. Creegan*, U.S. Army Research Laboratory – **POSTER WITHDRAWN**

Infrared Transmission and Path Radiance Through a Heavy Dust Cloud  
*James Williams*, U.S. Army Research Laboratory – **POSTER WITHDRAWN**

Simulating Atmospheric Effects of Images Used at the Center for Night Vision and Electro-Optics  
*James Williams, Alan Wetmore, David Tofsted and Richard Dutro*, U.S. Army Research Laboratory

Correlation of  $C_n^2$  with Image Distortion at the Rebal Test  
*F. R. Palacios, W. R. Watkins, S. B. Crow and D. R. Billingsley*, U.S. Army Research Laboratory

**SESSION V POSTERS:  
Weather Decision Aids**

The Integrated Weather Effect Decision Aid (IWEDA): A New Planning Tool  
*Robert R. Lee and Sue E. Bussells*, U.S. Army Research Laboratory

Weather and Terrain Analysis for Aerial Intelligence Preparation of the Battlefield  
*Gary McWilliams and Steve Kirby*, U.S. Army Research Laboratory

A Demonstration of the Updated Airland Battlefield Environment Software  
*David Sauter*, U.S. Army Research Laboratory; *John B. Spalding and Danforth C. Weems*, New Mexico State University

Local Spatial Influences on Temperature and Humidity  
*CPT Bruce L. Gwilliam*, United States Military Academy

## APPENDIX B

### LIST OF ATTENDEES

#### A

Mr. Jerry E. Albrecht  
Dynamics Research Corp  
P.O. Box 25349  
Scott AFB, IL 62225-0349  
Telephone: 618/256-6662  
Telefax: 618/256-2996

Mr. Neil Allen  
METSAT, Inc  
515 South Howes  
Ft Collins, CO 80521  
Telephone: 303/221-5420  
Telefax: 303/493-3410

LTC Lloyd L. Anderson, Jr.  
Detachment 14, 1st Weather Group  
Fort Hood, TX 76544-5076  
Telephone: 817/288-9819  
Telefax: 817/288-1930

Ms. Eleanor M. Arguello  
Physical Science Laboratory  
New Mexico State University  
P.O. Box 30002  
Las Cruces, NM 88003  
Telephone: 505/522-9120

Dr. Michael D. Arthur  
NSWC-DD  
Code J41  
Dahlgren, VA 22448  
Telephone: 703/663-4781

COL Grant Aufderhaar  
Office of Under Secretary of Defense  
Mil Asst for Env Science  
(R&AT) ELS, Room 3D129  
The Pentagon  
Washington, DC 20301-3080  
Telephone: 703/695-9604  
Telefax: 703/693-7042

Dr. Harry J. Auvermann  
ARL/BED  
ATTN: AMSRL-BE-M  
WSMR, NM 88002  
Telephone: 505/678-4224

Mr. Elton P. Avara  
ARL/BED  
ATTN: AMSRL-BE-M  
WSMR, NM 88002-5501  
Telephone: 505/678-1570  
Telefax: 505/678-8366

Ms. Scarlet Ayres  
ARL/BED  
ATTN: AMSRL-BE-S  
WSMR, NM 88002-5501

#### B

Dr. Walter D. Bach, Jr.  
Army Research Office  
P.O. Box 12211  
Research Triangle Park, NC 27709-2211  
Telephone: 919/549-4247  
Telefax: 919/549-4310

Dr. David P. Bacon  
Science Applications Int'l Corporation  
MS 2-3-1  
1710 Goodridge Drive  
McLean, VA 22102  
Telephone: 703/821-4594

Dr. Lee K. Balick  
EG&G Energy Measurements  
Mail Stop RSL-19  
P.O. Box 1912  
Las Vegas, NV 89125  
Telephone: 702/295-8603  
Telefax: 702/295-8040

Mr. T. L. Barber  
ARL/BED  
ATTN: AMSRL-BE-W  
WSMR, NM 88002-5501

Mr. Terry S. Barker  
Lockheed Austin Division  
Org. T2-30  
Environmental Systems, Bldg 320  
6800 Burleson Road  
Austin, TX 78744-1016  
Telephone: 512/386-1190

Mr. Roy E. Bates  
US Army CRREL  
CRL-RG  
72 Lyme Road  
Hanover, NH 03755  
Telephone: 603/646-4262  
Telefax: 603/646-4644

Mr. Jan Behunek  
METSAT, Inc.  
515 South Howes  
Ft. Collins, CO 80521  
Telephone: 303/221-5420  
Telefax: 303/493-3410

Dr. Ami Ben-Shalom  
EORD/Technion  
Haifa, 32000  
ISRAEL  
Telephone: 9724321058  
Telefax: 9724326678

Mr. Daniel R. Billingsley  
ARL/BED  
ATTN: MSRL-BE-M  
White Sands Missile Range, NM 88002-5501  
Telephone: 505/678-4313  
Telefax: 505/678-2432

Mr. Abel J. Blanco  
ARL/BED  
ATTN: AMSRL-BE-W  
WSMR, NM 88002-5501  
Telephone: 505/678-3924  
Telefax: 505/678-8366

Mr. Max P. Bleiweiss  
ARL/BED  
ATTN: AMSRL-BE-A  
WSMR, NM 88002-5501

Ms. Brenda Brathwaite  
ASTRO  
5321 Riggs Road  
Gaithersburg, MD 20783  
Telephone: 301/926-5327  
Telefax: 301/926-5506

Ms. Jan Breeden  
USA FSTC  
220 7th Street NE  
Charlottesville, VA 22901  
Telephone: 804/980-7870

Dr. Ralph J. Brewer  
OptiMetrics, Inc  
106 E. Idaho  
Suite C  
Las Cruces, NM 88005  
Telephone: 505/523-4986

Dr. Douglas R. Brown  
ARL/BED  
ATTN: AMSRL-BE-S  
WSMR, NM 88002  
Telephone: 505/678-2412  
Telefax: 505/678-2053

Mr. Brian R. Bullard  
Science and Technology Corporation  
555 Telshor Boulevard  
Suite 200  
Las Cruces, NM 88001  
Telephone: 505/525-2658

Mr. John F. Busic  
Naval Surface Warfare Center  
Dept J41  
Dahlgren, VA 22448-5000  
Telephone: 703/663-4837  
Telefax: 703/663-1693

Ms. Sue Bussells  
ARL/BED  
ATTN: AMSRL-BE-M  
WSMR, NM 88002  
Telephone: 505/678-2461  
Telefax: 505/678-8366

C

Ms. Anna Camenisch  
Physical Science Lab  
P.O. Box 30002  
Las Cruces, NM 88003-0002  
Telephone: 505/522-9322

Dr. Fernando Caracena  
NOAA-Environmental Research Labs-NSSL  
325 Broadway  
Boulder, CO 80303  
Telephone: 303/497-6269

Mrs. Thelma A. Chenault  
ARL/BED  
ATTN: SLCAS-BE-A  
WSMR, NM 88002  
Telephone: 505/678-6579  
Telefax: 505/678-2432

Mr. Hugh W. Church  
Sandia National Laboratories  
Organization 6612  
Albuquerque, NM 87185-5800  
Telephone: 505/845-8705  
Telefax: 505/844-0244

Mr. Ronald M. Cionco  
ARL/BED  
ATTN: AMSRL-BE-S  
WSMR, NM 88002-5501

Mr. Gary L. Clayton  
US Army Missile Command  
AMSMI-RD-BA  
Software Engineering Directorate  
Redstone Arsenal, AL 35898  
Telephone: 205/876-0755  
Telefax: 205/842-9210

Dr. James Cogan  
ARL/BED  
ATTN: AMSRL-BE-W  
WSMR, NM 88002-5501

Mr. Thomas D. Corey  
Air Force Tech Applications Center  
Molecular Science Division  
1030 S. Highway A1A  
Patrick AFB, FL 32925-3002  
Telephone: 407/494-4531  
Telefax: 407/494-5488

Mr. Michael G. Cotton  
U.S. Dept of Commerce  
National Telecommunications & Info Adm  
Institute for Telecomm Sciences  
325 Broadway  
Boulder, CO 80303-3328  
Telephone: 303/497-7346

Mr. James H. Cragin  
USA CRREL  
72 Lyme Road  
Hanover, NH 03755-1290  
Telephone: 603/646-4395  
Telefax: 603/646-4644

Mr. John Crain  
Science and Technology Corporation  
555 Telshor Blvd.  
Suite 200  
Las Cruces, NM 88001  
Telephone: 505/521-4353  
Telefax: 505/522-9062

Mr. Edward Creegan  
ARL/BED  
ATTN: AMSRL-BE-M  
WSMR, NM 88002-5501

Mr. Thomas A. Curran  
VIZ Manufacturing Company  
335 East Price Street  
Philadelphia, PA 19144-5782  
Telephone: 215/844-2626  
Telefax: 215/844-4410

## D

Dr. Roger E. Davis  
Science and Technology Corporation  
555 Telshor Blvd  
Suite 200  
Las Cruces, NM 88001  
Telephone: 505/521-4353  
Telefax: 505/522-9062

Mr. James A. Dawson  
Dynetics, Inc  
Drawer B  
Huntsville, AL 35814-5050  
Telephone: 205/922-9230  
Telefax: 205/922-9255

Mr. Robert E. De Kinder  
ARL/BED  
ATTN: AMSRL-BE-S  
WSMR, NM 88002-5501

Mr. Keith Deacon  
ARL/BED  
ATTN: AMSRL-BE-S  
WSMR, NM 88002-5501

Dr. Adarsh Deepak  
Science and Technology Corporation  
101 Research Drive  
Hampton, VA 23666  
Telephone: 804/865-1894  
Telefax: 804/865-1294

Mr. Robert Dickenshied  
ARL/BED  
ATTN: AMSRL-BE-W  
WSMR, NM 88002-5501

Mr. Dale H. Divis  
Tennessee Applied Physical Sciences  
Rt 3 Box 178  
Fayetteville, TN 37334  
Telephone: 615/732-4755

Mr. Gene Dobry  
DET 4 HQAWS  
Telephone: 904/884-5703

Mr. David W. DuBois  
SciTec Inc  
100 Wall Street  
Princeton, NJ 08543  
Telephone: 609/921-3892  
Telefax: 609/921-1926

Mr. Robert DuMais  
ARL/BED  
ATTN: AMSRL-BE-W  
WSMR, NM 88002-5501

COL Robert J. Dumont  
USAF  
Ofc of the Federal Coordinator for  
Meteorological Services  
Suite 900, 6010 Executive Boulevard  
Rockville, MD 20852  
Telephone: 301/770-3464  
Telefax: 301/443-2609

Mr. Clifton E. Dungey  
Telephone: 576-4598

## E

Mr. Frank Eaton  
ARL/BED  
ATTN: AMSRL-BE-W  
WSMR, NM 88002-5501

Mr. Kenneth E. Eis  
METSAT, Inc  
515 South Howes Street  
Ft Collins, CO 80521  
Telephone: 303/221-5420  
Telefax: 303/493-3410

Mr. James S. Ellis  
LLNL  
Telephone: 510/422-1808

Mr. John R. Elrick  
ARL/BED  
ATTN: AMSRL-BE-W  
WSMR, NM 88002-5501



Mr. Bob Endlich  
ARL/BED  
ATTN: AMSRL-BE-A  
WSMR, NM 88002-5501

Dr. Bernard F. Engebos  
ARL/BED  
ATTN: AMSRL-BE-M  
WSMR, NM 88005-5501  
Telephone: 505/678-1489

Mr. Gene W. Engelkemier  
Teledyne Brown Engineering  
MS 58  
Box 070007  
300 Sparkman Drive, NW  
Huntsville, AL 35807-7007  
Telephone: 205/726-2561

Ms. Joanne M. Esparza  
Physical Science Laboratory  
P.O. Box 30002  
Las Cruces, NM 88003-0002  
Telephone: 505/522-9117  
Telefax: 505/522-9389

Dr. Oskar M. Essenwanger  
University of Alabama in Huntsville  
Atmospheric & Environmental Science Dept  
Research Institute, Rm A-11  
Huntsville, AL 35899  
Telephone: 205/895-6296

COL Ronald Evans  
ARL/BED  
ATTN: AMSRL-BE  
WSMR, NM 88002-5501

## F

Mr. Dennis F. Flanigan  
ERDEC  
ATTN: SCBRD-RT  
APG, MD 21010-5423  
Telephone: 410/671-2760  
Telefax: 410/671-2742

MAJ Richard Fleming  
US Army Intelligence Center  
Attn: ATZS-CDW  
Staff Weather Office  
Ft Huachuca, AZ 85613-6000  
Telephone: 602/538-6472  
Telefax: 602/538-4482

Mr. Mark A. Flood  
US Army Topographic Engineering Center  
ATTN: CETEC-GL-AE  
Bldg 2592  
Ft Belvoir, VA 22060-5546  
Telephone: 703/355-2840  
Telefax: 703/355-3176

Mr. Jerrold S. Foster  
Command Control, Inc  
8800 Roswell Rod  
Suite 130  
Atlanta, GA 30350  
Telephone: 404/992-8430  
Telefax: 404/993-3603

Mr. John Fox  
ARL/BED  
ATTN: AMSRL-BE-M  
WSMR, NM 88002-5501  
Telephone: 505/678-2110  
Telefax: 505/678-2432

Dr. Kenneth Patrick Freeman  
Science and Technology Corporation  
P.O. Drawer 250  
WSMR, NM 88002  
Telephone: 505/678-8013  
Telefax: 505/678-6049

Mr. David Friedhelm  
318 O'Hair Drive  
Las Cruces, NM 88001

## G

Mr. Charles Gage  
DBA Systems Inc  
10560 Arrowhead Drive  
Fairfax, VA 22030  
Telephone: 703/934-6795  
Telefax: 703/385-5870

Dr. Geoffrey Y. Gardner  
Grumman Data Systems  
MSD12-25  
1111 Stewart Avenue  
Bethpage, NY 11714  
Telephone: 516/575-9082

Mr. Dennis Garvey  
ARL/BED  
ATTN: AMSRL-BE-A  
WSMR, NM 88002-5501

Mr. Chad George  
AMC Smart Weapons Mgmt Office  
Redstone Arsenal, AL

Mr. John C. Giever  
Physical Science Laboratory  
P.O. Box 30002  
Las Cruces, NM 88003-0002  
Telephone: 505/522-3280

Dr. Patti S. Gillespie  
ARL/BED  
ATTN: AMSRL-BE-M  
WSMR, NM 88002-5501

Mr. Paul J. Graf  
TRW Systems Integration Group  
One Federal Systems Park Drive  
FPI/3190  
Fairfax, VA 22033  
Telephone: 703/803-5177  
Telefax: 703/803-5173

Mr. Donald D. Grantham  
USAF Phillips Lab  
Geophysics Directorate  
PL/GPAA  
Hanscom AFB, MA 01731-5000  
Telephone: 617/377-2982  
Telefax: 617/377-2984

Mr. John Graves  
Optimetrix, Inc  
2107 Laurel Bush Road  
Suite 207-B  
Bel Air, MD 21015  
Telephone: 410/569-0293  
Telefax: 410/569-0295

Dr. Shlomit Grossman  
Israel Military Industries Ltd.  
Hancal Systems Engineering  
P.O. Box 1044/45  
Ramat  
Hasharon, 47100  
ISRAEL  
Telephone: 97235484265

## H

Mr. Daniel C. Haines  
Physical Science Laboratory  
New Mexico State University  
P.O. Box 30002  
Las Cruces, NM 88003-0002  
Telephone: 505/522-9373

Mr. Frank Hansen  
ARL/BED  
ATTN: AMSRL-BE-S  
WSMR, NM 88002-5501

Mr. Mike Hardaway  
US Army Topographic Engineering Center  
ATTN: ETEC-GL-VA  
Ft Belvoir, VA 22060-5546  
Telephone: 703/355-3852  
Telefax: 703/355-3176

Mr. James Harris  
ARL/BED  
ATTN: AMSRL-BE-W  
WSMR, NM 88002-5501

Mr. Carl Hess  
Science and Technology Corporation  
555 Telshor Blvd.  
Suite 200  
Las Cruces, NM 88001  
Telephone: 505/521-4353  
Telefax: 505/522-9062

Mr. John R. Hines  
ARL/BED  
ATTN: AMSRL-BE-W  
WSMR, NM 88002-5001

Dr. Donald B. Hodges  
Hughes STX  
109 Mass Avenue  
Lexington, MA 02173  
Telephone: 617/862-0713  
Telefax: 617/863-2357

Mr. Austin W. Hogan  
USA CRREL RC  
Hanover, NH 03755-1290

LtC Charles R. Holliday  
Air Force Global Weather Central  
Product Improvement Branch (DOA)  
Offutt AFB, NE 68113-4039  
Telephone: 402/294-5451

Mr. Donald W. Hoock  
ARL/BED  
ATTN: AMSRL-BE-M  
WSMR, NM 88002-5501

Dr. Mohammed Y. Hussain  
PSL-NMSU  
Applied Analysis/Development Eng  
Box 3548  
Las Cruces, NM 88003  
Telephone: 505/522-9345

Ms. Karen L. Hutchison  
Physical Science Laboratory  
New Mexico State University  
P.O. Box 30002  
Las Cruces, NM 88003-0002  
Telephone: 505/522-9412  
Telefax: 505/522-9434

## J

Ms. Joni Jarrett  
Topographic Engineering Center  
ATTN: USACE-TEC  
GL-AT 2592 Leaf Rd  
FT Belvoir, VA 22060-5546  
Telephone: 703/366-2825  
Telefax: 703/355-3176

Mr. Joe Johnson  
ARL/BED  
ATTN: AMSRL-BE-W  
WSMR, NM 88002-5501

Mr. Odell Johnson  
ARL/Technology Transfer  
ATTN: AMSRL-CP-TA  
WSMR, NM 88002-5501

## K

Mr. Jon P. Kahler  
OptiMetrics Inc.  
106 E. Idaho  
Suite C  
Las Cruces, NM 88005  
Telephone: 505/523-4986

Mr. Frank T. Kantrowitz  
ARL/BED  
ATTN: AMSRL-BE-A  
WSMR, NM 88002-5001

Mr. Dennis Kasperek  
Science and Technology Corporation  
555 Telshor Blvd.  
Suite 200  
Las Cruces, NM 88001  
Telephone: 505/521-4353  
Telefax: 505/522-9062

Mr. Joseph T. Kenny  
Harris Corp  
Info Sys Div R3/7753  
P.O. Box 98000  
Melbourne, FL 32902  
Telephone: 407/242-5618  
Telefax: 407/242-4249

Dr. Neal Harold Kilmer  
Physical Science Laboratory  
New Mexico State University  
P.O. Box 30002  
Las Cruces, NM 88003-0002  
Telephone: 505/522-9495

Mr. John D. Kincheloe  
ARL/BED  
ATTN: AMSRL-BE-S  
WSMR, NM 88002-5501

Mr. Thomas A. King  
NMSU/PSL  
P.O. Box 30002  
Las Cruces, NM 88003-0002  
Telephone: 505/678-1488  
Telefax: 505/678-4198

Mr. Steve Kirby  
ARL/BED  
ATTN: AMSRL-BE-M  
WSMR, NM 88002-5501  
Telephone: 505/678-4329  
Telefax: 505/678-8366

Mr. Frank J. Klein  
Science and Technology Corporation  
2140 Broken Circle Rd  
Colorado Springs, CO 80915  
Telephone: 719/550-1178

Ms. René Klein  
ARL  
9496 Luna Vista Dr, SP.3  
Las Cruces, NM 88001  
Telephone: 505/678-6780

Mr. Walter G. Klimek  
ARL  
ATTN: AMSRL-SL-NE  
Building E3330  
Aberdeen Proving Ground, MD 21010-5423  
Telephone: 410/671-2494  
Telefax: 410/671-3471

Dr. Lowell Krawitz  
General Electric, Astro-Space Div  
P.O. Box 800  
Princeton, NJ 08543-0800  
Telephone: 609/490-3386  
Telefax: 609/490-2856

## L

Mr. Steven LaMotte  
Physical Science Laboratory  
Box 30002  
Las Cruces, NM 88003-0002  
Telephone: 505/678-4419  
Telefax: 505/678-2058

Mr. Peter F. Lambeck  
Optimetrix Inc  
2107 Laurel Bush Road  
Suite 207-B  
Bel Air, MD 21015  
Telephone: 410/569-0293  
Telefax: 410/569-0295

Mr. Robert R. Lee  
ARL/BED  
ATTN: AMSRL-BE-M  
WSMR, NM 88002-5501  
Telephone: 505/678-4006  
Telefax: 505/678-8366

1LT Paul Henry Lewis  
USAF Environmental Technical  
Application Center  
859 Buchanan St  
Scott AFB, IL 62225-5438  
Telephone: 618/256-5412

Dr. Hans J. Liebe  
Institute for Telecomm Sciences  
U.S. Dept of Commerce - NTIA-ITS.S3  
325 Broadway  
Boulder, CO 80303-3328  
Telephone: 303/497-3310  
Telefax: 303/497-3680

Mr. Luis Linggi  
Physical Science Laboratory  
P.O. Box 30002  
Las Cruces, NM 88003-0002  
Telephone: 505/522-9100  
Telefax: 505/522-9389

Dr. Brian Locke  
Science and Technology Corporation  
555 Telshor Blvd.  
Suite 200  
Las Cruces, NM 88001  
Telephone: 505/521-4353  
Telefax: 505/522-9062

Mr. Merlin Louapre  
Aerojet Electronic Systems Div  
1100 W. Hollyvale  
Bldg 1/ Dept 3971  
Azusa, CA 91702  
Telephone: 818/812-1261  
Telefax: 818/969-9010

Mr. Darrell L. Lucas  
Dynamics Research Model  
Box 25349  
Scott AFB, IL 62225-0349  
Telephone: 618/256-6662  
Telefax: 618/256-2996

## M

Mr. Mat V. Maddix  
US Army Missile Command  
ATTN:AMSMI-RD-GC-T  
Redstone Arsenal, AL 35898  
Telephone: 205/876-2339  
Telefax: 205/876-6799

Ms. Lisa Manguso  
ARL/BED

Mr. David H. Marlin  
ARL/BED  
ATTN: AMSRL-BE-M  
WSMR, NM 88002-5501  
Telephone: 505/678-5447

Mr. Jon Martin  
ARL/BED  
ATTN: AMSRL-BE-A  
WSMR, NM 88002-5501

Mr. Steve J. McGee  
Physical Science Laboratory  
Box 30002  
Las Cruces, NM 88003-0002  
Telephone: 505/522-9374  
Telefax: 505/522-9389

Mr. Scott A. McLaughlin  
ARL/BED  
ATTN: AMSRL-BE-W  
WSMR, NM 88002-5501

Mr. Robert McPeck  
ARL/BED  
ATTN: AMSRL-BE-W  
WSMR, NM 88002-5501

Mr. Gary McWilliams  
ARL/BED  
ATTN: AMSRL-BE-M  
WSMR, NM 88002-5501  
Telephone: 505/678-4388  
Telefax: 505/678-8366

Dr. Robert H. Meyer  
Hughes Aircraft Company  
Electro-optical Systems  
P.O. Box 902, Bldg E51  
MS B215  
El Segundo, CA 90245  
Telephone: 310/616-2517  
Telefax: 310/616-2252

Mr. Ronald E. Meyers  
ARL/BED  
ATTN: AMSRL-BE-S  
WSMR, NM 88002-5501

Mr. Bruce T. Miers  
ARL/BED  
ATTN: AMSRL-BE-W  
WSMR, NM 88002-5501

Mr. Noah Montoya  
ARL/BED  
ATTN: AMSRL-BE-W  
WSMR, NM 88002-5501

Mr. Gene Morris  
ARL/BED  
ATTN: AMSRL/BE  
WSMR, NM 88002-5501

Ms. Patricia A. Morris  
USAE Waterways Experiment Station  
Halls Ferry Rd.  
Vicksburg, MS  
Telephone: 601/634-3065

Ms. Sheryl A. Morris  
ODCSINT-Pentagon  
Telephone: 703/695-5509

Mr. Frank Mullin  
TRW  
Telephone: 310/764-6431

## N

Mr. Ronald Nelson  
Science and Technology Corporation  
12452 Towner N.E.  
Albuquerque, NM 87112  
Telephone: 505/275-6663

Dr. Frank E. Niles  
ARL/BED  
ATTN: AMSRL-BE-M  
WSMR, NM 88002-5501  
Telephone: 505/678-3721  
Telefax: 505/678-8366

Dr. John Noble  
ARL/BED  
ATTN: AMSRL-BE-M  
WSMR, NM 88002-5501  
Telephone: 505/678-3751  
Telefax: 505/678-8366

Mr. James Norton  
Hughes STX Corporation  
4400 Forbes Blvd  
Lanham, MD 20706  
Telephone: 301/794-5002  
Telefax: 301/794-7106

## O

Dr. Sean G. O'Brien  
Physical Sciences Laboratory  
P.O. Box 30002  
Las Cruces, NM 88003-0002  
Telephone: 505/521-9560

LCDR Milton H. O'Bryant  
Defense Nuclear Agency  
6801 Telegraph Road  
Alexandria, VA 22310  
Telephone: 703/325-2987  
Telefax: 703/325-2957

Mr. Richard J. Okrasinski  
Physical Science Laboratory  
New Mexico State University  
P.O. Box 30002  
Las Cruces, NM 88003-0002  
Telephone: 505/522-9100  
Telefax: 505/522-9389

Mr. Robert Olsen  
ARL/BED  
ATTN: AMSRL-BE-M  
WSMR, NM 88002  
Telephone: 505/678-1939  
Telefax: 505/678-8366

Dr. Montie Orgill  
Science and Technology Corporation  
P.O. Drawer 250  
WSMR, NM 88002  
Telephone: 505/678-8013  
Telefax: 505/678-6049

Mr. Brian L. Orndorff  
ARL/BED  
ATTN: AMSRL-BE-S  
WSMR, NM 88002-5501

Dr. Clem Ota  
Science and Technology Corporation  
555 Telshor Blvd.  
Suite 200  
Las Cruces, NM 88001  
Telephone: 505/521-4353  
Telefax: 505/522-9062

Dr. Muhammad Owais  
Defense Nuclear Agency  
6801 Telegraph Road  
Alexandria, VA 22310  
Telephone: 703/325-2886  
Telefax: 703/325-2951

## P

Mr. Fernando R. Palacios  
ARL/BED  
ATTN: AMSRL-BE-M  
WSMR, NM 88002-5501  
Telephone: 505/678-4313  
Telefax: 505/678-2432

Mr. Jeffery E. Passner  
ARL/BED  
ATTN: AMSRL-BE-W  
WSMR, NM 88002-5501

LTC Douglas C. Pearson  
1st Weather Group  
Fort McPherson  
Atlanta, GA 30330-5000  
Telephone: 404/752-2105  
Telefax: 404/752-2744

Sgt Robert W. Platt  
Det 4, HQAWS  
Telephone: 904/884-5493

Mr. Bradley Poore  
ARL/BED  
ATTN: AMSRL-BE-A  
WSMR, NM 88002-5501

## R

Mr. John Raby  
ARL/BED  
ATTN: AMSRL-BE-A  
WSMR, NM 88002-5501

Mr. H. Rachele  
ARL/BED  
ATTN: AMSRL-BE-S  
WSMR, NM 88005-5501

Mr. Phil Raihl  
ARL/BED

CAPT Gregory A. Ramsay  
ESC/XRC  
78 Offutt Road  
Hanscom AFB, MA 01731  
Telephone: 617/271-5289  
Telefax: 617/271-4683

Mr. Don Reinke  
METSAT, Inc.  
515 South Howes  
Ft. Collins, CO 80521  
Telephone: 303/221-5420  
Telefax: 303/493-3410

Mr. Ronald Rodney  
Wright Lab Staff Meteorology  
WL/DOWA  
Wright-Patterson AFB, OH 45433-6543  
Telephone: 513/255-1978  
Telefax: 513/255-7552

Mr. Paul A. Roelle  
US Air Force  
DET 31 1WXG  
Ft. Polk, LA 71459  
Telephone: 318/531-2015

Dr. Michael Rollins  
Science and Technology Corporation  
555 Telshor Blvd.  
Suite 200  
Las Cruces, NM 88001  
Telephone: 505/521-4353  
Telefax: 505/522-9062

Dr. David Rosen  
ARL/BED  
ATTN: AMSRL-BE-W  
WSMR, NM 88002-5501

CPT Arnie Rothlein  
ARL/BED  
AMSRL-BE  
WSMR, NM 88002-5501

## S

Ms. Doreen Sasaki  
Hughes Aircraft  
Telephone: 310/616-5124

Ms. Barbara Sauter  
ARL/BED  
ATTN: AMSRL-BE  
WSMR, NM 88002-5501

Mr. David Sauter  
ARL/BED  
ATTN: AMSRL-BE-M  
WSMR, NM 88002-5501  
Telephone: 505/678-2078  
Telefax: 505/678-8366

Dr. Richard C. Savage  
Hughes Aircraft Co  
16800 E. Centretech Pkwy  
Aurora, CO 80011  
Telephone: 303/344-6176  
Telefax: 303/344-2903

Mrs. Kimberley Lynn Scasny  
Naval Research Laboratory, Monterey  
Code 7543  
Monterey, CA 93943  
Telephone: 408/647-4728

Mr. Ernest G. Schultz  
GE Astro-Space Division  
5933 W Century Blvd  
#220  
Los Angeles, CA 90045  
Telephone: 310/642-5261  
Telefax: 310/642-5284

Mr. Luke Scott  
US Army NVEOD  
ATTN: AMSEL-RD-NV-VMD-SMT  
Ft. Belvoir, VA 22060-5677  
Telephone: 703/704-1766  
Telefax: 703/704-1753

Dr. Mary Ann Seagraves  
ARL/BED  
ATTN: AMSRL-BE-W  
WSMR, NM 88002-5501

Mr. José M. Serna  
Physical Science Laboratory  
New Mexico State University  
P.O. Box 30002  
Las Cruces, NM 88003-0002  
Telephone: 505/522-9333

Mr. Doug Sheets  
ARL/BED

Dr. Richard Shirkey  
ARL/BED  
ATTN: AMSRL-BE-M  
WSMR, NM 88002-5001  
Telephone: 505/678-5470  
Telefax: 505/678-8366

Mr. Douglas Shoop  
ARL/BED  
ATTN: AMSRL-BE-W  
WSMR, NM 88002-5501



MSG Timothy Smith  
OL-N, AWS  
ATTN: AMSRL-BE-W  
WSMR, NM 88002-5501

Dr. John B. Spalding  
Physical Science Laboratory  
P.O. Box 30002  
Las Cruces, NM 88003-0002  
Telephone: 505/522-9298

Dr. Ralph Steinhoff  
ARL/BED  
ATTN: AMSRL-BE-A  
WSMR, NM 88002-5501

Mr. Vernon Stoltz  
Topographic Engineering Center  
ATTN: USACE-TEC  
GL-AT 2592 Leaf Rd  
FT Belvoir, VA 22060-5546  
Telephone: 703/355-2825  
Telefax: 703/355-3176

Mr. Robert A. Sutherland  
ARL/BED  
ATTN: AMSRL-BE-S  
WSMR, NM 88002-5501

## T

Mr. Paul Tattelman  
Phillips Laboratory  
GPAA  
Hanscom AFB, MA 01731  
Telephone: 617/377-5959  
Telefax: 617/377-2984

Mr. David D. Telles  
Physical Science Laboratory  
New Mexico State University  
P.O. Box 30002  
Las Cruces, NM 88003  
Telephone: 505/522-9371

Dr. Jean-Marc Thériault  
DREV-Defence Research Establishment  
Valcartier  
Phillips Laboratory/GPOA  
Hanscom AFB, MA 01731-5000  
Telephone: 617/377-4854  
Telefax: 617/377-3661

Dr. Friedrich Theunert  
German Military Geophysics Office  
Mont Royal  
Traben-Trarbach, D-5580  
GERMANY  
Telephone: 49654118341  
Telefax: 49654118296

Mr. Don Thornley  
US Army Tecom  
ATTN: AMSTE-TC-AM  
White Sands Missile Range, NM 88002-5504  
Telephone: 505/679-9106  
Telefax: 505/678-8457

Mr. Fidel Tibuni  
ARL/BED  
ATTN: AMSRL-BE-A  
WSMR, NM 88002-5501

Ms. Gail Tirrell-Vaucher  
Science and Technology Corporation  
P.O. Drawer 250  
WSMR, NM 88002-5501  
Telephone: 505/678-8013  
Telefax: 505/678-6049

Mr. Ian Derek Todd  
UK Meteorological Office  
London Road  
Bracknell, Berks, RG12 257  
UNITED KINGDOM  
Telephone: 0344856985  
Telefax: 0344856967

Mr. David H. Tofsted  
ARL/BED  
ATTN: AMSRL-BE-M  
WSMR, NM 88002-5501

Mr. George Tonn  
Hughes Aircraft  
Telephone: 703/759-1738

Dr. Richard Douglas Tooley  
Northrop Electronics Systems Division  
2301 W. 120th Street  
L110/N3-2  
Hawthorne, CA 90251-5032  
Telephone: 213/600-5927

Mr. Chan N. Touart  
Hughes STX Corp  
109 Massachusetts Ave  
Lexington, MA 02173  
Telephone: 617/863-0677

Mr. Arnold Tunick  
ARL/BED  
ATTN: AMSRL-BE-S  
WSMR, NM 88002-5501

LT Douglas A. Tunney  
3 ACR SWO  
OL-A Det 14  
1st WXG  
Fort Bliss, TX 79916-2418  
Telephone: 915/568-8702

#### V

Mr. Robert Valdez  
ARL/BED  
ATTN: AMSRL-BE-A  
WSMR, NM 88002-5501

Mr. Anthony Van de Wal  
ARL  
ATTN: AMSRL-SL-NO  
APG, MD 21010-5423  
Telephone: 410/671-2260  
Telefax: 410/671-3471

Dr. Frank D. Verderame  
Verderame Associates, Inc  
913 Juniper Place  
Alexandria, VA 22304  
Telephone: 703/823-1429

Mr. Edward Vidal  
ARL/BED  
ATTN: AMSRL-BE-W  
WSMR, NM 88002-5001

Dr. Thomas Vonder Haar  
METSAT, Inc  
515 South Howes  
Ft Collins, CO 80521  
Telephone: 303/221-5420  
Telefax: 303/493-3410

#### W

Mr. Arnold Wade  
ARL/BED  
ATTN: AMSRL-BE-A  
WSMR, NM 88002-5501

Dr. James Wallace  
Farfield, Inc.  
6 Thoreau Way  
Sudbury, MA 01776  
Telephone: 508/443-9214

Mr. Charles P. Warnick  
USA Intelligence Ctr & Ft Sam Houston  
ATTN: ATZS-CDC  
CDR, USAIC & FH  
Fort Huachuca, AZ 85613-6000  
Telephone: 602/538-7217  
Telefax: 602/538-2108

Mr. Wendell R. Watkins  
ARL/BED  
ATTN: AMSRL-BE-M  
WSMR, NM 88002-5501  
Telephone: 505/678-4313  
Telefax: 505/678-2432

Mr. Jason Weber  
US Army CERL  
P.O. Box 9005  
Champaign, IL 61826  
Telephone: 217/352-6511  
Telefax: 217/373-7251

Mr. Dan Weems  
Physical Science Laboratory  
New Mexico State University  
P.O. Box 30002  
Las Cruces, NM 88003  
Telephone: 505/522-9406

Dr. Alan Wetmore  
ARL/BED  
ATTN: AMSRL-BE-M  
WSMR, NM 88002-5501

Dr. John R. White  
US Army Edgewood RD&E Center  
ATTN: SMCCR-RSP-B  
APG, MD 21010  
Telephone: 410/671-4256  
Telefax: 410/671-4607

Mr. James Williams  
ARL/BED  
ATTN: AMSRL-BE-A  
WSMR, NM 88002-5501

## **Z**

Mr. Ict Zaoui  
DGA/ETBS/CETAM  
Route De Guerri  
Carrefour Onord BP 712  
Bourges Cedex, 18015  
FRANCE  
Telephone: 3348274597  
Telefax: 3348200218



# AUTHOR INDEX

Acosta, Ascencion, Jr.	425	Gammill, Troy D.	403
Allen, D. Neil	453	Gardner, Geoffrey Y.	13
Anderson, G.P.	91	Giever, John C.	3
Auermann, Harry J.	43	Gillespie, Patti S.	209
Avara, Elton P.	325	Giroux, Jean	91
Ayres, Scarlett D.	345	Goedecke, George H.	43
		Grunwald, Arthur A.	81
Balding, Jeff	397	Gutman, William M.	403
Barber, Ted L.	117, 123	Gwilliam, Bruce L.	523
Barnes, John	315		
Bebbs, Joseph F., Jr.	475	Hansen, Frank	69
Behunek, Jan L.	23	Hardaway, G. Michael	13
Billingsley, Daniel R.	133, 489	Harper, Alice	435
Bleiweiss, Max P.	175, 459	Hartman, Richard W.	145
Boehm, Albert R.	145	Hatch, William H.	357
Burlbaw, Edward J.	3	Henmi, Teizi	315
Bussells, Sue E.	501	Hines, John R.	357
		Hogan, Austin W.	53
Caracena, Fernando	189	Holliday, Charles R.	111
Chenault, Thelma	425	Hoock, Donald W.	3
Chetwynd, J.H.	91	Howell, Terry A.	165
Chintawongvanich, P.	367	Hufford, George A.	247
Cionco, Ronald M.	59	Hulsey, Randall J.	117
Cogan, James L.	101, 377, 413		
Cook, G.J.	123	Kantrowitz, Frank T.	403
Coté, Jacques	91	Kilmer, Neal H.	33
Cotton, Michael G.	247	Kincheloe, John D.	465
Crow, Samuel B.	489	King, Thomas A.	175
		Kirby, Steve	511
Davis, Roger E.	175	Klein, René	425
De Kinder, Robert E.	301, 475	Klett, James D.	237
Dumais, Robert E., Jr.	315		
Dutro, Richard	479	Lamotte, Steven J.	475
		Lee, Robert R.	501
Eaton, Frank D.	357	Lewis, Paul H.	145
Eis, Kenneth E.	23, 151, 453	Liebe, Hans J.	247
Elrick, John R.	393	Loncarich, Thomas C.	475
Endlich, Robert W.	199		
Essenwanger, Oskar	257	Marlin, David H.	227
		McLaughlin, Scott A.	357, 387
Foster, Jerrold S.	291	McPeck, Robert E.	81, 413
Fournier, Marc	91	McWilliams, Gary	511
Fox, John	367	Measure, Edward M.	117
		Miers, Bruce T.	325, 377

Nash, Kenneth A.	111	Vaucher, Gail T.	199
Nelson, Ronald J.	161	Vonder Haar, Thomas H.	23, 453
Noble, John M.	267, 397		
North, K.H.	111	Watkins, Wendell R.	133, 489
O'Brien, Sean G.	3	Weems, Danforth C.	517
Ohmstede, William D.	59	Wetmore, Alan	479
Okrasinski, Richard J.	123, 367	Williams, James	479
Olsen, Robert O.	123, 367		
Orgill, Montie M.	335	Young, Kenneth C.	291
Orndorff, Brian L.	305		
Palacios, Fernando R.	133, 489		
Passner, Jeffrey E.	287		
Payne, Kenneth C.	175		
Raby, John W.	199		
Rachele, Henry	33, 69		
Raihl, Phillip R.	393		
Reinke, Donald L.	23, 453		
Rice, Jerry V.B.	403		
Rollins, Michael	459		
Rosen, David L.	435		
Sauter, David	517		
Scasny, Kimberley	219		
Seagraves, Mary Ann	81		
Sierchio, J. Michael	219		
Smith, Timothy J.	393		
Spalding, John B.	517		
Steiner, Jean L.	165		
Sutherland, Robert A.	237, 335		
Szymber, Richard J.	115, 377, 413		
Thériault, Jean-Marc	91		
Tipton, Rebecca	459		
Todd, Ian D.	443		
Tofsted, David	479		
Touart, C.N.	277		
Tremback, Craig J.	23		
Tunick, Arnold	69, 165		
Turton, Jonathan D.	443		